# Constraints on the genesis and evolution of alkaline and carbonatitic rocks

**Dissertation**

der Mathematisch-Naturwissenschaftlichen Fakultät
der Eberhard Karls Universität Tübingen
zur Erlangung des Grades eines
Doktors der Naturwissenschaften
(Dr. rer. nat.)

vorgelegt von
M.Sc. Simon Johannes Braunger
aus Biberach an der Riß

Tübingen
2020

Gedruckt mit Genehmigung der Mathematisch-Naturwissenschaftlichen Fakultät der Eberhard Karls Universität Tübingen.

| | |
|---|---|
| Tag der mündlichen Qualifikation: | 15.10.2020 |
| Stellvertretender Dekan: | Prof. Dr. József Fortágh |
| 1. Berichterstatter: | Prof. Dr. Gregor Markl |
| 2. Berichterstatter: | PD Dr. Michael A. W. Marks |

# Danksagung (Acknowledgements)

Zuallererst möchte ich Prof. Dr. Gregor Markl für die Vergabe des Promotionsthemas und das mir damit entgegenbrachte Vertrauen danken. Besonderer Dank gilt ihm auch für die Finanzierung zu Beginn meiner Doktorarbeit und die stets gute Betreuung. Konstruktive Diskussionen sowie seine hilfreichen Anregungen und Kommentare haben zu vielen Ideen geführt, die so auch in den Publikationen wiederzufinden sind. Besonders dankbar bin ich ihm auch für die zeitnahe Bearbeitung und die kritische Auseinandersetzung mit den Manuskripten.
Großer Dank gilt auch PD Dr. Michael A. W. Marks für die intensive Betreuung während der Doktorarbeit. Insbesondere seine vielen Anregungen, Ideen und Tipps sowie seine kritischen Begutachtungen meiner Manuskript-Erstentwürfe haben einen bedeutsamen Anteil an dieser Arbeit. Danken möchte ich ihm auch für die Zeit und Mühe, die er in die Bearbeitung des Forschungsantrages (Deutsche Forschungsgemeinschaft; Nr. MA2563/12–1) investiert hat, welcher mir eine dreijährige Finanzierung ermöglichte. Auch bei Fragen und Sorgen jedweder Art konnte ich mich immer an ihn wenden.
PD Dr. Thomas Wenzel gebührt großer Dank für seine Unterstützung an der Mikrosonde. Nur durch sein analytisches Geschick konnten wir noch so kleine und komplexe Mineralphasen bestimmen. Dank gilt ihm auch für die Begutachtung der Manuskripte und seine hilfreichen und motivierenden Gespräche.
Dr. Udo Neumann und Dr. Sebastian Staude danke ich für ihre Hilfe bei der Erzmikroskopie. Bei Dr. Tatjana Epp möchte ich mich für ihre maßgebliche Hilfe bei statistischen Auswertungen und bei Manuel Scharrer für seine Hilfe bezüglich thermodynamischer Fragestellungen bedanken. Dank gilt auch Dr. Horst Hann, der mir mit seiner großen Erfahrung in verschiedensten geologischen Teilgebieten weiterhelfen konnte, und dabei auch immer eine spannende Geschichte abseits der Geologie zu erzählen hatte.
Beate Fritz und Claudia Jahn danke ich für die stets schnelle Bearbeitung der verschiedensten administrativen Angelegenheiten.
Den Mitautoren der Publikationen danke ich für die ausgezeichnete Zusammenarbeit.
Für die Bereitstellung von Probenmaterial danke ich insbesondere Dr. Benjamin F. Walter, Dr. R. Johannes Giebel, Prof. Dr. Anatoly Zaitsev, Dr. Jacques Mouttes, Dr. Mi Jung Lee, Dr. Corbin Cannon und Prof. Dr. Antonio Simonetti; für die Dünnschliffpräparation danke ich Simone Schafflick und Per Jeisecke. Mein Dank gilt auch Dr. Heinrich Taubald und Gabriele Stoschek für die in Tübingen durchgeführte Analytik.
Bedanken möchte ich mich an dieser Stelle auch bei allen Mitarbeitern des „European Union's Horizon 2020"-Forschungsprojektes „HiTechAlkCarb", mit denen ich viele konstruktive und inhaltsvolle Diskussionen führen durfte.
Anfang des Jahres 2019 hatte ich das große Glück, zu Forschungszwecken nach Tansania reisen zu dürfen. Für diese Möglichkeit und zwei unvergesslich schöne gemeinsame Wochen danke ich Prof. Dr. Gregor Markl, Prof. Dr. Anatoly Zaitsev, PD Dr. Michael Marks, Prof. Dr. Andrey Arzamastsev und Olga Ivashchenkova.
Für das Korrekturlesen dieser Dissertation danke ich Thomas Binder, Dr. R. Johannes Giebel, Manuel Scharrer und Curtis Rooks.
Bei meinen Kollegen und Studienfreunden Manuel Scharrer, Dr. Tatjana Epp, Rebekka Reich, Thomas Binder, Curtis Rooks, Dr. Benjamin F. Walter, Dr. R. Johannes Giebel, Dr. Sebastian Staude, Dr. Hans Eggenkamp, Marguerita Duchoslav, Petya Atanasova, Rainer Babiel, Dr. Steffan Kreißl, Dr. Maximilian Keim, Dr. Christoph Lauer, Gerald Buck, Anja Allabar, Frieder Lauxmann, Dr. Tobias Kiemle, Katharina Sandritter, Philipp Kortenbruck, Lutz Eberle und Rafael Vaudrin möchte ich mich für die vielen Diskussionen (nicht nur in Geologie-relevanten Themenbereichen), die tolle Arbeitsatmosphäre und die wunderschöne gemeinsame Zeit in Tübingen bedanken. Vielen Dank auch meinen Freunden Pascal Albrecht, Julian Gawatz, Judith Fetsch und Annika Träger.
Mein besonderer Dank für ihre bedingungslose Unterstützung gilt meiner Familie: meinen Eltern Eva und Hans Braunger, meiner Schwester Sarah Jöchle, meinem Schwager Timo Jöchle und meiner Oma Gertrud und meinem Opa Hans Braunger.
Vielen Dank für alles!

# Abstract

Alkaline complexes comprise a broad spectrum of mantle-derived silicate rocks which are of considerable scientific and economic interest. They reflect some of the most evolved igneous rocks on Earth, and may contain attractive levels of Rare Earth Elements (REE) and other High Field Strength Elements (HFSE) such as Zr, Hf, Nb, Ta. Some of these complexes are additionally associated with carbonatites. However, many questions regarding the crystallization conditions and processes of such peculiar rock types are still unanswered. This thesis focuses on two mineralogically contrasting alkaline complexes (and nearby localities), namely the Tarosero Volcanic Complex in northernTanzania, and the Kaiserstuhl Volcanic Complex in Southwest Germany.

The Tarosero volcano is one of the very few complexes that comprises extrusive agpaitic rocks. Early crystallization of OH-bearing amphibole prevented the exsolution of aqueous fluids, thus enabling the enrichment of halogens, REE/HFSE, and the late-stage formation of eudialyte. The variable evolved rocks formed under low redox conditions ($\Delta FMQ \leq 0$) and derived from a basaltic magma. Moreover, in the nearby Ogol basalts, multistage-magma mixing was demonstrated by various xenocryst phases.

The rocks of the Kaiserstuhl Volcanic Complex formed under high redox conditions ($\Delta FMQ = +1$ to $+2$) and derived from two parental magmas. Fractional crystallization of a basanitic magma produced the tephritic to phonolitic rock series, while fractional crystallization of an olivine melilititic magma with variable $CO_2$ concentrations resulted in the formation of the nephelinitic to limburgitic, or the melilititic to haüynitic rock series and the carbonatites. The magmatic to hydrothermal evolution of the carbonatites can be deciphered by textural and compositional variations in pyrochlore. Furthermore, unusual high amounts of mica in one carbonatite body (Badberg) indicate a steady and continuous supply of elements due to the interaction with the wall rock. The decomposition of silicate xenoliths raised the silica activity of the carbonatite magma, which additionally enabled the crystallization of clinopyroxene, and enhanced the incorporation of REE in apatite. However, despite the high geochemical contrast between primitive dyke magmas and potash salt rocks (at Buggingen), there is no evidence for magmatic interaction processes, presumably due to the relatively dry orthomagmatic melt conditions and the fast cooling of the dyke magma.

In addition, based on a worldwide compilation, combined with new results from seven carbonatite complexes (Kaiserstuhl, Sokli, Kovdor, Palabora, Oka, Magnet Cove, Jacupiranga), it was demonstrated that carbonatites and their associated silicate rocks indicate significantly higher magmatic redox conditions than alkaline rocks without association to carbonatites. This presumably is attributed to the prerequisite of a carbonate-bearing, and hence relatively oxidized mantle source for the genesis of carbonatites.

# Zusammenfassung

Alkaligesteinskomplexe umfassen ein breites Spektrum an aus Mantelschmelzen entstandenen Silikatgesteinen, die von beträchtlichem wissenschaftlichen und wirtschaftlichen Interesse sind. Sie stellen einige der am weitesten entwickelten magmatischen Gesteine der Erde dar und können attraktive Gehalte an Metallen der Seltenen Erden (REE) und anderen „High-Field-Strength“-Elementen (HFSE) enthalten (z.B. Zr, Hf, Nb, Ta). Manche dieser Komplexe sind zusätzlich mit Karbonatiten assoziiert. Viele Fragen bezüglich der Kristallisationsbedingungen und -prozesse solch ungewöhnlicher Gesteine sind jedoch noch unbeantwortet. Diese Arbeit konzentriert sich auf zwei mineralogisch gegensätzliche Alkalikomplexe (und nahe gelegene Lokalitäten), den Tarosero-Vulkankomplex in Nordtansania und den Kaiserstuhl-Vulkankomplex in Südwestdeutschland.

Der Vulkan Tarosero ist einer von nur wenigen Komplexen, die extrusive agpaitische Gesteine aufweisen. Die frühe Kristallisation von OH-haltigen Amphibolen verhinderte die Entweichung wässriger Fluide und ermöglichte so die Anreicherung von Halogenen, REE/HFSE, sowie die Bildung von spätmagmatischem Eudialyt. Die unterschiedlich hoch entwickelten Gesteine bildeten sich bei niedrigen Redoxbedingungen ($\Delta FMQ \leq 0$) und stammen von einem basaltischen Magma ab. In den nahegelegenen Ogol-Basalten konnte zudem anhand verschiedener Fremdmineraleinschlüsse ein mehrstufiger Magmamischungsprozess aufgezeigt werden.

Die Gesteine des Kaiserstuhl-Vulkankomplexes bildeten sich unter hohen Redoxbedingungen ($\Delta FMQ = +1$ bis $+2$) und stammen von zwei verschiedenen Stammmagmen ab. Fraktionierte Kristallisation eines basanitischen Magmas führte zur Bildung einer tephritischen bis phonolithischen Gesteinsserie, während die Fraktionierung eines olivinmelilithitischen Magmas mit variablen $CO_2$-Konzentrationen zur Bildung der nephelinitischen bis limburgitischen Gesteine, beziehungsweise. der melilithitischen bis haüynitischen Gesteinsserie inklusive der Karbonatite führte. Die magmatische bis hydrothermale Entwicklung der Karbonatite konnte durch texturelle und mineralchemische Unterschiede im Pyrochlor aufgezeigt werden. Zudem weißen ungewöhnlich hohe Glimmeranteile in einem Karbonatitkörper (Badberg) auf eine stetige und kontinuierliche Elementzufuhr aufgrund der Wechselwirkung mit dem Nebengestein hin. Die Zersetzung von silikatischen Xenolithen erhöhte zudem die

$SiO_2$-Aktivität des Karbonatitmagmas, was die Kristallisation von Klinopyroxen ermöglichte und einen erhöhten Einbau von Seltenen Erden (REE) in Apatit bewirkte. Trotz des hohen geochemischen Kontrastes zwischen primitiven Ganggesteinsmagmen und Kalisalzgesteinen (bei Buggingen) gibt es jedoch vermutlich aufgrund der relativ trockenen orthomagmatischen Schmelzbedingungen und einer schnellen Abkühlung des Magmas keinen Hinweis für magmatische Interaktionsprozesse.

Darüber hinaus konnte durch das weltweite Zusammentragen von Daten kombiniert mit neuen Ergebnissen aus sieben Karbonatitkomplexen (Kaiserstuhl, Sokli, Kovdor, Palabora, Oka, Magnet Cove, Jacupiranga) gezeigt werden, dass Karbonatite und die mit ihnen assoziierten Silikatgesteine signifikant höhere magmatische Redoxbedingungen anzeigen als Alkaligesteine ohne Assoziation zu Karbonatiten. Dies kann auf eine Karbonat-haltige und damit relativ oxidierte Mantelquelle zurückgeführt werden, die als notwendige Voraussetzung zur Bildung von Karbonatiten angesehen wird.

# List of publications in the dissertation

The present thesis deals with the publications listed below. The attached tables provide information about the authors' own contributions to the publications.

## Study 1

Zaitsev, A. N., Arzamastsev, A. A., Marks, M. A. W., **Braunger S.**, Wenzel, T., Spratt, J., Salge, T., and Markl, G., submitted. Multiple sources for basaltic volcanism in Laetoli area (Crater Highlands, Tanzania): evidence from mineralogy and geochemistry of the Ogol lavas. Journal of Petrology.

**Status of the publication process:** submitted

| Author | Author position | Scientific ideas (%) | Data generation (%) | Analysis and interpretation (%) | Paper writing (%) |
|---|---|---|---|---|---|
| Zaitsev, A. N. | 1 | 30 | 5 | 30 | 30 |
| Arzamastsev, A. A. | 2 | 30 | 5 | 30 | 30 |
| Marks, M. A. W. | 3 | 10 | 5 | 10 | 20 |
| **Braunger, S.** | **4** | **10** | **10** | **10** | **10** |
| Wenzel, T. | 5 | 10 | 35 | 0 | 0 |
| Spratt, J. | 6 | 0 | 30 | 5 | 0 |
| Salge T. | 7 | 0 | 5 | 5 | 0 |
| Markl, G. | 8 | 10 | 5 | 10 | 10 |

## Study 2

**Braunger, S.**, Marks, M. A. W., Zaitsev, A. N., Wenzel, T., and Markl, G., submitted. The Petrology of the Tarosero Volcanic Complex: Constraints on the formation of extrusive agpaitic rocks. Journal of Petrology.

**Status of the publication process:** submitted

| Author | Author position | Scientific ideas (%) | Data generation (%) | Analysis and interpretation (%) | Paper writing (%) |
|---|---|---|---|---|---|
| **Braunger, S.** | **1** | **75** | **95** | **70** | **75** |
| Marks, M. A. W. | 2 | 15 | 0 | 15 | 20 |
| Zaitsev, A. N. | 3 | 0 | 0 | 5 | 0 |
| Wenzel, T. | 4 | 0 | 5 | 5 | 0 |
| Markl, G. | 5 | 10 | 0 | 5 | 5 |

## Study 3

**Braunger, S.**, Marks, M.A.W., Walter, B.F., Neubauer, R., Reich, R., Wenzel, T., Parsapoor, A., Markl, G., 2018. The Petrology of the Kaiserstuhl Volcanic Complex, SW Germany: The Importance of Metasomatized and Oxidized Lithospheric Mantle for Carbonatite Generation. Journal of Petrology 59, 1731-1762. http://dx.doi.org/10.1093/petrology/egy078.

**Status of the publication process:** accepted and published

| Author | Author position | Scientific ideas (%) | Data generation (%) | Analysis and interpretation (%) | Paper writing (%) |
|---|---|---|---|---|---|
| **Braunger, S.** | **1** | **50** | **70** | **55** | **60** |
| Marks, M. A. W. | 2 | 30 | 0 | 20 | 20 |
| Walter, B. F. | 3 | 5 | 0 | 5 | 5 |
| Neubauer, R. | 4 | 0 | 10 | 5 | 0 |
| Reich, R. | 5 | 0 | 10 | 5 | 0 |
| Wenzel, T. | 6 | 0 | 5 | 5 | 5 |
| Parsapoor, A. | 7 | 0 | 5 | 0 | 5 |
| Markl, G. | 8 | 15 | 0 | 5 | 5 |

## Study 4

Walter, B.F., Parsapoor, A., **Braunger, S.**, Marks, M.A.W., Wenzel, T., Martin, M., Markl, G., 2018. Pyrochlore as a monitor for magmatic and hydrothermal processes in carbonatites from the Kaiserstuhl volcanic complex (SW Germany). Chemical Geology 498, 1-16. http://dx.doi.org/10.1016/j.chemgeo.2018.08.008.

**Status of the publication process:** accepted and published

| Author | Author position | Scientific ideas (%) | Data generation (%) | Analysis and interpretation (%) | Paper writing (%) |
|---|---|---|---|---|---|
| Walter, B. F. | 1 | 50 | 55 | 55 | 40 |
| Parsapoor, A. | 2 | 0 | 10 | 0 | 0 |
| **Braunger, S.** | **3** | **10** | **5** | **5** | **10** |
| Marks, M. A. W. | 4 | 30 | 10 | 30 | 30 |
| Wenzel, T. | 5 | 0 | 20 | 0 | 10 |
| Martin, M. | 6 | 0 | 0 | 5 | 0 |
| Markl, G. | 7 | 10 | 0 | 5 | 10 |

## Study 5

Giebel, R.J., Parsapoor, A., Walter, B.F., **Braunger, S.**, Marks, M.A.W., Wenzel, T., Markl, G., 2019. Evidence for Magma–Wall Rock Interaction in Carbonatites from the Kaiserstuhl Volcanic Complex (Southwest Germany). Journal of Petrology 60, 1163-1194. http://dx.doi.org/10.1093/petrology/egz028.

**Status of the publication process:** accepted and published

| Author | Author position | Scientific ideas (%) | Data generation (%) | Analysis and interpretation (%) | Paper writing (%) |
|---|---|---|---|---|---|
| Giebel, R. J. | 1 | 24 | 0 | 34 | 44 |
| Parsapoor, A. | 2 | 0 | 50 | 2 | 0 |
| Walter, B. F. | 3 | 21 | 30 | 15 | 7 |
| **Braunger, S.** | **4** | **22** | **0** | **24** | **12** |
| Marks, M. A. W. | 5 | 23 | 0 | 20 | 32 |
| Wenzel, T. | 6 | 0 | 20 | 0 | 0 |
| Markl, G. | 7 | 10 | 0 | 5 | 5 |

## Study 6

**Braunger, S.**, Scharrer, M., Marks, M. A. W., Wenzel, T., Markl, G., submitted. Hydrothermal halite precipitation in mafic volcanic rocks: the case of the Buggingen salt deposit, SW Germany. Canadian Mineralogist.

**Status of the publication process:** submitted

| Author | Author position | Scientific ideas (%) | Data generation (%) | Analysis and interpretation (%) | Paper writing (%) |
|---|---|---|---|---|---|
| **Braunger, S.** | **1** | **50** | **90** | **60** | **75** |
| Scharrer, M. | 2 | 15 | 0 | 20 | 5 |
| Marks, M. A. W | 3 | 10 | 0 | 10 | 10 |
| Wenzel, T. | 4 | 0 | 10 | 0 | 5 |
| Markl, G. | 5 | 25 | 0 | 10 | 5 |

## Study 7

**Braunger, S.**, Marks, M.A.W., Wenzel, T., Chmyz, L., Guitarrari Azzone, R., Markl, G., 2020. Do carbonatites and alkaline rocks reflect variable redox conditions in their upper mantle source? Earth and Planetary Science Letters 533, 116041. http://dx.doi.org/10.1016/j.epsl.2019.116041.

**Status of the publication process:** accepted and published

| Author | Author position | Scientific ideas (%) | Data generation (%) | Analysis and interpretation (%) | Paper writing (%) |
|---|---|---|---|---|---|
| **Braunger, S.** | **1** | **70** | **90** | **75** | **70** |
| Marks, M. A. W. | 2 | 20 | 0 | 15 | 20 |
| Chmyz, L. | 3 | 0 | 5 | 0 | 0 |
| Guitarrari Azzone, R. | 4 | 0 | 0 | 0 | 5 |
| Wenzel, T. | 5 | 0 | 5 | 5 | 0 |
| Markl, G. | 6 | 10 | 0 | 5 | 5 |

# Table of content

# 1 Introduction

This thesis was prepared at the Department of Earth Sciences at the Eberhard Karls University Tübingen and deals with the crystallization conditions and processes of variably evolved alkaline silicate rocks, and carbonatites. The resulting findings lead to a better understanding of alkaline magmatic systems in general and provide insights into the mantle source regions as well.

## 1.1 Thermodynamic terms

The thermodynamically stable mineral assemblage of a magmatic system depends on the intrinsic state variables pressure and temperature, as well as on its chemical composition. However, intrinsic parameters like the oxygen fugacity, the silica activity and the water activity are commonly used to describe a magmatic system in more detail and to depict magmatic processes, including e.g. fluid exsolution/degassing, fractional crystallization, melting from variable mantle sources or crustal contamination (e.g. Markl et al., 2001; Halama et al., 2004; Marks et al., 2008).

While fugacities are defined as the thermodynamically effective partial pressure of a system, activities represent the thermodynamically effective concentration of a component in a system. Besides experimentally calibrated approaches (e.g. Gudmundsson and Wood, 1995; Ridolfi and Renzulli, 2012), fugacities and activities can be calculated by appropriate in equilibrium mineral assemblages at a given pressure and temperature. The calculations are based on the minimization of the Gibbs free energy and may be executed by software like Perple_X (Connolly, 1990) or QUILF (Andersen et al., 1993), using internally consistent thermodynamic databases (e.g. Robie and Hemingway, 1995; Holland and Powell, 1998).

Since the absolute oxygen fugacity of a system typically strongly depends on the temperature, redox-sensitive buffer reactions are often used as a reference, such as the reaction (1) between fayalite, magnetite and quartz (FMQ buffer):

$$\underset{\text{Fayalite}}{3\ Fe_2SiO_4} + \underset{\text{Oxygen}}{O_2} = \underset{\text{Magnetite}}{2\ Fe_3O_4} + \underset{\text{Quartz}}{3\ SiO_2} \qquad \text{(Reaction 1)}$$

The logarithmic deviation of the oxygen fugacity from this buffer (ΔFMQ) is a common measure for the oxidation state of a magmatic system.

## 1.2 Alkaline silicate rocks: Definition, occurrence and formation

Alkaline silicate rocks comprise a broad spectrum of primitive (e.g. alkali basalt, olivine nephelinite/melilitite, basanite), intermediate (e.g. tephrite, foid monzograbbro) and evolved (e.g. phonolite, foid syenite, rhyolite, granite), mantle-derived rock types. They can be defined as those in which the content of alkali metals compared to silica and/or aluminum is too high to be solely incorporated into alkali feldspar. Thus, they contain foids, sodic pyroxenes, sodic amphiboles or other alkali-rich mineral phases (Fitton and Upton, 1987). Alkaline rocks are mainly present at continental rift systems and in intraplate continental provinces, but have also been reported at ocean-related settings and subduction zone environments (Wooley, 1987; Kogarko et al., 1995; Woolley, 2001, 2019). Although alkaline rock occurrences account for only ~1 % (~3300 localities) of all igneous rocks, they attained much attention over the last decades. This is largely due to their vast mineralogical and compositional variability, with some of them containing attractive levels for REE (Rare Earth Elements) and other HFSE (High Field Strength Elements; e.g. Kogarko, 1990; Goodenough et al., 2016; Smith et al., 2016).

### 1.2.1 Peralkaline rocks

Peralkaline rocks are defined by a molar (Na+K)/Al ratio >1, and form a volumetrically minor group of alkaline rocks with silica oversaturated to silica undersaturated compositions, such as granites/rhyolites, syenites/trachytes and nepheline syenites/phonolites (e.g. Le Maitre et al., 2002; Frost and Frost, 2008). They are typically characterized by high concentrations of halogens, Large Ion Lithophile Elements (LILE; e.g. Li, Na, K, Rb, Cs), REE and other HFSE (e.g. Zr, Hf, Nb, Ta). Peralkaline rocks can be further subdivided according to their mineralogy: the more common miaskitic rocks contain well-known HFSE-bearing minerals like zircon, baddeleyite or titanite, while agpaitic rocks are defined by rather unusual Na-Ca-HFSE and halogen-bearing minerals such as eudialyte and wöhlerite (Sørensen, 1997; Marks et al., 2011; Marks and Markl, 2017).

The high concentrations of incompatible elements in peralkaline rocks are assumed to derive by partial melting of a metasomatically pre-enriched (sub)lithospheric mantle (e.g. Fitton and Upton, 1987; Martin et al., 1994; Upton et al., 2003; Kogarko et al., 2010; Markl et al., 2010), with subsequent extensive fractional crystallization of the

parental basaltic, basanitic or nephelinitic magma (e.g. Marks and Markl, 2017 and references therein). Agpaitic rocks represent the most evolved stage and are characterized by the highest abundances of REE/HFSE in peralkaline systems. Volatile elements like alkali metals and halogens increase the solubility of REE and other HFSE (Watson, 1979; Keppler, 1993; Linnen and Keppler, 2002) and thus, need to be retained in the melt in order to form agpaitic minerals. This is generally reached by a combination of the following processes:

- a low water activity which inhibits the expulsion of alkali- and halogen-rich fluids (e.g. Kogarko, 1987; Markl et al., 2001; Marks and Markl, 2015)
- magma evolution under low redox conditions. This suppresses the early crystallization of magnetite, thus leading to an increase of the Fe concentration, which in turn enhances the solubility of halogens (Metrich and Rutherford, 1992; Giehl et al., 2013). Moreover, low redox conditions may prevent the escape of aqueous fluids by stabilizing $CH_4$+$O_2$ instead of $CO_2$+$H_2O$ mixtures (Markl et al., 2001)
- crystallization under closed system conditions, such as plutons, dykes and domes (Sørensen, 1992)

The last mentioned process is in accordance with the fact that almost all of the approximately 100 agpaitic occurrences represent intrusive rocks (Marks and Markl, 2017). Very rare extrusive peralkaline rocks with late stage agpaitic minerals (e.g. at Tarosero, Tanzania; Dawson, 1997) demonstrate a formation under open system conditions, and therefore require peculiar crystallization conditions. Moreover, agpaitic complexes mostly lack carbonatites, thus indicating contrasting formation processes compared to carbonatite complexes.

## 1.3 Carbonatites: Definition, occurrence and formation

Carbonatites are rocks of magmatic origin with a modal primary carbonate content of at least 30 vol.-% (Mitchell, 2005). Most occurrences (~60 %; Chakhmouradian et al., 2016) are mineralogically classified as calcite-carbonatites, and can be divided into coarse-grained carbonatites (sövites), and medium to fine-grained carbonatites (alvikites; Le Maitre et al., 2002). Other carbonatite types include dolomite-carbonatites (beforsites), ferrocarbonatites and natrocarbonatites, with the latter occurring at the only active carbonatite complex, the Oldoinyo Lengai in Tanzania (Dawson, 1962;

Keller and Krafft, 1990). Besides carbonate, carbonatites often consist of many other mineral phases, including phosphates (predominantly apatite), silicate minerals (e.g. olivine, clinopyroxene, mica, garnet), oxides (magnetite, ilmenite, pyrochlore, perovskite, baddeleyite) and sulfides (pyrrhotite, galena, pyrite). Some of these minerals might have formed due to the assimilation of wall rock, or they represent entrained xenocrysts (Barker, 2001; Vuorinen and Skelton, 2004; Chakhmouradian et al., 2008). Because of the presence of apatite and REE/HFSE-rich minerals like pyrochlore, perovskite and baddeleyite, carbonatites are not only of scientific interest but also provide economic potential (e.g. Kanazawa and Kamitani, 2006; Smith et al., 2016).

To date, there are about 550 known carbonatite occurrences, with over 90 % being intrusive rocks (Woolley and Kjarsgaard, 2008). About 80 % of the carbonatites are spatially and temporally associated with alkaline silicate rocks, suggesting a close genetic relationship between both rock types. Most of these silicate rocks are $SiO_2$-undersaturated and comprise variable primitive to evolved compositions. Mitchell (2005) divides carbonatites according to the dominant silicate rocks of the complex into common (I) nephelinite and (II) melilitite clan carbonatites, and rare (III) kimberlite, (IV) aillikite and (V) peralkaline (agpaitic) nephelinite clan carbonatites. Note that subvolcanic and plutonic equivalents are also included in this classification.

It is generally accepted that carbonatites and most of their associated alkaline silicate rocks have their origin in the lithospheric or sublithospheric (asthenospheric) mantle (Bell and Simonetti, 2010). Two hypotheses are discussed for the formation of carbonatites. They either form by low degree partial melting of a carbonated peridotite, leading directly to carbonatitic melts (Wallace and Green, 1988; Harmer et al., 1998; Ying et al., 2004), or by fractional crystallization of a carbonate-bearing, typically melilititic or nephelinitic, silicate melt. The latter process results in the genesis of carbonatites by the melt reaching its silicate-carbonate liquidus boundary (Lee and Wyllie, 1994, 1998), or by exceeding the carbonate solubility with consequent exsolution of a carbonatitic melt (Kjarsgaard and Peterson, 1991; Halama et al., 2005; Brooker and Kjarsgaard, 2011). These primary magmatic carbonatites are distinguished from so-called carbothermal carbonatites which form by $CO_2$-dominated residual fluids originating from a wide range of magmas (Mitchell, 2005). In some

cases, carbonatites are associated with phoscorites, ultramafic apatite-magnetite rocks which additionally contain forsterite, diopside or phlogopite, and commonly also carbonate (Russell, 1954; Krasnova et al., 2004b and references therein). Phoscorites are genetically related to carbonatites by crystal fractionation or liquid immiscibility from a common phosphate- and carbonate-rich magma (Rimskaya-Korsakova and Krasnova, 2002; Krasnova et al., 2004a; Lee et al., 2004; Giebel et al., 2019).

## 1.4 Redox conditions of the mantle

As stated above, alkaline magmatism is related to partial melting of the (sub)lithospheric mantle. Besides pressure and temperature, the melting point of the mantle strongly depends on phases such as $H_2O$, $CO_2$ and carbonate (Dasgupta and Hirschmann, 2006; Foley et al., 2009). However, whether these rather “oxidized” phases, or “reduced” phases such as graphite/diamond (C), carbides or $CH_4$ are stable in the mantle, is mainly controlled by the oxygen fugacity (Stagno, 2019). The redox conditions of the lithospheric mantle vary from ΔFMQ=-4 to ΔFMQ=+4, with considerable differences between various geodynamic settings (Frost and McCammon, 2008; Foley, 2011). Lithospheric mantle xenoliths found within cratons indicate relatively low redox conditions (ΔFMQ=-2.8) which are related to the pressure-dependent stability of reduced $Fe^{2+}$-bearing and oxidized $Fe^{3+}$-bearing mineral phases. The redox state of the mantle thus decreases by approximately 0.7 ΔFMQ units per Gigapascal (GPa) and is particularly low in the deeper parts of thick cratons (Ballhaus and Frost, 1994). Mantle xenoliths found at subduction zones are on average significantly more oxidized (ΔFMQ=+0.5) due to the interaction with slab-derived melts. The oxidative character of these melts may be caused by the oxidized subducted material (Foley, 2011), or by the fact that during partial melting, trivalent iron preferably partitions into the melt while divalent iron remains in its residue (Canil and O'Neill, 1996; Mallmann and O’Neill, 2009).

Although no asthenospheric xenoliths are recorded, it is assumed that the asthenosphere is slightly more reduced than the lithosphere because of the loss of oxidized melts and fluids which interact with the overlying mantle (Frost and McCammon, 2008). This is consistent with redox estimations on abyssal peridotites and redox calculations on mid-ocean ridge basalts, which are used as an approximation for the oxidation state of the asthenosphere (Christie et al., 1986; Bézos

and Humler, 2005; Foley, 2011). A relatively high redox state of the asthenospheric mantle is indicated by the redox conditions of ocean island basalts and associated xenoliths (ΔFMQ=+0.6; Ballhaus, 1993; Mallmann and O'Neill, 2007; Foley, 2011; Eguchi and Dasgupta, 2018). This might be related to the influence of subducted (oxidized) lithologies on the genesis of ocean island basalts (e.g. Weaver, 1991).

## 1.5 Redox conditions of alkaline silicate rocks and carbonatites

Redox estimates on magmatic rocks are assumed to provide deep insights into the oxidation state of the source region (Carmichael, 1991; Cottrell et al., 2020), although factors such as the melting degree, degassing processes or fractional crystallization complicate a direct link to the mantle source (Gaillard et al., 2015). Similar to the (sub)lithospheric mantle, the redox conditions during the formation of alkaline silicate rocks are highly diverse and vary between ΔFMQ=-4 and ΔFMQ=+5 (Carmichael, 1991; Marks and Markl, 2017). This redox variation is qualitatively visible in the mineralogy of the rocks, with clinopyroxene-garnet-titanite assemblages typically indicating high redox conditions above the FMQ buffer. Alkaline rocks with olivine, clinopyroxene and Fe-Ti oxides can demonstrate both oxidized and reduced formation conditions, while agpaitic rocks with their exotic minerals such as eudialyte or wöhlerite belong to the most reduced alkaline rocks (Marks and Markl, 2017).

Little is known about the redox conditions of carbonatites and their associated silicate rocks. The few previous studies either concentrate solely on the carbonatites (e.g. Mud Tank, Australia; Currie et al., 1992) or the silicate rocks (e.g. Tamazeght, Morocco; Marks et al., 2008). Many of these studies also deal with late to post-magmatic processes (Milani et al., 2016; Ivanyuk et al., 2017), or focus on rather atypical carbonatite occurrences, such as the graphite-bearing carbonatites of Newania (India; Doroshkevich et al., 2010) and Chagatai (Uzbekistan; Kogarko and Ryabchikov, 2013).

# 2 Objective

Alkaline silicate rocks and carbonatites are of great scientific interest due to the large spectrum of mineralogically variable rock types, and attained economic attention as an exploration target for “hi-tech” raw materials like REE and other HFSE (e.g. Zr, Hf, Nb, Ta). However, especially due to the large range of different rock types and their rarity with respect to igneous rocks in general, there are many unanswered questions concerning their crystallization conditions and processes.

Ideal places to investigate the formation and magmatic evolution of alkaline rocks are the Crater Highlands and the adjacent Gregory Rift in northern Tanzania. This region is known for its intense alkaline magmatism, with volcanoes typically belonging to the nephelinite/melilitite ± carbonatite series, or the basalt-trachyte series.
The Ogol lavas are considered as the most primitive basaltic rocks in the Crater Highlands, but despite their importance for the understanding of alkaline magmatism in this region, they are only poorly investigated. Study 1 (Chapter 4.1) provides a detailed petrological investigation of the Ogol lavas and focuses on:

- evaluating the role of crustal contamination and magma mixing;
- the genetic relationship between the Ogol lavas and the nearby volcanoes;
- the crystallization conditions (pressure, temperature).

Agpaitic rocks generally demonstrate a formation under closed system conditions (e.g. plutons, dykes, domes). However, the Tarosero Volcanic Complex (Gregory Rift, Tanzania) is one of the very few localities where extrusive agpaitic rocks have been reported. In order to shed light on the prerequisites to form such unusual rock types, Study 2 (Chapter 4.2) focuses on:

- the crystallization conditions of the different rock types at Tarosero (pressure, temperature, oxygen fugacity, silica activity, water activity);
- the genetic relationship between the various rock types.

The Kaiserstuhl Volcanic Complex (Germany) is a well-suited locality to study the evolutionary history of a carbonatite complex since it consists of various types of alkaline silicate rocks (e.g. nephelinites, tephrites, phonolites) and plutonic to volcanic facies of carbonatites. However, despite the broad spectrum of different lithologies,

there is no detailed petrological study for this volcano. The first study on the Kaiserstuhl (Study 3; Chapter 4.3) therefore deals with:

- the determination of the formation conditions of carbonatites and silicate rocks (pressure, temperature, oxygen fugacity, silica activity);
- the genetic relationship between the various rock types;
- the constraints of the mantle source(s).

The large crystallization interval of ubiquitous minerals like pyrochlore provides potential for a very detailed insight into the evolution of carbonatite magmas. The second study on the Kaiserstuhl (Study 4; Chapter 4.4) focuses on:

- the textural and geochemical differentiation of the pyrochlore types;
- the processes leading to the different pyrochlore types.

A high geochemical contrast between magmas and wall rocks allows for intense assimilation processes. However, the interaction between carbonatite magmas and silicate wall rocks is only poorly investigated (Study 5; Chapter 4.5). Likewise, little is known about the influence of salt-rich host rocks on the mineralization of primitive silicate dyke rocks (Study 6; Chapter 4.6). The studies on the Kaiserstuhl (Study 5) and at the nearby Buggingen (Study 6) deal with:

- the mineralogical/mineral chemical evidence for contamination/assimilation;
- the discrimination between magmatic and hydrothermal interaction processes;
- the influence of contamination/assimilation on the crystallizing mineral phases;
- the characterization of the mineral precipitation mechanism.

Little is known about the redox conditions during formation of carbonatites and their spatially associated alkaline silicate rocks. However, redox conditions of igneous rocks may provide insight into their mantle source and may help to understand the peculiar prerequisites to form carbonatites. Therefore, 7 carbonatite complexes (Kaiserstuhl, Sokli, Kovdor, Palabora, Oka, Magnet Cove, Jacupiranga) were investigated in Study 7 (Chapter 4.7), which concentrates on:

- the determination of the redox conditions for carbonatites and silicate rocks;
- the distinction between magmatic and post-magmatic redox conditions;
- the comparison of the redox conditions between alkaline complexes with and without associated carbonatites;
- the influence of the mantle redox state on the formation of alkaline rocks.

# 3 Selected study areas

The selected study areas for this thesis concentrate on two regions of alkaline magmatism: i) the North Tanzanian Divergence Zone where the Ogol lavas in the Laetoli area (Study 1) and the Tarosero Volcanic Complex (Study 2) were investigated, and ii) the Upper Rhine Graben in Southwest Germany with focus on the Kaiserstuhl Volcanic Complex (Studies 3-5) and the primitive dyke rocks at Buggingen (Study 6). Moreover, besides the Kaiserstuhl Volcanic Complex, six further carbonatite complexes were investigated (Study 7). These include Sokli (Finland) and Kovdor (Russia) on the Kola Peninsula, Palabora in South Africa, Oka in Canada, Magnet Cove in the USA, and Jacupiranga in Brazil. The differences in the formation age (Palaeoproterozoic to Neogene), the emplacement depth (plutonic, subvolcanic and volcanic), and the mineralogy of the carbonatites and associated silicate rocks reflect the typical spectrum of carbonatite occurrences worldwide (Mitchell, 2005; Woolley and Kjarsgaard, 2008). A more detailed description of the geology for these 6 complexes is given in Appendix VII.

## 3.1 Alkaline magmatism in the North Tanzanian Divergence Zone

The eastern branch of the East African Rift System is known for its intense magmatism. Rifting was initiated about 30 Ma ago by a mantle plume beneath Ethiopia, and evolved southwards along Pan-African suture zones (Hofmann et al., 1997; Chorowicz, 2005) towards the North Tanzanian Divergence Zone (Smith, 1994; Le Gall et al., 2008; Mana et al., 2015). Magmatic activity in this zone can be divided into two groups based on major faulting events (Dawson, 1992):

i) volcanoes older than 1.2 Ma which mainly consist of alkali basalts and trachytes to phonolites (e.g. Tarosero, Monduli, Ngorongoro, Lemagarut, Oldoinyo Sambu, Ketumbeine, Kilimanjaro), and rarely of nephelinites ± carbonatites (e.g. Burko, Sadiman, Essimingor, Mosonik);

ii) volcanoes younger 1.2 Ma which typically comprise nephelinites to phonolites ± carbonatites (e.g. Meru, Oldoinyo Lengai, Kerimasi, Kwahera, Hanang).

### 3.1.1 Ogol basalts

The Crater Highlands are situated next to the western escarpment of the Gregory Rift and consist of numerous volcanic centers (e.g. Lemagarut, Ngorongoro, Sadiman) in a ~100 km long zone between Lake Natron and Lake Eyasi. They mark the southern termination of the eastern branch of the East African Rift valley. The oldest magmatic activity in this region, beginning for 4.63 ± 0.05 Ma (Mollel et al., 2011), is attributed to the Sadiman volcano, west of which the Laetoli tuffs with the 3.66 Ma old Australopithecus afarensis footprints were discovered (Leakey and Hay, 1979). The ~2.3 Ma old Ogol basalt lavas (Mollel, 2007) erupted through fissures and cinder cones of up to 1.5 km in diameter and 150 m in height (Hay, 1987).

### 3.1.2 Tarosero Volcanic Complex

The Tarosero volcano is situated in the Gregory Rift, about 40 km northwest of Arusha. It was formed ~2.3 Ma ago (Macintyre et al., 1974; Mana et al., 2015) and extruded on a northerly dipping plateau of alkali basalt and trachyandesite lavas. The lava cone itself mainly consists of trachyte lavas (and rare tuffs), while smaller occurrences of extrusive rocks ranging from primitive basalts over peralkaline trachytes to agpaitic, eudialyte-bearing phonolites have also been described (Dawson, 2008).

## 3.2 Alkaline magmatism in the Upper Rhine Graben

Alkaline magmatism in the Upper Rhine Graben belongs to the European Cenozoic Volcanic Province (Wilson and Downes, 1991). The opening of the Upper Rhine Graben results from the stress regime induced by the Alpine orogeny and caused lithospheric thinning (Edel et al., 1975; Ziegler, 1982; Dèzes et al., 2004). This, in turn, enabled regional asthenospheric upwelling, and finally led to the emplacement of alkaline rocks along deep-reaching zones of weakness (Hüttner, 1996; Edel et al., 2006; Bourgeois et al., 2007).

### 3.2.1 Kaiserstuhl Volcanic Complex

The Kaiserstuhl Volcanic Complex is located about 20 km northwest of Freiburg. It was active 19 to 16 Ma ago (Kraml et al., 2006 and references therein) and was fed by several magma sources (Keller, 1978b, 1984a; Keller et al., 1990; Schleicher et al., 1990; Schleicher et al., 1991). A potassium-rich magma source led to the formation of the sodalite monzogabbros in the centre of the complex, and the tephritic rocks which

comprise most parts of the current exposure level. This rock series also includes the phonolite stocks at the central, the western and the eastern part of the volcano. Nosean syenites were rarely found in the central part, and have also been proved by scientific drillings at depth (Kirchheimer, 1973). The second magma source formed the volumetrically minor group of sodium-rich rocks such as the olivine nephelinites and limburgites, which mostly occur at the Limberg-Lützelberg complex near Sasbach. Melilite-bearing dyke rocks and the carbonatites are also believed to be genetically related to the second magma series, and predominantly are present in the central parts of the Kaiserstuhl complex. Besides two smaller occurrences at Kirchberg and Katharinenberg, there is a total of four large sövite bodies at Badberg, Haselschacher Buck, Orberg and Degenmatt. The westward dipping Tuniberg fault produces a vertical offset of ~1000 to ~3000 m, separating the carbonatite at the Badberg from the other three bodies (Groschopf et al., 1996; Beccaletto et al., 2010; Brauch et al., 2018). The banded Badberg carbonatite is inclined by 60° to the northwest, and contains cm- to m-sized silicate xenoliths (Blust, 1993). Extrusive carbonatites occur in the west at Kirchberg and Henkenberg as alternating sequences of carbonatitic tuffs, lavas, lapilli stones and silicate pyroclastics (Keller, 1978a, 1981, 1989). Beforsite and alvikite dykes mainly crosscut the subvolcanic rocks of the centre, but also occur in the distal parts of the complex (Katz and Keller, 1981; Katz-Lehnert, 1989).

### 3.2.2 Buggingen

Nephelinitic and melilititic dyke rocks frequently occur in the vicinity of the Kaiserstuhl Volcanic Complex, such as the olivine melilitite stock of Mahlberg in the north, or the olivine melilitites and monchiquites at Buggingen in the south (Wimmenauer, 1952; Dunworth and Wilson, 1998). At the latter, the primitive dyke rocks intruded into a potash salt deposit of Rupelian age (34 to 28 Ma; Braitsch et al., 1964; Sissingh, 1998). The deposit was mined at a depth level of 800 to 1000 m and belongs to the Upper Saliferous Zone, consisting of sylvite, halite, anhydrite, and marl layers (Esslinger, 1976). It is underlain by calcite- and dolomite-bearing marls (Middle Saliferous Zone), and overlain by anhydrite-, gypsum-, and halite-rich marls. The uppermost part of this sequence consists of bituminous marine shales (Fish Shale), and marine-brackish to limnic marls, which are cut off by unconformable Quaternary sands and gravel.

# 4 Individual studies

## 4.1 Evidence for multi-stage magma mixing in basaltic rocks

Title of publication:

*Multiple sources for basaltic volcanism in Laetoli area (Crater Highlands, Tanzania): evidence from mineralogy and geochemistry of the Ogol lavas.* (Study 1)

In the Crater Highlands, numerous eruptive centers are spatially and chronologically close together, with lava flows and tuffs of variable and partly unknown origin being intercalated (e.g. Mollel, 2007). Likewise, the intense alkaline magmatism provides potential for complex magma mixing processes at depth. We demonstrate such interaction processes by the Ogol basalts, which were investigated in terms of mineralogy, mineral chemistry (using the electron microprobe, EPMA) and whole-rock geochemistry (X-ray fluorescence analysis, XRF; inductively coupled plasma mass spectrometry, ICP-MS) including isotope analyses (thermal ionization mass spectrometer, TIMS).

The relative depletion of Cs, Rb and K in whole-rock samples (compared to Ocean Island Basalts) indicate a formation of the primary Ogol melts by partial melting of a mantle with residual amphibole and/or phlogopite. Moreover, the $(Tb/Yb)_N$ ratio demonstrates melting in the presence of residual garnet (Wang et al., 2002; Mana et al., 2015). Variable $(La/Sm)_N$ and Sr and Nd initial isotopic ratios in the basalts can be explained by assimilation and fractional crystallization (AFC) between the primary Ogol melts, the Tanzanian Craton granite-gneisses and the involvement of up to 5 % alkaline component. However, no mineralogical evidence for crustal contamination was found in the studied rock samples. Both major and trace element data, as well as Sr-Nd isotope ratios demonstrate that mixing with basaltic to trachyandesitic melts of the spatially associated Lemagarut volcanic system is the more likely process. Such magma mixing processes are in accordance with several xenocryst mineral phases in the Ogol lavas, including e.g. Fe-rich olivine cores, chemically distinct (and sometimes spongy) clinopyroxene varieties and embayed plagioclase. Further xenocryst phases comprise perovskite with ilmenite reaction rims, and schorlomite. Since these minerals are rather unusual in basaltic to trachyandesitic magmas, the involvement of an

alkaline component, possibly related to the nearby Sadiman volcano or the Laetoli tuffs (e.g. Zaitsev et al., 2012), is required. This conforms with highly alkaline, phonolitic glass ([Na+K]/Al=0.98-1.07) in the investigated Ogol basalts. The compositionally variable mantles and rims around the clinopyroxene xenocrysts suggest that magma mixing was a multistage process that happened at variable depths. The orthomagmatic crystallization conditions of the clinopyroxenes were determined by applying the clinopyroxene-liquid thermobarometer of Neave and Putirka (2017) using whole-rock compositions as a proxy for the melt composition. Although the basalts contain plenty of xenocrysts, rough estimates might be possible as the required liquid components of the pressure equation (Al, Na, K, Si) may only be slightly influenced by the dominant xenocryst phases olivine and clinopyroxene. The calculations indicate an orthomagmatic clinopyroxene crystallization temperature of ~1150-1220 °C at an upper-crustal depth of 3-12 km (0.1-0.4 GPa). Overall, the most primitive Ogol sample contains relatively few xenocrystals and might reflect the parental melt for the rocks of the Lemagarut volcano. These rocks are estimated to have evolved by fractionation of 50-60 % primary Ogol melt with addition of 5 % crustal material. However, a more detailed study of the Lemagarut volcano is needed to verify this assumption.

## 4.2 Prerequisites for the formation of extrusive agpaitic rocks

Title of publication: *The Petrology of the Tarosero Volcanic Complex: Constraints on the formation of extrusive agpaitic rocks.* (Study 2)

This study focuses on the genesis of the Tarosero Volcanic Complex in northern Tanzania, which is one of the very rare examples involving extrusive agpaitic rocks. It mainly consists of trachyte lavas and some trachytic tuffs, but additionally comprises minor occurrences of extrusive basalts, andesites, latites, as well as peralkaline trachytes, olivine trachytes and phonolites, with the latter occasionally containing interstitial eudialyte (Dawson, 2008). The magmatic evolution of this volcano is demonstrated by a mineralogical, mineral chemical (EPMA) and geochemical investigation (XRF; ICP-MS; Combustion Ion Chromatography, CIC) of the different rock types, combined with calculations of the intrinsic parameters and fractional crystallization models.

Intrinsic parameters including pressure, temperature, silica activity and oxygen fugacity were calculated by several thermo(oxy)barometers and in-equilibrium mineral assemblages. Pressure estimates for the different rock types illustrate a multi-level magmatic system. While clinopyroxene phenocrysts in the basalts demonstrate a pressure of 1.1 ± 0.2 GPa (~25-40 km depth) which might reflect magmatic underplating at the Moho (Prodehl et al., 1997), amphiboles of the intermediate andesite and the trachytes demonstrate pressures of 0.7 GPa and 0.9 ± 0.1 GPa, respectively (depths of 20-30 km). Peralkaline rocks typically evolve in a shallow-level plumbing system (~2-4 km depth; Mahood, 1984; Novak and Mahood, 1986; Spandler and Morris, 2016; Marks and Markl, 2017) which is in agreement with coarse-grained cumulates that indicate a nearby magma chamber. The liquidus temperature was determined to be 1000-1290 °C in the basalts and decreases to ~900-1100 °C in the intermediate andesites, latites and trachytes. The groundmass assemblage illustrates temperatures around 850 °C. Experimental constraints for the stability of aenigmatite and arfvedsonite determine the groundmass formation of the peralkaline rocks to 750 ±50 °C (Ernst, 1962; Bailey, 1969; Thompson and Chisholm, 1969; Scaillet and Macdonald, 2001; Giehl et al., 2013; Giehl et al., 2014), which conforms with the feldspar solvus of ≥700 °C. Silica activity calculations mostly yield values of $a_{SiO2}$=0.4 ±0.2. The redox conditions typically vary between ΔFMQ=0 and ΔFMQ=-1, while there is a large uncertainty in the peralkaline rocks with values ranging from ΔFMQ=-5 to ΔFMQ=0.

The relatively low K, Cs and Rb abundances in primitive mantle-normalized incompatible element pattern of the primitive and intermediate rock types indicate a derivation of a mantle source with residual amphibole±phlogopite (e.g. Halliday et al., 1995; Mana et al., 2015). A genetic link between the various investigated rocks at Tarosero is suggested by the continuous trend in the mineral composition and the very similar ages for the primitive basalts and the peralkaline rock types (Macintyre et al., 1974; Mana et al., 2015). Moreover, the negative Eu and Sr anomalies of the evolved rock types, as well as the low Sr concentration in eudialyte demonstrate extensive plagioclase fractionation which is typical for a basaltic rather than a basanitic or a nephelinitic parental magma (Marks et al., 2011). Fractional crystallization based on the phenocryst phases (olivine + clinopyroxene) cannot explain the evolution from the basalts to the intermediate latites (nor does the additional fractionation of the

groundmass minerals titanomagnetite + plagioclase). Hence, the genetic relationship between these two rock types remains enigmatic. However, fractional crystallization of variable amounts of olivine, clinopyroxene, plagioclase, magnetite, ilmenite and apatite, accompanied by minor crustal contamination, enables the magmatic evolution from the latites via the trachytes towards the peralkaline trachytes and phonolites. Contamination and assimilation in the evolved rock types is in accordance with trace element modelling and Sr-Nd-Pb isotope data of Mana (2013) and Mana et al. (2015). The agpaitic composition of some phonolites is reached by further fractional crystallization of alkali feldspar and minor amphibole. In contrast to the trachytes and all other peralkaline rocks, the peralkaline olivine trachytes are characterized by olivine phenocrysts but lack clinopyroxene and calcic amphibole phenocrysts. The mineral chemistry of olivine, Fe-Ti-oxides and interstitial amphibole implies a close genetic relation with the intermediate latites. The derivation of the peralkaline olivine trachytes from the latites can also be modelled by fractional crystallization (olivine, clinopyroxene, magnetite, ilmenite, plagioclase) and minor crustal contamination.

Alkali metals and halogens in the melt increase the solubility for REE and other HFSE and support the formation of agpaitic minerals (Watson, 1979; Keppler, 1993; Linnen and Keppler, 2002). In case of the extrusive agpaitic rocks at Tarosero, the early crystallization of OH-bearing amphibole resulted in relatively dry late-magmatic conditions which prevented the exsolution of fluid phases and the consequent loss of water-soluble alkali metals and halogens (e.g. Kogarko, 1987; Markl et al., 2001; Liebscher and Heinrich, 2007; Marks and Markl, 2015). Moreover, the low redox conditions (below FMQ) suppressed intense crystallization of magnetite, hence increasing the Fe concentration of the melt, which additionally enhanced the solubility of Cl (Metrich and Rutherford, 1992; Giehl et al., 2013). Finally, the concentration of REE/HFSE could increase during fractionation, leading to the late-stage crystallization of eudialyte in the most evolved peralkaline phonolites.

In contrast to the peralkaline trachytes/phonolites, the peralkaline olivine trachytes are characterized by much lower REE/HFSE concentrations and the lack of agpaitic minerals. A high water activity is demonstrated by the relatively high OH-contents in the interstitial amphiboles and the absence of clinopyroxene and sodalite (Bailey, 1969; Scaillet and Macdonald, 2001; Andersen and Sørensen, 2005; Giehl et al., 2014). Fractional crystallization under rather low crustal pressures presumably

impeded the transition from olivine to OH-bearing amphibole as the dominant phenocryst phase, thus resulting in an increasing water activity during magma evolution. We suggest that the evolution towards the peralkaline olivine trachytes was accompanied by significant amounts of fluid exsolutions, which prevented the enrichment of Cl, REE and other HFSE, and the final crystallization of eudialyte.

## 4.3 The evolution of silicate magmas in carbonatite complexes

Title of publication: *The Petrology of the Kaiserstuhl Volcanic Complex, SW Germany: The Importance of Metasomatized and Oxidized Lithospheric Mantle for Carbonatite Generation.* (Study 3)

In this study, we demonstrate the evolutionary history for the Kaiserstuhl Volcanic Complex and give implications for the required conditions to form carbonatite complexes in general. The whole-rock major element composition was determined by XRF, the trace elements by ICP-MS, and the mineral chemistry was analyzed using the electron microprobe (EPMA).

The following four rock groups were distinguished at the Kaiserstuhl based on their mineralogy and geochemistry: (I) primitive nephelinitic to limburgitic rocks; (II) melilititic to haüynitic dyke rocks; (III) tephritic to phonolitic rocks including the monchiquite dykes; (IV) and carbonatites, from which the olivine- and monticellite-bearing varieties were investigated in more detail.
Rock groups I and II are characterized by a molar Na/K ratio > 2, while the tephritic to phonolitic rocks (group III) typically have a Na/K ratio < 2. Strontium isotope studies reveal the same division, with the carbonatites being assigned to the Na-rich rock series (Schleicher et al., 1990; Schleicher et al., 1991).

Intrinsic parameters including pressure, temperature, silica activity and oxygen fugacity were determined by various thermo(oxy)barometers and appropriate in-equilibrium mineral assemblages. A subvolcanic emplacement depth of approximately 1 km (~0.03 GPa) was calculated for the tephritic rocks based on their amphibole composition. Core analyses typically indicate higher pressure estimates than rim analyses and may reflect a continuous crystallization over a distance of 2– 4 km during

the ascent from the magma chamber. The orthomagmatic crystallization temperature decreases from more than 1100 °C in the primitive rocks (olivine nephelinites, monchiquites) towards ~880 °C in the evolved phonolitic rocks and the carbonatites. The silica activity increases from the nephelinitic to the limburgitic rocks ($a_{SiO2}$=0.4-0.9), which is in accordance with the absence of plagioclase in the former. The presence of perovskite in the melilititic to haüynitic group demonstrates a silica activity ≤ 0.2, while a decline of the silica activity is observed from the tephritic to the more evolved phonolitic rocks ($a_{SiO2}$=0.7-0.2). In the carbonatites, the absence of clinopyroxene (diopside), but the presence of monticellite indicates a silica activity ≤ 0.05. Calculated redox conditions for the different rock types typically show high mean values (ΔFMQ=+1 to +2), although lower redox estimates are possible for rocks with an insufficiently well determined lower silica activity constraint.

The importance of fractional crystallization for producing the various lithologies at the Kaiserstuhl was demonstrated by mass balance calculations which are based on the assumption that phenocrysts mainly control the fractionation process. Due to the high formation temperature and the primitive composition, the monchiquite was used as the parental magma for the evolution towards the tephritic and phonolitic rocks. Fractional crystallization of garnet caused a depletion of heavy REE in the remaining melt. In the most evolved phonolitic rocks, fractionation of titanite is mirrored by relatively low concentrations of middle REE (e.g. Nicholls and Harris, 1980; Prowatke and Klemme, 2005). Increasing Zr/Hf, Y/Ho and Nb/Ta ratios during melt evolution strengthen the assumption of garnet and/or titanite fractionation. However, the chemical composition of the most evolved phonolitic rocks requires the additional accumulation of nosean and alkali feldspar.

The olivine melilitite from the Mahlberg north of the Kaiserstuhl is assumed to reflect the parental magma for the olivine nephelinites (Wilson et al., 1995; Dunworth and Wilson, 1998; Ulianov et al., 2007) and hence, was used as the starting composition for the further magma evolution. Depending on the olivine/melilite fractionation ratio, the magma evolved towards the nephelinitic-limburgitic (low olivine/melilite ratio) or the melilititic-haüynitic rock series (high olivine/melilite ratio). A high $CO_2$ partial pressure favors the crystallization of melilite, indicating that the magma evolution is controlled by polybaric melting, or by differences in the redox conditions of the parental magmas

(Mysen et al., 1976; Dunworth and Wilson, 1998). Evolution towards the haüynitic composition additionally requires accumulation of haüyne, clinopyroxene and melilite. Based on the $^{87}Sr/^{86}Sr$ isotope ratio (Schleicher et al., 1990), the carbonatites are assigned to the sodium-dominated rock series, and thus presumably originate from the same magma source. This conforms with the relatively high carbonate content of the haüyne melilitites, which are considered to represent the genetic link between the silicate rocks and the carbonatites (Keller, 1984a; Hubberten et al., 1988). However, liquid immiscibility between the carbonatites and haüyne melilitites illustrating the conjugated silicate melt was ruled out as the hypothetically unexsolved precursor melt (haüyne melilitite+carbonatite) cannot be modelled by fractional crystallization of the parental olivine melilitites. The lack of an appropriate silicate conjugate might be related to decarbonation processes in the silicate magmas. We therefore suppose that the precursor melt for the carbonatites is present at greater depths where the pressure is high enough to suppress $CO_2$ degassing.

The relatively high potassium concentrations for the tephritic to phonolitic rocks, as well as the presence of rare mica xenocrysts (presumably of lithospheric mantle origin) indicate the derivation of a phlogopite- and amphibole-bearing lithospheric mantle (Wilson and Downes, 1991; Wilson and Downes, 1992). Based on the isotope systematics and the trace element chemistry of the olivine melilitites and olivine nephelinites (Wilson et al., 1995; Dunworth and Wilson, 1998; Ulianov et al., 2007), the source for the sodium-rich rock group is assumed to be the lithospheric mantle that had been previously metasomatized by carbonate-rich melts. Since the redox conditions steadily decrease with depth (Ballhaus and Frost, 1994), such carbonate-bearing liquids may be the result of lithospheric thinning: Diamond or graphite that has been stored at the base of the lithosphere gets oxidized to carbonate, thereby lowering the melting point and finally producing carbonated melts (Foley, 2011). Metasomatism commonly goes along with an increase of the oxidation state of the mantle (Rudnick et al., 1993; Rudnick et al., 1994a; Foley, 2011; Martin et al., 2017), which presumably is reflected by the high redox conditions for the rocks of the Kaiserstuhl. The lithological similarities between the Kaiserstuhl and many other carbonatite complexes indicate that high redox conditions are a common feature for carbonatite complexes worldwide. A metasomatically overprinted (sub)lithospheric mantle therefore might be an important prerequisite for the formation of such complexes (see also Study 7).

## 4.4 Multi-stage evolution of carbonatite magmas monitored by pyrochlore

Title of publication:

*Pyrochlore as a monitor for magmatic and hydrothermal processes in carbonatites from the Kaiserstuhl volcanic complex (SW Germany).* (Study 4)

Pyrochlore group minerals are common accessory phases in carbonatites and show significant variations in their chemical composition (e.g. Hogarth et al., 2000). Thus, they may be suitable to distinguish diverse carbonatite formation stages. In this study, we investigated pyrochlore in the sövite bodies, the extrusive carbonatites, and the alvikite and beforsite dykes of the Kaiserstuhl Volcanic Complex. Based on a textural, mineral chemical and geochemical analyses, we decipher the evolution of such a carbonatitic system. The whole-rock chemistry was determined using XRF (major elements) and ICP-MS (trace elements), while the mineral composition was determined by the electron microprobe (EPMA).

Four main pyrochlore types were distinguished at the Kaiserstuhl: (I) irregularly shaped pyrochlore cores that contain up to 22 wt.% $UO_2$ and 9 wt.% $Ta_2O_5$; (II) oscillatory-zoned pyrochlore rich in CaO (up to 23 wt.%) and $Na_2O$ (up to 11 wt.%); (III) patchy pyrochlore zones that are characterized by high REE oxide concentrations of up to 18 wt.%, and which overgrew the before-mentioned pyrochlore types; (IV) unzoned pyrochlore crystals with high compositional variations between the different rock samples.

Irregularly shaped, U- and Ta-rich pyrochlore cores surrounded by an oscillatory-zoned pyrochlore generation occur in several carbonatites worldwide and are typically interpreted to represent the multi-stage magmatic evolution of a carbonatitic magma (Hogarth et al., 2000; Chakhmouradian and Williams, 2004; Lee et al., 2006). However, at the Kaiserstuhl, pyrochlore type I mainly occurs at the Badberg carbonatite pipe, which is characterized by cm- to m-sized silicate xenoliths (former nosean syenites). A xenocrystic origin of these U-Ta-rich pyrochlore cores is unlikely since pyrochlore could not be observed in the pristine nosean syenites. We rather suggest that the compositionally distinct pyrochlore generation formed by assimilation processes due to the (partly) resorption of the xenoliths (see also Study 5). This conforms with the

xenolith clasts of the inner part of the carbonatite pipe which are more strongly disaggregated than those of the peripheral zone.

The oscillatory zoned pyrochlore type II appears in all sövites and is considered a typical orthomagmatic feature, due to the faster crystal growth rate compared to the diffusion rate in tranquil conditions (Hogarth et al., 2000). The patchy pyrochlore zones (type III) mainly occur at the Orberg and illustrate a late magmatic to hydrothermal overprint. This is in agreement with the evolved character of these carbonatites, as demonstrated by the high whole-rock Nb/Ta and Zr/Hf ratios that could be caused by extensive fractionation of pyrochlore (Chakhmouradian, 2006). High REE concentrations in the whole-rock analyses and pyrochlore from Orberg also point towards an evolved magma composition.

Unzoned pyrochlore, restricted to the extrusive carbonatites, the alvikites and the beforsites, impedes a genetic discrimination. However, especially the tuffs at Henkenberg contain fragments of silicate rocks and may represent the volcanic equivalent to the sövites at the Badberg, which is also consistent with the similar pyrochlore composition in both carbonatite types.

## 4.5 Interaction processes between carbonatite magmas and silicate wall rocks

Title of publication:

*Evidence for Magma–Wall Rock Interaction in Carbonatites from the Kaiserstuhl Volcanic Complex (Southwest Germany).* (Study 5)

The low density and the low viscosity of carbonatitic melts enables them to ascend rapidly (Treiman and Schedl, 1983; Jones et al., 2013). Hence, even though the chemical contrast is large, contamination processes between carbonatites and crustal rocks are usually considered to play a negligibly role. However, if contamination by silicate rocks occurred, it is difficult to detect by means of radiogenic isotopes like Sr, Nd and Pb. Carbonatites generally have much higher concentrations of these elements, thereby buffering their isotope systems against crustal contamination. On the contrary, carbonatites offer considerable potential for magma-wall rock interactions due to their high geochemical contrast to most silicate rocks, their high liquidus temperature (1000 °C), and their high volatile contents (e.g. Treiman and Essene,

1984; Jago and Gittins, 1991; Vuorinen and Skelton, 2004; Chakhmouradian et al., 2008; Guzmics et al., 2011). Based on a textural and a mineral chemical investigation (EPMA) of the sövite bodies and the extrusive carbonatites, this study provides evidence for contamination processes in the carbonatitic magma system of the Kaiserstuhl Volcanic Complex.

Besides calcite, the carbonatites at the Kaiserstuhl typically consist of apatite, mica, spinel group minerals and pyrochlore. The extrusive carbonatites are characterized by nepheline, garnet and clinopyroxene. Olivine occurs in few sövites at Haselschacher Buck and at Katharinenberg, while small occurrences of monticellite-bearing carbonatites were found at the Orberg.

The sövites at the Badberg are peculiar since they contain euhedral clinopyroxene, high proportions of large mica crystals, and cm- to m-sized silicate xenoliths (calcite foidolites). These calcite foidolites largely consist of former nosean/haüyne (which has been completely altered to zeolite minerals), interstitial clinopyroxene, calcite, apatite, rare titanite and relict garnet which is surrounded by an interstitial garnet generation. Despite the textural similarity to the haüynolites, we suggest that the calcite foidolites represent the interaction product between the carbonatitic magma and the nosean syenites because of the chemical composition of the garnet relicts and the fact that the nosean syenites underlie the Badberg carbonatite (Kirchheimer, 1973). The contrasting mineral abundances and textures compared to the nosean syenites (higher foid content; lack of magnetite and alkali feldspar; interstitial clinoyproxene and garnet) demonstrates intense resorption and recrystallization processes.

The contact towards the calcite foidolite is characterized by a black wall of euhedral mica, which sometimes additionally comprise an inner zone of clinopyroxene, garnet and calcite. On a larger scale, similar observations can be drawn by the decrease of xenolith abundance, but the increase of mica content from the marginal towards the central part of the carbonatite body. This presumably is related to a more intense resorption of the nosean syenites due to a longer prevailing heat flow in the inner part of the carbonatitic magma pipe compared to the faster cooled pipe margins.

While the Badberg carbonatite is mica-rich and characterized by large mica grains up to 2 cm, all other carbonatites at the Kaiserstuhl are mica-poor and contain much smaller crystal sizes (< 2 mm). The micas at the Badberg are also chemically distinguishable from the other carbonatite types, as they contain comparably low

concentrations of Mg and Ba, but high contents of Mn and Fe. Especially the high proportion of Fe is atypical for mica in carbonatites (e.g. Lee et al., 2003; Krasnova et al., 2004a; Giebel et al., 2019), and implies an element supply by assimilation with the nosean syenite. Resorption of clinopyroxene, magnetite and alkali feldspar may have provided significant amounts of Fe, K, Al, and Si required for the crystallization of abundant mica.

The chemical composition of the apatites at the Badberg is also unique at the Kaiserstuhl. While the cores have a similar composition compared to the other carbonatite bodies, the rims demonstrate a relatively high britholite substitution ($Ca^{2+} + P^{5+} \leftrightarrow REE^{3+} + Si^{4+}$). The sharp contact between the core and the compositionally distinct apatite rim (rather than a continuous transition) argues against magmatic differentiation, although the comparably high Sr concentration of the Badberg apatites may reflect a high evolution stage of the carbonatite magma. However, a hydrothermal origin can be excluded since a high britholite component typically indicates magmatic crystallization conditions (T > 600 °C), whereas a hydrothermal overprint results in the crystallization of REE-poor apatite and separate REE-minerals (Anenburg et al., 2018; Anenburg and Mavrogenes, 2018). Thus, the high REE concentration in the apatite rims is the result of charge balancing due to the high incorporation of Si, which was provided by the (partly) resorption of the silicate xenoliths (Klemme and Dalpé, 2003; Hammouda et al., 2010). The enhanced incorporation of REE in early crystallizing apatite led to rather low REE concentrations in late-stage pyrochlore compared to the carbonatites without evidence of crustal contamination and/or assimilation. An elevated Si activity in the Badberg carbonatites is also indicated by the presence of euhedral clinopyroxene (Barker, 2001). The chemical composition is similar to the recrystallized, interstitial clinopyroxenes of the calcite foidolites, but differs from the clinoyproxenes of all other silicate rocks at the Kaiserstuhl (see also Study 3), hence ruling out a xenocrystic origin. This contrasts with garnet, clinopyroxene and some spinel group minerals of the extrusive carbonatites where the chemical composition indicates that the minerals represent xenocrysts entrapped from various silicate rocks.

Similar to the Badberg, many carbonatites worldwide have high modal amounts of mica (e.g. Brod et al., 2001; Lee et al., 2003; Reguir et al., 2009; Giebel et al., 2019). However, experiments on carbonatitic melts demonstrate that the solubility for elements such as Si and Al is strictly limited (Brooker and Kjarsgaard, 2011; Weidendorfer et al., 2017). Based on mass balance calculations, we conclude that a

maximum of approximately 7 % mica can crystallize from a carbonatitic melt. Note that these calculations were examined by assuming that sufficient K, Mg and $H_2O$ are available, and mica is the sole crystallizing mineral phase. We therefore suggest that the high mica content of many carbonatites can only be explained by a continuous interaction with silicate rocks and a consequently steady supply of elements such as Si and Al. The occurrence and composition of silicate minerals like mica and clinopyroxene hence may be a useful indicator for contamination and assimilation processes during the emplacement of carbonatitic magmas.

## 4.6 Interaction processes between silicate magmas/rocks and potash salt rocks

Title of publication:

*Hydrothermal halite precipitation in mafic volcanic rocks: the case of the Buggingen salt deposit, SW Germany.* (Study 6)

Olivine melilitites and monchiquites intruded into the potash salt deposit at Buggingen. Similar to the carbonatite magma-silicate wall rock interaction mentioned in Study 5, the large geochemical contrast between primitive dyke rocks and salt-rich host rocks provides potential for intense magmatic to hydrothermal assimilation processes. Based on a detailed mineralogical and mineral chemical characterization (EPMA), we reveal the influence of the wall rock on the mineralization of the dyke rocks.

The dyke rocks are characterized by spheroidal textures that show a contrasting mineralization depending on whether they adjoin the salt rocks or the bituminous Fish Shales. Roundish textures associated with the salt layer mainly comprise smectite, calcite, halite and sometimes anhydrite, while those associated with the Fish Shale consist of smectite, calcite, zeolite and analcime. As spheroidal textures are present in all investigated dyke rocks, independent of the host rock, we suggest that the halite inclusions do not illustrate salt-magma mingling, or salt-liquid immiscibility caused by intense magmatic assimilation with the salt rocks. The absence of salt rock-melt interactions might be related to a low orthomagmatic water content of the primitive melts, which inhibited intense fluid exsolution and a consequent dissolution of the salt. Moreover, the dyke magma presumably cooled too fast in order to melt the salt and

enable liquid mingling and/or assimilation processes (Knipping, 1989). The halite-bearing textures are interpreted as amygdules and hydrothermally altered ocelli. NaCl-bearing fluids derived from the salt layers reacted with the dyke rock groundmass and formed smectites and zeolites, thereby cementing the fluid paths and increasing the Na concentration of the fluid. The absence of halite in the groundmass indicates that the initial fluid was not saturated in NaCl. As soon as the fluid entered a vesicle or an ocellus where the calcite-bearing interior (Hurrle, 1973) was previously dissolved, smectite formed at the marginal areas and the fluid became trapped. Water extraction by clay mineral swelling finally led to the precipitation of halite. Datolite was observed in pseudomorphs after olivine, associated with halite or with serpentine/smectite. The required boron for the formation of datolite most likely derives from the clay-rich layers of the host rock (e.g. Leeman and Sisson, 1996; Garrett, 1998) and was incorporated/adsorbed into serpentine/smectite during alteration of olivine. Subsequent breakdown of serpentine/smectite during interaction with a second fluid batch provided Si and B for the formation of datolite.

## 4.7 The relationship between the redox conditions of alkaline silicate rocks, carbonatites, and the mantle source

Title of publication:
*Do carbonatites and alkaline rocks reflect variable redox conditions in their upper mantle source?* (Study 7)

In our first study on the Kaiserstuhl (Study 3), we conclude that the high redox estimates for the various rock types may be a common characteristic for carbonatite complexes and suggest that the rocks may reflect a high oxidation state of their mantle source. This assumption was tested by a worldwide compilation of the intrinsic parameters of alkaline rocks and carbonatites, including new results from the carbonatite complexes Sokli, Kovdor, Palabora, Magnet Cove, Oka and Jacupiranga.

The chemical composition of the minerals was determined using the electron microprobe (EPMA). Based on these results, the formation conditions (temperature and oxygen fugacity) for the carbonatites (including phoscorites) and silicate rocks were calculated by several thermo(oxybaro)meters and thermodynamically stable

mineral equilibria. Temperatures typically vary between 900 and 500 °C, while the redox calculations indicate relatively oxidized conditions (ΔFMQ≈0 to +3) for all rock types.

Including literature data, the reported crystallization temperature for carbonatites strongly depends on the applied geothermometer and ranges from ~1000 °C to less than 200 °C. The highest values correspond to calculations based on melt inclusions (e.g. Guzmics et al., 2011), while the lowest values can be explained by late magmatic to post-magmatic diffusion or exsolution processes (e.g. Haynes et al., 2003; Milani et al., 2016). The transition from magmatic to hydrothermal/carbothermal conditions can be determined by fluid inclusions which illustrate homogenization temperatures of up to 600 °C (Rankin, 1975). This is in broad accordance with experimental constrains of the carbonatite eutectic (~650 °C; Lee et al., 2000) and with melt inclusions in late-stage carbonate crystals (530 °C; Sokolov, 2014). We therefore conclude that magmatic carbonatites typically crystallize between ~1000 and 500 °C. To minimize the potential effect of fractional crystallization or thermal re-equilibration, we only consider redox estimates for temperatures above 600 °C.

Based on a worldwide compilation, carbonatites (ΔFMQ=+1.3) and their associated alkaline silicate rocks at continental settings (ΔFMQ=+1.4) formed on average under significantly higher redox conditions than alkaline silicate rocks at continental settings which are not associated with carbonatites (ΔFMQ=-1.1). We suggest that these redox variations reflect the heterogeneity of their mantle source, although some variations may result from variable melting degrees, fractionation of Fe-bearing minerals and degassing processes (Carmichael, 1991; Gaillard et al., 2015). The prerequisite of a carbonated and relatively oxidized mantle for the formation of carbonatite complexes conforms with the high redox estimates for mantle xenoliths that show evidence for metasomatism processes involving carbonate-rich liquids (up to ΔFMQ=+3.5; Rudnick et al., 1994b; Woodland et al., 1996; Uenver-Thiele et al., 2017). Such xenoliths may not only represent the interaction between the lithospheric mantle and ascending (carbonate-bearing) melts/fluids but may reflect a possible mantle source for the formation of carbonatite complexes as well. Since carbonatites are typically associated with nephelinitic to melililitic rocks, the source region for most carbonatite complexes can be estimated to depths of 75 to 130 km (Wyllie et al., 1990; Hirose and Kushiro, 1993; Gudfinnsson and Presnall, 2005). At such depths, the stability of carbonate

requires redox conditions above that of the average asthenospheric and lithospheric mantle (Foley, 2011), roughly in the same range than those for carbonatites and associated silicate rocks.

Carbonatites and alkaline silicate rocks at the seven investigated complexes all indicate oxidized formation conditions. However, the various rock types do not always originate from the same mantle source (e.g. Kaiserstuhl, see Study 3), hence demonstrating that oxidation processes must have affected multiple mantle domains. An increasing redox state of the mantle may result from subduction and digestion of oxidized (and eventually carbonate-bearing) crustal material (Yaxley and Brey, 2004; Foley, 2011; Rohrbach and Schmidt, 2011), or by the interaction with ascending asthenospheric liquids. Note that partial melts presumably have a higher oxidation state than the precursor solid (Canil and O'Neill, 1996; Frost and McCammon, 2008; Mallmann and O'Neill, 2009).

A rather high oxidation state and enough carbonate in the mantle, however, is not the sole prerequisite for the formation of carbonatite complexes. The mantle beneath subduction zones, for example, is relatively oxidized, but carbonatites are absent presumably due to the reversed temperature gradient of the mantle wedge. Ascending carbonate-bearing melts would react with the hot overlying mantle, whereby they would be strongly modified and diluted (Yaxley et al., 2019). Ocean island basalts and spatially associated xenoliths also indicate oxidized conditions (Ballhaus, 1993; Mallmann and O'Neill, 2007; Foley, 2011). Such environments typically lack carbonatites because of a too thin lithosphere which prevents the parental melts to evolve into the carbonatite-silicate miscibility gap (Weidendorfer et al., 2017). Further reasons for the absence of carbonatites at alkaline complexes that formed under oxidized conditions include $CO_2$ degassing processes, the complete crystallization of the silicate melt before an exsolved/residual carbonatite magma could form, or lack of outcrop.

# 5 Conclusion and implications

This thesis provides new and improved insights into the crystallization conditions and processes of variably evolved alkaline silicate rocks and carbonatites. It was shown that the rock type and the mineral assemblage may strongly vary as a function of the mantle source conditions, magma mixing, and crustal contamination/assimilation processes. Especially alkaline complexes that comprise agpaitic rocks reflect contrasting crystallization conditions and magma evolution processes compared to alkaline complexes associated with carbonatites. This can be impressively demonstrated by the Tarosero Volcanic Complex (Tanzania) and the Kaiserstuhl Volcanic Complex (Germany).

In general, the main prerequisite for the formation of agpaitic rocks is the retention of volatiles in the melt. Thus, almost all agpaitic occurrences represent intrusive rocks. In case of the extrusive agpaitic rocks at Tarosero, the near-liquidus crystallization of OH-bearing amphibole resulted in a low water activity at late-magmatic conditions which prevented the exsolution of fluids and water-soluble halogens. Consequently, the solubility of REE and other HFSE was kept high in the melt residue, which finally supported the formation of interstitial eudialyte. The rocks from Tarosero derive from a basaltic magma source and evolved by extensive fractional crystallization at low redox conditions ($\Delta FMQ \leq 0$).

This stands in great contrast to the rocks of the carbonatite-bearing Kaiserstuhl volcano. A K-basanitic magma produced the tephritic to phonolitic rock series, while an olivine melilititic magma is responsible for the nephelinitic to limburgitic rock series, the melilititic to haüynitic rock series and the carbonatites. Fractional crystallization at high redox conditions ($\Delta FMQ = +1$ to $+2$) is the key process for the evolution of such magmas.

In fact, carbonatites and associated silicate rocks at continental settings reveal on average significantly higher redox conditions ($\Delta FMQ \approx +1.4$) than alkaline complexes without carbonatites ($\Delta FMQ = -1.1$). Especially agpaitic rocks typically demonstrate reduced formation conditions (Marks and Markl, 2017). The redox variations presumably reflect the heterogeneity of the oxidation state of the mantle source. This is consistent with the prerequisite of a relatively oxidized, carbonate-bearing mantle for the formation of carbonatites, and may explain why carbonatites are absent at most agpaitic complexes. However, there are few exceptions where carbonatites are

spatially associated with agpaitic rocks (e.g. Magnet Cove, Oldoinyo Lengai, Khibina, Kovdor, Tamazeght, Kontozero, Kaiserstuhl; Erickson and Blade, 1963; Dawson and Frisch, 1971; Kramm and Kogarko, 1994; Pekov et al., 2001; Marks et al., 2008; Petrovsky et al., 2012; Marks and Markl, 2017). It remains doubtful that these agpaitic occurrences all derive from separate, relatively reduced mantle sources. Indeed, agpaitic rocks can also derive from primitive nephelinitic magmas (Marks et al., 2011; Schilling et al., 2011), which may also be parental to carbonatites. However, redox calculations for presumably nephelinite-derived agpaitic rocks are restricted to the Tamazeght Carbonatite Complex and “have to be taken as rough estimates” (Marks et al., 2008). Further investigations on such rocks are needed to make generally valid statements about their redox conditions. Moreover, there are several further processes that have to be considered to relate the oxidation state of the mantle with its magmatic derivatives. For example, we demonstrated evidence for multi-stage magma mixing in the Ogol basalts of the Laetoli area. Mixing of several magmas with contrasting redox conditions, however, may result in an intermediate oxidation state, which does not reflect the redox conditions of the mantle source. At the Kaiserstuhl, we showed that carbonatite magma-wall rock interactions caused an increasing silica activity of the magma, and it seems likely that such processes may also affect the redox conditions. Variable melting degrees, degassing and fractional crystallization may also influence the oxidation state of a magmatic system (Gaillard et al., 2015). Thus, further work on such processes are appreciated in order to more precisely link the redox conditions of igneous rocks to their mantle source.

# 6 References

Andersen, D.J., Lindsley, D.H., Davidson, P.M., 1993. Quilf - a Pascal Program to Assess Equilibria among Fe-Mg-Mn-Ti Oxides, Pyroxenes, Olivine, and Quartz. Computers & Geosciences 19, 1333-1350. http://dx.doi.org/10.1016/0098-3004(93)90033-2.

Andersen, T., Sørensen, H., 2005. Stability of naujakasite in hyperagpaitic melts, and the petrology of naujakasite lujavrite in the Ilímaussaq alkaline complex, South Greenland. Mineralogical Magazine 69, 125-136. http://dx.doi.org/10.1180/0026461056920240.

Anenburg, M., Burnham, A.D., Mavrogenes, J.A., 2018. REE Redistribution Textures in Altered Fluorapatite: Symplectites, Veins, and Phosphate-Silicate-Carbonate Assemblages from the Nolans Bore P-REE-Th Deposit, Northern Territory, Australia. The Canadian Mineralogist 56, 331-354. http://dx.doi.org/10.3749/canmin.1700038.

Anenburg, M., Mavrogenes, J.A., 2018. Carbonatitic versus hydrothermal origin for fluorapatite REE-Th deposits: Experimental study of REE transport and crustal “antiskarn” metasomatism. American Journal of Science 318, 335-366. http://dx.doi.org/10.2475/03.2018.03.

Bailey, D., 1969. The stability of acmite in the presence of H2O. American Journal of Science 267, 1-16.

Ballhaus, C., 1993. Redox States of Lithospheric and Asthenospheric Upper-Mantle. Contributions to Mineralogy and Petrology 114, 331-348. http://dx.doi.org/Doi 10.1007/Bf01046536.

Ballhaus, C., Frost, B.R., 1994. The Generation of Oxidized CO2-Bearing Basaltic Melts from Reduced CH4-Bearing Upper-Mantle Sources. Geochimica Et Cosmochimica Acta 58, 4931-4940. http://dx.doi.org/10.1016/0016-7037(94)90222-4.

Barker, D.S., 2001. Calculated silica activities in carbonatite liquids. Contributions to Mineralogy and Petrology 141, 704-709. http://dx.doi.org/10.1007/s004100100281.

Beccaletto, L., Capar, L., Cruz-Mermy, D., Rupf, I., Nitsch, E., Oliviero, G., Elsass, P., Perrin, A., Marc, S., 2010. The GeORG project - Geological Potential of the Upper Rhine Graben - Situation, goals and first scientific results, 23ème RST, Bordeaux, France.

Bell, K., Simonetti, A., 2010. Source of parental melts to carbonatites–critical isotopic constraints. Mineralogy and Petrology 98, 77-89. http://dx.doi.org/10.1007/s00710-009-0059-0.

Bézos, A., Humler, E., 2005. The Fe3+/ΣFe ratios of MORB glasses and their implications for mantle melting. Geochimica et Cosmochimica Acta 69, 711-725. http://dx.doi.org/10.1016/j.gca.2004.07.026.

Blust, G., 1993. Petrographie und Geochemie der silikatischen Ganggesteine der Bohrung KB3 Steinreise. Albert-Ludwigs-University Freiburg, p. 83.

Bourgeois, O., Ford, M., Diraison, M., Veslud, C.L.C.d., Gerbault, M., Pik, R., Ruby, N., Bonnet, S., 2007. Separation of rifting and lithospheric folding signatures in the NW-Alpine foreland. International Journal of Earth Sciences 96, 1003-1031. http://dx.doi.org/10.1007/s00531-007-0202-2.

Braitsch, O., Gunzert, G., Wimmenauer, W., Thiel, R., 1964. Über ein Datolithvorkommen am Basaltkontakt im Kaliwerk Buggingen (Südbaden).

Beiträge zur Mineralogie und Petrographie 10, 111-124. http://dx.doi.org/10.1007/BF01192540.

Brauch, K., Pohl, C., Symons, G., Tauchnitz, M., 2018. Paper on Instrument Test and Best Practice for Carbonatites and Alkaline Rocks. Horizon2020 Internal Report, HiTechAlkCarb Project.

Brod, J.A., Gaspar, J.C., de Araújo, D.P., Gibson, S.A., Thompson, R.N., Junqueira-Brod, T.C., 2001. Phlogopite and tetra-ferriphlogopite from Brazilian carbonatite complexes: petrogenetic constraints and implications for mineral-chemistry systematics. Journal of Asian Earth Sciences 19, 265-296. http://dx.doi.org/10.1016/S1367-9120(00)00047-X.

Brooker, R., Kjarsgaard, B., 2011. Silicate–carbonate liquid immiscibility and phase relations in the system SiO2–Na2O–Al2O3–CaO–CO2 at 0· 1–2· 5 GPa with applications to carbonatite genesis. Journal of Petrology 52, 1281-1305. http://dx.doi.org/10.1093/petrology/egq081.

Canil, D., O'Neill, H.S.C., 1996. Distribution of Ferric Iron in some Upper-Mantle Assemblages. Journal of Petrology 37, 609-635. http://dx.doi.org/10.1093/petrology/37.3.609.

Carmichael, I.S.E., 1991. The redox states of basic and silicic magmas: a reflection of their source regions? Contributions to Mineralogy and Petrology 106, 129-141. http://dx.doi.org/10.1007/BF00306429.

Chakhmouradian, A., Williams, C., 2004. Mineralogy of high-field-strength elements (Ti, Nb, Zr, Ta, Hf) in phoscoritic and carbonatitic rocks of the Kola Peninsula, Russia. Phoscorites and carbonatites from mantle to mine: the key example of the Kola Alkaline Province 10, 293-340.

Chakhmouradian, A.R., 2006. High-field-strength elements in carbonatitic rocks: Geochemistry, crystal chemistry and significance for constraining the sources of carbonatites. Chemical Geology 235, 138-160. http://dx.doi.org/10.1016/j.chemgeo.2006.06.008.

Chakhmouradian, A.R., Mumin, A.H., Demény, A., Elliott, B., 2008. Postorogenic carbonatites at Eden Lake, Trans-Hudson Orogen (northern Manitoba, Canada): Geological setting, mineralogy and geochemistry. Lithos 103, 503-526. http://dx.doi.org/10.1016/j.lithos.2007.11.004.

Chakhmouradian, A.R., Reguir, E.P., Zaitsev, A.N., 2016. Calcite and dolomite in intrusive carbonatites. I. Textural variations. Mineralogy and Petrology 110, 333-360. http://dx.doi.org/10.1007/s00710-015-0390-6.

Chorowicz, J., 2005. The East African rift system. Journal of African Earth Sciences 43, 379-410. http://dx.doi.org/10.1016/j.jafrearsci.2005.07.019.

Christie, D.M., Carmichael, I.S.E., Langmuir, C.H., 1986. Oxidation states of mid-ocean ridge basalt glasses. Earth and Planetary Science Letters 79, 397-411. http://dx.doi.org/10.1016/0012-821X(86)90195-0.

Connolly, J.A.D., 1990. Multivariable Phase-Diagrams - an Algorithm Based on Generalized Thermodynamics. American Journal of Science 290, 666-718. http://dx.doi.org/10.2475/ajs.290.6.666.

Cottrell, E., Birner, S., Brounce, M., Davis, F., Waters, L., Kelley, K., 2020. Oxygen fugacity across tectonic settings, AGU Geophysical Monograph Redox 28variables and mechanisms in magmatism and volcanism. Earth and Space Science Open Archive, Wiley, p. 61. http://dx.doi.org/10.1002/essoar.10502445.1.

Currie, K., Knutson, J., Temby, P., 1992. The Mud Tank carbonatite complex, central Australia—an example of metasomatism at mid-crustal levels. Contributions to Mineralogy and Petrology 109, 326-339. http://dx.doi.org/10.1007/BF00283322.

Dasgupta, R., Hirschmann, M.M., 2006. Melting in the Earth's deep upper mantle caused by carbon dioxide. Nature 440, 659-662. http://dx.doi.org/10.1038/nature04612.

Dawson, J.B., 1962. The geology of Oldoinyo Lengai. Bulletin Volcanologique 24, 349-387. http://dx.doi.org/10.1007/BF02599356.

Dawson, J.B., 1992. Neogene tectonics and volcanicity in the North Tanzania sector of the Gregory Rift Valley: contrasts with the Kenya sector. Tectonophysics 204, 81-92. http://dx.doi.org/10.1016/0040-1951(92)90271-7.

Dawson, J.B., 1997. Neogene–Recent rifting and volcanism in northern Tanzania: relevance for comparisons between the Gardar province and the East African Rift valley. Mineralogical Magazine 61, 543-548. http://dx.doi.org/10.1180/minmag.1997.061.407.06.

Dawson, J.B., 2008. The Gregory rift valley and Neogene-recent volcanoes of northern Tanzania. Geological Society of London, p. 102.

Dawson, J.B., Frisch, T., 1971. Eucolite from oldoinyo Lengai, Tanzania. Lithos 4, 297-303. http://dx.doi.org/10.1016/0024-4937(71)90008-9.

Dèzes, P., Schmid, S.M., Ziegler, P.A., 2004. Evolution of the European Cenozoic Rift System: interaction of the Alpine and Pyrenean orogens with their foreland lithosphere. Tectonophysics 389, 1-33. http://dx.doi.org/10.1016/j.tecto.2004.06.011.

Doroshkevich, A.G., Ripp, G., Viladkar, S., 2010. Newania carbonatites, Western India: example of mantle derived magnesium carbonatites. Mineralogy and Petrology 98, 283-295. http://dx.doi.org/10.1007/s00710-009-0076-z.

Dunworth, E.A., Wilson, M., 1998. Olivine melilitites of the SW German Tertiary volcanic province: Mineralogy and petrogenesis. Journal of Petrology 39, 1805-1836. http://dx.doi.org/10.1093/petrology/39.10.1805.

Edel, J.-B., Whitechurch, H., Diraison, M., 2006. Seismicity wedge beneath the Upper Rhine Graben due to backwards Alpine push? Tectonophysics 428, 49-64. http://dx.doi.org/10.1016/j.tecto.2006.08.009.

Edel, J.B., Fuchs, K., Gelbke, C., Prodehl, C., 1975. Deep Structure of Southern Rhinegraben Area from Seismic Refraction Investigations. Journal of Geophysics-Zeitschrift für Geophysik 41, 333-356.

Eguchi, J., Dasgupta, R., 2018. Redox state of the convective mantle from CO2-trace element systematics of oceanic basalts. Geochemical Perspectives Letters 8, 17-21. http://dx.doi.org/10.7185/geochemlet.1823.

Erickson, R.L., Blade, L.V., 1963. Geochemistry and petrology of the alkalic igneous complex at Magnet Cove, Arkansas, Professional Paper, - ed. http://dx.doi.org/10.3133/pp425.

Ernst, W.G., 1962. Synthesis, Stability Relations, and Occurrence of Riebeckite and Riebeckite-Arfvedsonite Solid Solutions. The Journal of Geology 70, 689-736. http://dx.doi.org/10.1086/626866.

Esslinger, G., 1976. Vorkommen und Tektonik der Basalte im Kalisalzlager Buggingen (Südbaden). Jahresheft des Geologischen Landesamtes in Baden-Württemberg 18, 7-18.

Fitton, J.G., Upton, B.G.J., 1987. Alkaline igneous rocks. The Geological Society of London, London.

Foley, S.F., 2011. A reappraisal of redox melting in the Earth's mantle as a function of tectonic setting and time. Journal of Petrology 52, 1363-1391. http://dx.doi.org/10.1093/petrology/egq061.

Foley, S.F., Yaxley, G.M., Rosenthal, A., Buhre, S., Kiseeva, E.S., Rapp, R.P., Jacob, D.E., 2009. The composition of near-solidus melts of peridotite in the presence of CO2 and H2O between 40 and 60 kbar. Lithos 112, 274-283. http://dx.doi.org/10.1016/j.lithos.2009.03.020.

Frost, B.R., Frost, C.D., 2008. A Geochemical Classification for Feldspathic Igneous Rocks. Journal of Petrology 49, 1955-1969. http://dx.doi.org/10.1093/petrology/egn054.

Frost, D.J., McCammon, C.A., 2008. The redox state of Earth's mantle. Annual Review of Earth and Planetary Sciences 36, 389-420. http://dx.doi.org/10.1146/annurev.earth.36.031207.124322.

Gaillard, F., Scaillet, B., Pichavant, M., Iacono-Marziano, G., 2015. The redox geodynamics linking basalts and their mantle sources through space and time. Chemical Geology 418, 217-233. http://dx.doi.org/10.1016/j.chemgeo.2015.07.030.

Garrett, D.E., 1998. Borates: Handbook of deposits, processing, properties, and use. Elsevier.

Giebel, R.J., Marks, M.A., Gauert, C.D., Markl, G., 2019. A model for the formation of carbonatite-phoscorite assemblages based on the compositional variations of mica and apatite from the Palabora Carbonatite Complex, South Africa. Lithos 324, 89-104. http://dx.doi.org/10.1016/j.lithos.2018.10.030.

Giehl, C., Marks, M., Nowak, M., 2013. Phase relations and liquid lines of descent of an iron-rich peralkaline phonolitic melt: an experimental study. Contributions to Mineralogy and Petrology 165, 283-304. http://dx.doi.org/10.1007/s00410-012-0809-6.

Giehl, C., Marks, M.A.W., Nowak, M., 2014. An experimental study on the influence of fluorine and chlorine on phase relations in peralkaline phonolitic melts. Contributions to Mineralogy and Petrology 167, 977. http://dx.doi.org/10.1007/s00410-014-0977-7.

Goodenough, K.M., Schilling, J., Jonsson, E., Kalvig, P., Charles, N., Tuduri, J., Deady, E.A., Sadeghi, M., Schiellerup, H., Müller, A., Bertrand, G., Arvanitidis, N., Eliopoulos, D.G., Shaw, R.A., Thrane, K., Keulen, N., 2016. Europe's rare earth element resource potential: An overview of REE metallogenetic provinces and their geodynamic setting. Ore Geology Reviews 72, 838-856. http://dx.doi.org/10.1016/j.oregeorev.2015.09.019.

Groschopf, R., Kessler, G., Leiber, J., Maus, H., Ohmert, W., Schreiner, A., Wimmenauer, W., 1996. Geologische Karte von Baden-Württemberg 1:50000: Erläuterungen zum Blatt Freiburg i. Br. und Umgebung. Geologisches Landesamt Baden-Württemberg, 364.

Gudfinnsson, G.H., Presnall, D.C., 2005. Continuous gradations among primary carbonatitic, kimberlitic, melilititic, basaltic, picritic, and komatiitic melts in equilibrium with garnet lherzolite at 3–8 GPa. Journal of Petrology 46, 1645-1659. http://dx.doi.org/10.1093/petrology/egi029.

Gudmundsson, G., Wood, B.J., 1995. Experimental tests of garnet peridotite oxygen barometry. Contributions to Mineralogy and Petrology 119, 56-67. http://dx.doi.org/10.1007/BF00310717.

Guzmics, T., Mitchell, R.H., Szabo, C., Berkesi, M., Milke, R., Abart, R., 2011. Carbonatite melt inclusions in coexisting magnetite, apatite and monticellite in

Kerimasi calciocarbonatite, Tanzania: melt evolution and petrogenesis. Contributions to Mineralogy and Petrology 161, 177-196. http://dx.doi.org/10.1007/s00410-010-0525-z.

Halama, R., Marks, M., Brügmann, G., Siebel, W., Wenzel, T., Markl, G., 2004. Crustal contamination of mafic magmas: evidence from a petrological, geochemical and Sr–Nd–Os–O isotopic study of the Proterozoic Isortoq dike swarm, South Greenland. Lithos 74, 199-232. http://dx.doi.org/10.1016/j.lithos.2004.03.004.

Halama, R., Vennemann, T., Siebel, W., Markl, G., 2005. The Grønnedal-Ika carbonatite–syenite complex, South Greenland: carbonatite formation by liquid immiscibility. Journal of Petrology 46, 191-217. http://dx.doi.org/10.1093/petrology/egh069.

Halliday, A.N., Lee, D.-C., Tommasini, S., Davies, G.R., Paslick, C.R., Godfrey Fitton, J., James, D.E., 1995. Incompatible trace elements in OIB and MORB and source enrichment in the sub-oceanic mantle. Earth and Planetary Science Letters 133, 379-395. http://dx.doi.org/10.1016/0012-821X(95)00097-V.

Hammouda, T., Chantel, J., Devidal, J.-L., 2010. Apatite solubility in carbonatitic liquids and trace element partitioning between apatite and carbonatite at high pressure. Geochimica et Cosmochimica Acta 74, 7220-7235. http://dx.doi.org/10.1016/j.gca.2010.09.032.

Harmer, R.E., Lee, C.A., Eglington, B.M., 1998. A deep mantle source for carbonatite magmatism: evidence from the nephelinites and carbonatites of the Buhera district, SE Zimbabwe. Earth and Planetary Science Letters 158, 131-142. http://dx.doi.org/10.1016/S0012-821x(98)00053-3.

Hay, R.L., 1987. Geology of the Laetoli area. Clarendon, Oxford.

Haynes, E.A., Moecher, D.P., Spicuzza, M.J., 2003. Oxygen isotope composition of carbonates, silicates, and oxides in selected carbonatites: constraints on crystallization temperatures of carbonatite magmas. Chemical Geology 193, 43-57. http://dx.doi.org/10.1016/S0009-2541(02)00244-9.

Hirose, K., Kushiro, I., 1993. Partial melting of dry peridotites at high pressures: determination of compositions of melts segregated from peridotite using aggregates of diamond. Earth and Planetary Science Letters 114, 477-489. http://dx.doi.org/10.1016/0012-821x(93)90077-M.

Hofmann, C., Courtillot, V., Féraud, G., Rochette, P., Yirgu, G., Ketefo, E., Pik, R., 1997. Timing of the Ethiopian flood basalt event and implications for plume birth and global change. Nature 389, 838-841. http://dx.doi.org/10.1038/39853.

Hogarth, D.D., Williams, C.T., Jones, P., 2000. Primary zoning in pyrochlore group minerals from carbonatites. Mineralogical Magazine 64, 683-697. http://dx.doi.org/10.1180/002646100549544.

Holland, T.J.B., Powell, R., 1998. An internally consistent thermodynamic data set for phases of petrological interest. Journal of Metamorphic Geology 16, 309-343. http://dx.doi.org/10.1111/j.1525-1314.1998.00140.x.

Hubberten, H.W., Katz-Lehnert, K., Keller, J., 1988. Carbon and Oxygen Isotope Investigations in Carbonatites and Related Rocks from the Kaiserstuhl, Germany. Chemical Geology 70, 257-274. http://dx.doi.org/10.1016/0009-2541(88)90097-6.

Hurrle, H., 1973. Ocelli-und Mandelbildung der Melilithankaratrite im Kalisalzlager Buggingen und im Kristallin des Schwarzwaldes. Verlag nicht ermittelbar.

Hüttner, R., 1996. Tektonik im Grundgebirge. Landesamt für Geologie, Rohstoffe und Bergbau Baden-Württemberg, Freiburg im Breisgau, Germany.

Ivanyuk, G.Y., Kalashnikov, A.O., Pakhomovsky, Y.A., Bazai, A.V., Goryainov, P.M., Mikhailova, J.A., Yakovenchuk, V.N., Konopleva, N.G., 2017. Subsolidus Evolution of the Magnetite-Spinel-UlvöSpinel Solid Solutions in the Kovdor Phoscorite-Carbonatite Complex, NW Russia. Minerals 7, 215. http://dx.doi.org/10.3390/min7110215.

Jago, B.C., Gittins, J., 1991. The role of fluorine in carbonatite magma evolution. Nature 349, 56-58. http://dx.doi.org/10.1038/349056a0.

Kanazawa, Y., Kamitani, M., 2006. Rare earth minerals and resources in the world. Journal of Alloys and Compounds 408-412, 1339-1343. http://dx.doi.org/10.1016/j.jallcom.2005.04.033.

Katz-Lehnert, K., 1989. Petrologie der Gangkarbonatite im Kaiserstuhl. Albert-Ludwigs University Freiburg, Freiburg, p. 290.

Katz, K., Keller, J., 1981. Comb-layering in carbonatite dykes. Nature 294, 350-352. http://dx.doi.org/10.1038/294350a0.

Keller, J., 1978a. Karbonatitische Schmelzen im Oberflächenvulkanismus des Kaiserstuhls. Fortschritte der Mineralogie 56, 1-58.

Keller, J., 1978b. Primary olivine nephelinitic magmas in the Rhinegraben riftvalley volcanism (Central Europe), Abstract presented at the Int. Geodynamics Conf.'Magma Genesis', pp. 270-271.

Keller, J., 1981. Carbonatitic volcanism in the Kaiserstuhl alkaline complex: evidence for highly fluid carbonatitic melts at the Earth's surface. Journal of Volcanology and Geothermal Research 9, 423-431. http://dx.doi.org/10.1016/0377-0273(81)90048-2.

Keller, J., 1984a. Der jungtertiäre Vulkanismus Südwestdeutschlands: Exkursionen im Kaiserstuhl und Hegau. Fortschr. Mineral 62, 2-35.

Keller, J., 1989. Extrusive carbonatites and their significance, in: Bell, K. (Ed.), Carbonatites: genesis and evolution. . Unwin Hyman, London, pp. 70-88.

Keller, J., Brey, G., Lorenz, V., Sachs, P., Schleicher, H., 1990. IAVCEI 1990: Pre-conference Excursion 2A: Volcanism and Petrology of the Upper Rhinegraben (Urach-Hegau-Kaiserstuhl). IAVCEI International Volcanic Congress Mainz.

Keller, J., Krafft, M., 1990. Effusive natrocarbonatite activity of Oldoinyo Lengai, June 1988. Bulletin of Volcanology 52, 629-645. http://dx.doi.org/10.1007/BF00301213.

Keppler, H., 1993. Influence of fluorine on the enrichment of high field strength trace elements in granitic rocks. Contributions to Mineralogy and Petrology 114, 479-488. http://dx.doi.org/10.1007/BF00321752.

Kirchheimer, F., 1973. Weitere Mitteilungen über das Vorkommen radioaktiver Substanzen in Süddeutschland. Jahresh. Geol. Landesamtes Baden-Württemb. 15, 33-125.

Kjarsgaard, B., Peterson, T., 1991. Nephelinite-Carbonatite Liquid Immiscibility at Shombole Volcano, East-Africa - Petrographic and Experimental-Evidence. Mineralogy and Petrology 43, 293-314. http://dx.doi.org/Doi 10.1007/Bf01164532.

Klemme, S., Dalpé, C., 2003. Trace-element partitioning between apatite and carbonatite melt. American Mineralogist 88, 639-646. http://dx.doi.org/10.2138/am-2003-0417.

Knipping, B.J., 1989. Basalt Intrusions in Evaporites. Lecture Notes in Earth Sciences, Berlin Springer Verlag 24.

Kogarko, L., Kononova, V., Orlova, M., Woolley, A., 1995. Alkaline rocks of the world, Part 2: Former Soviet Union. London, Chapman & Hall.

Kogarko, L.N., 1987. Alkaline rocks of the eastern part of the Baltic Shield (Kola Peninsula). Geological Society, London, Special Publications 30, 531. http://dx.doi.org/10.1144/GSL.SP.1987.030.01.26.

Kogarko, L.N., 1990. Ore-forming potential of alkaline magmas. Lithos 26, 167-175. http://dx.doi.org/10.1016/0024-4937(90)90046-4.

Kogarko, L.N., Lahaye, Y., Brey, G.P., 2010. Plume-related mantle source of super-large rare metal deposits from the Lovozero and Khibina massifs on the Kola Peninsula, Eastern part of Baltic Shield: Sr, Nd and Hf isotope systematics. Mineralogy and Petrology 98, 197-208. http://dx.doi.org/10.1007/s00710-009-0066-1.

Kogarko, L.N., Ryabchikov, I.D., 2013. Diamond potential versus oxygen regime of carbonatites. Petrology 21, 316-335. http://dx.doi.org/10.1134/S0869591113040048.

Kraml, M., Pik, R., Rahn, M., Selbekk, R., Carignan, J., Keller, J., 2006. A New Multi-Mineral Age Reference Material for 40Ar/39Ar,(U-Th)/He and Fission Track Dating Methods: The Limberg t3 Tuff. Geostandards and Geoanalytical Research 30, 73-86. http://dx.doi.org/10.1111/j.1751-908X.2006.tb00914.x.

Kramm, U., Kogarko, L.N., 1994. Nd and Sr isotope signatures of the Khibina and Lovozero agpaitic centres, Kola Alkaline province, Russia. Lithos 32, 225-242. http://dx.doi.org/10.1016/0024-4937(94)90041-8.

Krasnova, N., Balaganskaya, E., Garcia, D., 2004a. Kovdor—classic phoscorites and carbonatites. Phoscorites and Carbonatites from Mantle to Mine: the Key Example of the Kola Alkaline Province. Mineralogical Society, London, 99-132.

Krasnova, N., Petrov, T., Balaganskaya, E., Garcia, D., Moutte, J., Zaitsev, A., Wall, F., 2004b. Introduction to phoscorites: occurrence, composition, nomenclature and petrogenesis. Phoscorites and Carbonatites from Mantle to Mine: the Key Example of the Kola Alkaline Province", eds. F. Wall and AN Zaitev, The Mineralogical Society of Great Britain and Ireland, London, 45-74.

Le Gall, B., Nonnotte, P., Rolet, J., Benoit, M., Guillou, H., Mousseau-Nonnotte, M., Albaric, J., Deverchère, J., 2008. Rift propagation at craton margin.: Distribution of faulting and volcanism in the North Tanzanian Divergence (East Africa) during Neogene times. Tectonophysics 448, 1-19. http://dx.doi.org/10.1016/j.tecto.2007.11.005.

Le Maitre, R., Streckeisen, A., Zanettin, B., Le Bas, M., Bonin, B., Bateman, P., Bellieni, G., Dudek, A., Efremova, A., Keller, J., 2002. Igneous rocks. A classification and glossary of terms. Recommendations of the IUGS Subcomission on the Systematics of Igneous Rocks. Cambridge University Press, Cambridge.

Leakey, M.D., Hay, R.L., 1979. Pliocene footprints in the Laetolil Beds at Laetoli, northern Tanzania. Nature 278, 317-323. http://dx.doi.org/10.1038/278317a0.

Lee, M., Garcia, D., Moutte, J., Williams, C., Wall, F., 2004. Carbonatites and phoscorites from the Sokli Complex, Finland. Phoscorites and Carbonatites from Mantle to Mine: the Key Example of the Kola Alkaline Province", eds. F. Wall and AN Zaitev, The Mineralogical Society of Great Britain and Ireland, London, 133-162.

Lee, M.J., Garcia, D., Moutte, J., Lee, J.I., 2003. Phlogopite and tetraferriphlogopite from phoscorite and carbonatite associations in the Sokli massif, Northern Finland. Geosciences Journal 7, 9-20. http://dx.doi.org/10.1007/Bf02910260.

Lee, M.J., Lee, J.I., Garcia, D., Moutte, J., Williams, C.T., Wall, F., Kim, Y., 2006. Pyrochlore chemistry from the Sokli phoscorite-carbonatite complex, Finland:

Implications for the genesis of phoscorite and carbonatite association. Geochemical Journal 40, 1-13. http://dx.doi.org/10.2343/geochemj.40.1.

Lee, W.-J., Fanelli, M., Cava, N., Wyllie, P., 2000. Calciocarbonatite and magnesiocarbonatite rocks and magmas represented in the system CaO-MgO-CO 2-H 2 O at 0.2 GPa. Mineralogy and Petrology 68, 225-256. http://dx.doi.org/10.1007/s007100050011.

Lee, W.-j., Wyllie, P.J., 1994. Experimental Data Bearing on Liquid Immiscibility, Crystal Fractionation, and the Origin of Calciocarbonatites and Natrocarbonatites. International Geology Review 36, 797-819. http://dx.doi.org/10.1080/00206819409465489.

Lee, W.-J., Wyllie, P.J., 1998. Processes of Crustal Carbonatite Formation by Liquid Immiscibility and Differentiation, Elucidated by Model Systems. Journal of Petrology 39, 2005-2013. http://dx.doi.org/10.1093/petroj/39.11-12.2005.

Leeman, W., Sisson, V., 1996. Geochemistry of boron and its implications for crustal and mantle processes. Boron: mineralogy, petrology and geochemistry. Rev. Mineral. 33, 645-708.

Liebscher, A., Heinrich, C.A., 2007. Fluid-fluid interactions. Walter de Gruyter GmbH & Co KG.

Linnen, R.L., Keppler, H., 2002. Melt composition control of Zr/Hf fractionation in magmatic processes. Geochimica et Cosmochimica Acta 66, 3293-3301. http://dx.doi.org/10.1016/S0016-7037(02)00924-9.

Macintyre, R.M., Mitchell, J.G., Dawson, J.B., 1974. Age of Fault Movements in Tanzanian Sector of East African Rift System. Nature 247, 354-356. http://dx.doi.org/10.1038/247354a0.

Mahood, G.A., 1984. Pyroclastic rocks and calderas associated with strongly peralkaline magmatism. Journal of Geophysical Research: Solid Earth 89, 8540-8552. http://dx.doi.org/10.1029/JB089iB10p08540.

Mallmann, G., O'Neill, H.S.C., 2007. The effect of oxygen fugacity on the partitioning of Re between crystals and silicate melt during mantle melting. Geochimica et Cosmochimica Acta 71, 2837-2857. http://dx.doi.org/10.1016/j.gca.2007.03.028.

Mallmann, G., O'Neill, H.S.C., 2009. The Crystal/Melt Partitioning of V during Mantle Melting as a Function of Oxygen Fugacity Compared with some other Elements (Al, P, Ca, Sc, Ti, Cr, Fe, Ga, Y, Zr and Nb). Journal of Petrology 50, 1765-1794. http://dx.doi.org/10.1093/petrology/egp053.

Mana, S., 2013. Magmatic evolution of the north Tanzanian divergence zone, east African rift system. Rutgers The State University of New Jersey-New Brunswick, p. 138.

Mana, S., Furman, T., Turrin, B.D., Feigenson, M.D., Swisher, C.C., III, 2015. Magmatic activity across the East African North Tanzanian Divergence Zone. Journal of the Geological Society 172, 368-389. http://dx.doi.org/10.1144/jgs2014-072.

Markl, G., Marks, M., Schwinn, G., Sommer, H., 2001. Phase Equilibrium Constraints on Intensive Crystallization Parameters of the Ilímaussaq Complex, South Greenland. Journal of Petrology 42, 2231-2257. http://dx.doi.org/10.1093/petrology/42.12.2231.

Markl, G., Marks, M.A.W., Frost, B.R., 2010. On the Controls of Oxygen Fugacity in the Generation and Crystallization of Peralkaline Melts. Journal of Petrology 51, 1831-1847. http://dx.doi.org/10.1093/petrology/egq040.

Marks, M.A., Schilling, J., Coulson, I.M., Wenzel, T., Markl, G., 2008. The alkaline–peralkaline Tamazeght complex, High Atlas Mountains, Morocco: mineral chemistry and petrological constraints for derivation from a compositionally heterogeneous mantle source. Journal of Petrology 49, 1097-1131. http://dx.doi.org/10.1093/petrology/egn019.

Marks, M.A.W., Hettmann, K., Schilling, J., Frost, B.R., Markl, G., 2011. The Mineralogical Diversity of Alkaline Igneous Rocks: Critical Factors for the Transition from Miaskitic to Agpaitic Phase Assemblages. Journal of Petrology 52, 439-455. http://dx.doi.org/10.1093/petrology/egq086.

Marks, M.A.W., Markl, G., 2015. The Ilímaussaq Alkaline Complex, South Greenland, in: Charlier, B., Namur, O., Latypov, R., Tegner, C. (Eds.), Layered Intrusions. Springer Netherlands, Dordrecht, pp. 649-691.

Marks, M.A.W., Markl, G., 2017. A global review on agpaitic rocks. Earth-Science Reviews 173, 229-258. http://dx.doi.org/10.1016/j.earscirev.2017.06.002.

Martin, A.M., Medard, E., Righter, K., Lanzirotti, A., 2017. Intraplate mantle oxidation by volatile-rich silicic magmas. Lithos 292, 320-333. http://dx.doi.org/10.1016/j.lithos.2017.09.002.

Martin, H., Bonin, B., Capdevila, R., Jahn, B.M., Lameyre, J., Wang, Y., 1994. The Kuiqi Peralkaline Granitic Complex (SE China): Petrology and Geochemistry. Journal of Petrology 35, 983-1015. http://dx.doi.org/10.1093/petrology/35.4.983.

Metrich, N., Rutherford, M.J., 1992. Experimental study of chlorine behavior in hydrous silicic melts. Geochimica et Cosmochimica Acta 56, 607-616. http://dx.doi.org/10.1016/0016-7037(92)90085-W.

Milani, L., Bolhar, R., Cawthorn, R.G., Frei, D., 2016. In situ LA–ICP-MS and EPMA trace element characterization of Fe–Ti oxides from the phoscorite–carbonatite association at Phalaborwa, South Africa. Mineralium Deposita 52, 747-768. http://dx.doi.org/10.1007/s00126-016-0696-2.

Mitchell, R.H., 2005. Carbonatites and carbonatites and carbonatites. Can Mineral 43, 2049-2068. http://dx.doi.org/10.2113/gscanmin.43.6.2049.

Mollel, G.F., 2007. Petrochemistry and geochronology of Ngorongoro volcanic highland complex (NVHC) and its relationship to Laetoli and Olduvai Gorge, Tanzania. Rutgers University-Graduate School-New Brunswick.

Mollel, G.F., Swisher, C.C., Feigenson, M.D., Carr, M.J., 2011. Petrology, Geochemistry and Age of Satiman, Lemagurut and Oldeani: Sources of the Volcanic Deposits of the Laetoli Area, in: Harrison, T. (Ed.), Paleontology and Geology of Laetoli: Human Evolution in Context: Volume 1: Geology, Geochronology, Paleoecology and Paleoenvironment. Springer Netherlands, Dordrecht, pp. 99-119.

Mysen, B.O., Eggler, D.H., Seitz, M.G., Holloway, J.R., 1976. Carbon-Dioxide in Silicate Melts and Crystals .1. Solubility Measurements. American Journal of Science 276, 455-479. http://dx.doi.org/DOI 10.2475/ajs.276.4.455.

Neave, D.A., Putirka, K.D., 2017. A new clinopyroxene-liquid barometer, and implications for magma storage pressures under Icelandic rift zones. American Mineralogist 102, 777-794. http://dx.doi.org/10.2138/am-2017-5968.

Nicholls, I.A., Harris, K.L., 1980. Experimental Rare-Earth Element Partition-Coefficients for Garnet, Clinopyroxene and Amphibole Coexisting with Andesitic and Basaltic Liquids. Geochimica Et Cosmochimica Acta 44, 287-308. http://dx.doi.org/Doi 10.1016/0016-7037(80)90138-6.

Novak, S.W., Mahood, G.A., 1986. Rise and fall of a basalt-trachyte-rhyolite magma system at the Kane Springs Wash Caldera, Nevada. Contributions to Mineralogy and Petrology 94, 352-373. http://dx.doi.org/10.1007/BF00371444.

Pekov, I., Ekimenkova, I., Chukanov, N., RASTSVE-TAEVA, R., Kononkova, N., Pekova, N., Zadov, A., 2001. Feklichevite Na11Ca9 (Fe3+, Fe2+) 2Zr3Nb [Si25O73](OH, H2O, Cl, O) 5, a new mineral of the eudialyte group from the Kovdor Massif, Kola Peninsula. Zap. Vser. Mineral. Obshchest 130, 55-65.

Petrovsky, M.N., Savchenko, E.A., Kalachev, V.Y., 2012. Formation of eudialyte-bearing phonolite from Kontozero carbonatite paleovolcano, Kola Peninsula. Geology of Ore Deposits 54, 540-556. http://dx.doi.org/10.1134/S1075701512070057.

Prodehl, C., Fuchs, K., Mechie, J., 1997. Seismic-refraction studies of the Afro-Arabian rift system — a brief review. Tectonophysics 278, 1-13. http://dx.doi.org/10.1016/S0040-1951(97)00091-7.

Prowatke, S., Klemme, S., 2005. Effect of melt composition on the partitioning of trace elements between titanite and silicate melt. Geochimica Et Cosmochimica Acta 69, 695-709. http://dx.doi.org/10.1016/j.gca.2004.06.037.

Rankin, A., 1975. Fluid inclusion studies in apatite from carbonatites of the Wasaki area of western Kenya. Lithos 8, 123-136. http://dx.doi.org/10.1016/0024-4937(75)90020-1.

Reguir, E.P., Chakhmouradian, A.R., Halden, N.M., Malkovets, V.G., Yang, P., 2009. Major- and trace-element compositional variation of phlogopite from kimberlites and carbonatites as a petrogenetic indicator. Lithos 112, 372-384. http://dx.doi.org/10.1016/j.lithos.2009.05.023.

Ridolfi, F., Renzulli, A., 2012. Calcic amphiboles in calc-alkaline and alkaline magmas: thermobarometric and chemometric empirical equations valid up to 1,130° C and 2.2 GPa. Contributions to Mineralogy and Petrology 163, 877-895. http://dx.doi.org/10.1007/s00410-011-0704-6.

Rimskaya-Korsakova, O., Krasnova, N., 2002. Geology of the deposits of Kovdor massif. St. Petersburg State University, St. Petersburg, Russia.

Robie, R.A., Hemingway, B.S., 1995. Thermodynamic properties of minerals and related substances at 298.15 K and 1 bar (105 Pascals) pressure and at higher temperatures. US Government Printing Office, Washington.

Rohrbach, A., Schmidt, M.W., 2011. Redox freezing and melting in the Earth's deep mantle resulting from carbon–iron redox coupling. Nature 472, 209-212. http://dx.doi.org/10.1038/nature09899.

Rudnick, R., McDonough, W.F., Orpin, A., 1994a. Northern Tanzanian peridotite xenolith: a comparison with Kaapvaal peridotites and evidence for carbonatite interaction with ultra-refractory residues, Proc. 5th Int'l Kimberlite conference. CPRM, pp. 336-353.

Rudnick, R., McDonough, W.F., Orpin, A.R., 1994b. Northern Tanzanian peridotite xenolith: a comparison with Kaapvaal peridotites and evidence for carbonatite interaction with ultra-refractory residues, Proc. 5th Int'l Kimberlite conference. CPRM, pp. 336-353.

Rudnick, R.L., Mcdonough, W.F., Chappell, B.W., 1993. Carbonatite Metasomatism in the Northern Tanzanian Mantle - Petrographic and Geochemical Characteristics. Earth and Planetary Science Letters 114, 463-475. http://dx.doi.org/10.1016/0012-821x(93)90076-L.

Russell, H., 1954. The mineralogy and petrology of the carbonatite at Loolekop, Eastern Transvaal. South African Journal of Geology 57, 197-208.

Scaillet, B., Macdonald, R.A.Y., 2001. Phase Relations of Peralkaline Silicic Magmas and Petrogenetic Implications. Journal of Petrology 42, 825-845. http://dx.doi.org/10.1093/petrology/42.4.825.

Schilling, J., Wu, F.-Y., McCammon, C., Wenzel, T., Marks, M., Pfaff, K., Jacob, D., Markl, G., 2011. The compositional variability of eudialyte-group minerals. Mineralogical Magazine 75, 87-115. http://dx.doi.org/10.1180/minmag.2011.075.1.87.

Schleicher, H., Baumann, A., Keller, J., 1991. Pb Isotopic Systematics of Alkaline Volcanic-Rocks and Carbonatites from the Kaiserstuhl, Upper Rhine Rift-Valley, Frg. Chemical Geology 93, 231-243. http://dx.doi.org/10.1016/0009-2541(91)90116-9.

Schleicher, H., Keller, J., Kramm, U., 1990. Isotope Studies on Alkaline Volcanics and Carbonatites from the Kaiserstuhl, Federal-Republic-of-Germany. Lithos 26, 21-35. http://dx.doi.org/10.1016/0024-4937(90)90038-3.

Sissingh, W., 1998. Comparative Tertiary stratigraphy of the Rhine Graben, Bresse Graben and Molasse Basin: correlation of Alpine foreland events. Tectonophysics 300, 249-284. http://dx.doi.org/10.1016/S0040-1951(98)00243-1.

Smith, M., 1994. Stratigraphic and structural constraints on mechanisms of active rifting in the Gregory Rift, Kenya. Tectonophysics 236, 3-22. http://dx.doi.org/10.1016/0040-1951(94)90166-X.

Smith, M.P., Moore, K., Kavecsánszki, D., Finch, A.A., Kynicky, J., Wall, F., 2016. From mantle to critical zone: A review of large and giant sized deposits of the rare earth elements. Geoscience Frontiers 7, 315-334. http://dx.doi.org/10.1016/j.gsf.2015.12.006.

Sokolov, S.V., 2014. The formation conditions of labuntsovite-group minerals in the Kovdor massif, Kola Peninsula. Geology of Ore Deposits 56, 671-674. http://dx.doi.org/10.1134/S1075701514080108.

Sørensen, H., 1992. Agpaitic nepheline syenites: a potential source of rare elements. Applied Geochemistry 7, 417-427. http://dx.doi.org/10.1016/0883-2927(92)90003-L.

Sørensen, H., 1997. The agpaitic rocks− an overview. Mineralogical Magazine 61, 485-498. http://dx.doi.org/10.1180/minmag.1997.061.407.02.

Spandler, C., Morris, C., 2016. Geology and genesis of the Toongi rare metal (Zr, Hf, Nb, Ta, Y and REE) deposit, NSW, Australia, and implications for rare metal mineralization in peralkaline igneous rocks. Contributions to Mineralogy and Petrology 171, 104. http://dx.doi.org/10.1007/s00410-016-1316-y.

Stagno, V., 2019. Carbon, carbides, carbonates and carbonatitic melts in the Earth's interior. Journal of the Geological Society, jgs2018-2095. http://dx.doi.org/10.1144/jgs2018-095.

Thompson, R.N., Chisholm, J.E., 1969. Synthesis of aenigmatite. Mineralogical Magazine 37, 253-255. http://dx.doi.org/10.1180/minmag.1969.037.286.15.

Treiman, A.H., Essene, E.J., 1984. A Periclase-Dolomite-Calcite Carbonatite from the Oka Complex, Quebec, and Its Calculated Volatile Composition. Contributions to Mineralogy and Petrology 85, 149-157. http://dx.doi.org/10.1007/Bf00371705.

Uenver-Thiele, L., Woodland, A.B., Seitz, H.-M., Downes, H., Altherr, R., 2017. Metasomatic Processes Revealed by Trace Element and Redox Signatures of the Lithospheric Mantle Beneath the Massif Central, France. Journal of Petrology 58, 395-422. http://dx.doi.org/10.1093/petrology/egx020.

Ulianov, A., Muntener, O., Ulmer, P., Pettke, T., 2007. Entrained macrocryst minerals as a key to the source region of olivine nephelinites: Humberg, Kaiserstuhl, Germany. Journal of Petrology 48, 1079-1118. http://dx.doi.org/10.1093/petrology/egm011.

Upton, B.G.J., Emeleus, C.H., Heaman, L.M., Goodenough, K.M., Finch, A.A., 2003. Magmatism of the mid-Proterozoic Gardar Province, South Greenland: chronology, petrogenesis and geological setting. Lithos 68, 43-65. http://dx.doi.org/10.1016/S0024-4937(03)00030-6.

Vuorinen, J.H., Skelton, A.D.L., 2004. Origin of silicate minerals in carbonatites from Alnö Island, Sweden: magmatic crystallization or wall rock assimilation? Terra Nova 16, 210-215. http://dx.doi.org/10.1111/j.1365-3121.2004.00557.x.

Wallace, M.E., Green, D.H., 1988. An Experimental-Determination of Primary Carbonatite Magma Composition. Nature 335, 343-346. http://dx.doi.org/10.1038/335343a0.

Wang, K., Plank, T., Walker, J.D., Smith, E.I., 2002. A mantle melting profile across the Basin and Range, SW USA. Journal of Geophysical Research: Solid Earth 107, ECV 5-1-ECV 5-21. http://dx.doi.org/10.1029/2001JB000209.

Watson, E.B., 1979. Zircon saturation in felsic liquids: Experimental results and applications to trace element geochemistry. Contributions to Mineralogy and Petrology 70, 407-419. http://dx.doi.org/10.1007/BF00371047.

Weaver, B.L., 1991. The origin of ocean island basalt end-member compositions: trace element and isotopic constraints. Earth and Planetary Science Letters 104, 381-397. http://dx.doi.org/10.1016/0012-821X(91)90217-6.

Weidendorfer, D., Schmidt, M.W., Mattsson, H.B., 2017. A common origin of carbonatite magmas. Geology 45, 507-510. http://dx.doi.org/10.1130/G38801.1.

Wilson, M., Downes, H., 1991. Tertiary—Quaternary extension-related alkaline magmatism in western and central Europe. Journal of Petrology 32, 811-849. http://dx.doi.org/10.1093/petrology/32.4.811.

Wilson, M., Downes, H., 1992. Mafic Alkaline Magmatism Associated with the European Cenozoic Rift System. Tectonophysics 208, 173-182. http://dx.doi.org/10.1016/0040-1951(92)90343-5.

Wilson, M., Rosenbaum, J.M., Dunworth, E.A., 1995. Melilitites: partial melts of the thermal boundary layer? Contributions to Mineralogy and Petrology 119, 181-196. http://dx.doi.org/10.1007/BF00307280.

Wimmenauer, W., 1952. Petrographische Untersuchungen an einigen basischen Eruptivgesteinen des Oberrheingebietes. N. Jb. Miner. 83, 375-432.

Woodland, A.B., Kornprobst, J., McPherson, E., Bodinier, J.L., Menzies, M.A., 1996. Metasomatic interactions in the lithospheric mantle: Petrologic evidence from the Lherz massif, French Pyrenees. Chemical Geology 134, 83-112. http://dx.doi.org/10.1016/S0009-2541(96)00082-4.

Wooley, A., 1987. Alkaline rocks and carbonatites of the world, part 1: North and South America. University of Texas Press and British Museum of National History, Austin and London.

Woolley, A.R., 2001. Alkaline rocks and carbonatites of the world: Africa. Geological Society of London, p. 372.

Woolley, A.R., 2019. Alkaline Rocks and Carbonatites of the World, Part 4: Antarctica, Asia and Europe (excluding the former USSR), Australasia and Oceanic Islands. Geological Society of London, London.

Woolley, A.R., Kjarsgaard, B.A., 2008. Carbonatite occurrences of the world: map and database. Geological Survey of Canada, p. 28. http://dx.doi.org/10.4095/225115.

Wyllie, P.J., Baker, M.B., White, B.S., 1990. Experimental Boundaries for the Origin and Evolution of Carbonatites. Lithos 26, 3-19. http://dx.doi.org/Doi 10.1016/0024-4937(90)90037-2.

Yaxley, G.M., Brey, G.P., 2004. Phase relations of carbonate-bearing eclogite assemblages from 2.5 to 5.5 GPa: implications for petrogenesis of carbonatites. Contributions to Mineralogy and Petrology 146, 606-619. http://dx.doi.org/10.1007/s00410-003-0517-3.

Yaxley, G.M., Ghosh, S., Kiseeva, E.S., Mallik, A., Spandler, C., Thomson, A.R., Walter, M.J., 2019. CO2-rich melts in Earth, Deep Carbon: Past to Present. Cambridge University Press.

Ying, J., Zhou, X., Zhang, H., 2004. Geochemical and isotopic investigation of the Laiwu–Zibo carbonatites from western Shandong Province, China, and implications for their petrogenesis and enriched mantle source. Lithos 75, 413-426.

Zaitsev, A.N., Marks, M.A.W., Wenzel, T., Spratt, J., Sharygin, V.V., Strekopytov, S., Markl, G., 2012. Mineralogy, geochemistry and petrology of the phonolitic to nephelinitic Sadiman volcano, Crater Highlands, Tanzania. Lithos 152, 66-83. http://dx.doi.org/10.1016/j.lithos.2012.03.001.

Ziegler, P.A., 1982. Triassic rifts and facies patterns in Western and Central Europe. Geologische Rundschau 71, 747-772. http://dx.doi.org/10.1007/BF01821101.

# Appendix I

Submitted manuscript

*Study 1*

Zaitsev, A. N., Arzamastsev, A. A., Marks, M. A. W., Braunger S., Wenzel, T., Spratt, J., Salge, T., and Markl, G., submitted. Multiple sources for basaltic volcanism in Laetoli area (Crater Highlands, Tanzania): evidence from mineralogy and geochemistry of the Ogol lavas. Journal of Petrology.

# Multiple sources for basaltic volcanism in Laetoli area (Crater Highlands, Tanzania): evidence from mineralogy and geochemistry of the Ogol lavas

Antoly N. Zaitsev[1,2*], Andrei A. Arzamastsev[3,4], Michael A.W. Marks[5], Simon Braunger[5], Thomas Wenzel[5], John Spratt[2], Tobias Salge[2] and Gregor Markl[5]

[1]Department of Mineralogy, St. Petersburg State University, University Emb. 7/9, St. Petersburg, 199034, Russia; [2]Imaging and Analysis Centre, Department of Earth Sciences, Natural History Museum, Cromwell Road, London, SW7 5BD, UK; [3]Department of Petrography, St. Petersburg State University, University Emb. 7/9, St. Petersburg, 199034, Russia; [4]Institute of Precambrian Geology and Geochronology, Russian Academy of Sciences, Makarova Emb. 2, St. Petersburg, 199034, Russia; [5]Universität Tübingen, Mathematisch-Naturwissenschaftliche Fakultät, FB Geowissenschaften, Wilhelmstrasse 56, D-72074 Tübingen, Germany

*Corresponding author. E-mail: a.zaitsev@spbu.ru

Running title: Ogol basalts

## ABSTRACT

The southern part of the eastern branch of the East African Rift is characterized by extensive magmatism since the late Miocene. In the Crater Highlands, part of the North Tanzanian Divergence zone, effusive and pyroclastic rocks reflect nephelinitic and basaltic compositions that formed between 4.6 and 0.8 Ma. The former are best represented by the Sadiman volcano (4.6-4.0 Ma) and the latter occur in the giant Ngorongoro crater (2.3-2.0 Ma), the Lemagarut volcano (2.4-2.2 Ma) and as a small volcanic field in the Laetoli area (2.3 Ma), where basaltic rocks known as Ogol lavas were erupted through fissures and several cinder cones. Compositionally, they are alkaline basalts with 46.0-47.9 wt % $SiO_2$, 3.0-4.3 wt % of $Na_2O+K_2O$, Mg# of 61 to 55, and high Cr and Ni content (450-975 and 165-222 ppm respectively). A detailed textural and compositional analysis of the major minerals (olivine, clinopyroxene, spinel-group minerals, plagioclase) in the rocks reveals their heterogeneity. Most samples contain appreciable proportions of xenocrystic minerals, with large variations between samples. The primary mineral assemblage that crystallized from the Ogol magmas comprises forsterite ($Fo_{89.5-84.2}$), Cr-bearing diopside to augite, magnesiochromite-chromite, magnetite-ulvöspinel, andesine-oligoclase and apatite, with glass of phonolitic composition in the groundmass. Xenocrysts that derive from distinct sources include forsterite ($Fo_{84.1-72.5}$) with reverse zonation, rounded and embayed clinopyroxene cores of variable composition (at least four different populations), Cr-free magnetite-ulvöspinel and oligoclase. These xenocrysts as well as observed variations in major and trace element contents, variable $^{87}Sr/^{86}Sr_{(i)}$ (0.70377-0.70470) and $^{143}Nd/^{144}Nd_{(i)}$ (0.51246-0.51261) isotopic ratios provide evidence of multi-stage magma mixing between Ogol and Lemagarut basaltic melts. Elevated alkalinity, which positively correlates with isotope ratios and the presence of xenocrystic perovskite and schorlomite, indicate additional mixing with alkaline melts and/or assimilation of alkaline rocks (related to the Sadiman volcano and/or the Laetolil tuffs). Contamination by crustal granite-gneisses did not exceed 5 %. Due to their heterogeneity, estimates on the crystallization conditions for the Ogol rocks are difficult. Nevertheless, clinopyroxene-liquid thermobarometry indicates crystallization temperatures of around 1150-1220 °C and records upper-crustal depths of 3-12 km (1-4 kbar). Despite the fact that Ogol basalts

46 are hybrid rocks that formed under open-system conditions, they seems to be the best examples of near-
47 primary basaltic melts within the Crater Highlands.
48
49 **Key words:** basalt; Crater Highlands; Laetoli; magma mixing; xenocryst
50
51 **INTRODUCTION**
52
53 The eastern branch of the East African Rift (EAR) that opened along the border of Tanzanian craton is
54 known as a region of intense magmatism developed since the late Miocene to Recent. Numerous
55 volcanic centers in the North Tanzanian Divergence zone (NTD; Fig. 1; Baker *et al.,* 1972) produced a
56 wide variety of lavas and pyroclastic rocks ranging in composition from undersaturated peralkaline
57 rocks and carbonatites to subalkaline basalts. Models for the structure of the NTD and the sequence of
58 magmatic events directly depend on the accuracy of geochronological data, most of which were obtained
59 in the 1960s and 1970s using low-precision methods, e.g. whole-rock K-Ar data (reviewed in Dawson,
60 2008). Recent $^{40}Ar/^{39}Ar$ ages allow to decipher the mixture of undersaturated peralkaline and basic rocks
61 forming eruptive centers of different age and discriminate distinct pulses of igneous activity in the NTD
62 (Mollel, 2007; Nonnotte *et al.,* 2008; Mana *et al.,* 2012, 2015; Peirce & Mana, 2018).
63 The main source of magmatism in the NTD area is probably the metasomatized subcontinental
64 lithospheric mantle (Mana *et al.,* 2015), but the composition of potential primary magmas remains
65 unclear. Recent nephelinite-phonolite volcanic activity, which produced several centers along the axis
66 of Gregory rift in Lake Natron - Engaruka area may relate to olivine melilitite primary melts (Keller *et*
67 *al.,* 2006), However, the basalt-trachybasalt-trachyandesite-trachyte series documented from
68 Lemagarut, Ngorongoro and Oldeani volcanoes and the Olduvai Gorge can not be easily explained by
69 fractionation of such parental melts. Basaltic rocks known as Ogol lavas, forming lava flows in the
70 Laetoli area, 30 km west of the Ngorongoro caldera (Mollel, 2007), have characteristics that allow them
71 to be classified as primary magmas of basalt-trachyte series. In the present study we use the
72 geochemistry and mineralogy of a suite of mafic Ogol lavas to constrain their origin, their depth of
73 melting and source region character. We integrate these results with evolutionary paths of basalt-trachyte

series in adjacent volcanoes and evaluate the role of possible crustal contamination and magma mixing.

## GEOLOGICAL SETTING

### Regional geology

The Crater Highlands and adjacent Gregory Rift are parts of a much larger volcanic province, extending from the Afar triple junction southwards to the Mozambique margin along the western and eastern borders of the Tanzanian Craton, including numerous complexes in Ethiopia, Kenya and Tanzania. In the NTD zone in the southern end of the southerly-propagating eastern branch of the EAR system, the distribution of volcanoes is controlled by lineaments and faults along the boundary of the Neoarchean Tanzanian Craton and the Proterozoic Mozambique belt (Smith, 1994) (Fig. 1).

The earliest manifestation of volcanic activity is represented by an alkali picrite-nephelinite-phonolite series from Essimingor volcano dated to 5.91±0.02 Ma (Mana *et al.,* 2012). Further alkaline magma eruptions throughout the NTD zone formed Sadiman, Mosonik, Engelosin, Tarosero and other minor centers ranging in age from 4.6 to 2.3 Ma (Dawson, 2008). Silica undersaturated alkaline magma eruptions were replaced and superimposed by Lemagarut, Ngorongoro, Monduli, Olduvai, Olmoti, Oldeani volcanoes, calderas and minor centers in which basalts and basanites are the predominant rock types. Vast basalt lava beds spread along the southern end of Gregory Rift in the Engaruka-Manyara area.

Based on $^{40}Ar/^{39}Ar$ age determinations basaltic magmatism lasted from 2.4 Ma to 1.6 Ma (Manega, 1993; Foster *et al.,* 1997; Mollel, 2007). Since 1.3 Ma renewal of magmatism was marked by ongoing activity in the axial part of NTD, and its lateral eastward spreading. Alkaline rocks ranging in composition from primitive olivine melilitite to highly evolved phonolite, sporadically associated with carbonatite form the Embagai, Burko, Kerimasi, Meru, and Oldoinyo Lengai volcanoes and numerous minor craters and cones in the Lake Natron-Engaruka area (Dawson, 2008; Mattsson *et al.,* 2013).

In multiphase volcanic centers, such as Kilimanjaro and Ketumbeine, early mafic magmatism started at 2.2 Ma (simultaneously with Ngorongoro and other basaltic centers) followed by phonolitic eruptions dated to 1.3 and 0.5 Ma, respectively (Nonnotte *et al.,* 2008; Peirce & Mana, 2018). A recent

study (Mana *et al.,* 2015) provides evidence of consistent younging of NTD magmatism along two main trends: one from west to east (Essimingor to Kilimanjaro) and another from SW to NE (Sadiman to Gelai).

**Crater Highlands**

The Crater Highlands comprise numerous eruptive centers in a 100 km-long elevated area between lakes Natron and Eyasi at the southern termination of the eastern branch of the EAR (Fig. 2). Seismic tomography reveals a thick mantle keel (exceeding 200 km) beneath the craton (Ritsema *et al.,* 1998; Adams *et al.,* 2012), considerably thicker than the lithosphere beneath the Eastern Rift north of Lake Natron, which is less than 100 km thick (Birt *et al.,* 1997). Although the contact between Archaean and Late Proterozoic crust is west of the Crater Highlands, outcrops of gneissic-granitic basement indicate that Archaean lithosphere underlies much of this rift sector. Recent local magnetotelluric and tomography studies (Plasman *et al.,* 2019) indicate the presence of a melt accumulation zone at 40 km depth below the Crater Highlands, potentially connected to the volcanic edifices at the surface. The Eyasi fault system, which delimits the westward distribution of magmatism in upland area, is interpreted as a narrow vertical conduit linking the surface to a deeper conductive structure between two large basement terrains (Plasman *et al.,* 2019).

The earliest volcanic activity, beginning at 4.63±0.05 Ma (Mollel *et al.,* 2011), produced large volumes of interlayered phonolitic tuffs, tuff breccias and nephelinitic lava flows erupted from Sadiman volcano (Zaitsev *et al.,* 2011; 2012). Superimposed tuffs west of Sadiman, in particular the Laetolil Footprint Tuff, where 3.66 Ma *Australopithecus afarensis* footprints were discovered (Leakey & Hay, 1979), may have been erupted from Mosonik volcano (Zaitsev *et al.,* 2015; 2019). Since about 2.4 Ma, mafic magmatism predominates in the Crater Highlands. Eruptions from the Lemagarut volcano occurred between 2.40±0.01 Ma and 2.22±0.10 Ma and the giant Ngorongoro volcano was active between 2.25±0.02 Ma to 2.01±0.02 Ma (Mollel *et al.,* 2008; 2011), erupting basalts, basanites and their evolved derivatives (trachyandesite, trachydacite and trachyte). The youngest manifestations of mafic magmatism is represented by the Oldeani volcano which was active between 1.61±0.01 Ma and 1.52±0.02 Ma (Mollel, 2007).

**Ogol lavas**

Basaltic lavas (local name Ogol lavas) erupted through fissures and cinder cones ranging from 0.5 to 1.5 km in diameter and 50 to 150 m in height (Hay, 1987; Supplementary Data Fig. S1). The major localities (as named on Quarter degree sheet 52 Endulen; Pickering, 1964) are Oldoinyo Mati (Ndonyamati), Oldoinyo Emusenge (Norsigidok), Oldoinyo Ildolaunya (Ndolanya) and Oldoinyo Naisiusiu hills (Fig. 3). Outcrops with well exposed lava flows are limited, but rounded lava blocks up to 2.5 m in diameter are widespread (Supplementary Data Fig. S1). The Ogol lavas are massive (common) to vesicular (rare), fine- to medium-grained, and have aphanitic (rare) to porphyritic (common) textures. The proportions of phenocrysts (olivine and pyroxene) are highly variable and range from approximately 1 to 30 vol. % (Supplementary Data Fig. S2). The Ogol lavas overlie the Ndolanya (3.58-2.66 Ma) and Laetolil (4.36-3.66 Ma) beds and are partly overlain by the Naibadad beds (2.15-2.06 Ma) (Hay, 1987; Dawson, 2008; Deino, 2011). The eastern part of the flows is superimposed by basalts and basaltic andesites of Lemagarut volcano. Mollel (2007) reported two $^{40}Ar/^{39}Ar$ ages (2.31±0.01 Ma and 2.27±0.05 Ma) collected from the northeast trending Ogol lava flow west of Lemagarut volcano.

Despite their importance for the understanding of basaltic volcanism in the Crater Highlands (Mollel, 2007) as well as in anthropological studies in Laetoli (Adelsberger *et al.,* 2011), the Ogol lavas are poorly studied. They were originally described as vogesites (Hay, 1987) and subsequently classified as basalts (Mg#=49-59) with olivine and augite as phenocrysts, and plagioclase, augite and Ti-rich magnetite as groundmass phases (Mollel, 2007). Although, this study provided high precision ages (see above), geochemical and mineralogical data are limited and incomplete. A more extensive geochemical study was published by Adelsberger *et al.* (2011). Based on whole-rock data, the rocks were classified as basalts and basanites with each one sample of tephrite and picrobasalt. The basaltic and some of the basanitic samples are relatively primitive (Mg# of 55-61) with appreciable Cr (496-1091 ppm) and Ni (188-248 ppm). Three basanitic samples are more evolved, Mg#=47-48, with 297-338 ppm Cr and 77-95 ppm Ni. A picrobasalt is strongly enriched in Fe and depleted in Mg (Mg# of 20) and is low in Cr (32 ppm) and Ni (8 ppm) and unusually high P (2.1 wt % $P_2O_5$).

## SAMPLES AND METHODS

For this study we investigated 15 samples of Ogol lavas and 12 samples of lavas from the western part of the Lemagarut volcano (Fig. 3). Crystalline basement rocks are not exposed in the Laetoli area, but at the Eyasi plateau about 15 km south and south-west from the Laetoli area. We collected 8 samples from basement rocks of the Tanzania craton, comprising granite-gneisses, green and melanocratic schists and garnet amphibolites with an age of about 2.7 Ga (Supplementary Data Table S1; Pickering, 1964; Fletcher *et al.,* 2018).

Mineral identification was based on petrographic studies of polished thin sections (Leica DM 2500P microscope and Hitachi S–3400N scanning electron microscope, St. Petersburg State University) and XRD measurements of powder samples using a Bruker D8 Focus XRD system (St. Petersburg State University).

Whole-rock samples (lavas and basement rocks) were analysed for major and trace elements by X-ray fluorescence (XRF) and inductively coupled plasma mass-spectrometry (ICP-MS) at the Karelian Research Centre RAS (Petrozavodsk). Powders were fused into glass disks using ca. 3 g of sample mixed with lithium tetraborate ($Li_2B_4O_7$). Glass disks were analyzed by XRF using an ARL ADVANT"X X-ray sequential fluorescence spectrometer. Loss on ignition (LOI) was determined gravimetrically. The uncertainties were 1–5% for elements with concentrations of >0.5 wt % and up to 12% for elements with concentrations of <0.5 wt %. The concentrations of trace elements were determined by ICP-MS using an X Series 2 instrument. Powdered samples were digested in acid mixture in open vessels following the standard procedure described by Svetov *et al.* (2015). The accuracy of the analyses was monitored by analyzing USGS reference materials BHVO-2 and BIR-1a, and in-house 1412 and SGD-2a reference materials. Precision is generally < 1% for Sr, Y, Zr, Nb, Cr, Ni, Cu, Zn, V, La, Ce, Pr, Nd; < 3% for Ba, Sr, Rb, Cs, Sc, Co, Sm, Eu, Gd, Tb, Dy, Ho, Er, Hf, Ta, Yb, Lu, Pb Th and U.

Mineral compositions (olivine, clinopyroxene, spinel and plagioclase) were obtained by electron microprobe analysis (wavelength-dispersive X-ray spectrometry mode) using a JEOL 8900 Superprobe (Tübingen University) and Cameca SX-100 (Natural History Museum, London) instruments operated

at same analytical conditions (20 kV, 20 nA with a beam diameter of 1 μm for olivine, clinopyroxene and spinel, and 10 μm for plagioclase). Well-characterized natural and synthetic compounds were used for calibration. Glass compositions were obtained by using a Hitachi S–3400N scanning electron microscope (St. Petersburg State University) equipped with an Oxford Instruments X-Max 20 spectrometer (20 kV, 1.0 nA and defocused beam 10-15 μm in diameter).

The Rb-Sr and Sm-Nd isotopic compositions of the 10 Ogol samples, 3 Lemagarut samples, and 3 basement rocks samples were analysed using a multi-collector TRITON mass-spectrometer operated in static mode (VSEGEI, St. Petersburg). Detailed information on sample preparation and analysis procedure is given in Zaitsev *et al.* (2019).

## WHOLE-ROCK GEOCHEMISTRY

Whole-rock geochemical data for 13 Ogol samples are given in Table 1. The studied samples have relatively low $SiO_2$ (46.0-47.9 wt %) and $Na_2O+K_2O$ (3.0-4.3 wt %) contents, and are rich in MgO (8.8-11.7 wt %), CaO (10.0-12.3 wt %) and $Fe_2O_{3total}$ (13.2-15.5 wt %), with Mg# values (calculated as $100*Mg/(Mg+0.9Fe_{total})$) ranging from 61 to 55. In a Total Alkali vs $SiO_2$ diagram (Le Bas *et al.,* 1986) most Ogol samples plot in the alkaline basalt field (Fig. 4a). For further comparison and discussion, we use published (Nonnotte, 2007; Mollel, 2007; Mollel *et al.,* 2008; Adelsberger *et al.,* 2011) and our unpublished data from adjacent Lemagarut volcano and Ngorongoro caldera that are relevant to evaluating 2.4-2.2 Ma magmatism in the Crater Highlands. Data from the nearby located but older nephelinitic Sadiman volcano (Zaitsev *et al.,* 2012) are also considered as they are important for future discussion on mineralogy of the basalts (see below).

The Ogol basalts are not compositionally uniform, particularly a suite of three samples is high in $TiO_2$ (4.1-4.2 wt %), low in MgO (7.6-8.0 wt %) and low in $SiO_2$ (45.0-45.6 wt %) (Adelsberger *et al.,* 2011). Overall, there are negative correlations between the contents of MgO and $SiO_2$, $Al_2O_3$, $Na_2O$, $K_2O$ and $P_2O_5$ (Fig. 4b, c) and less evident positive correlations of MgO with $Fe_2O_3$ and CaO. The contents of compatible elements, such as Cr and Ni, are variable and high, with 297-1091 ppm and 77-248 ppm, respectively (Fig. 4d). The lowest Cr (297-338 ppm) and Ni (77-95 ppm) contents are observed

in high Ti and low Mg-Si basalt (Adelsberger *et al.,* 2011).

The Ogol lavas are broadly enriched in incompatible trace elements with respect to the primitive mantle and are characterized by slightly positive Ba and Pb anomalies and negative U, K and P anomalies (Fig. 5a), some samples display marked positive Zr and Hf anomalies. The contents of rare earth elements (REE) range from 206 to 276 ppm (Table 1) and there is a tendency of increasing REE content with decreasing MgO. Chondrite-normalized REE patterns are enriched in light REE (LREE) with $(La/Yb)_N$ ratios of 17.8-25.0 and $(La/Lu)_N$ ratios of 20.5-27.2 (Fig. 5b).

Considerable scatter in the major and trace element data of the studied samples argue against simple closed-system fractional crystallization or mixing between two hypothetic endmembers. The reasons for that will be understandable based on the following detailed petrographic descriptions and mineral chemical investigations.

## PETROGRAPHY AND MINERAL CHEMISTRY

The studied Ogol samples are characterized by variable structures, textures and proportions of mineral crystals (Supplementary Data Fig. S2). In this study we prefer not to use the term “pheno- and microphenocrysts”, because, as recent studied showed, phenocrysts in volcanic rocks commonly represent very complex mineral assemblage. They consists of autocrysts (or phenocrysts sensu stricto), primary minerals that are cogenetic with their host rock; antecrysts, crystals that crystallized from the same magmatic system, but have been recycled one or several times before inclusion in the specific sample; microlites, crystallized during magma degassing magma on eruption, and xenocrysts, i.e. these crystals were entrained from other sources (e.g. Jerram & Martin, 2008; Ubide et al., 2014; Shane et al 2019). Therefore, the terms macro- and microcrysts will be used for petrographic description of the Ogol basalts. The only macrocrysts (>500 μm) are olivine and clinopyroxene, with the latter being commonly more abundant (Fig. 6). They are generally 1-3 (rarely up to 5) mm in size, few of them reaching megacrystic size of 9 x 3 mm (olivine) and 9 x 8 mm (clinopyroxene). Microcrysts (100-500 μm) include olivine, clinopyroxene and rare plagioclase and spinel (not spinel s.s., but spinel as a mineral group). Groundmass minerals (<100 μm) are olivine (rare), clinopyroxene, plagioclase and spinel. Textural data

suggest the presence of several populations of olivine, clinopyroxene and spinel. Macro-, microcrysts and groundmass crystals are characterized by different morphologies, zonation patterns, internal structures and compositions.

Mosaic mapping of thin sections and blocks showed that apatite is relatively abundant in the groundmass, and rare pyrhhotite and chalcopyrite occurs as inclusions in clinopyroxene. Previously, these minerals have not been found in the Ogol basalts (Mollel, 2007; Adelsberger *et al.,* 2011). Ilmenite was mentioned by Adelsberger *et al.* (2011) as a groundmass mineral but was not identified in our samples as a primary mineral. As Adelsberger *et al.* (2011) did not describe (abundant) spinel in Ogol basalts, we suggest that they may have mixed up ilmenite with spinel.

The majority of the studied samples show variable degrees of alteration and the most altered samples (A16-24 and A16-25) derive from Oldoinyo Ildolanya hill. Olivine is partly to fully replaced by fine-grained brown hydrous Mg, Fe-rich silicate (not precisely identified); calcite is a common secondary mineral and fills vesicles and forms veins and veinlets. SEM/EDS studies also indicate the presence of a montmorillonite, sodalite, Na-K feldspar and Na (+/-K) zeolite. This mineral assemblage is considered to be a result of glass alteration. Further secondary minerals include Sr-bearing baryte (veinlets and small nests), and rare Ba-bearing celestine, Ba-Mn hydroxide and dolomite (Fig. 6b). Exceptions are two samples from the Oldoinyo Emusenge hill (A16-05 and A16-06) that show only little alteration (Fig. 6a).

**Olivine**

Most olivine macrocrysts (and some of the larger microcrysts) are “hopper crystals” (Fig. 7) but they also occur as euhedral to subhedral crystals, partly showing initial stages of skeletal growth at crystal edges (Fig. 7b, e). Few grains are angular to sub-angular (Fig. 7g, f) and their morphology suggest that they represent fragments of broken crystals, showing a kink-banded texture. The overall compositional range (311 analyses from 10 samples) is $Fo_{89.5}$ to $Fo_{72.5}$ (Table 2, Fig. 8) and based on their internal structures and compositions, we distinguish four forsterite populations with

(1) Normal zonation (Mg-rich core with Fe-rich rim, macro- and rare microcrysts),

(2) Reverse zonation (Fe-rich core with Mg-rich rim, macro- and extremely rare microcrysts),

(3) Repetitive zonation (Fe-rich core, Mg-riched mantle and Fe-rich rim, extremely rare macrocrysts),

(4) No zonation (majority of microcrysts and groundmass crystals, rare crystal fragments of various size).

The proportion between normally and reversely zoned crystals is highly variable. In samples from Oldoinyo Emusenge (A16-05 and A16-06) reversely zoned forsterite is extremely rare, in other samples normally zoned and reversely zoned forsterite occur in similar amounts, and in sample A19-64 reversely zoned forsterite dominates. Forsterite grains showing repetitive zonation are extremely rare, with only two crystals observed in one sample (A19-01). Angular to sub-angular grains (unzoned or with partial rim) are less common, but abundant in a sample from Oldoinyo Naisiusiu (A19-08).

Normally zoned forsterite has a core composition with $Fo_{89.5}$ to $Fo_{84.2}$ with NiO between 0.44 and 0.20 wt %. Both Fo and Ni contents decrease towards the rim with $Fo_{85.9\text{-}80.7}$ and 0.31-0.17 wt % NiO. In reversely zoned forsterite, the cores are variable in composition ($Fo_{72.5}$ to $Fo_{84.1}$; 0.05-0.31 wt % NiO) and their rims are always higher in Fo ($Fo_{80.2\text{-}86.0}$) and NiO (0.18-0.32 wt %). A single forsterite megacryst (sample A19-08) is compositionally similar to the cores in reversely zoned forsterite, but it is normally zoned with a Fo and Ni rich core ($Fo_{79.2\text{-}77.6}$, 0.22-0.17 wt % NiO) and a Fo and Ni depleted rim ($Fo_{77.3\text{-}76.4}$; 0.15-0.14 wt % NiO). Microcrysts and groundmass forsterite has a composition similar to that of rim on forsterite crystals with both zonation types. Aphanitic samples (A19-04a, b and c) contain zoned microcrysts (which are very close to 500 μm size) with a core enriched in both Fo and NiO (e.g. $Fo_{86.6\text{-}85.4}$ and 0.36-0.33 wt % NiO). These values are similar to those from forsterite cores in porphyritic basalt varieties. Two macrocrysts with repetitive zonation contain Fe-enriched core and rim with similar composition ($Fo_{79.0\text{-}80.2}$, 0.07-0.10 wt % NiO) and mantle which is slightly enriched in Mg ($Fo_{82.1\text{-}82.9}$, 0.18-0.23 wt % NiO). Angular to sub-angular forsterite fragments are generally rare, but abundant in one sample (A19-08; Fig. 7h). The composition of these fragments is highly variable ($Fo_{86.3\text{-}75.4}$; 0.32-0.10 wt % NiO). Besides, minor Ca, Mn and traces of Cr were detected (Table 2) with generally high Ca and low Mn in high-Fo olivine and low Ca and high Mn in low-Fo olivine.

**Clinopyroxene**

Clinopyroxene occurs as euhedral to subhedral macro-, microcrysts and groundmass crystals, with a single megacryst (Fig. 9, Supplementary Data Fig. S2). Compared to forsterite, clinopyroxene occurs more often as fragments of broken crystals. Most clinopyroxene grains are colourless, with few crystals containing greenish cores. In some samples microcrysts define a trachytoid texture and rarely they occur as glomerocrysts. Based on variable shapes, zonation patterns, internal structures, and compositions, we distinguish six populations of clinopyroxene. In total 342 spot analyses were obtained from 12 samples. Most analyses indicate diopsidic to augitic compositions, with rarely hedenbergite and aegirine-augite compositions in greenish cores.

Population I (common) is represented by cores of euhedral to subhedral macro- and microcrysts (Fig. 9a, b, d), typically not in optical continuity with the mantle or rim zones. These cores are characterized by a variable morphology (round, oval, embayed) and sometimes show strong resorption at their boundary with the mantle or rim. Their Mg# values (calculated as $100*Mg/(Mg+Fe^{2+})$) and contents of Cr, Al and Ti point to three varieties (Ia, Ib and Ic - Table 3). Variety Ia is augite ($Di_{60-68}Hed_{12-16}others_{19-25}$) with Mg# between 85 and 80, low Cr (always below detection limit) and high Al (3.2-3.8 wt % $Al_2O_3$) and Ti (1.3-1.7 wt % $TiO_2$). Variety Ib ($Di_{51-63}Hed_{14-20}others_{22-33}$) has Mg# of 81-73, contains higher Cr (0.05-0.4 wt % $Cr_2O_3$) and high, but variable Al and Ti (2.3-4.7 wt % $Al_2O_3$ and 0.6-1.6 wt % $TiO_2$). Variety Ic ($Di_{68-76}Hed_{6-11}others_{16-21}$) with high Mg# values of 94-87 is rather Cr-rich (0.4-1.4 wt % $Cr_2O_3$) but depleted in Al and Ti (0.3-0.5 wt % $TiO_2$ and 0.8-1.8 wt % $Al_2O_3$). Varieties Ia and Ic contain similar amounts of $Na_2O$ (0.5-0.6 and 0.4-0.7 wt % respectively), variety Ib is slightly enriched in Na (typically 0.7-1.0 wt % $Na_2O$, with two spot analysis of 0.5 wt %).

Population II (less common, but abundant in some samples) occurs as rounded and embayed cores in macrocrysts (Fig. 9c). A prominent feature is their large size, typically 1-4 mm, and up to 9 x 8 mm and their irregular extinction. Unlike population I, these crystals do not have a mantle zone. Augite ($Di_{60-75}Hed_{8-14}others_{16-29}$) has a relatively high Mg# (90-83) and contains elevated Cr (0.3-0.7 wt % $Cr_2O_3$). Other minor components are Al (1.3-2.9 wt % $Al_2O_3$), Ti (0.4-1.0 wt % $TiO_2$) and Na (0.5-0.7 wt % $Na_2O$) (Table 3).

Population III (common) is augite ($Di_{54-74}Hed_{10-21}others_{13-30}$) with a characteristic spongy texture

(Fig. 9d, e) that occurs as cores in euhedral to subhedral macro- and microcrysts or as mantle around augite I. In the latter case it forms either complete or discontinuous mantle zone. The mineral has a variable Mg# (86-74), contains relatively little Cr (0.1-0.4 wt % $Cr_2O_3$ with one spot analysis of 0.8 wt %) and variable amounts of Al (1.6-4.0 wt % $Al_2O_3$), Ti (0.5-1.9 wt % $TiO_2$) and Na (0.3-0.9 wt % $Na_2O$) (Table 3).

Despite the observed compositional differences between augite I, II and III, there is a common feature for these three populations – a negative correlation between values of Mg# and content of Al and Ti (Figs. 11-12). The behavior of Cr is different: augite with Mg# between 85 and 73 contains Cr at approximately similar and relatively low level, while high Mg# augite (94-85) shows a positive correlation between Mg# and Cr (Fig. 10).

Population IV (generally rare, but common in some samples) occurs as greenish cores in euhedral to subhedral micro- and rarely macrocrysts, typically not in optical continuity with the rim of the crystals (Fig. 9f, g). Some of these cores contain inclusions of Ti-rich garnet (schorlomite), titanite and/or apatite (Figs. 9f, 18b). Clinopyroxene IV is compositionally very diverse ($Di_{18-76}Hed_{10-62}Aeg_{3-20}others_{2-23}$); minerals are characterized by a highly variable Mg# values (86-26) and Al, Ti and Na contents (0.4-5.1 wt % $Al_2O_3$, 0.3-2.2 wt % $TiO_2$ and 0.8-3.8 wt % $Na_2O$) (Table 3). The Cr contents are below the detection limit with the exception of one crystal (Fig. 9g) that contains 0.17-0.24 wt % $Cr_2O_3$. Also, this crystal contains a mantle zone while others do not.

Population V (common) occurs as two varieties. One occurs as mantles around cores of populations I, III and rarely IV (Fig. 9a, b, d, e, g) and generally shows oscillatory zoning, with rare continuous growth zonation. Another represents euhedral to subhedral macro- (rare), microcrysts (common) and groundmass (common) crystals with oscillatory-type or rarely sector-type zoning (Fig. 9h, i). This augite ($Di_{56-76}Hed_{6-21}others_{12-30}$) has high Mg# values with a range from 93 to 73 and the high Cr contents (up to 1.4 wt % $Cr_2O_3$), which decrease towards the rims (Table 3, (Fig. 10). In contrast, Al and Ti increase from the inner mantle/core (1.2 wt % $Al_2O_3$ and 0.4 wt % $TiO_2$) towards the outer mantle/rim (5.7 wt % $Al_2O_3$ and 3.6 wt % $TiO_2$). These compositional variations are related to the size of the crystals: macrocrysts have a core with higher Mg# values and lower Al-Ti contents compared with microcrysts and groundmass crystals, which have lower Mg# and higher Al-Ti contents. Variable

Na (0.2-0.7 wt % $Na_2O$) correlate positively with Cr (Fig. 13), suggesting a minor kosmochlor $NaCr(Si_2O_6)$ component (up to 4 mol.%). However, molar Na/Cr ratio is always ≥1 (up to 9.2), suggesting that parts of Na is incorporated as aegirine and/or jadeite components (Fig. 13).

Population VI (common) is augite ($Di_{49-69}Hed_{12-26}others_{14-29}$), which forms thin rims around almost all macro-, microcrysts and groundmass crystals (Fig. 9). The latter (particularly those < 50 μm) can be completely composed by this population. This augite has variable Mg# values (85-69), contains low Cr (commonly below detection limit), and is characterized by high and variable contents of Al (1.7-6.1 wt % $Al_2O_3$), (1.3-3.6 wt % $TiO_2$) (Table 3, Figs. 10-12) and variable Na (0.3-0.7 wt % $Na_2O$) with no obvious relationship between Na and Cr (Fig. 13).

**Spinel**

Opaque minerals compose an essential part of the groundmass. They are rarely present as microcrysts and also occur as inclusions in forsterite and augite macrocrysts. The crystals are different in morphology, size, internal zonation, and compositional data show the presence of two distinct solid solutions series (magnesiochromite-chromite$_{ss}$ and magnetite-ulvöspinel$_{ss}$) (Table 4, Figs. 14, 15).

Euhedral spinel inclusions (up to 180 x 90 μm in size) in forsterite macrocrysts with normal zonation and microcrysts (up to 160 x 110 μm in size) are considered to be the earliest opaque phases to crystallize (Fig. 14a). They are Ti-poor (1.7-3.3 wt % $TiO_2$) and Al-rich (6.3-8.9 wt % $Al_2O_3$) magnesiochromite-chromite$_{ss}$. From core to rim contents of Mg and Cr decrease, while Al and Ti increase (Fig. 15). Spinel inclusions (up to 30 μm in size) in forsterite with reverse zonation are characterized by high and variable Ti (12.1-21.7 wt % $TiO_2$) and low Cr (3.5-8.5 wt % $Cr_2O_3$) contents (Fig. 15), while having similar Mg and Al (5.4-7.8 wt % MgO and 7.9-9.6 wt % $Al_2O_3$) as euhedral chromite (see above).

Strongly zoned euhedral to subhedral spinel-group minerals occur as rare microcrysts (up to 230 x 100 μm) and groundmass crystals (Fig. 14b, c). They consist of a chromite core rimmed by "titanomagnetite" (magnetite-ulvöspinel$_{ss}$). Chromite is a low Ti variety (2.0-3.8 wt % $TiO_2$) with elevated Al (6.5-10.4 wt % $Al_2O_3$) and Mg (3.6-9.6 wt % MgO). The boundary between chromite and magnetite-ulvöspinel$_{ss}$ is gradational with considerable compositional changes over a distance of 5-10

μm (Fig. 15). Magnetite-ulvöspinel$_{ss}$ is Ti-rich (11.2-26.7 wt % $TiO_2$), Cr-poor (1.5-15.7 wt % $Cr_2O_3$) and contains less Al (1.1-4.6 wt % $Al_2O_3$) and Mg (2.0-4.0 wt % MgO) compared to the core chromite (Fig. 15). One of the studied samples (A19-64) contains texturally and compositionally similar zoned microcrysts with chromite cores and magnetite-ulvöspinel$_{ss}$ rims, but the latter contains ilmenite exsolution lamellae (Fig. 14d). All magnetite-ulvöspinel$_{ss}$ in this sample, either occurring as rim on chromite or as euhedral to subhedral crystals in groundmass contain exsolved ilmenite lamellae. Cr-bearing magnetite-ulvöspinel$_{ss}$ (2.2-10.4 wt % $Cr_2O_3$, 14.2-19.9 wt % $TiO_2$, Fig. 15) occurs as inclusions in clinopyroxene (typically in varieties II, III, V and VI). Groundmass spinel with grain sizes between 1 and 50 μm (rarely up to 100 μm) occurs as euhedral to subhedral crystals (Fig. 14e). Compositionally they are magnetite-ulvöspinel$_{ss}$ with low Cr (0.2-3.8 wt % $Cr_2O_3$), and high Ti (18.2 to 25.6 wt % $TiO_2$; Fig. 15). Few crystal cores are relatively enriched in Cr (4.1-9.9 and 16.1-17.9 wt % $Cr_2O_3$).

All studied samples contain additional anhedral and rather homogeneous spinel (up to 330 x 260 μm; Fig. 14f) with Mg, Al and Ti (2.3-4.1 wt % MgO, 1.7-4.0 wt % $Al_2O_3$ and 14.5-21.8 wt % $TiO_2$) at levels similar to groundmass magnetite-ulvöspinel (Fig. 15). However, these grains are very low in Cr (mostly below the detection limit, Fig. 15) and compositionally different grains are present within a single specimen, e.g. the sample A19-08 contains crystals (150 – 300 μm in size) with quite different Ti content (14.5-14.7, 17.0-17.1 and 20.0-20.8 wt % $TiO_2$).

**Plagioclase**

Plagioclase occurs as subhedral tabular laths to anhedral grains (mostly 20 to 70 μm in size, and rarely up to 200 μm in length; Fig. 16a) that form polycrystalline aggregates (Supplementary Data Fig. S3). Plagioclase is andesine-oligoclase solid solution ($An_{0.28-0.37}Ab_{0.58-0.66}Or_{0.04-0.06}$) with predominance of andesine compositions (Table 5); they contain minor Sr (0.4-0.6 wt % SrO) and Ba (0.2-0.4 wt % BaO). A single microcryst contains a strongly corroded core with labradorite composition ($An_{0.66}Ab_{0.33}Or_{0.01}$), rimed by Ca-enriched andesine ($An_{0.42}Ab_{0.55}Or_{0.03}$). It is unclear if this core is a xenocryst or a primary crystallized phase, but with subsequent reaction with a melt. In addition to microcrysts, sample A19-08 contains relatively large embayed plagioclase grains (250 x 180 to 520 x 490 μm; Fig. 16b) of oligoclase composition ($An_{0.20-0.29}Ab_{0.67-0.71}Or_{0.04-0.09}$).

**Apatite**

Apatite is a common accessory mineral in all studied samples and occurs as needle- or spindle-like crystals up to 120 μm in length and 10 μm in thickness (Fig. 16c, Supplementary Data Fig. S4). Because of small crystals size WDS analysis was not possible, and SEM/EDS analysis show that the mineral is close to an ideal fluorapatite with minor Si (ca. 1.0 wt % $SiO_2$). No peaks from other cations have been found on ED spectra.

**Other minerals**

A sample from the Oldoinyo Naisiusiu hill (A19-08) contains rare, but relatively large grains of perovskite (up to 160 x 210 μm in size) (Fig. 18a), a mineral which is not a typical phase in basaltic rocks. It is always surrounded by a 10-50 μm thick rim of Mg-bearing ilmenite. The latter, in turn, contains numerous tiny inclusions of REE-rich mineral(s) (not precisely identified). In addition, the sample contains grains of green clinopyroxene with inclusions of schorlomite, titanite and apatite (Fig. 18b). These were also observed as rare minerals in some of the other samples.

**Glass**

Glass is an essential component in the studied samples (Supplementary Data Fig. S3). Fresh, unaltered glass is, however, rare (Fig. 16d), but well preserved in two samples from Oldoinyo Emusenge hill (A16-05 and A16-06). The glass contains 58.7-60.2 wt % $SiO_2$, 18.9-19.4 wt % $Al_2O_3$ and 13.3-14.6 wt % $Na_2O+K_2O$ (Table 5) and corresponds to a phonolite on TAS classification diagram (Fig. 4a). It is strongly depleted in Mg (0.5-0.7 wt % MgO) and Ca (0.4-0.9 wt % CaO) and slightly enriched in Fe (4.4-4.7 wt % $Fe_2O_{3total}$). SEM/EDS analysis shows presence of P (up to 0.5 wt % $P_2O_5$), Cl (up to 0.4 wt %) and S (up to 0.2 wt % $SO_3$). The analytical totals are typically between 95 and 98 wt % (Table 5) and this can be an indication of presence of other volatile components, e.g. $H_2O$. During alteration the glass was transformed to a fine-grained assemblage of montmorillonite, K-Na feldspar, Na±K zeolite and sodalite (Fig. 17).

## Sr-Nd ISOTOPES

Limited published Sr and Nd isotope compositions for the Ogol basalts are controversial. While the data presented by Mollel (2007) are relatively uniform ($^{87}Sr/^{86}Sr$ = 0.70371-0.70381 and $^{143}Nd/^{144}Nd$ = 0.51255-0.51261), the data from Adelsberger *et al.* (2011) show wide variations ($^{87}Sr/^{86}Sr$ = 0.70350-0.70577 and $^{143}Nd/^{144}Nd$ = 0.51221-0.51257). The highest Sr (0.70577) and lowest Nd (0.51221) rations were found in sample OL-22E (Adelsberger *et al.,* 2011), which is compositionally quite different from all other Ogol basalts ("picrobasalt" with low Mg, Cr and Ni contents and high Ti and P contents, see above) and is probably not directly related with them. In the present study we analysed 10 samples of the Ogol basalts for their Sr and Nd isotopic composition; complemented by three lava samples from the Lemagarut volcano and three samples of basement samples (Table 6). All measured $^{87}Sr/^{86}Sr$ and $^{143}Nd/^{144}Nd$ values were corrected for an age of 2.3 Ma.

Our new data (Fig. 19) confirm variable isotopic composition of the studied basalts ($^{87}Sr/^{86}Sr_{initial}$ = 0.70377-0.70470 and $^{143}Nd/^{144}Nd_{initial}$ =0.51246-0.51261). The data show a negative correlation between $^{87}Sr/^{86}Sr_{initial}$ and $^{143}Nd/^{144}Nd_{initial}$ ratios, with a sample from Oldoinyo Emusenge hill (A16-05) showing lowest $^{87}Sr/^{86}Sr_{initial}$ and highest $^{143}Nd/^{144}Nd_{initial}$ and a sample from Oldoinyo Mati hill (A19-02) haven the highest $^{87}Sr/^{86}Sr_{initial}$ and lowest $^{143}Nd/^{144}Nd_{initial}$ values.

Sr-Nd isotopic data for basalts to trachyandesites from the contemporaneously erupting Lemagarut volcano partly overlap with those for the Ogol basalts, forming a continuous field (Table 6; Fig. 19). One sample of Lemagarut trachyandesite (Mollel, 2007), has a low $^{143}Nd/^{144}Nd$ ratio of 0.51219, which is quite different from all other samples. The reason for low $^{143}Nd/^{144}Nd$ ratio is unknown, but can potentially be explained by alteration. Significant changes in Nd isotope compositions were observed for nephelinitic rocks from the nearby Sadiman volcano, where highly altered nephelinitic tuffs have much low $^{143}Nd/^{144}Nd$ ratio compared with fresh, unaltered tuffs and lavas (Zaitsev *et al.,* 2019).

In contrast to Ogol and Lemagarut, basaltic rocks from the Ngorongoro volcano are characterized by irregular distribution of measured $^{87}Sr/^{86}Sr$ and $^{143}Nd/^{144}Nd$ ratios (Fig. 19). Majority of samples from Ngorongoro show similar, to Ogol and Lamagarut, ranges for Sr and Nd isotopic

compositions ($^{87}Sr/^{86}Sr$ = 0.70405-0.70533 and $^{143}Nd/^{144}Nd$ =0.51227-0.51277), and three samples have extremely high $^{87}Sr/^{86}Sr$ ratio of 0.70634, 0.70801 and 0.71317 (Nonnotte, 2007; Mollel *et al.,* 2008).

Importantly, the Sr and Nd isotopic data for the Ogol basalts, as well as the basaltic rocks from Lamagarut and Ngorongoro correlate with their major element whole-rock data (Fig. 20). The $^{87}Sr/^{86}Sr$ ratios correlate positively with $SiO_2$, $Al_2O_3$, $Na_2O$, $K_2O$ and negatively with MgO, $TiO_2$, $Fe_2O_3$ and CaO, while $^{143}Nd/^{144}Nd$ ratio shows the opposite relationships.

## DISCUSSION

Basaltic magmatism is a common phenomenon for the Eastern branch of the East African Rift and numerous publications present detailed discussions on the origin and evolution of basaltic magmas based on whole-rock geochemical (major and trace elements) and radiogenic isotope (Sr, Nd and Pb) data (see recent reviewers by Rooney 2017; 2020a; b; c; d). However, only few publications (e.g. Paslick *et al.,* 1996) provide detailed textural and mineralogical descriptions of the basaltic rocks, which is, however, extremely important for sound genetic interpretations of multi-reservoir melting and contamination processes, as is evident from the observations presented above.

### Distinguishing different crystal populations

The textural and compositional differences between the various populations of olivine, clinopyroxene, spinel group minerals and plagioclase in the studied samples (see above) show that besides primary minerals (autocrysts and microlites) which crystallized from a particular melt batch erupted as lava, variable amounts of their crystal load is xenocrystic.

As primary minerals we consider groundmass phases and some, but not all, macro- and microcrysts:

(1) Forsterite macro- and microcrysts with normal zonation and unzoned microcrysts (Fig. 7a, b).

(2) Clinopyroxene cores and mantles with characteristic oscillatory-type, rarely sector-type or continuous growth zonation (population V) and augite rims (population VI; Fig. 9).

(3) Magnesiochromite-chromite as inclusions in forsterite with normal zonation and microcrysts,

494 magnetite-ulvöspinel rims arround those and discrete magnetite-ulvöspinel crystals in groundmass (Fig.
495 14a-e).
496 (4) Microcrysts and groundmass andesine-oligoclase and apatite (Fig. 16a,c).
497 All other crystals were probably entrained from additional sources and are considered to
498 represent xenocrystic material, however, some of them can represent antecrysts:
499 (1) Forsterite crystals (and angular fragments thereof) that show reverse and repetitive zonations (Fig.
500 7c-f) and their Cr-bearing magnetite-ulvöspinel inclusions.
501 (2) Rounded and embayed clinopyroxene cores (populations I-IV) and angular fragments thereof (Fig.
502 9a-g), including perovskite, rimmed by ilmenite and schorlomite ± apatite and titanite (Figs. 9f, 18a-b)
503 that occur as inclusions in population IV (green cores).
504 (3) Anhedral, low-Cr magnetite-ulvöspinel (Fig. 14f) and embayed oligoclase macro- and microcrysts
505 (Fig. 16b).
506 The presence of abundant and texturally/compositionally diverse xenocrystic minerals suggest
507 an open-system and multi-stage crystallization history for the Ogol basalts and the involvement of
508 several sources during their evolution and these are considered in the following.
509
510 **Potential sources of xenocrystic minerals**
511 Importantly, macrocrystic forsterite (normal zonation) and xenocrystic forsterite (reverse zonation)
512 occurs in the same sample, and rim compositions for both types are very similar (Fig. 8). This indicates
513 that xenocrystic forsterite cores were entrained in the magma before eruption with a residence time long
514 enough for partial equilibration. Unzoned angular fragments (occasionally with partial rims only) point
515 to entrainment close to the surface, only shortly before lava eruption and with no time for equilibration
516 with the surrounding melt. A forsterite megacryst with Fe-rich core and normal zonation (see above)
517 was also likely entrained before eruption, because the crystal rim has a quite different composition from
518 rims on normally zoned Fe-poor forsterite in the same sample. Forsterite with repetitive zonation (Fe-
519 rich core – Fe-depleted mantle – Fe-rich rim, Fig. 7e, f), although being extremely rare, is example of
520 multi-stage growth in melt (or melts) with variable Mg#.
521 All studied forsterite crystals show elevated contents of Ca and Mn (0.17-0.42 wt % CaO and

0.12-0.38 wt % MnO) compared to mantle forsterite ($Fo_{\geq 90}$) which has typically up to 0.1 wt % and rarely up to 0.2 wt % oxides (e.g. Dawson, 2002; Koornneef *et al.,* 2009). Therefore, we assume that the Ogol lavas contain basaltic forsterite only and none of the xenocrysts derive from mantle lithologies. Two possible scenarios can explain the occurrence of both low and high Fe forsterite: (1) mixing of relatively primitive magma with evolved magma batches related to the differentiation of the primary Ogol magmas and (2) mixing with evolved melts derived from the Lemagarut volcanic system, which was active at the same time as the Ogol magmas erupted. The second scenario is supported by the occurrence of embayed oligoclase crystals in the Ogol basalts (Fig. 16b), as their morphology and composition suggest that they represent xenocrysts. Lavas of basaltic trachyandesite with plagioclase as phenocrysts have been observed in the Laetoli area (samples A16-21 and A16-28, Supplementary Data Table S1) and on the western lower slope of the Lemagarut volcano; our unpublished data show that these plagioclase phenocrysts are compositionally similar to those found in the Ogol basalts.

Green core clinopyroxenes (population IV) with inclusions of schorlomite, titanite and apatite (Figs. 9f, 18b), as well as discrete perovskite crystals (Fig. 18a) provide strong evidence for the additional contribution of evolved alkaline sources - either by mixing between the basaltic Ogol melts and nephelinitic melts or by assimilation/fragmentation of already crystallized alkaline rocks (foidolitic) at depth. However, no nephelinitic rocks with an age of ca. 2.3 Ma are known in the Laetoli area. Here, alkaline magmatism (Sadiman volcano, Laetoli tuffs, Engolsin cone) is older (>3 Ma) and we can only speculate that alkaline magmas were still present in mantle after 3.0 Ma and mixed with Ogol melts. This assumption is somewhat supported by alkaline volcanoes in the Gregory Rift, which were active at 2.3 Ma, e.g. Tarosero volcano (Mana *et al.,* 2015; Braunger *et al.,* 2020, submitted). At Crater Highlands alkaline magmatism was reactivated around 1.2 Ma (Fig. 1) with the Embagai volcano being active at 1.2-0.8 Ma (Fig. 2). Alternatively, the minerals can simply derive from small-scale assimilation of unexposed rocks related to the Sadiman volcano or even from the Laetolil tuffs by rising basaltic melts. One of the studied green core crystals (Fig. 9g) is different from the others as it shows a distinct patchy zonation, contains 0.17-0.24 wt % $Cr_2O_3$, and is mantled by augite population V. Note that all other green cores are rimmed by augite VI only and some grains even do not have the rim. This suggests that entrainment of this crystal happened at a different depth level and time, but the detailed origin of this

550 crystal remains unclear. Augite population Ia (Fig. 9a) could be also related to an alkaline source because
551 of the lack of Cr. It is always mantled by augite V, these crystals had a long residence time in the melt
552 and therefore, another, probably deeper mixing event, compared to clinopyroxene IV, is considered.

553 Rounded and embayed clinopyroxene cores (populations Ib, Ic) are mantled by primary augite
554 V followed by a rim of augite VI, while clinopyroxene II cores are rimmed by augite VI but lack a
555 mantle of augite V. This may suggest different residence times in melt(s). Compositionally, they are
556 also different, but plotting all together they show gradational changes. From augite Ic, via augite II, to
557 augite Ib we observe decreasing Mg# (94-73) and $Cr_2O_3$ (from 1.4 to to 0.05 wt %), accompanied by
558 increasing $Al_2O_3$ (from 0.8 to 4.7 wt %) and $TiO_2$ (from 0.3 to 1.6 wt %) content (Figs. 10-12). These
559 variations suggest minerals crystallization from melts with different compositions. All cores of augite
560 Ib and Ic, and even megacrystic augite II are relatively homogeneous (Fig. 9) with small compositional
561 variations within a single crystal. We suggest that they crystallized in closed-system intermediate
562 magma chambers under equilibrium conditions. The compositional variations in augite Ib, I c and II are
563 similar with those of primary augite V (Figs. 10-12). This indicates basaltic melt compositions that may
564 derive from the Lemagarut magmatic system, and were mixed with Ogol melts.

565 Alternatively, high Mg# and Cr augite Ic may derive from mantle rocks. Although mantle
566 xenoliths are not known from basaltic or nephelinitic rocks of the Crater Highlands, they occur, for
567 example, at Lashaine volcano within the Gregory Rift, at Labait volcano located on the eastern edge of
568 the Tanzanian Craton and other localities. Clinopyroxene from Lashaine (Dawson, 2002) is enriched in
569 Cr and Na (1.7-3.1 wt % $Cr_2O_3$ and 1.2-2.5 wt % $Na_2O$) compared with mineral from Ogol, but
570 clinopyroxene occurring in glassy melt pockets, veinlets and veins shows similar levels of Cr and Na
571 (0.2-1.8 wt % $Cr_2O_3$ and 0.3-0.8 wt % $Na_2O$) as augite Ic. However, as no "true" mantle minerals (e.g.
572 low Ca-Mn and high Fo olivine, high Cr-Na clinopyroxene and/or orthopyroxene) were found in the
573 Ogol basalts we suggest a basaltic source is more likely for augite Ic.

574 Spongy clinopyroxene cores and mantles (population III) are compositionally similar to augite
575 populations Ib, II and even partly overlap with augite Ic (Fig. 9d, e) and are always overgrown by augite
576 V, indicating relatively long residence time in the melts. The large compositional variations for augite
577 III (Figs. 10-12) are interpreted to represent magmatic differentiation. Spongy- or sieve-textured

minerals, mainly plagioclase and pyroxene, are known in various volcanic rocks and two models were suggested to explain origin of the texture (e.g. Nelson & Montana, 1992; Stewart & Pearce, 2004; Shane *et al.,* 2019). The formation of spongy-textured crystals can be related to magma mixing processes or due to rapid decompression during melt ascent.

**Primary minerals**

Primary orthomagmatic phenocrysts of forsterite and clinopyroxene (population V) are Mg-rich ($Fo_{89.5}$ and Mg# of 94, respectively) and crystallized from rather primitive melts with Mg# of 72.5-70.5 during forsterite crystallization (assuming crystal/melt equilibrium with $Kd_{Fe/Mg}$(ol/liq) = 0.30-0.35, depending of pressure; Ulmer, 1989). Primary forsterite with lower Mg contents (down to $Fo_{84.2}$) reflect magmatic differentiation, magma mixing processes, or combinations thereof.

Similarly, the compositional variation of augite V is explained, characterized by well-developed zonation with a decrease of Mg# and Cr from core to rim (in case of mantle from inner to outer parts) and a simultaneous increase in Al and Ti (Fig. 11, 12). Augite VI that occurs as rims around pheno- and microphenocrysts and as groundmass crystals, formed somewhat later but from the same evolving magma. Based on its textural context and evolved composition (low Mg# and high content of Al and Ti), we suggest that augite VI crystallized immediately before and during eruptions of melts.

Two compositionally distinct spinel group minerals crystallized during magmatic differentiation. The change from magnesiochromite-$chromite_{ss}$ to magnetite-$ulvöspinel_{ss}$ indicates not only changes in melt composition, but is further related to changes in physical-chemical conditions, such as temperature and oxygen fugacity (Hill & Roeder, 1974).

**Ogol primary melt composition**

The relatively high concentrations of Cr and Ni in the studied samples allow them to be considered as candidates for primary magma compositions, not only for the Ogol rocks, but also for the Lemagarut and even Ngorongoro volcanoes (see above). The Ogol basalts are relatively primitive (Table 1), but show continuous variations in contents of major and trace elements (Fig. 4). With 11.5 wt % MgO (Mg# = 61), 975 pm Cr and 222 ppm Ni, a sample from Oldoinyo Emusenge hill (A16-05; Fig. 6a) could

approximate the composition of a primary magma in equilibrium with its mantle source. Out of all studied samples, A16-05 contains the most Mg-rich olivine ($Fo_{89.5-87.5}$) and clinopyroxene V (Mg# of 94-85) and magnesiochromite. Also, it is characterized by the lowest $^{87}Sr/^{86}Sr_i$ (0.703768) and highest $^{143}Nd/^{144}Nd_i$ (0.512614) ratios compared to the Ogol as well as Lemagarut basalts. However, even this sample contains few high-Fe forsterite as well as xenocrystic augite (populations Ib, Ic, II and IV). Therefore, we suggest that its composition is close but not exactly corresponds to a primary melt composition. The presence of relatively Fe-rich and Ni-poor forsterite causes a decrease of Mg and Ni and an increase of Fe compared to an initial composition (Fig. 21). Likewise, abundant augite xenocrysts mainly influence Mg, Fe and Cr content of the whole rock. The lack of trace element data for primary and xenocrystic minerals, do not allow a more detailed discussion on possible changes, particularly for trace elements, of melts initial composition.

Despite the modification of the studied samples by variable amounts of xenocrystic minerals (see above), their minor and trace elements distribution is similar to that of OIB (Fig. 5), except for Ba and Cs. The relative depletion of the Ogol basalts in K could reflect partial melting in the presence of a K-bearing phase (amphibole and/or phlogopite) as suggested for other volcanic rocks in the NTD zone (e.g. Mana *et al.,* 2015). Both minerals are known in mantle xenoliths from Eledoi and Pello Hill where they form metasomatic veins (Dawson & Smith, 1988) and giant mantle-derived amphibole and mica megacrysts (up to 12 cm in size) occur at Deeti cone (Johnson *et al.,* 1977; Zaitsev *et al.,* 2013). The high values of ($(Tb/Yb)_{CN}$ = 2.48-2.83) observed in the Ogol basalts indicate melting of enriched lithosphere in the presence of residual garnet (Wang *et al.,* 2002). Such a mantle source for the basalts is also supported by relatively high values of Ce/Pb ratio of 17.3-24.9.

**Crystallization depth and temperature of the Ogol basalts**

Based on the clinopyroxene-only barometer of Nimis & Ulmer (1998), there is no clear evidence for a deep (mantle) origin of the various xenocrysts (populations I-IV). Also, pressure estimates for xenocrysts and orthomagmatic clinopyroxene (populations V and VI) are rather similar, with many of them illustrating negative, and thus, geologically meaningless crystallization depths though (Supplementary Data Fig. S5). Apparently, such pressure estimates are not suitable in this case. It is

known that melt composition influences clinopyroxene composition as well. Therefore, we used augite populations V and VI to constrain the crystallization pressure and temperature by applying the clinopyroxene-liquid barometer of Neave & Putirka (2017) combined with the thermometer equation 33 from Putirka (2008).

As a proxy for the liquid composition in equilibrium with augite, we used whole-rock compositions, being aware that (i) the whole rock composition cannot represent the coexisting liquid for both augite populations V and VI, as these crystallized over certain intervals and partly during different stages, and that (ii) mineral removal as well as accumulation/xenocryst entrainment result in discrepancies between equilibrium melts and the whole rock compositions. Correction of the whole rock composition by removing xenocrystals was rejected because the amount of xenocrysts cannot be determined exactly. We still applied the thermobarometer, since the required liquid components of the pressure equation solely involve the Al, Na, K and Si concentration (Neave & Putirka, 2017). The aluminum and alkali metal budget of the whole rock compositions is mainly controlled by plagioclase, and the relatively high $SiO_2$ concentration of the basalts (~45 wt %) acts as a buffer, hence diminishing the effect of olivine, clinopyroxene or spinel contamination. Note that the temperature equation 33 (Putirka, 2008) depends on further liquid components (Ca, Mg, Fe, Ti concentration), on which xenocryst contamination, however, has little effect (Supplementary Data Fig. S6). For obtaining reliable results, two important criteria for the pressure calculations have to be satisfied (e.g. Putirka *et al.,* 1996; Putirka, 2008; Neave & Putirka, 2017). Firstly, the Fe and Mg concentrations of clinopyroxene and the coexisting liquid must be in accordance with the assumed Fe-Mg exchange coefficient of $K_D[Fe\text{-}Mg]^{cpx\text{-}liq}=0.27\pm0.3$ (Fig. 22a). Equally important is that the observed augite composition conforms with the predicted values (Fig. 22b), for which we used 5 percentage points as cutoff. If these requirements are not fulfilled, clearly meaningless pressure variations down to -25 kbar are calculated (Fig. 22c). Data that meet these requirements (Fig. 22c), however, suggest formation depths for augite V typically between 1 and 4 kbar (uncertainty of ± 1.4 kbar) at a temperature of ~1150-1220 °C (uncertainty of ± 45 °C). The calculated pressures indicate upper-crustal crystallization depths for augite V of approximately 3-12 km, which is consistent with several basaltic magmas at other localities (e.g. Eimeishan; Icelandic rift zone; Tao *et al.,* 2015; Neave & Putirka, 2017). Groundmass augite VI does

not meet the equilibrium constraints, which is related to the relatively evolved composition of late stage augite VI compared to early magmatic augite V (Fig. 22a). The groundmass assemblage of augite VI, forsterite and magnetite-ulvöspinel$_{ss}$, however, would be suitable for calculating equilibrium temperature, silica activity and oxygen fugacity using the QUIlF software package (Andersen *et al.,* 1993). While late stage augite and magnetite-ulvöspinel$_{ss}$ are in textural equilibrium, there is, however, no clear evidence that forsterite crystallized contemporaneously. Indeed, the high uncertainty (>100 °C) of the calculated temperature and oxygen fugacity (above 3 log units), as well as the failure to calculate the silica activity (iteration limit) clearly points towards chemical disequilibrium between forsterite on the one hand, and augite VI + magnetite-ulvöspinel$_{ss}$ on the other hand (Table 7). Hence, we consider the calculated results as not reliable.

**Magma mixing and contamination of the Ogol basalts**

The variability of the Ogol basalts in mineralogy, whole rock compositions, incompatible trace element ratios (e.g. Ce/Pb, La/Sm) and Sr-Nd isotopic ratios reflect the contribution from different components, two of them (basaltic and alkaline) were suggested above. Furthermore, assimilation of crustal rocks composing the Tanzania Craton may contribute as considered for other volcanic rocks in the Gregory rift and Crater Highlands (e.g. Mana *et al.,* 2015; Mollel *et al.,* 2008).

Archean basement exposed in the southwestern part of the NTD zone close to Laetoli, allows to consider granite-gneisses and associated garnet amphibolites (Table 1S) as possible contaminants. Garnet amphibolite is unlikely to explain the observed $^{87}Sr/^{86}Sr$ and $^{143}Nd/^{144}Nd$ variations as up to 25 % assimilation would be needed to cover this range and such a voluminous addition would be reflected in the whole rock composition of the Ogol basalts (Fig. 19). Assimilation of granite-gneisses would only require <3 % bulk assimilation but the assimilation line between Ogol basalts and granite-gneiss is shifted to higher $^{143}Nd/^{144}Nd$ values. An alternative explanation for the observed variations is the addition of an alkaline source, for which data from the Sadiman volcano were used (sample Sad-10; Zaitsev *et al.,* 2012). A plot of $(La/Sm)_N$ against $^{87}Sr/^{86}Sr$ and $^{143}Nd/^{144}Nd$ ratios with data from assimilation and fractional crystallization (AFC) modeling between Ogol basalt, Tanzanian Craton

granite-gneiss and Sadiman nephelinite suggests involvement up to 5% of alkaline component (Fig. 23). The combination of contamination with granite-gneisses and mixing with alkaline melts or contamination by unexposed Sadiman plutonic rocks can explain the observed geochemical characteristics. Involvement of alkaline source is further supported by relatively high alkalinity ratios (molar Na+K)/Al) of 0.98-1.07 of phonolitic glass and xenocrystic green core pyroxene (population IV) with perovskite and schorlomite (see above). At the same time, abundant xenocrysts (high-Fe forsterite, diverse clinopyroxene cores and mantles, embayed plagioclase) suggest that mixing with other basaltic melts is a further important process in evolution of Ogol melts.

Much of the compositional variation of the Ogol basalts (Fig. 4) could be explained by crystal fractionation processes and subsequent mixing between different melt batches which related to fractionation of primary Ogol magma only. However, as shown above, whole rock data show that major and trace elements correlate with variable Sr and Nd isotope ratios (Figs. 19, 20). This is strong evidence against closed-system evolution of Ogol melts, because Sr and Nd isotopic ratios should not change during differentiation under closed-system condition. Although, we cannot completely exclude that fractionation of primary Ogol magmas took place, our mineralogical and geochemical data suggest that mixing with melts related to the Lemagarut volcanic system is more likely process. Rocks composing the Lemagarut volcano vary from relatively primitive basaltic rocks (Mg# = 58-56 and 537-495 ppm Cr) to highly evolved trachyandesite (Mg# = 27-30 and 15-3.4 ppm Cr) (Mollel, 2007). Our data show that the former contains olivine with compositions similar to Ogol phenocrysts with reverse zonation and the latter is rich in oligoclase-andesine$_{ss}$ phenocrysts. Diagrams showing relationships between major elements and isotopic ratios (Figs. 19, 20) support mixing between Ogol and Lemagarut derived melts. For example, mixing with evolved Lemagarut basaltic trachyandesite (Supplementary Data Table S1) would explain the enrichment of Zr and Hf observed for some Ogol basalts (Fig. 5a).

The detailed relationships between Ogol and Lemagarut may be more complex. Although Hay (1987) assumed that Ogol lavas erupted from a series of individual vents, Mollel *et al.* (2011) provide some arguments in favor of close genetical relation of Ogol and Lemagarut eruptions and suggested that Ogol basalts may represent distal flows from the Lemagarut volcano. Limited mineralogical data for the Lemagarut rocks (Mollel *et al.,* 2011) does not allow to discuss possible genetic relations with Ogol

718 rocks. At this stage we can only speculate that the volcanic series of Ogol and Lemagarut may record
719 an uniform evolutionary history reflected by the composition of a single parental melt and the onset of
720 cotectic crystallization of olivine, pyroxene, magnetite and plagioclase. Linear correlations in major
721 element abundances in Ogol and Lemagarut lavas are unlikely to reflect crystallization along a liquid
722 line of descent. Simple AFC modelling indicates that Lemagarut derivatives could be result of
723 fractionation of 50 – 60 % Ogol melt with addition of 5 % of the crustal material. A detailed study of
724 the Lemagarut volcano is needed to prove or disprove this idea.
725
726 **CONCLUSIONS**
727
728 The textural, mineralogical and geochemical heterogeneity of the Ogol basalts suggests that these
729 represent hybride rocks that formed under open-system conditions. The major findings we consider to
730 be important for formation and evolution of the Ogol basalts (Fig. 24) include
731 (1) formation of a primary Ogol melts during partial melting of amphibole- (and phlogopite?)
732 and garnet-bearing lithospheric material;
733 (2) although small degrees of fractional crystallization may explain the compositional variations
734 of the studied samples, the presence of abundant xenocrysts (Fe-rich olivine, clinopyroxene with
735 variable composition, plagioclase, perovskite and schorlomite) and variable Sr and Nd initial isotopic
736 ratios suggest that magma mixing with other melts from different sources was important;
737 (3) there is no clear evidence for a deep (mantle) origin of the various clinopyroxene xenocrysts.
738 Early orthomagmatic augite (population V) crystallized at a temperature of ~1150-1220 °C, and an
739 upper-crustal depth of 3-12 km (1-4 kbar). Late stage augite (population VI) and magnetite-ulvöspinel$_{ss}$
740 are in textural equilibrium, while thermodynamic calculations indicate that groundmass forsterite did
741 not form contemporaneously;
742 (4) magma mixing between Ogol and Lemagarut melts can explain the observed chemical
743 variations of the Ogol basalts. Magma mixing was not a single-stage process but happened at different
744 depths with variable crystals residence time in melts during ascent to the surface;
745 (5) mixing with mantle-derived alkaline melts and/or contamination with alkaline rocks

crystallized beneath the Sadiman volcano or even from the Laetolil tuffs did occur, but was a relatively minor process;

(6) small-scale contamination of the Ogol melts by crustal granite-gneises may have occurred. However, this assumption is based on geochemical modeling only, and no mineralogical evidence for this was found.

Overall, the Ogol basalts, particularly from Oldoinyo Emusenge volcanic cone, seem to be the best examples of near-primary basaltic melts within the Crater Highlands region. They could also be considered as parental to the Lemgarut volcano, but more data are needed to solve this question.

**ACKNOWLEDGEMENTS**

We would like to thank Ngorongoro Conservation Area Authorities (Tanzania) and GMP Consulting Engineers Ltd. (Arusha, Tanzania) for help with organization of field work, and particularly Larissa Leach and Jumanne S. (J-Four) Pyuza for great help with export of samples. Olga Ivashchenkova is thanked for held during field work. We thank the Tanzania Commission for Science and Technology for granting permission to conduct research.

**FUNDING**

This work was supported by the Alexander von Humboldt Stiftung, Russian Foundation for Basic Research (grant 18-05-00835), The Natural History Museum (London) and St. Petersburg State University (Resource Centres of X-ray Diffraction Studies and Geo-Environmental Research and Modelling).

**SUPPLEMENTARY DATA**

Supplementary data are available at Journal of Petrology online.

774 **REFERENCES**

775


776 Adams, A., Nyblade, A. & Weeraratne, D. (2012). Upper mantle shear wave velocity structure beneath
777 the East African plateau: evidence for a deep, plateau wide low velocity anomaly. *Geophysical*
778 *Journal International* **189**, 123-142.

779 Adelsberger, K.A., Wirth, K.R., Mabulla, A.Z.P. & Bowman, D.C. (2011). Geochemical and
780 mineralogic characterization of Middle Stone Age tools of Laetoli, Tanzania, and comparisons
781 with possible source materials. In: Harrison, T. (ed.) *Paleontology and Geology of Laetoli:*
782 *Human Evolution in Context. Vol.1: Geology, Geochronology, Paleoecology and*
783 *Paleoenvironment.* Dordrecht: Springer, pp. 143-166.

784 Andersen, D. J., Lindsley, D. H. & Davidson, P. M. (1993). Quilf - a Pascal program to assess equilibria
785 among Fe-Mg-Mn-Ti oxides, pyroxenes, olivine, and quartz. *Computers & Geosciences* **19**,
786 1333-1350.

787 Baker, B.H., Mohr, P.A. & Williams, L.A.J. (1972). *Geology of the Eastern Rift System of Africa*.
788 Geological Society of America, Special Papers, 136.

789 Birt, C., Maguire, P.K.H., Khan, M.A. & Thybo, A. (1997). A combined interpretation of the KRISP
790 '94 seismic and gravity data: evidence for a mantle plume beneath the East African plateau.
791 *Tectonophysics* **278**, 211-242.

792 Braunger, S., Marks, M.A.W., Wenzel, T., Zaitsev, A.N. & Markl, G. (2020). The petrology of the
793 Tarosero volcanic complex: constraints on the formation of extrusive agpaitic rocks. *Journal of*
794 *Petrology* (submitted).

795 Dawson, J.B. (2002). Metasomatism and partial melting in upper-mantle peridotite xenoliths from the
796 Lashaine volcano, northern Tanzania. *Journal of Petrology* **43**, 1749-1777.

797 Dawson, J.B. (2008). *The Gregory Rift Valley and Neogene-Recent Volcanoes of Northern Tanzania*.
798 Geological Society of London, Memoirs, 33.

799 Dawson, J.B. & Smith, J.V. (1988). Metasomatised and veined upper-mantle xenoliths from Pello
800 Hill, Tanzania: evidence for anomalously-light mantle beneath the East African Rift Valley.
801 *Contributions to Mineralogy and Petrology* **100**, 510-527.

802 Deino, A.L. (2011). $^{40}Ar/^{39}Ar$ dating of Laetoli, Tanzania. In: Harrison, T. (ed.) *Paleontology and*
803 *Geology of Laetoli: Human Evolution in Context. Volume 1: Geology, Geochronology,*
804 *Paleoecology and Paleoenvironment*. Dordrecht: Springer, pp. 77-97.

805 Deino, A.L. (2012). $^{40}Ar/^{39}Ar$ dating of Bed I, Olduvai Gorge, Tanzania, and the chronology of early
806 Pleistocene climate change. *Journal of Human Evolution* **63**, 251-273

807 Fletcher, A.W., Abdelsalam, M.G., Emishaw, L., Estella A. Atekwana, E.A., Laó-Dávila, D.A. & Ismail,
808 A. (2018). Lithospheric controls on the rifting of the Tanzanian Craton at the Eyasi Basin,
809 Eastern Branch of the East African Rift System. *Tectonics* **37**, 1-15.

Foster, A., Ebinger, C., Mbede, E. & Rex, D. (1997). Tectonic development of the northern sector of the East African Rift System. *Journal of Geological Society, London* **154**, 689-700.

Frey, F., Green, D. and Roy, S. (1978). Integrated models of basalt petrogenesis: a study of quartz tholeiites to olivine melilitites from South Eastern Australia utilizing geochemical and experimental petrological data. *Journal of Petrology* **19**, 463–513.

Hay, R.L. (1987). Geology of the Laetoli area. In: Leakey, M.D. & Harris, J.M. (eds.) *Laetoli: A Pliocene Site in Northern Tanzania*. Oxford: Clarendon, pp. 23–47.

Hill, R. & Roeder, P. (1974). The crystallization of spinel from basaltic liquid as a function of oxygen fugacity. *Journal of Geology* **82**, 709-729.

Jerram, D.A. & Martin, V.M. (2008). Understanding crystal populations and their significance through the magma plumbing system. In: Annen, C. & Zellmer, G.F. (eds.) *Dynamics of Crustal Magma Transfer, Storage and Differentiation*. Geological Society, London, Special Publications. 304, pp. 133-148.

Johnson, L.H., Jones, A.P., Church, A.A. & Taylor, W.R. (1997). Ultramafic xenoliths and megacrysts from a melilitite tuff cone, Deeti, northern Tanzania. *Journal of African Earth Sciences* **25**, 29-42.

Keller, J., Zaitsev, A.N. & Wiedenmann, D. (2006). Primary magmas at Oldoinyo Lengai: the role of olivine melilitites. *Lithos* **91**, 150-172.

Koornneef, J.M., Davies, G.R., Döpp, S.P., Vukmanovic, Z., Nikogosian, I.K. & Mason, P.R.D. (2009). Nature and timing of multiple metasomatic events in the sub-cratonic lithosphere beneath Labait, Tanzania. *Lithos* **112S**, 896-912.

Le Bas, M.J, Le Maitre, R.W., Streckeisen, A. & Zanettin, B. (1986). A chemical classification of volcanic rocks based on the total alkali-silica diagram. *Journal of Petrology* **27**, 745-750.

Le Gall, B., Nonnotte, P., Rolet, J., Benoit, M., Guillou, H., Mousseau-Nonnotte, M., Albaric, J. & Deverchère, J. (2008). Rift propagation at craton margin. Distribution of faulting and volcanism in the North Tanzanian Divergence (East Africa) during Neogene times. *Tectonophysics* **448**, 1-19.

Leakey, M.D. & Hay, R.L. (1979). Pliocene footprints in the Laetolil Beds at Laetoli, northern Tanzania. *Nature* **278**, 317-323.

Mana, S., Furman, T., Carr, M.J., Mollel, G.F., Mortlock, R.A., Feigenson, M.D., Turrin, B.D. & Swisher III C.C. (2012). Geochronology and geochemistry of the Essimingor volcano: melting of metasomatized lithospheric mantle beneath the North Tanzanian Divergence zone (East African Rift). *Lithos* **155**, 310-325.

Mana, S., Furman, T., Turrin, B.D., Feigenson, M.D. & Swisher III, C.C. (2015). Magmatic activity across the East African North Tanzanian Divergence Zone. *Journal of the Geological Society* **172**, 368-389.

Manega, P. C. (1993). *Geochronology, geochemistry and isotope study of the Plio-Pleistocene hominid sites and the Ngorongoro Volcanic Highlands in northern Tanzania*. PhD thesis, University of Colorado, USA

Mattsson, H.B., Nandedkar, R.H. & Ulmer, P. (2013). Petrogenesis of the melilititic and nephelinitic rock suites in the Lake Natron–Engaruka monogenetic volcanic field, northern Tanzania. *Lithos* **179**, 175-192.

Mollel, G.F. (2007). *Petrochemistry and Geochronology of Ngorongoro Volcanic Highland Complex (NVHC) and its Relationship to Laetoli and Olduvai Gorge, Tanzania*. PhD thesis, Rutgers University, USA.

Mollel, G.F., Swisher III, C.C., Feigenson, M.D. & Carr, M.J. (2008). Geochemical evolution of Ngorongoro Caldera, Tanzania: implications for crust-magma interaction. *Earth and Planetary Science Letters* **271**, 337-347.

Mollel G.F., Swisher III, C.C., Feigenson M.D. & Carr M.J. (2011). Petrology, geochemistry, and age of Satiman, Lemagurut and Oldeani: sources of the volcanic deposits of the Laetoli area. In: Harrison, T. (ed.) *Paleontology and Geology of Laetoli: Human Evolution in Context. Vol.1: Geology, Geochronology, Paleoecology and Paleoenvironment.* Dordrecht: Springer, pp. 99-120.

Neave D. A. & Putirka K. D. (2017). A new clinopyroxene-liquid barometer, and implications for magma storage pressures under Icelandic rift zones. *American Mineralogist* **102**, 777-794.

Nelson, S. T. & Montana, A. (1992). Sieve-textured plagioclase in volcanic rocks produced by rapid decompression. *American Mineralogist* **77**, 1242-1249.

Nimis, P. & Ulmer, P. (1998). Clinopyroxene geobarometry of magmatic rocks Part 1: An expanded structural geobarometer for anhydrous and hydrous, basic and ultrabasic systems. *Contributions to Mineralogy and Petrology* **133**, 122-135.

Nonnotte, P. (2007). *Etude volcano-tectonique de la zone de Divergence Nord Tanzanienne (Terminaison Sud du Rift Kenyan). Caractérisation pétrologique et géochimique du volcanisme récent (8 Ma – Actuel) et du manteau source*. Doctorat These, Université de Bretagne Occidentale, France.

Nonnotte, P., Guillou, H., Le Gall, B., Benoit, M., Cotten, J. & Scaillet, S. (2008). New K-Ar age determinations of Kilimanjaro volcano in the North Tanzanian diverging rift, East Africa. *Journal of Volcanology and Geothermal Research* **173**, 99-112.

Paslick, C., Halliday, A.N., James, D. & Dawson, J.B. (1995). Enrichment of Continental lithosphere by OIB melts: isotopic evidence from the volcanic province of northern Tanzania. *Earth and Planetary Science Letters* **130**, 109-126.

Paslick, C.R., Halliday, A.N., Lange, R.A., James, D. & Dawson, J.B. (1996). Indirect crustal contamination: evidence from isotopic and chemical disequilibria in minerals from alkali basalts and nephelinites from northern Tanzania. *Contributions to Mineralogy and Petrology* **125**, 277-

292.

Peirce S. & Mana S. (2018). Fractional crystallization history recorded by the lava flows of Ketumbeine volcano, North Tanzania. *Geological Society of America Abstracts with Programs* **50** (2), 10.1130/abs/2018NE-311204

Pickering, R. (1964). Endulen. Tanzania Geological Survey. Quarter Degree Sheet 52.

Plasman, M., Hautot, S., Tarits, P., Gautier, S., Tiberi, C., Le Gall, B., Mtelela, K. & Gama, R. (2019). Lithospheric structure of a transitional magmatic to amagmatic continental rift system - insights from magnetotelluric and local tomography studies in the North Tanzanian Divergence, East African Rift. *Geosciences* **9**, 462.

Putirka K. D. (2008). Thermometers and Barometers for Volcanic Systems. *Reviews in Mineralogy and Geochemistry* **69**, 61-120.

Putirka, K., Johnson, M., Kinzler, R., Longhi, J. & Walker, D. (1996). Thermobarometry of mafic igneous rocks based on clinopyroxene-liquid equilibria, 0–30 kbar. *Contributions to Mineralogy and Petrology* **123**, 92-108.

Ritsema, J., Nyblade, A.A., Owens, T.J., Langston, C.A. & VanDecar, J.C. (1998). Upper mantle seismic velocity structure beneath Tanzania, east Africa: Implications for the stability of cratonic lithosphere. *Journal of Geophysical Research* **103**, 21201–21213.

Rooney, T.O. (2017). The Cenozoic magmatism of East-Africa: Part I - Flood basalts and pulsed magmatism. Lithos *Lithos* **286–287**, 264-301.

Rooney, T.O. (2020a). The Cenozoic magmatism of East Africa: Part II – Rifting of the mobile belt. *Lithos* **360–361**, 105291.

Rooney, T.O. (2020b). The Cenozoic magmatism of East Africa: Part III – Rifting of the craton. *Lithos* **360–361**, 105390.

Rooney, T.O. (2020c). The Cenozoic magmatism of East Africa: Part IV – The terminal stages of rifting preserved in the Northern East African Rift System. *Lithos* **360–361**, 105381.

Rooney, T.O. (2020d). The Cenozoic magmatism of East Africa: Part V – Magma sources and processes in the East African Rift. *Lithos* **360–361**, 105296.

Smith, M. (1994). Stratigraphic and structural constraints on mechanisms of active rifting in the Gregory Rift, Kenya. *Tectonophysics* **236**, 3-22.

Svetov, S.A., Stepanova, A.V., Chazhengina, S.Yu., Svetova, E.N. Rybnikova, Z.P., Mikhailova, A.I., Paramonov, A.S., Utitsyna, V.L., Ekhova, M.V. & Kolodey, B.S. (2015). Precision geochemical (ICP-MS, LA-ICP-MS) analysis of rock and mineral compositions:the method and accuracy estimation in the case study of Early Precambiran mafic complexes. *Proceedings of Karelian Research Centre of RAS* **7**, 54-73.

Shane, P., Cocker, K., Coote, A., Stirling, C.H. & Reid, M.R. (2019). The prevalence of plagioclase antecrysts and xenocrysts in andesite magma, exemplified by lavas of the Tongariro volcanic complex, New Zealand. *Contributions to Mineralogy and Petrology* **174**, 89.

Stewart, M.L. & Pearce, T. (2004) Sieve-textured plagioclase in dacitic magma: interference imaging results. *American Mineralogists* **89**, 348-351.

Sun, S.-S. & McDonough, W.F. (1989). Chemical and isotopic systematics of oceanic basalts: Implications for mantle composition and processes. In: Saunders, A.D. & Norry, M.J. (eds.) *Magmatism in the Ocean Basins*. London: Geological Society. Special Publications 42, 313-345.

Tao, Y., Putirka, K., Hu, R.-Z. & Li, C. (2015). The magma plumbing system of the Emeishan large igneous province and its role in basaltic magma differentiation in a continental setting. *American Mineralogist* **100**, 2509-2517.

Ubide T., Galé, C., Larrea, P., Arranz, E. & Lago, M. (2014). Antecrysts and their effect on rock compositions: The Cretaceous lamprophyre suite in the Catalonian Coastal Ranges (NE Spain). *Lithos* **206-207**, 214-233.

Ulmer, P. (1989). The dependence of the $Fe^{2+}$-Mg cation-partitioning between olivine and basaltic liquid on pressure, temperature and composition. An experimental study to 30 kbars. *Contributions to Mineralogy and Petrology* **1989**, 261-273.

Wang, K., Plank, T., Walker, J. D. & Smith, E. I. (2002). A mantle melting profile across the Basin and Range, SW USA. *Journal of Geophysical Research* **107**, B1, 2017.

Wass, S.Y. (1979). Multiple origins of clinopyroxenes in alkaline basaltic rocks. *Lithos* **12**, 115-132.

Zaitsev, A.N., Wenzel, T., Spratt, J., Williams, T.C., Strekopytov, S., Sharygin, V.V., Petrov, S.V., Golovina, T.A., Zaitseva, E.O. & Markl, G. (2011). Was Sadiman volcano a source for the Laetoli Footprint Tuff? *Journal of Human Evolution* **61**, 121-124.

Zaitsev, A.N., Marks, M.A.W., Wenzel, T., Spratt, J., Sharygin, V.V., Strekopytov, S. & Markl, G. (2012). Mineralogy, geochemistry and petrology of the phonolitic to nephelinitic Sadiman volcano, Crater Highlands, Tanzania. *Lithos* **152**, 66–83.

Zaitsev, A.N., Avdontseva, E.Yu., Britvin, S.N., Demeny, A., Homonnay. Z., Jeffries, T.E., Keller, J., Krivovichev, V.G., Markl, G., Platonova, N.V., Siidra, O.I., Spratt, J. & Vennemann, T. (1993). Oxo-magnesio-hastingsite, $NaCa_2(Mg_2Fe^{3+})(Al_2Si_6)O_{22}O_2$, a new anhydrous amphibole from the Deeti volcanic cone, Gregory rift, northern Tanzania. *Mineralogical Magazine* **77**, 773-2792.

Zaitsev, A.N., Spratt, J., Sharygin, V.V., Wenzel, T., Zaitseva, O.A. & Markl, G. (2015). Mineralogy of the Laetolil footprint tuff: a comparison with possible volcanic sources from the Crater Highlands and Gregory rift. *Journal of African Earth Sciences* **111**, 214-221.

Zaitsev, A.N., McHenry, L., Savchenok, A.I, Strekopytov, S., Spratt, J.,Humphreys-Williams, E., Sharygin, V.V., Bogomolov, E.S., Chakhmouradian, A.R., Zaitseva, O.A., Arzamastsev, A.A., Reguir, E.P., Leach, L., Leach, M. & Mwankunda J. (2019). Stratigraphy, mineralogy and geochemistry of the Upper Laetolil tuffs including a new Tuff 7 site with footprints of *Australopithecus afarensis*, Laetoli, Tanzania. *Journal of African Earth Sciences* **158**, 103561.

**Table 1:** Whole-rock geochemical data for the studied Ogol basalts

| Sample | A16-05 | A16-06 | A16-25 | A16-26 | A19-01 | A19-02 | A19-06 | A19-07 | A19-08 | A19-64 | A19-4c | A19-4b |
|---|---|---|---|---|---|---|---|---|---|---|---|---|
| Latitude | 741220 | 740683 | 739808 | 745223 | 748761 | 748497 | 740867 | 742655 | 734090 | 741124 | 747201 | 747201 |
| Longitude | 9642114 | 9642261 | 9644377 | 9643513 | 9641516 | 9641340 | 9639339 | 9641864 | 9643749 | 9635170 | 9640489 | 9640489 |
| $SiO_2$, wt % | 45.90 | 45.16 | 46.19 | 45.60 | 46.68 | 44.95 | 45.03 | 46.31 | 46.68 | 47.27 | 46.61 | 47.12 |
| $TiO_2$ | 3.06 | 3.54 | 2.99 | 2.98 | 2.80 | 2.77 | 3.37 | 3.01 | 2.75 | 2.70 | 2.85 | 2.86 |
| $Al_2O_3$ | 7.59 | 8.45 | 10.00 | 8.99 | 9.44 | 9.61 | 8.94 | 9.96 | 9.85 | 10.13 | 10.16 | 10.00 |
| $Fe_2O_{3total}$ | 14.37 | 15.45 | 13.72 | 14.07 | 13.79 | 13.47 | 14.53 | 13.90 | 13.17 | 13.44 | 13.47 | 13.23 |
| MnO | 0.18 | 0.19 | 0.18 | 0.19 | 0.17 | 0.18 | 0.19 | 0.18 | 0.18 | 0.18 | 0.21 | 0.18 |
| MgO | 11.50 | 10.97 | 8.54 | 9.58 | 10.22 | 10.46 | 9.42 | 9.60 | 9.36 | 8.82 | 9.15 | 9.24 |
| CaO | 12.32 | 11.23 | 10.82 | 12.13 | 11.30 | 9.98 | 12.04 | 10.81 | 11.03 | 10.35 | 10.98 | 11.04 |
| $Na_2O$ | 2.27 | 1.90 | 2.81 | 2.19 | 2.16 | 2.97 | 2.09 | 2.76 | 2.67 | 2.62 | 2.80 | 2.89 |
| $K_2O$ | 1.06 | 1.00 | 1.37 | 1.25 | 1.11 | 1.20 | 1.16 | 1.35 | 1.30 | 1.19 | 1.44 | 1.37 |
| $P_2O_5$ | 0.34 | 0.41 | 0.43 | 0.39 | 0.39 | 0.39 | 0.40 | 0.41 | 0.45 | 0.38 | 0.49 | 0.50 |
| $S_{total}$ | | 0.03 | 0.09 | 0.05 | | 0.02 | 0.01 | 0.02 | 0.02 | 0.01 | | 0.02 |
| LOI | 0.89 | 1.36 | 2.36 | 2.14 | 1.48 | 3.66 | 2.25 | 1.22 | 2.09 | 2.53 | 1.29 | 1.02 |
| Total | 99.48 | 99.69 | 99.50 | 99.56 | 99.54 | 99.66 | 99.43 | 99.53 | 99.55 | 99.62 | 99.45 | 99.47 |
| Mg# | 61 | 58 | 55 | 57 | 59 | 61 | 56 | 58 | 58 | 57 | 57 | 58 |
| Li, ppm | 7.60 | 7.21 | 6.98 | 8.21 | 7.19 | 7.35 | 9.13 | 8.34 | 9.05 | 9.55 | 11.32 | 9.57 |
| Be | 1.43 | 1.38 | 1.91 | 1.51 | 1.51 | 1.72 | 1.45 | 2.09 | 1.81 | 1.58 | 2.09 | 1.91 |
| Sc | 36.3 | 25.7 | 26.7 | 27.0 | 29.5 | 30.1 | 28.9 | 28.0 | 27.8 | 29.1 | 29.3 | 30.3 |
| V | 293 | 266 | 205 | 232 | 257 | 251 | 280 | 245 | 228 | 214 | 238 | 245 |
| Cr | 975 | 519 | 497 | 542 | 479 | 450 | 520 | 450 | 458 | 520 | 572 | 569 |
| Co | 78.4 | 57.4 | 53.7 | 55.9 | 70.0 | 60.3 | 64.9 | 61.1 | 58.9 | 62.9 | 63.2 | 64.2 |
| Ni | 222 | 197 | 171 | 183 | 183 | 165 | 190 | 174 | 172 | 185 | 196 | 198 |
| Cu | 190 | 143 | 138 | 139 | 147 | 166 | 169 | 143 | 152 | 138 | 175 | 189 |
| Zn | 118 | 105 | 114 | 106 | 110 | 109 | 114 | 112 | 107 | 118 | 111 | 120 |
| Ga | 15.2 | 13.0 | 17.7 | 14.7 | 16.6 | 13.5 | 18.3 | 15.0 | 14.8 | 16.1 | 15.2 | 16.1 |
| Rb | 20.1 | 15.8 | 22.8 | 19.5 | 21.2 | 20.6 | 20.3 | 23.7 | 13.7 | 17.5 | 25.3 | 22.6 |
| Sr | 560 | 608 | 846 | 757 | 614 | 924 | 665 | 765 | 733 | 855 | 827 | 842 |
| Y | 19.1 | 19.2 | 21.6 | 19.5 | 19.7 | 18.6 | 19.7 | 20.7 | 20.2 | 20.2 | 22.2 | 22.8 |
| Zr | 194 | 186 | 362 | 358 | 179 | 192 | 198 | 208 | 203 | 202 | 218 | 233 |
| Nb | 50.5 | 47.8 | 59.2 | 52.5 | 53.8 | 52.8 | 54.6 | 60.4 | 62.8 | 58.0 | 66.1 | 69.1 |
| Cs | 0.15 | 0.18 | 1.42 | 0.13 | 0.22 | 0.13 | 0.14 | 0.16 | 0.31 | 0.13 | 0.20 | 0.27 |
| Ba | 781 | 362 | 910 | 854 | 622 | 658 | 987 | 1076 | 732 | 638 | 979 | 1130 |
| La | 38.2 | 42.7 | 52.1 | 47.5 | 47.3 | 47.2 | 45.8 | 52.3 | 54.1 | 46.9 | 59.2 | 60.9 |

| | | | | | | | | | | | | |
|---|---|---|---|---|---|---|---|---|---|---|---|---|
| Ce | 86.9 | 84.6 | 99.9 | 89.6 | 88.7 | 93.5 | 94.1 | 104 | 105 | 93.5 | 119 | 119 |
| Pr | 10.2 | 10.9 | 12.1 | 11.1 | 11.2 | 10.7 | 11.0 | 11.7 | 11.8 | 10.7 | 13.1 | 13.1 |
| Nd | 41.8 | 44.6 | 48.6 | 44.5 | 41.9 | 42.6 | 44.0 | 46.5 | 45.9 | 41.1 | 51.6 | 50.8 |
| Sm | 8.43 | 9.24 | 9.51 | 9.01 | 8.19 | 8.25 | 8.84 | 8.87 | 8.77 | 8.05 | 9.52 | 9.67 |
| Eu | 2.50 | 2.53 | 2.86 | 2.61 | 2.32 | 2.43 | 2.57 | 2.68 | 2.65 | 2.42 | 2.90 | 2.88 |
| Gd | 7.04 | 7.48 | 7.90 | 7.25 | 6.88 | 6.82 | 7.11 | 7.28 | 7.10 | 6.70 | 7.81 | 7.73 |
| Tb | 0.96 | 0.98 | 1.02 | 0.95 | 0.98 | 0.90 | 1.02 | 1.03 | 0.97 | 0.95 | 1.07 | 1.07 |
| Dy | 4.74 | 4.93 | 5.38 | 4.82 | 4.69 | 4.70 | 4.95 | 4.91 | 4.96 | 4.64 | 5.17 | 5.27 |
| Ho | 0.88 | 0.81 | 0.86 | 0.79 | 0.85 | 0.90 | 0.90 | 0.94 | 0.96 | 0.88 | 1.06 | 1.00 |
| Er | 1.97 | 2.15 | 2.36 | 2.11 | 2.01 | 2.00 | 2.09 | 2.18 | 2.07 | 2.07 | 2.24 | 2.21 |
| Tm | 0.27 | 0.25 | 0.30 | 0.25 | 0.27 | 0.29 | 0.29 | 0.31 | 0.30 | 0.30 | 0.31 | 0.32 |
| Yb | 1.54 | 1.59 | 1.87 | 1.58 | 1.67 | 1.63 | 1.66 | 1.76 | 1.70 | 1.72 | 1.82 | 1.75 |
| Lu | 0.20 | 0.21 | 0.25 | 0.21 | 0.20 | 0.21 | 0.21 | 0.23 | 0.23 | 0.22 | 0.25 | 0.24 |
| Hf | 5.29 | 5.42 | 9.41 | 9.30 | 5.51 | 4.96 | 5.56 | 5.58 | 5.29 | 5.03 | 5.49 | 5.58 |
| Ta | 2.99 | 3.25 | 3.55 | 3.25 | 2.96 | 3.24 | 3.24 | 3.63 | 3.60 | 3.26 | 3.80 | 3.72 |
| Pb | 5.03 | 4.82 | 4.01 | 5.07 | 4.81 | 5.00 | 4.71 | 5.49 | 5.48 | 4.69 | 6.59 | 5.77 |
| Th | 5.08 | 5.27 | 6.61 | 5.89 | 5.50 | 6.21 | 5.64 | 6.76 | 7.18 | 6.01 | 7.69 | 7.48 |
| U | 0.89 | 1.05 | 1.46 | 0.85 | 1.12 | 1.27 | 0.85 | 0.97 | 1.38 | 1.23 | 0.84 | 0.89 |

LOI - loss on ignition. Mg# = 100*Mg/(Mg + 0.9*$Fe_{total}$). Map datum WGS84, Latitude and longtitude in UTM coordinate system, zone 36M.

**Table 2:** Selected compositions of forsterite

| Sample | 16-05 | | | | | 16-06 | | 19-04c | | 16-05 | | 16-06 | | 19-07 | | 16-06 | | 19-08 | |
|---|---|---|---|---|---|---|---|---|---|---|---|---|---|---|---|---|---|---|---|
| Zonation | normal | | | | | | | | | reverse | | | | | | unzoned | | | |
| Crystal | pheno | pheno | | pheno | | pheno | | micro | | pheno | | pheno | | pheno | | micro | gm | fragment | fragment |
| | core | core | rim | core | rim | core | rim | core | rim | core | rim | core | rim | core | rim | core | core | core | core |
| Analysis | 26 | 7 | 9 | 3 | 5 | 18 | 20 | 150 | 151 | 16 | 19 | 14 | 19 | 71 | 73 | 52 | 13 | 139 | 145 |
| $SiO_2$ | 41.60 | 41.13 | 40.02 | 40.61 | 39.64 | 40.65 | 40.10 | 41.42 | 40.53 | 38.23 | 39.68 | 38.38 | 39.53 | 39.72 | 40.26 | 39.65 | 39.65 | 40.83 | 39.41 |
| $TiO_2$ | | | 0.03 | | | | | 0.03 | 0.03 | | | 0.03 | | | | | | | |
| $Al_2O_3$ | | 0.03 | 0.05 | | | | 0.03 | | 0.03 | | | 0.03 | | | 0.03 | | | 0.03 | |
| FeO | 9.25 | 9.93 | 15.95 | 10.99 | 17.38 | 13.22 | 15.26 | 12.95 | 17.26 | 24.65 | 16.29 | 23.42 | 17.66 | 19.93 | 17.28 | 15.69 | 17.23 | 16.19 | 21.49 |
| MgO | 48.62 | 48.23 | 43.05 | 48.37 | 43.42 | 45.73 | 44.03 | 45.72 | 42.35 | 37.50 | 44.00 | 38.26 | 43.02 | 40.13 | 42.38 | 44.63 | 43.32 | 43.49 | 38.66 |
| MnO | 0.16 | 0.15 | 0.30 | 0.13 | 0.25 | 0.19 | 0.23 | 0.20 | 0.33 | 0.30 | 0.21 | 0.26 | 0.23 | 0.32 | 0.32 | 0.21 | 0.23 | 0.18 | 0.29 |
| CaO | 0.31 | 0.34 | 0.42 | 0.34 | 0.36 | 0.29 | 0.25 | 0.33 | 0.31 | 0.27 | 0.37 | 0.27 | 0.34 | 0.17 | 0.34 | 0.31 | 0.38 | 0.26 | 0.25 |
| NiO | 0.33 | 0.28 | 0.17 | 0.33 | 0.20 | 0.23 | 0.22 | 0.35 | 0.25 | 0.05 | 0.21 | 0.14 | 0.20 | 0.13 | 0.21 | 0.25 | 0.19 | 0.20 | 0.11 |
| $Cr_2O_3$ | 0.08 | 0.10 | 0.05 | 0.09 | 0.11 | 0.06 | 0.03 | 0.06 | 0.06 | | | | | | 0.04 | 0.06 | | | |
| Total | 100.34 | 100.18 | 100.03 | 100.86 | 101.36 | 100.37 | 100.16 | 101.05 | 101.14 | 101.00 | 100.76 | 100.79 | 100.98 | 100.40 | 100.87 | 100.80 | 101.00 | 101.19 | 100.21 |
| Si | 1.013 | 1.007 | 1.009 | 0.994 | 0.995 | 1.008 | 1.007 | 1.018 | 1.016 | 0.996 | 0.996 | 0.996 | 0.996 | 1.015 | 1.012 | 0.993 | 0.997 | 1.016 | 1.017 |
| Ti | | | 0.001 | | | | | 0.001 | 0.001 | | | 0.001 | | | | | | | |
| Al | | 0.001 | 0.001 | | | | 0.001 | | 0.001 | | | 0.001 | | | 0.001 | | | 0.001 | |
| Total | 1.013 | 1.008 | 1.011 | 0.994 | 0.995 | 1.008 | 1.008 | 1.019 | 1.018 | 0.996 | 0.996 | 0.998 | 0.996 | 1.015 | 1.013 | 0.993 | 0.997 | 1.017 | 1.017 |
| Mg | 1.765 | 1.761 | 1.619 | 1.766 | 1.624 | 1.691 | 1.648 | 1.675 | 1.582 | 1.456 | 1.647 | 1.480 | 1.617 | 1.529 | 1.589 | 1.666 | 1.624 | 1.614 | 1.487 |
| Fe | 0.188 | 0.203 | 0.336 | 0.225 | 0.365 | 0.274 | 0.320 | 0.266 | 0.362 | 0.537 | 0.342 | 0.508 | 0.372 | 0.426 | 0.363 | 0.329 | 0.362 | 0.337 | 0.464 |
| Mn | 0.003 | 0.003 | 0.006 | 0.003 | 0.005 | 0.004 | 0.005 | 0.004 | 0.007 | 0.007 | 0.004 | 0.006 | 0.005 | 0.007 | 0.007 | 0.004 | 0.005 | 0.004 | 0.006 |
| Ca | 0.008 | 0.009 | 0.011 | 0.009 | 0.010 | 0.008 | 0.007 | 0.009 | 0.008 | 0.008 | 0.010 | 0.008 | 0.009 | 0.005 | 0.009 | 0.008 | 0.010 | 0.007 | 0.007 |
| Ni | 0.006 | 0.006 | 0.003 | 0.006 | 0.004 | 0.005 | 0.005 | 0.007 | 0.005 | 0.001 | 0.004 | 0.003 | 0.004 | 0.003 | 0.004 | 0.005 | 0.004 | 0.004 | 0.002 |
| Cr | 0.002 | 0.002 | 0.001 | 0.002 | 0.002 | 0.001 | 0.001 | 0.001 | 0.001 | | | | | | 0.001 | 0.001 | | | |
| Total | 1.973 | 1.984 | 1.977 | 2.010 | 2.010 | 1.983 | 1.986 | 1.962 | 1.965 | 2.008 | 2.008 | 2.005 | 2.007 | 1.969 | 1.973 | 2.014 | 2.006 | 1.966 | 1.966 |
| Fo | 89.5 | 88.8 | 81.9 | 87.8 | 80.8 | 85.3 | 83.0 | 85.4 | 80.5 | 72.5 | 82.0 | 73.8 | 80.5 | 77.6 | 80.5 | 82.7 | 81.0 | 82.1 | 75.6 |

Fo – forsterite end-member, mol. %.

**Table 3:** Selected analyses of clinopyroxene

| Sample | 16-05 | 16-06 | 16-25 | 16-26 | 19-04a | 16-06 | 19-04c | 19-07 | 19-08 | | 19-64 | 16-26 | | 19-07 | 19-04a | | 19-08 | 16-06 | |
|---|---|---|---|---|---|---|---|---|---|---|---|---|---|---|---|---|---|---|---|
| Population | Ia | | Ib | | Ic | | | II | | | | III | | | IV | | | | |
| Analysis | 26 | 31 | 43 | 33 | 1 | 49 | 113 | 97 | 123 | 134 | 3 | 102 | 53 | 110 | 14 | 6 | 125 | 21 | 23 |
| $SiO_2$ | 50.19 | 49.32 | 51.33 | 53.41 | 53.89 | 53.44 | 54.62 | 53.68 | 54.32 | 52.90 | 54.19 | 50.99 | 53.18 | 52.88 | 51.58 | 47.61 | 51.69 | 50.74 | 50.76 |
| $TiO_2$ | 1.67 | 1.57 | 1.30 | 0.63 | 0.51 | 0.42 | 0.42 | 0.64 | 0.50 | 0.84 | 0.43 | 1.93 | 0.83 | 0.93 | 0.52 | 1.99 | 0.51 | 0.95 | 0.97 |
| $Al_2O_3$ | 3.34 | 3.82 | 4.00 | 2.35 | 1.81 | 1.05 | 1.32 | 2.50 | 1.85 | 2.56 | 1.30 | 3.23 | 2.30 | 2.14 | 1.26 | 5.10 | 0.69 | 3.36 | 3.40 |
| $Cr_2O_3$ | | | 0.21 | 0.31 | 1.37 | 0.89 | 0.53 | 0.38 | 0.71 | 0.32 | 0.47 | 0.20 | 0.23 | 0.32 | | | | 0.24 | 0.17 |
| $Fe_2O_3$ | 3.03 | 4.36 | | | | 2.29 | | | | 0.41 | 0.24 | 0.16 | | 0.78 | 3.33 | 4.44 | 6.32 | 4.06 | 3.54 |
| FeO | 5.31 | 4.36 | 8.65 | 6.68 | 3.54 | 2.22 | 4.01 | 5.57 | 4.63 | 5.72 | 3.60 | 7.77 | 6.53 | 4.52 | 10.93 | 8.15 | 14.07 | 6.46 | 4.50 |
| MnO | 0.17 | 0.21 | 0.18 | 0.13 | 0.09 | 0.09 | 0.10 | 0.11 | 0.10 | 0.13 | 0.09 | 0.18 | 0.12 | 0.11 | 0.45 | 0.31 | 0.80 | 0.29 | 0.17 |
| MgO | 14.20 | 13.97 | 13.69 | 16.16 | 17.14 | 18.06 | 18.28 | 17.08 | 17.42 | 15.88 | 18.23 | 13.41 | 15.60 | 16.18 | 8.42 | 8.75 | 4.46 | 12.52 | 15.36 |
| NiO | | | | 0.03 | 0.09 | | 0.05 | 0.04 | 0.05 | | 0.08 | 0.04 | 0.03 | 0.03 | | | | | |
| CaO | 21.88 | 22.06 | 19.63 | 19.24 | 21.39 | 21.43 | 20.74 | 19.96 | 20.75 | 20.95 | 20.86 | 22.37 | 20.99 | 22.41 | 21.25 | 22.47 | 17.35 | 20.34 | 20.32 |
| $Na_2O$ | 0.58 | 0.57 | 0.81 | 0.53 | 0.70 | 0.50 | 0.50 | 0.65 | 0.62 | 0.65 | 0.50 | 0.48 | 0.46 | 0.41 | 1.84 | 1.27 | 3.71 | 1.38 | 0.75 |
| Total | 100.37 | 100.25 | 99.80 | 99.47 | 100.52 | 100.39 | 100.57 | 100.61 | 100.95 | 100.36 | 100.00 | 100.76 | 100.26 | 100.73 | 99.58 | 100.08 | 99.60 | 100.34 | 99.94 |
| Si | 1.859 | 1.832 | 1.908 | 1.972 | 1.952 | 1.940 | 1.971 | 1.947 | 1.960 | 1.934 | 1.966 | 1.887 | 1.953 | 1.927 | 1.977 | 1.812 | 2.017 | 1.889 | 1.874 |
| Al | 0.141 | 0.167 | 0.092 | 0.028 | 0.048 | 0.045 | 0.029 | 0.053 | 0.040 | 0.066 | 0.034 | 0.113 | 0.047 | 0.073 | 0.023 | 0.188 | | 0.110 | 0.126 |
| $Fe^{3+}$ | | 0.001 | | | | 0.015 | | | | | | | | | | | | | |
| Total | 2.000 | 2.000 | 2.000 | 2.000 | 2.000 | 2.000 | 2.000 | 2.000 | 2.000 | 2.000 | 2.000 | 2.000 | 2.000 | 2.000 | 2.000 | 2.000 | 2.017 | 2.000 | 2.000 |
| Mg | 0.784 | 0.774 | 0.759 | 0.890 | 0.926 | 0.977 | 0.984 | 0.923 | 0.937 | 0.866 | 0.986 | 0.740 | 0.854 | 0.879 | 0.481 | 0.496 | 0.259 | 0.695 | 0.846 |
| $Fe^{2+}$ | 0.164 | 0.136 | 0.269 | 0.206 | 0.107 | 0.067 | 0.121 | 0.169 | 0.140 | 0.175 | 0.109 | 0.240 | 0.200 | 0.138 | 0.350 | 0.259 | 0.459 | 0.201 | 0.139 |
| $Fe^{3+}$ | 0.085 | 0.121 | | | | 0.048 | | | | 0.011 | 0.007 | 0.004 | | 0.021 | 0.096 | 0.127 | 0.186 | 0.114 | 0.098 |
| Al | 0.005 | | 0.083 | 0.074 | 0.029 | | 0.027 | 0.054 | 0.039 | 0.045 | 0.022 | 0.027 | 0.053 | 0.019 | 0.034 | 0.041 | 0.032 | 0.037 | 0.022 |
| Ti | 0.047 | 0.044 | 0.036 | 0.017 | 0.014 | 0.011 | 0.011 | 0.017 | 0.013 | 0.023 | 0.012 | 0.054 | 0.023 | 0.026 | 0.015 | 0.057 | 0.015 | 0.027 | 0.027 |
| Mn | 0.005 | 0.007 | 0.006 | 0.004 | 0.003 | 0.003 | 0.003 | 0.003 | 0.003 | 0.004 | 0.003 | 0.005 | 0.004 | 0.003 | 0.014 | 0.010 | 0.027 | 0.009 | 0.005 |
| Cr | | | 0.006 | 0.009 | 0.039 | 0.026 | 0.015 | 0.011 | 0.020 | 0.009 | 0.014 | 0.006 | 0.007 | 0.009 | | | | 0.007 | 0.005 |
| Ni | | | | 0.001 | 0.003 | | 0.002 | 0.001 | 0.001 | | 0.002 | 0.001 | 0.001 | 0.001 | | | | | |
| Ca | 0.868 | 0.878 | 0.782 | 0.761 | 0.830 | 0.833 | 0.802 | 0.776 | 0.802 | 0.821 | 0.811 | 0.887 | 0.826 | 0.875 | 0.873 | 0.916 | 0.725 | 0.811 | 0.804 |
| Na | 0.042 | 0.041 | 0.058 | 0.038 | 0.049 | 0.035 | 0.035 | 0.045 | 0.044 | 0.046 | 0.035 | 0.035 | 0.032 | 0.029 | 0.137 | 0.093 | 0.281 | 0.100 | 0.054 |
| Total | 2.000 | 2.000 | 2.000 | 2.000 | 1.999 | 2.000 | 2.000 | 2.000 | 2.000 | 2.000 | 2.000 | 2.000 | 2.000 | 2.000 | 2.000 | 2.000 | 1.983 | 2.000 | 2.000 |
| Mg# | 83 | 85 | 74 | 81 | 90 | 94 | 89 | 85 | 87 | 83 | 90 | 75 | 81 | 86 | 58 | 66 | 36 | 78 | 86 |

**Table 3:** Continued

| Sample | 16-05 | | | 19-07 | | 16-26 | | 16-05 | | | 19-06 | | 16-26 | | 16-05 | 16-06 | 19-06 | 19-07 | 16-26 |
|---|---|---|---|---|---|---|---|---|---|---|---|---|---|---|---|---|---|---|---|
| Population | V (mantle) | | | | | | | V (core) | | | | | | | VI | | | | |
| Analysis | 28 | 27 | 25 | 92 | 91 | 46 | 44 | 60 | 61 | 62 | 30 | 32 | 73 | 74 | 3 | 31 | 39 | 104 | 78 |
| $SiO_2$ | 52.24 | 51.10 | 52.41 | 54.39 | 52.43 | 53.38 | 52.20 | 50.27 | 52.63 | 50.04 | 51.86 | 52.30 | 54.08 | 53.37 | 51.46 | 48.94 | 50.29 | 49.04 | 46.44 |
| $TiO_2$ | 0.76 | 1.31 | 0.91 | 0.55 | 1.26 | 0.53 | 1.12 | 1.30 | 0.74 | 1.79 | 1.19 | 1.30 | 0.81 | 0.97 | 1.34 | 1.99 | 1.87 | 2.59 | 3.65 |
| $Al_2O_3$ | 1.91 | 2.20 | 1.24 | 1.76 | 2.45 | 1.58 | 1.67 | 2.97 | 1.46 | 2.94 | 2.31 | 1.65 | 1.71 | 1.81 | 1.72 | 2.91 | 3.01 | 4.40 | 4.87 |
| $Cr_2O_3$ | 1.33 | 0.57 | 0.46 | 1.06 | 0.62 | 1.09 | 0.52 | 1.24 | 0.61 | 0.45 | 0.98 | 0.22 | 0.56 | 0.36 | 0.16 | | 0.06 | | 0.05 |
| $Fe_2O_3$ | 1.37 | 2.90 | 2.18 | | 0.29 | | | 3.30 | 2.16 | 3.13 | 0.38 | 0.79 | | | 2.42 | 4.06 | 1.48 | 1.40 | 3.30 |
| FeO | 3.86 | 3.45 | 3.62 | 4.41 | 5.23 | 5.23 | 6.24 | 3.25 | 4.40 | 4.14 | 4.83 | 5.79 | 6.53 | 7.03 | 5.10 | 5.50 | 6.17 | 6.85 | 8.69 |
| MnO | 0.09 | 0.10 | 0.10 | 0.09 | 0.12 | 0.17 | 0.12 | 0.10 | 0.14 | 0.12 | 0.11 | 0.12 | 0.17 | 0.14 | 0.16 | 0.16 | 0.11 | 0.16 | 0.18 |
| MgO | 16.56 | 15.71 | 16.31 | 17.39 | 15.57 | 16.45 | 14.87 | 15.73 | 17.58 | 14.76 | 15.43 | 15.82 | 15.66 | 15.11 | 15.37 | 13.98 | 14.07 | 12.93 | 11.46 |
| NiO | | | | 0.03 | | | | | | | | | 0.03 | | | | | | |
| CaO | 21.14 | 22.46 | 22.87 | 21.11 | 22.51 | 19.96 | 22.01 | 21.12 | 20.04 | 22.54 | 22.24 | 21.85 | 20.69 | 21.24 | 22.39 | 21.65 | 22.03 | 22.09 | 20.57 |
| $Na_2O$ | 0.56 | 0.42 | 0.30 | 0.65 | 0.41 | 0.60 | 0.37 | 0.61 | 0.44 | 0.43 | 0.46 | 0.35 | 0.47 | 0.44 | 0.30 | 0.43 | 0.48 | 0.56 | 0.68 |
| Total | 99.82 | 100.22 | 100.40 | 101.43 | 100.88 | 98.99 | 99.12 | 99.89 | 100.21 | 100.34 | 99.79 | 100.19 | 100.71 | 100.48 | 100.42 | 99.62 | 99.57 | 100.02 | 99.90 |
| Si | 1.919 | 1.882 | 1.922 | 1.955 | 1.914 | 1.975 | 1.947 | 1.857 | 1.925 | 1.851 | 1.914 | 1.926 | 1.981 | 1.965 | 1.900 | 1.838 | 1.877 | 1.831 | 1.764 |
| Al | 0.081 | 0.096 | 0.054 | 0.045 | 0.086 | 0.025 | 0.053 | 0.129 | 0.063 | 0.128 | 0.086 | 0.072 | 0.019 | 0.035 | 0.075 | 0.129 | 0.123 | 0.169 | 0.218 |
| $Fe^{3+}$ | | 0.022 | 0.024 | | | | | 0.014 | 0.012 | 0.020 | | 0.002 | | | 0.025 | 0.034 | | | 0.018 |
| Total | 2.000 | 2.000 | 2.000 | 2.000 | 2.000 | 2.000 | 2.000 | 2.000 | 2.000 | 2.000 | 2.000 | 2.000 | 2.000 | 2.000 | 2.000 | 2.000 | 2.000 | 2.000 | 2.000 |
| Mg | 0.907 | 0.863 | 0.892 | 0.932 | 0.847 | 0.907 | 0.827 | 0.866 | 0.959 | 0.814 | 0.849 | 0.869 | 0.855 | 0.829 | 0.846 | 0.783 | 0.783 | 0.720 | 0.649 |
| $Fe^{2+}$ | 0.119 | 0.106 | 0.111 | 0.132 | 0.160 | 0.162 | 0.195 | 0.100 | 0.135 | 0.128 | 0.149 | 0.178 | 0.200 | 0.216 | 0.158 | 0.173 | 0.193 | 0.214 | 0.276 |
| $Fe^{3+}$ | 0.038 | 0.058 | 0.036 | | 0.008 | | | 0.078 | 0.048 | 0.067 | 0.011 | 0.020 | | | 0.042 | 0.081 | 0.041 | 0.039 | 0.076 |
| Al | 0.002 | | | 0.029 | 0.020 | 0.044 | 0.021 | | | | 0.014 | | 0.055 | 0.043 | | | 0.009 | 0.025 | |
| Ti | 0.021 | 0.036 | 0.025 | 0.015 | 0.035 | 0.015 | 0.031 | 0.036 | 0.020 | 0.050 | 0.033 | 0.036 | 0.022 | 0.027 | 0.037 | 0.056 | 0.052 | 0.073 | 0.104 |
| Mn | 0.003 | 0.003 | 0.003 | 0.003 | 0.004 | 0.005 | 0.004 | 0.003 | 0.004 | 0.004 | 0.003 | 0.004 | 0.005 | 0.004 | 0.005 | 0.005 | 0.004 | 0.005 | 0.006 |
| Cr | 0.039 | 0.017 | 0.013 | 0.030 | 0.018 | 0.032 | 0.015 | 0.036 | 0.018 | 0.013 | 0.029 | 0.006 | 0.016 | 0.011 | 0.005 | | 0.002 | | 0.002 |
| Ni | | | | 0.001 | | | | | | | | | 0.001 | | | | | | |
| Ca | 0.832 | 0.887 | 0.899 | 0.813 | 0.881 | 0.792 | 0.880 | 0.836 | 0.785 | 0.893 | 0.879 | 0.862 | 0.812 | 0.838 | 0.886 | 0.871 | 0.881 | 0.884 | 0.837 |
| Na | 0.040 | 0.030 | 0.021 | 0.045 | 0.029 | 0.043 | 0.027 | 0.044 | 0.031 | 0.031 | 0.033 | 0.025 | 0.033 | 0.031 | 0.021 | 0.031 | 0.035 | 0.041 | 0.050 |
| Total | 2.000 | 2.000 | 2.000 | 2.000 | 2.000 | 2.000 | 2.000 | 2.000 | 2.000 | 2.000 | 2.000 | 2.000 | 2.000 | 2.000 | 2.000 | 2.000 | 2.000 | 2.000 | 2.000 |
| Mg# | 88 | 89 | 89 | 88 | 84 | 85 | 81 | 90 | 88 | 86 | 85 | 83 | 81 | 79 | 84 | 82 | 80 | 77 | 70 |

$Fe_2O_3$ and FeO calculated from charge balance (4 cations and 6 O), Mg# = 100*Mg/(Mg+$Fe^{2+}$).

**Table 4:** Selected analyses of spinel-group minerals

| Sample | 16-05 | | 19-06 | | 19-07 | 19-06 | | 19-04c | | | | 16-05 | 19-06 | | | | 19-04a | 19-08 | 19-04a |
|---|---|---|---|---|---|---|---|---|---|---|---|---|---|---|---|---|---|---|---|
| Variety | 1 | | | | 2 | 3 | | | | | | 4 | 5 | | | | | 6 | |
| | core | rim | core | rim | core | core | rim | core | rim | core | rim | core | core | rim | core | rim | core | core | core |
| Analysis | 1 | 4 | 30 | 32 | 62 | 8 | 12 | 93 | 96 | 39 | 40 | 73 | 49 | 50 | 44 | 46 | 9 | 88 | 23 |
| MgO | 12.69 | 8.51 | 9.82 | 9.89 | 5.44 | 9.58 | 3.07 | 4.81 | 3.53 | 5.49 | 2.07 | 3.94 | 2.51 | 1.69 | 2.55 | 1.84 | 2.28 | 2.58 | 3.24 |
| $Al_2O_3$ | 7.65 | 7.17 | 8.38 | 8.40 | 7.89 | 7.03 | 4.46 | 7.45 | 1.80 | 8.28 | 3.44 | 2.81 | 6.10 | 2.69 | 5.02 | 3.01 | 1.23 | 1.99 | 3.05 |
| $SiO_2$ | 0.09 | 0.09 | 0.07 | 0.08 | 0.09 | 0.06 | 0.05 | | 0.03 | 0.07 | 0.08 | 0.03 | 0.03 | 0.10 | 0.04 | 0.08 | 0.04 | 0.12 | 0.07 |
| CaO | | 0.12 | | | | | 0.16 | 0.05 | 0.08 | | 0.12 | 0.08 | 0.04 | 0.05 | 0.06 | 0.14 | | | |
| $TiO_2$ | 1.77 | 2.12 | 3.19 | 3.19 | 15.30 | 2.06 | 19.41 | 2.73 | 18.01 | 3.47 | 23.39 | 14.19 | 15.14 | 25.57 | 18.48 | 25.00 | 22.06 | 17.13 | 21.17 |
| $V_2O_3$ | 0.10 | 0.09 | 0.21 | 0.18 | 0.57 | 0.12 | 0.35 | 0.12 | 0.26 | 0.20 | 0.33 | 0.28 | 0.32 | 0.35 | 0.36 | 0.37 | 0.32 | 0.60 | 0.38 |
| $Cr_2O_3$ | 53.91 | 50.81 | 44.62 | 44.04 | 6.17 | 51.56 | 9.61 | 44.17 | 3.27 | 42.48 | 2.02 | 10.36 | 17.88 | 0.75 | 9.91 | 1.06 | 1.79 | 0.04 | 0.08 |
| MnO | 0.11 | 0.19 | 0.16 | 0.14 | 0.32 | 0.14 | 0.56 | 0.50 | 0.65 | 0.25 | 0.63 | 0.55 | 0.49 | 0.70 | 0.56 | 0.65 | 0.74 | 0.56 | 0.68 |
| NiO | 0.18 | 0.13 | 0.15 | 0.18 | 0.08 | 0.14 | 0.03 | 0.05 | 0.09 | 0.12 | 0.04 | 0.09 | 0.03 | 0.03 | | | 0.07 | 0.05 | 0.05 |
| ZnO | 0.02 | 0.10 | 0.07 | 0.06 | 0.07 | 0.10 | 0.08 | 0.24 | 0.07 | 0.10 | 0.09 | 0.13 | 0.15 | 0.09 | 0.10 | 0.08 | 0.10 | 0.11 | 0.08 |
| $Fe_2O_3$ | 7.95 | 9.20 | 12.54 | 13.11 | 26.66 | 8.93 | 17.90 | 12.64 | 30.27 | 12.12 | 17.71 | 29.10 | 14.82 | 14.99 | 17.78 | 15.88 | 24.08 | 34.18 | 26.45 |
| FeO | 14.99 | 21.55 | 20.76 | 20.65 | 38.30 | 19.80 | 44.59 | 27.38 | 41.84 | 27.65 | 49.20 | 37.82 | 41.69 | 51.49 | 44.47 | 50.93 | 47.49 | 42.87 | 45.92 |
| Total | 99.47 | 100.07 | 99.96 | 99.90 | 100.88 | 99.50 | 100.28 | 100.15 | 99.90 | 100.21 | 99.11 | 99.38 | 99.18 | 98.49 | 99.34 | 99.03 | 100.22 | 100.22 | 101.16 |
| $Fe^{2+}$ | 0.367 | 0.557 | 0.499 | 0.496 | 0.706 | 0.506 | 0.812 | 0.726 | 0.782 | 0.705 | 0.863 | 0.761 | 0.845 | 0.881 | 0.842 | 0.874 | 0.847 | 0.837 | 0.803 |
| Mg | 0.625 | 0.430 | 0.490 | 0.494 | 0.280 | 0.484 | 0.164 | 0.250 | 0.192 | 0.282 | 0.113 | 0.213 | 0.135 | 0.093 | 0.137 | 0.101 | 0.125 | 0.141 | 0.173 |
| Mn | 0.003 | 0.005 | 0.005 | 0.004 | 0.009 | 0.004 | 0.017 | 0.015 | 0.020 | 0.007 | 0.019 | 0.017 | 0.015 | 0.022 | 0.017 | 0.020 | 0.023 | 0.017 | 0.021 |
| Ni | 0.005 | 0.003 | 0.004 | 0.005 | 0.002 | 0.004 | 0.001 | 0.001 | 0.003 | 0.003 | 0.001 | 0.003 | 0.001 | 0.001 | 0.000 | 0.000 | 0.002 | 0.002 | 0.002 |
| Zn | 0.001 | 0.003 | 0.002 | 0.001 | 0.002 | 0.002 | 0.002 | 0.006 | 0.002 | 0.002 | 0.002 | 0.003 | 0.004 | 0.003 | 0.003 | 0.002 | 0.003 | 0.003 | 0.002 |
| Total | 1.000 | 0.999 | 1.000 | 1.000 | 1.000 | 1.000 | 0.996 | 0.998 | 0.998 | 1.000 | 0.998 | 0.998 | 1.000 | 1.000 | 0.999 | 0.997 | 1.000 | 1.000 | 1.000 |
| Cr | 1.408 | 1.362 | 1.182 | 1.167 | 0.168 | 1.380 | 0.272 | 1.216 | 0.094 | 1.159 | 0.058 | 0.298 | 0.509 | 0.022 | 0.283 | 0.031 | 0.052 | 0.001 | 0.002 |
| $Fe^{3+}$ | 0.198 | 0.235 | 0.316 | 0.331 | 0.693 | 0.228 | 0.482 | 0.331 | 0.831 | 0.315 | 0.488 | 0.796 | 0.401 | 0.418 | 0.484 | 0.439 | 0.665 | 0.942 | 0.713 |
| Al | 0.298 | 0.286 | 0.331 | 0.332 | 0.321 | 0.280 | 0.188 | 0.306 | 0.078 | 0.336 | 0.149 | 0.120 | 0.259 | 0.117 | 0.214 | 0.130 | 0.053 | 0.086 | 0.129 |
| Ti | 0.044 | 0.054 | 0.080 | 0.080 | 0.398 | 0.052 | 0.522 | 0.072 | 0.494 | 0.090 | 0.645 | 0.388 | 0.410 | 0.713 | 0.503 | 0.691 | 0.609 | 0.472 | 0.570 |
| $Fe^{2+}$ | 0.047 | 0.054 | 0.083 | 0.083 | 0.401 | 0.054 | 0.522 | 0.072 | 0.494 | 0.093 | 0.645 | 0.388 | 0.410 | 0.715 | 0.503 | 0.691 | 0.610 | 0.477 | 0.572 |
| V | 0.003 | 0.002 | 0.006 | 0.005 | 0.016 | 0.003 | 0.010 | 0.003 | 0.008 | 0.006 | 0.010 | 0.008 | 0.009 | 0.010 | 0.011 | 0.011 | 0.010 | 0.018 | 0.011 |
| Total | 1.997 | 1.994 | 1.998 | 1.998 | 1.997 | 1.998 | 1.996 | 2.000 | 1.998 | 1.998 | 1.994 | 1.998 | 1.998 | 1.995 | 1.997 | 1.994 | 1.998 | 1.996 | 1.997 |
| Si | 0.003 | 0.003 | 0.002 | 0.003 | 0.003 | 0.002 | 0.002 | | 0.001 | 0.002 | 0.003 | 0.001 | 0.001 | 0.004 | 0.001 | 0.003 | 0.001 | 0.004 | 0.002 |
| Ca | | 0.005 | | | | | 0.006 | 0.002 | 0.003 | | 0.005 | 0.003 | 0.001 | 0.002 | 0.002 | 0.006 | | | |

Varieties (1) – microphenocrystals, inclusions in forsterite (Fo = 84-89 mol.%), (2) – inclusions in forsterite (Fo = 74-78 mol.%), (3) zoned microphenocrystals and inclusions in forsterite (Fo = 84-87 mol.%), (4) – inclusions in diopside, (5) groundmass crystals, (6) xenocrystals. $Fe_2O_3$ and FeO calculated from charge balance (3 cations and 4 O).

**Table 5:** Selected analyses of plagioclase and glass

| Sample | 16-05 plagioclase | | | 16-26 | | | 16-05 glass | | |
|---|---|---|---|---|---|---|---|---|---|
| Analysis | 2 | 6 | 12 | 1 | 3 | 5 | 1 | 11 | 15 |
| $SiO_2$ | 60.01 | 59.90 | 61.23 | 59.49 | 60.69 | 61.81 | 57.56 | 58.96 | 58.72 |
| $TiO_2$ | | | | | | | 0.47 | 1.11 | 0.85 |
| $Al_2O_3$ | 24.81 | 24.56 | 23.53 | 25.31 | 24.27 | 24.00 | 19.06 | 18.54 | 18.76 |
| $Fe_2O_3$ | 0.56 | 0.80 | 0.77 | 0.57 | 0.51 | 0.57 | 4.29 | 4.58 | 4.30 |
| CaO | 7.25 | 6.87 | 6.01 | 7.72 | 6.53 | 5.76 | 0.87 | 0.44 | 0.84 |
| MgO | 0.04 | 0.05 | 0.04 | 0.06 | 0.03 | 0.02 | 0.71 | 0.49 | 0.52 |
| MnO | | 0.02 | | | 0.02 | 0.02 | 0.08 | 0.09 | 0.07 |
| $Na_2O$ | 6.55 | 6.97 | 7.47 | 6.76 | 7.17 | 7.52 | 8.75 | 7.47 | 7.55 |
| $K_2O$ | 0.74 | 0.83 | 0.97 | 0.70 | 0.90 | 1.12 | 5.52 | 5.53 | 5.47 |
| SrO | 0.51 | 0.65 | 0.45 | 0.50 | 0.49 | 0.45 | | | |
| BaO | 0.19 | 0.23 | 0.23 | 0.27 | 0.26 | 0.45 | 0.03 | 0.03 | 0.05 |
| $P_2O_5$ | | | | | | | 0.49 | 0.51 | 0.40 |
| $SO_3$ | | | | | | | | | 0.16 |
| Cl | | | | | | | 0.27 | 0.28 | 0.35 |
| $-O=Cl_2$ | | | | | | | 0.06 | 0.06 | 0.08 |
| Total | 100.66 | 100.87 | 100.71 | 101.38 | 100.87 | 101.71 | 98.03 | 97.96 | 97.96 |
| Si | 2.674 | 2.672 | 2.727 | 2.642 | 2.700 | 2.727 | | | |
| Al | 1.303 | 1.291 | 1.235 | 1.325 | 1.273 | 1.248 | | | |
| $Fe^{3+}$ | 0.019 | 0.027 | 0.026 | 0.019 | 0.017 | 0.019 | | | |
| Total | 3.996 | 3.990 | 3.988 | 3.986 | 3.989 | 3.993 | | | |
| Ca | 0.346 | 0.328 | 0.287 | 0.367 | 0.311 | 0.272 | | | |
| Na | 0.566 | 0.603 | 0.645 | 0.582 | 0.618 | 0.643 | | | |
| K | 0.042 | 0.047 | 0.055 | 0.040 | 0.051 | 0.063 | | | |
| Mn | 0.000 | 0.001 | 0.000 | 0.000 | 0.001 | 0.001 | | | |
| Mg | 0.003 | 0.003 | 0.003 | 0.004 | 0.002 | 0.002 | | | |
| Sr | 0.013 | 0.017 | 0.012 | 0.013 | 0.013 | 0.011 | | | |
| Ba | 0.003 | 0.004 | 0.004 | 0.005 | 0.005 | 0.008 | | | |
| Total | 0.973 | 1.003 | 1.006 | 1.011 | 1.001 | 1.000 | | | |

P, S and Cl were not analysed in plagioclase.

**Table 6:** Rb-Sr and Sm-Nd data for samples of the Ogol and Lemagarut lavas and the Precambrian rocks

| Sample | Rb ppm | Sr ppm | $^{87}Rb/^{86}Sr_m$ | $^{87}Sr/^{86}Sr_m$ | $^{87}Sr/^{86}Sr_i$ | Sm ppm | Nd ppm | $^{147}Sm/^{144}Nd_m$ | $^{143}Nd/^{144}Nd_m$ | $^{143}Nd/^{144}Nd_i$ | εNd |
|---|---|---|---|---|---|---|---|---|---|---|---|
| Ogol lavas | | | | | | | | | | | |
| A16-05 | 20.9 | 562 | 0.1077 | 0.703771±9 | 0.703768 | 8.17 | 40.8 | 0.1211 | 0.512616±6 | 0.512614 | -0.41 |
| A16-06 | 17.1 | 735 | 0.0670 | 0.703903±15 | 0.703901 | 9.79 | 51.2 | 0.1158 | 0.512579±3 | 0.512577 | -1.13 |
| A16-25 | 24.2 | 786 | 0.0890 | 0.703907±17 | 0.703904 | 9.69 | 52.5 | 0.1117 | 0.512553±4 | 0.512551 | -1.63 |
| A16-26 | 23.3 | 845 | 0.0796 | 0.704088±10 | 0.704085 | 9.28 | 49.8 | 0.1126 | 0.512561±3 | 0.512559 | -1.48 |
| A19-02 | 23.9 | 991 | 0.0696 | 0.704704±11 | 0.704702 | 8.59 | 43.6 | 0.1191 | 0.512462±4 | 0.512460 | -3.41 |
| A19-4c | 28.2 | 851 | 0.0958 | 0.704367±10 | 0.704364 | 9.98 | 54.6 | 0.1106 | 0.512511±5 | 0.512509 | -2.45 |
| A19-06 | 24.3 | 752 | 0.0931 | 0.704180±16 | 0.704177 | 9.39 | 48.7 | 0.1166 | 0.512572±3 | 0.512570 | -1.26 |
| A19-07 | 27.0 | 823 | 0.0948 | 0.704075±9 | 0.704072 | 9.46 | 50.9 | 0.1124 | 0.512546±3 | 0.512544 | -1.77 |
| A19-08 | 15.2 | 784 | 0.0561 | 0.704325±9 | 0.704323 | 9.10 | 49.5 | 0.1111 | 0.512493±5 | 0.512491 | -2.80 |
| A19-64 | 19.4 | 881 | 0.0635 | 0.704359±9 | 0.704357 | 8.33 | 43.7 | 0.1152 | 0.512541±5 | 0.512539 | -1.87 |
| Lemagarut lavas | | | | | | | | | | | |
| A16-21 | 56.2 | 1043 | 0.1557 | 0.705000±10 | 0.704995 | 14.4 | 84.7 | 0.1029 | 0.512422±3 | 0.512420 | -4.19 |
| A16-28 | 69.6 | 1086 | 0.1852 | 0.704949±13 | 0.704943 | 13.1 | 76.0 | 0.1039 | 0.512421±3 | 0.512419 | -4.21 |
| A16-29 | 46.1 | 1397 | 0.0953 | 0.704980±19 | 0.704977 | 11.7 | 63.3 | 0.1117 | 0.512414±2 | 0.512412 | -4.34 |
| Precambrian basement | | | | | | | | | | | |
| A16-10 | 4.08 | 124 | 0.0950 | 0.704687±11 | 0.704684 | 4.00 | 13.9 | 0.1741 | 0.512378±5 | 0.512375 | -5.07 |
| A16-12 | 222 | 146 | 4.4560 | 0.862926±14 | 0.862783 | 3.80 | 21.8 | 0.1053 | 0.511058±5 | 0.511056 | -30.79 |
| A16-16c | 17.0 | 336 | 0.1465 | 0.709289±14 | 0.709284 | 3.27 | 15.5 | 0.1276 | 0.511452±6 | 0.511450 | -23.12 |

A16-10 – green schist, A16-12 – granite-gneiss, A16-16c – garnet amphibolite. M – measured, I – initial (calculated for 2.3 Ma). $^{143}Nd/^{144}Nd$ radio is normalized to $^{146}Nd/^{144}Nd = 0.7219$, error is 2 standard error of the mean in the last sign. digits.

**Table 7:** Selected results for intrinsic parameters calculated based on groundmass olivine-clinopyroxene-Ti-magnetite assemblages using QUIlF (Andersen *et al.*, 1993)

| Assemblage | Olivine | Clinopyroxene | Spinel | Pressure (kbar) | Temperature (°C) | | Oxygen fugacity | | | Silica activity |
|---|---|---|---|---|---|---|---|---|---|---|
| | | | | (Fixed) | Absolute | Uncertainty | Absolute | ΔFMQ | Uncertainty | |
| Groundmass | A19-4a-47 (micro; core) | A19-4a-2 (VI) | A19-4a-9 (5; core) | 1 | 745 | 158 | -11.2 | 4.7 | 3.4 | - |
| Groundmass | A19-4a-48 (micro; mantle) | " | " | 1 | 754 | 161 | -11.1 | 4.6 | 3.4 | - |
| Groundmass | A19-4c-146 (micro; core) | A19-4c-108 (VI) | A19-4c-88 (5; core) | 1 | 832 | 156 | -8.8 | 5.2 | 2.9 | - |
| Groundmass | A19-4c-147 (micro; mantle) | A19-4c-122 (VI) | A19-4c-89 (5; core) | 1 | 771 | 149 | -10.2 | 5.1 | 3.1 | - |
| Groundmass | A19-4c-151 (micro; rim) | " | " | 1 | 809 | 117 | -11.0 | 3.4 | 2.2 | - |
| Groundmass | A19-06-25 (pheno; rim) | A19-06-34 (VI) | A19-06-48 (5; core) | 1 | 743 | 182 | -11.4 | 4.5 | 3.9 | - |
| Groundmass | A19-06-23 (micro; rim) | A19-06-40 (VI) | A19-06-51 (5; rim) | 1 | 775 | 166 | -10.8 | 4.3 | 3.4 | - |

Pressure was fixed at 1 bar; silica activity could not be calculated (iteration limit).

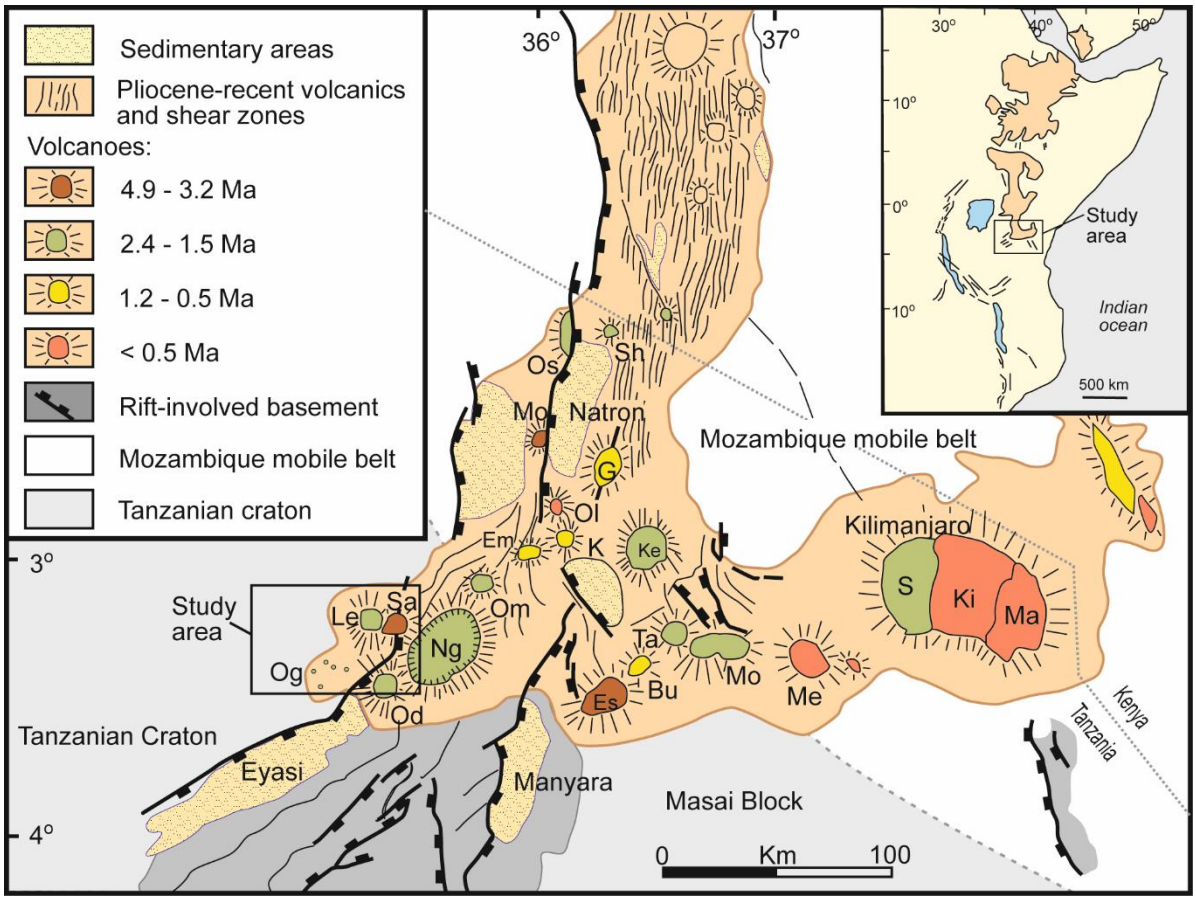


**Fig. 1.** Main structural and magmatic features in the North Tanzania Divergence zone (modified from Le Gall *et al.,* 2008). Volcanoes: Bu, Burko; Em, Embagai; Es, Essimingor; G, Gelai; K, Kerimasi; Ke., Ketumbeine; Ki, Kibo; Kw, Kwaraha; Le, Lemagarut; M, Monduli; Ma, Mawenzi; Me, Meru; Mo, Mosonik; Ng, Ngorongoro; Og, Ogol; Os, Oldoinyo Shira, Ol, Oldonyo Lengai; S, Shira; Sa, Sadiman, Sh, Shombole; Ta, Tarosero. Age data are from Mollel (2007), Dawson (2008, and references therein), Nonnotte *et al.* (2008), Mana *et al.* (2012; 2015) and Peirce & Mana (2018).

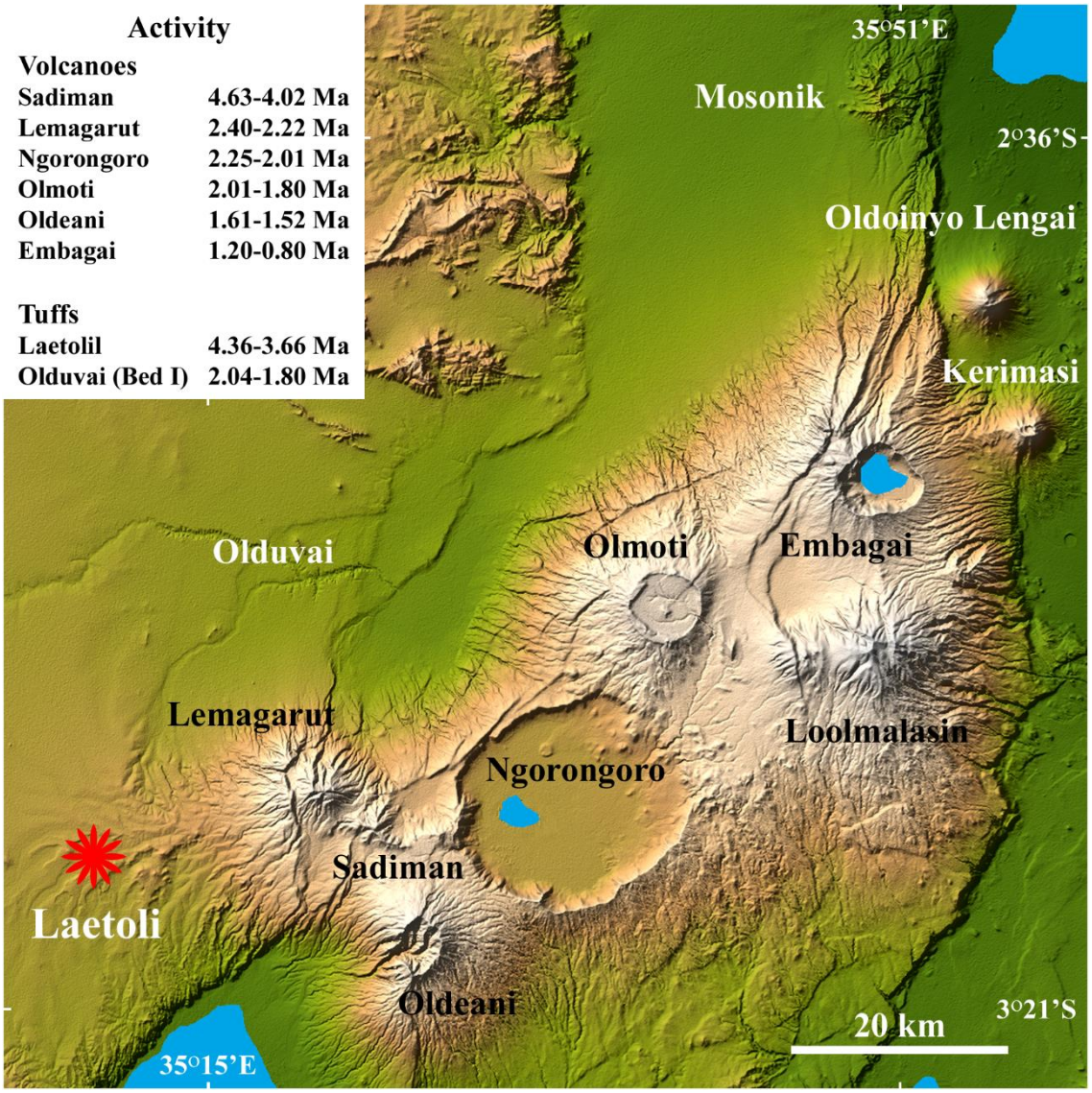


**Fig. 2.** Major volcanoes and tuffs in the Crater Highlands (shaded and coloured SRTM elevation model, February 2000). Courtesy NASA/JPL/NIMA. Age data are from Mollel (2007) and Deino (2011; 2012).

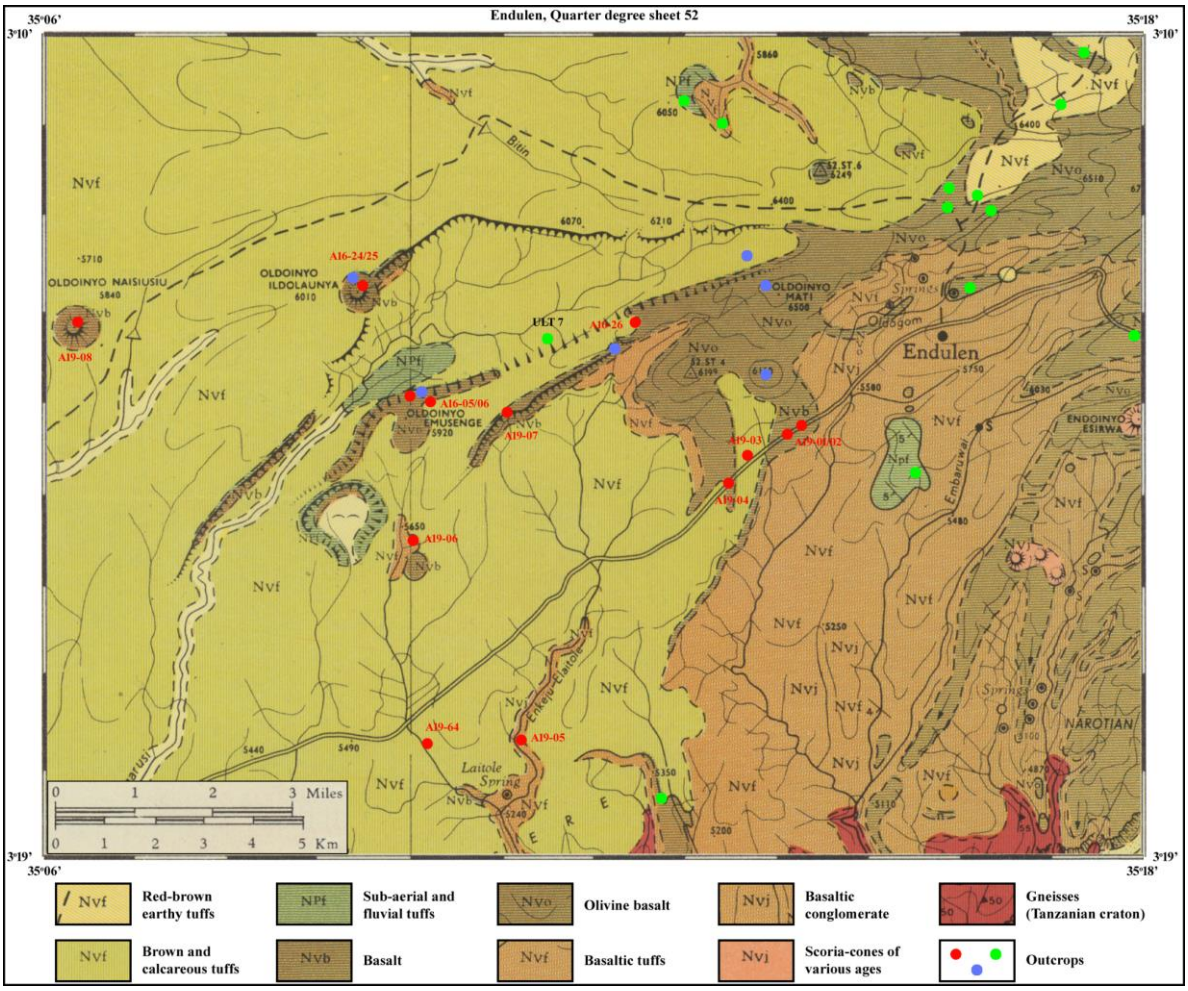


**Fig. 3.** Cropped Quarter degree sheet 52 Endulen (Pickering, 1964) showing geology of the Laetoli area. Outcrops with Ogol basalts are shown by red (this study) and blue (Mollel, 2007; Adelsberger *et al.,* 2011) dots; green dots are outcrops with Lemagarut basalts, Laetolil tuffs and tuffs with nephelinite xenoliths (likely to be from Sadiman).

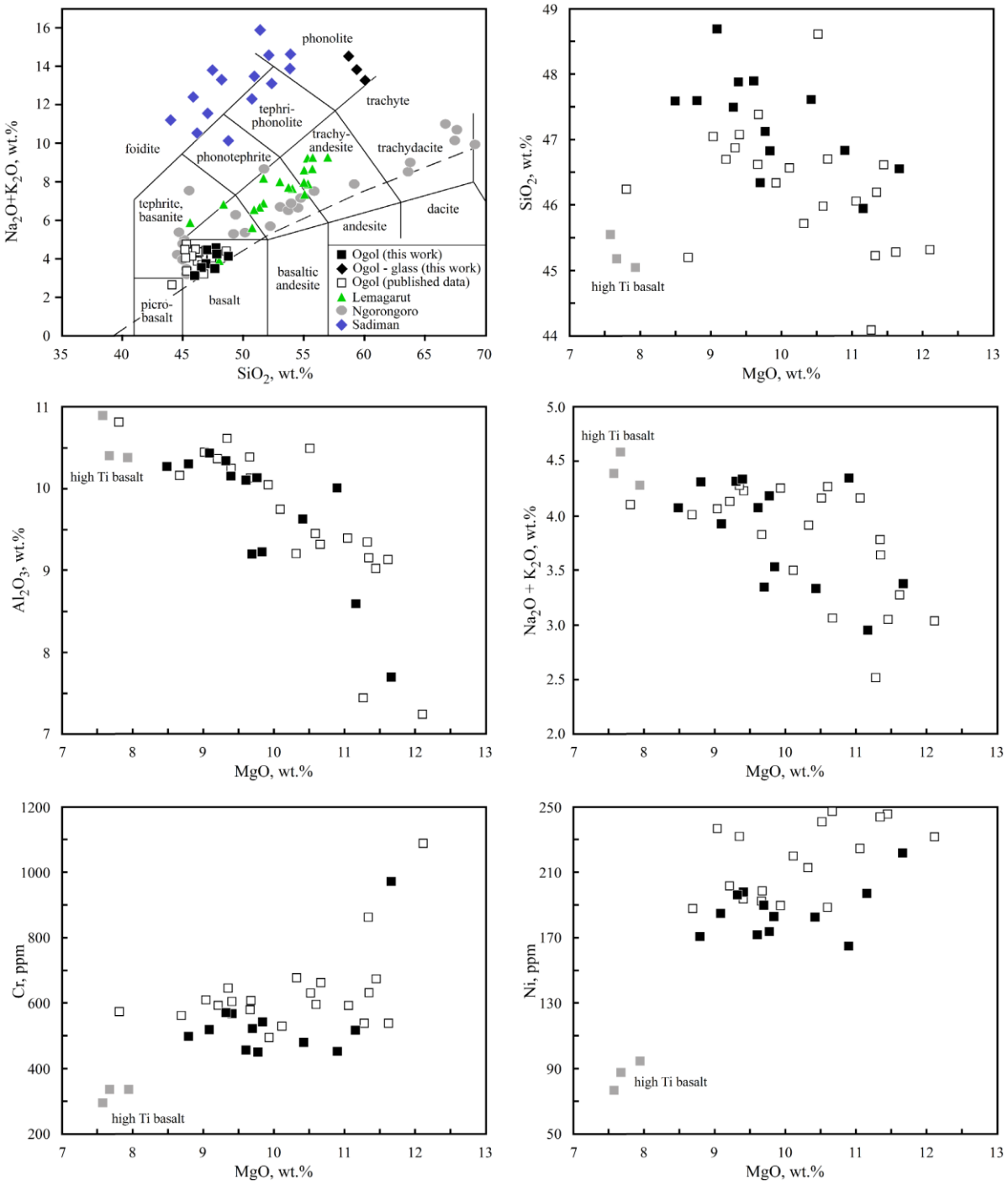


**Fig. 4.** Compositional variations for the Ogol basalts. (a) Total alkali vs $SiO_2$ diagram (TAS; Le Bas *et al.,* 1986). The dashed line divides alkaline and tholeiitic basalts. Compositions of basaltic series from the Lemagarut and Ngorongoro volcanoes and nephelinites from the Sadiman volcano are shown for comparison; (b-f) Major and compatible element variations. Published data are from Nonnotte (2007), Mollel (2007), Adelsberger *et al.* (2011), Mollel *et al.* (2011) and Zaitsev *et al.* (2012).

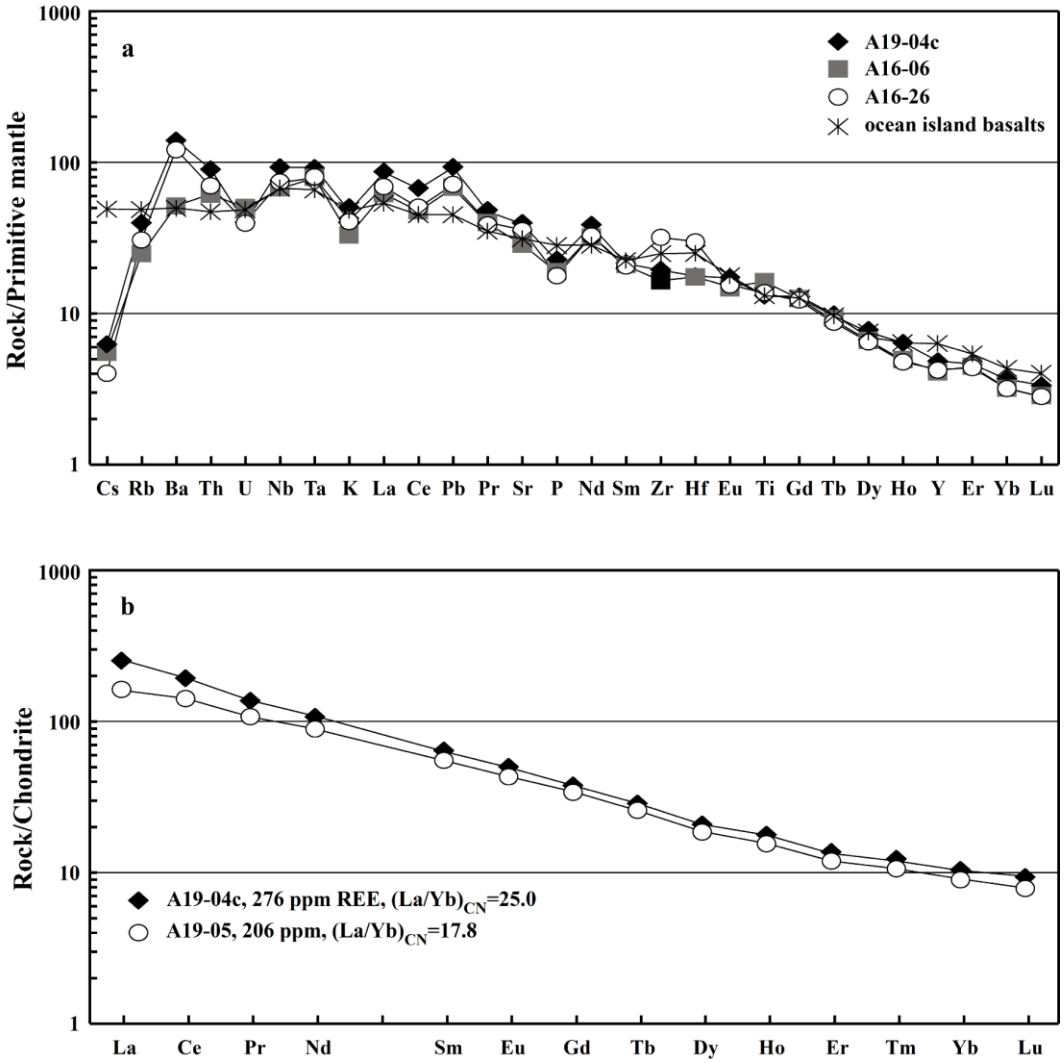


**Fig. 5.** Primitive mantle- and chondrite-normalised plots for selected Ogol basalt samples. Data for ocean island basalts, normalizing values for primary mantle and chondrite are from Sun & McDonough (1989). For Pb and Ce recommended normalizing values of 0.071 and 0.0079 ppm respectively were used (Sun & McDonough, 1989).

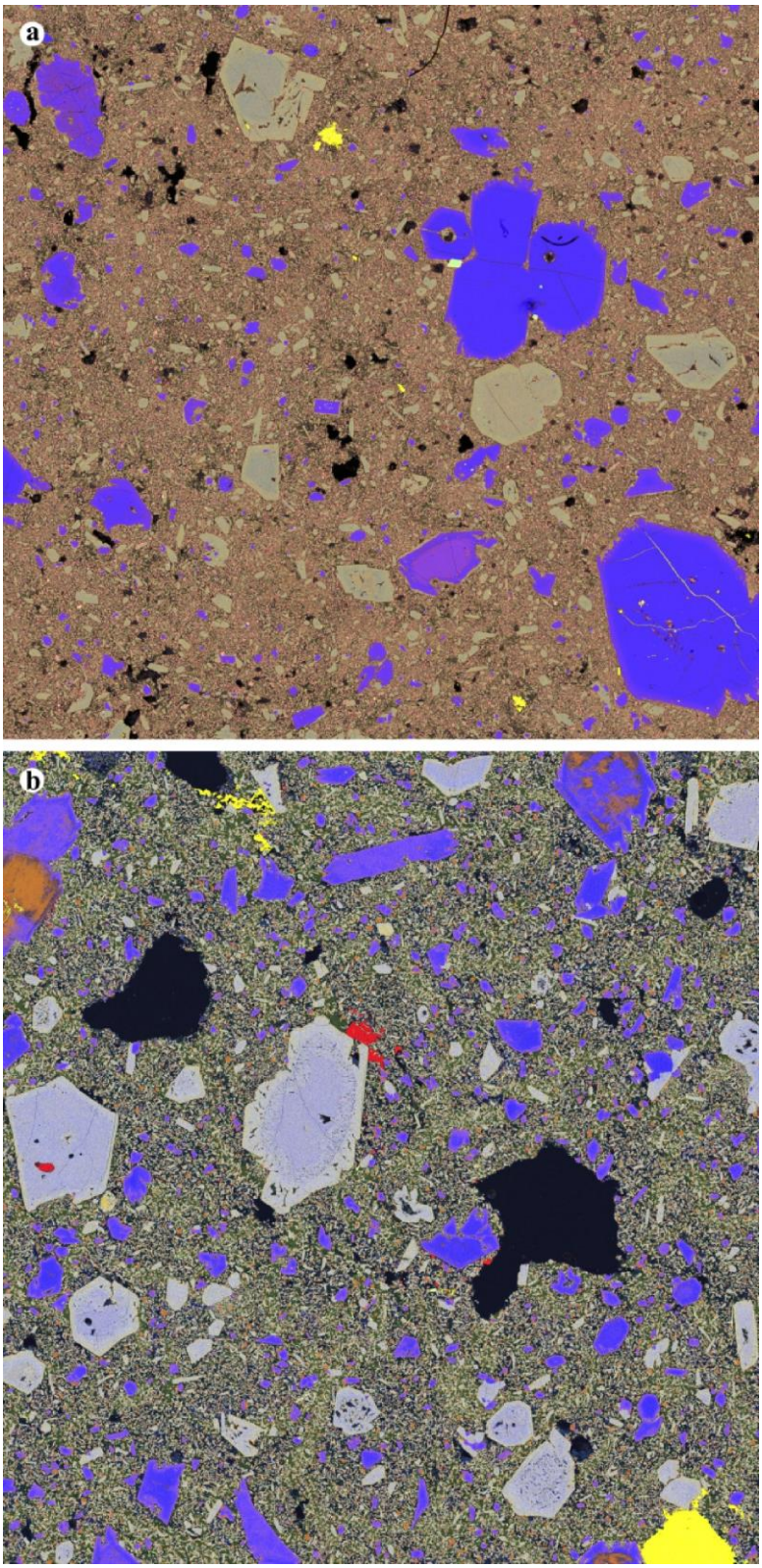


**Fig. 6.** False-coloured BSE montage maps of the Ogol basalts. (a) sample A16-05, field of view 9.48 x 9.22 mm, blue – olivine, beige – clinopyroxene, light green – magnesiochromite, pink in groundmass – magnetite, yellow – calcite, black – holes; (b) A16-26, field of view 9.48 x 10.20 mm, blue – olivine, orange-brown – olivine alteration, light violet to light gray – clinopyroxene, orange-brown in groundmass – magnetite, yellow – calcite, red – baryte.

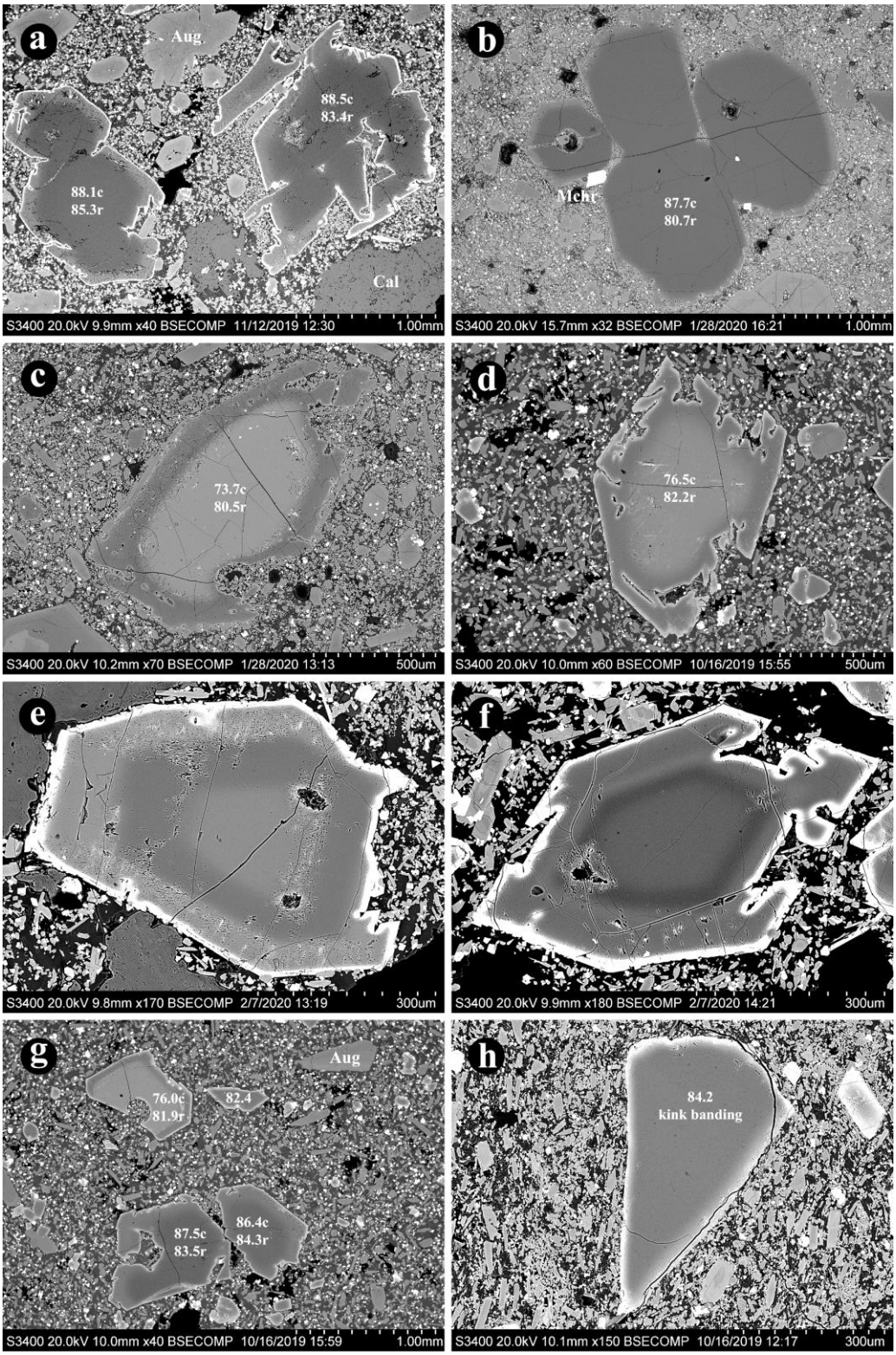


**Fig. 7.** Forsterite morphology and zonation. (a) hopper forsterite with normal zonation, A19-06, (b) euhedral to subhedral forsterite with normal zonation, Mchr – magnesiochromite, A16-05, (c) hopper forsterite with reverse zonation, A16-05, (d) hopper forsterite with reverse zonation, A19-07, (e) euhedral forsterite with repetitive zonation, A19-01, (f) hopper forsterite with repetitive zonation, A19-01, (g) forsterite with normal zonation, fragment of forsterite with reverse zonation and angular microphenocrystals (A19-07), (h) fragment of unzoned forsterite, A19-08. Numbers are Fo values (mol. %), c – core, r – rim. BSE images.

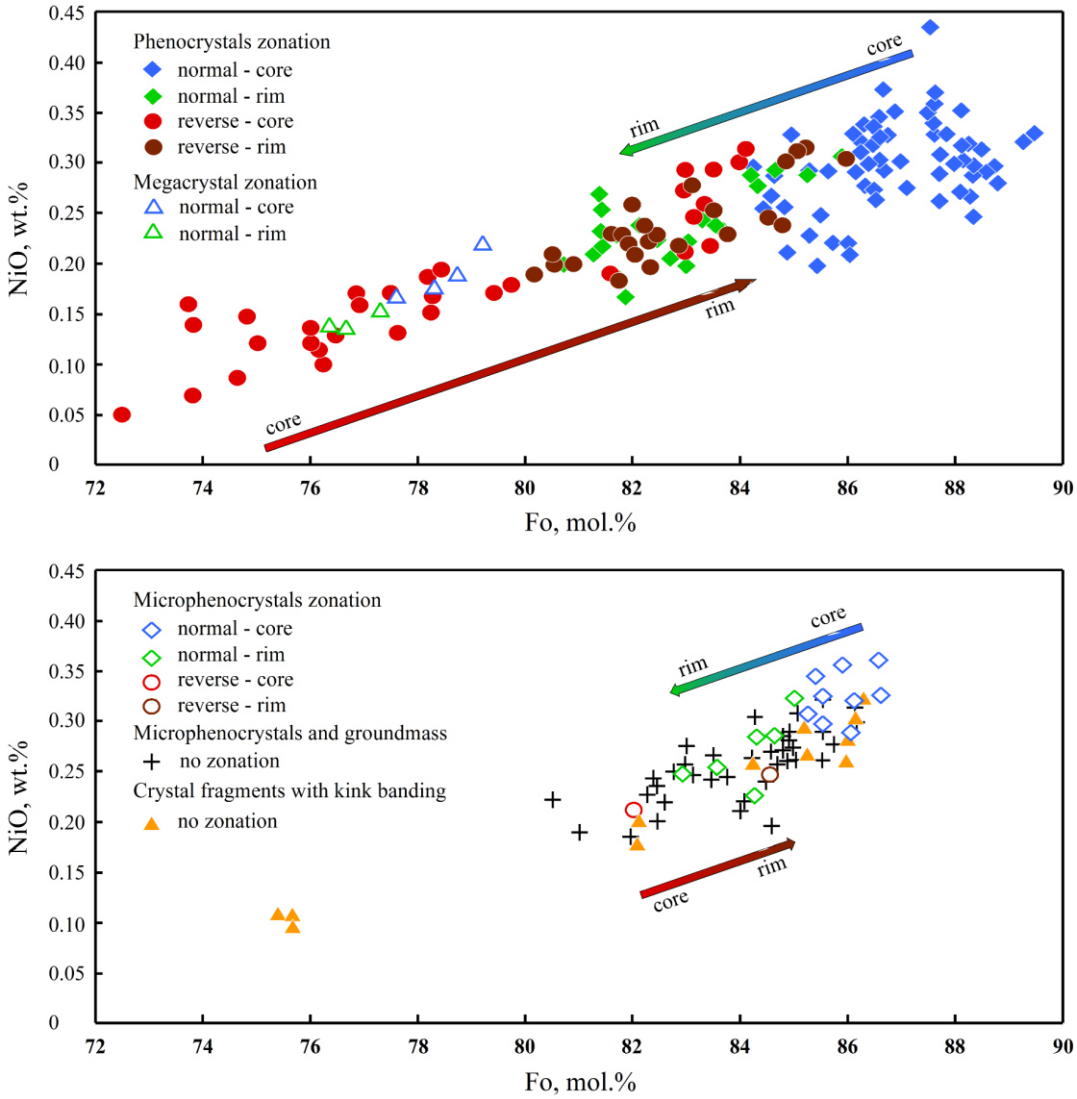


**Fig. 8.** Forsterite composition, Fo (mol. %) vs NiO (wt %) in the Ogol basalts.

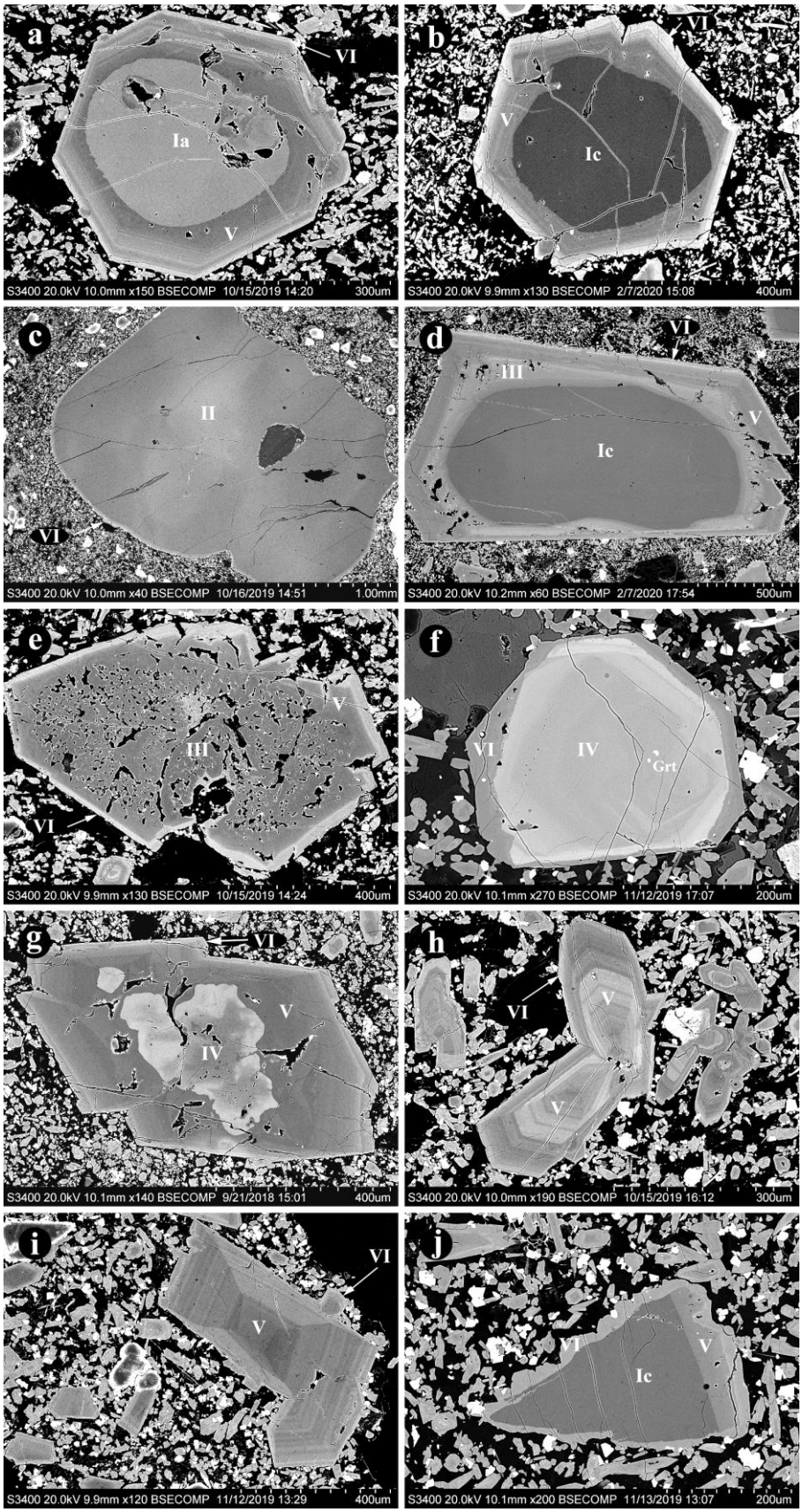


**Fig. 9.** Clinopyroxene morphology and zonation. I – VI – clinopyroxene population, (a, e) sample A19-64, (b) A19-01, (c) A19-08, (d) A19-02, (f) A19-04a, (g) A16-06, (h) A19-06, (i) A16-05, (j) A19-04b. Crt – schorlomite, BSE images.

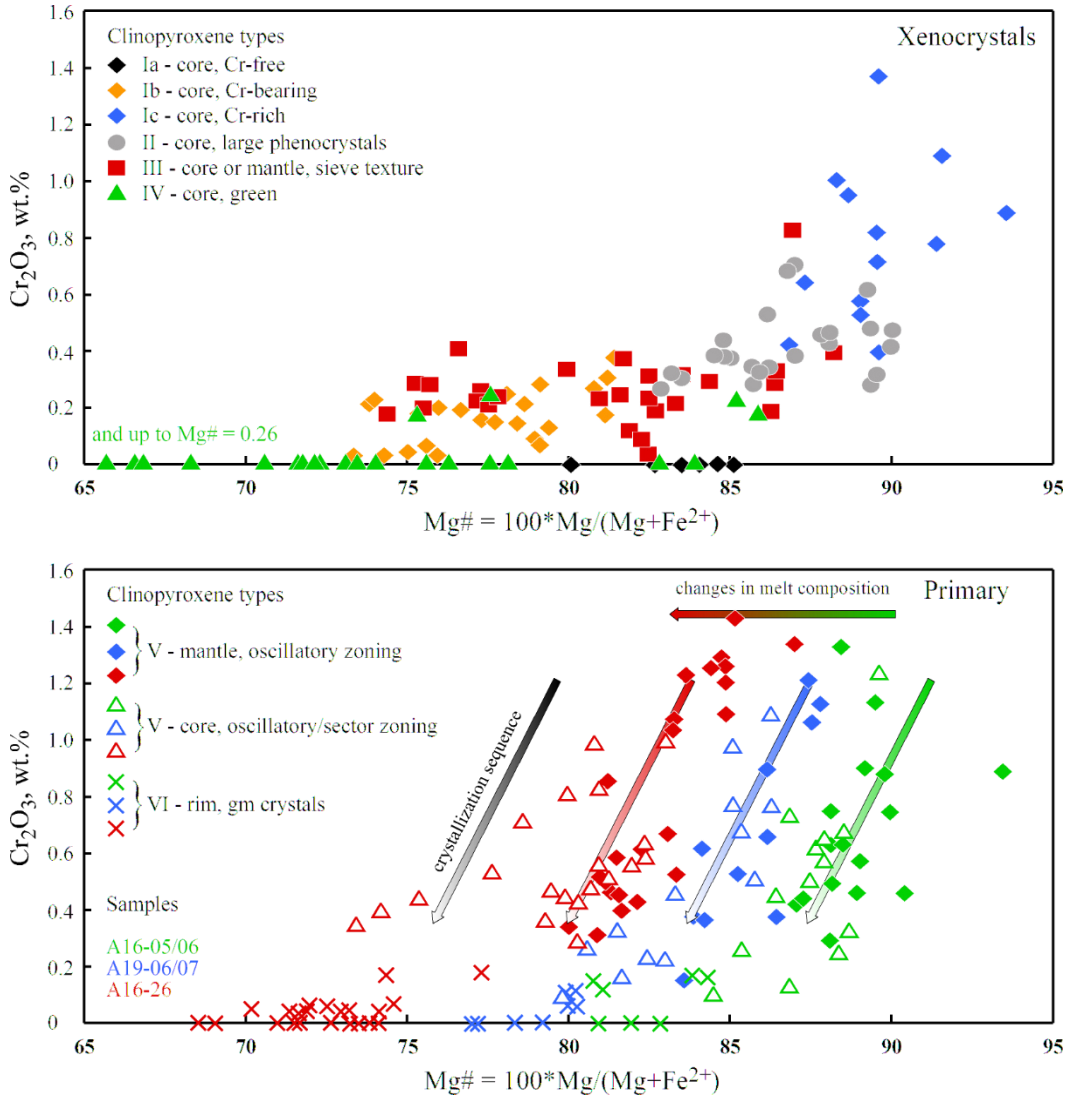


**Fig. 10.** Relationships between Mg# (100*Mg/(Mg=$Fe^{2+}$) from at %) and $Cr_2O_3$ (wt %) in clinopyroxene. Arrow "crystallization sequence" show compositional changes in population V (core to rim) and from population V to VI.

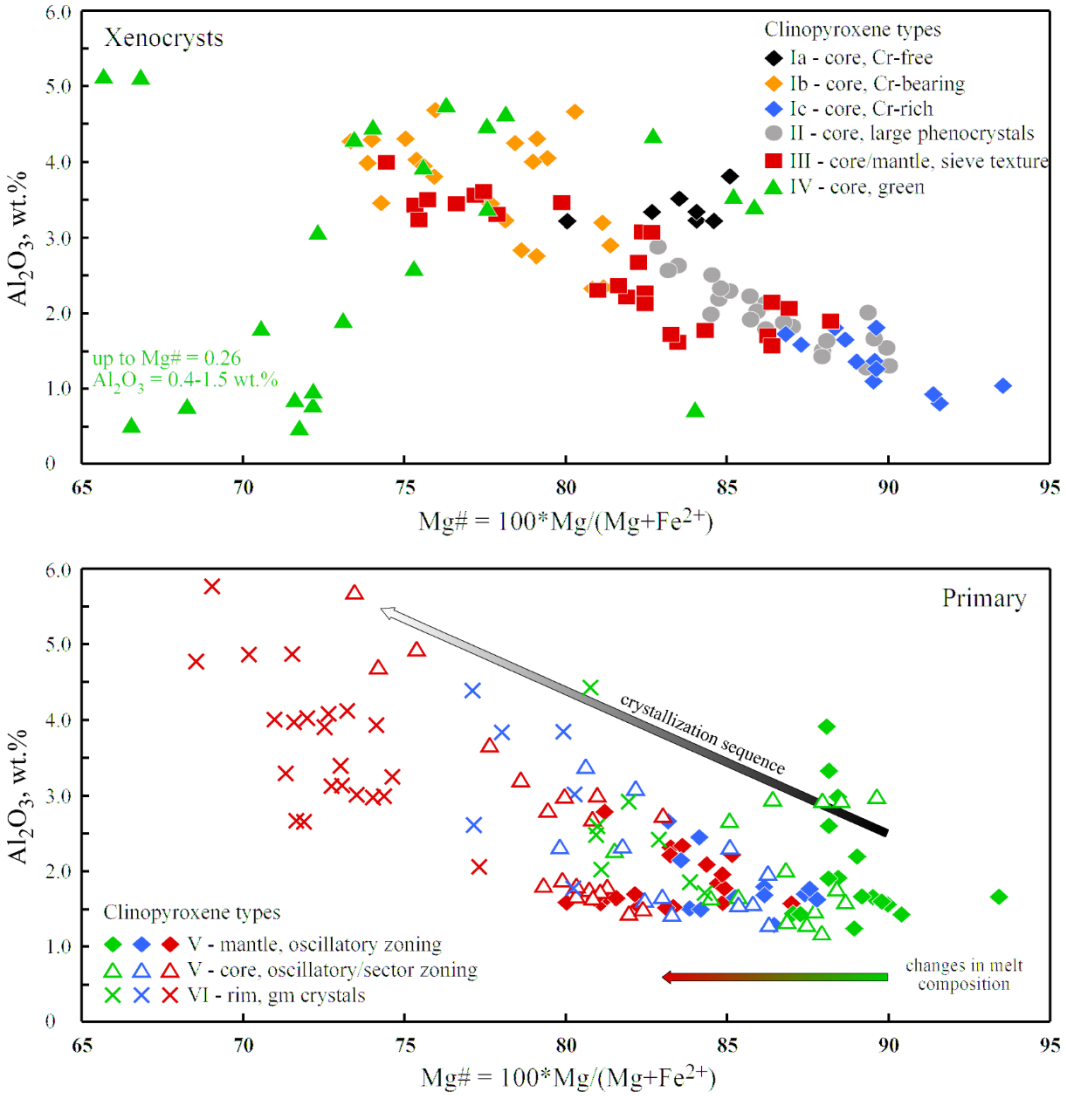


**Fig. 11.** Relationships between Mg# (100*Mg/(Mg=$Fe^{2+}$) from at %) and $Al_2O_3$ (wt %) in clinopyroxene. Arrow "crystallization sequence" show compositional changes in population V (core to rim) and from population V to VI.

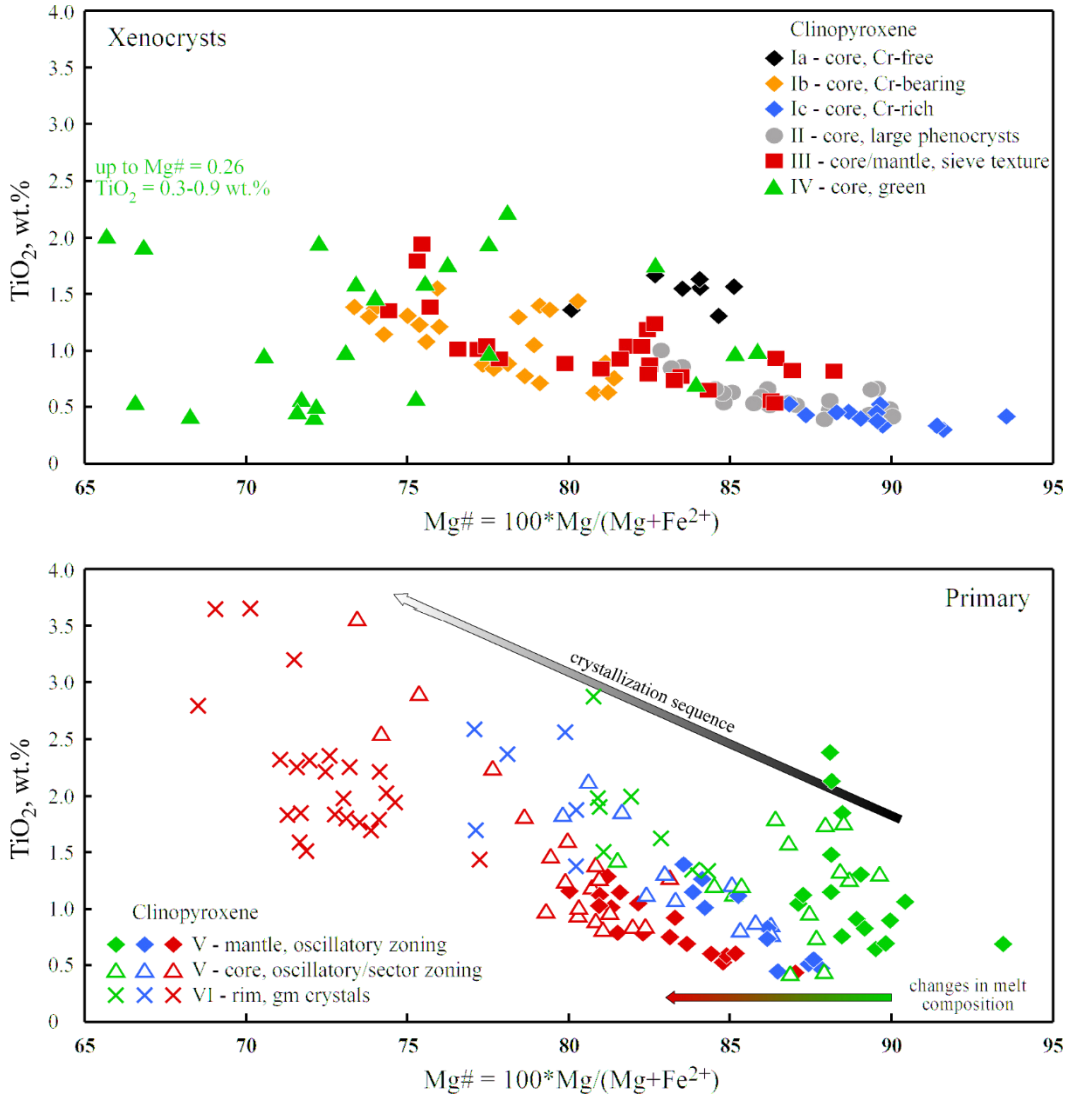


**Fig. 12.** Relationships between Mg# (100*Mg/(Mg=$Fe^{2+}$) from at %) and $TiO_2$ (wt %) in clinopyroxene. Arrow "crystallization sequence" show compositional changes in population V (core to rim) and from population V to VI.

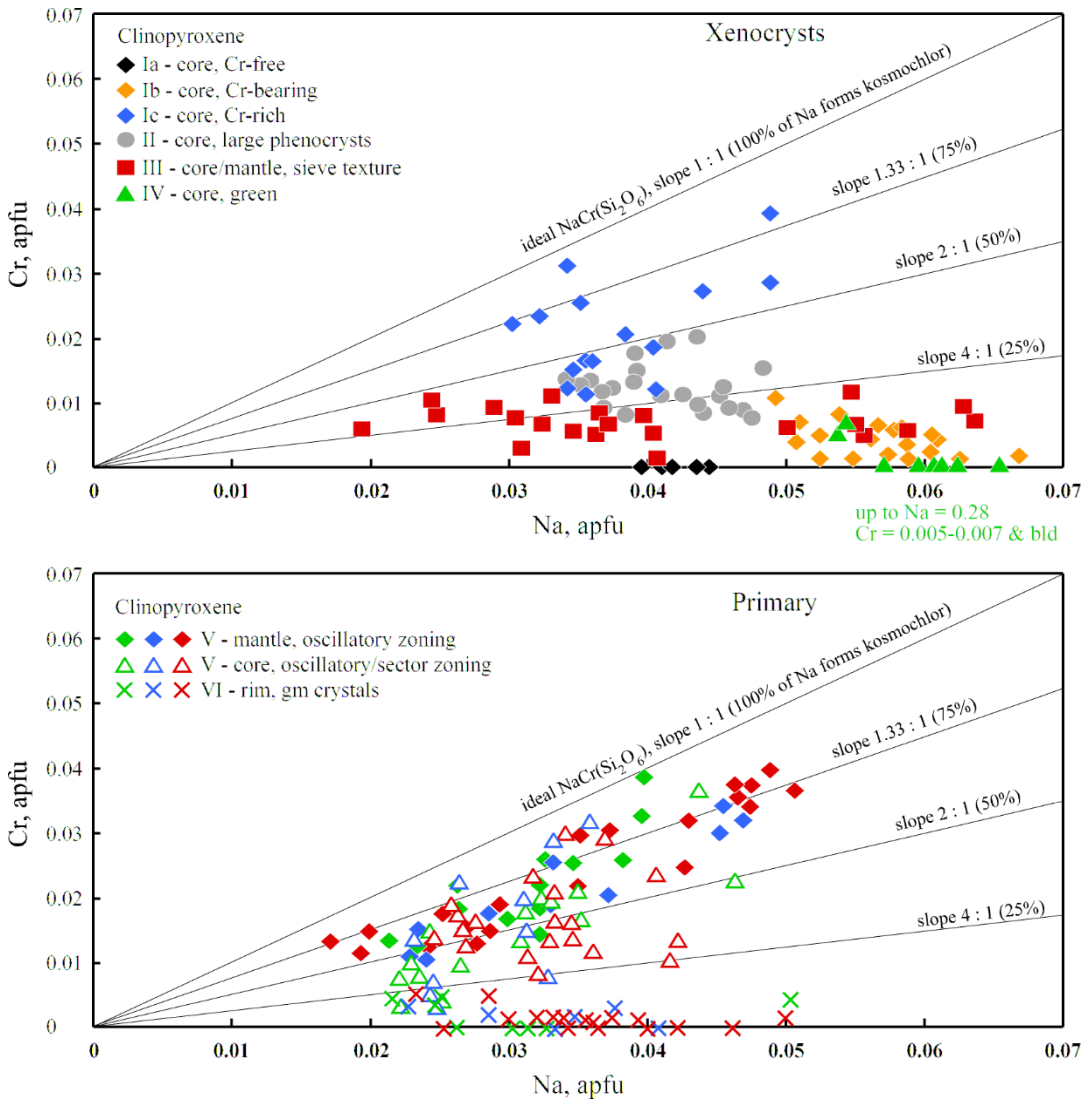


**Fig. 13.** Relationships between Na and Cr (apfu) in clinopyroxene.

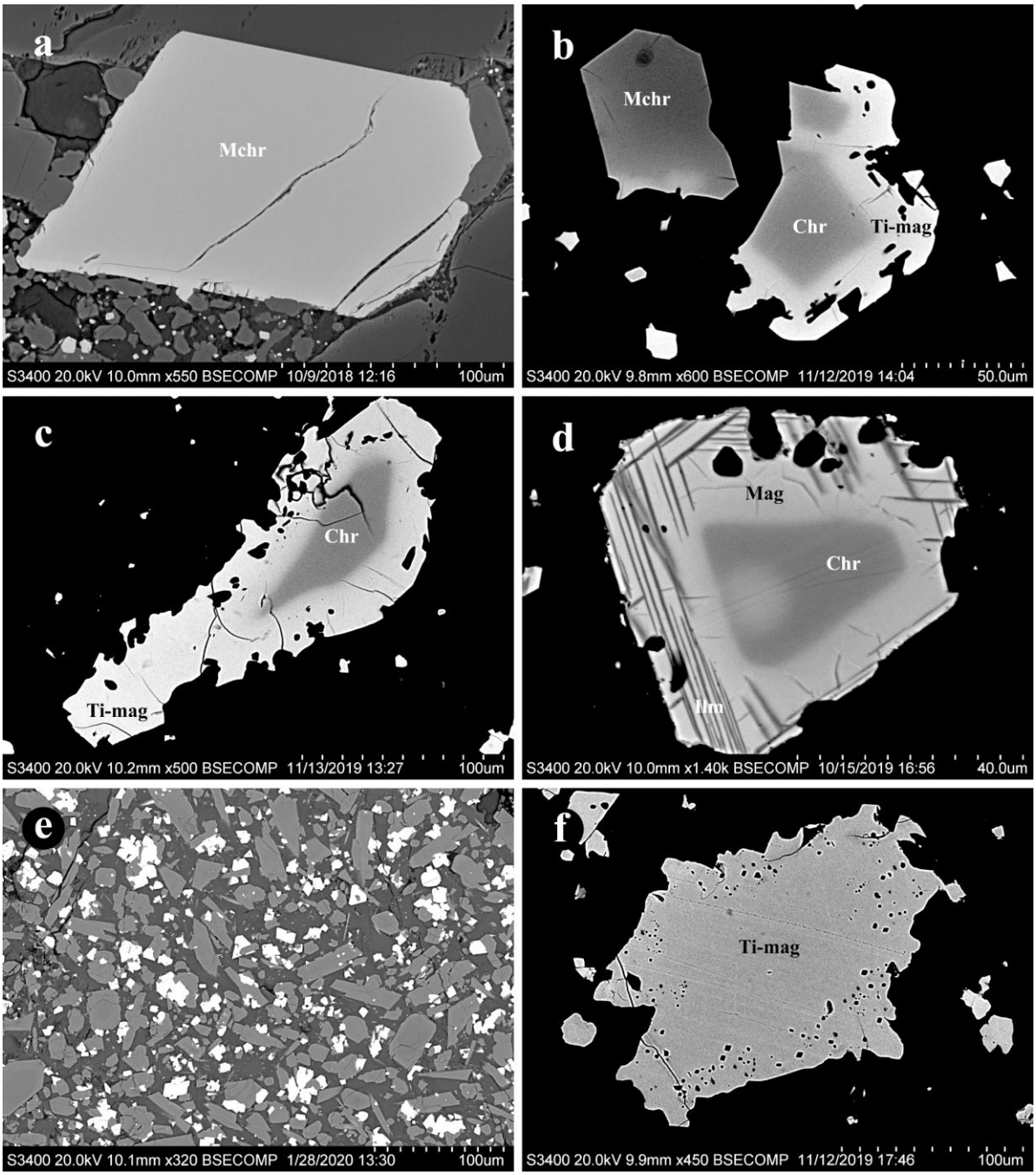


**Fig. 14.** Morphology and zonation of spinel-group minerals. (a) euhedral magnesiochromite (Mchr) at contact forsterite phenocrystal and groundmass, A16-05; (b) euhedral magnesiochromite in forsterite phenocrystals and zoned chromite (Chr) - magnetite-ulvöspinel (Ti-mag) at contact forsterite phenocrystal and groundmass, A19-06, (c) zoned chromite (Chr) - magnetite-ulvöspinel (Ti-mag) microphenocrystal, A19-04b, (d) zoned chromite (Chr) - magnetite (Mag) microphenocrystals with ilmenite exsolution (Ilm) in magnetite, A19-64, (e) euhedral to subhedral magnetite-ulvöspinel (white) in groundmass, A16-05, (f) unhedral magnetite-ulvöspinel xenocrystal, A19-04a. BSE images.

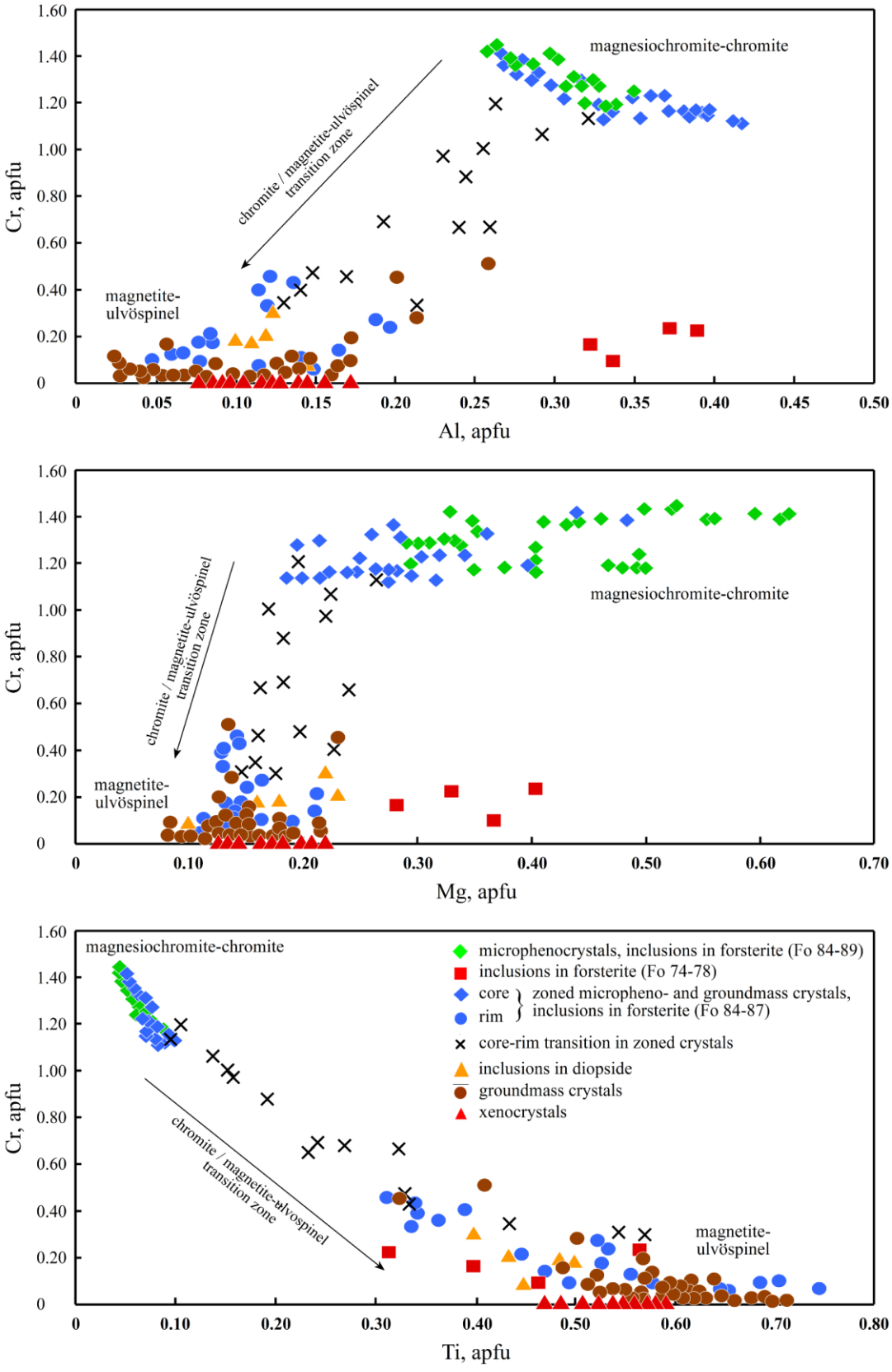


**Fig. 15.** Compositional variations of spinel-group minerals.

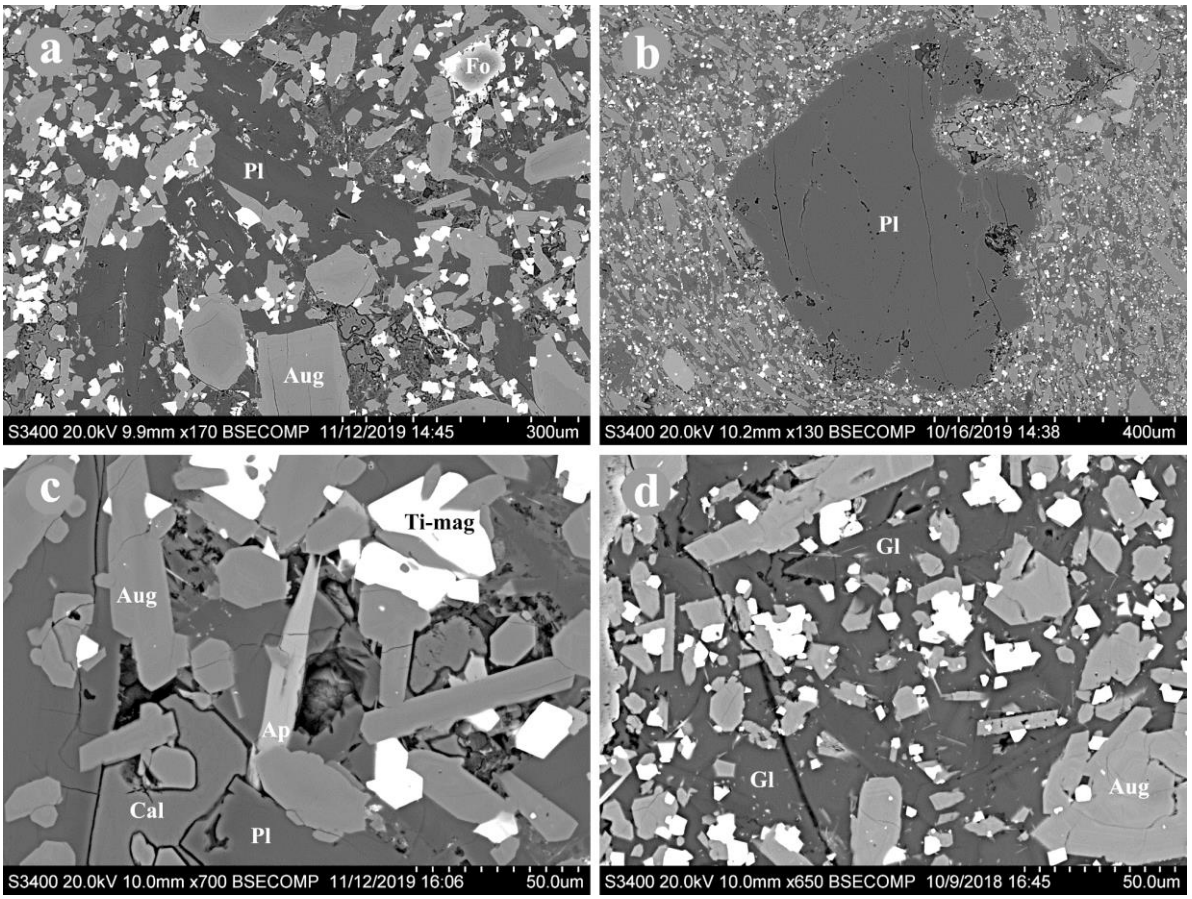


**Fig. 16.** Microphenocrysts and groundmass minerals. (a) andesine (Pl) microphenocrystals, A19-06, (b) oligoclase (Pl) xenocrystal, A19-08, (c) apatite (Ap) microphenocrystal, A19-07, (d) glass (Gl) with apatite microlites (gray), A16-06. Fo forsterite, Aug augite, Ti-mag magnetite-ulvöspinel, Cal calcite. BSE images.

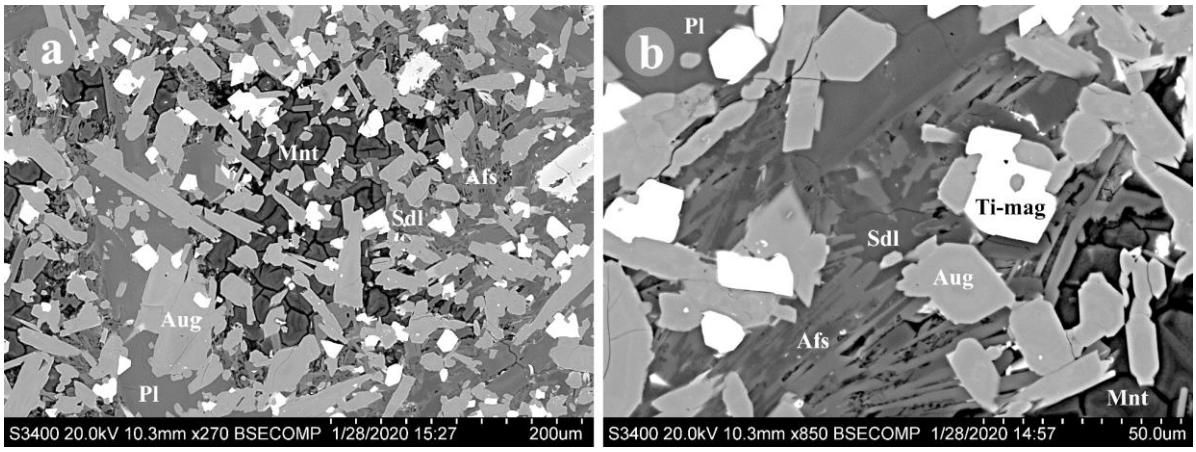


**Fig. 17.** Glass alteration to montmorillonite (Mnt), K-Na feldspar (Afs), Na zeolite (not shown) and sodalite (Sdl). Pl andesine, Aug augite, Ti mag magnetite-ulvöspinel$_{ss}$, A16-26. BSE images.

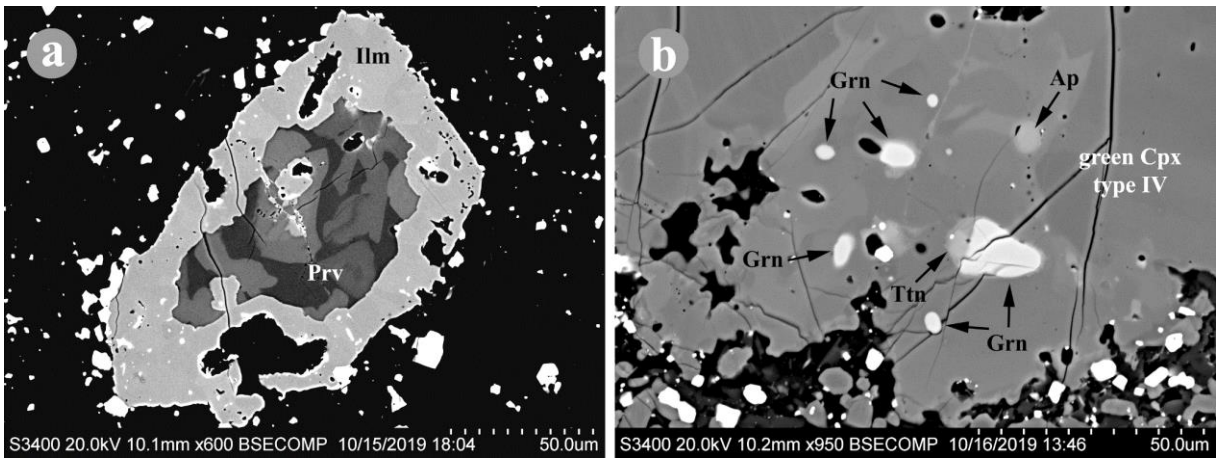


**Fig. 18.** Xenocrysts in the Ogol basalts. (a) perovskite (Prv) with ilmenite (Ilm) reaction rim, white inclusions in ilmenite are REE-rich minerals, (b) schorlomite (Grn), titanite (Ttn) and apatite (Ap) in green clinopyroxene of type IV, A19-08. BSE images.

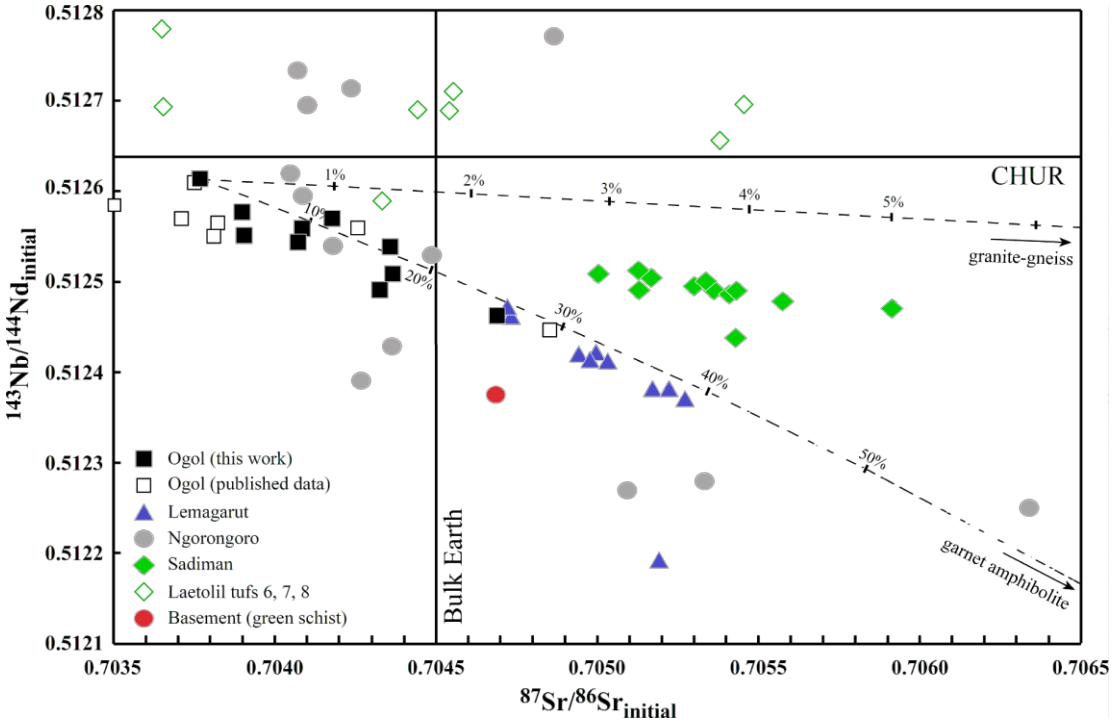


**Fig. 19.** Sr and Nd initial ratios (2.3 Ma) for the Ogol basalts, Lemagarut, Ngorongoro and Sadiman volcanoes, Laetolil tuffs and green schist from the Tanzania Craton. Data are from this study and Paslick *et al.* (1995, 1996), Mollel (2007), Nonnotte (2007), Adelsberger *et al.* (2011) and Zaitsev *et al.* (2019). Dashed lines show mixing isotope models between Ogol basalt (A16-05), granite-gneiss (A16-12) and garnet amphibolite (A16-16c).

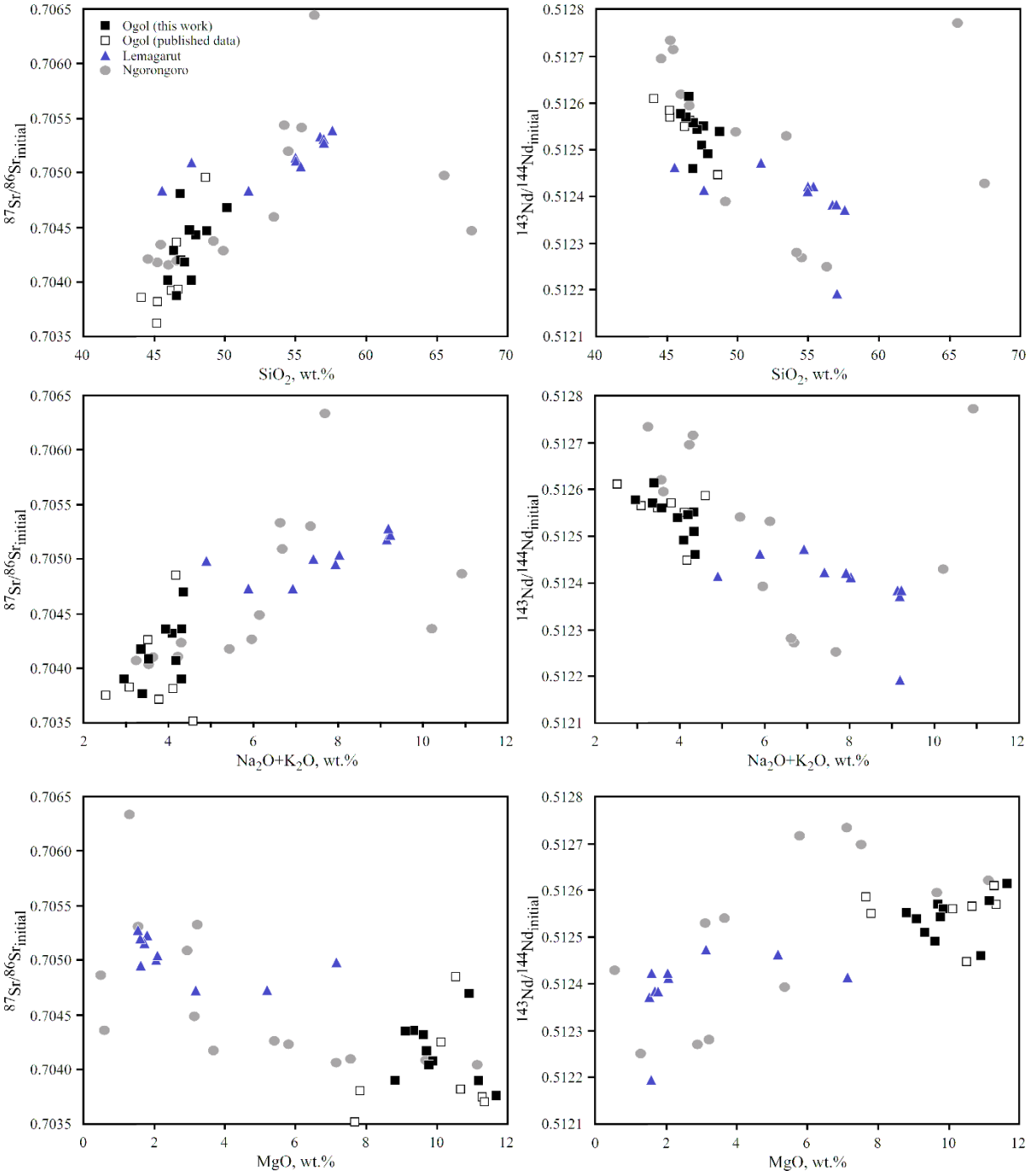


**Fig. 20.** Relationships between Sr / Nd initial ratios and major elements for the Ogol basalts and Lemagarut and Ngorongoro volcanoes. Data are from this study and Mollel (2007), Nonnotte (2007) and Adelsberger *et al.* (2011).

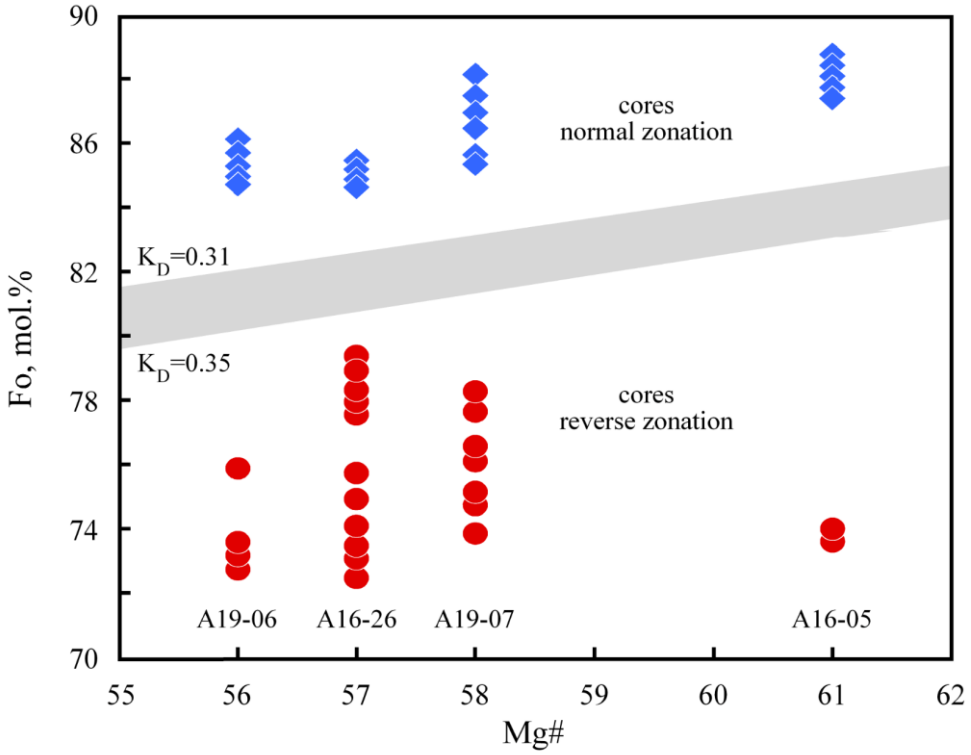


**Fig. 21.** Whole rocks Mg# (100*Mg/(Mg+$Fe^{2+}$)) vs forsterite composition. Only cores of phenocrysts with normal and reverse zonation were used for the plot. The gray field represent olivine/melt equilibrium compositions for $K_D$=0.31-0.35 (Ulmer, 1989).

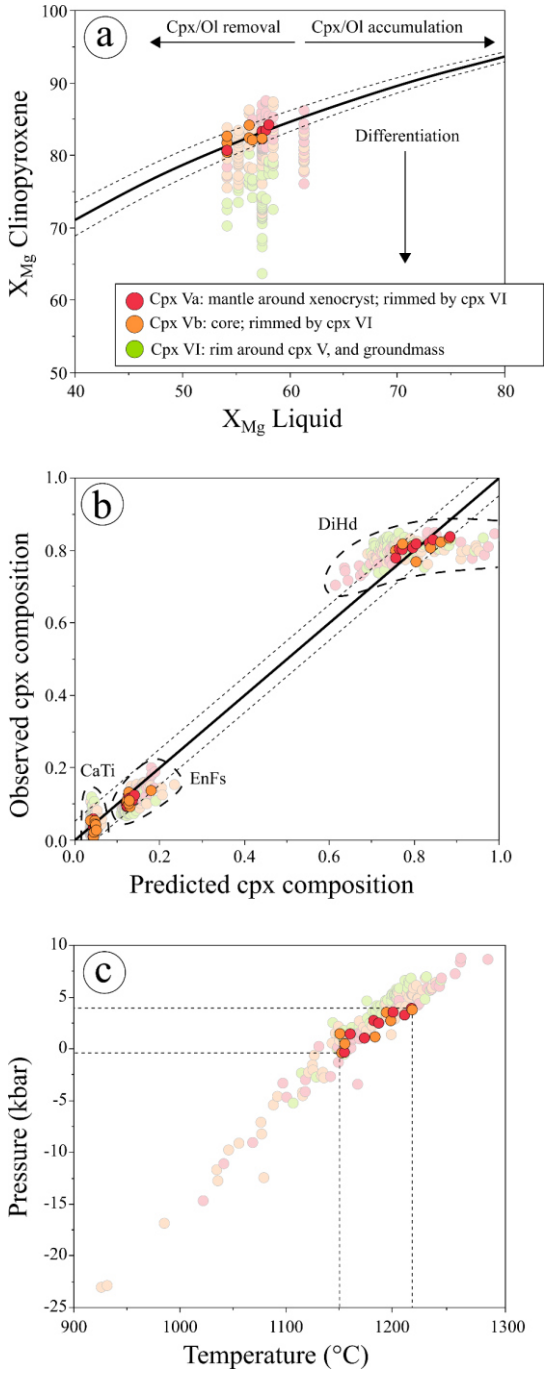


**Fig. 22.** Clinopyroxene-liquid thermobarometry for the Ogol basalts according to Neave & Putirka (2017), paired with the temperature equation 33 from Putirka (2008). The whole rock composition was used as a proxy for the coexisting liquid to clinopyroxene. (a) Rhodes diagram ($X_{Mg}$ clinopyroxene vs $X_{Mg}$ liquid) for the studied basalts. $X_{Mg}$ is the molar Mg/[Mg+$Fe_{tot}$]*100. The curves illustrate the equilibrium interval between clinopyroxene and liquid by assuming an exchange coefficient $K_{D(Fe\text{-}Mg)}^{cpx\text{-}liq}$ of 0.27±0.3; (b) Observed clinopyroxene compositions vs predicted clinopyroxene compositions including diopside-hedenbergite (DiHd), enstatite-ferrosilite (EnFs) and Ti-Tschermak's clinopyroxene (CaTi; Putirka, 2008). The accepted range of equilibrium is indicated by the dashed lines (± 5 %, absolute). The predicted DiHd component sometimes exceeds 1.0 (up to 2.3), with the corresponding pressure calculations giving extraordinary low values <-5 kbar; (c) Pressure-temperature correlation of the applied thermobarometer. Highlighted are the results that fulfill the equilibrium constraints.

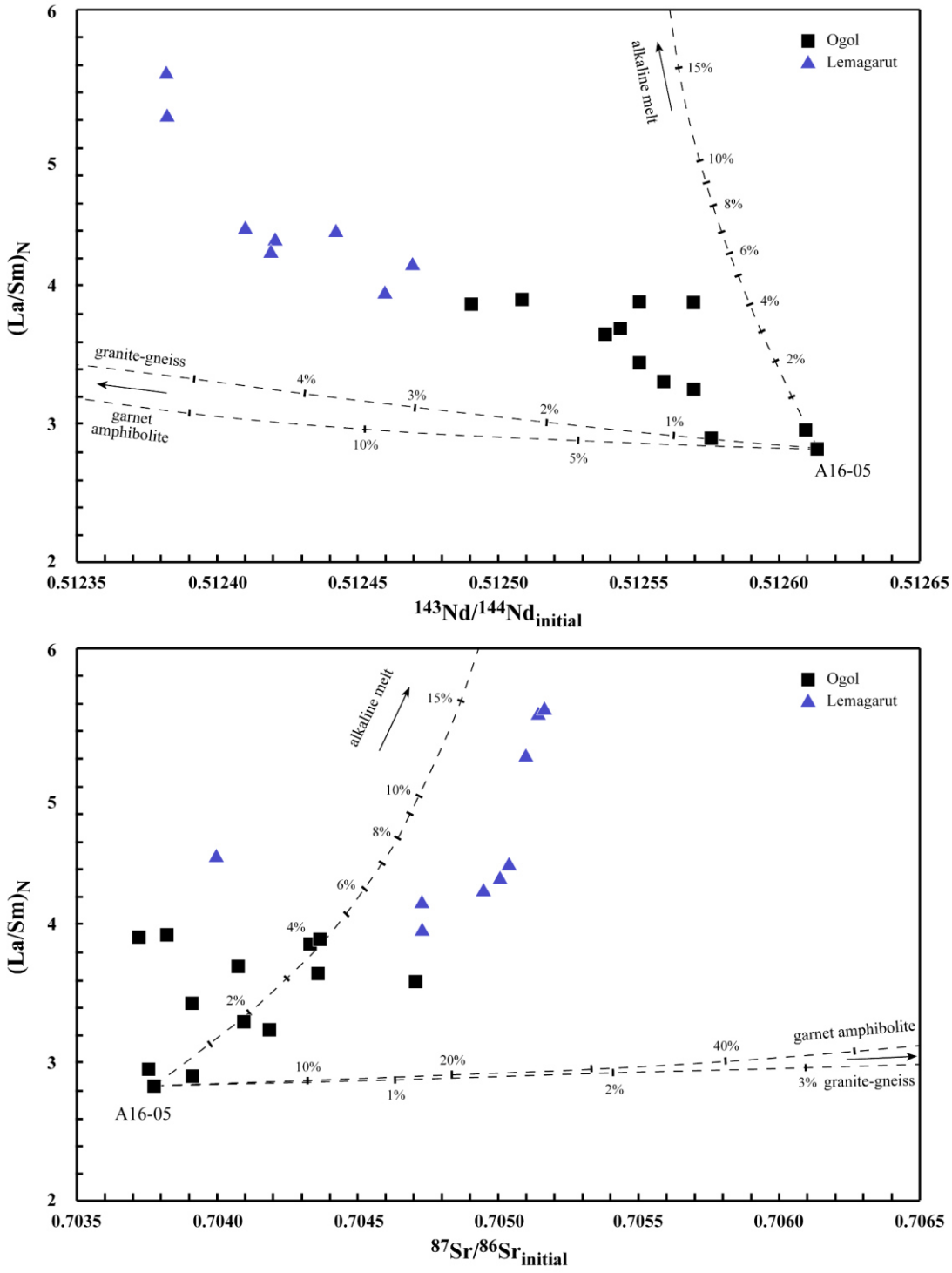


**Fig. 23.** Nd and Sr initial isotope rations vs $(La/Sm)_N$. Dashed lines show variations of the Ogol primitive basalt (A16-05) during fractional crystallization with crustal contamination of Precambrina granite-gneiss (A16-12), garnet amphibolite (A16-15c) or mixing with alkaline melt (sample Sad-10 from Zaitsev *et al.,* 2012). AFC model, R = 0.8 (ratio of mass assimilation rate to the fractional crystallization rate).

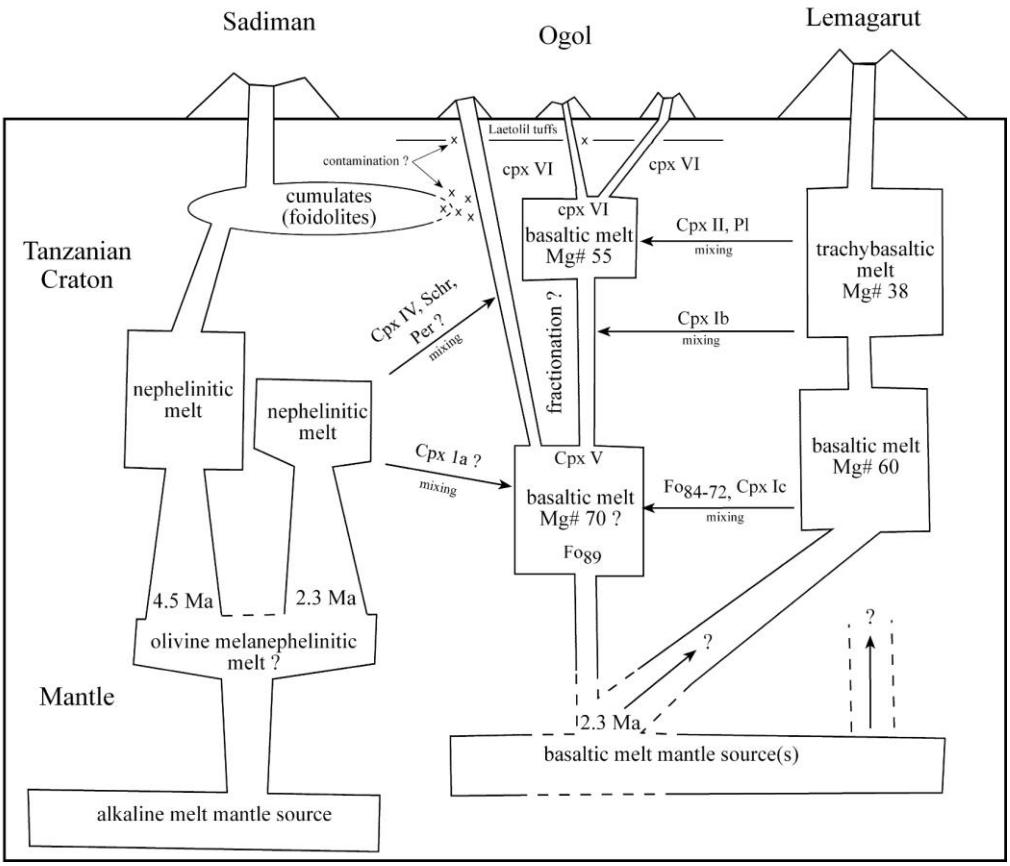


**Fig. 24.** Schematic diagram showing possible relationships between magmatic systems of Ogol, Lemagarut and Sadiman. The horizontal and vertical sketches are not to scale.

# Appendix II

Submitted manuscript

*Study 2*

Braunger, S., Marks, M. A. W., Zaitsev, A. N., Wenzel, T., and Markl, G., submitted. The Petrology of the Tarosero Volcanic Complex: Constraints on the formation of extrusive agpaitic rocks. Journal of Petrology.

# The Petrology of the Tarosero Volcanic Complex:

## Constraints on the formation of extrusive agpaitic rocks

Braunger, S.[1*], Marks, M.A.W.[1], Wenzel, T.[1], Zaitsev, A.N.[2,3] and Markl, G.[1]

[1]Department of Geosciences, Eberhard Karls Universität Tübingen, Wilhelmstr. 56, D-72074 Tübingen, Germany

[2]Department of Mineralogy, St. Petersburg State University, University Emb. 7/9, St. Petersburg, 199034, Russia

[3]Imaging and Analysis Centre, Department of Earth Sciences, Natural History Museum, Cromwell Road, London, SW7 5BD, UK

* = corresponding author: Email: simonbraunger@hotmail.com; Telephone: +49-(0)7071-29-73155; Fax: +49-(0)7071-29-3060.

**ABSTRACT**

The Quaternary Tarosero volcano is situated in the East African Rift of northern Tanzania and mainly consists of trachyte lavas and some trachytic tuffs. In addition, there are minor occurrences of extrusive basalts, andesites, latites, as well as peralkaline trachytes, olivine trachytes and phonolites. Some of the peralkaline phonolites contain interstitial eudialyte, making Tarosero one of the few known occurrences for extrusive agpaitic rocks. This study investigates the genetic relationships between the various rock types and focuses on the peculiar formation conditions of the extrusive agpaitic rocks using a combination of whole-rock geochemistry, mineral chemistry, petrography, thermodynamic calculations and fractional crystallization models. The Tarosero rocks derive from an amphibole- and phlogopite-bearing mantle source and formed at redox conditions around or below the fayalite-magnetite-quartz buffer (FMQ). During multi-level magmatic fractionation at depths between ~35 km and the shallow

crust, temperature decreased from > 1100 °C at near-liquidus conditions in the basalts to ~ 700 °C in the peralkaline residue. The andesite shows a considerably lower silica activity of $a_{SiO2}$=0.15 and a low molar Na/K ratio of 1.5 compared to the other intermediate rock types ($a_{SiO2}$≥0.4; Na/K=2.5-3.0), indicating a different parental magma source. The genetic relationships between the primitive basalts and the intermediate latites cannot be explained by simple fractional crystallization. However, latites evolved towards the trachytes by high-pressure fractionation of clinopyroxene, magnetite and olivine. Further low-pressure fractional crystallization of plagioclase and alkali feldspar, with minor contributions of clinopyroxene, amphibole, magnetite and ilmenite, resulted in the formation of the peralkaline trachytes and phonolites. Fractionation towards the peralkaline rocks was probably accompanied by minor crustal contamination. In general, agpaitic magmas evolve under closed system conditions which impedes the escape of volatile phases. For the extrusive rocks at Tarosero, exsolution of fluids and halogens was prevented by a low water activity due to the early crystallization of OH-bearing amphibole. This resulted in high concentrations of Rare Earth Elements (REE), High Field Strength Elements (HFSE) and the formation of eudialyte in the most evolved peralkaline phonolites. In contrast, the peralkaline olivine trachytes contain olivine instead of amphibole phenocrysts, demonstrating a derivation from the latites by fractional crystallization (plagioclase, clinopyroxene, magnetite, olivine) and assimilation at comparably low-pressure conditions. Due to the lack of a mineral phase acting as a water sink, exsolution of fluids and loss of water-soluble elements prevented an enrichment of REE, HFSE and the final crystallization of eudialyte.

**KEY WORDS**

Eudialyte; extrusive agpaitic rocks; fractional crystallization; peralkaline; Tarosero

## INTRODUCTION

Peralkaline rocks mainly occur in rift-related intraplate settings, and are defined by a molar (Na+K)/Al ratio > 1 (e.g. Le Maitre *et al.*, 2002, Frost & Frost, 2008). Although they represent a volumetrically minor group of igneous rocks with both, silica undersaturated and silica oversaturated varieties (e.g. Dawson, 1998, Markl *et al.*, 2001, Marks *et al.*, 2003, Macdonald & Scaillet, 2006, Mann *et al.*, 2006, Ren *et al.*, 2006, Ridolfi *et al.*, 2006, Zaitsev *et al.*, 2012, Estrade *et al.*, 2014, Cucciniello *et al.*, 2017), peralkaline rocks are of economic and scientific interest due to their high abundances of incompatible elements, including High Field Strength Elements (HFSE), Rare Earth Elements (REE) and volatiles (e.g. Kogarko, 1990, Sørensen, 1992, Bailey *et al.*, 2001, Kalashnikov *et al.*, 2016, Smith *et al.*, 2016). Most peralkaline rocks form by partial melting of a metasomatically enriched mantle source (e.g. Fitton & Upton, 1987, Martin *et al.*, 1994, Upton *et al.*, 2003, Kogarko *et al.*, 2010, Markl *et al.*, 2010), followed by subsequent intense fractional crystallization under variable redox conditions (see details in Marks & Markl, 2017 and references therein).

Among the peralkaline rocks, the more common miaskitic types contain well-known HFSE-bearing minerals, such as zircon, baddeleyite, titanite or perovskite, the relatively rare apgaitic rocks, however, contain Na-Ca-HFSE-bearing and halogen-rich minerals such as eudialyte or wöhlerite instead (e.g. Sørensen, 1997, Marks *et al.*, 2011, Marks & Markl, 2017). Agpaitic rocks belong to the most evolved and most reduced alkaline rocks at all (Marks & Markl, 2017). A major prerequisite for the formation of agpaitic rocks is the retention of volatiles in the melt (e.g. Marks & Markl, 2001, Marks & Markl, 2015). This is most likely reached in closed systems (Sørensen, 1992) and is in accordance with the fact that most of the about 100 occurrences of agpaitic rocks are plutonic. However, the relatively few extrusive agpaitic rocks (e.g. at Oktyabr'sky, Tarosero and Kontozero; Krivdik & Tkachuk, 1988, Dawson, 1997, Petrovsky *et al.*, 2012) raise questions on how halogens and other volatiles can be prevented from escaping to the atmosphere within a volcanic system.

The Tarosero Volcanic Complex in northern Tanzania is a well-suited locality to investigate such formation processes as it comprises variably evolved alkaline to peralkaline extrusive rocks, including rare and highly evolved agpaitic phonolites (Dawson, 2008). To date, no detailed study exists about the

mineralogy and petrology of this volcano. We present a detailed mineralogical, mineral chemical and geochemical investigation of the Tarosero rocks. Combined with thermodynamic calculations of the prevailing crystallization conditions and fractional crystallization models, we decipher the genetic relationships between the various rock types, and suggest processes to form the highly evolved, agpaitic extrusive rocks in the volcanic environment at Tarosero.

## GEOLOGY

The Tarosero volcano in northern Tanzania is situated in the eastern branch of the East African Rift valley, with the Kenyan and Tanzanian parts also known as the Gregory Rift. Rifting was initiated by plume activity beneath Ethiopia 30 Ma ago and proceeded southwards along Pan-African suture zones (e.g. Hofmann *et al.*, 1997 and references therein, Chorowicz, 2005). Volcanic magmatism in northern Tanzania is linked to the North Tanzanian Divergence Zone (Fig. 1a; Le Gall *et al.*, 2008), which formed along pre-existing zones of crustal weakness between the Tanzanian craton to the west and the Mozambique mobile belt to the east (Smith, 1994).

Magmatism can be divided into two groups based on major faulting events (Dawson, 1992, Dawson, 2008): a pre-1.2 Ma group of mainly alkali basalt-phonolite (e.g. Tarosero, Monduli, Ngorongoro, Oldoinyo Sambu, Ketumbeine, Kilimanjaro) and rather rare nephelinite±carbonatite volcanoes (e.g. Burko, Essimingor, Mosonik), and a post-1.2 Ma group comprising volcanoes essentially of the nephelinite-phonolite±carbonatite association (e.g. Meru, Oldoinyo Lengai, Kerimasi, Kwahera, Hanang).

The Tarosero rocks have been dated to 2.4 - 1.9 Ma using K-Ar-dating (Macintyre *et al.*, 1974), with the youngest ages being related to the rocks of the summit area. However, recent $^{40}Ar/^{39}Ar$-dating indicate 2.35 to 2.33 Ma for the peak region (Mana *et al.* (2015). The complex is a so-called lava cone that extruded onto a nowadays northerly-dipping lava plateau of alkali basalts and trachyandesites of which the volcanic center is unknown (Dawson, 2008). The complex is situated just west of the

Lembolos graben and mainly consists of trachyte lavas and minor trachytic tuffs, while primitive rocks like basalts and more evolved peralkaline phonolites are also present (Fig. 1b).

## SAMPLE LOCALITIES

In total, 73 samples deriving from 15 localities were examined in the course of this study. Of these, 28 samples were investigated in detail by means of electron microprobe and whole-rock analyses (Table 1). Samples were taken from the central part of the complex, including the cone itself, as well as from the southern part, where more primitive to intermediate rocks (basalts, andesites, latites) occur. In a deep gorge at the western flank of the complex, trachytic and phonolitic bolders were sampled. These derive from eroded or almost inaccessible parts of the central area of the volcano and were transported by ephemeral rivers.

## PETROGRAPHY

The Tarosero rocks are classified according to the guidelines of the IUGS, Subcommission on the Systematics of Igneous Rocks (Le Maitre *et al.*, 2002). We distinguish the following six rock groups:

### Basalt

Basalts contain up to 2 mm large euhedral olivine, typically rimmed by iddingsite (Fig. 2a). Chromian spinel was found once as inclusion in olivine. Clinopyroxene occurs as up to several mm large, partly rounded crystals (Fig. 2b) that sometimes reveal a slightly darker rim. The groundmass consists of olivine, clinopyroxene, euhedral magnetite, rare ilmenite laths and tabular plagioclase.

### Andesite

The andesite reveals a layered, tuff-like structure and contains up to several mm large macrocrysts of euhedral to partly rounded amphibole, euhedral to subhedral clinopyroxene (Fig. 2c) and elongated plagioclase crystals in a fine-grained groundmass (Fig. 2d). Magnetite occurs as phenocrysts (Fig. 2d) and as inclusions in amphibole and clinopyroxene. Apatite is ubiquitous.

**Latite**

Latites contain several mm large and randomly arranged tabular plagioclase (Fig. 2e), euhedral to subhedral and partly altered olivine, and subhedral clinopyroxene. Ilmenite and magnetite occur as independent microphenocrysts, with the latter commonly surrounding ilmenite (Fig. 2f). The groundmass mineralogy is similar to that of the phenocrysts with additional amphibole (Fig. 2f) and apatite. The latter is occasionally replaced by monazite.

**Sodalite-bearing trachyte**

Sodalite-bearing trachytes (for the sake of simplicity in the following called "trachytes") are characterized by several mm large, randomly arranged plagioclase phenocrysts with a sieved core and a rim of alkali feldspar (Fig. 2g). Euhedral and sometimes concentrically zoned clinopyroxene, euhedral magnetite, subhedral amphibole (Fig. 2h) and rare ilmenite occur as phenocrysts and as inclusions in plagioclase. Amphibole macrocrysts are surrounded by fine-grained clinopyroxene and magnetite (Fig. 2h). The groundmass mainly consists of alkali feldspar, and minor plagioclase, fluorite and subhedral to interstitial sodalite. Carbonate was found in vugs within large plagioclase grains, apatite is ubiquitous.

**Peralkaline (sodalite-bearing) alkali feldspar trachyte and peralkaline phonolite**

Peralkaline (sodalite-bearing) alkali feldspar trachytes (in the following called "peralkaline trachytes") and peralkaline phonolites reveal a flow structure with oriented phenocrysts of tabular alkali feldspar. Some of these rocks contain abundant dark brown amphibole macrocryts (type I), bright green clinopyroxene I and magnetite. Clinopyroxene I is typically enclosed by dark green clinoyproxene II (Fig. 3a), while amphibole I is replaced by magnetite and bright brown amphibole II (Fig. 3b). The amount of euhedral to subhedral sodalite, which commonly is altered to clay minerals and Fe-rich hydroxides, strongly varies between the samples. Interstitial phases are alkali feldspar, clinopyroxene II, aenigmatite and brownish amphibole IIIa (Fig. 3c), whereas late-stage interstitial blue amphibole IIIb (Fig. 3d) only occurs in peralkaline phonolites with low contents of mafic phenocrysts. In peralkaline phonolites, sodalite is commonly enclosed by amphibole IIIb and can contain inclusions of aenigmatite (Fig. 3d). Some of the peralkaline phonolites contain interstitial eudialyte (Fig. 3e), which is, however,

frequently replaced by un-identified Zr-rich alteration phases. Further late-stage (probably hydrothermal) phases are Mn-(hydr)oxides that mainly occur along cracks of alkali feldspar crystals and rare REE-F-carbonates (bastnäsite; Fig. 3f). Apatite is rare. An agpaitic phonolite (TA-030) additionally contains coarse-grained cumulates that mainly consist of alkali feldspar and dark brown amphibole I, which is altered to bright brown amphibole II and magnetite when in direct contact to the peralkaline phonolite (Fig. 3g). Agpaitic phonolite TA-021 contains a several mm large xenocrystic plagioclase fragments with inclusions of clinopyroxene, magnetite and olivine.

**Peralkaline olivine-bearing alkali feldspar trachyte**

Peralkaline olivine-bearing alkali feldspar trachytes (in the following called "peralkaline olivine trachytes") are characterized by oriented alkali feldspar laths, subhedral magnetite, and olivine that is commonly altered to iron (hydr)oxides (Fig. 3h) and also occurs as inclusions in alkali feldspar. The groundmass mainly consists of small alkali feldspar laths, interstitial brown to dark blue amphibole and aenigmatite (Fig. 3h). Apatite is very rare, and clinopyroxene is absent.

## METHODS

### Whole-rock analyses

For this study, major and trace elements of 25 rock samples were determined. Major element analyses were done at the Department of Geosciences, University of Tübingen (Germany) with a wavelength dispersive XRF (Bruker AXS S4 Pioneer; Rh-tube at 4kW) using 32 references materials (compiled in Govindaraju, 1989). The rock samples were ground with an agate mill for 10 minutes. After drying at 105 °C, each 1.5 g of rock powder was mixed with 7.5 g MERCK spectromelt A12 (mixture of 66% Li-tetraborate and 34% Li-metaborate), and melted at 1200°C to fused beads using an Oxiflux system (CBR analytical service). Detection limits and analytical errors are in the 1-10 µg/g, and 0.1 % (relative) range, respectively.

Trace elements were analysed by ICP-MS (X-series 2, Thermo Fisher Scientific) at the Institute for Applied Geosciences, Karlsruhe Institute of Technology (Germany). Each 100 mg of powdered sample

was pre-oxidized (65 % $HNO_3$, subboiled) and digested in a mixture of 40 % HF (suprapur) and 65 % $HClO_4$ (normatom) heated for 16 h at 120 °C in closed Teflon vessels to ensure complete silicate decomposition. Afterwards, the acids were evaporated to incipient dryness and the residue was re-dissolved in 65 % $HNO_3$ (subboiled) and evaporated again. This step was repeated three times for purification purposes and the final residue was dissolved in 50 mL of ultrapure water. Due to the high concentrations of Ba and light REE, mathematical corrections for Eu, Gd, Tb and Er were required: $^{151/153}$Eu was corrected for BaO, $^{157}$Gd for PrO, $^{158}$Gd for CeO and $^{159}$Tb and $^{167}$Er for NdO interferences. The mean value of both isotopes are reported for Eu and Gd. The quality of the whole procedure was ensured by adding six blanks, certified reference materials SY-2, SY-3 (Govindaraju, 1994) and CRM-TMDW-A (High-Purity standards, Inc.) that were included in the digestion (accuracy: mainly ± 10 %).

Bulk halogen (F, Cl, Br) and S concentrations of 25 powdered whole-rock samples were determined by Combustion Ion Chromatography (CIC) at the University of Tübingen. For this purpose, a 930 Compact IC Flex chromatograph (Metrohm) with chemical suppression and a peristaltic pump for regeneration (100 mmol/l $H_2SO_4$) connected to a combustion oven and an autosampler for solid samples (MMS 5000; Analytik Jena), was used. Based on the frequent analysis of standard solutions (single element 1000 mg/l solutions; Roth), reference material GSN (granite), and replicate analyses for a subset of the samples, the long-term reproducibility (1σ) for solid samples of the measurements is generally within a 10 % margin for F, Cl and S, while Br may vary by ~20 % because of its relatively low concentrations. Effective detection limits are in the order of 10 µg/g for F and Cl, around 5 µg/g for S and 0.3 µg/g for Br. See also Epp *et al.* (2019) and Epp *et al.* (2020) for a more detailed description of the method.

**Mineral analyses**

Mineral compositions were determined using a JEOL JXA 8900 electron microprobe in wavelength dispersive mode at the Department of Geosciences, University of Tübingen (Germany). An acceleration voltage of 15 kV was used for feldspar, sodalite, clinopyroxene, aenigmatite and amphibole, respectively 20 kV for olivine, oxides and eudialyte (see Supplementary Table 1 for a compilation of the WDS configurations). Peak counting times for major elements were between 16 s and 30 s, and between 30 and 60 s for minor elements, while the background counting times were half as long. Both, synthetic

and natural standards were used for calibration. Peak overlap corrections involving Ti-V, V-Cr (oxides), F-Fe (amphibole), Ba-Ti (feldspar), Hf-Ti and Hf-Sr (eudialyte) were implemented and the raw data was converted using the implemented ZAF (for olivine, clinopyroxene, oxides, amphibole, aenigmatite) and φρz corrections (Armstrong, 1991). The beam current was set to 20 nA, except for sodalite and eudialyte, which were analyzed with 5 nA. Sodium diffusion and destruction of the grains was additionally avoided by widening the beam spot to 2 µm (feldspar, amphibole), respectively 5 µm (sodalite). Eudialyte was also measured with a 5 µm beam spot (instead of the recommended 20 µm; e.g. Johnsen & Grice, 1999, Pfaff *et al.*, 2010) due to the small grain size. The standard deviation for the major elements is typically < 1 %, but reaches up to ~6 % for Fe in sodalite, and for Zr in eudialyte as a result of the analytical conditions (low beam current) required to prevent the destruction of the grains.

**Thermodynamic calculation of intrinsic parameters**

Several thermometers and (oxy)barometers, as well as thermodynamic calculations were used to quantify the intrinsic parameters pressure (P), temperature (T), oxygen fugacity ($f_{O2}$) and silica activity ($a_{SiO2}$) for suitable samples. Pressure and temperature were estimated using an amphibole thermo(oxy)barometer (Ridolfi & Renzulli, 2012), and clinopyroxene-liquid barometers with their pressure independent thermometers (Putirka *et al.*, 1996, Putirka *et al.*, 2003, Putirka, 2008, Neave & Putirka, 2017). Whole-rock analyses were used as proxies for liquid compositions and special care was taken to exclude samples that exhibit coarse-grained cumulates or xenoliths (see above). Temperature was additionally estimated using ilmenite-magnetite equilibria Andersen & Lindsley (1985) applying solid solution models of Stormer (1983), the QUILF software package Andersen *et al.* (1993), which is based on coexisting olivine-Fe-Ti oxides±clinopyroxene, and feldspar solvus thermometry Fuhrman & Lindsley (1988). Oxygen fugacity was calculated using the magnetite-melt oxybarometer of Arató & Audétat (2017), which is based on the Fe and Ti partitioning between melt and mineral. Redox conditions were also estimated by the ilmenite-magnetite oxybarometer, and both, $f_{O2}$ and $a_{SiO2}$ could be determined using the QUILF software. Moreover, several redox and/or silica sensitive reactions (reactions 1-4) were calculated using the Perple_X software package (Connolly (1990) with the

implemented database of Holland & Powell (1998). Aenigmatite-involving reaction (5) was executed according to Marsh (1975).

(1): 2 $Fe_3O_4$ (magnetite) + 3 $SiO_2$ = $O_2$ + 3 $Fe_2SiO_4$ (fayalite)

(2): $NaAlSiO_4$ (nepheline)+ 2 $SiO_2$ = $NaAlSi_3O_8$ (albite)

(3): $NaAlSi_2O_6$ (jadeite)+ $SiO_2$ = $NaAlSi_3O_8$ (albite)

(4): $CaAlAlSiO_6$ (Ca-Tschermak's pyroxene) + $SiO_2$ = $CaAl_2Si_2O_8$ (anorthite)

(5): $Fe_3O_4$ (magnetite)+ 6 $SiO_2$ + 6 $NaFeSi_2O_6$ (aegirine) + 3 $Fe_2TiO_4$ (ulvöspinel) = 3 $Na_2Fe_5TiSi_6O_{20}$ (aenigmatite) + 2 $O_2$

All mineral equilibria calculations were corrected by the activities for endmember components of olivine, clinopyroxene, Fe-Ti oxides and feldspar (Wood, 1979, Holland, 1990, Andersen *et al.*, 1993, Holland & Powell, 2003). Aegirine and aenigmatite activities were calculated using mixing-on-site models.

### Fractional crystallization modeling

Fractional crystallization models were executed in the system $SiO_2$-$TiO_2$-$Al_2O_3$-$Fe_2O_3$-MnO-MgO-CaO-$Na_2O$-$K_2O$-$P_2O_5$, assuming that phenocryst phases are primarily responsible for the fractionation process. Whole-rock analyses were used as a proxy for the initial melt composition, while the target composition was computed using the Least Square Fitting Method.

## RESULTS

### Whole-rock data

New whole-rock data of 25 samples, augmented by analyses from literature (Cooper, 1972, Mana *et al.*, 2015), represent the large compositional variation for the Tarosero rocks (Table 2). According to the

whole-rock chemistry using the TAS diagram (Fig. 4a) and further subdivision schemes (Le Bas *et al.*, 1986, Le Maitre *et al.*, 2002), the rocks can be mainly divided into basalts, basaltic trachyandesites (shoshonite), trachyandesites (benmoreites) and trachytes. Trachytes are further subdivided into comenditic and pantelleritic varieties (Fig. 4b; MacDonald, 1974). Note that the geochemical study of Cooper (1972) did not mention eudialyte in the peralkaline trachytes/phonolites at all. This might be related to the strong alteration of the grains, and/or to the very small size of the crystals which prevents an easy recognition by transmitted light microscopy.

Concentrations of $Na_2O+K_2O$ and $SiO_2$ generally increase from primitive to evolved rocks, although "fine-grained peralkaline trachytes" of Cooper (1972) show a rough negative correlation between $Na_2O+K_2O$ and $SiO_2$ (Fig. 4a). The alkalinity index (A.I.=[Na+K]/Al) is lowest in basalts (~0.4) and highest in eudialyte-bearing peralkaline phonolites (~1.2). A positive correlation exists between A.I. and $Na_2O+K_2O$ (Fig. 4c), negative ones with CaO (Fig. 4d), $TiO_2$ (Fig. 4e) and MgO (Fig. 4f). The $Al_2O_3$ concentration rises in basalts towards the andesite, whereas trachytes and the peralkaline rocks show a negative correlation with A.I. (Fig. 4g). Latites slightly deviate from this trend with an intermediate A.I. and $Al_2O_3$ composition. A complex pattern is also illustrated by $Fe_2O_3$ (Fig. 5h) which decreases from primitive to intermediate rock types, but increases towards agpaitic peralkaline phonolites. The molar Na/K ratio (Table 2) roughly decreases from the primitive rocks (molar Na/K=4.5-1.5) to the peralkaline rock group, but is exceptionally low in the andesite (molar Na/K=1.5).

Compatible trace elements like Ni (<440 µg/g) and Cr (<710 µg/g) are only elevated within the basalts, while incompatible elements such as REE (Fig. 5a) and HFSE (Fig. 5b & c) increase from the primitive towards the peralkaline trachytes and peralkaline phonolites. Peralkaline trachyte TA-078 contains large amounts of hydrothermal bastnäsite and has the highest REE concentrations, while peralkaline olivine trachytes have rather low REE contents similar to the trachytes.

Primitive mantle-normalized (Palme & O'Neill, 2003) incompatible element patterns for basalts, the andesite, latites and trachytes are very similar, except for the lack of negative P and Ti anomalies in basalts (Fig. 6a), the peralkaline rocks are characterized by strongly negative Ba, Sr, P and Ti anomalies. Primitive mantle-normalized REE abundances generally decrease from light REE (LREE) to heavy REE

(HREE), with increasing $La_N/Lu_N$ ratios from basalts via latites-trachytes to peralkaline rocks. Negative Eu anomalies are only present in the peralkaline rocks (Fig. 6b). Some of the peralkaline rocks, and most pronounced the peralkaline olivine trachytes comprise strongly negative Ce anomalies, but have a less prominent Eu anomaly (Fig. 6b).

Halogen concentrations are highly variable (Supplementary Table 2): Fluorine ranges between 680 and 2050 µg/g and commonly shows a variation of more than 1000 µg/g within a specific rock type (Fig. 7a). Chlorine (Fig. 7b) is typically below 250 µg/g but much higher (up to ~2700 µg/g) for rocks containing unaltered/relict sodalite grains (trachytes, peralkaline phonolites). Bromine mostly varies between 0.7 and 3.7 µg/g, and $SO_4$ between 5 and 100 µg/g. The pattern for the F/Cl ratio (~1-100) and the Br/Cl ratio (~0.001-0.1) are very similar (Fig. 7c & d), with samples containing fresh sodalite illustrating the lowest values.

## Mineral data

*Olivine*

Olivine compositions vary largely (Table 3; see Supplementary Table 2 for all mineral data), with macrocrysts in basalts being $Fa_{12-19}$ and groundmass olivines $Fa_{39-42}$. In latites, olivine is $Fa_{41-60}$, in peralkaline olivine trachytes $Fa_{66-85}$ and olivine in the plagioclase fragment of peralkaline phonolite TA-021 has an intermediate composition ($Fa_{48-50}$). The tephroite component (0.2-6.2 mol%) increases with the fayalite component (Fig. 8a). Nickel contents reach 0.008 apfu (~0.4 wt.% NiO) in basalts but are otherwise mostly below the detection limit (0.01 wt.% NiO). Calcium contents range from 0.006 apfu (~0.2 wt.% CaO) in basalts to 0.017 apfu (~0.5 wt.% CaO) in peralkaline olivine trachytes (Fig. 8b).

*Clinopyroxene*

Clinopyroxene evolves from diopside-hedenbergite$_{ss}$ in primitive and intermediate rocks and reaches about 80 mol% aegirine component in interstitial clinopyroxene of the peralkaline rocks (Table 4; Fig. 9a). Tschermak's components ($CaXXSiO_6$; X= Al, Ti, $Fe^{3+}$) reach 17 mol% in basalts and the andesite. The Mn content (up to 0.04 apfu; 1.2 wt.% MnO) increases from the primitive to the evolved rock types, but decreases with the aegirine content in interstitial clinopyroxenes of the peralkaline rocks (Fig. 9b).

310 Clinopyroxenes of the primitive rocks have the highest Ti (0.09 apfu; 3.3 wt.% $TiO_2$) and the lowest Zr
311 contents (generally below 0.001 apfu; 0.09 wt.% $ZrO_2$), the latter reaches up to 0.07 apfu (3.8 wt.%
312 $ZrO_2$) in peralkaline rocks (Figs. 9c & d).

313 *Oxides*

314 Spinel-group minerals represent magnetite-ulvöspinel solid solutions (Table 5; Fig. 10a). The Ti
315 concentrations decrease from the basalts (~75 mol% ulvöspinel) via the intermediate rock types (~65-
316 55 mol% ulvöspinel) towards the peralkaline trachytes/phonolites (~40-30 mol% ulvöspinel). Spinel-
317 group minerals in the peralkaline olivine trachytes, however, reveal rather high ulvöspinel components
318 between 70 and 60 mol%. Manganese (up to 0.08 apfu; 2.5 wt.% MnO) and Zn (0.011 apfu; 0.4 wt.%
319 ZnO) are positively correlated and are highest in peralkaline rocks (Fig. 10b). One basalt (TA-048)
320 additionally contains a Cr-spinel inclusion in olivine (Cr=1.1 apfu; Mg=0.5 apfu). Ilmenite has the
321 highest Ti content in the latites ($Ilm_{71-81}Hem_{11-16}Prph_{2-5}Gk_{3-13}$), followed by the basalts ($Ilm_{62-74}Hem_{14-27}Prph_{0-1}Gk_{9-14}$) and the trachytes ($Ilm_{64-68}Hem_{15}Prph_3Gk_{14-18}$).

323 *Aenigmatite*

324 Aenigmatite-group minerals are characterized by a low rhönite component and intermediate
325 compositions between the aenigmatite and the wilkinsonite endmember (Table 6; Fig. 11a). Mean Ti
326 contents increase from eudialyte-free peralkaline trachytes/phonolites ($\approx Aen_{35-54}Wlk_{43-63}Rhn_{1-5}$) via
327 agpaitic phonolites ($\approx Aen_{34-65}Wlk_{34-63}Rhn_{0-5}$) and peralkaline olivine trachytes ($\approx Aen_{58-71}Wlk_{27-41}Rhn_{0-2}$). Eudialyte-free and eudialyte-bearing peralkaline trachytes/phonolites have similar Mg contents (0.1-
329 0.3 apfu; 0.05-1.3 wt.% MgO), while Zr contents (<0.4 apfu; 0.5 wt.% $ZrO_2$) of the former are on
330 average slightly higher (Fig. 11b). Peralkaline olivine trachytes have the lowest magnesium and
331 zirconium concentrations (≤0.1 apfu).

332 *Amphibole*

333 Amphibole compositions cover the whole spectrum from calcic to sodic species (Table 7). Amphibole
334 I (macrocrysts) reveals the highest Ca and lowest Si contents, while amphibole II (altered rim) and
335 especially amphibole III (interstitial) are more sodic and silicic (Fig. 12a; nomenclature according to

Hawthorne *et al.*, 2012). The concentration of F as well as $X_{Mg}$ (=Mg/[Mg+$Fe^{2+}$]) increase from amp I to amp II (Fig. 12b), while Ti decreases (Fig. 12c). Amphibole III has a large range for $X_{Mg}$ (0-0.5), which differs from amphibole IIIa ($X_{Mg}$=0.4-0.5) and amphibole IIIb ($X_{Mg}$=0-0.3). In peralkaline phonolites, amph IIIb is low in Ti (<0.1 apfu) and F (1.2-1.6 apfu), while in amph IIIb Ti increases down to $X_{Mg}$=0.05 and subsequently decreases for $X_{Mg}$<0.05. Fluorine in peralkaline olivine trachytes negatively correlates with Ti, hence showing the reverse pattern with respect to $X_{Mg}$. The Zr concentration is the highest for amp III with $X_{Mg}$ between 0.15 and 0.55 (Fig. 12d), Cl is typically low (≤ 0.01 apfu; 0.04 wt.%).

*Feldspar*

Plagioclase and alkali feldspar in the primitive to intermediate rocks vary in composition from $An_{58}Ab_{40}Or_2$ over $An_{11}Ab_{78}Or_{11}$ to $An_2Ab_{58}Or_{40}$ (Table 8; Fig. 13a). Feldspars of the peralkaline rocks are typically characterized by very low anorthite components ($An_1Ab_{70}Or_{29}$ to $An_0Ab_{63}Or_{37}$), while higher Ca contents only occur in some feldspar cores of the peralkaline trachytes ($An_{12}Ab_{76}Or_{12}$), in the cumulate of sample TA-030 ($An_{11}Ab_{4780}Or_{11}$) and the xenolith in sample TA-021 ($An_{21}Ab_{72}Or_7$). Strontium is elevated (>0.01 apfu; 0.4 wt.% SrO) in plagioclase from andesite, trachytes and some anorthite-rich alkali feldspars of the peralkaline trachytes. Iron reaches up to 0.08 apfu (2.2 wt.% $Fe_2O_3$) in the peralkaline rocks, but is also elevated in the plagioclases of the basalts and the groundmass plagioclases of the andesite (0.02-0.05 apfu; Fig. 13b). Barium is always below 0.01 apfu (0.5 wt.% BaO).

*Sodalite*

Sodalite has almost Cl-endmember compositions (Table 9), with S typically being below the detection limit (~0.05 wt.% $SO_3$). The analyzed sodalite grains contain minor K (mostly <0.15 apfu; Fig. 14a) and Ca (<0.01 apfu; 0.06 wt.% CaO). Notable are rather high contents of $Fe^{3+}$ (0.2-0.8 apfu) that correlate negatively with Al (Fig. 14b), suggesting a coupled substitution between Al+$Fe^{3+}$ and Si (Fig. 14c). Charge balancing may be maintained by the exchange mechanism of $Na^+$+($Al^{3+}$, $Fe^{3+}$) = □+$Si^{4+}$. Sodalites with elevated K, Si, and $Fe^{3+}$ concentrations show low analytical totals down to 96 wt.%.

*Eudialyte*

Eudialyte (formula based on Si+Al+Zr+Ti+Hf+Nb=29 cations; Johnsen & Grice, 1999) reveals Na contents of 11 to 14 apfu, and is characterized by Ca (3.6-5.1 apfu) and REE concentrations (0.3-0.8 apfu) which are typical of foid-bearing rocks (Table 10; Supplementary Figure 1a; Schilling *et al.*, 2011, Estrade *et al.*, 2018). The contents of Fe (2.7-3.5 apfu) and Si (25.8-26.5 apfu) partly exceed the typical maximum site occupation (Fe=3 apfu; Si=26 apfu). This might in part be related to the analytical conditions (see above), although high Fe concentrations above 3 apfu for eudialyte from Tarosero were also reported by Dawson (1997). We also consider the possibility that the formula calculation based on the simplified assumption of Si+Al+Zr+Ti+Hf+Nb= 29 cations may not be useful in all cases. Contrary to the current literature data on eudialyte-group minerals, there is a positive correlation between Fe and Mn (Supplementary Figure 1b). Zirconium varies between 2.0 and 2.9 apfu. Chlorine typically ranges between 1.7 and 1.9 apfu, while strontium mostly is below the detection limit (<0.05 apfu; 0.16 wt.% SrO).

## DISCUSSION

### Crystallization conditions of the Tarosero rocks

Intrinsic parameters like P, T, $f_{O2}$, $a_{SiO2}$, and $a_{H2O}$ strongly affect the stability of mineral phases, and are therefore of great importance to understand the evolution of magmatic systems. Based on these data and their combination with whole-rock data and fractional crystallization calculations, we propose a possible petrological evolution for the Tarosero Volcanic Complex.

*Crystallization pressure*

Pressure estimates for basalts were executed using the recently calibrated clinopyroxene-liquid barometer of Neave & Putirka (2017) with the independent temperature estimate of Putirka (2008; Equation 33). Temperatures range between 1140 and 1210 °C and pressures vary between 4 and 6 kbar, corresponding to a crustal depth of 12 to 18 km. However, clinopyroxene-liquid models of Putirka *et al.* (1996) and Putirka *et al.* (2003) imply much higher pressures of 11±2 kbar, respectively ~25-40 km

388 depth. This is consistent with the absence of plagioclase macrocrysts in the Tarosero basalts, since
389 experiments demonstrated that plagioclase typically does not occur as a near-liquidus phase above 10
390 kbar (Green & Ringwood, 1967). The pressure estimates conform with magmatic underplating at the
391 Moho, which is assumed to occur at depths < 35 km along the rift axis in southern Kenya (e.g. Prodehl
392 *et al.*, 1997). Pressure calculations for the intermediate andesite and the trachytes were determined by
393 applying the amphibole barometer of Ridolfi & Renzulli (2012). The calculated pressures of 7 kbar and
394 9±1 kbar, respectively, demonstrate rather deep crystallization depths of 20-30 km, although the results
395 must be considered with caution since recent studies indicate that amphibole-related pressure estimates
396 are highly sensitive to the temperature and liquid composition (Erdmann *et al.*, 2014, Putirka, 2016).
397 However, the estimates are in good agreement with magma fractionation, ascent and storage at shallower
398 crustal levels compared to the more primitive basalts. Peccerillo *et al.* (2007) suppose that trachyte-
399 dominated volcanoes commonly form by high-pressure fractionation. Moreover, the fine-grained
400 reaction rim around the amphiboles and the sieve-textured plagioclase cores in trachytes (see above;
401 Figs. 3g & h) might reflect rapid decompression during ascent from a deep magma chamber to the
402 surface (e.g. Nelson & Montana, 1992, Rutherford & Devine, 2003, Buckley *et al.*, 2006). Peralkaline
403 magmas typically evolve in shallow-level magma plumbing systems of approximately 2-4 km depth
404 (e.g. Mahood, 1984, Novak & Mahood, 1986, Spandler & Morris, 2016, Marks & Markl, 2017). The
405 coarse-grained cumulate in peralkaline phonolite TA-030 (see above; Fig. 3g), consisting mainly of
406 large amphibole and feldspar crystals, is a further hint for a shallow magma chamber. In subsequent
407 calculations (T, $a_{SiO2}$, $f_{O2}$) on such a multi-level magmatic differentiation system, we assumed a pressure
408 of 11 kbar for the basalts, 9 kbar for the trachytes (and the latites), 7 kbar for the andesite and 1 kbar for
409 the peralkaline rocks. Calculations based on groundmass minerals were done at atmospheric conditions
410 (1 bar).

411 *Estimates for T, $f_{O2}$ and $a_{SiO2}$*

412 Based on texturally coexisting olivine-clinopyroxene macrocryst pairs, near liquidus temperatures for
413 the basalts were determined to ~1000 °C, while clinopyroxene-liquid thermometers yield higher
414 temperatures (1290-1140 °C). The early groundmass assemblages indicate temperatures of 850-920 °C

(olivine-clinopyroxene-magnetite and ilmenite-magnetite, respectively). However, the latter two estimates must be considered with caution since i) only one fresh ilmenite-magnetite pair was found (all other groundmass magnetites of sample TA-048 are strongly altered to hematite) and ii) groundmass olivines of TA-042 are completely altered to iddingsite, hence olivine-clinopyroxene-magnetite equilibria could only be applied by combining mineral data of both samples (TA-048 and TA-042). These results agree with minimum temperature estimates based on the feldspar solvus (850 °C; accoring to Fuhrman & Lindsley, 1988). Computed redox conditions vary between ΔFMQ= -0.2 and ΔFMQ +0.3 (Fig. 15) with the relatively high redox conditions during groundmass formation being in good accordance with the elevated $Fe^{3+}$-content in plagioclase (Fig. 13b). Silica activity calculations based on olivine-clinopyroxene-magnetite equilibria (reactions 3+4) yield values of $a_{SiO2}$=0.8, whereas late magmatic clinopyroxene-feldspar equilibria indicate a decrease of the silica activity to $a_{SiO2}$=0.4±0.2, possibly due to the early clinopyroxene crystallization.

The early magmatic crystallization temperature for the andesite, the latites and the trachytes are estimated to ~1100-900 °C using amphibole and ilmenite+magnetite±olivine assemblages. Groundmass feldspars crystallized above 850 °C. Redox conditions for these rocks are typically rather reduced (ΔFMQ=-1–0; Fig. 15). However, the groundmass plagioclases of the andesite show similarly high $Fe^{3+}$-concentrations compared to the basalts and may record increasing redox conditions during the late magmatic stage (Fig. 13b). Silica activity can be constrained to $a_{SiO2}$=0.4±0.2 (reactions 3+4), except for the andesite which shows a comparatively low silica activity of $a_{SiO2}$=0.15

The maximum temperature for the groundmass assemblage of the peralkaline rock groups can be assumed to be around 750 °C ± 50 based on experimentally synthesized aenigmatite and arfvedsonite (Ernst, 1962, Bailey, 1969, Thompson & Chisholm, 1969, Scaillet & Macdonald, 2001, Giehl *et al.*, 2013, Giehl *et al.*, 2014), consistent with a feldspar solvus ≥700 °C. Redox conditions during crystallization of the peralkaline trachytes and peralkaline phonolites was roughly estimated by an equilibrium reaction including magnetite, clinopyroxene and aenigmatite (reaction 5). Since oxides typically do not coexist with aenigmatite (Nicholls & Carmichael, 1969), this reaction reflects the redox conditions that prevailed during termination of magnetite and onset of aenigmatite crystallization. The

high uncertainty of the exact mineral compositions during this transition results in a large possible redox range of ΔFMQ=-5 to ΔFMQ=0 (Fig. 15) and a high uncertainty for the silica activity ($a_{SiO2}$=0.2-0.8). Oxygen fugacity estimates for the peralkaline olivine trachytes (ΔFMQ=-2.6-0) were computed using coexisting olivine, magnetite, and a silica activity >0.3 due to the absence of nepheline but the presence of alkali feldspar (reactions 1+2).

**Source region for the rocks from Tarosero**

The high concentrations of incompatible elements in peralkaline rocks are commonly related to a metasomatically enriched mantle source (Martin *et al.*, 1994, Upton *et al.*, 2003, Markl *et al.*, 2010) which is also assumed for Tarosero based on trace element fractionation models (Mana *et al.*, 2015). The low Cs and Rb abundances and the negative K anomaly in the primitive rocks from Tarosero suggest the presence of a K-bearing mineral phase in the mantle source (Fig. 6a). Since the primitive mantle-normalized Ba/Ce ratio of ≥1 illustrates a residual phase that only incorporates minor amounts of Ba, we suggest that amphibole rather than phlogopite is the dominant potassium phase in the mantle (Mana *et al.*, 2015). However, contributions of other residual mineral phases like olivine, pyroxene or garnet increase the Ba/Ce ratio, and hence, might be balanced by the presence of phlogopite (Halliday *et al.*, 1995). Radiogenic Sr-Nd-Pb isotope values indicate the involvement of several mantle components, with the least evolved samples trending towards the isotope composition of the Kenya Plume (Aulbach *et al.*, 2011), while more evolved rocks might be contaminated by crustal components (Mana *et al.*, 2015).

**Genetic relationship between the rock types at Tarosero**

Continuous trends in mineral compositions (e.g. clinopyroxene, magnetite, amphibole) suggest a genetic link between the investigated rock types , as do the very similar ages for primitive basalts and the evolved rocks of the volcano (Macintyre *et al.*, 1974, Mana *et al.*, 2015). Besides basanitic and nephelinitic melts, alkali basaltic melts are candidates for the source of peralkaline rocks (e.g. Kramm & Kogarko, 1994, Schilling *et al.*, 2011, Andersen *et al.*, 2014, Estrade *et al.*, 2014, Spandler & Morris, 2016). In the case of Tarosero, negative Eu anomalies in the evolved rocks (Fig. 6b) indicate extensive plagioclase fractionation, which is a common characteristic of many peralkaline rocks (e.g. Sørensen, 1992, Ridolfi

469 *et al.*, 2006) and is typical of their derivation from basaltic, rather than from basanitic or nephelinitic
470 magmas (Marks *et al.*, 2011). Similarly, the low Sr concentrations in eudialyte (Table 10) and the
471 negative Sr anomaly in the peralkaline suite (Fig. 6a) supports this assumption (e.g. Kramm & Kogarko,
472 1994, Schilling *et al.*, 2011).

473 *Evolution from the primitive to intermediate compositions*

474 Based on the arguments presented above, we computed fractional crystallization models. Due to the
475 exceptionally low Na/K ratio (Table 2) and the low silica activity of the andesite, we excluded this rock
476 type from further modelling and suggest that it is derived from a different magma source. In the absence
477 of a better suited primitive rock type, we first tested if the basalts from Tarosero represent suitable
478 parental magmas for the latites and the more evolved rocks.

479 Fractional crystallization based on the phenocryst phases olivine and clinopyroxene (path 1a in Fig. 16)
480 does not result in an evolutionary path from the basaltic composition towards the intermediate latites
481 (note that no clinopyroxene fractionation is required for the best fit; see Supplementary Table 3) nor
482 does the addition of titanomagnetite (path 1b) or titanomagnetite + plagioclase fractionation (path 1c).
483 While the fractionation of titanomagnetite could be suggested by negative Ti anomalies (Fig. 6a), the
484 lack of a negative Eu and Sr anomaly in latites argues against extensive plagioclase fractionation. We
485 conclude that the investigated basalts do not represent a parental magma for the latites. Unfortunately,
486 no other primitive rock type was sampled in the field which could represent a suitable parental magma
487 composition. Since extensive plagioclase fractionation can be ruled out for the rather high alkalinity
488 index A.I. of the latites (A.I.=0.74-0.84), we assume that these rocks derive from a mantle source
489 involving partial melting of phlogopite (A.I. ≈ 1). However, we emphasize that both, the basalts and the
490 latites might also represent a tectonic window of the underlying plateau lavas for which the genetic
491 relationship to the more evolved rock types at Tarosero is still enigmatic (Dawson, 2008).

492 *Evolution models from intermediate to the evolved (peralkaline) rocks*

493 The evolution from latites towards trachytes can be modelled by fractionation of minor amounts (<10
494 %) of clinopyroxene, magnetite and olivine. However, the slightly elevated alkalinity index of trachytes

compared to latites additionally requires minor plagioclase fractionation (path 2 in Fig. 16). The lack of a Eu anomaly in the whole-rock analyses could in part be explained by fractional crystallization of apatite (Watson & Green, 1981), as indicated by the negative P anomaly (Fig. 6a). Absence of intense plagioclase fractionation is also demonstrated by the increasing Sr concentration in plagioclase (Fig. 13b) and whole-rock analyses (Fig. 6a) from latites towards trachytes. Fractionation of the mafic minerals is consistent with the steeper REE pattern compared to the more primitive rocks (e.g. White, 2013). The presence of ilmenite in both rock types might be a further hint for a genetic link. Late, interstitial amphibole in latites becomes an early precipitating mineral phase in the trachytes, presumably due to the increase of the water concentration of the melt because of ongoing fractionation of water-free minerals.

The presence of amphibole in trachytes and the more evolved peralkaline trachytes/ phonolites could be a hint for a close genetic relationship between them. The composition of the latter can be reached by fractionation of large amounts (>20 %) of plagioclase, minor magnetite, and traces (< 1 %) of ilmenite and apatite (path 3), in addition to minor contamination and assimilation with $SiO_2$-rich rocks (for simplicity modelled as quartzite). Contamination with crustal material for the evolved rocks at Tarosero has already been proposed by Mana (2013) and Mana *et al.* (2015) based on the trace element modelling and Sr-Nd-Pb isotope data. As soon as the melt becomes peralkaline, plagioclase crystallization is suppressed (Scaillet & Macdonald, 2001). This is in agreement with the absence of plagioclase in the peralkaline trachytes and phonolites. The agpaitic compositions of the peralkaline phonolites can be reached by further fractionation of alkali feldspar, minor amphibole and traces of magnetite and apatite (path 4).

Peralkaline olivine trachytes are mineralogically distinct as they lack clinopyroxene and calcic amphibole (relics) but contain olivine instead (see above). Based on the mineralogy (olivine, Fe-Ti-oxides; interstitial amphibole) and the mineral chemistry (Fig. 9, Fig. 12), these rocks are closely related to latites. We therefore suggest that they derive from latites by fractionation of plagioclase, minor clinopyroxene, olivine, magnetite and apatite, accompanied by minor crustal contamination (path 5).

## Hydrothermal overprint of the peralkaline rocks

Several peralkaline rocks at Tarosero are characterized by negative Ce anomalies in their primitive mantle-normalized REE patterns (Fig. 17a). The low solubility of $Ce^{4+}$ (Bouchaud *et al.*, 2012) in aqueous fluids compared to REE in their trivalent oxidation state directly affects the REE distribution in hydrothermally altered samples. Leaching of REE by an aqueous fluid results in a positive Ce anomaly in the peralkaline rocks, while precipitation of REE-bearing minerals from the same fluid has the opposite effect. Indeed, peralkaline trachyte TA-078 contains the highest REE concentrations of all samples (Fig. 5) due to the hydrothermal formation of bastnäsite (Fig. 3f), consistent with a strongly negative Ce anomaly. Since $Eu^{2+}$ is more soluble than $Eu^{3+}$ at temperatures > 250 °C (Sverjensky, 1984, Bilal, 1991), the (high temperature) hydrothermal overprint should have the opposite effect on Eu abundances. However, the strongly negative Eu anomaly in the peralkaline rocks, caused by the intense fractionation of plagioclase, generally may hide this effect. Moreover, peralkaline rocks with high initial REE concentrations are somewhat buffered against distinctive REE anomalies (Fig. 17b). Hence, peralkaline olivine trachytes with their comparatively low REE concentrations show the strongest negative Ce anomalies and are also characterized by a comparably small Eu anomaly (Fig. 17a; Fig. 6b).

## Constraints for the formation of extrusive agpaitic rocks

Agpaitic rocks are typically related to intrusive complexes, and the occurrence of extrusive agpaitic rocks is restricted to rather few localities (e.g. at Oktyabr'sky, Tarosero and Kontozero; Krivdik & Tkachuk, 1988, Dawson, 1997, Petrovsky *et al.*, 2012). The rarity of volcanic equivalents might, in part, arise from erosion, alteration, or overlooking of small-grained agpaitic minerals. However, the major prerequisite for the formation of agpaitic rocks is the retention of the volatile halogens in the magma during fractionation (e.g. Marks & Markl, 2001, Marks & Markl, 2015). This requires special conditions which are discussed in the following section.

### *General constraints for the formation of agpaitic rocks*

Most agpaitic rocks are plutonic and hence, indicate a magmatic system that prevents the easy escape of volatile phases (Sørensen, 1992). Redox conditions below the FMQ buffer are a further common

548 characteristic for agpaitic rocks (Marks & Markl, 2017 and references therein). This is in agreement
549 with the fact that low redox conditions suppress the early crystallization of magnetite, thereby increasing
550 the Fe concentrations of the melt. High Fe concentrations in turn enhances the solubility of halogens
551 like Cl (Metrich & Rutherford, 1992, Giehl *et al.*, 2013), which is required for the formation of agpaitic
552 minerals. Besides the redox conditions, the water activity is the crucial parameter in the evolution of
553 agpaitic complexes since a low $a_{H2O}$ typically prevents expulsion of water-rich fluids. This prevention
554 results in an enrichment of typically water-soluble elements like alkali metals and halogens in the melt
555 (e.g. Kogarko, 1987, Markl *et al.*, 2001, Liebscher & Heinrich, 2007, Marks & Markl, 2015), which
556 increase the solubility for REE and HFSE (Watson, 1979, Keppler, 1993, Linnen & Keppler, 2002) and
557 support formation of HFSE-enriched minerals.

558 The necessary conditions for the formation of agpaitic minerals can be reached during orthomagmatic,
559 late-magmatic and hydrothermal stages (Marks & Markl, 2017). In the agpaitic phonolite lavas from
560 Oktyabr'sky (Krivdik & Tkachuk, 1988) and Kontozero (Petrovsky *et al.*, 2012), eudialyte occurs as
561 (micro)phenocrysts, which indicates melt saturation in HFSE and chlorine at early magmatic stages prior
562 to the lava extrusion. In contrast, peralkaline lavas at Tarosero may contain interstitial eudialyte,
563 illustrating a process that retains halogens in the late-magmatic melt residue.

564 *Crystallization conditions and implications for the formation of the peralkaline trachytes/phonolites*

565 The oxygen fugacity during the formation of the peralkaline trachytes/phonolites was estimated to
566 ΔFMQ=-5-0, seemingly low enough to suppress extensive magnetite fractionation, which caused Fe-
567 enrichment during evolution towards the most evolved peralkaline phonolites (Figs. 4b & c). The
568 increasing Fe concentrations enhance the Cl solubility of the melt, as demonstrated by the increasing
569 amount of orthomagmatic to late-magmatic sodalite (Fig. 3d). Experimental work of Giehl *et al.* (2013)
570 illustrated that besides low redox conditions, a low water activity is a further prerequisite to suppress
571 magnetite crystallization. We suggest that the water activity during evolution from the trachytes to the
572 peralkaline magma was kept low due to the near liquidus crystallization of OH-rich amphibole. The
573 relatively dry late-magmatic conditions prevented fluid exsolution and the escape of volatile elements
574 such as alkali metals and halogens. The enrichment of these elements during magma evolution increased

575 the solubility for REE and HFSE, and supported the late-stage formation of interstitial eudialyte. Due to
576 the onset of eudialyte crystallization, the most evolved clinopyroxenes (Fig. 9d) and amphiboles (Fig.
577 12d), as well as aenigmatite in the eudialyte-bearing peralkaline phonolites (Fig. 11b) reveal low Zr
578 concentrations (Markl *et al.*, 2001). However, there are several peralkaline phonolites which do not
579 contain eudialyte but still have high concentrations of HFSE (and REE). We suggest that late-stage
580 clinopyroxene with up to ~3 wt. % $ZrO_2$ (Table 4) rather than altered eudialyte dominates the HFSE
581 budget in these rocks (q.v. Andersen *et al.*, 2012).

582 Notable, the intermediate trachytes show similarly high F concentrations and even higher Cl
583 concentrations (Figs. 7a & b) than most of the agpaitic phonolites. Rather high F concentrations in the
584 trachytes might be related to the dry late-magmatic conditions which impeded the loss of F by exsolving
585 fluids and resulted in the crystallization of fluorite. Increasing F concentrations during magma evolution
586 towards the agpaitic phonolites might have been prevented by fractionation of amphibole with up to 0.5
587 apfu F (Fig. 12b), although the relatively large scatter in F concentrations of both rock types may suggest
588 variable F loss to the atmosphere. Moreover, the variable F concentrations are in part related to a
589 hydrothermal overprint as demonstrated by sample TA-078 which contains abundant REE-F-carbonates
590 (bastnäsite; Fig. 3f; Fig. 7a). The relatively low Cl contents in the peralkaline rocks may also result from
591 post-magmatic alteration processes. While interstitial sodalite in the trachytes is pristine, sodalite in the
592 peralkaline trachytes/phonolites is strongly altered and replaced by (Cl-free) Fe-hydroxides and clay
593 minerals (note that the beginning of sodalite alteration is marked by constant Cl but, elevated K, Si, and
594 $Fe^{3+}$ concentrations, and low analytical totals which may demonstrate microscale porosity; Fig. 14). We
595 suppose that the initial Cl concentration of the peralkaline magma was much higher than that of the
596 trachytes, hence evolving towards REE- and HFSE-rich compositions that finally crystallized interstitial
597 eudialyte.

598 *Crystallization conditions and implications for the formation of the peralkaline olivine trachytes*

599 Peralkaline olivine trachytes at Tarosero reveal much lower REE and HFSE concentrations compared
600 to the peralkaline trachytes/phonolites (Fig. 5) and do not contain agpaitic minerals. A discrimination of
601 the two peralkaline rock series based on the oxygen fugacity is unfeasible because of the high uncertainty

of the redox calculations. However, we suggest that the peralkaline olivine trachytes formed under high water activities, which are indicated by the lack of clinopyroxene (Bailey, 1969, Scaillet & Macdonald, 2001, Andersen & Sørensen, 2005), and the higher OH-contents in the interstitial amphiboles compared to those of the peralkaline trachytes/phonolites (Fig. 12b). The absence of sodalite is further evidence for a high water activity since preliminary work of Giehl *et al.* (2014) demonstrated sodalite stability only for peralkaline melts with low $H_2O$ concentrations. An increasing water activity during magma evolution results from the fractionation of olivine instead of OH-rich amphibole. Fractionation under relatively low crustal pressures, and hence low fluid pressures, may have prevented the change from olivine to amphibole as the dominant phenocryst phase during evolution from the latites towards the trachytes (e.g. Ernst, 1962). We therefore suppose that the formation of the peralkaline olivine trachytes was accompanied by significant amounts of fluid exsolutions. The consequent loss of volatiles phases resulted in a peralkaline melt with low solubilities of HFSE and REE. Furthermore, exsolving halogen-rich aqueous fluids have the potential to transport significant amounts of HFSE which additionally leads to a decrease of these elements in the remaining melt (Migdisov *et al.*, 2009, Migdisov *et al.*, 2011, Timofeev *et al.*, 2015).

The high water activity presumably prevented the crystallization of (Ti-rich) aenigmatite during the beginning of interstitial amphibole formation. Hence, in contrast to the eudialyte-bearing peralkaline phonolites, the Ti content of amphibole increased during evolution of the peralkaline olivine trachytes (Fig. 12c). Contrary to most peralkaline trachytes/phonolites, the lack of fractionation of F-bearing amphibole phenocrysts resulted in rather high F concentrations in the peralkaline olivine trachytes (Fig. 7a). Late-stage aenigmatite formation might be correlated with a sudden lowering of the water activity in the melt residue due to the expulsion of fluids, as indicated by the changing OH/F and Ti pattern in amphibole at $X_{Mg}$=0.5 (Fig. 12c). We speculate that during this process, most of the remaining REE, HFSE and chlorine could escape from the melt residue, hence preventing the crystallization of eudialyte.

## SUMMARY AND CONCLUSION

The Tarosero volcano covers a broad spectrum from primitive to evolved rock types that formed by partial melting of an amphibole- and phlogopite-bearing mantle combined with multi-level differentiation at depths ≤ 35 km. All rock types formed under relatively reduced conditions (≤ FMQ buffer), which is typical of peralkaline complexes associated with agpaitic rocks.

Basalts represent the most primitive rocks at Tarosero but fractional crystallization models cannot cross the gap towards the latites, indicating that the basalts do not reflect their parental magma source. The high alkalinity index A.I. of the latites presumably illustrates a derivation from a mantle source involving partial melting of phlogopite. However, starting from the intermediate latites, fractional crystallization of mainly plagioclase, and variable amounts of clinopyroxene, olivine, magnetite and ilmenite, accompanied by minor crustal contamination can reproduce the observed composition of peralkaline rocks. The most evolved peralkaline phonolites require additional alkali feldspar and minor amphibole fractionation. They are characterized by interstitial eudialyte, which indicates that halogens were (partly) prevented from escaping to the atmosphere. Generally, agpaitic rocks are plutonic to subvolcanic rocks, hence illustrating a magmatic system that prevents the easy loss of volatile phases. In case of the extrusive rocks at Tarosero, fluid exsolution and loss of water-soluble halogens was impeded by a low water activity in the late-magmatic conditions caused by the early crystallization of OH-bearing amphibole. In contrast, peralkaline olivine trachytes are characterized by much lower HFSE and REE concentrations and the absence of agpaitic minerals. We suggest that melt evolution towards this rock type occurred at lower pressure, hence crystallizing fayalite instead of amphibole phenocrysts. The lack of an early water-sink led to an increase of the water activity and the expulsion of halogen-bearing fluids. Finally, this prevented the crystallization of agpaitic assemblages in these rocks.

## ACKNOWLEDGMENTS

We would like to thank Simone Schafflick for sample preparation in Tübingen. Moreover, we are very thankful to Olga Ivashchenkova and Andrey Arzamastsev, with whom we had a pleasant stay in Tanzania. Many thanks to J4 who drove us to the most remote and inaccessible places, and to the whole team in Tanzania who supported us during the field trip in 2019. Special thanks go to Larissa Leach who took care of the export of the samples.

## FUNDING

This work was supported by the Deutsche Forschungsgemeinschaft [grant number MA2563/12–1] and the Alexander von Humboldt Stiftung.

## REFERENCES

Andersen, D. & Lindsley, D. H. (1985). New (and final!) models for the Ti-magnetite/ilmenite geothermometer and oxygen barometer. *Abstracts of American Geophysical Union 1985 Spring Meeting*: American Geophysical Union.

Andersen, D. J., Lindsley, D. H. & Davidson, P. M. (1993). Quilf - a Pascal Program to Assess Equilibria among Fe-Mg-Mn-Ti Oxides, Pyroxenes, Olivine, and Quartz. *Computers & Geosciences* **19**, 1333-1350.

Andersen, T., Carr, P. & Erambert, M. (2012). Late-magmatic mineral assemblages with siderite and zirconian pyroxene and amphibole in the anorogenic Mt Gibraltar microsyenite, New South Wales, Australia, and their petrological implications. *Lithos* **151**, 46-56.

Andersen, T., Elburg, M. A. & Erambert, M. (2014). Extreme peralkalinity in delhayelite- and andremeyerite-bearing nephelinite from Nyiragongo volcano, East African Rift. *Lithos* **206**, 164-178.

Andersen, T. & Sørensen, H. (2005). Stability of naujakasite in hyperagpaitic melts, and the petrology of naujakasite lujavrite in the Ilímaussaq alkaline complex, South Greenland. *Mineralogical magazine* **69**, 125-136.

Arató, R. & Audétat, A. (2017). FeTiMM – A new oxybarometer for mafic to felsic magmas. *Geochemical Perspectives Letters* **5**, 19-23.

681 Armstrong, J. T. (1991). Quantitative elemental analysis of individual microparticles with electron beam
682 instruments. *Electron probe quantitation*: Springer, 261-315.
683 Aulbach, S., Rudnick, R. L. & McDonough, W. F. (2011). Evolution of the lithospheric mantle beneath
684 the East African Rift in Tanzania and its potential signatures in rift magmas. *Geological Society*
685 *of America Bulletin* **Special Papers 478**, 105-125.
686 Bailey, D. (1969). The stability of acmite in the presence of H2O. *American Journal of Science* **267**, 1-
687 16.
688 Bailey, J. C., Gwozdz, R., Rose-Hansen, J. & Sørensen, H. (2001). Geochemical overview of the
689 Ilímaussaq alkaline complex, South Greenland. *Geology of Greenland Survey Bulletin* **190**, 35-
690 53.
691 Bilal, B. A. (1991). Thermodynamic Study of Eu3+ /Eu2+ Redox Reaction in Aqueous Solutions at
692 Elevated Temperatures and Pressures by Means of Cyclic Voltammetry. *Zeitschrift für*
693 *Naturforschung A*, 1108.
694 Bouchaud, B., Balmain, J., Bonnet, G. & Pedraza, F. (2012). pH-distribution of cerium species in aqueous
695 systems. *Journal of Rare Earths* **30**, 559-562.
696 Braunger, S. (2016). Geothermometry in Agpaitic Syenites based on Mn Partitioning between
697 Aenigmatite, Clinopyroxene and Eudialyte-group minerals. *Department of Geosciences*.
698 Tübingen: Eberhard Karls Universität Tübingen, 174.
699 Buckley, V. J. E., Sparks, R. S. J. & Wood, B. J. (2006). Hornblende dehydration reactions during magma
700 ascent at Soufrière Hills Volcano, Montserrat. *Contributions to Mineralogy and Petrology* **151**,
701 121-140.
702 Bussweiler, Y., Foley, S. F., Prelevic, D. & Jacob, D. E. (2015). The olivine macrocryst problem: New
703 insights from minor and trace element compositions of olivine from Lac de Gras kimberlites,
704 Canada. *Lithos* **220**, 238-252.
705 Chorowicz, J. (2005). The East African rift system. *Journal of African Earth Sciences* **43**, 379-410.
706 Connolly, J. A. D. (1990). Multivariable Phase-Diagrams - an Algorithm Based on Generalized
707 Thermodynamics. *American Journal of Science* **290**, 666-718.
708 Cooper, J. P. (1972). Geochemistry of Tarosero Volcano: Northern Tanzania. *Department of Geology*:
709 University of Manchester, 76.
710 Cucciniello, C., Melluso, L., le Roex, A. P., Jourdan, F., Morra, V., de' Gennaro, R. & Grifa, C. (2017).
711 From olivine nephelinite, basanite and basalt to peralkaline trachyphonolite and comendite in
712 the Ankaratra volcanic complex, Madagascar: 40Ar/39Ar ages, phase compositions and bulk-
713 rock geochemical and isotopic evolution. *Lithos* **274-275**, 363-382.
714 Dawson, J. B. (1992). Neogene tectonics and volcanicity in the North Tanzania sector of the Gregory
715 Rift Valley: contrasts with the Kenya sector. *Tectonophysics* **204**, 81-92.

716 Dawson, J. B. (1997). Neogene–Recent rifting and volcanism in northern Tanzania: relevance for
717 comparisons between the Gardar province and the East African Rift valley. *Mineralogical*
718 *magazine* **61**, 543-548.
719 Dawson, J. B. (1998). Peralkaline Nephelinite–Natrocarbonatite Relationships at Oldoinyo Lengai,
720 Tanzania. *Journal of Petrology* **39**, 2077-2094.
721 Dawson, J. B. (2008). The Gregory rift valley and Neogene-recent volcanoes of northern Tanzania.
722 Geological Society of London, 102.
723 Dawson, J. B. & Pickering, R. (1964). Geological Map of Monduli. Geological Survey Division, Quarter
724 Degree Sheet 54.
725 Epp, T., Marks, M. A. W., Ludwig, T., Kendrick, M. A., Eby, N., Neidhardt, H., Oelmann, Y. & Markl, G.
726 (2019). Crystallographic and fluid compositional effects on the halogen (Cl, F, Br, I)
727 incorporation in pyromorphite-group minerals. *American Mineralogist* **104**, 1673-1688.
728 Epp, T., Neidhardt, H., Pagano, N., Marks, M. A. W., Markl, G. & Oelmann, Y. (2020). Vegetation canopy
729 effects on total and dissolved Cl, Br, F and I concentrations in soil and their fate along the
730 hydrological flow path. *Science of The Total Environment* **712**, 135473.
731 Erdmann, S., Martel, C., Pichavant, M. & Kushnir, A. (2014). Amphibole as an archivist of magmatic
732 crystallization conditions: problems, potential, and implications for inferring magma storage
733 prior to the paroxysmal 2010 eruption of Mount Merapi, Indonesia. *Contributions to*
734 *Mineralogy and Petrology* **167**, 1016.
735 Ernst, W. G. (1962). Synthesis, Stability Relations, and Occurrence of Riebeckite and Riebeckite-
736 Arfvedsonite Solid Solutions. *The Journal of Geology* **70**, 689-736.
737 Estrade, G., Beziat, D., Salvi, S., Tiepolo, M., Paquette, J. L. & Rakotovao, S. (2014). Unusual evolution
738 of silica-under- and -oversaturated alkaline rocks in the Cenozoic Ambohimirahavavy Complex
739 (Madagascar): Mineralogical and geochemical evidence. *Lithos* **206**, 361-383.
740 Estrade, G., Salvi, S. & Béziat, D. (2018). Crystallization and destabilization of eudialyte-group minerals
741 in peralkaline granite and pegmatite: a case study from the Ambohimirahavavy complex,
742 Madagascar. *Mineralogical magazine* **82**, 375-399.
743 Fitton, J. G. & Upton, B. G. J. (1987). *Alkaline igneous rocks*. London: The Geological Society of London.
744 Foley, S. F., Prelevic, D., Rehfeldt, T. & Jacob, D. E. (2013). Minor and trace elements in olivines as
745 probes into early igneous and mantle melting processes. *Earth and Planetary Science Letters*
746 **363**, 181-191.
747 Frost, B. R. & Frost, C. D. (2008). A Geochemical Classification for Feldspathic Igneous Rocks. *Journal of*
748 *Petrology* **49**, 1955-1969.
749 Fuhrman, M. L. & Lindsley, D. H. (1988). Ternary-Feldspar Modeling and Thermometry. *American*
750 *Mineralogist* **73**, 201-215.

751 Giehl, C., Marks, M. & Nowak, M. (2013). Phase relations and liquid lines of descent of an iron-rich
752 peralkaline phonolitic melt: an experimental study. *Contributions to Mineralogy and Petrology*
753 **165**, 283-304.
754 Giehl, C., Marks, M. A. W. & Nowak, M. (2014). An experimental study on the influence of fluorine and
755 chlorine on phase relations in peralkaline phonolitic melts. *Contributions to Mineralogy and*
756 *Petrology* **167**, 977.
757 Govindaraju, K. (1989). 1989 compilation of working values and sample description for 272
758 geostandards. *Geostandards and Geoanalytical Research* **13**, 1-113.
759 Govindaraju, K. (1994). 1994 Compilation of Working Values and Sample Description for 383
760 Geostandards (Vol 18, Pg 53, 1994). *Geostandards Newsletter* **18**, 331-331.
761 Green, D. H. & Ringwood, A. E. (1967). The genesis of basaltic magmas. *Contributions to Mineralogy*
762 *and Petrology* **15**, 103-190.
763 Halliday, A. N., Lee, D.-C., Tommasini, S., Davies, G. R., Paslick, C. R., Godfrey Fitton, J. & James, D. E.
764 (1995). Incompatible trace elements in OIB and MORB and source enrichment in the sub-
765 oceanic mantle. *Earth and Planetary Science Letters* **133**, 379-395.
766 Hawthorne, F. C., Oberti, R., Harlow, G. E., Maresch, W. V., Martin, R. F., Schumacher, J. C. & Welch,
767 M. D. (2012). Nomenclature of the amphibole supergroup. *American Mineralogist* **97**, 2031-
768 2048.
769 Hofmann, C., Courtillot, V., Féraud, G., Rochette, P., Yirgu, G., Ketefo, E. & Pik, R. (1997). Timing of the
770 Ethiopian flood basalt event and implications for plume birth and global change. *Nature* **389**,
771 838-841.
772 Holland, T. & Powell, R. (2003). Activity–composition relations for phases in petrological calculations:
773 an asymmetric multicomponent formulation. *Contributions to Mineralogy and Petrology* **145**,
774 492-501.
775 Holland, T. J. B. (1990). Activities of Components in Omphacitic Solid-Solutions - an Application of
776 Landau Theory to Mixtures. *Contributions to Mineralogy and Petrology* **105**, 446-453.
777 Holland, T. J. B. & Powell, R. (1998). An internally consistent thermodynamic data set for phases of
778 petrological interest. *Journal of metamorphic Geology* **16**, 309-343.
779 Irvine, T. N. & Baragar, W. R. A. (1971). A Guide to the Chemical Classification of the Common Volcanic
780 Rocks. *Canadian Journal of Earth Sciences* **8**, 523-548.
781 Johnsen, O. & Grice, J. D. (1999). The crystal chemistry of the eudialyte group. *The Canadian*
782 *Mineralogist* **37**, 865-891.
783 Kalashnikov, A. O., Konopleva, N. G., Pakhomovsky, Y. A. & Ivanyuk, G. Y. (2016). Rare Earth Deposits
784 of the Murmansk Region, Russia—A Review. *Economic Geology* **111**, 1529-1559.

785 Keppler, H. (1993). Influence of fluorine on the enrichment of high field strength trace elements in
786 granitic rocks. *Contributions to Mineralogy and Petrology* **114**, 479-488.
787 Kogarko, L. N. (1987). Alkaline rocks of the eastern part of the Baltic Shield (Kola Peninsula). *Geological*
788 *Society, London, Special Publications* **30**, 531.
789 Kogarko, L. N. (1990). Ore-forming potential of alkaline magmas. *Lithos* **26**, 167-175.
790 Kogarko, L. N., Lahaye, Y. & Brey, G. P. (2010). Plume-related mantle source of super-large rare metal
791 deposits from the Lovozero and Khibina massifs on the Kola Peninsula, Eastern part of Baltic
792 Shield: Sr, Nd and Hf isotope systematics. *Mineralogy and Petrology* **98**, 197-208.
793 Kramm, U. & Kogarko, L. N. (1994). Nd and Sr isotope signatures of the Khibina and Lovozero agpaitic
794 centres, Kola Alkaline province, Russia. *Lithos* **32**, 225-242.
795 Krivdik, S. & Tkachuk, V. (1988). Eudialyte Bearing Peral kaline Phonolites and Nepheline Syenite Dikes
796 of the Oktyabr'sky Pluton, the Ukrainian Shield. *Geokhimiya* **26**, 1133-1139.
797 Le Bas, M. J., Maitre, R. W. L., Streckeisen, A., Zanettin, B. & Rocks, I. S. o. t. S. o. I. (1986). A Chemical
798 Classification of Volcanic Rocks Based on the Total Alkali-Silica Diagram. *Journal of Petrology*
799 **27**, 745-750.
800 Le Gall, B., Nonnotte, P., Rolet, J., Benoit, M., Guillou, H., Mousseau-Nonnotte, M., Albaric, J. &
801 Deverchère, J. (2008). Rift propagation at craton margin.: Distribution of faulting and
802 volcanism in the North Tanzanian Divergence (East Africa) during Neogene times.
803 *Tectonophysics* **448**, 1-19.
804 Le Maitre, R., Streckeisen, A., Zanettin, B., Le Bas, M., Bonin, B., Bateman, P., Bellieni, G., Dudek, A.,
805 Efremova, A. & Keller, J. (2002). Igneous rocks. A classification and glossary of terms.
806 Recommendations of the IUGS Subcomission on the Systematics of Igneous Rocks. Cambridge
807 University Press, Cambridge.
808 Liebscher, A. & Heinrich, C. A. (2007). *Fluid-fluid interactions*: Walter de Gruyter GmbH & Co KG.
809 Linnen, R. L. & Keppler, H. (2002). Melt composition control of Zr/Hf fractionation in magmatic
810 processes. *Geochimica et Cosmochimica Acta* **66**, 3293-3301.
811 Macdonald, R. (1974). Nomenclature and petrochemistry of the peralkaline oversaturated extrusive
812 rocks. *Bulletin Volcanologique* **38**, 498-516.
813 Macdonald, R. & Scaillet, B. (2006). The central Kenya peralkaline province: Insights into the evolution
814 of peralkaline salic magmas. *Lithos* **91**, 59-73.
815 Macintyre, R. M., Mitchell, J. G. & Dawson, J. B. (1974). Age of Fault Movements in Tanzanian Sector
816 of East African Rift System. *Nature* **247**, 354-356.
817 Mahood, G. A. (1984). Pyroclastic rocks and calderas associated with strongly peralkaline magmatism.
818 *Journal of Geophysical Research: Solid Earth* **89**, 8540-8552.

819 Mana, S. (2013). Magmatic evolution of the north Tanzanian divergence zone, east African rift system.
820 Rutgers The State University of New Jersey-New Brunswick, 138.
821 Mana, S., Furman, T., Turrin, B. D., Feigenson, M. D. & Swisher, C. C., III. (2015). Magmatic activity
822 across the East African North Tanzanian Divergence Zone. *Journal of the Geological Society*
823 **172**, 368-389.
824 Mann, U., Marks, M. & Markl, G. (2006). Influence of oxygen fugacity on mineral compositions in
825 peralkaline melts: The Katzenbuckel volcano, Southwest Germany. *Lithos* **91**, 262-285.
826 Markl, G., Marks, M., Schwinn, G. & Sommer, H. (2001). Phase Equilibrium Constraints on Intensive
827 Crystallization Parameters of the Ilímaussaq Complex, South Greenland. *Journal of Petrology*
828 **42**, 2231-2257.
829 Markl, G., Marks, M. A. W. & Frost, B. R. (2010). On the Controls of Oxygen Fugacity in the Generation
830 and Crystallization of Peralkaline Melts. *Journal of Petrology* **51**, 1831-1847.
831 Marks, M. & Markl, G. (2001). Fractionation and assimilation processes in the alkaline augite syenite
832 unit of the Ilimaussaq intrusion, South Greenland, as deduced from phase equilibria. *Journal*
833 *of Petrology* **42**, 1947-1969.
834 Marks, M., Vennemann, T., Siebel, W. & Markl, G. (2003). Quantification of magmatic and
835 hydrothermal processes in a peralkaline syenite–alkali granite complex based on textures,
836 phase equilibria, and stable and radiogenic isotopes. *Journal of Petrology* **44**, 1247-1280.
837 Marks, M. A. W., Hettmann, K., Schilling, J., Frost, B. R. & Markl, G. (2011). The Mineralogical Diversity
838 of Alkaline Igneous Rocks: Critical Factors for the Transition from Miaskitic to Agpaitic Phase
839 Assemblages. *Journal of Petrology* **52**, 439-455.
840 Marks, M. A. W. & Markl, G. (2015). The Ilímaussaq Alkaline Complex, South Greenland. In: Charlier,
841 B., Namur, O., Latypov, R. & Tegner, C. (eds.) *Layered Intrusions*. Dordrecht: Springer
842 Netherlands, 649-691.
843 Marks, M. A. W. & Markl, G. (2017). A global review on agpaitic rocks. *Earth-Science Reviews* **173**, 229-
844 258.
845 Marsh, J. S. (1975). Aenigmatite stability in silica-undersaturated rocks. *Contributions to Mineralogy*
846 *and Petrology* **50**, 135-144.
847 Martin, H., Bonin, B., Capdevila, R., Jahn, B. M., Lameyre, J. & Wang, Y. (1994). The Kuiqi Peralkaline
848 Granitic Complex (SE China): Petrology and Geochemistry. *Journal of Petrology* **35**, 983-1015.
849 Metrich, N. & Rutherford, M. J. (1992). Experimental study of chlorine behavior in hydrous silicic melts.
850 *Geochimica et Cosmochimica Acta* **56**, 607-616.
851 Migdisov, A. A., Williams-Jones, A. E., van Hinsberg, V. & Salvi, S. (2011). An experimental study of the
852 solubility of baddeleyite (ZrO2) in fluoride-bearing solutions at elevated temperature.
853 *Geochimica et Cosmochimica Acta* **75**, 7426-7434.

Migdisov, A. A., Williams-Jones, A. E. & Wagner, T. (2009). An experimental study of the solubility and speciation of the Rare Earth Elements (III) in fluoride- and chloride-bearing aqueous solutions at temperatures up to 300°C. *Geochimica et Cosmochimica Acta* **73**, 7087-7109.

Neave, D. A. & Putirka, K. D. (2017). A new clinopyroxene-liquid barometer, and implications for magma storage pressures under Icelandic rift zones. *American Mineralogist* **102**, 777-794.

Nelson, S. T. & Montana, A. (1992). Sieve-textured plagioclase in volcanic rocks produced by rapid decompression. *American Mineralogist* **77**, 1242-1249.

Nicholls, J. & Carmichael, J. S. E. (1969). Peralkaline acid liquids: A petrological study. *Contributions to Mineralogy and Petrology* **20**, 268-294.

Novak, S. W. & Mahood, G. A. (1986). Rise and fall of a basalt-trachyte-rhyolite magma system at the Kane Springs Wash Caldera, Nevada. *Contributions to Mineralogy and Petrology* **94**, 352-373.

Palme, H. & O'Neill, H. S. C. (2003). Cosmochemical estimates of mantle composition. *Treatise on geochemistry* **2**, 568.

Peccerillo, A., Donati, C., Santo, A. P., Orlando, A., Yirgu, G. & Ayalew, D. (2007). Petrogenesis of silicic peralkaline rocks in the Ethiopian rift: Geochemical evidence and volcanological implications. *Journal of African Earth Sciences* **48**, 161-173.

Petrovsky, M. N., Savchenko, E. A. & Kalachev, V. Y. (2012). Formation of eudialyte-bearing phonolite from Kontozero carbonatite paleovolcano, Kola Peninsula. *Geology of Ore Deposits* **54**, 540-556.

Pfaff, K., Wenzel, T., Schilling, J., Marks, M. A. & Markl, G. (2010). A fast and easy-to-use approach to cation site assignment for eudialyte-group minerals. *Neues Jahrbuch für Mineralogie-Abhandlungen: Journal of Mineralogy and Geochemistry* **187**, 69-81.

Prodehl, C., Fuchs, K. & Mechie, J. (1997). Seismic-refraction studies of the Afro-Arabian rift system — a brief review. *Tectonophysics* **278**, 1-13.

Putirka, K. (2016). Amphibole thermometers and barometers for igneous systems and some implications for eruption mechanisms of felsic magmas at arc volcanoes. *American Mineralogist* **101**, 841-858.

Putirka, K., Johnson, M., Kinzler, R., Longhi, J. & Walker, D. (1996). Thermobarometry of mafic igneous rocks based on clinopyroxene-liquid equilibria, 0–30 kbar. *Contributions to Mineralogy and Petrology* **123**, 92-108.

Putirka, K. D. (2008). Thermometers and Barometers for Volcanic Systems. *Reviews in Mineralogy and Geochemistry* **69**, 61-120.

Putirka, K. D., Mikaelian, H., Ryerson, F. & Shaw, H. (2003). New clinopyroxene-liquid thermobarometers for mafic, evolved, and volatile-bearing lava compositions, with

applications to lavas from Tibet and the Snake River Plain, Idaho. *American Mineralogist* **88**, 1542-1554.

Ren, M. H., Omenda, P. A., Anthony, E. Y., White, J. C., Macdonald, R. & Bailey, D. K. (2006). Application of the QUILF thermobarometer to the peralkaline trachytes and pantellerites of the Eburru volcanic complex, East African Rift, Kenya. *Lithos* **91**, 109-124.

Ridolfi, F. & Renzulli, A. (2012). Calcic amphiboles in calc-alkaline and alkaline magmas: thermobarometric and chemometric empirical equations valid up to 1,130° C and 2.2 GPa. *Contributions to Mineralogy and Petrology* **163**, 877-895.

Ridolfi, F., Renzulli, A., Macdonald, R. & Upton, B. G. J. (2006). Peralkaline syenite autoliths from Kilombe volcano, Kenya Rift Valley: Evidence for subvolcanic interaction with carbonatitic fluids. *Lithos* **91**, 373-392.

Rutherford, M. J. & Devine, J. D. (2003). Magmatic Conditions and Magma Ascent as Indicated by Hornblende Phase Equilibria and Reactions in the 1995–2002 Soufrière Hills Magma. *Journal of Petrology* **44**, 1433-1453.

Scaillet, B. & Macdonald, R. A. Y. (2001). Phase Relations of Peralkaline Silicic Magmas and Petrogenetic Implications. *Journal of Petrology* **42**, 825-845.

Schilling, J., Wu, F.-Y., McCammon, C., Wenzel, T., Marks, M., Pfaff, K., Jacob, D. & Markl, G. (2011). The compositional variability of eudialyte-group minerals. *Mineralogical magazine* **75**, 87-115.

Smith, M. (1994). Stratigraphic and structural constraints on mechanisms of active rifting in the Gregory Rift, Kenya. *Tectonophysics* **236**, 3-22.

Smith, M. P., Moore, K., Kavecsánszki, D., Finch, A. A., Kynicky, J. & Wall, F. (2016). From mantle to critical zone: A review of large and giant sized deposits of the rare earth elements. *Geoscience Frontiers* **7**, 315-334.

Sørensen, H. (1992). Agpaitic nepheline syenites: a potential source of rare elements. *Applied Geochemistry* **7**, 417-427.

Sørensen, H. (1997). The agpaitic rocks− an overview. *Mineralogical magazine* **61**, 485-498.

Spandler, C. & Morris, C. (2016). Geology and genesis of the Toongi rare metal (Zr, Hf, Nb, Ta, Y and REE) deposit, NSW, Australia, and implications for rare metal mineralization in peralkaline igneous rocks. *Contributions to Mineralogy and Petrology* **171**, 104.

Stormer, J. C. (1983). The Effects of Recalculation on Estimates of Temperature and Oxygen Fugacity from Analyses of Multicomponent Iron Titanium-Oxides. *American Mineralogist* **68**, 586-594.

Sverjensky, D. A. (1984). Europium redox equilibria in aqueous solution. *Earth and Planetary Science Letters* **67**, 70-78.

Thompson, R. N. & Chisholm, J. E. (1969). Synthesis of aenigmatite. *Mineralogical magazine* **37**, 253-255.

923 Timofeev, A., Migdisov, A. A. & Williams-Jones, A. E. (2015). An experimental study of the solubility
924 and speciation of niobium in fluoride-bearing aqueous solutions at elevated temperature.
925 *Geochimica et Cosmochimica Acta* **158**, 103-111.
926 Upton, B. G. J., Emeleus, C. H., Heaman, L. M., Goodenough, K. M. & Finch, A. A. (2003). Magmatism
927 of the mid-Proterozoic Gardar Province, South Greenland: chronology, petrogenesis and
928 geological setting. *Lithos* **68**, 43-65.
929 Watson, E. B. (1979). Zircon saturation in felsic liquids: Experimental results and applications to trace
930 element geochemistry. *Contributions to Mineralogy and Petrology* **70**, 407-419.
931 Watson, E. B. & Green, T. H. (1981). Apatite/liquid partition coefficients for the rare earth elements
932 and strontium. *Earth and Planetary Science Letters* **56**, 405-421.
933 White, W. M. (2013). *Geochemistry*: John Wiley & Sons.
934 Wood, B. (1979). Activity-composition relationships in Ca (Mg, Fe) Si 2 O 6-CaAl 2 SiO 6 clinopyroxene
935 solid solutions. *American Journal of Science* **279**, 854-875.
936 Woolley, A. R. (2001). Alkaline rocks and carbonatites of the world: Africa. Geological Society of
937 London, 372.
938 Zaitsev, A. N., Marks, M. A. W., Wenzel, T., Spratt, J., Sharygin, V. V., Strekopytov, S. & Markl, G. (2012).
939 Mineralogy, geochemistry and petrology of the phonolitic to nephelinitic Sadiman volcano,
940 Crater Highlands, Tanzania. *Lithos* **152**, 66-83.

941

Table 1: List of investigated samples. Locality numbers as indicated in Fig. 1b.

| Locality # | Rock type | Sample # | Coordinates (WGS84) | | Mineral assemblage | | | | | | | | EPMA data | WR data |
|---|---|---|---|---|---|---|---|---|---|---|---|---|---|---|
| | | | Latitude (°N) | Longitude (°E) | Ol | Cpx | Amp | Ox | Aen | Fsp | Sdl | Eud | | |
| 1 | Peralkaline phonolite (agpaitic) | TA-008 | -3.192030 | 36.359916 | | x | x | x | x | x | x | x | x | x |
| 2 | Peralkaline olivine trachyte | TA-005 | -3.206808 | 36.353964 | x | | x | x | x | x | | | x | |
| 2 | Peralkaline olivine trachyte | TA-006 | -3.201757 | 36.354662 | x | | x | x | x | x | | | x | x |
| 2 | Peralkaline olivine trachyte | TA-007 | -3.197472 | 36.356970 | x | | x | x | x | x | | | | x |
| 6 | Trachyte | TA-116 | -3.224889 | 36.325347 | | x | x | x | | x | | | x | x |
| 6 | Trachyte | TA-118 | -3.224892 | 36.325351 | | x | x | x | | x | | | x | x |
| 7 | Peralkaline trachyte | TA-054 | -3.228092 | 36.313845 | | x | x | x | x | x | x | | x | x |
| 7 | Peralkaline trachyte | TA-056 | -3.228055 | 36.313871 | | x | x | x | x | x | | | | x |
| 7 | Peralkaline phonolite | TA-059 | -3.228727 | 36.314917 | | x | x | x | x | x | x | | | x |
| 7 | Peralkaline phonolite | TA-065 | -3.228132 | 36.316177 | | x | x | x | x | x | x | | | x |
| 7 | Peralkaline phonolite (agpaitic) | TA-070 | -3.230712 | 36.317713 | | x | x | x | x | x | x | x | | x |
| 7 | Peralkaline phonolite (agpaitic) | TA-072 | -3.230712 | 36.317713 | | x | x | x | x | x | x | x | x | x |
| 7 | Peralkaline phonolite | TA-073 | -3.230712 | 36.317713 | | x | x | x | x | x | x | | x | x |
| 9 | Peralkaline trachyte | TA-078 | -3.254544 | 36.317459 | | x | x | x | x | x | | | x | x |
| 9 | Peralkaline phonolite | TA-079 | -3.254544 | 36.317459 | | x | x | x | x | x | x | | | x |
| 9 | Peralkaline phonolite | TA-080 | -3.254887 | 36.316688 | | x | x | x | x | x | x | | | x |
| 10 | Latite | TA-045 | -3.293488 | 36.301786 | x | x | x | x | | x | | | x | x |
| 11 | Basalt | TA-042 | -3.306456 | 36.301439 | x | x | | x | | x | | | x | x |
| 11 | Andesite | TA-044 | -3.303982 | 36.301464 | | x | x | x | | x | | | x | x |
| 12 | Basalt | TA-048 | -3.313556 | 36.291862 | x | x | | x | | x | | | x | x |
| 12 | Basalt | TA-049 | -3.313556 | 36.291862 | x | x | | x | | x | | | | x |
| 12 | Latite | TA-046 | -3.313651 | 36.293727 | x | x | x | x | | x | | | x | x |
| 15 | Trachyte | TA-026 | -3.227314 | 36.234362 | | x | x | x | | x | | | | x |
| 15 | Peralkaline phonolite (agpaitic) | TA-021 | -3.227316 | 36.235095 | x | x | x | x | x | x | x | x | x | |
| 15 | Peralkaline phonolite (agpaitic) | TA-022 | -3.227497 | 36.235158 | | x | x | x | x | x | x | x | x | x |
| 15 | Peralkaline phonolite (agpaitic) | TA-030 | -3.227910 | 36.233296 | | x | x | x | x | x | x | x | x | |
| 15 | Peralkaline phonolite | TA-034 | -3.227886 | 36.231895 | | x | x | x | x | x | x | | | x |
| 15 | Peralkaline phonolite | TA-035 | -3.227886 | 36.231895 | | x | x | x | x | x | x | | x | x |

Abbreviations: Ol=Olivine; Cpx=Clinopyroxene; Amp=Amphibole; Ox=Oxides; Fsp=Feldspar; Sdl=Sodalite; Aen=Aenigmatite; Eud=Eudialyte; EPMA=electron microprobe analysis ; WR=whole-rock

Table 2: Whole-rock analyses from the Tarosero Volcanic Complex.

| Rock type | Basalt | | | Andesite | Latite | | Trachyte | | | Peralkaline trachyte/phonolite | | | | | | | | | | Peralkaline phonolite (agpaitic) | | | | Peralkaline olivine trachyte | |
|---|---|---|---|---|---|---|---|---|---|---|---|---|---|---|---|---|---|---|---|---|---|---|---|---|---|
| Thin section | TA-042 | TA-048 | TA-049 | TA-044 | TA-045 | TA-046 | TA-026 | TA-116 | TA-118 | TA-054 | TA-056 | TA-078 | TA-034 | TA-035 | TA-059 | TA-065 | TA-073 | TA-079 | TA-080 | TA-008 | TA-022 | TA-070 | TA-072 | TA-006 | TA-007 |
| *wt.%* | | | | | | | | | | | | | | | | | | | | | | | | | |
| $SiO_2$ | 45.94 | 43.43 | 42.69 | 48.08 | 52.84 | 54.70 | 56.26 | 58.61 | 57.53 | 58.74 | 57.78 | 61.34 | 59.56 | 58.50 | 57.46 | 62.27 | 61.24 | 60.34 | 60.19 | 60.91 | 54.39 | 58.03 | 60.08 | 59.79 | 60.69 |
| $TiO_2$ | 3.66 | 3.36 | 4.78 | 1.45 | 1.57 | 1.60 | 0.87 | 0.91 | 0.91 | 0.46 | 0.48 | 0.51 | 0.51 | 0.49 | 0.46 | 0.60 | 0.51 | 0.48 | 0.50 | 0.49 | 0.46 | 0.48 | 0.47 | 0.51 | 0.47 |
| $Al_2O_3$ | 12.69 | 11.60 | 13.88 | 19.33 | 15.75 | 16.35 | 18.32 | 19.20 | 18.76 | 15.24 | 13.06 | 15.38 | 15.78 | 15.30 | 13.18 | 16.78 | 15.89 | 13.98 | 14.59 | 14.01 | 12.70 | 13.26 | 14.36 | 16.15 | 14.77 |
| $Fe_2O_3$ (tot) | 16.07 | 15.79 | 16.91 | 7.51 | 8.50 | 8.60 | 4.73 | 4.82 | 4.94 | 6.05 | 9.41 | 5.95 | 6.37 | 6.29 | 9.00 | 5.73 | 6.57 | 8.14 | 9.46 | 8.38 | 8.70 | 9.14 | 8.06 | 6.36 | 6.10 |
| MnO | 0.20 | 0.21 | 0.25 | 0.23 | 0.26 | 0.23 | 0.15 | 0.16 | 0.18 | 0.24 | 0.19 | 0.15 | 0.25 | 0.23 | 0.46 | 0.19 | 0.21 | 0.19 | 0.22 | 0.36 | 0.27 | 0.34 | 0.22 | 0.15 | 0.19 |
| MgO | 7.12 | 6.84 | 4.78 | 1.05 | 1.68 | 1.83 | 1.07 | 1.05 | 1.00 | 0.68 | 0.64 | 0.57 | 0.49 | 0.62 | 0.45 | 0.55 | 0.63 | 0.46 | 0.47 | 0.50 | 0.45 | 0.39 | 0.61 | 0.27 | 0.27 |
| CaO | 9.61 | 9.89 | 10.25 | 3.54 | 3.96 | 4.11 | 2.81 | 2.93 | 3.00 | 1.07 | 1.13 | 1.03 | 0.86 | 1.16 | 1.11 | 0.98 | 1.17 | 1.05 | 0.94 | 0.95 | 1.24 | 1.17 | 1.19 | 0.39 | 0.57 |
| $Na_2O$ | 2.83 | 2.42 | 2.81 | 3.87 | 6.02 | 6.13 | 7.70 | 7.01 | 7.61 | 6.92 | 6.53 | 6.92 | 7.07 | 7.00 | 6.51 | 7.22 | 7.05 | 6.66 | 6.53 | 7.44 | 6.65 | 6.91 | 6.69 | 6.78 | 7.51 |
| $K_2O$ | 0.99 | 0.84 | 1.39 | 3.83 | 3.08 | 3.11 | 4.19 | 4.21 | 4.15 | 4.92 | 4.54 | 4.84 | 5.25 | 5.29 | 4.70 | 5.26 | 5.16 | 4.71 | 4.99 | 4.87 | 4.83 | 4.75 | 4.98 | 4.94 | 5.09 |
| $P_2O_5$ | 0.58 | 0.46 | 1.97 | 0.46 | 0.63 | 0.62 | 0.21 | 0.21 | 0.22 | 0.08 | 0.09 | 0.11 | 0.08 | 0.05 | 0.09 | 0.10 | 0.07 | 0.09 | 0.10 | 0.09 | 0.08 | 0.08 | 0.07 | 0.08 | 0.07 |
| SrO | 0.07 | 0.08 | 0.11 | 0.14 | 0.11 | 0.10 | 0.19 | 0.15 | 0.14 | 0.02 | 0.02 | 0.02 | 0.01 | 0.03 | 0.02 | 0.01 | 0.09 | 0.02 | 0.01 | 0.01 | 0.06 | 0.02 | 0.03 | 0.00 | 0.00 |
| BaO | 0.05 | 0.05 | 0.08 | 0.15 | 0.15 | 0.12 | 0.12 | 0.22 | 0.13 | 0.26 | 0.02 | 0.06 | 0.02 | 0.02 | 0.05 | 0.04 | 0.08 | 0.14 | 0.01 | 0.04 | 0.07 | 0.09 | 0.11 | 0.04 | 0.02 |
| LOI | 0.50 | 1.15 | 0.21 | 3.53 | 0.54 | 0.24 | 0.90 | 1.23 | 0.86 | 1.21 | 0.54 | 1.14 | 0.66 | 0.89 | 1.48 | 0.61 | 0.76 | 1.28 | 1.08 | 1.14 | 1.20 | 1.21 | 1.22 | 1.68 | 0.32 |
| Total | 100.31 | 96.14 | 100.12 | 93.15 | 95.10 | 97.73 | 97.54 | 100.69 | 99.42 | 95.88 | 94.42 | 98.01 | 96.89 | 95.87 | 94.96 | 100.33 | 99.41 | 97.55 | 99.09 | 99.20 | 91.09 | 95.85 | 98.10 | 97.13 | 96.05 |
| Na/K (molar) | 4.35 | 4.36 | 3.08 | 1.54 | 2.97 | 3.00 | 2.79 | 2.53 | 2.79 | 2.14 | 2.18 | 2.17 | 2.05 | 2.01 | 2.11 | 2.09 | 2.08 | 2.15 | 1.99 | 2.32 | 2.09 | 2.21 | 2.04 | 2.09 | 2.24 |
| A.I. | 0.45 | 0.42 | 0.44 | 0.54 | 0.84 | 0.82 | 0.94 | 0.84 | 0.91 | 1.10 | 1.20 | 1.08 | 1.10 | 1.13 | 1.20 | 1.05 | 1.08 | 1.15 | 1.11 | 1.25 | 1.27 | 1.25 | 1.14 | 1.02 | 1.21 |
| *µg/g* | | | | | | | | | | | | | | | | | | | | | | | | | |
| V | 392 | 366 | 292 | 17 | 29 | 28 | 19 | 19 | 19 | 7 | 4 | 7 | 3 | 3 | 3 | 6 | 8 | 4 | 5 | 3 | 3 | 4 | 4 | 1 | 0 |
| Cr | 362 | 710 | 23 | 2 | 1 | 1 | 1 | 1 | 0 | 6 | 2 | 6 | 0 | 1 | 1 | 1 | 7 | 2 | 1 | 2 | 1 | 1 | 2 | 0 | 0 |
| Co | 69 | 74 | 51 | 6 | 6 | 6 | 4 | 4 | 4 | 5 | 2 | 3 | 2 | 2 | 3 | 2 | 4 | 2 | 3 | 3 | 3 | 3 | 2 | 1 | 0 |
| Ni | 193 | 303 | 21 | 0 | 2 | 1 | 1 | 1 | 1 | 6 | 1 | 4 | 1 | 1 | 2 | 3 | 4 | 1 | 2 | 1 | 1 | 2 | 2 | 0 | 0 |
| Cu | 90 | 116 | 25 | 4 | 2 | 2 | 5 | 5 | 5 | 7 | 9 | 19 | 5 | 5 | 11 | 4 | 7 | 12 | 4 | 13 | 11 | 9 | 10 | 2 | 1 |
| Zn | 141 | 159 | 170 | 149 | 172 | 173 | 113 | 118 | 108 | 285 | 300 | 389 | 252 | 264 | 324 | 195 | 244 | 368 | 210 | 413 | 416 | 356 | 624 | 182 | 223 |
| Rb | 20 | 15 | 26 | 64 | 65 | 64 | 81 | 73 | 80 | 166 | 208 | 181 | 192 | 202 | 240 | 184 | 196 | 201 | 289 | 274 | 330 | 303 | 262 | 133 | 141 |
| Zr | 230 | 201 | 281 | 632 | 508 | 484 | 554 | 557 | 552 | 1574 | 3144 | 2566 | 1679 | 1701 | 3173 | 1447 | 1693 | 2942 | 3131 | 2697 | 3180 | 3187 | 2849 | 1083 | 992 |
| Nb | 52 | 41 | 42 | 185 | 125 | 101 | 164 | 174 | 172 | 307 | 685 | 445 | 352 | 359 | 562 | 292 | 321 | 561 | 667 | 558 | 648 | 666 | 551 | 203 | 212 |
| Cs | 0 | 0 | 0 | 1 | 0 | 0 | 1 | 0 | 1 | 2 | 1 | 0 | 1 | 3 | 3 | 1 | 1 | 0 | 4 | 3 | 4 | 2 | 10 | 0 | 0 |
| Hf | 7 | 6 | 7 | 12 | 13 | 12 | 12 | 13 | 12 | 37 | 75 | 62 | 41 | 41 | 76 | 34 | 41 | 71 | 77 | 66 | 77 | 77 | 69 | 26 | 25 |
| Ta | 4 | 3 | 3 | 11 | 9 | 7 | 8 | 10 | 10 | 21 | 50 | 32 | 25 | 25 | 41 | 21 | 22 | 40 | 48 | 38 | 45 | 48 | 40 | 13 | 13 |
| Pb | 3 | 3 | 4 | 11 | 13 | 13 | 17 | 16 | 16 | 33 | 71 | 61 | 35 | 35 | 78 | 22 | 38 | 68 | 24 | 62 | 75 | 61 | 51 | 9 | 14 |
| U | 1 | 1 | 2 | 4 | 3 | 2 | 4 | 3 | 3 | 9 | 30 | 21 | 4 | 7 | 26 | 3 | 15 | 25 | 7 | 23 | 18 | 23 | 27 | 3 | 6 |
| Sc | 30 | 31 | 17 | 1 | 7 | 7 | 1 | 1 | 1 | 1 | 1 | 2 | 1 | 1 | 1 | 2 | 1 | 1 | 1 | 1 | 1 | 1 | 1 | 2 | 2 |
| Y | 32 | 27 | 45 | 41 | 69 | 51 | 32 | 45 | 33 | 116 | 140 | 570 | 88 | 85 | 112 | 66 | 72 | 140 | 60 | 347 | 156 | 164 | 160 | 32 | 38 |
| La | 48 | 36 | 94 | 122 | 120 | 124 | 115 | 135 | 116 | 306 | 477 | 1602 | 174 | 235 | 466 | 130 | 235 | 351 | 221 | 833 | 521 | 556 | 351 | 142 | 214 |
| Ce | 93 | 73 | 201 | 239 | 259 | 237 | 212 | 224 | 217 | 590 | 875 | 1852 | 468 | 477 | 953 | 233 | 501 | 727 | 396 | 937 | 872 | 926 | 581 | 49 | 141 |
| Pr | 12 | 10 | 25 | 24 | 27 | 27 | 21 | 23 | 21 | 51 | 83 | 244 | 32 | 39 | 83 | 27 | 39 | 65 | 36 | 153 | 90 | 99 | 60 | 30 | 64 |
| Nd | 47 | 40 | 98 | 79 | 102 | 100 | 69 | 74 | 67 | 165 | 284 | 780 | 101 | 133 | 279 | 88 | 138 | 197 | 114 | 489 | 303 | 314 | 186 | 97 | 206 |
| Sm | 10 | 8 | 18 | 13 | 18 | 17 | 11 | 11 | 10 | 27 | 40 | 124 | 16 | 21 | 40 | 15 | 22 | 33 | 18 | 79 | 47 | 48 | 33 | 16 | 33 |
| Eu | 3 | 3 | 5 | 4 | 6 | 5 | 3 | 3 | 3 | 4 | 5 | 17 | 2 | 3 | 5 | 2 | 3 | 4 | 2 | 10 | 6 | 6 | 4 | 3 | 5 |
| Gd | 9 | 8 | 15 | 10 | 16 | 15 | 8 | 9 | 8 | 24 | 32 | 110 | 14 | 17 | 30 | 12 | 18 | 27 | 13 | 69 | 37 | 37 | 29 | 11 | 18 |
| Tb | 1 | 1 | 2 | 1 | 2 | 2 | 1 | 1 | 1 | 4 | 5 | 16 | 2 | 2 | 4 | 2 | 3 | 4 | 2 | 10 | 5 | 5 | 5 | 1 | 2 |
| Dy | 7 | 6 | 10 | 8 | 12 | 10 | 6 | 7 | 6 | 21 | 27 | 92 | 13 | 15 | 24 | 11 | 15 | 25 | 11 | 59 | 31 | 31 | 31 | 8 | 11 |
| Ho | 1 | 1 | 2 | 1 | 2 | 2 | 1 | 1 | 1 | 4 | 5 | 17 | 3 | 3 | 4 | 2 | 3 | 5 | 2 | 11 | 6 | 6 | 6 | 1 | 2 |
| Er | 3 | 3 | 4 | 4 | 6 | 5 | 3 | 4 | 3 | 11 | 14 | 43 | 8 | 8 | 12 | 7 | 8 | 14 | 6 | 31 | 16 | 16 | 18 | 3 | 4 |
| Tm | 0 | 0 | 0 | 1 | 1 | 1 | 0 | 0 | 0 | 1 | 2 | 5 | 1 | 1 | 2 | 1 | 1 | 2 | 1 | 4 | 2 | 2 | 3 | 0 | 1 |
| Yb | 2 | 2 | 3 | 3 | 5 | 4 | 3 | 3 | 3 | 9 | 12 | 32 | 8 | 7 | 11 | 8 | 7 | 13 | 6 | 24 | 14 | 14 | 17 | 3 | 4 |
| Lu | 0 | 0 | 0 | 0 | 1 | 1 | 0 | 0 | 0 | 1 | 2 | 4 | 1 | 1 | 2 | 1 | 1 | 2 | 1 | 3 | 2 | 2 | 2 | 0 | 1 |
| Th | 5 | 4 | 10 | 25 | 20 | 19 | 26 | 26 | 25 | 58 | 149 | 123 | 61 | 66 | 144 | 53 | 65 | 125 | 125 | 112 | 145 | 148 | 128 | 33 | 35 |

LOI: Loss of ignition; A.I.: Alkalinity index

Table 3: Selected EPMA analyses for olivine from the Tarosero Volcanic Complex.

| Rock type | ————Basalt———— | | ————Latite———— | | Peralkaline phonolite (agpaitic) | Peralkaline olivine trachyte | |
|---|---|---|---|---|---|---|---|
| Thin section | TA-042_1 | TA-048 | TA-045 | TA-046 | TA-021 | TA-005 | TA-005 |
| | macrocryst | groundmass | macrocryst | groundmass | xenolith | macrocryst | macrocryst |
| *wt.%* | | | | | | | |
| $SiO_2$ | 40.60 | 35.28 | 34.75 | 33.62 | 34.34 | 30.64 | 32.02 |
| $TiO_2$ | bdl | 0.07 | 0.03 | 0.08 | 0.02 | 0.02 | 0.04 |
| $Al_2O_3$ | 0.03 | 0.02 | bdl | 0.02 | 0.02 | 0.00 | bdl |
| FeO | 15.07 | 36.53 | 39.24 | 45.48 | 41.11 | 58.82 | 53.69 |
| MnO | 0.20 | 0.54 | 1.37 | 1.80 | 1.73 | 4.25 | 3.37 |
| MgO | 44.58 | 27.73 | 25.06 | 19.24 | 23.02 | 6.37 | 11.74 |
| NiO | 0.31 | 0.07 | bdl | 0.02 | bdl | bdl | bdl |
| CaO | 0.25 | 0.27 | 0.30 | 0.39 | 0.29 | 0.46 | 0.36 |
| Total | 101.04 | 100.51 | 100.76 | 100.65 | 100.52 | 100.58 | 101.23 |
| | | | | | | | |
| *Formula based on 4 oxygens* | | | | | | | |
| Si | 1.01 | 0.98 | 0.98 | 0.99 | 0.99 | 0.99 | 0.99 |
| Ti | bdl | 0.00 | 0.00 | 0.00 | 0.00 | 0.00 | 0.00 |
| Al | 0.00 | 0.00 | bdl | 0.00 | 0.00 | 0.00 | bdl |
| Fe | 0.31 | 0.85 | 0.93 | 1.12 | 0.99 | 1.59 | 1.38 |
| Mn | 0.00 | 0.01 | 0.03 | 0.04 | 0.04 | 0.12 | 0.09 |
| Mg | 1.65 | 1.15 | 1.06 | 0.84 | 0.99 | 0.31 | 0.54 |
| Ni | 0.01 | 0.00 | bdl | 0.00 | bdl | bdl | bdl |
| Ca | 0.01 | 0.01 | 0.01 | 0.01 | 0.01 | 0.02 | 0.01 |
| Sum cations | 2.99 | 3.01 | 3.01 | 3.01 | 3.01 | 3.01 | 3.01 |

bdl: below detection limit

Table 4: Selected EPMA analyses for clinopyroxene from the Tarosero Volcanic Complex.

| Rock type | Basalt | | Andesite | Latite | | Trachyte | | Peralkaline trachyte/phonolite | | Peralkaline phonolite (agpaitic) | | | |
|---|---|---|---|---|---|---|---|---|---|---|---|---|---|
| Thin section | TA-042_1 large | TA-048 Small | TA-044 large | TA-046 large | TA-046 Small | TA-116 large | TA-118 Small | TA-073 large | TA-054 interstitial | TA-072 large | TA-072 interstitial | TA-030 cumulate | TA-021 xenolith |
| *wt.%* | | | | | | | | | | | | | |
| $SiO_2$ | 53.84 | 49.31 | 48.11 | 51.63 | 51.56 | 52.39 | 49.61 | 52.34 | 50.48 | 52.27 | 50.87 | 52.35 | 52.09 |
| $TiO_2$ | 0.51 | 2.03 | 2.12 | 0.74 | 1.05 | 1.01 | 1.77 | 0.32 | 0.24 | 0.40 | 0.27 | 0.36 | 0.61 |
| $ZrO_2$ | bdl | bdl | 0.03 | bdl | 0.03 | 0.04 | 0.82 | 0.05 | 2.55 | 0.05 | 3.27 | 0.04 | 0.03 |
| $Al_2O_3$ | 1.99 | 3.89 | 5.65 | 1.75 | 1.57 | 2.30 | 1.49 | 0.51 | 0.46 | 0.71 | 0.33 | 0.59 | 1.19 |
| $Cr_2O_3$ | 0.53 | 0.13 | 0.04 | bdl | bdl | bdl | bdl | bdl | bdl | bdl | bdl | bdl | bdl |
| $Fe_2O_3$* | 0.02 | 1.97 | 3.29 | 1.57 | 0.90 | 0.00 | 3.78 | 1.64 | 16.57 | 1.70 | 19.28 | 1.65 | 3.08 |
| FeO* | 5.34 | 9.31 | 6.39 | 8.87 | 10.20 | 9.48 | 13.69 | 13.50 | 10.45 | 13.47 | 7.28 | 15.22 | 9.00 |
| MnO | 0.13 | 0.24 | 0.33 | 0.54 | 0.59 | 0.54 | 0.98 | 1.04 | 0.94 | 1.03 | 0.67 | 1.20 | 0.72 |
| MgO | 17.92 | 13.30 | 11.28 | 14.13 | 13.21 | 12.42 | 6.11 | 9.83 | 0.95 | 10.30 | 0.95 | 8.83 | 13.64 |
| CaO | 20.02 | 19.68 | 22.27 | 20.08 | 20.30 | 21.12 | 19.42 | 20.22 | 8.77 | 19.58 | 6.60 | 19.64 | 20.24 |
| $Na_2O$ | 0.37 | 0.49 | 0.88 | 0.45 | 0.47 | 0.89 | 2.32 | 1.06 | 8.13 | 1.07 | 9.68 | 1.21 | 0.62 |
| $K_2O$ | 0.02 | 0.02 | bdl | bdl | 0.02 | 0.02 | 0.07 | bdl | 0.02 | bdl | bdl | bdl | bdl |
| F | bdl | bdl | bdl | bdl | bdl | bdl | bdl | bdl | bdl | bdl | bdl | bdl | bdl |
| Cl | bdl | bdl | bdl | bdl | bdl | bdl | bdl | bdl | bdl | bdl | bdl | bdl | bdl |
| Total | 100.67 | 100.36 | 100.39 | 99.75 | 99.91 | 100.21 | 100.03 | 100.51 | 99.56 | 100.58 | 99.20 | 101.08 | 101.22 |
| *Formula based on 4 cations and 6 oxygens* | | | | | | | | | | | | | |
| Si | 1.95 | 1.85 | 1.80 | 1.93 | 1.94 | 1.96 | 1.93 | 1.99 | 2.00 | 1.99 | 2.01 | 2.00 | 1.94 |
| Ti | 0.01 | 0.06 | 0.06 | 0.02 | 0.03 | 0.03 | 0.05 | 0.01 | 0.01 | 0.01 | 0.01 | 0.01 | 0.02 |
| Zr | bdl | bdl | 0.00 | bdl | 0.00 | 0.00 | 0.02 | 0.00 | 0.05 | 0.00 | 0.06 | 0.00 | 0.00 |
| Al | 0.08 | 0.17 | 0.25 | 0.08 | 0.07 | 0.10 | 0.07 | 0.02 | 0.02 | 0.03 | 0.02 | 0.03 | 0.05 |
| Cr | 0.02 | 0.00 | 0.00 | bdl | bdl | bdl | bdl | bdl | bdl | bdl | bdl | bdl | bdl |
| $Fe^{3+}$ | 0.00 | 0.06 | 0.09 | 0.04 | 0.03 | 0.00 | 0.11 | 0.05 | 0.49 | 0.05 | 0.57 | 0.05 | 0.09 |
| $Fe^{2+}$ | 0.16 | 0.29 | 0.20 | 0.28 | 0.32 | 0.30 | 0.45 | 0.43 | 0.35 | 0.43 | 0.24 | 0.49 | 0.28 |
| Mn | 0.00 | 0.01 | 0.01 | 0.02 | 0.02 | 0.02 | 0.03 | 0.03 | 0.03 | 0.03 | 0.02 | 0.04 | 0.02 |
| Mg | 0.97 | 0.74 | 0.63 | 0.79 | 0.74 | 0.69 | 0.35 | 0.56 | 0.06 | 0.58 | 0.06 | 0.50 | 0.76 |
| Ca | 0.78 | 0.79 | 0.89 | 0.81 | 0.82 | 0.84 | 0.81 | 0.83 | 0.37 | 0.80 | 0.28 | 0.80 | 0.81 |
| Na | 0.03 | 0.04 | 0.06 | 0.03 | 0.03 | 0.06 | 0.17 | 0.08 | 0.62 | 0.08 | 0.74 | 0.09 | 0.04 |
| K | 0.00 | 0.00 | bdl | bdl | 0.00 | 0.00 | 0.00 | bdl | 0.00 | bdl | bdl | bdl | bdl |
| Total cations | 4.00 | 4.00 | 4.00 | 4.00 | 4.00 | 4.00 | 4.00 | 4.00 | 4.00 | 4.00 | 4.00 | 4.00 | 4.00 |
| F | bdl | bdl | bdl | bdl | bdl | bdl | bdl | bdl | bdl | bdl | bdl | bdl | bdl |
| Cl | bdl | bdl | bdl | bdl | bdl | bdl | bdl | bdl | bdl | bdl | bdl | bdl | bdl |
| Total anions | 4.00 | 4.00 | 4.00 | 4.00 | 4.00 | 4.00 | 4.00 | 4.00 | 4.00 | 4.00 | 4.00 | 4.00 | 4.00 |
| Mg# | 0.85 | 0.71 | 0.75 | 0.73 | 0.69 | 0.69 | 0.43 | 0.55 | 0.13 | 0.56 | 0.18 | 0.49 | 0.71 |

bdl: below detection limit; *Fe2O3-FeO ratio was calculated.

Table 5: Selected EPMA analyses for magnetite and ilmenite from the Tarosero Volcanic Complex.

| Rock type | ——————Basalt—————— | | | Andesite | ————Latite———— | | ———Trachyte——— | | Peralkaline trachyte/phonolite | | ——Peralkaline phonolite (agpaitic) —— | | | Peralkaline olivine trach |
|---|---|---|---|---|---|---|---|---|---|---|---|---|---|---|
| Thin section | TA-048 | TA-042_1 | TA-048 | TA-044 | TA-045 | TA-046 | TA-118 | TA-116 | TA-054 | TA-73 | TA-008_2 | TA-030 | TA-021 | TA-006 |
| Mineral | Cr-Spinel | Magnetite | Ilmenite | Magnetite | Magnetite | Ilmenite | Magnetite | Ilmenite | Magnetite | Magnetite | Magnetite | Magnetite cumulate | Magnetite xenolith | Magnetite |
| *wt.%* | | | | | | | | | | | | | | |
| $SiO_2$ | 0.08 | 0.08 | 0.05 | 0.09 | 0.05 | bdl | 0.07 | bdl | 0.06 | 0.08 | 0.13 | 0.07 | 0.05 | 0.09 |
| $TiO_2$ | 2.01 | 25.60 | 45.04 | 22.20 | 22.97 | 49.47 | 20.49 | 48.66 | 16.14 | 14.91 | 14.74 | 20.14 | 21.46 | 21.07 |
| $Al_2O_3$ | 13.56 | 0.92 | 0.14 | 3.56 | 2.34 | 0.08 | 1.83 | 0.15 | 0.35 | 0.37 | 0.08 | 0.47 | 1.59 | bdl |
| $V_2O_3$ | 0.20 | 0.32 | 0.19 | 0.09 | 0.18 | bdl | 0.07 | 0.03 | 0.10 | 0.05 | 0.03 | 0.13 | 0.16 | bdl |
| $Nb_2O_5$ | bdl | bdl | 0.08 | bdl | bdl | 0.08 | bdl | 0.29 | 0.05 | 0.17 | 0.09 | bdl | bdl | 0.13 |
| $Cr_2O_3$ | 45.07 | 0.12 | 0.09 | bdl | bdl | bdl | bdl | bdl | 0.18 | 0.28 | bdl | 0.12 | 0.04 | bdl |
| $Fe_2O_3$* | 10.07 | 19.49 | 15.20 | 23.41 | 22.99 | 7.43 | 28.07 | 8.72 | 37.21 | 39.01 | 39.97 | 29.80 | 26.22 | 27.81 |
| FeO* | 19.22 | 49.59 | 35.30 | 46.85 | 47.37 | 39.11 | 45.04 | 33.55 | 43.95 | 43.04 | 43.10 | 47.22 | 47.24 | 48.85 |
| MnO | 0.06 | 0.63 | 0.38 | 1.11 | 0.96 | 1.21 | 1.48 | 1.45 | 1.69 | 1.58 | 1.61 | 2.20 | 1.77 | 1.69 |
| MgO | 11.07 | 3.06 | 2.78 | 2.87 | 2.81 | 2.37 | 2.39 | 5.06 | 0.30 | 0.26 | 0.04 | 0.29 | 1.40 | 0.02 |
| NiO | 0.18 | 0.04 | bdl | bdl | bdl | bdl | bdl | bdl | bdl | bdl | 0.03 | 0.03 | bdl | bdl |
| ZnO | 0.06 | 0.09 | 0.02 | 0.14 | 0.15 | 0.04 | 0.18 | 0.05 | 0.21 | 0.20 | 0.26 | 0.27 | 0.22 | 0.32 |
| Total | 101.58 | 99.94 | 99.28 | 100.33 | 99.80 | 99.79 | 99.61 | 97.95 | 100.24 | 99.94 | 100.06 | 100.73 | 100.14 | 99.98 |
| *Formula based on 3 cations and 4 oxygens, respectively 2 cations and 3 oxygens for ilmenite* | | | | | | | | | | | | | | |
| Si | 0.00 | 0.00 | 0.00 | 0.00 | 0.00 | bdl | 0.00 | bdl | 0.00 | 0.00 | 0.00 | 0.00 | 0.00 | 0.00 |
| Ti | 0.05 | 0.70 | 0.85 | 0.60 | 0.63 | 0.93 | 0.57 | 0.91 | 0.46 | 0.42 | 0.42 | 0.57 | 0.60 | 0.60 |
| Al | 0.51 | 0.04 | 0.00 | 0.15 | 0.10 | 0.00 | 0.08 | 0.00 | 0.02 | 0.02 | 0.00 | 0.02 | 0.07 | bdl |
| V | 0.00 | 0.00 | 0.00 | 0.00 | 0.00 | bdl | 0.00 | 0.00 | 0.00 | 0.00 | 0.00 | 0.00 | 0.00 | bdl |
| Nb | bdl | bdl | 0.00 | bdl | bdl | 0.00 | bdl | 0.00 | 0.00 | 0.00 | 0.00 | bdl | bdl | 0.00 |
| Cr | 1.14 | 0.00 | 0.00 | bdl | bdl | bdl | bdl | bdl | 0.01 | 0.01 | bdl | 0.00 | 0.00 | bdl |
| $Fe^{3+}$ | 0.24 | 0.54 | 0.29 | 0.64 | 0.63 | 0.14 | 0.78 | 0.16 | 1.06 | 1.11 | 1.14 | 0.84 | 0.73 | 0.79 |
| $Fe^{2+}$ | 0.51 | 1.52 | 0.74 | 1.41 | 1.45 | 0.82 | 1.39 | 0.70 | 1.38 | 1.36 | 1.37 | 1.47 | 1.46 | 1.54 |
| Mn | 0.00 | 0.02 | 0.01 | 0.03 | 0.03 | 0.03 | 0.05 | 0.03 | 0.05 | 0.05 | 0.05 | 0.07 | 0.06 | 0.05 |
| Mg | 0.53 | 0.17 | 0.10 | 0.15 | 0.15 | 0.09 | 0.13 | 0.19 | 0.02 | 0.01 | 0.00 | 0.02 | 0.08 | 0.00 |
| Ni | 0.00 | 0.00 | bdl | bdl | bdl | bdl | bdl | bdl | bdl | bdl | 0.00 | 0.00 | bdl | bdl |
| Zn | 0.00 | 0.00 | 0.00 | 0.00 | 0.00 | 0.00 | 0.00 | 0.00 | 0.01 | 0.01 | 0.01 | 0.01 | 0.01 | 0.01 |
| Total cations | 3.00 | 3.00 | 2.00 | 3.00 | 3.00 | 2.00 | 3.00 | 2.00 | 3.00 | 3.00 | 3.00 | 3.00 | 3.00 | 3.00 |

bdl: below detection limit; *Fe2O3-FeO ratio was calculated.

Table 6: Selected EPMA analyses for aenigmatite from the Tarosero Volcanic Complex.

| Rock type | Peralkaline trachyte/phonolite | | ——Peralkaline phonolite (agpaitic) —— | | | ——Peralkaline olivine trachyte—— | | |
|---|---|---|---|---|---|---|---|---|
| Thin section | TA-054 | TA-073 | TA-008 | TA-072 | TA-022 | TA-005 | TA-006 | TA-006 |
| *wt.%* | | | | | | | | |
| $SiO_2$ | 39.71 | 42.16 | 39.22 | 40.13 | 40.42 | 41.70 | 41.43 | 41.57 |
| $TiO_2$ | 5.70 | 5.71 | 6.54 | 6.02 | 5.82 | 7.76 | 6.49 | 7.55 |
| $ZrO_2$ | 0.39 | 0.09 | 0.27 | 0.24 | 0.20 | 0.08 | 0.13 | 0.05 |
| $Al_2O_3$ | 1.60 | 0.45 | 1.09 | 1.46 | 1.32 | 0.19 | 0.28 | 0.24 |
| $Cr_2O_3$ | bdl | bdl | bdl | bdl | bdl | bdl | bdl | bdl |
| $Fe_2O_3$* | 11.96 | 9.24 | 11.12 | 10.84 | 10.92 | 5.74 | 8.37 | 6.93 |
| FeO* | 31.31 | 32.78 | 31.21 | 31.92 | 31.95 | 36.60 | 34.88 | 35.60 |
| MnO | 1.55 | 1.58 | 1.52 | 1.63 | 1.75 | 1.64 | 1.38 | 1.51 |
| MgO | 0.96 | 0.58 | 1.04 | 1.14 | 0.66 | 0.16 | 0.14 | 0.27 |
| CaO | 0.71 | 0.28 | 0.88 | 0.62 | 0.47 | 0.22 | 0.25 | 0.23 |
| $Na_2O$ | 7.35 | 7.91 | 7.30 | 7.31 | 7.56 | 7.53 | 7.63 | 7.66 |
| $K_2O$ | 0.06 | 0.04 | 0.04 | 0.07 | 0.02 | 0.03 | 0.02 | 0.03 |
| F | bdl | bdl | bdl | bdl | bdl | bdl | bdl | bdl |
| Cl | bdl | bdl | bdl | bdl | bdl | bdl | bdl | bdl |
| Total | 101.29 | 100.83 | 100.23 | 101.37 | 101.10 | 101.66 | 101.00 | 101.63 |
| | | | | | | | | |
| *Formula based on 14 cations and 20 oxygens* | | | | | | | | |
| Si | 5.61 | 5.94 | 5.60 | 5.65 | 5.71 | 5.88 | 5.88 | 5.86 |
| Ti | 0.61 | 0.61 | 0.70 | 0.64 | 0.62 | 0.82 | 0.69 | 0.80 |
| Zr | 0.03 | 0.01 | 0.02 | 0.02 | 0.01 | 0.01 | 0.01 | 0.00 |
| Al | 0.27 | 0.08 | 0.18 | 0.24 | 0.22 | 0.03 | 0.05 | 0.04 |
| Cr | bdl | bdl | bdl | bdl | bdl | bdl | bdl | bdl |
| $Fe^{3+}$ | 1.27 | 0.98 | 1.20 | 1.15 | 1.16 | 0.61 | 0.89 | 0.73 |
| $Fe^{2+}$ | 3.70 | 3.87 | 3.73 | 3.76 | 3.78 | 4.32 | 4.14 | 4.20 |
| Mn | 0.19 | 0.19 | 0.18 | 0.19 | 0.21 | 0.20 | 0.17 | 0.18 |
| Mg | 0.20 | 0.12 | 0.22 | 0.24 | 0.14 | 0.03 | 0.03 | 0.06 |
| Ca | 0.11 | 0.04 | 0.13 | 0.09 | 0.07 | 0.03 | 0.04 | 0.03 |
| Na | 2.01 | 2.16 | 2.02 | 2.00 | 2.07 | 2.06 | 2.10 | 2.09 |
| K | 0.01 | 0.01 | 0.01 | 0.01 | 0.00 | 0.01 | 0.00 | 0.01 |
| Total cations | 14.00 | 14.00 | 14.00 | 14.00 | 14.00 | 14.00 | 14.00 | 14.00 |
| F | bdl | bdl | bdl | bdl | bdl | bdl | bdl | bdl |
| Cl | bdl | bdl | bdl | bdl | bdl | bdl | bdl | bdl |
| Total anions | bdl | bdl | bdl | bdl | bdl | bdl | bdl | bdl |

bdl: below detection limit; *Fe2O3-FeO ratio was calculated.

Table 7: Selected EPMA analyses for amphibole from the Tarosero Volcanic Complex.

| Rock type | Andesite | Latite | Trachyte | ——Peralkaline trachyte/phonolite—— | | | ————Peralkaline phonolite (agpaitic) ———— | | | | —Peralkaline olivine trachyte— | |
|---|---|---|---|---|---|---|---|---|---|---|---|---|
| Thin section | TA-044 | TA-045 | TA-118 | TA-078 | TA-073 | TA-054 | TA-072 | TA-021 | TA-008 | TA-030 | TA-006 | TA-006 |
| | large | interstitial | large | large | altered rim | interstitial | large | altered rim | interstitial | cumulate | interstitial | interstitial |
| *wt.%* | | | | | | | | | | | | |
| $SiO_2$ | 40.01 | 51.03 | 40.53 | 43.87 | 50.00 | 50.60 | 44.94 | 50.91 | 50.90 | 46.53 | 50.11 | 49.48 |
| $TiO_2$ | 6.14 | 1.48 | 5.69 | 3.21 | 1.08 | 0.14 | 2.91 | 1.09 | 1.05 | 2.30 | 1.44 | 3.73 |
| $ZrO_2$ | 0.05 | 0.08 | 0.03 | 0.05 | bdl | 0.03 | bdl | bdl | 0.07 | 0.06 | 0.08 | 0.08 |
| $Al_2O_3$ | 12.74 | 1.40 | 11.53 | 8.00 | 3.37 | 0.44 | 6.79 | 2.13 | 1.79 | 5.07 | 0.24 | 0.47 |
| $Cr_2O_3$ | bdl | bdl | bdl | bdl | 0.05 | bdl | 0.04 | bdl | bdl | bdl | bdl | bdl |
| $Fe_2O_3$* | 0.00 | 0.00 | 0.00 | 0.00 | 1.60 | 5.46 | 1.32 | 3.13 | 2.71 | 0.00 | 3.40 | 0.00 |
| FeO* | 13.51 | 18.85 | 13.81 | 15.09 | 12.99 | 27.28 | 15.52 | 13.07 | 17.50 | 20.62 | 30.45 | 31.29 |
| MnO | 0.30 | 0.61 | 0.36 | 0.56 | 0.78 | 1.59 | 0.71 | 1.00 | 1.02 | 0.92 | 1.76 | 1.35 |
| MgO | 10.16 | 10.98 | 10.82 | 11.85 | 13.85 | 1.95 | 11.74 | 13.21 | 10.63 | 9.98 | 0.51 | 1.34 |
| CaO | 11.81 | 6.46 | 11.27 | 10.12 | 8.06 | 2.59 | 9.93 | 6.54 | 6.01 | 8.58 | 2.26 | 2.31 |
| $Na_2O$ | 2.89 | 5.38 | 3.15 | 3.90 | 5.25 | 7.63 | 4.13 | 6.07 | 6.18 | 4.05 | 7.89 | 7.89 |
| $K_2O$ | 1.08 | 1.19 | 0.98 | 1.12 | 1.26 | 1.58 | 1.10 | 1.29 | 1.33 | 1.26 | 1.23 | 0.99 |
| F | bdl | 3.25 | bdl | 0.98 | 3.27 | 2.92 | 1.07 | 3.18 | 3.36 | 1.00 | 2.66 | 2.02 |
| Cl | 0.01 | 0.03 | 0.02 | 0.03 | bdl | 0.01 | 0.02 | bdl | bdl | 0.01 | 0.03 | 0.02 |
| $H_2O$* | 1.98 | 0.44 | 1.98 | 1.52 | 0.48 | 0.53 | 1.50 | 0.52 | 0.42 | 1.51 | 0.63 | 0.93 |
| Total | 100.68 | 99.80 | 100.15 | 99.87 | 100.66 | 101.51 | 101.25 | 100.79 | 101.55 | 101.45 | 101.57 | 101.04 |
| *Formula based on 16 cations and 23 oxygens* | | | | | | | | | | | | |
| Si | 6.04 | 7.75 | 6.13 | 6.60 | 7.37 | 7.94 | 6.70 | 7.51 | 7.59 | 7.04 | 7.93 | 7.82 |
| Ti | 0.70 | 0.17 | 0.65 | 0.36 | 0.12 | 0.02 | 0.33 | 0.12 | 0.12 | 0.26 | 0.17 | 0.44 |
| Zr | 0.00 | 0.01 | 0.00 | 0.00 | bdl | 0.00 | bdl | bdl | 0.00 | 0.00 | 0.01 | 0.01 |
| Al | 2.27 | 0.25 | 2.05 | 1.42 | 0.58 | 0.08 | 1.19 | 0.37 | 0.31 | 0.90 | 0.05 | 0.09 |
| Cr | bdl | bdl | bdl | bdl | 0.01 | 0.00 | 0.00 | bdl | bdl | bdl | bdl | bdl |
| $Fe^{3+}$ | 0.00 | 0.00 | 0.00 | 0.00 | 0.18 | 0.64 | 0.15 | 0.35 | 0.30 | 0.00 | 0.40 | 0.00 |
| $Fe^{2+}$ | 1.70 | 2.39 | 1.75 | 1.90 | 1.60 | 3.58 | 1.94 | 1.61 | 2.18 | 2.61 | 4.03 | 4.14 |
| Mn | 0.04 | 0.08 | 0.05 | 0.07 | 0.10 | 0.21 | 0.09 | 0.12 | 0.13 | 0.12 | 0.24 | 0.18 |
| Mg | 2.29 | 2.49 | 2.44 | 2.66 | 3.04 | 0.46 | 2.61 | 2.90 | 2.36 | 2.25 | 0.12 | 0.32 |
| Ca | 1.91 | 1.05 | 1.83 | 1.63 | 1.27 | 0.44 | 1.59 | 1.03 | 0.96 | 1.39 | 0.38 | 0.39 |
| Na | 0.85 | 1.59 | 0.92 | 1.14 | 1.50 | 2.32 | 1.20 | 1.73 | 1.79 | 1.19 | 2.42 | 2.42 |
| K | 0.21 | 0.23 | 0.19 | 0.22 | 0.24 | 0.32 | 0.21 | 0.24 | 0.25 | 0.24 | 0.25 | 0.20 |
| Total cations | 16.00 | 16.00 | 16.00 | 16.00 | 16.00 | 16.00 | 16.00 | 16.00 | 16.00 | 16.00 | 16.00 | 16.00 |
| F | bdl | 1.55 | bdl | 0.47 | 1.53 | 1.45 | 0.51 | 1.49 | 1.58 | 0.48 | 1.33 | 1.01 |
| Cl | 0.00 | 0.01 | 0.00 | 0.01 | bdl | 0.00 | 0.00 | bdl | 0.00 | 0.00 | 0.01 | 0.00 |
| OH | 2.00 | 0.44 | 2.00 | 1.53 | 0.47 | 0.55 | 1.49 | 0.51 | 0.42 | 1.52 | 0.66 | 0.98 |
| Total anions | 2.00 | 2.00 | 2.00 | 2.00 | 2.00 | 2.00 | 2.00 | 2.00 | 2.00 | 2.00 | 2.00 | 2.00 |

bdl: below detection limit; *Fe2O3-FeO ratio and H2O was calculated.

Table 8: Selected EPMA analyses for feldspar from the Tarosero volcanic complex.

| Rock type | ———Basalt——— | | ——Andesite—— | | ————Latite———— | | | ——Trachyte—— | | Peralkaline trachyte/phonolite | | | ——Peralkaline phonolite (agpaitic)—— | | | | Peralkaline olivine trachy | |
|---|---|---|---|---|---|---|---|---|---|---|---|---|---|---|---|---|---|---|
| Thin section | TA-042 | TA-042 | TA-044 | TA-044 | TA-046 | TA-046 | TA-046 | TA-118 | TA-116 | TA-078 | TA-054 | TA-035 | TA-021 | TA-022 | TA-030 | TA-021 | TA-006 | TA-005 |
| Mineral | afs | pl | pl | pl | pl | pl | afs | pl | afs | afs | afs | afs | afs | afs | afs | pl | afs | afs |
| | small | small | large | small | large | small | small | large | small | large | large | small | large | small | cumulate | xenolith | large | small |
| *wt.%* | | | | | | | | | | | | | | | | | | |
| $SiO_2$ | 64.58 | 56.60 | 56.91 | 59.18 | 57.97 | 58.64 | 64.12 | 60.90 | 65.98 | 64.23 | 67.31 | 66.72 | 67.01 | 67.40 | 65.73 | 62.91 | 66.89 | 67.22 |
| $TiO_2$ | 0.34 | 0.19 | 0.11 | 0.28 | 0.08 | 0.09 | 0.14 | 0.06 | 0.13 | 0.07 | 0.04 | 0.05 | 0.08 | 0.02 | 0.06 | 0.08 | 0.05 | 0.06 |
| $Al_2O_3$ | 19.86 | 26.32 | 26.64 | 24.07 | 25.54 | 25.28 | 20.95 | 24.21 | 19.57 | 21.45 | 19.07 | 18.74 | 19.04 | 18.86 | 20.83 | 22.78 | 19.07 | 19.07 |
| $Fe_2O_3$ | 0.71 | 1.15 | 0.34 | 1.09 | 0.39 | 0.54 | 0.53 | 0.31 | 0.51 | 0.25 | 0.39 | 0.46 | 0.51 | 0.50 | 0.16 | 0.29 | 0.25 | 0.48 |
| BaO | 0.06 | 0.06 | 0.15 | 0.21 | 0.08 | 0.11 | 0.33 | 0.24 | bdl | 0.30 | 0.05 | 0.07 | 0.03 | bdl | 0.52 | 0.16 | 0.15 | 0.09 |
| SrO | bdl | 0.07 | 0.59 | 0.54 | 0.30 | 0.31 | 0.09 | 0.72 | bdl | 0.54 | bdl | bdl | bdl | bdl | 0.08 | 0.13 | bdl | bdl |
| CaO | 1.44 | 10.26 | 8.69 | 6.34 | 7.87 | 7.33 | 2.49 | 5.41 | 0.70 | 2.39 | 0.21 | 0.23 | 0.22 | 0.04 | 1.67 | 4.02 | 0.27 | 0.15 |
| $Na_2O$ | 6.61 | 5.30 | 5.98 | 7.57 | 6.78 | 6.63 | 7.95 | 7.66 | 6.99 | 8.68 | 8.19 | 7.77 | 7.71 | 7.58 | 8.32 | 8.30 | 7.49 | 8.06 |
| $K_2O$ | 6.31 | 0.80 | 0.53 | 0.57 | 0.61 | 0.89 | 3.09 | 1.05 | 6.06 | 2.26 | 5.01 | 5.77 | 5.65 | 6.12 | 3.18 | 1.28 | 5.82 | 4.89 |
| Total | 99.91 | 100.74 | 99.93 | 99.84 | 99.62 | 99.83 | 99.68 | 100.55 | 99.95 | 100.18 | 100.27 | 99.81 | 100.25 | 100.53 | 100.54 | 99.94 | 99.99 | 100.02 |
| *Formula based on 8 oxygens* | | | | | | | | | | | | | | | | | | |
| Si | 2.91 | 2.54 | 2.57 | 2.67 | 2.62 | 2.64 | 2.87 | 2.72 | 2.95 | 2.86 | 2.99 | 2.99 | 2.98 | 2.99 | 2.91 | 2.80 | 2.99 | 2.99 |
| Ti | 0.01 | 0.01 | 0.00 | 0.01 | 0.00 | 0.00 | 0.00 | 0.00 | 0.00 | 0.00 | 0.00 | 0.00 | 0.00 | 0.00 | 0.00 | 0.00 | 0.00 | 0.00 |
| Al | 1.05 | 1.39 | 1.42 | 1.28 | 1.36 | 1.34 | 1.11 | 1.27 | 1.03 | 1.13 | 1.00 | 0.99 | 1.00 | 0.99 | 1.09 | 1.19 | 1.00 | 1.00 |
| $Fe^{3+}$ | 0.02 | 0.04 | 0.01 | 0.04 | 0.01 | 0.02 | 0.02 | 0.01 | 0.02 | 0.01 | 0.01 | 0.02 | 0.02 | 0.02 | 0.01 | 0.01 | 0.01 | 0.02 |
| Ba | 0.00 | 0.00 | 0.00 | 0.00 | 0.00 | 0.00 | 0.01 | 0.00 | bdl | 0.01 | 0.00 | 0.00 | 0.00 | bdl | 0.01 | 0.00 | 0.00 | 0.00 |
| Sr | bdl | 0.00 | 0.02 | 0.01 | 0.01 | 0.01 | 0.00 | 0.02 | bdl | 0.01 | bdl | bdl | bdl | bdl | 0.00 | 0.00 | bdl | bdl |
| Ca | 0.07 | 0.49 | 0.42 | 0.31 | 0.38 | 0.35 | 0.12 | 0.26 | 0.03 | 0.11 | 0.01 | 0.01 | 0.01 | 0.00 | 0.08 | 0.19 | 0.01 | 0.01 |
| Na | 0.58 | 0.46 | 0.52 | 0.66 | 0.59 | 0.58 | 0.69 | 0.66 | 0.61 | 0.75 | 0.70 | 0.67 | 0.67 | 0.65 | 0.71 | 0.72 | 0.65 | 0.69 |
| K | 0.36 | 0.05 | 0.03 | 0.03 | 0.04 | 0.05 | 0.18 | 0.06 | 0.35 | 0.13 | 0.28 | 0.33 | 0.32 | 0.35 | 0.18 | 0.07 | 0.33 | 0.28 |
| Total cations | 5.01 | 4.99 | 4.99 | 5.01 | 5.01 | 4.99 | 4.99 | 5.00 | 4.99 | 5.01 | 5.00 | 5.01 | 5.00 | 5.00 | 4.99 | 4.99 | 5.00 | 4.99 |

afs: alkali feldspar; pl: plagioclase; bdl: below detection limit

Table 9: Selected EPMA analyses for sodalite group minerals from the Tarosero Volcanic Complex.

| Rock type | Peralkaline trachyte/phonolite | | Peralkaline phonolite (agpaitic) | |
|---|---|---|---|---|
| Thin section | TA-054 | TA-035 | TA-022 | TA-008_2 |
| *wt.%* | | | | |
| $SiO_2$ | 41.37 | 38.62 | 42.19 | 42.44 |
| $Al_2O_3$ | 23.12 | 28.49 | 21.78 | 21.86 |
| $Fe_2O_3$ | 5.60 | 1.87 | 6.00 | 5.48 |
| CaO | bdl | bdl | bdl | bdl |
| $Na_2O$ | 23.71 | 25.35 | 24.62 | 21.90 |
| $K_2O$ | 0.34 | 0.15 | 0.12 | 0.76 |
| $SO_3$ | bdl | bdl | 0.06 | bdl |
| Cl | 6.85 | 6.99 | 6.77 | 6.86 |
| Total | 99.45 | 99.89 | 100.01 | 97.75 |
| | | | | |
| *Formula based on 25 oxygens* | | | | |
| Si | 6.75 | 6.25 | 6.86 | 7.01 |
| Al | 4.45 | 5.44 | 4.17 | 4.25 |
| $Fe^{3+}$ | 0.69 | 0.23 | 0.73 | 0.68 |
| Ca | bdl | bdl | bdl | bdl |
| Na | 7.50 | 7.96 | 7.76 | 7.01 |
| K | 0.07 | 0.03 | 0.02 | 0.16 |
| Total cations | 19.47 | 19.91 | 19.56 | 19.11 |
| $SO_3$ | bdl | bdl | 0.01 | bdl |
| Cl | 1.90 | 1.92 | 1.87 | 1.92 |
| Total anions | 1.90 | 1.92 | 1.87 | 1.92 |

bdl: below detection limit

Table 10: Selected EPMA analyses for eudialyte group minerals from the Tarosero volcanic complex.

| Rock type | Peralkaline phonolite (agpaitic) | | | | | |
|---|---|---|---|---|---|---|
| Thin section | TA-030 | TA-072 | TA-030 | TA-022 | TA-030 | Dawson, 1997 |
| *wt.%* | | | | | | |
| $SiO_2$ | 52.51 | 52.03 | 53.16 | 52.03 | 51.43 | 50.10 |
| $TiO_2$ | 0.29 | 0.22 | 0.37 | 0.22 | 0.41 | 0.18 |
| $ZrO_2$ | 11.01 | 11.27 | 9.42 | 9.75 | 8.80 | 11.30 |
| $HfO_2$ | 0.30 | 0.26 | 0.13 | 0.26 | 0.13 | bdl |
| $Al_2O_3$ | 0.09 | 0.17 | 0.51 | 0.18 | 0.16 | 0.20 |
| FeO | 7.01 | 7.60 | 6.63 | 7.75 | 6.77 | 7.50 |
| MnO | 1.23 | 1.56 | 1.25 | 1.52 | 1.25 | 1.24 |
| CaO | 8.34 | 7.83 | 7.23 | 8.25 | 8.25 | 8.70 |
| $Na_2O$ | 13.59 | 13.88 | 11.58 | 12.23 | 13.44 | 12.90 |
| $K_2O$ | 0.33 | 0.31 | 0.71 | 0.33 | 0.34 | 0.33 |
| $Nb_2O_5$ | 0.54 | 0.52 | 0.90 | 0.71 | 1.01 | 0.55 |
| SrO | 0.17 | bdl | bdl | 0.18 | bdl | bdl |
| $La_2O_3$ | 0.59 | 0.48 | 0.84 | 0.59 | 0.62 | 0.57 |
| $Ce_2O_3$ | 1.13 | 1.15 | 1.74 | 1.17 | 1.40 | 0.94 |
| $Nd_2O_3$ | 0.38 | 0.37 | 0.65 | 0.44 | 0.49 | 0.58 |
| $Y_2O_3$ | 0.38 | 0.37 | 0.66 | 0.50 | 0.69 | bdl |
| Cl | 2.19 | 2.05 | 2.07 | 2.19 | 2.27 | 2.13 |
| Total | 99.57 | 99.60 | 97.37 | 97.78 | 96.95 | 96.74 |
| | | | | | | |
| *Formula based on Si+Al+Zr+Ti+Hf+Nb=29 cations* | | | | | | |
| Si | 26.02 | 25.93 | 26.10 | 26.22 | 26.30 | 25.84 |
| Ti | 0.11 | 0.08 | 0.14 | 0.08 | 0.16 | 0.07 |
| Zr | 2.66 | 2.74 | 2.26 | 2.40 | 2.19 | 2.84 |
| Hf | 0.04 | 0.04 | 0.02 | 0.04 | 0.02 | bdl |
| Al | 0.05 | 0.10 | 0.29 | 0.11 | 0.09 | 0.12 |
| $Fe^{2+}$ | 2.90 | 3.17 | 2.72 | 3.27 | 2.90 | 3.23 |
| Mn | 0.52 | 0.66 | 0.52 | 0.65 | 0.54 | 0.54 |
| Ca | 4.43 | 4.18 | 3.80 | 4.45 | 4.52 | 4.81 |
| Na | 13.06 | 13.41 | 11.02 | 11.95 | 13.33 | 12.90 |
| K | 0.21 | 0.19 | 0.44 | 0.21 | 0.22 | 0.22 |
| Nb | 0.12 | 0.12 | 0.20 | 0.16 | 0.23 | 0.13 |
| Sr | 0.05 | bdl | bdl | 0.05 | bdl | bdl |
| La | 0.11 | 0.09 | 0.15 | 0.11 | 0.12 | 0.11 |
| Ce | 0.20 | 0.21 | 0.31 | 0.22 | 0.26 | 0.18 |
| Nd | 0.07 | 0.07 | 0.11 | 0.08 | 0.09 | 0.11 |
| Y | 0.10 | 0.10 | 0.17 | 0.13 | 0.19 | bdl |
| Total cations | 50.64 | 51.07 | 48.26 | 50.12 | 51.16 | 51.09 |
| Cl | 1.84 | 1.73 | 1.72 | 1.87 | 1.97 | 1.86 |

bdl: below detection limit

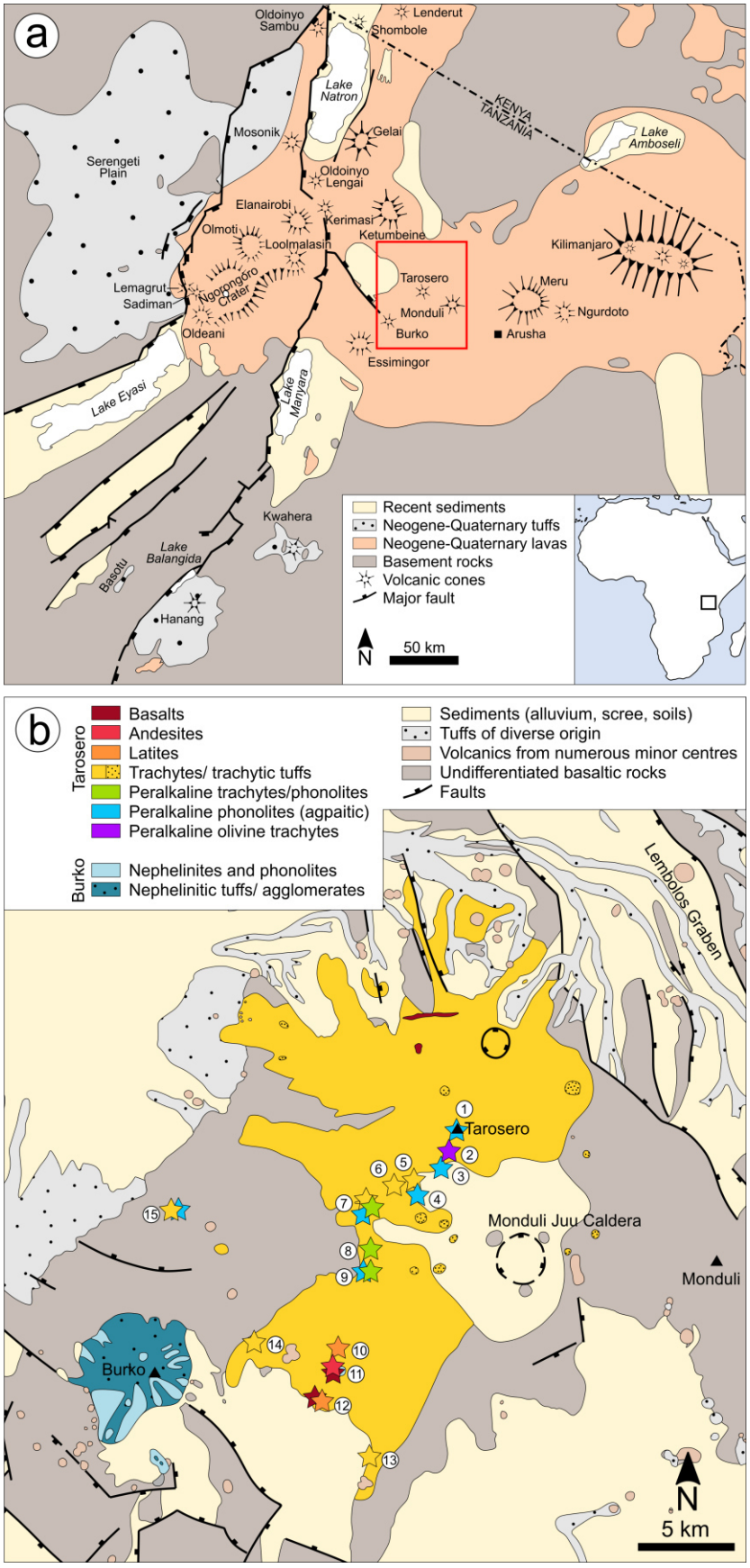


Fig. 1: Geology of northern Tanzania. a) North Tanzanian Divergence Zone (modified after Woolley, 2001). Red square represents the study area. b) Geological map of the Tarosero Volcanic Complex (modified after Dawson & Pickering, 1964), including the sample localities (indicated by the stars). The numbers refer to the samples listed in Table 1.

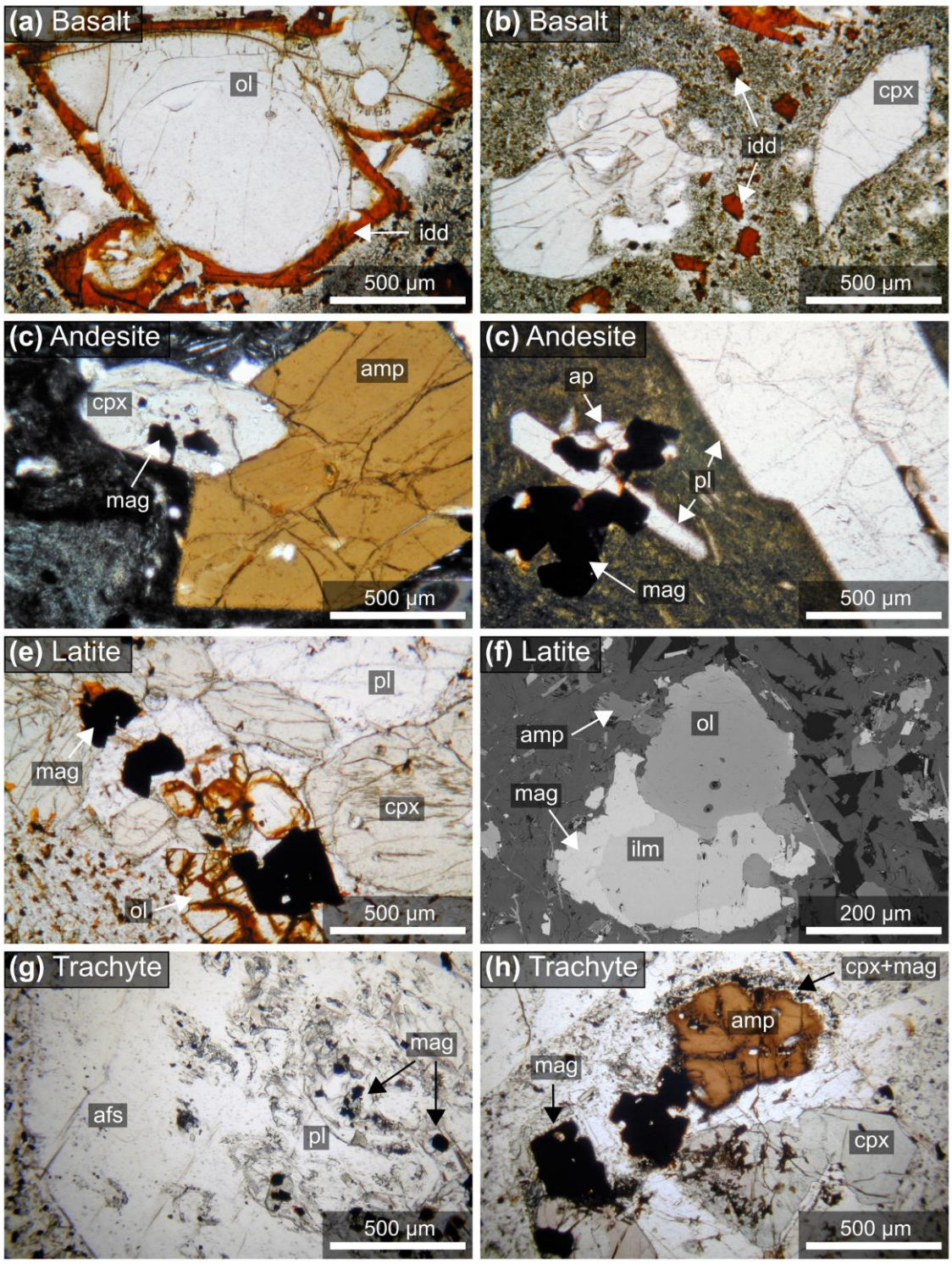


Fig. 2: Mineral textures in the primitive to intermediate rock types from Tarosero. a) Basalt with euhedral olivine (ol) crystals that are surrounded by iddingsite (idd). b) Basalt with rounded clinopyroxene (cpx) macrocrysts and small altered (to iddingsite) olivine grains. c) Andesite consisting of large euhedral amphibole (amp), and clinopyroxene with inclusions of magnetite (mag). d) Andesite showing magnetite and plagioclase (pl) phenocrysts, and small apatite (ap) in a very fine-grained groundmass. e) Latite with olivine, clinopyroxene, magnetite and plagioclase. f) Latite containing olivine, ilmenite rimmed by magnetite, and small anhedral amphibole grains. g) Trachyte showing a sieved-textured plagioclase surrounded by alkali feldspar (afs). h) Trachyte with subhedral clinopyroxene, magnetite and a dark brown amphibole that is partly rimmed by an alteration zone of fine-grained clinopyroxene and magnetite.

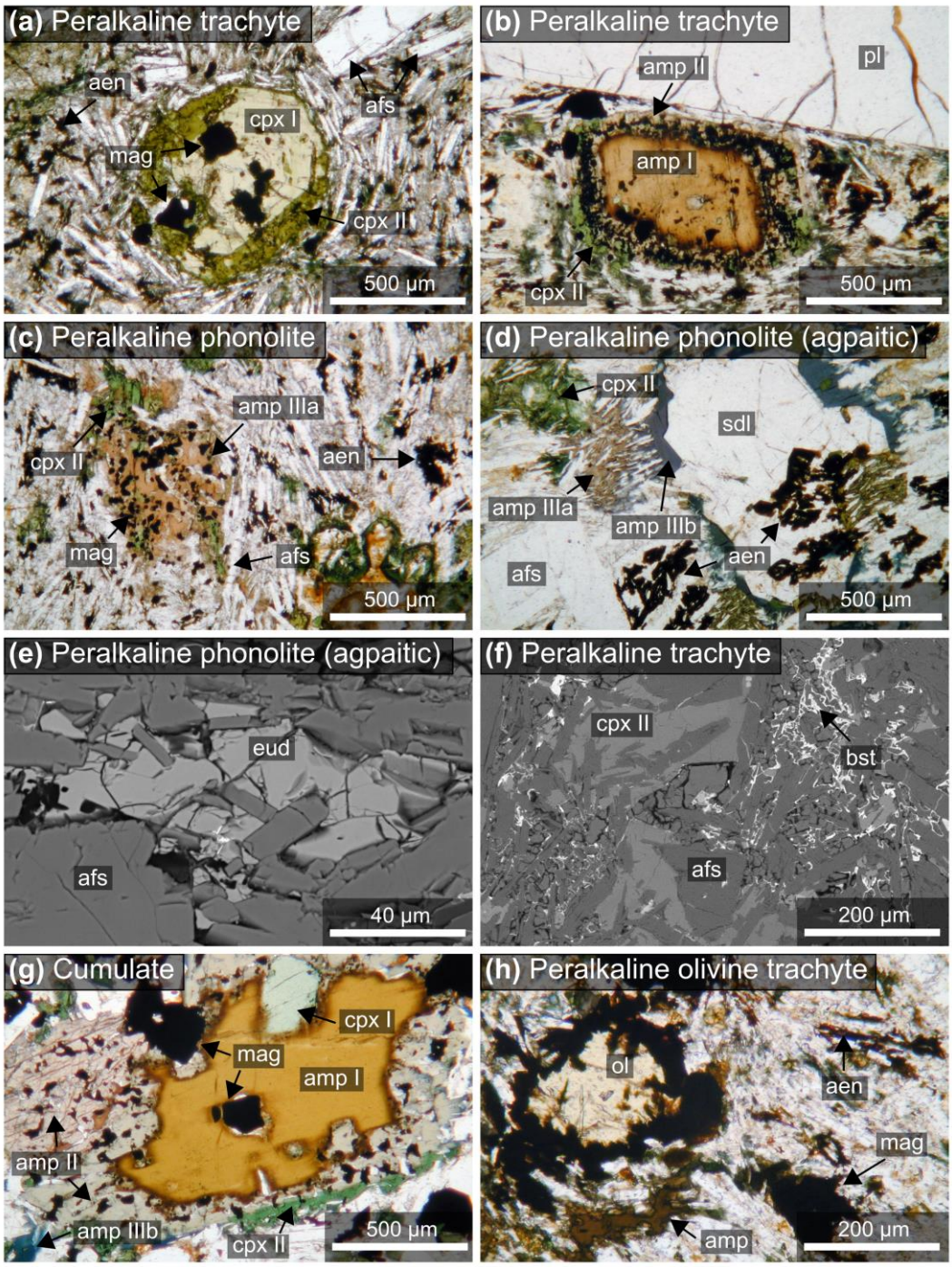


Fig. 3: Mineral textures in evolved rock types from Tarosero. a) Peralkaline trachyte containing bright green clinopyroxene (cpx I) with magnetite (mag) inclusions, surrounded by a dark green clinopyroxene generation (cpx II). The groundmass mainly consists of alkali feldspar laths and small aenigmatite (aen) grains. b) Peralkaline trachyte with a plagioclase (pl) crystal, and dark amphibole (amp I) which is rimmed by bright brown amphibole (amp II), dark green clinopyroxene and magnetite. c) Peralkaline phonolite with bright brown interstitial amphibole IIIa, dark green clinopyroxene II, aenigmatite and alkali feldspar laths. d) Peralkaline phonolite showing alkali feldspar laths, and a subhedral sodalite (sdl) grain with inclusions of aenigmatite, which is surrounded by blue amphibole IIIb. e) Peralkaline phonolite with interstitial eudialyte (eud). f) Peralkaline trachyte with interstitial bastnäsite (bst). g) Cumulate in a peralkaline phonolite consisting of dark brown anhedral amphibole I, surrounded by bright brown amphibole II, dark green clinopyroxene and blue amphibole IIIb. h) Peralkaline olivine trachyte with partly altered olivine and a fine-grained groundmass of magnetite, amphibole and aenigmatite.

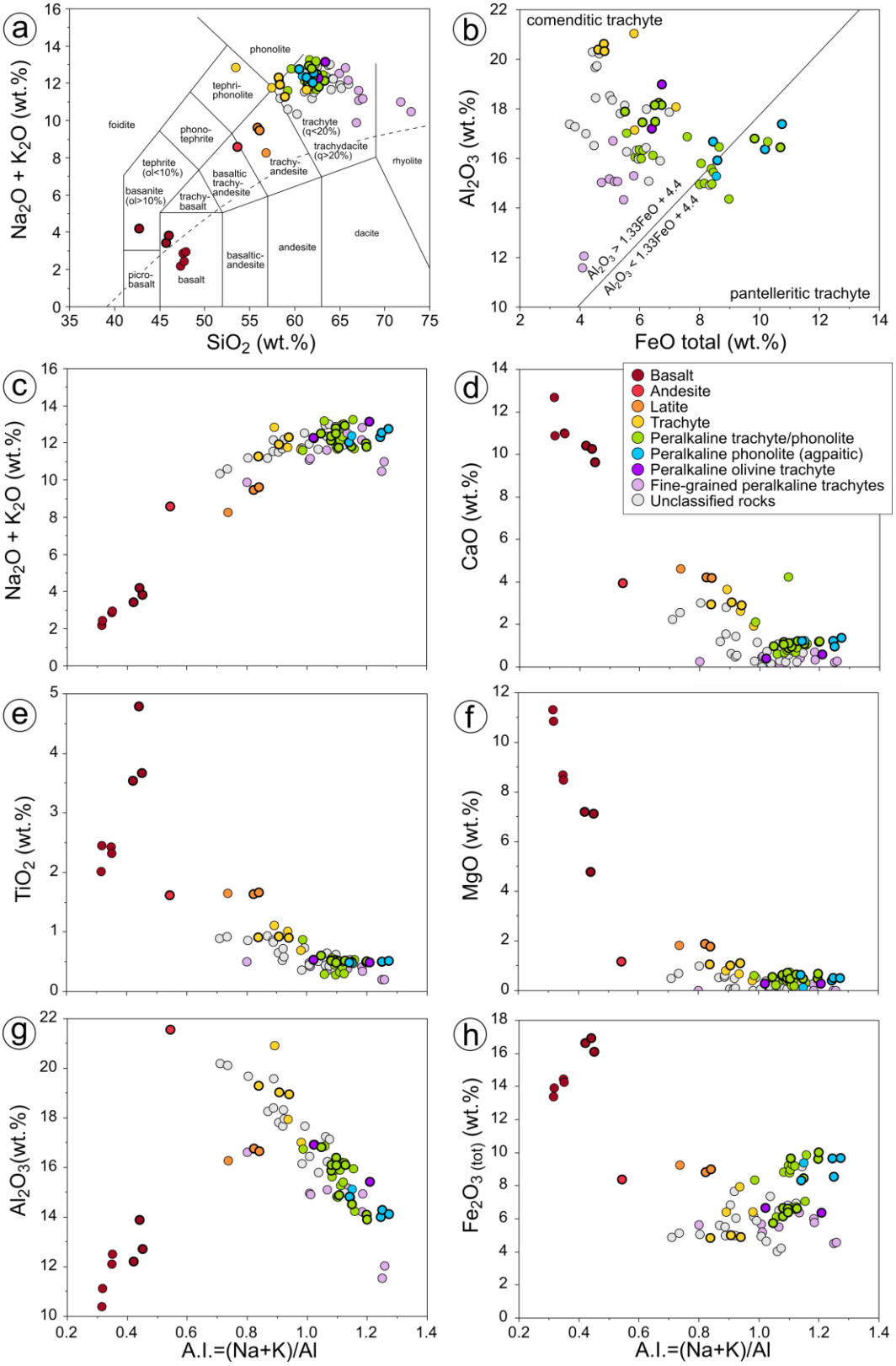


Fig. 4: Whole-rock major element composition for the rocks from Tarosero. a) TAS diagram showing the total alkalies ($Na_2O+K_2O$) vs $SiO_2$ (in wt. %). The dashed line divides the alkaline field (high alkali content) from the subalkaline fiel (according to Irvine & Baragar, 1971). b) Concentration (in wt. %) of $Al_2O_3$ vs total FeO (all Fe expressed as FeO). c-h) Concentration (in wt. %) of $Na_2O+K_2O$ (c), CaO (d), $TiO_2$ (e), MgO (f), $Al_2O_3$ (g) and $Fe_2O_3$ (h) vs the alkalinity index A.I. (molar [Na+K]/Al). Bold-rimmed data are from this study, literature data are from Cooper (1972) and Mana *et al.* (2015).

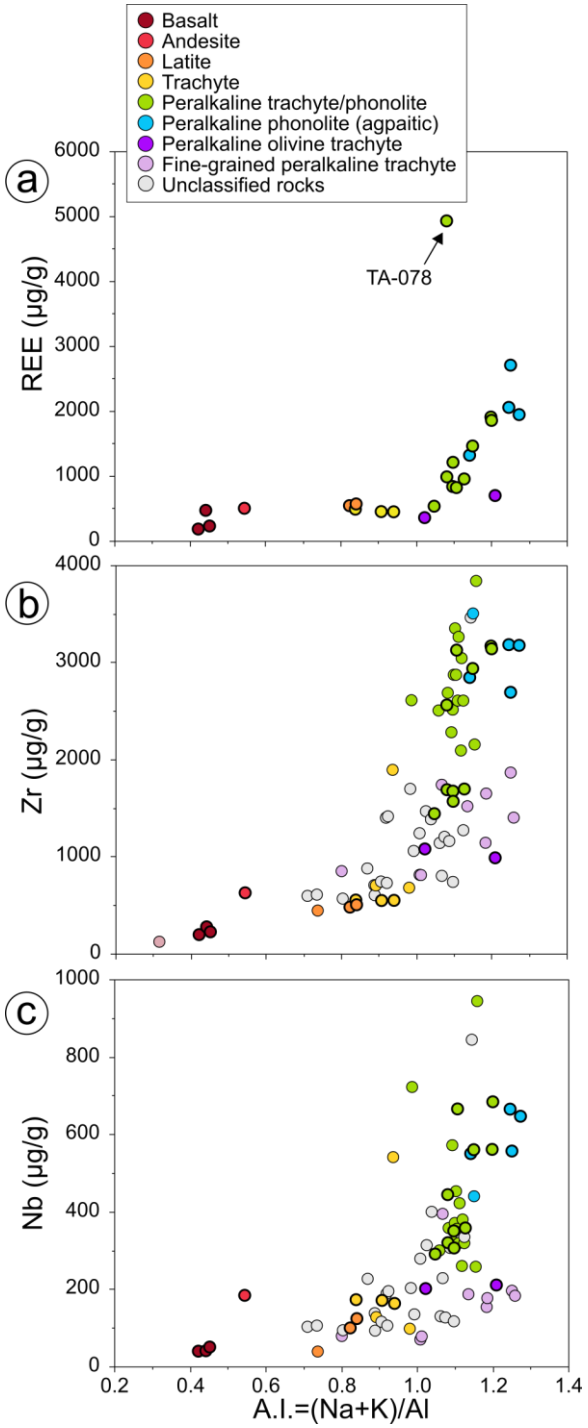


Fig. 5: Whole-rock trace element concentrations for the rocks from Tarosero. a) Concentration (in µg/g) of REE (a), Zr (b) and Nb (c) vs the alkalinity index A.I. (molar [Na+K]/Al). Sample TA-078 contains large amounts of REE-F-carbonates (bastnäsite). Bold-rimmed data are from this study, literature data are from Cooper (1972) and Mana *et al.* (2015).

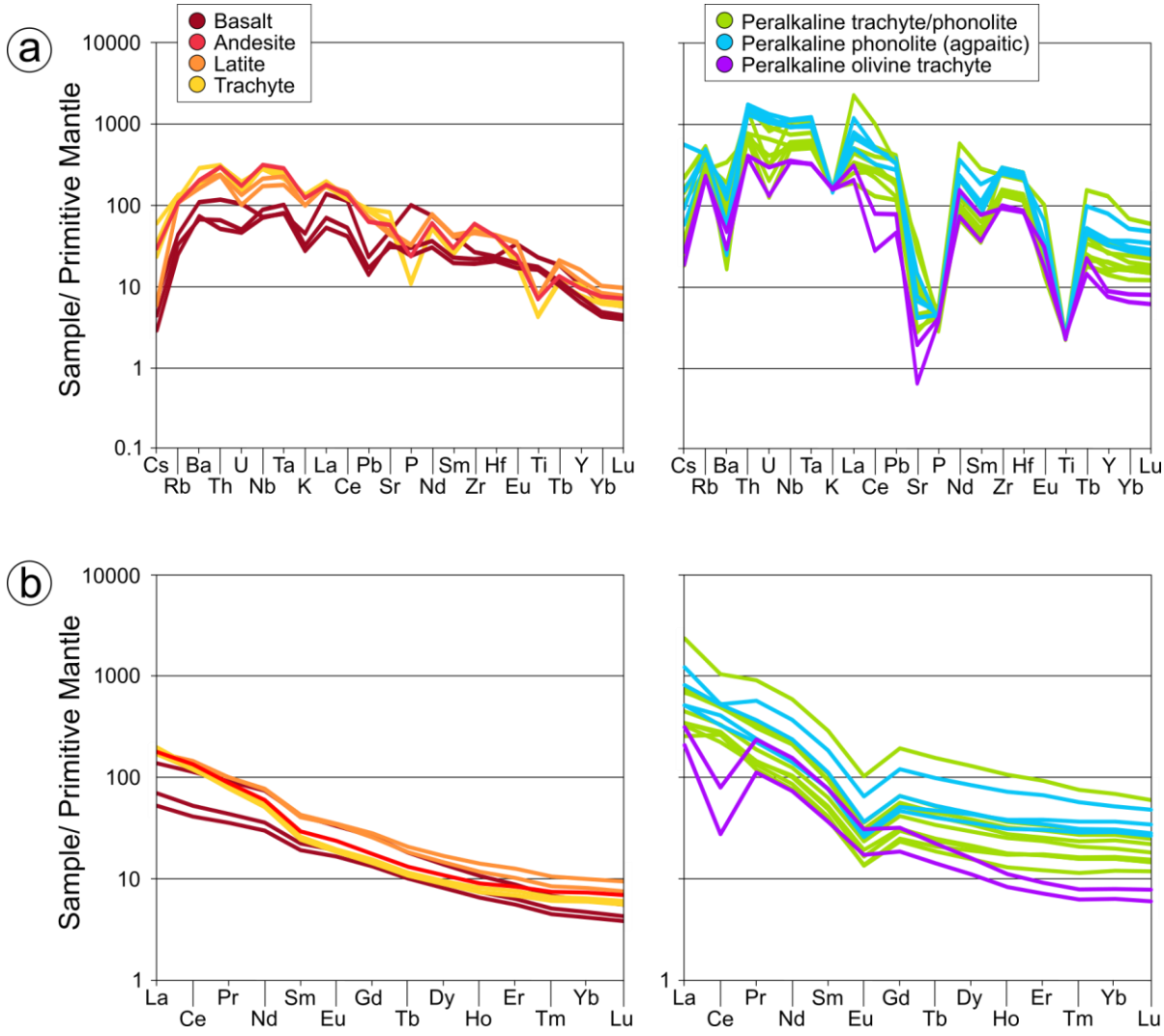


Fig. 6: Primitive mantle-normalized element pattern for the rocks from Tarosero. a) Incompatible element variation diagram. b) Rare earth elements pattern diagram. Normalization values are from Palme & O'Neill (2003).

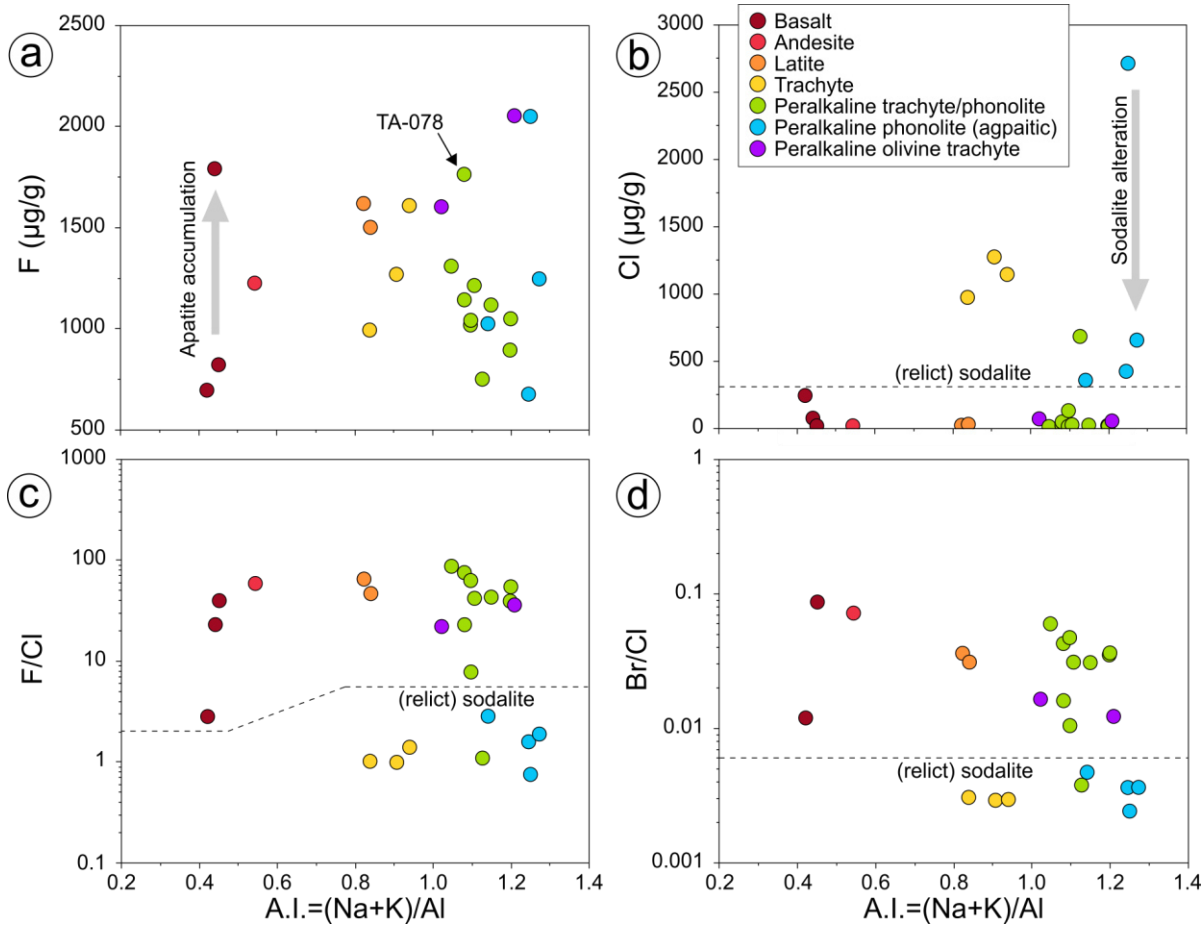


Fig. 7: Halogen composition for the rocks from Tarosero. a-b) Concentration (in µg/g) of fluorine (a) and chlorine (b) vs the alkalinity index A.I.. c-d) Ratio of F/Cl and Br/Cl vs the alkalinity index A.I.. Apatite accumulation explains the large variation in the F concentration of the basalts. The presence of relict sodalite conforms with high Cl concentrations, respectively low F/Cl and Br/Cl ratios.

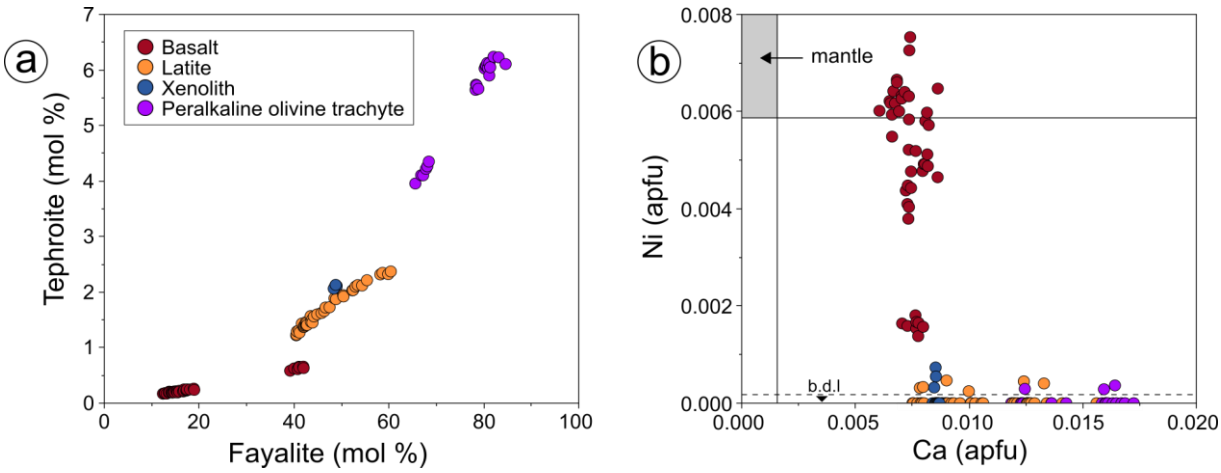


Fig. 8: Olivine composition from the rocks from Tarosero. a) The tephroite component (in mol %) positively correlates with fayalite (mol %). b) Concentration (in apfu) of Ni vs Ca. The grey field indicates the typical mantle olivine composition (Foley *et al.*, 2013, Bussweiler *et al.*, 2015).

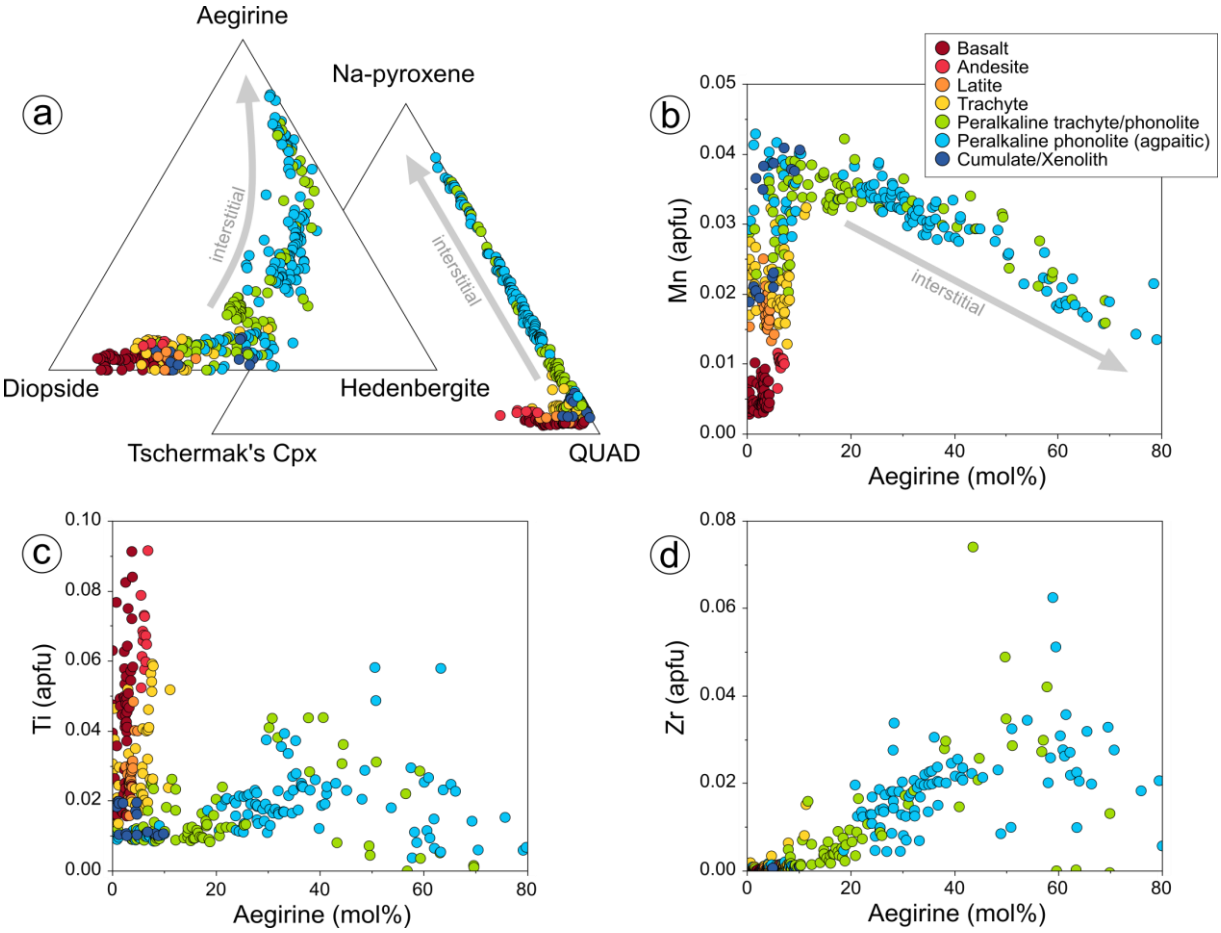


Fig. 9: Clinopyroxene composition from the rocks from Tarosero. a) Diopside ($CaMgSi_2O_6$)-aegirine ($NaFeSi_2O_6$)-hedenbergite ($CaFeSi_2O_6$) and Tschermak's clinopyroxene ($CaXXSiO_6$)-Na-pyroxene ($NaFeSi_2O_6$+$NaAlSi_2O_6$-QUAD ($CaMgSi_2O_6$+$CaFeSi_2O_6$) triangles. b-d) Concentration (in apfu) of Mn (b), Ti (c) and Zr (d) vs the aegirine component (mol %). Grey arrows highlight the evolution trend of the interstitial clinopyroxenes.

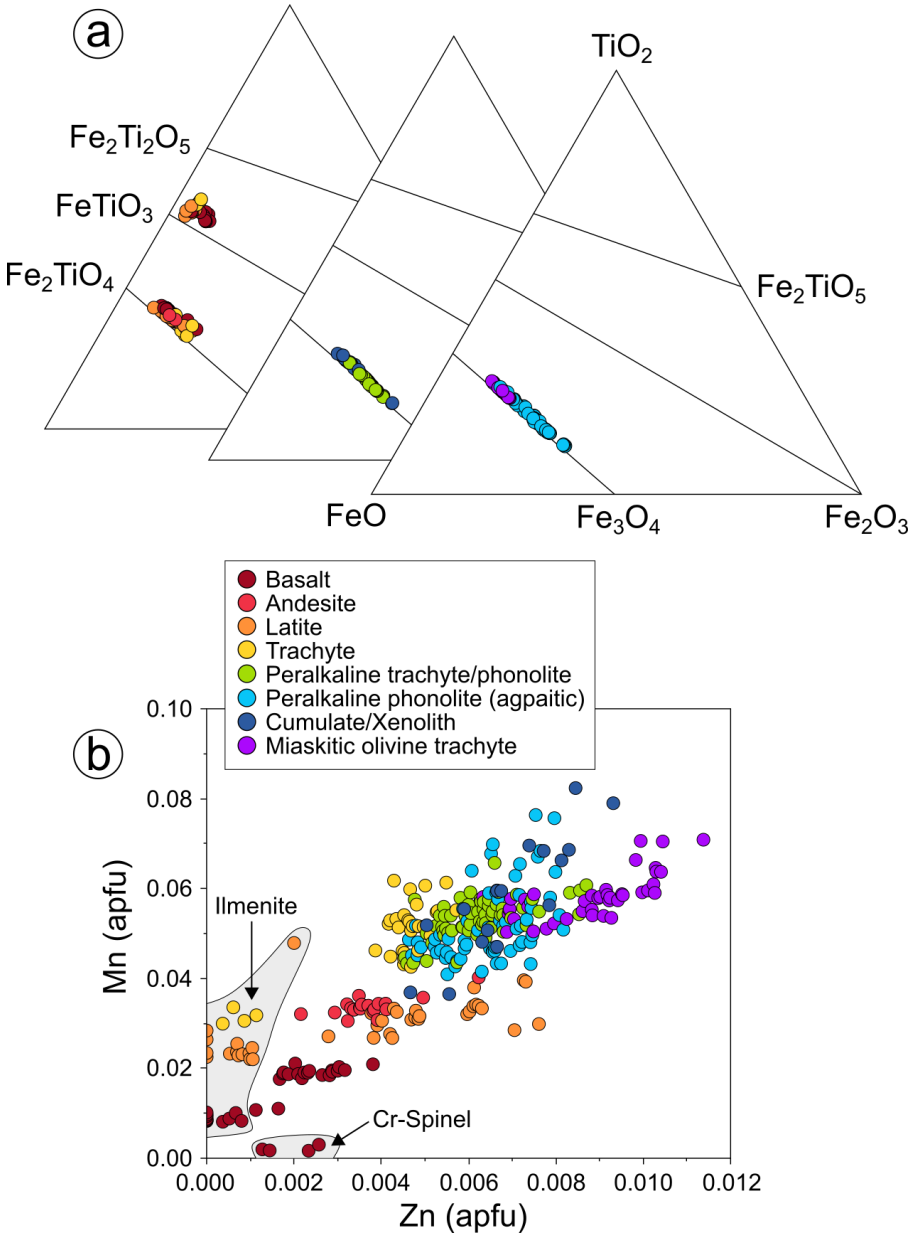


Fig. 10: Oxide composition from the rocks from Tarosero. a) Ternary FeO-$TiO_2$-$Fe_2O_3$ (molar) diagram illustrating the composition of (Ti)-magnetite and ilmenite. b) Correlation diagram of Mn (apfu) vs Zn (apfu). Grey fields indicate the compositional range for ilmenite and Cr-spinel.

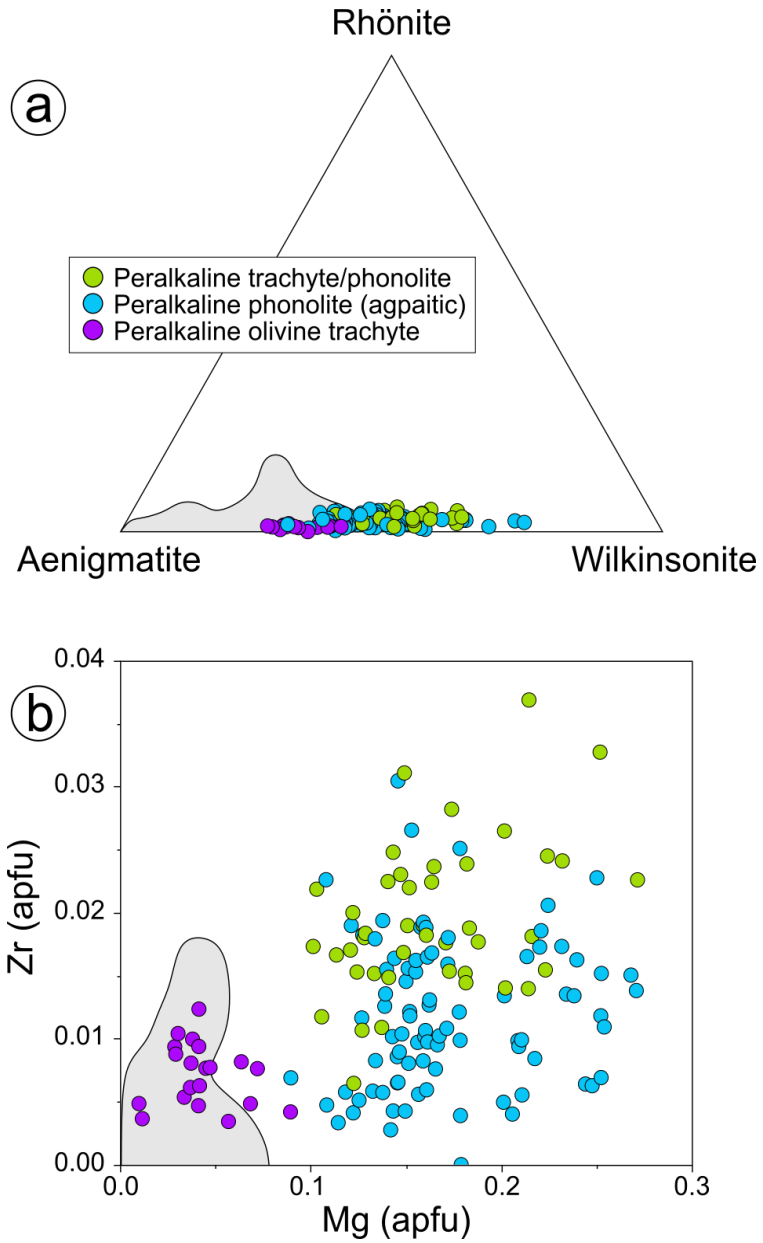


Fig. 11: Aenigmatite group composition from the rocks from Tarosero. a) Aenigmatite ($Na_2Fe_5TiSi_6O_{20}$)-Rhönite ($Ca_2[Mg,Fe,Ti]_6[Si,Al]_6O_{20}$)-Wilkinsonite ($Na_2Fe_6Si_6O_{20}$) triangle showing the compositional range of aenigmatite group minerals. b) Correlation diagram of Zr (apfu) vs Mg (apfu). Grey fields represent aenigmatite data from Ilímaussaq and Puklen (Gardar Province, Greenland; Braunger, 2016).

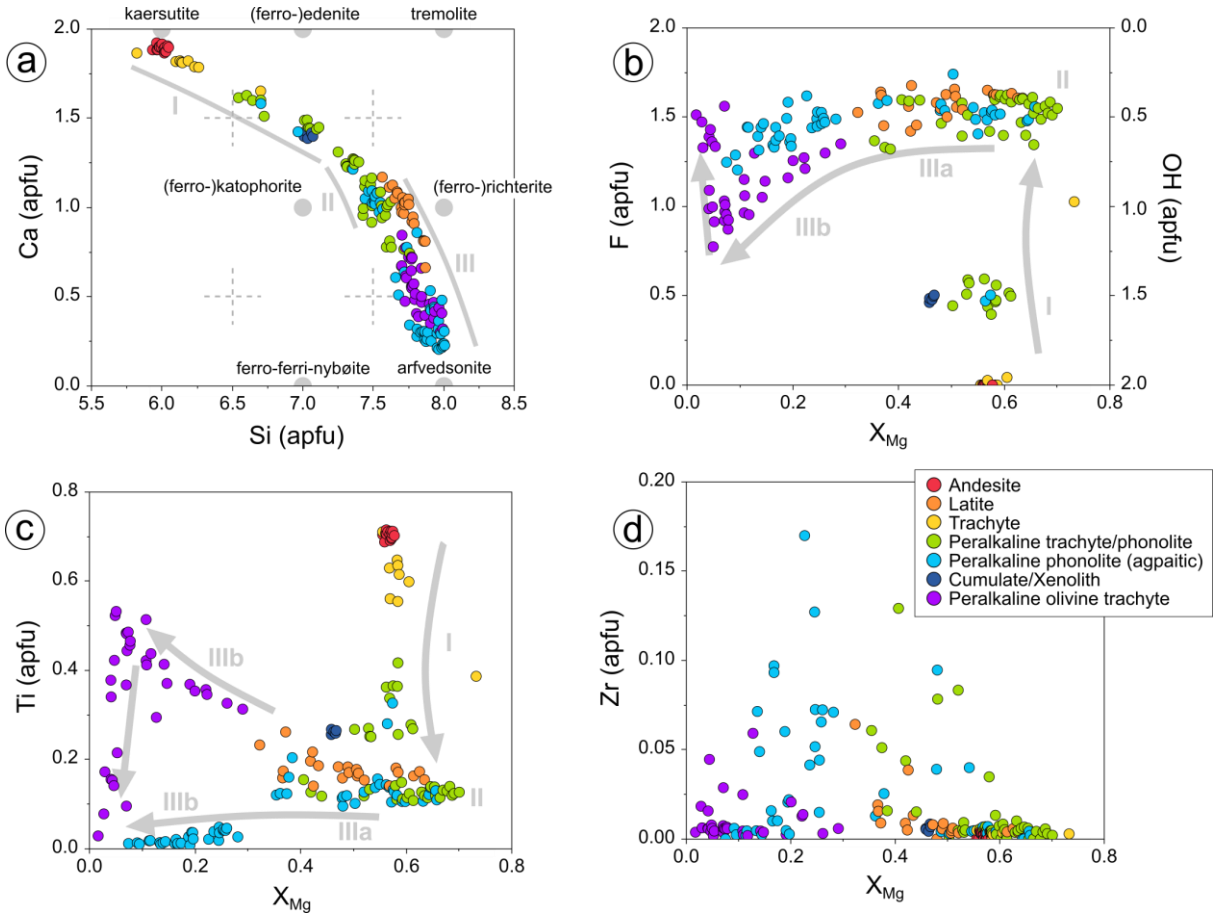


Fig. 12: Amphibole composition from the rocks from Tarosero. a) Classification (according to Hawthorne *et al.*, 2012) and correlation diagram illustrating the Ca vs Si concentration (in apfu). b-d) Concentration of Ti (b), Zr (c), F and OH (d) vs $X_{Mg}$ (=Mg/[Mg+$Fe^{2+}$]). The grey arrows indicate evolution paths for the amphibole generations I to III.

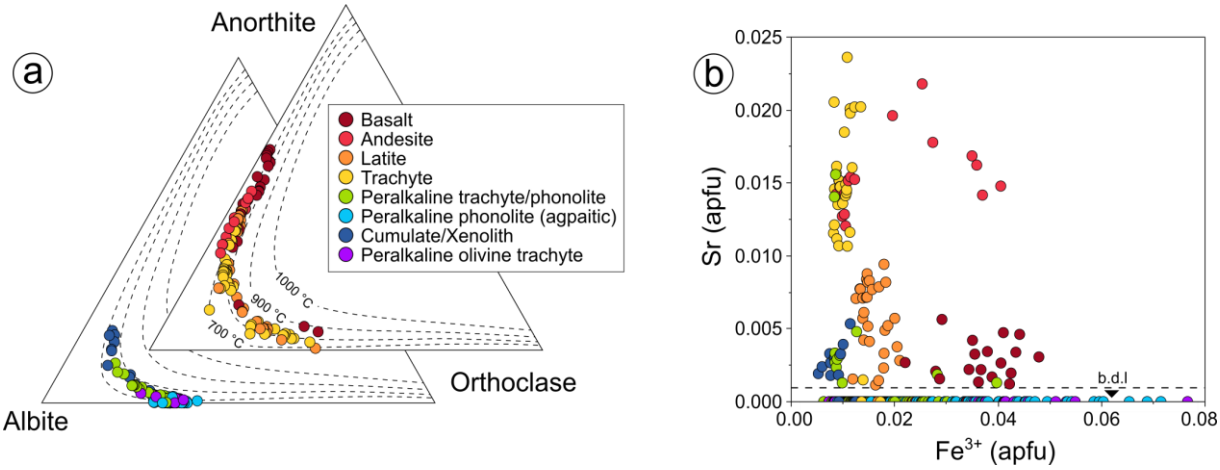


Fig. 13: Feldspar composition from the rocks from Tarosero. a) Ternary albite-anorthite-orthoclase diagram. Isotherms (dashed lines) according to Fuhrman & Lindsley (1988) at a pressure of 1 bar. b) Correlation diagram illustrating the concentration of Sr (apfu) vs $Fe^{3+}$ (apfu).

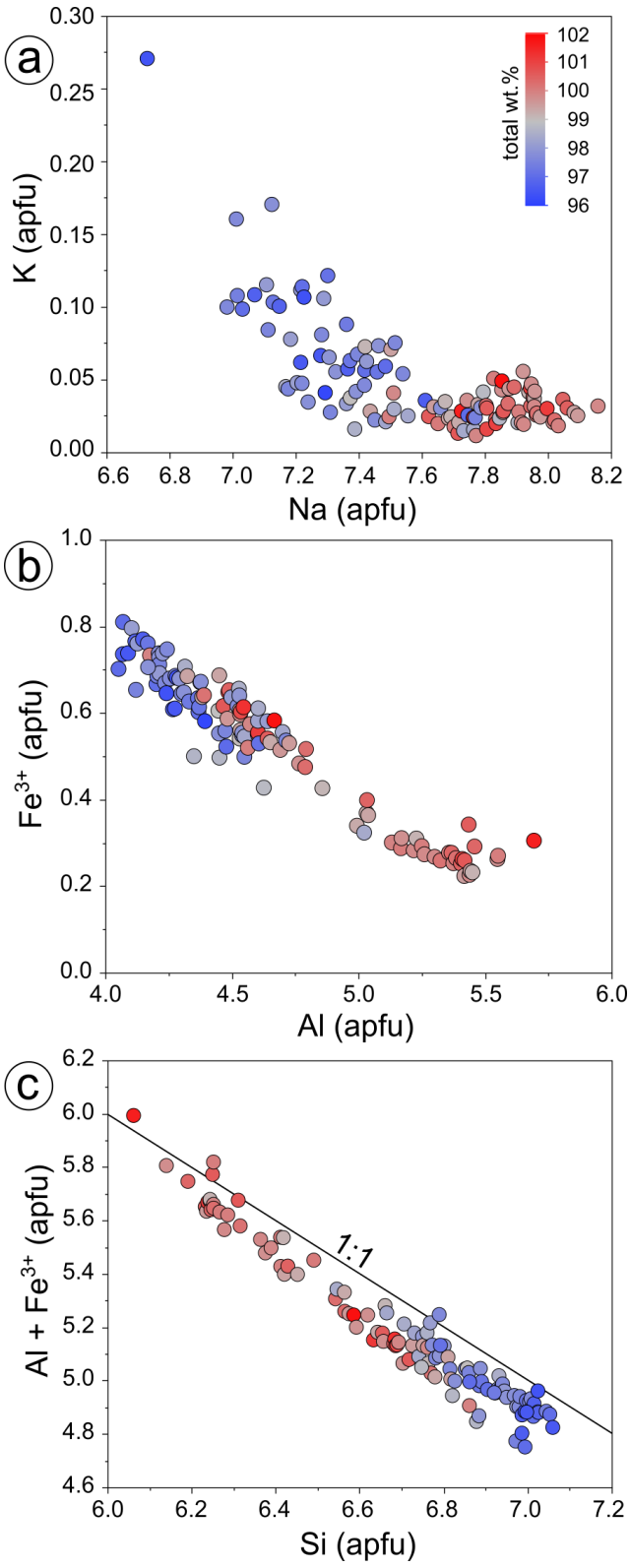


Fig. 14: Sodalite composition of the peralkaline trachytes and peralkaline phonolites from Tarosero. a-c) Correlation diagrams illustrating the K vs Na concentration (a), the $Fe^{3+}$ vs Al concentration (b) and the Al+$Fe^{3+}$ vs Si concentration (c). The variable weight percent totals of the analyses are highlighted by the colour gradient.

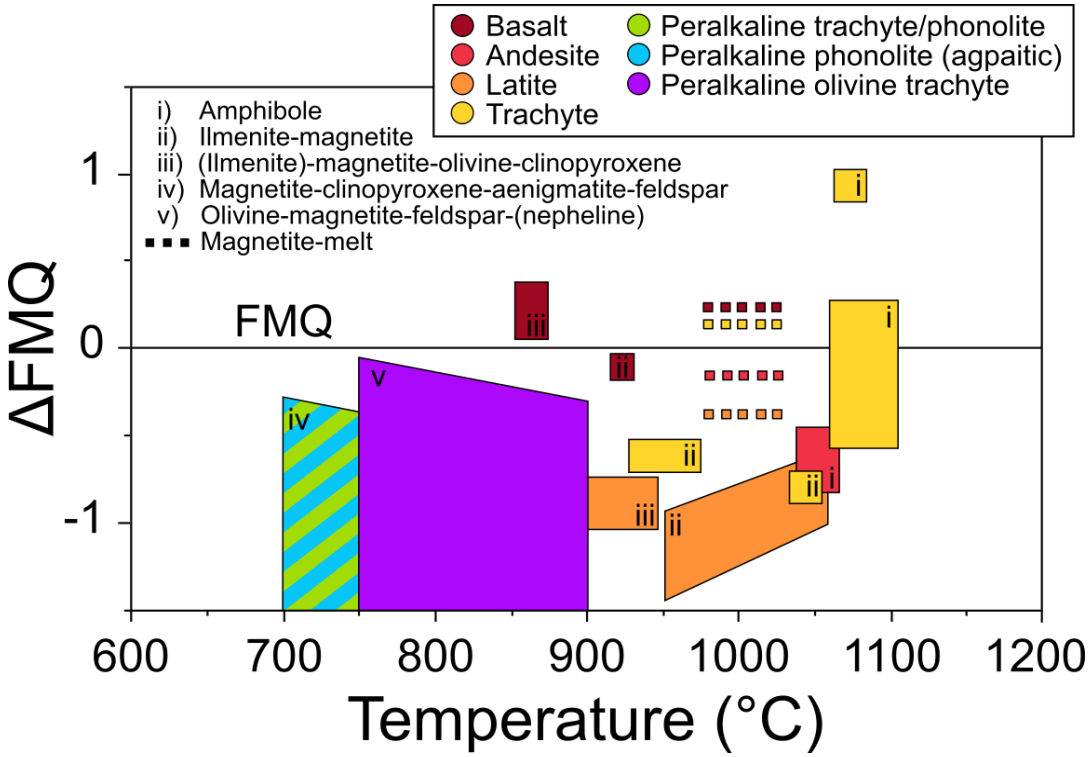


Fig. 15: Estimated temperature vs redox conditions (expressed as ΔFMQ) for the rocks from Tarosero. The numbers i-v) indicate the applied thermo- and oxybarometers. The dotted lines refer to the magnetite-melt oxybarometer of Arató & Audétat (2017), whereas the corresponding temperature has been chosen arbitrarily. See text for further information.

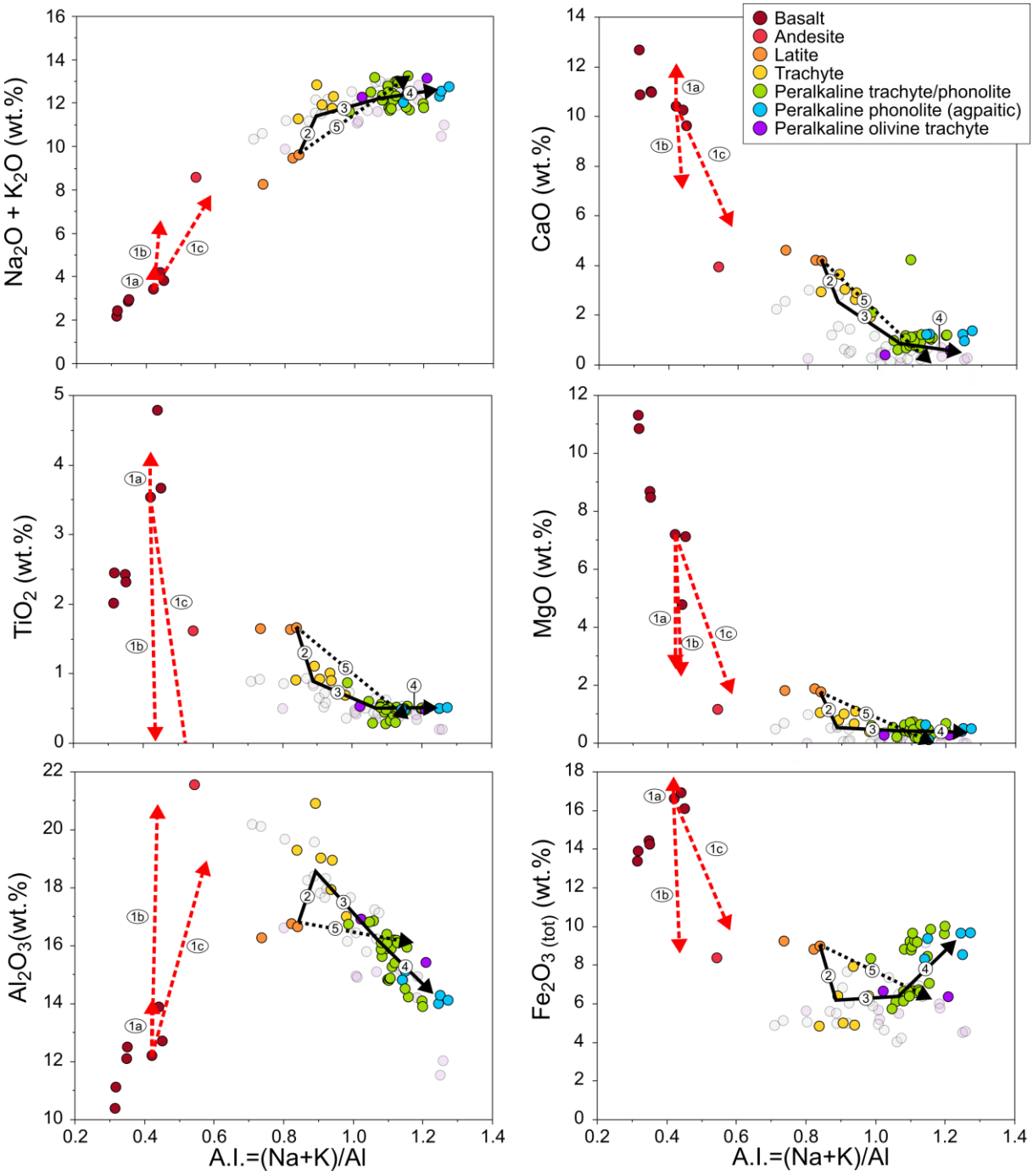


Fig. 16: Fractionation path for the rocks from Tarosero. Numbers refer to Supplementary Table 3. See text for more information.

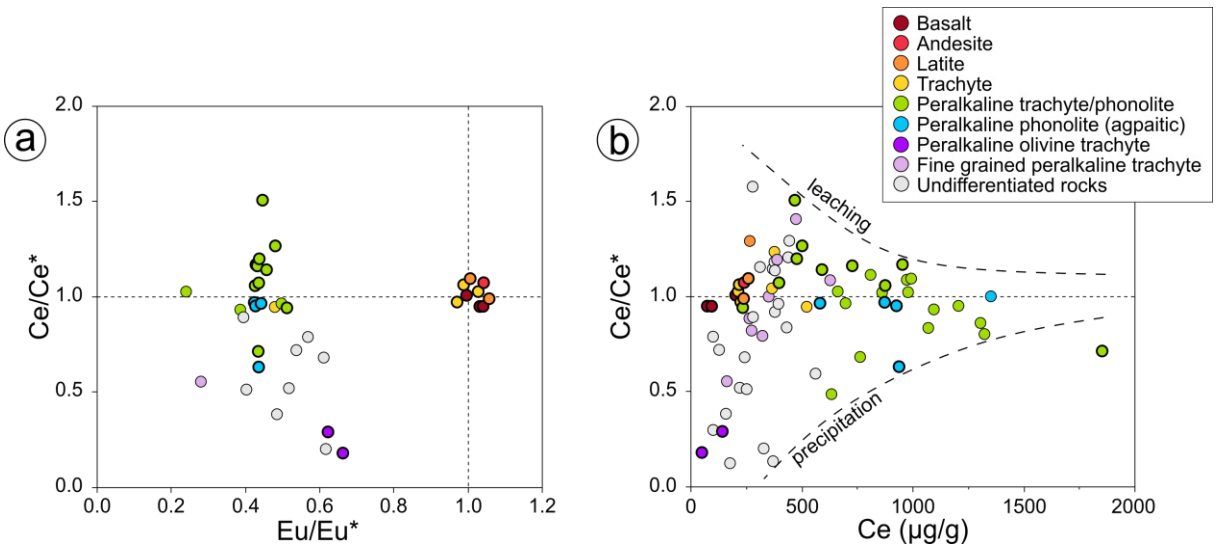


Fig. 17: Ce anomaly vs Eu anomaly (a) and Ce anomaly vs Ce concentration (in µg/g) for the rocks from Tarosero. Anomalies were calculated as $Ce/Ce^*=Ce_N/(La_N*Pr_N)^{0.5}$, respectively $Eu/Eu^*=Eu_N/(Sm_N*Gd_N)^{0.5}$.

# Appendix III

Accepted publication

*Study 3*

Braunger, S., Marks, M.A.W., Walter, B.F., Neubauer, R., Reich, R., Wenzel, T., Parsapoor, A., Markl, G., 2018. The Petrology of the Kaiserstuhl Volcanic Complex, SW Germany: The Importance of Metasomatized and Oxidized Lithospheric Mantle for Carbonatite Generation. Journal of Petrology 59, 1731-1762. http://dx.doi.org/10.1093/petrology/egy078.

JOURNAL OF PETROLOGY

*Journal of Petrology*, 2018, Vol. 59, No. 9, 1731–1762
doi: 10.1093/petrology/egy078
Advance Access Publication Date: 8 August 2018
Original Article

OXFORD

# The Petrology of the Kaiserstuhl Volcanic Complex, SW Germany: The Importance of Metasomatized and Oxidized Lithospheric Mantle for Carbonatite Generation

**S. Braunger *, M. A. W. Marks, B. F. Walter, R. Neubauer, R. Reich, T. Wenzel, A. Parsapoor and G. Markl**

Fachbereich Geowissenschaften, Eberhard Karls Universität Tübingen, Wilhelmstr. 56, D-72074 Tübingen, Germany

*Corresponding author. Fachbereich Geowissenschaften, Eberhard Karls Universität Tübingen, Wilhelmstr. 56, D-72074 Tübingen, Germany. Telephone: +49-(0)7071-29-73155. Fax: +49-(0)7071-29-3060. E-mail: simon-johannes.braunger@student.uni-tuebingen.de

Received February 22, 2018; Accepted July 31, 2018

## ABSTRACT

The Miocene Kaiserstuhl Volcanic Complex (Southwest Germany) consists largely of tephritic to phonolitic rocks, accompanied by minor nephelinitic to limburgitic and melilititic to haüynitic lithologies associated with carbonatites. Based on whole-rock geochemistry, petrography, mineralogy and mineral chemistry, combined with mineral equilibrium calculations and fractional crystallization models using the Least Square Fitting Method, we suggest that the Kaiserstuhl was fed by at least two distinct magma sources. The most primitive rock type of the tephritic to phonolitic group is rare monchiquite (basanitic lamprophyre) evolving towards tephrite, phonolitic tephrite, phonolitic noseanite, nosean phonolite and tephritic phonolite by fractional crystallization of variable amounts of clinopyroxene, amphibole, olivine, spinel/magnetite, garnet, titanite, plagioclase and nosean. During this evolution, temperature and silica activity ($a\mathrm{SiO_2}$) decrease from about 1100°C and $a\mathrm{SiO_2} = 0{\cdot}6$–$0{\cdot}8$ to 880°C and $a\mathrm{SiO_2} = \sim 0{\cdot}2$. At the same time, oxygen fugacity ($f\mathrm{O_2}$) increases from $\Delta\mathrm{FMQ}^* = +2$–$3$ to $\Delta\mathrm{FMQ}^* = +3$–$5$, with $\Delta\mathrm{FMQ}^*$ being defined as the log $f\mathrm{O_2}$ deviation from the silica activity-corrected FMQ buffer curve. Nephelinitic rocks probably derive by fractionation of mostly olivine, spinel/magnetite, melilite, perovskite and nepheline from an olivine melilititic magma. The nephelinitic rocks were formed at similarly high crystallization temperatures (>1000°C) and evolve towards limburgite (hyalo-nepheline basanite) by an increase of silica activity from about $a\mathrm{SiO_2} = 0{\cdot}4$–$0{\cdot}5$ to $a\mathrm{SiO_2} = 0{\cdot}5$–$0{\cdot}9$, whilst redox conditions are buffered to $\Delta\mathrm{FMQ}^*$ values of around +3. Haüyne melilitite and the more evolved (melilite) haüynite may equally be derived from an olivine melilitite by more intense olivine and less melilite fractionation combined with the accumulation of haüyne, clinopyroxene and spinel. These rocks were crystallized at very low silica activities ($a\mathrm{SiO_2} \leq 0{\cdot}2$) and highly oxidized conditions ($\Delta\mathrm{FMQ}^* = +4$–$6$). Even higher oxygen fugacities ($\Delta\mathrm{FMQ}^* = +6$–$7$) determined for the carbonatite suggests a close genetic relation between these two groups. The assemblage of carbonatites with highly oxidized silicate rocks is typical of many carbonatite occurrences worldwide, at least for those associated with melilititic to nephelinitic silicate rocks. Therefore, we suggest that the existence of highly oxidized carbonate-bearing sublithospheric mantle domains is an important prerequisite to form such complexes.

**Key words:** alkaline magmatism; carbonatites; fractional crystallization; Kaiserstuhl; mantle sources; redox conditions

## INTRODUCTION

Most of the about 500 known carbonatite occurrences worldwide are spatially and temporally associated with alkaline rocks, which implies that both rock groups are genetically closely related (e.g. Woolley, 2001; Woolley & Kjarsgaard, 2008). Two major hypotheses for the formation of carbonatites are discussed: (1) partial melting of a carbonate-bearing peridotite leading to primary carbonatitic magmas (e.g. Wallace & Green, 1988; Harmer *et al.*, 1998; Ying *et al.*, 2004) and (2) fractional crystallization of a carbonate-bearing (nephelinititc to melilititic) parental silicate melt resulting in the formation of exsolved/residual carbonatitic magmas (Gittins, 1989, Kjarsgaard & Peterson, 1991; Gittins & Jago, 1998; Halama *et al.*, 2005; Brooker & Kjarsgaard, 2011).

The source region for most carbonatites and associated alkaline rocks is the (sub)lithospheric mantle (Bell & Simonetti, 2010). The oxidation state of the Earth's lithospheric mantle, however, varies over several orders of magnitude, which is commonly expressed as the log-deviation from the synthetic fayalite–magnetite–quartz (FMQ) buffer (e.g. Frost, 1991). For example, subduction-related peridotites record an average oxidation state of $\Delta$FMQ $> +0{\cdot}5$, whereas cratonic mantle lithosphere shows a much more reduced average oxidation state of almost $\Delta$FMQ $=$ -3 (e.g. Frost & McCammon, 2008; Foley, 2011 and references therein). Highly variable redox conditions (and silica activities) during the crystallization of alkaline rocks are reflected in their diverse mineralogy, as rocks with olivine–augite-Fe–Ti oxide assemblages record $fO_2$ values that are several log units lower than rocks with garnet–augite–titanite assemblages (e.g. Marks *et al.*, 2008*a*; Marks & Markl, 2017). Only few attempts have been undertaken to determine the redox conditions during the crystallization of carbonatites, probably due to the lack of suitable mineral assemblages. The few estimated $fO_2$ values all cluster around (Friel & Ulmer, 1974; Gaspar & Wyllie, 1983; Treiman & Essene, 1984; Ryabchikov *et al.*, 2008) or below the FMQ buffer (Milani *et al.*, 2016). The oxidation state of alkaline rocks associated with carbonatites has rarely been determined. In some cases, they are assumed to have been formed at $fO_2$ conditions around the FMQ buffer (Ryabchikov & Kogarko, 2006), whereas in other cases highly oxidized conditions (4 to 5 log units above FMQ) have been suggested (Halama *et al.*, 2005; Marks *et al.*, 2008*a*). This apparent discrepancy between the redox states of carbonatites and associated silicate rocks is noteworthy, since carbonatitic magma production might be triggered by hydrous redox (e.g. Taylor & Green, 1987), or carbonate redox melting (Foley, 2011). However, to date no attempt has been made to determine the redox conditions for carbonatites and associated alkaline silicate rocks at a given locality.

The Kaiserstuhl Volcanic Complex (KVC) in south western Germany is a well-suited locality for such investigations, as it consists of a variety of alkaline silicate rocks (primitive olivine-bearing tephritic/basanitic and nephelinitic rocks as well as evolved and garnet-bearing phonolites), which are closely associated with carbonatitic rocks (e.g. Keller *et al.*, 1990; Wimmenauer, 2003). However, despite being a classical carbonatite locality, published mineral and whole-rock compositional data for the KVC are fragmentary. No comprehensive petrological study of the KVC exists to date and the detailed genetic relationships between the various rock types are not fully understood (e.g. Schleicher *et al.*, 1990, 1991; Panina *et al.*, 2000). In order to shed light on the formation and evolution of the KVC and similar complexes in general, we present a detailed geochemical, mineralogical and mineral chemical characterization of the different rock types. Combined with fractional crystallization computations and thermodynamic estimates for the crystallization conditions ($P$, $T$, $aSiO_2$, $fO_2$), we show how these parameters influence the mineralogical and geochemical evolution of silicate magmas and how the various KVC rocks are genetically related to one another.

## GEOLOGY

The KVC is part of the European Cenozoic Volcanic Province, situated in the southern part of the Upper Rhine Graben, about 20 km NW of Freiburg, southwest Germany (Fig. 1a; Wilson & Downes, 1991). The Upper Rhine Graben formed as a consequence of the stress field induced by the Alpine Orogeny, which caused lithospheric thinning below the KVC (Edel *et al.*, 1975; Ziegler, 1982). This enabled regional asthenospheric upwelling and the formation of the KVC, which was active between 19 and 16 Ma (e.g. Wimmenauer, 2003; Kraml *et al.*, 2006 and references therein).

The KVC was probably fed by several magma sources: a hypothetical K-basanitic magma produced large volumes of tephrites, sodalite monzogabbros, phonolitic tephrites and phonolites (Wimmenauer, 1962; Keller, 1984*a*). A volumetrically minor sodic rock series consists of olivine nephelinites, basanitic nephelinites and limburgites that are mainly present at the spatially associated Limberg-Lützelberg Complex near Sasbach (Fig. 1a). Melilite-bearing dyke rocks [haüyne melilitites and (melilite) haüynites] and intrusive as well as extrusive carbonatites are largely restricted to the central part of the KVC and are believed to be genetically related to the latter group (e.g. Keller, 1978, 1984*a*; Keller *et al.*, 1990; Schleicher *et al.*, 1990, 1991).

The original size of the Kaiserstuhl volcano during its active period is difficult to reconstruct because of: (i) intense deposition of Quarternary sediments in the Rhine valley and (ii) long-lasting tectonic activity in the Rhine graben during and after the formation of the KVC. Along the eastern flank of the KVC a considerable amount of erosion happened, probably due to westward tilting of parts of the area (Wimmenauer, 2003). Based on published and ongoing geophysical

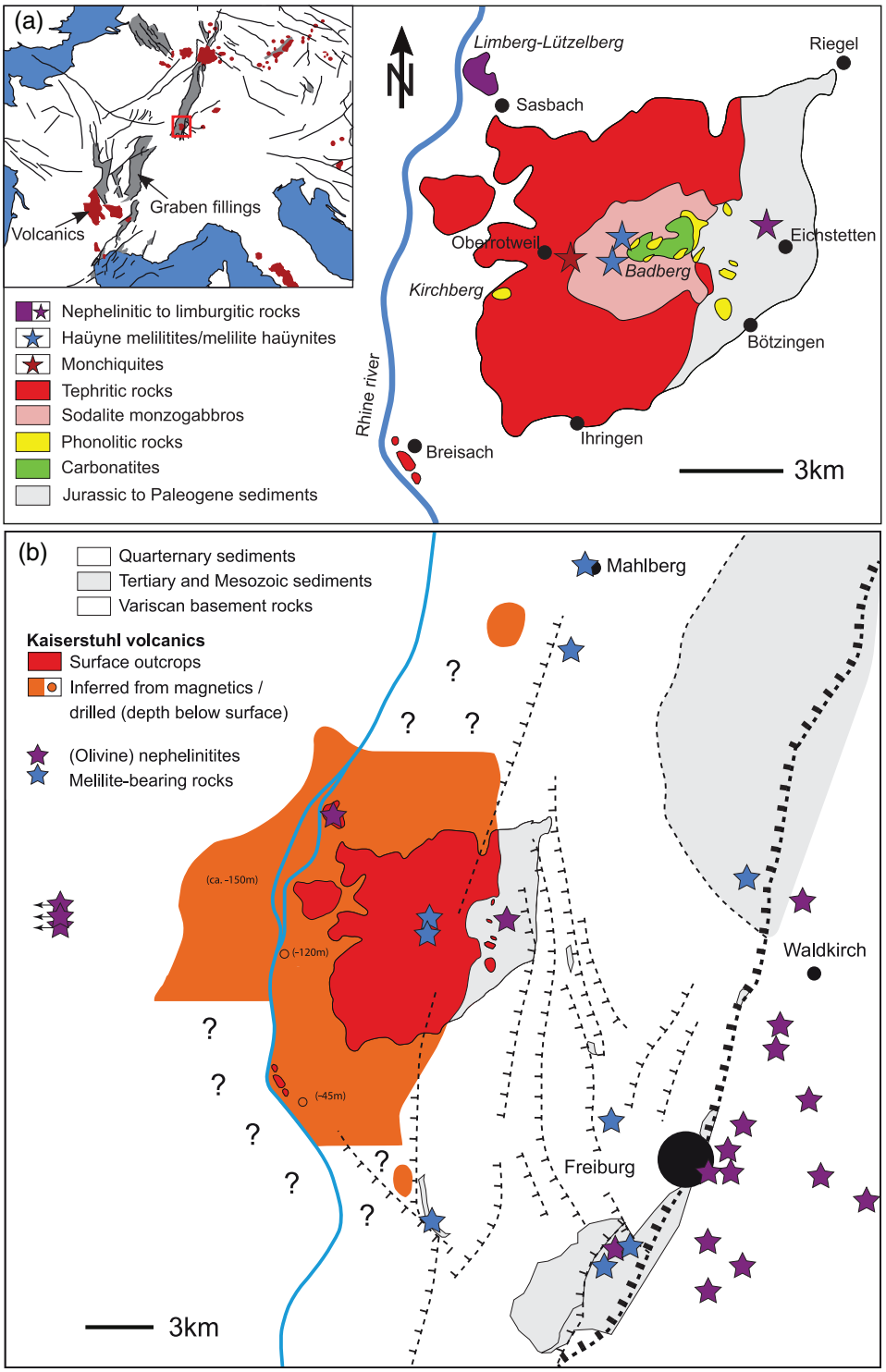


**Fig. 1.** Geology of the Kaiserstuhl Volcanic Complex. (a) Geological map of the European Cenozoic Volcanic Province and the Kaiserstuhl Volcanic Complex. Modified after Keller *et al.* (1990). (b) Sketch map showing the surface exposure of the Kaiserstuhl volcanic rocks combined with sub-surface information from drill holes (Groschopf *et al.* 1996) and geomagnetic work (Pucher, 1991; Bouiflane, 2008; terratec Geophysical Services, unpubl. data). Purple and blue stars indicate the known occurrences of nephelinitic and melilititic rocks, respectively (after Wimmenauer, 1952).

investigations (Pucher, 1991; Bouiflane, 2008; terratec Geophysical Services, unpublished data) and drill-core data (Groschopf *et al.*, 1996; Wimmenauer, 2003) in the immediate vicinity, large volumes of volcanic rocks are hidden below the surface north, east and south of the KVC (Fig. 1b). Thus, the KVC as we see it today is no more than the diminished ruin of a once much larger volcanic complex that originally consisted of a group of

volcanic centres, comparable in size to, e.g. the Mt. Vulture Volcanic Complex (Italy). Further, nephelinitic and melilititic rocks occur in the immediate vicinity of the KVC (purple and blue stars on Fig. 1b), with the most prominent one being the olivine melilitite stock of Mahlberg (e.g. Wimmenauer, 1952; Dunworth & Wilson, 1998). Together with the melilititic rocks of the well-known volcanic fields of Urach (about 150 km NE) and Hegau (about 100 km SE), such strongly $SiO_2$-undersaturated magmas are prominently present on a regional scale, at least partly contemporaneous with the volcanic activity at Kaiserstuhl.

## SAMPLE LOCALITIES

In total, more than 150 samples from surface outcrops and drill holes at Orberg (KB2 1991; Sigmund, 1996) and Horberig (KB3 1991; Blust, 1993) were examined for this study (Table 1; Supplementary Data Fig. S1; supplementary data are available for downloading at http://www.petrology.oxfordjournals.org). Out of these, 89 were investigated in detail by means of whole-rock and/or mineral analyses.

Most samples were taken from the centre of the KVC, which shows the greatest diversity of rock types (carbonatites, melilite- and haüyne-bearing rocks, tephritic and phonolitic rocks). However, several samples from the Limberg-Lützelberg complex and the phonolite quarries at Kirchberg and Fohberg (NW of Bötzingen), as well as rare olivine tephrites (near Breisach), and tephritic and nephelinitic rocks in the western and eastern part of the KVC were also included.

## PETROGRAPHY

The large variety of KVC rocks was classified following the scheme of the *International Union of Geological Sciences, Subcommission on the Systematics of Igneous Rocks*, as summarized in Le Maitre *et al.* (2002), avoiding the (still frequently used) local names wherever possible (Table 2). We distinguish the following four rock groups:

### Nephelinitic to limburgitic rocks

Olivine nephelinites and a basanitic nephelinite contain phenocrysts of olivine (partly altered to goethite and yellow clay minerals) and clinopyroxene (Fig. 2a), the latter additionally occurring as a subhedral to anhedral groundmass phase. Subhedral to anhedral spinel was only found as inclusions in olivine phenocrysts. Magnetite appears as inclusions in the rim areas of olivine and clinopyroxene phenocrysts and as a groundmass phase, where it occasionally shows a composite texture with ilmenite. Rarely, anhedral biotite appears in the nepheline-dominated matrix (Fig. 2a) that might also contain some subhedral plagioclase (HTAC1433).

Limburgites (hyalo-nepheline basanites) have a glassy groundmass and contain olivine (both as euhedral and anhedral grains that are partly altered to iddingsite; Fig. 2b) and sector-or oscillatory zoned euhedral clinopyroxene phenocrysts (rarely with greenish cores). The latter also occurs as small groundmass needles. Subhedral to euhedral spinel appears as inclusions in olivine and as a groundmass phase, locally evolving towards magnetite (Fig. 2c). Magnetite also occurs as inclusions in clinopyroxene.

Olivine tephrites contain several mm in size, rounded macrocrysts of olivine (frequently altered to iddingsite) that may contain spinel inclusions, and euhedral, strongly altered olivine in the groundmass (Fig. 2d). Oscillatory-zoned rose-brownish clinopyroxene appears in variable sizes and commonly contains magnetite inclusions in its darker rim areas (Fig. 2e) as well as rare inclusions of olivine. Plagioclase forms subhedral grains in the groundmass and dominates over alkali feldspar.

### Melilititic to haüynitic rocks

Haüyne melilitites, melilite haüyinites and haüynites occur as porphyritic dyke rocks and contain variable amounts of melilite, haüyne, clinopyroxene, and magnetite phenocrysts (Fig. 2f). All of these phases also occur in their groundmass. In haüyne melilitites, perovskite appears as phenocrysts and as smaller cruciform-twinned crystals in the matrix (Fig. 2g). Melilite haüynites and haüynites, however, lack perovskite phenocrysts, but contain euhedral garnet instead (Fig. 2h). Haüyne is zoned with the cores containing exsolved Fe-sulfides. Further felsic mineral phases are nepheline and rare alkali feldspar, which occurs as small flakes and represents a late mineral phase. Apatite is ubiquitous. Notably, a large proportion of calcite is found in haüyne melilitites as individual anhedral grains (Fig. 2f), within cracks and as an alteration product of melilite.

Coarse-grained haüynolites and melteigites appear as cm- to dm-sized xenoliths in the foiditic and phonolitic rocks (Bakhashwin, 1975; Seeger, 2015). Yellowish euhedral clinopyroxene occurs in variable modal amounts and sizes, typically with greenish rims (Fig. 3a). Oscillatory zoned garnet is present as euhedral to subhedral crystals, in places intergrown with clinopyroxene (Fig. 3b). Haüyne (commonly replaced by natrolite) is only present in the haüynolites, whereas nepheline occurs as an intercumulus phase in melteigites. The latter can additionally contain tabular plagioclase (Fig. 3c). Occasionally, magnetite, pyrite and pyrrhotite can be observed. Titanite and apatite are ubiquitous, while perovskite (Fig. 3d) is only present in some melteigites.

### Tephritic to phonolitic rocks

This heterogeneous group of rocks constitutes the dominant part of the KVC (see details in Kim, 1985) and can be divided into primitive (monchiquites), intermediate (tephrites, phonolitic tephrites/sodalite monzogabbros, mesocratic tephritic phonolites and melanocratic phonolites)

**Table 1:** Location with UTM coordinates of the investigated samples.

| Number | Sample | Location | UTM coordinates | Name |
|---|---|---|---|---|
| 1 | HTAC1446 | Limberg | 32 U 396072 5333966 | Limburgite |
| 2 | HTAC1443 | Limberg | 32 U 396167 5333725 | Limburgite |
| 3 | HTAC1438 | Limberg | 32 U 396187 5333554 | Limburgite |
| 4 | HTAC1436 | Ltzelberg | 32 U 396526 5333258 | Olivine nephelinite |
| 5 | HTAC1415 | Katharinenberg | 32 U 402288 5329644 | Olivine sövite |
| 6 | HTAC1433 | Eichstetten/ Schenkelgrub | 32 U 404972 5328280 | Basanitic nephelinite |
| 7 | HTAC1412 | Orberg | 32 U 402482 5329092 | Phonolitic tephrite |
| 7 | HTAC1393 | Orberg | 32 U 402484 5329085 | Phonolitic tephrite |
| 8 | HTAC1356 | Orberg | 32 U 402640 5328781 | Monticellite sövite |
| 8 | HTAC0231 | Orberg | 32 U 402626 5329020 | (Wollastonite-bearing) nosean phonolite |
| 8 | HTAC0232 | Orberg | 32 U 402665 5329041 | Phonolitic tephrite |
| 9 | HTAC1291 | Orberg Drilling KB2 | 32 U 402477 5328680 | Phonolitic noseanite |
| 10 | HTAC290 | Degenmatt | 32 U 403049 5328638 | Mesocratic tephritic phonolite |
| 10 | HTAC291 | Degenmatt | 32 U 403041 5328629 | Phonolitic noseanite |
| 10 | HTAC293 | Degenmatt | 32 U 403038 5328620 | (Wollastonite-bearing) nosean phonolite |
| 11 | HTAC299 | Degenmatt | 32 U 403001 5328410 | Phonolitic noseanite |
| 12 | HTAC1354 | Haselschacher Buck | 32 U 402323 5328107 | Olivine sövite |
| 13 | HTAC1391 | Schelingen | 32 U 401885 5328418 | Sodalite monzogabbro |
| 14 | HTAC0243 | Schelingen | 32 U 401542 5328576 | (Wollastonite-bearing) nosean phonolite |
| 14 | HTAC0244 | Schelingen | 32 U 401528 5328580 | Phonolitic tephrite |
| 14 | HTAC1397 | Schelingen | 32 U 401660 5328612 | Phonolitic tephrite |
| 14 | HTAC1386 | Schelingen | 32 U 401660 5328612 | (Wollastonite-bearing) nosean phonolite |
| 14 | HTAC1407 | Schelingen | 32 U 401660 5328612 | Phonolitic noseanite |
| 15 | HTAC1411 | Oberbergen-Schelingen | 32 U 401064 5328504 | Phonolitic tephrite |
| 16 | HTAC1365 | Hessleter Buck | 32 U 400021 5328614 | Hayne melilitite |
| 16 | HTAC1427 | Pulverbuck | 32 U 399970 5328595 | Phonolitic tephrite/ sodalite monzogabbro |
| 16 | HTAC1406 | Pulverbuck | 32 U 399918 5328612 | Phonolitic tephrite |
| 17 | HTAC1383 | Pulverbuck | 32 U 399856 5328950 | Tephritic phonolite |
| 17 | HTAC1400 | Pulverbuck | 32 U 399842 5328960 | Tephrite |
| 18 | HTAC1341 | Mondhalde | 32 U 399084 5328736 | (Wollastonite-bearing) nosean phonolite |
| 19 | HTAC252 | Horberig | 32 U 400563 5327867 | Phonolitic noseanite |
| 19 | HTAC1332, 1425 | Horberig | 32 U 400587 5327839 | Hayne melilitite |
| 19 | HTAC1333 | Horberig | 32 U 400587 5327839 | Melilite haynite |
| 19 | HTAC1336 | Horberig | 32 U 400563 5327837 | Phonolitic noseanite |
| 20 | HTAC1387 | Horberig | 32 U 400636 5327773 | Phonolitic noseanite |
| 20 | HTAC0218 | Horberig | 32 U 400801 5329041 | Phonolitic tephrite (continued) |
| 20 | HTAC1374 | Horberig | 32 U 400729 5327814 | (Wollastonite-bearing) nosean phonolite |
| 20 | HTAC1379 | Horberig | 32 U 400851 5327912 | Phonolitic noseanite/ (Plagioclase-bearing) melteigite |
| 20 | HTAC1382 | Horberig | 32 U 400652 5327827 | (Wollastonite-bearing) nosean phonolite |
| 20 | GM1430 | Horberig | 32 U 400652 5327810 | Nosean phonolite/haynolite |
| 20 | PS2, 6-8, 10a | Horberig | 32 U 400652 5327810 | Nosean phonolite |
| 20 | PS3, 4 | Horberig | 32 U 400652 5327810 | Nosean phonolite/haynolite |
| 20 | PS5 | Horberig | 32 U 400652 5327810 | Nosean phonolite/melteigite |
| 21 | HTAC1110 | Horberig Drilling KB3 | 32 U 400940 5327843 | Melanocratic phonolite |
| 21 | HTAC1113, 1125, 1133, 1217 | Horberig Drilling KB3 | 32 U 400940 5327843 | Melilite haynite |
| 21 | HTAC1117 | Horberig Drilling KB3 | 32 U 400940 5327843 | Phonolitic tephrite |
| 21 | HTAC1120 | Horberig Drilling KB3 | 32 U 400940 5327843 | Melanocratic phonolite |
| 21 | HTAC1125, 1133, 1217 | Horberig Drilling KB3 | 32 U 400940 5327843 | Melilite haynite |
| 21 | HTAC1172 | Horberig Drilling KB3 | 32 U 400940 5327843 | Hayne melilitite |
| 21 | HTAC1241 | Horberig Drilling KB3 | 32 U 400940 5327843 | Mesocratic tephritic phonolite |
| 22 | HTAC213 | Horberig | 32 U 400849 5327828 | Haynite |
| 22 | HTAC214 | Horberig | 32 U 400849 5327828 | Phonolitic noseanite/ (Wollastonite-bearing) nosean phonolite |
| 22 | HTAC216 | Horberig | 32 U 400796 5327784 | Phonolitic noseanite |
| 22 | HTAC217 | Horberig | 32 U 400729 5327814 | Phonolitic noseanite |
| 23 | HTAC201 | Badloch | 32 U 401181 5327456 | Mesocratic tephritic phonolite |

(continued)

**Table 1:** Continued

| Number | Sample | Location | UTM coordinates | Name |
|---|---|---|---|---|
| 23 | HTAC202 | Badloch | 32 U 401242 5327438 | Phonolitic noseanite |
| 24 | HTAC267 | East of Badloch | 32 U 401359 5327451 | Mesocratic tephritic phonolite |
| 24 | HTAC1360 | East of Badloch | 32 U 401366 5327465 | Haynite |
| 24 | HTAC1390 | East of Badloch | 32 U 401501 5327470 | (Wollastonite-bearing) nosean phonolite |
| 24 | HTAC0268 | East of Badloch | 32 U 401856 5327550 | Nosean syenite |
| 25 | HTAC1398 | Endhalde | 32 U 403779 5326955 | (Wollastonite-bearing) nosean phonolite |
| 26 | HTAC1376, 1377, 1378 | Fohberg | 32 U 403676 5325793 | (Wollastonite-bearing) nosean phonolite/Haynolite |
| 27 | HTAC1389 | Fohberg | 32 U 403881 5325801 | (Wollastonite-bearing) nosean phonolite |
| 28 | HTAC1345 | Fohberg | 32 U 403655 5325623 | (Wollastonite-bearing) nosean phonolite |
| 29 | HTAC1344 | Totenkopf | 32 U 399812 5327020 | Sodalite monzogabbro |
| 30 | HTAC1408 | Totenkopf | 32 U 399669 5327099 | Phonolitic tephrite |
| 31 | HTAC1396, 1402 | Oberrotweil | 32 U 398380 5327327 | Monchiquite |
| 32 | HTAC1369 | Henkenberg Drilling II | 32 U 396571 5327640 | Monchiquite |
| 33 | HTAC1343 | Sponeck | 32 U 394700 5329987 | Sodalite monzogabbro |
| 34 | HTAC1351, 1392 | Kirchberg | 32 U 396728 5326421 | Tephritic phonolite |
| 34 | HTAC1375 | Kirchberg | 32 U 396728 5326421 | (Wollastonite-bearing) nosean phonolite |
| 35 | HTAC1424 | Bchsenberg | 32 U 396249 5325222 | Tephrite |
| 36 | HTAC1423 | Ihringen-Breisach | 32 U 397401 5321607 | Olivine tephrite |
| 37 | HTAC1434 | Breisach | 32 U 393825 5320779 | Olivine tephrite |

Numbers refer to Supplementary Data Fig. S1.

**Table 2:** Average modal mineralogy of investigated Kaiserstuhl rocks

| | Olivine | Clinopyroxene | Spinel/magnetite | Garnet | Amphibole/mica | Titanite | Perovskite | Plagioclase | Alkali feldspar | SGM[1] | Nepheline | Melilite | Wollastonite | Apatite | Carbonate | Colour code | Old (local) name |
|---|---|---|---|---|---|---|---|---|---|---|---|---|---|---|---|---|---|
| **Nephelinitic to limburgitic rocks** | | | | | | | | | | | | | | | | | |
| Olivine nephelinite | 22 | 42 | 8 | | 2 | | | | | | 26 | | | | | | Olivine nephelinite |
| Basanitic nephelinite | 18 | 46 | 8 | | 2 | | | 6 | | | 20 | | | | | | Olivine nephelinite |
| Limburgite | 16 | 46 | 10 | | | | | X | | | X | | | | | | Limburgite |
| Olivine tephrite | 8 | 42 | 8 | | | | | 32 | 4 | 6 | | | | Tr | | | Olivine tephrite |
| **Melilitic to haüynitic rocks** | | | | | | | | | | | | | | | | | |
| Haüyne melilitite | | 6 | 8 | | 6 | | 4 | | | 26 | 8 | 34 | | Tr | 8 | | Bergalite |
| Melilite haüynite | | 20 | 8 | 16 | 2 | | 2 | | | 36 | 8 | 8 | | Tr | | | Haüynophyre |
| Haüynite | | 24 | 6 | 18 | | | Tr | | 4 | 40 | 8 | | | Tr | | | Haüynophyre |
| Haüynolite | | 6 | 2 | 10 | | Tr | | | | 82 | | | | Tr | | | |
| (Plagioclase-bearing) melteigite | | 70 | 8 | 2 | 4 | Tr | Tr | 6 | | | 10 | | | Tr | | | |
| Melteigite | | 76 | 6 | 6 | | Tr | Tr | | | | 12 | | | Tr | | | |
| **Tephritic to phonolitic rocks** | | | | | | | | | | | | | | | | | |
| Monchiquite | 10 | 44 | 10 | | 4 | | | X | | | X | | | | | | Olivine monchiquite |
| Tephrite | | 38 | 10 | | 2 | | | 32 | 6 | 12 | | | | Tr | | | Tephrite |
| Phonolitic tephrite/sodalite monzogabbro | | 36 | 8 | | 4 | Tr | | 32 | 12 | 8 | | | | Tr | | | Phonolitic tephrite/essexite |
| Mesocratic tephritic phonolite | | 30 | 14 | | 10 | | | 10 | 24 | 12 | | | | Tr | | | Gauteite |
| Melanocratic phonolite | | 40 | 8 | | 8 | | | | 22 | 22 | | | | Tr | | | Shonkinite porphyry |
| Phonolitic noseanite | | 18 | | 14 | | | | | 20 | 36 | 8 | | 4 | Tr | | | Tinguaite |
| Nosean phonolite/syenite | | 14 | | 10 | | Tr | | | 48 | 28 | | | | Tr | | | Phonolite/ledmorite-foid syenite |
| (Wollastonite-bearing) nosean phonolite | | 6 | | 2 | | | | | 68 | 14 | | | 10 | Tr | | | Phonolite |
| Tephritic phonolite | | 6 | Tr | 2 | | Tr | | 10 | 76 | 6 | | | | Tr | | | Phonolite |
| **Carbonatites** | | | | | | | | | | | | | | | | | |
| Olivine sövite | 10 | | 8 | | | | | | | | | | | Tr | 82 | | Magnetite-Forsterite-Sövite |
| Monticellite sövite | 14[2] | | 4 | | Tr | | | | | | | | | 2 | 80 | | Magnetite-Monticellite-Sövite |

(X) Minerals are present in the glass matrix. (Tr) Trace minerals. ([1]) SGM, Sodalite group Minerals; ([2]) Monticellite instead of olivine.

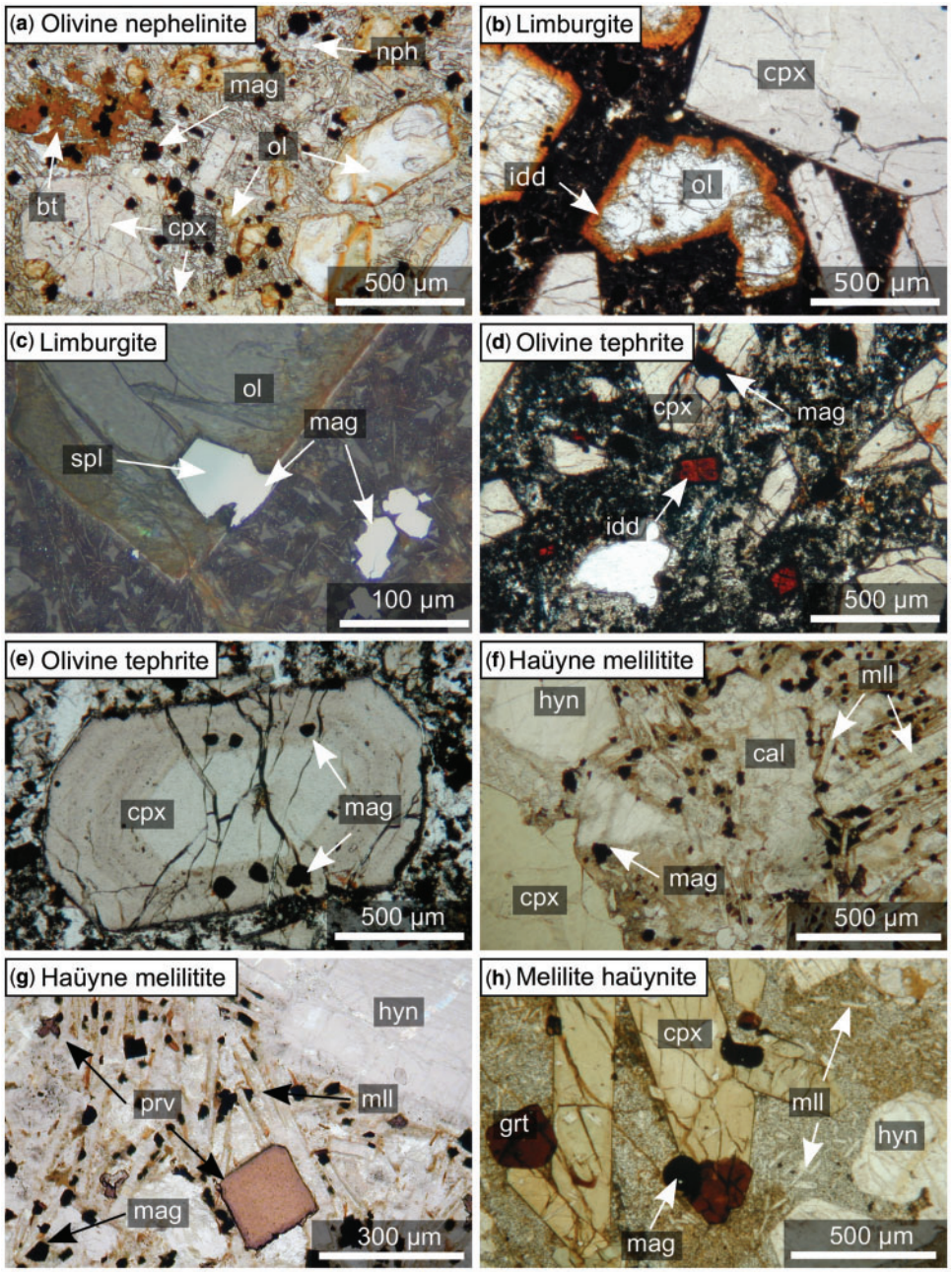


**Fig. 2.** Mineral textures in nephelinitic to limburgitic and melilititic to haüynitic rocks. (a) Olivine (ol) and clinopyroxene (cpx) phenocrysts in olivine nephelinite with nepheline (nph), biotite (bt) and magnetite (mag) being typical groundmass phases (HTAC1436-2). (b) Clinopyroxene and olivine macrocrysts set in a largely glassy groundmass in limburgite HTAC1446. Red olivine rim consists of iddingsite (idd). (c) Combined transmitted and reflected light image of limburgite HTAC1446. A spinel (spl) inclusion in olivine gradually evolves into magnetite. (d) In olivine tephrites, groundmass olivines are totally replaced by iddingsite (HTAC 1423–2). (e) Magnetite inclusions in zoned clinopyroxene (olivine tephrite HTAC1423–1). (f) The main mineral phases of haüyne melilitites are melilite (mll), magnetite, calcite (cal), clinopyroxene and haüyne (hyn; HTAC1365). (g) Perovskite (prv) phenocrysts and cruciform-twinned groundmass perovskite in haüyne melilitite (HTAC1332). (h) Melilite haüynite (HTAC1133) containing phenocrysts of garnet (grt), clinopyroxene, magnetite and haüyne.

and evolved members (phonolitic noseanites, nosean phonolites/nosean syenites, and tephritic phonolites), with systematically changing mineralogical features.

Monchiquites contain olivine and clinopyroxene phenocrysts (rarely with greenish cores); the latter mineral also occurs as a groundmass phase. In one sample (HTAC1396a), needle-shaped olivine was observed embedded in zeolite minerals as an inclusion in clinopyroxene. Spinel generally occurs as inclusions in olivine, whereas magnetite is mostly present in clinopyroxene and in the matrix. If present in the groundmass, spinel is always rimed by magnetite (Fig. 4a). The groundmass is largely glassy.

Tephrites are porphyritic and contain euhedral yellowish pale green and oscillatory zoned phenocrysts of clinopyroxene (rarely with greenish cores), which is

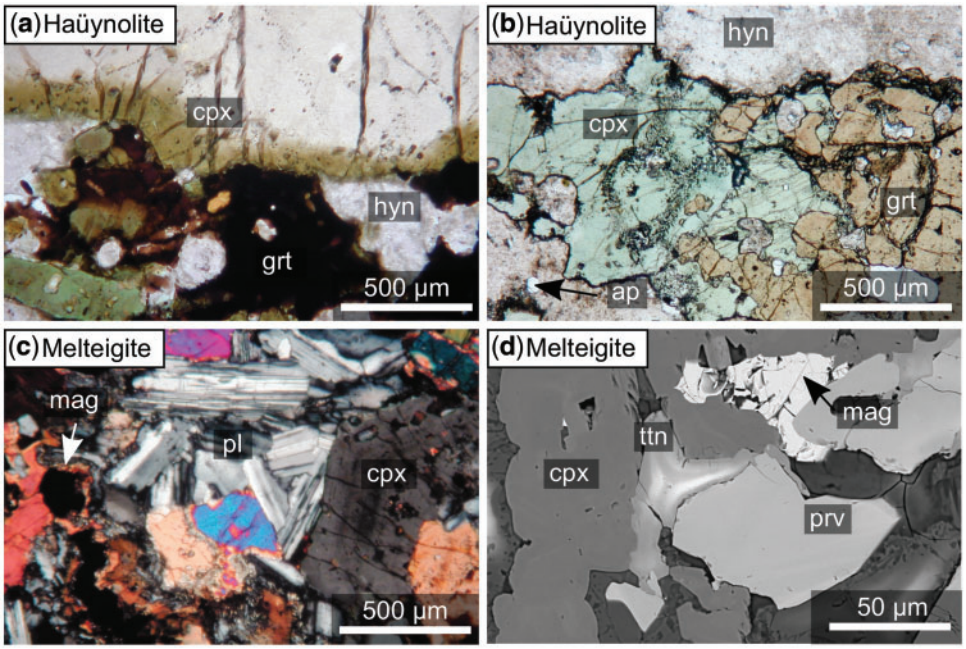


**Fig. 3.** Mineral textures in haüynolites and melteigites. (a) Garnet co-precipitated with dark green clinopyroxene (haüynolite GM1430C). (b) Intergrowth of clinopyroxene and garnet in haüynolite HTAC1376, with haüyne being altered to zeolites. (c) Plagioclase, clinopyroxene and magnetite assemblage in melteigite HTAC1379. (d) Perovskite overgrown by titanite in melteigite HTAC1379.

also present as a groundmass phase. Magnetite mainly appears in the matrix, but occurs as inclusions in marginal zones of pyroxene or is partially surrounded by clinopyroxene (Fig. 4b). The amount, type and size of feldspar grains varies strongly among individual samples. Plagioclase occurs as a groundmass phase and is partly altered to zeolites. Alkali feldspar occasionally surrounds plagioclase, but also appears as individual grains. Contrary to rarely occurring leucite crystals, which are always completely replaced by analcime, euhedral sodalite was only partially affected by this late stage alteration. Some of the more evolved and hence alkali feldspar-bearing samples contain up to 1 mm biotite and amphibole phenocrysts (Fig. 4c). Biotite additionally occurs as small grains in the groundmass, and apatite is the most common accessory mineral. Sodalite monzogabbros are mineralogically very similar to tephrites but have an equigranular and medium-grained texture. Amphibole always occurs as subhedral to euhedral crystals (Fig. 4c), whereas biotite is generally anhedral (Fig. 4d). Both minerals partly replace oscillatory zoned clinopyroxene and mostly subhedral magnetite. The latter additionally occurs as inclusions in clinopyroxene. One sample (HTAC1344) contains composite ilmenite–magnetite intergrowths. Alkali feldspar may enclose tabular plagioclase, but also occurs as euhedral crystals. Apatite and titanite are common accessory phases.

Most phonolitic rocks (phonolitic noseanites, nosean phonolites) have an alkali feldspar-dominated groundmass and lack plagioclase, magnetite and olivine, but contain variable amounts of garnet and wollastonite, except for mesocratic tephritic phonolites and a melanocratic phonolite, which are mineralogically very similar to the above-described tephritic rocks. Phonolitic noseanites (Fig. 4e) contain phenocrysts of bright green and locally needle-shaped clinopyroxene, brown garnet, nosean, nepheline and strongly altered wollastonite. Porphyritic nosean phonolites comprise euhedral bright green clinopyroxene I and variable amounts of subsequently crystallized dark green clinopyroxene II (Fig. 4f). Euhedral and oscillatory zoned brown garnet (Fig. 4g) is in places replaced by a darker garnet generation, which is associated with clinopyroxene II (Fig. 4f). Few samples contain magnetite and titanite, in one sample (HTAC1345) titanite replaces garnet. Magnetite- and titanite-free samples, however, contain euhedral wollastonite, often replaced by natrolite. Euhedral nosean is commonly replaced by analcime, natrolite or calcite. Oscillatory zoned alkali feldspar can be present as tabular phenocrysts and as smaller grains in the groundmass. Coarse-grained nosean syenites are rare and were only found in drill cores south of Badberg (Bakhashwin, 1975) and as xenoliths within the phonolitic rocks (Czygan, 1977). They contain tabular alkali feldspar, nosean (commonly replaced by natrolite), euhedral and greenish clinopyroxene (in some cases with a yellowish core), euhedral to subhedral oscillatory zoned garnet and blocky apatite. Magnetite is only present in one sample (HTAC268B). Titanite is ubiquitous, generally subhedral to euhedral. Only in one sample (HTAC1375) it is absent and wöhlerite ($Na_2Ca_4ZrNb[F|O_3|(Si_2O_7)_2]$) is present instead.

Tephritic phonolites (Kirchberg and Oberrotweil localities) are distinguished from nosean phonolites and phonolitic noseanites, as they contain anhedral garnet, show small amounts of nosean, and contain

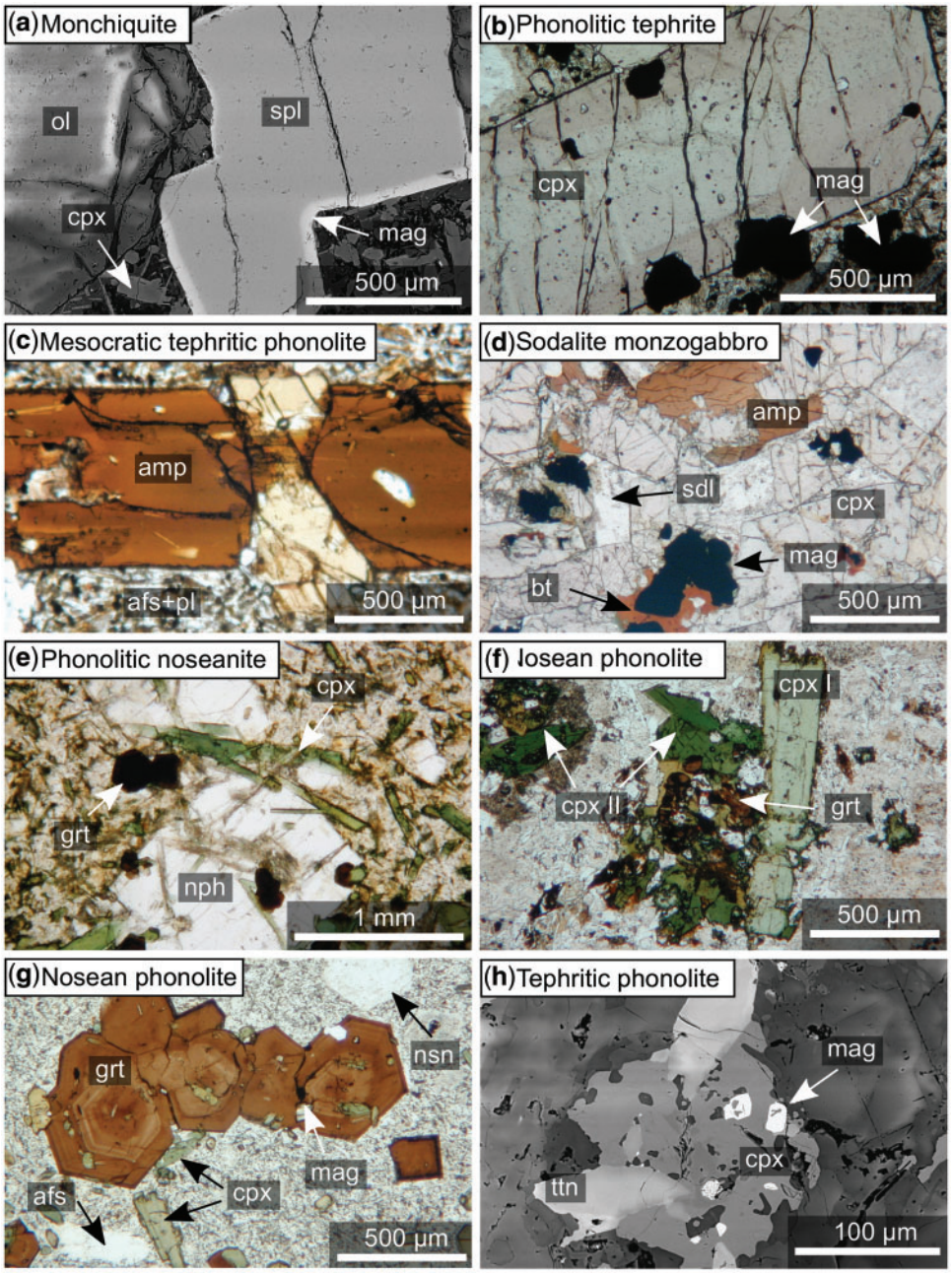


**Fig. 4.** Mineral textures in tephritic to phonolitic rocks. (a) Spinel rimmed by magnetite in monchiquite HTAC1396a (BSE-image). (b) Magnetite aligned in dark clinopyroxene rims (phonolitic tephrite HTAC1411b). (c) Amphibole phenocrysts (amp) embedded in fine-grained plagioclase and alkali feldspar in mesocratic tephritic phonolite HTAC1241. (d) Typical texture of a sodalite monzogabbro with amphibole, clinopyroxene, sodalite (sdl), minor amounts of biotite and magnetite (HTAC1391). (e) Phonolitic noseanites contain nepheline phenocrysts (HTAC216). (f) Two clinopyroxene generations in nosean phonolites (HTAC1345). Late-stage garnet is always associated with clinopyroxene II. (g) Zoned garnet associated with clinopyroxene, magnetite, nosean (nsn) and alkali feldspar in nosen phonolite PS8. (h) Tephritic phonolites (HTAC1351) contain the coexisting mineral assemblage of clinopyroxene, titanite and magnetite (BSE image).

plagioclase phenocrysts. Texturally, clinopyroxene, titanite and magnetite coexist with each other in these rocks (Fig. 4h). One nosean phonolite (HTAC1375) is transitional to tephritic phonolite as it shows the same mineral characteristics except for the absence of plagioclase crystals. Rare trachytes occur southwest of the Badberg (Sutherland, 1967; Koberski, 1992) and were reported from drill hole KB2 (Sigmund, 1996). They are characterized by alkali feldspar phenocrysts, the absence of garnet and minor amounts of feldspathoid minerals.

## Carbonatites

Carbonatites of the KVC include coarse-grained calcite-carbonatite (sövites), medium- to fine-grained calcite-

carbonatite (alvikites), rare medium- to fine-grained dolomite-carbonatite (beforsites) and minor extrusive rocks (lapillistones, tuffs, lavas) and have been described elsewhere in great detail (e.g. Keller, 1978, 1981; Lehnert, 1989). Three sövites from Orberg, Haselschacher Buck and Katharinenberg have been chosen for this study. In addition to calcite, they contain magnetite, phlogopite, pyrochlore and apatite along with rare monticellite (Orberg; Fig. 5a) or olivine (Fig. 5b).

## METHODS

### Whole-rock analyses

Major elements were analysed at the Department of Geosciences, University of Tübingen (Germany), with a wavelength dispersive Bruker AXS S4 Pioneer XRF device (Rh-tube at 4 kW) with 32 standardised samples (compiled in Govindaraju, 1989). Prior to preparation, the samples were ground with an agate mill for 10 minutes. For the fused beads 1.5 g of dried sample powder (at 105 °C) was mixed with 7.5 g MERCK spectromelt A12 (mixture of 66 % Li-tetraborate and 34 % Li-metaborate) and melted at 1200 °C beads using an Oxiflux system from CBR analytical service. Detection limits and analytical errors are sample specific and usually in the range of 0.1 % (relative).

Trace elements were determined by ICP-MS (X-series 2, Thermo Fisher Scientific) at the Institute for Applied Geosciences, Karlsruhe Institute of Technology (Germany) after $HNO_3$-HF-$HClO_4$ acid digestions of powdered material (100 mg). To ensure a complete silicate decomposition, 40% HF (suprapur), 65% $HClO_4$ (normatom) and the pre-oxidized (65% $HNO_3$, subboiled) sample were heated in a closed Teflon vessel for 16 h at 120°C. After evaporating the acids to incipient dryness, the residue was redissolved in 65% $HNO_3$ (subboiled) and evaporated again (three times) for purification purposes. The final residue was dissolved in 50 ml of ultrapure water. The quality assurance of the ICP-MS measurement of the trace elements was done by including the certified reference material CRM-TMDW-A (High-Purity standards, Inc.) into the protocol (accuracy: ± 10% for most elements). Mathematical corrections of Eu, Gd, Tb and Er were necessary due to high concentrations of Ba and light REE; $^{151/153}$Eu was corrected for BaO interferences, $^{157}$Gd for PrO and $^{158}$Gd for CeO interferences, $^{159}$Tb and $^{167}$Er for NdO interferences. The mean value of both isotopes is given for Eu and Gd. To assure the quality of the whole procedure, six blanks and two certified reference materials (SY-2, SY-3; Govindaraju, 1994) were included in the digestion (accuracy: mainly ± 10%). The reproducibility (± 5% for most elements) was checked by digesting a phonolitic sample in triplicate.

### Mineral analyses

Mineral analyses were performed using a JEOL JXA 8900 electron microprobe in wave-length dispersive mode at the Department of Geosciences, University of Tübingen (Germany). Depending on the mineral, an acceleration voltage of 15 kV (felsic minerals) or 20 kV was chosen. The beam current was set to 20 nA, except for garnet, titanite and perovskite analyses which were acquired using a current of 12 nA. The peak counting times for major elements were 16 s and between 30 and 60 s for minor elements. Background counting times were half as long as the peak counting. For calibration, natural and synthetic standards were used. Peak overlap corrections involving Ba–Ti, V–Ti, F–Fe, Sm–Ce and Pr–La were implemented as well as an internal ZAF (garnet, titanite and perovskite) or φrz correction of the raw data (Armstrong, 1991). Garnet, titanite and perovskite analyses were performed with a 5 μm beam diameter since test measurements executed with a smaller beam size led to fluctuating probe currents and visible destruction of the grains due to the long measurement time. Amphibole and biotite were measured with a 2 μm beam spot. Sodium diffusion in felsic minerals was avoided by measuring Na first and widening the beam diameter to 10 μm

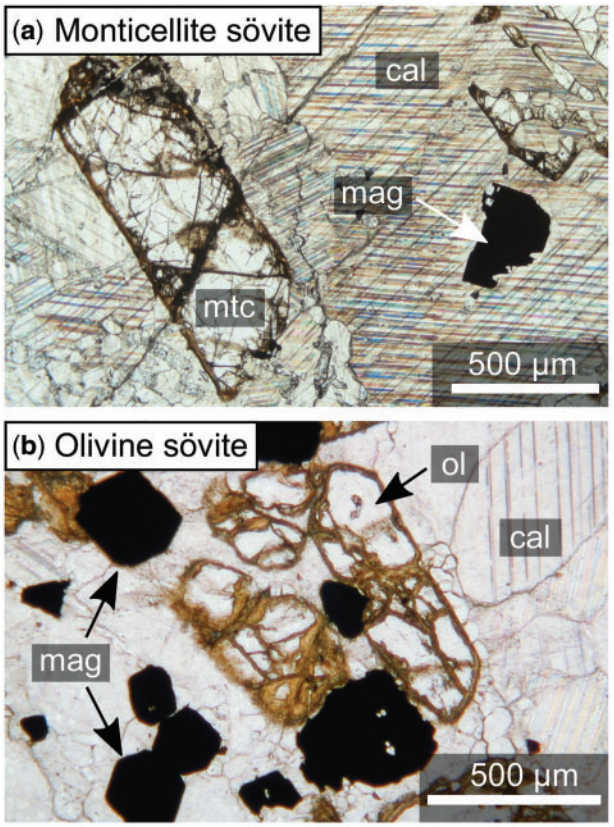


**Fig. 5.** Mineral textures in carbonatites. (a) Sövite carbonatite with monticellite (mtc) and magnetite macrocrysts (HTAC1356). (b) Sövite with olivine and magnetite phenocrysts (HTAC1354).

### Quantification of intrinsic parameters

In order to constrain the crystallization conditions (*P*, *T*, $fO_2$, $aSiO_2$) for the various rock types, several

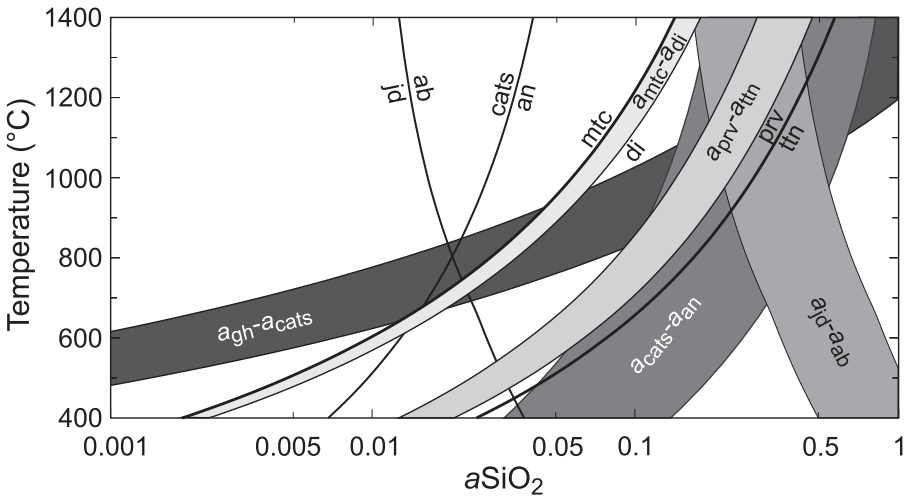


**Fig. 6.** Temperature-$a\mathrm{SiO_2}$ plot illustrating the temperature dependence of the reactions used to determine silica activity. Thick lines represent reactions at unit activities, while the broad fields show their position when typical endmember activities are used.

geothermobarometers were applied and various activity-corrected phase diagrams were computed. Phase diagrams were computed and plotted using the Perple_X software package of Connolly (1990), implemented with the thermodynamic database of Holland & Powell (1998). Thermodynamic properties of titanite and perovskite were taken from Robie & Hemingway (1995) and were checked for internal consistency. Activities for endmember components of alkali feldspar, plagioclase, pyroxene, garnet, Fe–Ti oxides and olivine group minerals were obtained using the solution models of Holland & Powell (2003), Holland (1990), Wood (1979), Cosca *et al.* (1986) and Andersen *et al.* (1993), respectively. Nepheline, melilite, perovskite and titanite activities were calculated using a mixing-on-site model and by assuming oxygen substitution in titanite only being possible in one O site (Tropper & Manning, 2008). Based on the analyses of Weisenberger *et al.* (2014), wollastonite was treated as a pure phase.

Pressure estimations for some of the rocks were possible by applying the temperature-dependent Al-in hornblende barometer of Anderson & Smith (1995). Temperatures have been estimated using the feldspar solution model of Fuhrman & Lindsley (1988) and the amphibole-plagioclase thermometer of Holland & Blundy (1994). For applying the clinopyroxene-liquid thermometer of Putirka *et al.* (1996), we used the whole-rock data as a proxy for the liquid composition. Oxygen fugacity was calculated using the recently calibrated oxybarometer of Arató & Audétat (2017), which is based on the FeO and $TiO_2$ contents of magnetite and the melt. Similar to the clinopyroxene-liquid thermometer, calculations were only performed for samples where xenoliths, xenocrysts or mineral accumulations could be excluded. Combined $f\mathrm{O_2}$, $a\mathrm{SiO_2}$ and temperature estimations for some rocks were possible with the QUILF software of Andersen *et al.* (1993). For other rock types, we used combinations of the following silica-sensitive (reactions 1–7; Fig. 6) and redox-dependent phase equilibria (reactions 8–15):

1. $NaAlSiO_4 + SiO_2 = NaAlSi_2O_6$
2. $NaAlSiO_4 + 2\ SiO_2 = NaAlSi_3O_8$
3. $NaAlSi_2O_6 + SiO_2 = NaAlSi_3O_8$
4. $CaTiO_3 + SiO_2 = CaTiSiO_5$
5. $CaAlASiO_6 + SiO_2 = CaAl_2Si_2O_8$
6. $CaMgSiO_4 + SiO_2 = CaMgSi_2O_6$
7. $2\ Ca_2Al_2SiO_7 + 2\ SiO_2 = CaAlAlSiO_6 + Ca_3Al_2Si_3O_{12}$
8. $9\ CaFeSi_2O_6 + 2\ O_2 = 3\ Ca_3Fe_2Si_3O_{12} + Fe_3O_4 + 9\ SiO_2$
9. $2\ CaSiO_3 + 4\ CaFeSi_2O_6 + O_2 = 2\ Ca_3Fe_2Si_3O_{12} + 4\ SiO_2$
10. $16\ CaFeSi_2O_6 + 2\ CaTiSiO_5 + 3\ O_2 = 2\ Fe_2TiO_4 + 6\ Ca_3Fe_2Si_3O_{12} + 16\ SiO_2$
11. $16\ CaFeSi_2O_6 + 2\ CaTiO_3 + 3\ O_2 = 2\ Fe_2TiO_4 + 6\ Ca_3Fe_2Si_3O_{12} + 14\ SiO_2$
12. $3\ CaFeSi_2O_6 + 3\ FeTiO_3 + O_2 = 3\ CaTiSiO_5 + 2\ Fe_3O_4 + 3\ SiO_2$
13. $2\ CaFeSi_2O_6 + 2\ Fe_2TiO_4 + O_2 = 2\ CaTiO_3 + 2\ Fe_3O_4 + 4\ SiO_2$
14. $2\ CaTiSiO_5 + 2\ Fe_3O_4 + 2\ SiO_2 = 2\ CaFeSi_2O_6 + 2\ Fe_2TiO_4 + O_2$
15. $3\ Fe_2SiO_4 + O_2 = 2\ Fe_3O_4 + 3\ SiO_2$

Relative oxygen fugacity (ΔFMQ) is generally expressed as the deviation from the temperature-dependent FMQ buffer curve in log $f\mathrm{O_2}$ units. However, the use of ΔFMQ is not consistent in the literature. Importantly, this buffer curve is also strongly $a\mathrm{SiO_2}$-dependent and may shift by several log units. Therefore, it is necessary to state $a\mathrm{SiO_2}$ values along with relative oxygen fugacity estimates (e.g. Marks *et al.*, 2008*a*; Zaitsev *et al.*, 2012). We present our results relative to $a\mathrm{SiO_2}$-corrected FMQ buffer curves, expressed as ΔFMQ*.

## Fractional crystallization calculations

Fractional crystallization was modelled using a least squares fitting method based on the assumption that

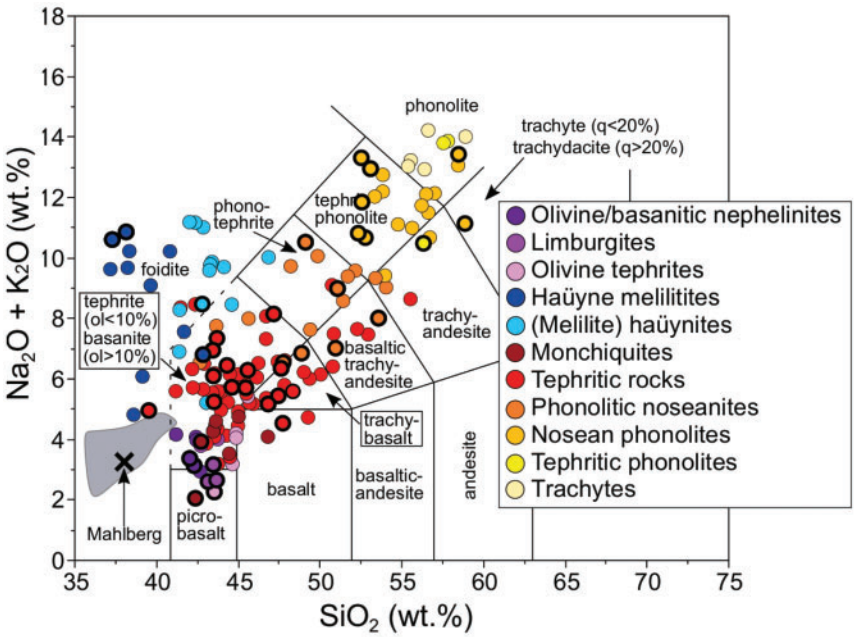


**Fig. 7.** Total alkalies ($Na_2O+K_2O$) vs $SiO_2$ for the silicate rocks of the KVC. New analyses are shown with thick rims, literature data from Bakhashwin (1975), Czygan (1977), Kim (1985), Keller *et al.* (1990), Blust (1993), Panina *et al.* (2000), Sigmund (1996), Wimmenauer (2003) and Grapes & Keller (2010). Grey area illustrates the compositional range of olivine melilitites from SW Germany (Keller *et al.*, 1990; Wilson *et al.*, 1995). Note that the loss of ignition of haüyne melilitites and olivine melilitites may reach ~10 wt %, which is not taken into account in this diagram, as all data are normalized to 100% (anhydrous), ignoring volatile components.

phenocrysts represent the principal products of that process. Whole-rock analyses were used as a proxy for the initial melt compositions and compositional data for the various mineral phases were used to compute the target melt. The quality of the outcome was evaluated by the residual sum of squares ($SSQ=[SiO_2^{target}-SiO_2^{calculated}]^2+[TiO_2^{target}-TiO_2^{calculated}]^2+\ldots$).

## RESULTS

### Whole-rock data

New whole-rock analyses (Supplementary Data Table S1) together with literature data (Bakhashwin, 1975; Czygan, 1977; Kim, 1985; Keller *et al.*, 1990; Blust, 1993; Sigmund, 1996; Panina *et al.*, 2000; Wimmenauer, 2003; Grapes & Keller, 2010) provide a comprehensive overview of the compositional variation of the various lithologies at the KVC (Figs 7–9). The classic TAS diagram (Fig. 7) illustrates an increase of ($Na_2O+K_2O$) and $SiO_2$ concentrations from primitive olivine melilitites, which do not occur at the KVC but are present at several localities in SW Germany (Mahlberg, Urach, Hegau), through olivine/basanitic nephelinites, limburgites, olivine tephrites and monchiquites to tephritic and phonolitic rocks. Haüyne melilitites, melilite haüynites, and haüynites, however, form a distinct group with highly elevated alkali contents.

Two rock series can be distinguished based on the molar Na/K ratio (Fig. 8). The monchiquite is the most primitive rock of the low Na/K group ($< \sim 2$) and shows the highest contents of MgO. With decreasing MgO concentration, major elements either increase ($Na_2O+K_2O$, $Al_2O_3$) or decrease (CaO, $Fe_2O_3$). The correlation between MgO and $Fe_2O_3$ is typical of oxidized rock suites (Giehl *et al.*, 2013; Marks & Markl, 2017). The concentration of $TiO_2$ deviates slightly from this trend as the tephritic rocks show higher values than the monchiquites. The second group shows Na/K ratios $\geq 2$. From olivine melilitites via olivine/basanitic nephelinites, towards limburgites and olivine tephrites (with decreasing MgO), $Al_2O_3$ steadily increases, whereas $Na_2O+K_2O$, CaO, $Fe_2O_3$ and $TiO_2$ remain almost constant. Haüyne melilitites and (melilite) haüynites deviate from this pattern by higher $Na_2O+K_2O$, CaO and $Al_2O_3$ and lower $Fe_2O_3$ and $TiO_2$ concentrations, which additionally either positively (CaO, $Fe_2O_3$, $TiO_2$) or negatively ($Na_2O+K_2O$, $Al_2O_3$) correlate with MgO.

With decreasing MgO, compatible elements such as Ni (up to 560 ppm) or Cr (up to 1400 ppm) steadily decrease, whereas incompatible elements such as Zr ($\leq$770 ppm), Nb ($\leq$620 ppm), La ($\leq$350 ppm), Ce ($\leq$630 ppm) and Pb ($\leq$35 ppm) increase (Fig. 9). However, REE and HFSE concentrations in the haüyne melilitites and (melilite) haüynites are similar or even higher than those of the phonolitic rocks, which have lower MgO.

Primitive-mantle normalized (Palme & O'Neill, 2003) REE patterns of whole-rocks (Fig. 10) show a decrease from light to heavy REE. The normalized REE concentrations increase in parallel from monchiquite via tephrite to phonolitic tephrite. Phonolitic noseanites and especially nosean phonolites have steeper patterns and flatten out towards the HREE. The REE pattern of the

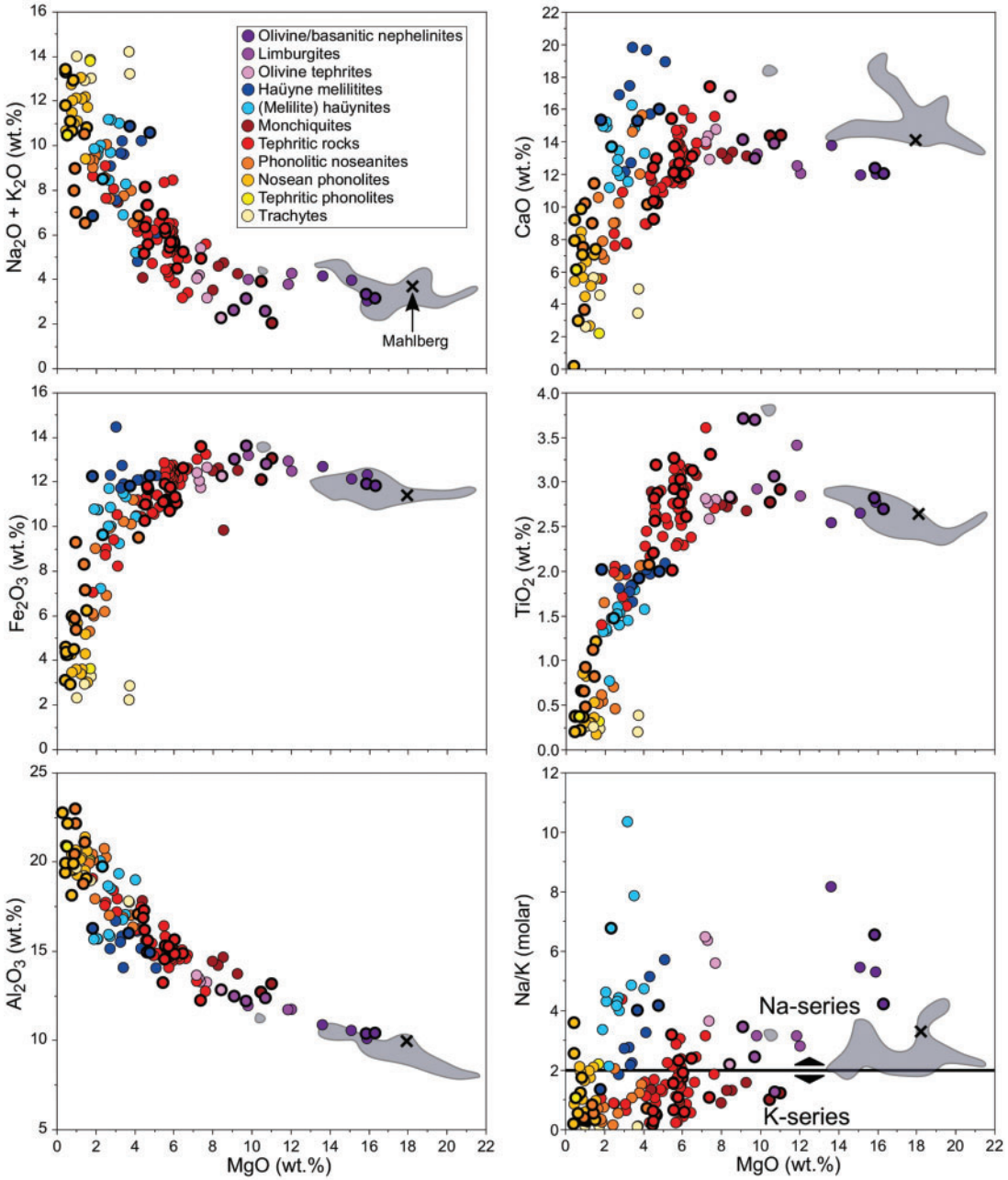


**Fig. 8.** Correlation diagrams for the various volcanic rocks of the KVC. Olivine melilitites from SW Germany are shown as a grey field (data from Keller *et al.*, 1990; Wilson *et al.*, 1995).

tephritic phonolite is less steep and increases from Ho to Lu. The nephelinitic to limburgitic rocks show a similar pattern to the monchiquites, whereas the melilititic to haüynitic rocks exhibit elevated concentrations and are depressed in the middle REE.

## Mineral data

### *Olivine group*

Olivine in the KVC is invariably Mg-rich (Fig. 11a; Supplementary Data Table S2), with $Fo_{96–90}$ in carbonatites, $Fo_{90–79}$ in olivine nephelinites (due to growth zonation), $Fo_{86–79}$ in limburgites and $Fo_{86–77}$ in monchiquites. Rounded macrocrysts in olivine tephrites are $Fo_{85–83}$, whereas groundmass olivines are $Fo_{72–71}$ (including data from Kim, 1985, shown as rectangles in Fig. 11a). The larnite component is highest in olivine/basanitic nephelinites and monchiquites (up to 0·9 mol %) among the silicate rocks, whereas in some carbonatite samples, the larnite component exceeds 1 mol %. The Ni content roughly correlates with Ca and is highest in the olivine/basanitic nephelinite macrocrysts (up to 0·007 apfu; Fig. 11b). The composition of some of these grains is typical of mantle olivines (e.g. Foley *et al.*, 2013; Bussweiler *et al.*, 2015). Olivine from carbonatite samples is distinctly higher in Mn (0·04–0·06 apfu) compared to olivine from the silicate rocks (≤0·01 apfu; Fig. 11c). Monticellite only

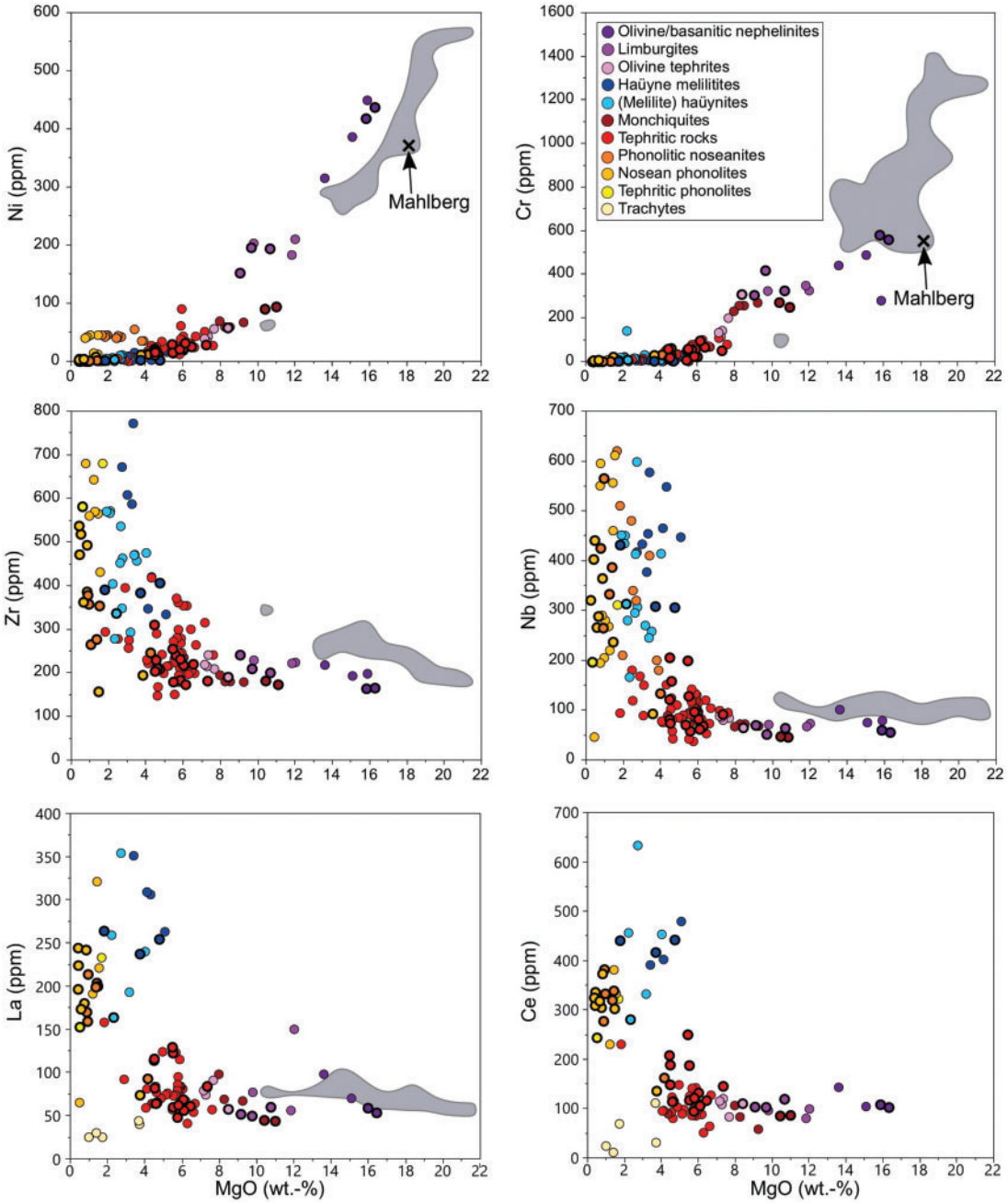


**Fig. 9.** Whole-rock trace element concentrations (in ppm) of Ni, Cr, Zr, Nb, La and Ce vs MgO (wt %). Olivine melilitites from SW Germany are shown as a grey field (data from Keller *et al.*, 1990; Wilson *et al.*, 1995).

occurs in one carbonatite sample (HTAC1356), with $CaMgSiO_4$ ranging between 75 and 77 mol % and Mn content between 0·05 and 0·06 apfu.

### *Clinopyroxene*

Diopside and hedenbergite (≈QUAD), aegirine and Tschermak's pyroxenes ($CaFe^{3+}Fe^{3+}SiO_6$, $CaTiAl_2O_6$ and $CaAlAlSiO_6$) are the most important clinopyroxene endmember components in the KVC rocks (Fig. 12a). All samples contain at least some pyroxenes with a diopside component that exceeds 50 mol %, but especially in haüynolites, melteigites and the phonolitic rocks, clinopyroxene compositions evolve towards higher hedenbergite and aegirine contents (Fig. 12b). Except for late-stage clinopyroxenes, especially of the haüyne melilitites and nosean phonolites, pyroxenes of the tephritic phonolites have the lowest diopside component. Olivine/basanitic nephelinites and limburgites show the highest Ti concentrations, followed by the tephritic rocks. Those from nosean phonolites and tephritic phonolites have the lowest Ti values

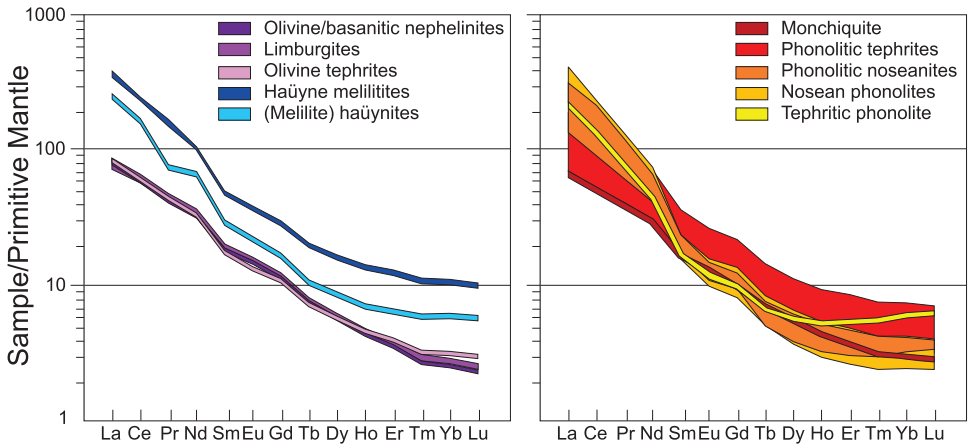


**Fig. 10.** Primitive mantle normalized rare earth element patterns for whole-rock analyses of various KVC rocks (normalizing values from Palme & O'Neill, 2003).

(Supplementary Data Table S3). In some clinopyroxenes of the mafic rock groups, Cr is elevated, with the highest values (up to 0·04 apfu) observed in clinopyroxene from olivine/basanitic nephelinites.

*Spinel group.* Members of the spinel group in the KVC rocks vary in composition between rock types (Fig. 13). Limburgites, olivine tephrites (Fig. 13a) and monchiquites (Fig. 13b) contain Cr-rich spinel with XCr [=Cr/(Cr+Al)] of up to 0·64 and Mg contents between 0·22 and 0·60 apfu (Supplementary Data Table S4). They mainly occur as inclusions in olivine, but are also present within the groundmass, where they either show a continuous or an abrupt (in monchiquites) decrease of the Cr- and a corresponding increase of the Ti-concentration from core to rim. These Ti-rich magnetites have higher ulvöspinel and spinel components ($Mag_{33–62}Usp_{25–57}Sp_{4–23}$) compared to the magnetites of phonolitic rocks, haüynolites and plagioclase-absent melteigites ($Mag_{7–91}Usp_{8–29}Sp_{0–3}$). Magnetites of the plagioclase-bearing melteigite ($Mag_{41–68}Usp_{27–51}Sp_{5–10}$) resemble those of the tephritic rocks ($Mag_{36–67}Usp_{25–57}Sp_{4–19}$). Magnetites from carbonatites have Mn contents (Fig. 13a) that are distinctively higher (up to 0·22 apfu) than those of the silicate rocks (up to 0·07 apfu). The content of Mg varies between 0 and 0·5 apfu and is lowest in the phonolitic rocks, whereas in the carbonatites, it locally reaches levels found in magnesioferrite.

Olivine/basanitic nephelinites and one sodalite monzogabbro contain primary ilmenite as intergrowths with magnetite, whereas ilmenite in the carbonatite sample HTAC1282 is present as individual grains. The composition varies between $Ilm_{57–76}Hem_{4–14}Pph_{1–20}Gk_{1–32}$ with the highest pyrophanite and lowest geikielite contents observed in the carbonatite.

### *Garnet*

Garnets in the KVC rocks are andradite-schorlomite solid solutions (Fig. 14a), and the positive correlation between $TiFe^{3+}$ and SiAl (Fig. 14b) illustrates the main substitution process involving grossular (0–30%), andradite (50–90%) and schorlomite (0–38%) endmember components (calculated after Locock, 2008). Morimotoite (0–34%) represents the remaining component (Fig. 14c). The content of Zr (generally <0·03 apfu) is elevated in some garnets of the tephritic phonolites (up to 0·08 apfu; Supplementary Data Table S5), whereas the total amount of REE is always below 0·03 apfu. There is a general decrease of Mg and Ti from the core towards the rim, and based on these two elements, several compositional subgroups representing the different garnet-bearing lithologies can be distinguished (Fig. 14d).

### *Amphibole*

Amphibole in sodalite monzogabbros and melanocratic phonolites is kaersutite, whereas Ti-poor amphibole in a phonolitic tephrite is magnesiopargasite (Leake *et al.*, 1997, 2004; Ridolfi *et al.*, 2018 Fig. 15a). Charge balance is maintained by coupled substitutions involving Na, K, Ti, Ca and Al (Fig. 15b), but is more complex in magnesiopargasites (HTAC1117), probably due to higher amounts of calculated $Fe^{3+}$ (0.90-1.07 apfu versus 0.56-0.88 apfu; Supplementary Data Table S6). Amongst the halogens, F (up to 0·3 apfu) is distinctively higher than Cl (<0·04 apfu), reaching the highest values in sodalite monzogabbros. There is, however, no correlation between F and $X_{Mg}$ [Mg/(Mg+Fe+Mn+Ti+$Al^{VI}$); Fig. 15c].

### *Mica*

Micas of the KVC form solid solutions consisting of phlogopite, annite, eastonite and siderophyllite (Fig. 15d). The Si+Al deficit in many analyses (except for the phonolitic tephrites) indicates incorporation of Ti or $Fe^{3+}$ in the tetrahedral site (Farmer & Boettcher, 1981). Variable Ba contents (up to about 0·5 apfu; Supplementary Data Table S7) are incorporated by the coupled substitution Ba + Al = Si + K (Fig. 15e). Similar to amphiboles (see above), Cl is <0·04 apfu while F reaches up to 1 apfu (Fig. 15e). The correlation between F and $X_{Mg}$ (Mg/(Mg+Fe+Mn+Ti+$Al^{VI}$) for most of the analyses (Fig. 1f)

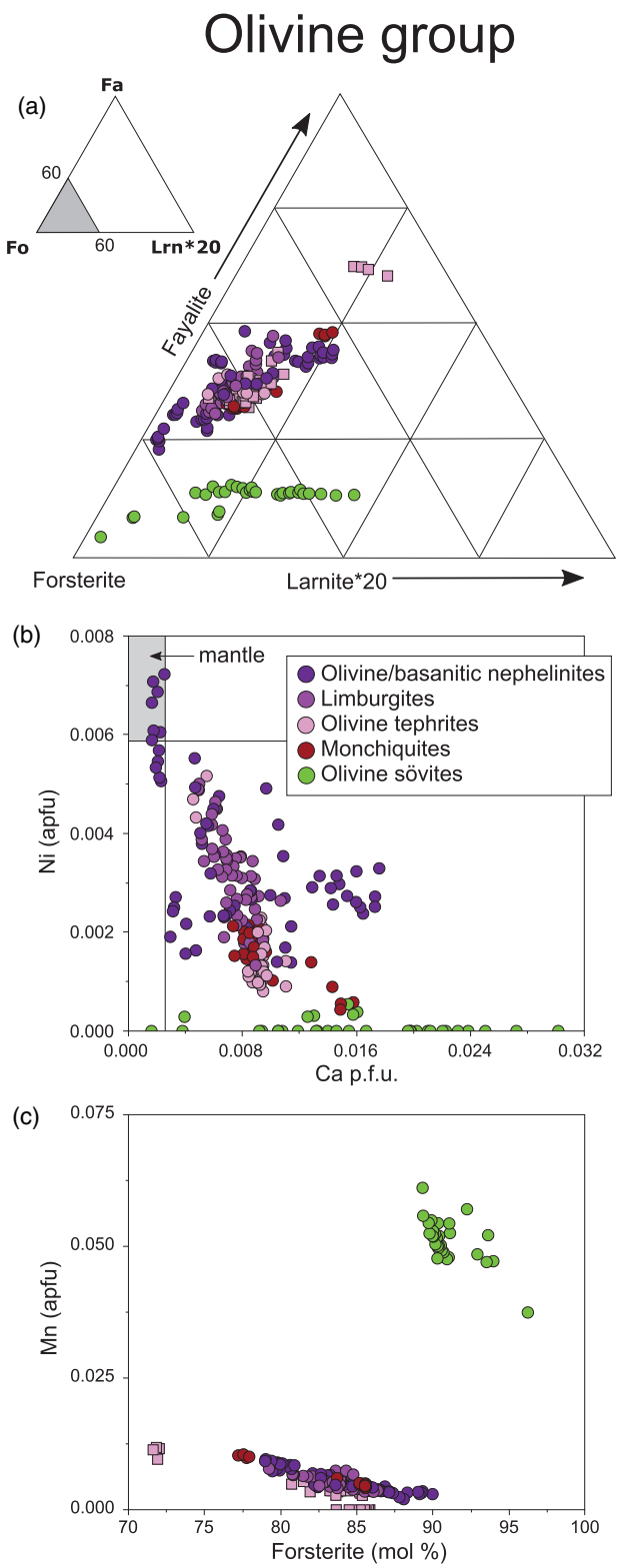


**Fig. 11.** Olivine compositions from the KVC rocks. (a) Forsterite–fayalite–larnite triangle with the larnite component being exaggerated by a factor of 20. (b) Contents of Ni (apfu) vs Ca (apfu). The upper left corner (grey) represents typical mantle olivine compositions (e.g. Foley *et al.*, 2013; Bussweiler *et al.*, 2015). Rectangles are data from Kim (1985). (c) Amount of Mn (apfu) vs forsterite content (mol %).

implies the well-known F–Fe avoidance (e.g. Munoz, 1984; Speer, 1984; Léger *et al.*, 1996). Exceptions correspond to very early (xeno-)crystic (phonolitic tephrite HTAC1117) and late-stage mica (haüyne melilitites).

*Titanite and perovskite.* Titanite shows a 2: 1 correlation between Ti and (Al + OH + F) (Fig. 16a), indicating coupled substitutions Al + OH = Ti + O and Al + F = Ti + O (e.g. Carswell *et al.*, 1996; Markl & Piazolo, 1999; Tropper & Manning, 2008). However, $Fe^{3+}$ is also relevant in this substitution process because the sum of Al and $Fe^{3+}$ clearly correlates with F (up to 0·2 apfu in titanites from sodalite monzogabbro HTAC1343; Fig. 16b; Supplementary Data Table S8). Titanite in the tephritic phonolites has the highest REE (up to 0·02 apfu), Nb (up to 0·07 apfu) and Zr (up to 0·07 apfu) contents. Late-stage titanite, which formed at the expense of garnet (wollastonite-bearing nosean phonolite HTAC1345, see above) incorporates the highest amounts of Sr (up to 0·026 apfu). In perovskites, minor substitutions of Ca with Na (up to 0·044 apfu; Supplementary Data Table S9) and REE (up to 0·029 apfu), and Ti with Al (up to 0·007 apfu) and Nb (up to 0·074 apfu) were detected, whereas Zr is generally below the detection limit.

### *Feldspar*

Plagioclase is generally unzoned and varies in composition from $An_{82}Ab_{17}Or_1$ to $An_{22}Ab_{70}Or_8$. The highest anorthite component is present in some phonolitic tephrites and the lowest in tephritic phonolites (Fig. 17a). Olivine tephrites and tephritic phonolites contain plagioclase with the highest Sr contents (up to 0·056 apfu; Supplementary Data Table S10), whereas the remaining feldspar analyses (including alkali feldspar) show a broad range down to the detection limit. Alkali feldspar composition ranges from $An_{10}Ab_{65}Or_{25}$ to $An_0Ab_{03}Or_{97}$. In alkali feldspar from phonolitic rocks, Ba may reach up to 0·18 apfu; in the remaining rock types, Ba is generally $<$0·04 apfu.

### *Nepheline*

Nepheline composition varies between $Ne_{70}Ks_{27}Qtz_{03}$ and $Ne_{82}Ks_{17}Qtz_{01}$. The Ca content is lower (0·02–0·13 apfu; Supplementary Data Table S11) in haüyne melilitites, melilite haüynites and phonolitic noseanites than in the melteigites (0·13–0·25 apfu). The highest $Fe^{3+}$ concentrations (0·16 apfu) occur in nepheline from haüyne melilitites and melilite haüynites, while the lowest (0·01 apfu) were observed in the melteigites.

*Sodalite group.* Minerals of the sodalite group (Fig. 17b) are Cl-dominated (sodalite-rich) in tephritic rocks, but mostly S-rich (nosean and haüyne) in phonolitic and in melilitic to haüynitic rocks, respectively (Fig. 18). In melilititic to haüynitic rocks, large grains have distinctively higher S contents than smaller grains and show a

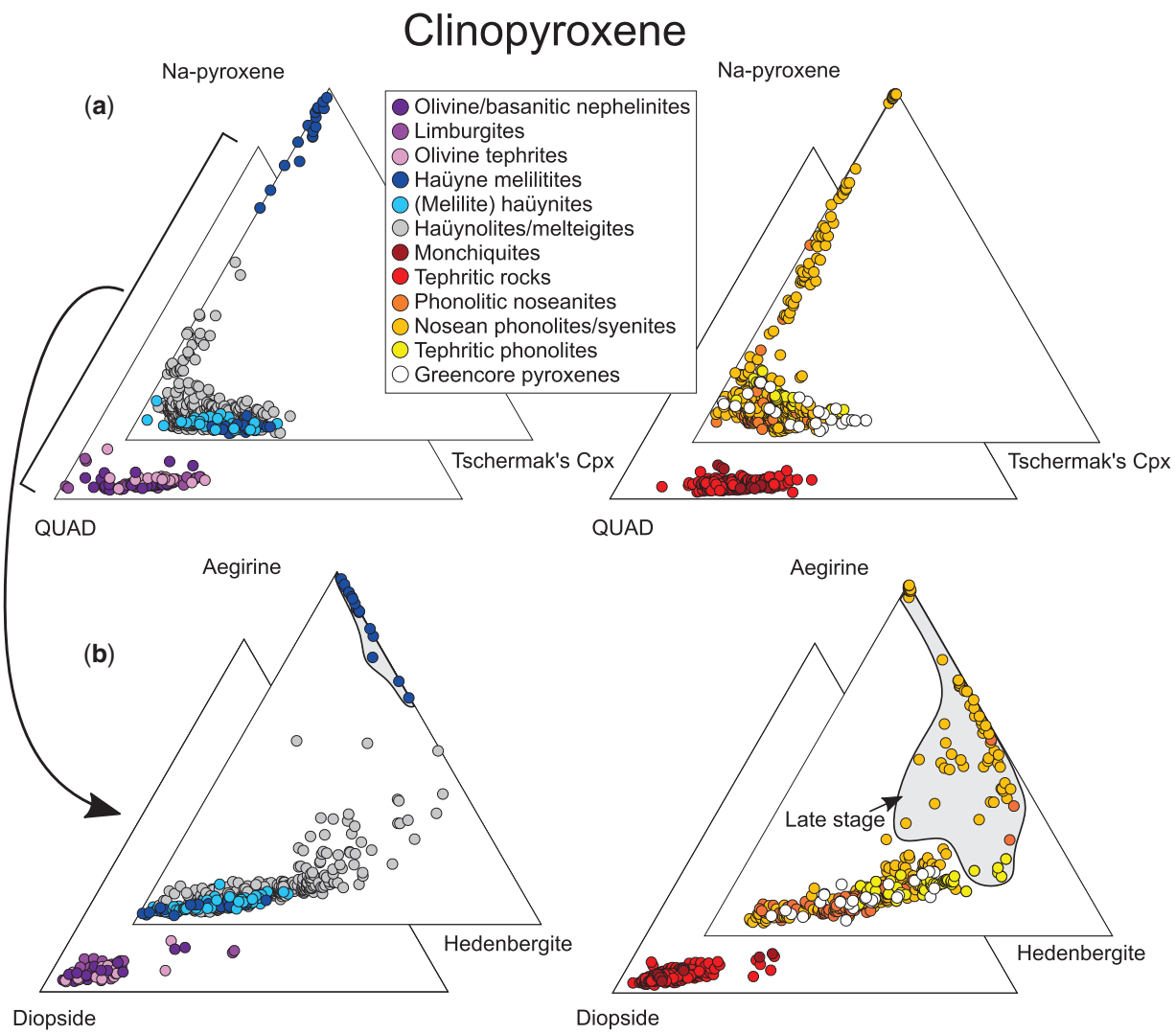


**Fig. 12.** Pyroxene compositions from the KVC rocks. (a) Na-pyroxene ($NaFeSi_2O_6$+$NaAlSi_2O_6$)-QUAD ($CaMgSi_2O_6$+$CaFeSi_2O_6$)-Tschermaks pyroxene ($CaFeFeSiO_6$+$CaTiAl_2O_6$+$CaAlAlSiO_6$) triangles. (b) Diopside–hedenbergite–aegirine triangles.

decrease in S from core to rim. The contents of K and Fe reach up to 1·0 and 0·4 apfu, respectively (Supplementary Data Table S12).

*Melilite group.* Melilite in haüyne melilitites has a higher akermanite and a lower soda melilite component compared to melilite haüynites (Fig. 17c). In haüyne melilitites, melilite phenocrysts have slightly higher MgO and CaO concentrations (Supplementary Data Table S13) than the groundmass grains.

## DISCUSSION

### Crystallization conditions of the KVC rocks

In this section, various geothermobarometers are applied to the KVC rocks to derive estimates of the crystallization conditions ($P$, $T$, $fO_2$, $aSiO_2$) of the various lithologies. These are then combined with fractional crystallization calculations to reconstruct the petrological evolution of this composite volcano.

#### *Depth of emplacement*

The only means to estimate the emplacement depth of the KVC rocks is via Al-in amphibole barometry, requiring equilibrium amphibole–plagioclase assemblages and independent T estimates (Anderson & Smith, 1995). The results of these calculations depend on redox-sensitive Tschermak and $Fe^{3+}$-Al substitutions in the amphibole structure, and it has been suggested to apply this barometer only to specific amphibole compositions with intermediate Fe contents and significant calculated $Fe^{3+}$ ($Fe_{tot}/[Fe_{tot}+Mg]$ = 0·40–0·65; $(Fe^{3+}/[Fe^{3+}+Fe^{2+}] > 0·25$), otherwise pressure may be overestimated (Anderson & Smith, 1995). Although some KVC amphibole compositions do not fulfil all requirements, we applied this barometer since the investigated

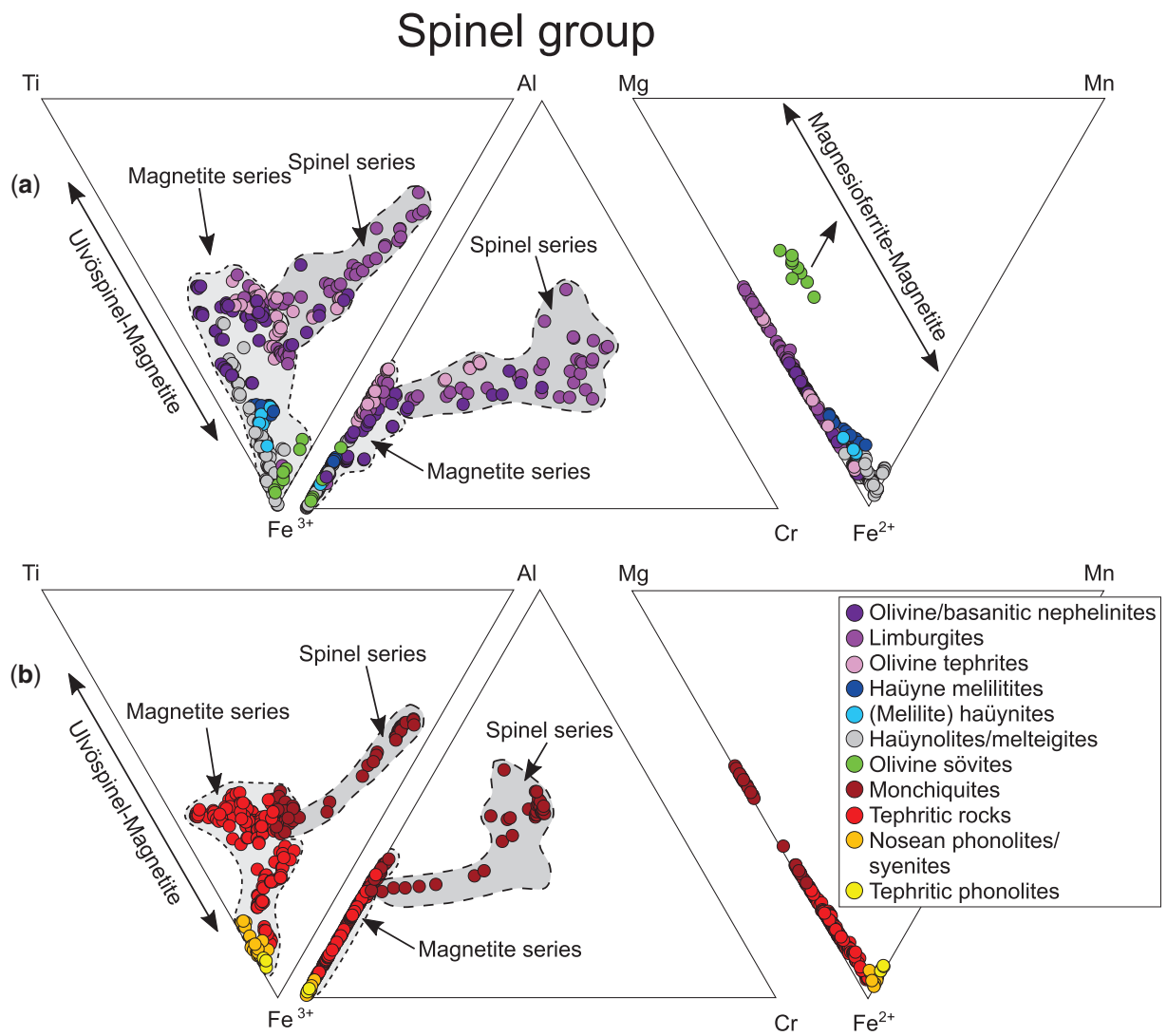


**Fig. 13.** Spinel compositions from the KVC rocks. (a) Nephelinitic to limburgitic rocks, melilititic to haüynitic rocks and olivine sövites. (b) Tephritic to phonolitic rocks.

amphiboles formed at high redox conditions (see below).

Four suitable samples of phonolitic tephrite and sodalite monzogabbro yielded a temperature of 920°C (two feldspar solvus thermometry; Fuhrman & Lindsley, 1988) and a calculated pressure range between 0·1 to 1·7 kbar (uncertainty of ±0·6 kbar). The highest values derive from a sample that contains abundant 'green-core' clinopyroxenes (HTAC1117), implying that some clinopyroxenes (and amphiboles) from this sample may have been entrapped at greater depth (or may have formed at higher temperature). For the remaining samples, pressures <0·9 kbar (average of 0·3 kbar) were calculated. In these samples, pressures calculated from amphibole rim analyses are lower than those calculated from core analyses (Fig. 18a). The calculated pressure range may reflect continuous crystallization during ascent from a magma chamber over a distance of about 2–4 km to sub-surface emplacement. Thus, a shallow level plumbing system not very different from what is assumed for Mt. Vulture (e.g. Beccaluva *et al.*, 2002) can be envisaged, with potential magma storage at shallow sub-surface levels. Temperature calculation according to the thermometer of Holland & Blundy (1994) strongly depends on pressure, but overlaps with the results of the two-feldspar thermometer (Fuhrman & Lindsley, 1988) if a mean pressure of 0·3 kbar and no Ti on the tetrahedral site of the amphibole is assumed. This pressure was used for all subsequent calculations.

### *Estimates of T–aSiO$_2$–fO$_2$ conditions*

Olivine–clinopyroxene–magnetite assemblages in olivine/basanitic nephelinites and the slightly more evolved limburgites and olivine tephrites yield equilibration temperatures of 1000–1050°C, 990–1030°C, and 1000–1150°C, respectively (Fig. 18b and Supplementary Data Table S14). We interpret these as near-liquidus temperatures. For the same rocks, the clinopyroxene-liquid

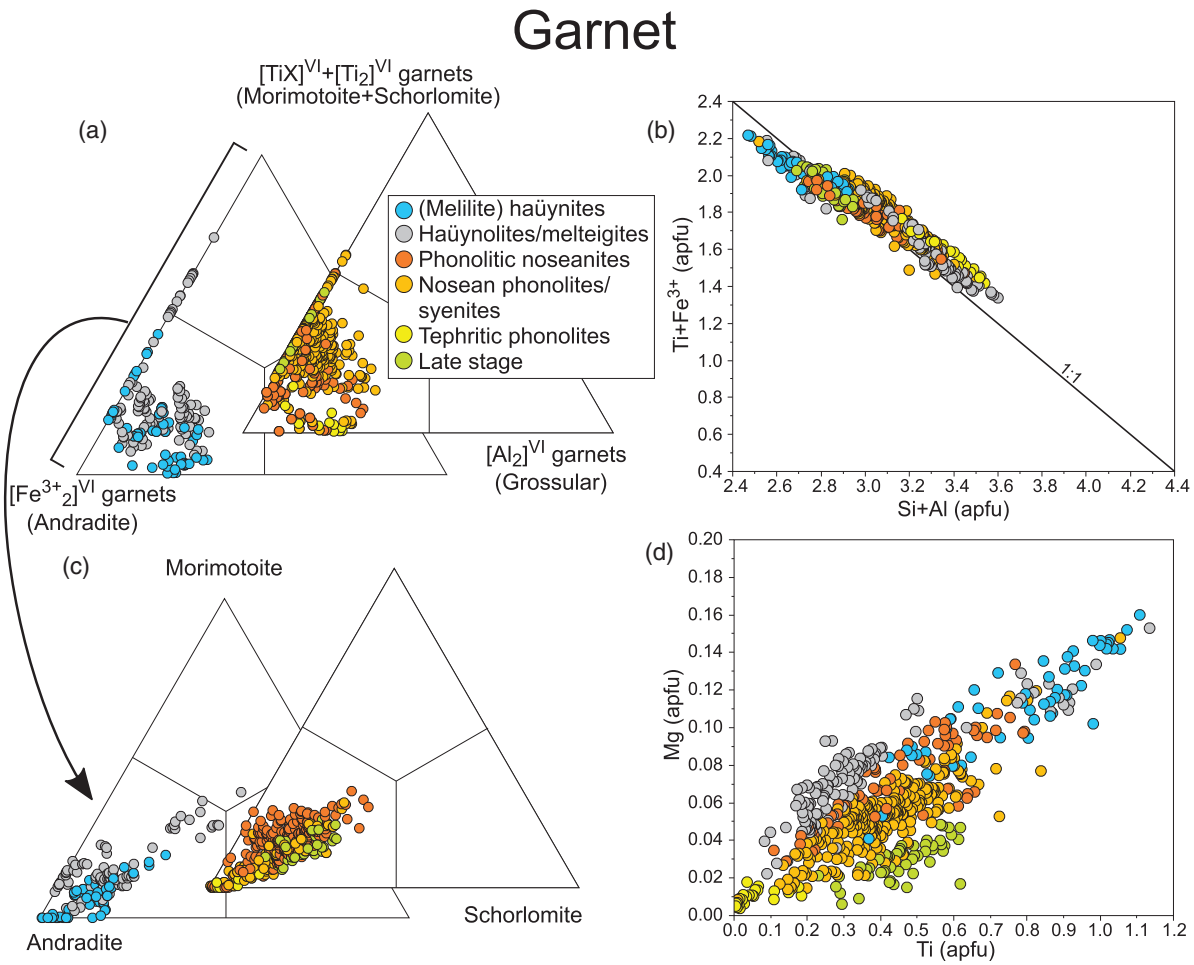


**Fig. 14.** Correlation and compositions diagrams for garnet from the KVC rocks. (a) Garnet composition based on the octahedral-site occupancy. (b) $TiFe^{3+}$ apfu vs Si+Al apfu diagram illustrating a good 1: 1-correlation (solid line). (c) Garnet composition expressed as andradite-morimotoite-schorlomite endmembers. (d) Mg apfu vs Ti apfu subdivides various garnet types and lithologies into specific groups.

thermometer of Putirka *et al.* (1996) indicates higher temperatures (1130–1260°C). However, these values have to be treated with caution, because the whole-rock data were used as proxies for melt compositions and in some samples, xenocrysts of olivine and clinopyroxene were identified based on characteristic textures (Ulianov *et al.*, 2007; see above). Calculated $aSiO_2$ values for this rock group (Fig. 18c) increase from olivine nephelinites ($aSiO_2$=0·4–0·5), through the basanitic nephelinite ($aSiO_2$=0·7–0·8) to limburgites and olivine tephrites (0·5–0·9). This is in agreement with the absence of feldspar in the former but its appearance in the latter and can be explained by fractionation of olivine (see below). Redox conditions are estimated to around $\Delta FMQ^* = +2–3$ (Fig. 18c). However, application of the magnetite-melt oxybarometer of Arató & Audétat (2017) reveals slightly lower values ($\Delta FMQ^* = +1–2$), which may be related to the methodological limitations mentioned above.

For haüyne melilitites and slightly more evolved (melilite) haüynites similarly high crystallization temperatures were estimated (1060–1120°C and 950–1010°C, respectively; Fig. 18b and Supplementary Data Table S14). Their estimated silica activity, however, is very low ($aSiO_2$ <0·22) and highly oxidized conditions ($\Delta FMQ^* = +4–6$) are determined (Fig. 18c). This is in accordance with their mineralogy, i.e. the abundance of melilite, feldspathoid minerals and garnet, whilst olivine and feldspar are scarce or absent. Due to the absence of suitable phases, no constraints on the crystallization temperature of coarse-grained foidolitic cumulates could be calculated. The absence of K-rich minerals, the occurrence of perovskite and the composition of the sodalite-group minerals in the foidolitic xenoliths suggest that these rocks are rather related to the haüyne melilitites and haüynites than to the phonolitic rock group. Based on their mineralogical similarity, a comparable crystallization history as for haüyne melilitites and (melilite) haüynites can be assumed. The minimum silica activity of titanite-bearing and perovskite-lacking haüynolites is around 0·1, the transition from perovskite to titanite in some melteigites

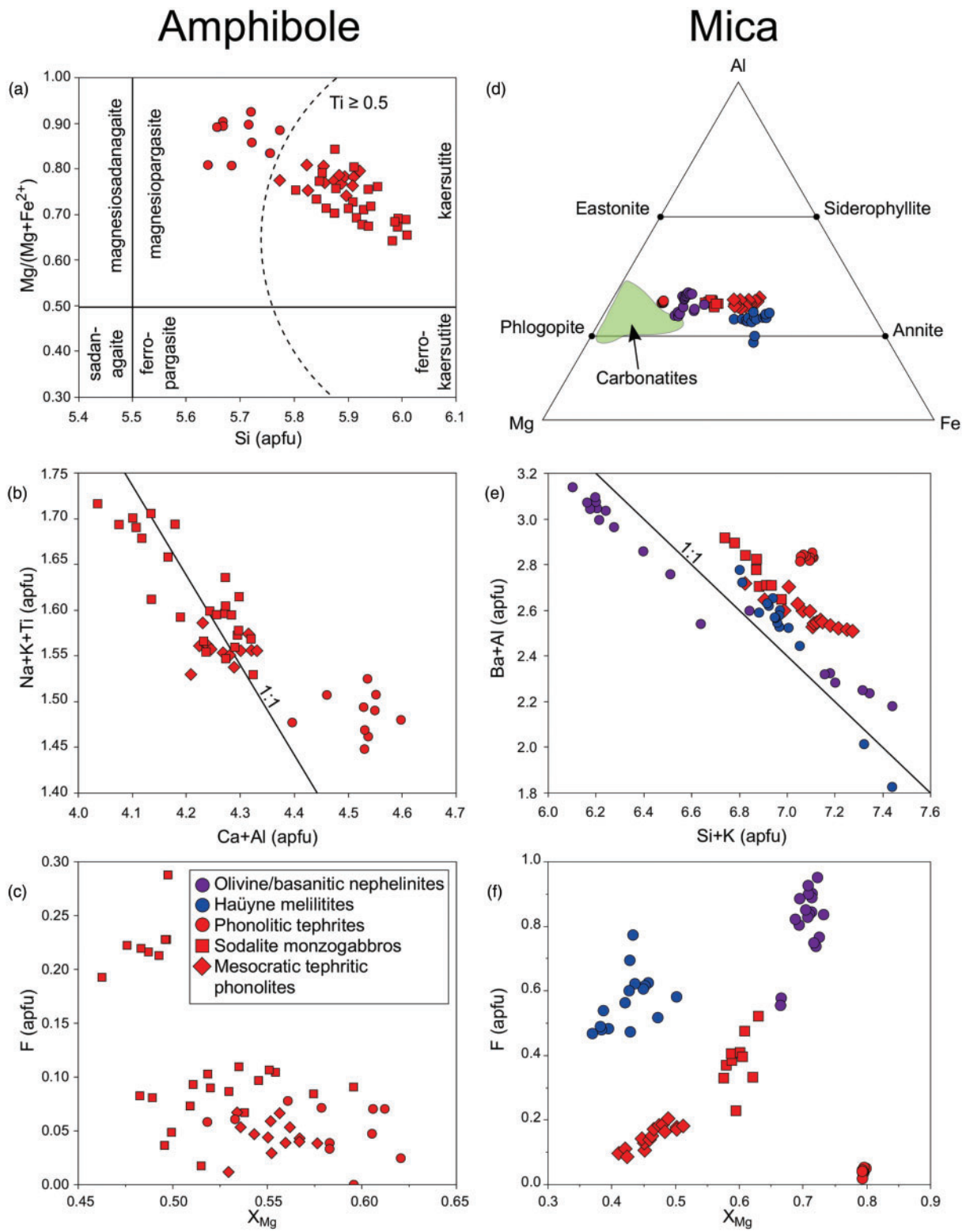


**Fig. 15.** (a) Classification and correlation diagrams for amphibole (a–c) and mica (d–f) from the KVC rocks. (a) Amphiboles are classified as magnesiopargasite or kaersutite (after Leake *et al.*, 1997, 2004). (b) Correlation of Na+K+Ti apfu vs Ca+Ba+Al apfu (c) Correlation diagram of F apfu vs $X_{Mg}$ ($Mg/(Mg+Fe+Mn+Ti+Al^{VI})$). (d) Mica composition based on the amount of Mg, Al and Fe. Green area represents the compositional range of carbonatites at the KVC (unpublished data). (e) Diagram showing a good 1:1 correlation between Ba+Al apfu and Si+K apfu (f) Correlation diagram of F apfu vs $X_{Mg}$ ($Mg/(Mg+Fe+Mn+Ti+Al^{VI})$).

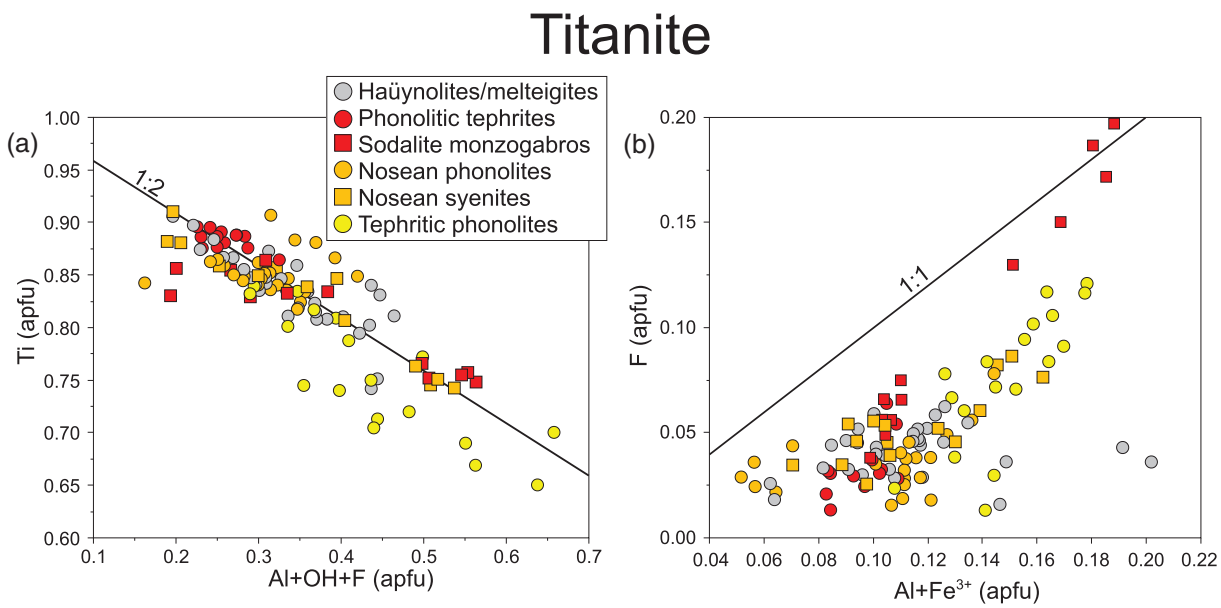


**Fig. 16.** Titanite compositions from the KVC rocks. (a) Correlation of Ti apfu vs Al+OH+F apfu (b) Correlation of Al+$Fe^{3+}$ apfu vs F apfu, illustrating the additional influence of $Fe^{3+}$.

(Fig. 3d) suggests $aSiO_2$ values of 0·1–0·15. High $fO_2$ conditions ($\Delta FMQ^* = +3$–6; Fig. 18c), similar to haüyne melilitites and (melilite) haüynites are indicated.

Tephritic to phonolitic rocks reveal variable T–$aSiO_2$–$fO_2$ conditions. Estimated near-liquidus temperatures decrease with evolution from primitive monchiquites (~1040–1100°C) towards tephrites and phonolites (~960–880°C), based on QUILF calculations, two-feldspar thermometry (Fig. 17a) and hornblende–plagioclase thermometry (Supplementary Data Table S14). Again, the clinopyroxene-liquid thermometer of Putirka *et al.* (1996) generally yields distinctively higher temperatures (up to 1220°C), as do melt inclusion-homogenization data (up to 1170°C; Panina *et al.*, 2000). Silica activity decreases (Fig. 18c) from monchiquites ($aSiO_2 = 0·6$–0·8) via tephritic ($aSiO_2 = \sim 0·5$) to phonolitic rocks ($aSiO_2 = \sim 0·2$), probably as a consequence of intense clinopyroxene fractionation (see below). Estimated $fO_2$ (Fig. 18c) increases from monchiquites ($\Delta FMQ^* = +2$–3) towards tephritic ($\Delta FMQ^* = +3$–4) and phonolitic rocks ($\Delta FMQ^* = +3$–5). This is in accordance with the change of the mafic liquidus assemblage from olivine–clinopyroxene–spinel in primitive rocks (monchiquites) to clinopyroxene–garnet–titanite in the more evolved rocks (compare Marks *et al.*, 2008*a*). Similarly, the shift from sulfate-poor sodalite-group minerals in tephrites towards sulfate-rich members (nosean/haüyne) in the more evolved phonolitic rocks (Fig. 17b), paralleled by a decrease in ulvöspinel component in magnetites (Fig. 13), implies increasingly oxidized conditions.

For carbonatites, the crystallization temperature is constrained to 840–900°C (Fig. 18c and Supplementary Data Table S14) based on the Fe–Mg exchange reaction between olivine and magnetite (QUILF). Reaction (6) allows determination of a maximum $aSiO_2$ value of 0·05, using a monticellite endmember component of 0·8 and a diopside activity of 1. However, monticellite is a very rare phase in the KVC carbonatites and diopside is absent in the investigated samples. Therefore, this estimate may not be representative of all carbonatites in the KVC. Nevertheless, $aSiO_2$ in carbonatites is certainly low, and perovskite-bearing carbonatites record an upper silica activity limit of 0·2. Redox estimates for the investigated samples ($\Delta FMQ^* = +6$–7) are distinctively higher than previous $fO_2$ estimates on other carbonatites, which fall between $\Delta FMQ = -0·8$ and $+1·0$ (Friel & Ulmer, 1974; Gaspar & Wyllie, 1983; Treiman & Essene, 1984; Ryabchikov *et al.*, 2008; Milani *et al.*, 2016). This apparent discrepancy is caused by the fact that the cited publications present $\Delta FMQ$ calculations at $aSiO_2$ values of 1. However, if they are corrected to low silica activities (=FMQ*, as is done here), much more oxidized values emerge. The association of carbonatites with quite oxidized silicate rocks is not uncommon at other localities, such as Mt. Vulture, Italy (e.g. De Fino *et al.*, 1982; Beccaluva *et al.*, 2002; Panina & Stoppa, 2009), Magnet Cove, USA (e.g. Flohr & Ross, 1990), Tamazeght, Morocco (e.g. Marks *et al.*, 2008*a*), Oldoinyo Lengai (e.g. Zaitsev *et al.*, 2012) or Kerimasi (e.g. Guzmics *et al.*, 2012). In case of the KVC, carbonatites represent the most oxidized lithologies, but it remains to be tested if this is true for other carbonatite complexes.

## Genetic relationships between the various KVC rocks

Based on their MgO, Ni and Cr contents (Figs 8 and 9), olivine/basanitic nephelinities, limburgites and monchiquites represent the most primitive rock types of the KVC. Their contrasting mineralogy, mineral chemistry, petrology, and geochemistry (see above),

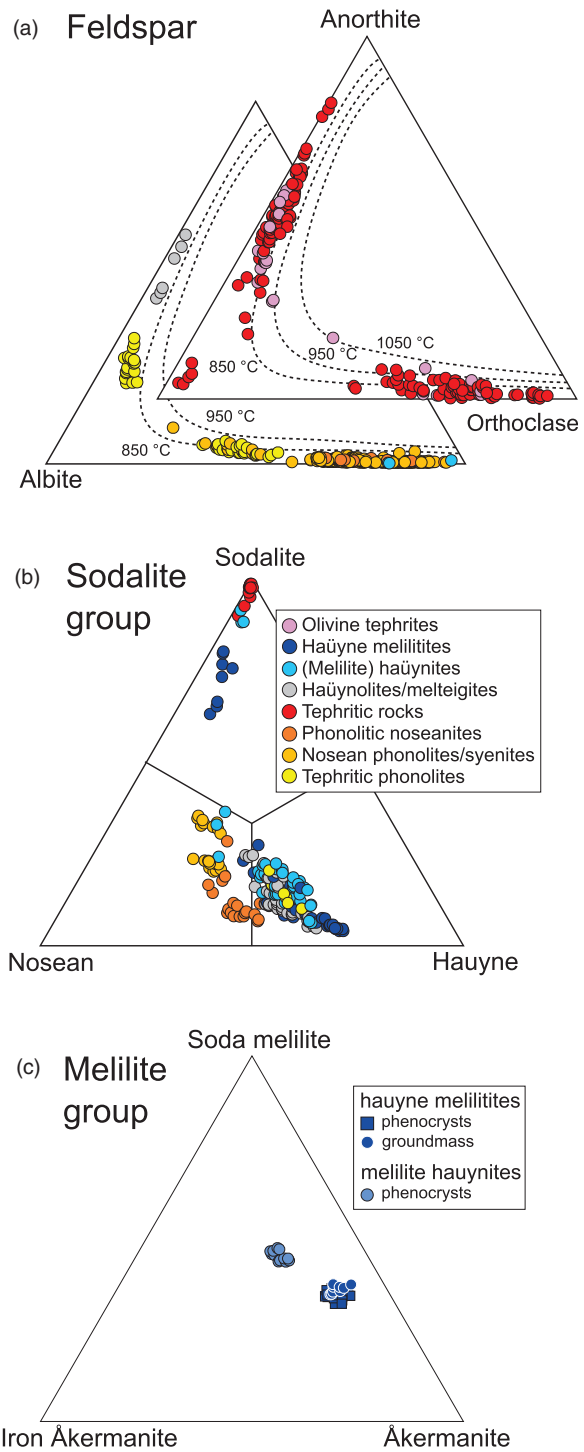


**Fig. 17.** (a) Feldspar compositions in the KVC rocks illustrated in the albite–anorthite–orthoclase triangle. Isotherms (dashed lines) represent the feldspar solvus after Fuhrman & Lindsley (1988). (b) Nosean–sodalite–haüyne triangle showing the compositional range of sodalite-group minerals. (c) Melilite composition of haüyne melilitites and melilite haüynites in the iron akermanite–soda melilite–akermanite triangle.

however, makes a common parental magma unlikely. Monchiquites and olivine/basanitic nephelinites probably represent the most primitive members of at least two distinct parental magmas, as previously suggested by Keller (1984*b*) and Schleicher *et al.* (1990). The association of feldspar-free nephelinitic/melilititic rocks with plagioclase-normative, primitive basanitic/tephritic rocks is a common association world-wide (e.g. Melluso *et al.*, 2016) and is, for example, very similar to the rock associations known from Mt. Vulture (Italy), including the occurrence of associated calciocarbonatite (e.g. De Fino *et al.*, 1982; Melluso *et al.*, 1996; Rosatelli *et al.*, 2000, 2007; Beccaluva *et al.*, 2002; Stoppa *et al.*, 2008). We tested the importance of fractional crystallization of monchiquitic/basanitic and nephelinitic/melilititic magmas for producing the lithological and geochemical variation observed in the KVC rocks by means of mass balance calculations using phenocryst assemblages as potential fractionating phases (Supplementary Data Table S15 and Fig. 2). The results of these calculations are discussed in the following sections.

### *A model for the evolution of tephritic to phonolitic rocks*

The evolution from tephritic to phonolitic rocks is mirrored by an increasing hedenbergite component in clinopyroxene (Fig. 12), decreasing Ti and Mg contents in magnetite (Fig. 13) and decreasing Mg concentrations in garnet (Fig. 14), and is further strengthened by whole-rock data (Figs 7 and 8). The evolution from monchiquites towards tephrites can be modelled by the fractionation of clinopyroxene and minor amounts of olivine and spinel. Further fractionation of clinopyroxene and magnetite explains the evolution towards phonolitic tephrites and the compositional variation of most phonolites requires further fractionation of clinopyroxene, plagioclase, haüyne/nosean, as well as garnet and titanite. The importance of garnet and titanite fractionation at this stage is further supported by whole-rock REE systematics. Except for an increasing total amount of REE, the REE pattern does not change during evolution from monchiquites via tephrites to phonolitic tephrites (Fig. 10), as the fractionating phases incorporate negligible amounts of REE (Schnetzler & Philpotts, 1970; Grutzeck *et al.*, 1974; Hanson, 1980). With the onset of garnet and titanite crystallization, this situation changes; as garnet prefers the heavy REE (e.g. Schnetzler & Philpotts, 1970; Shimizu & Kushiro, 1975; Nicholls & Harris, 1980; Marks *et al.*, 2008*b*), garnet fractionation leads to a depletion of heavy REE in the remaining melt. Titanite has high Kd values for REE and preferentially incorporates the middle REE (e.g. Simmons & Hedge, 1978; Prowatke & Klemme, 2005). Accordingly, total REE concentration decreases and the resulting REE patterns for evolved tephritic phonolites are trough-shaped (Figs 10 and 19). Similarily, Zr/Hf ratios are almost constant in monchiquites and phonolitic tephrites, but strongly increase towards the phonolitic rocks (Fig. 19). The Nb/Ta and Y/Ho ratios behave in a similar way, except for four phonolitic tephrites, which show anomalous high ratios. (Note that these samples

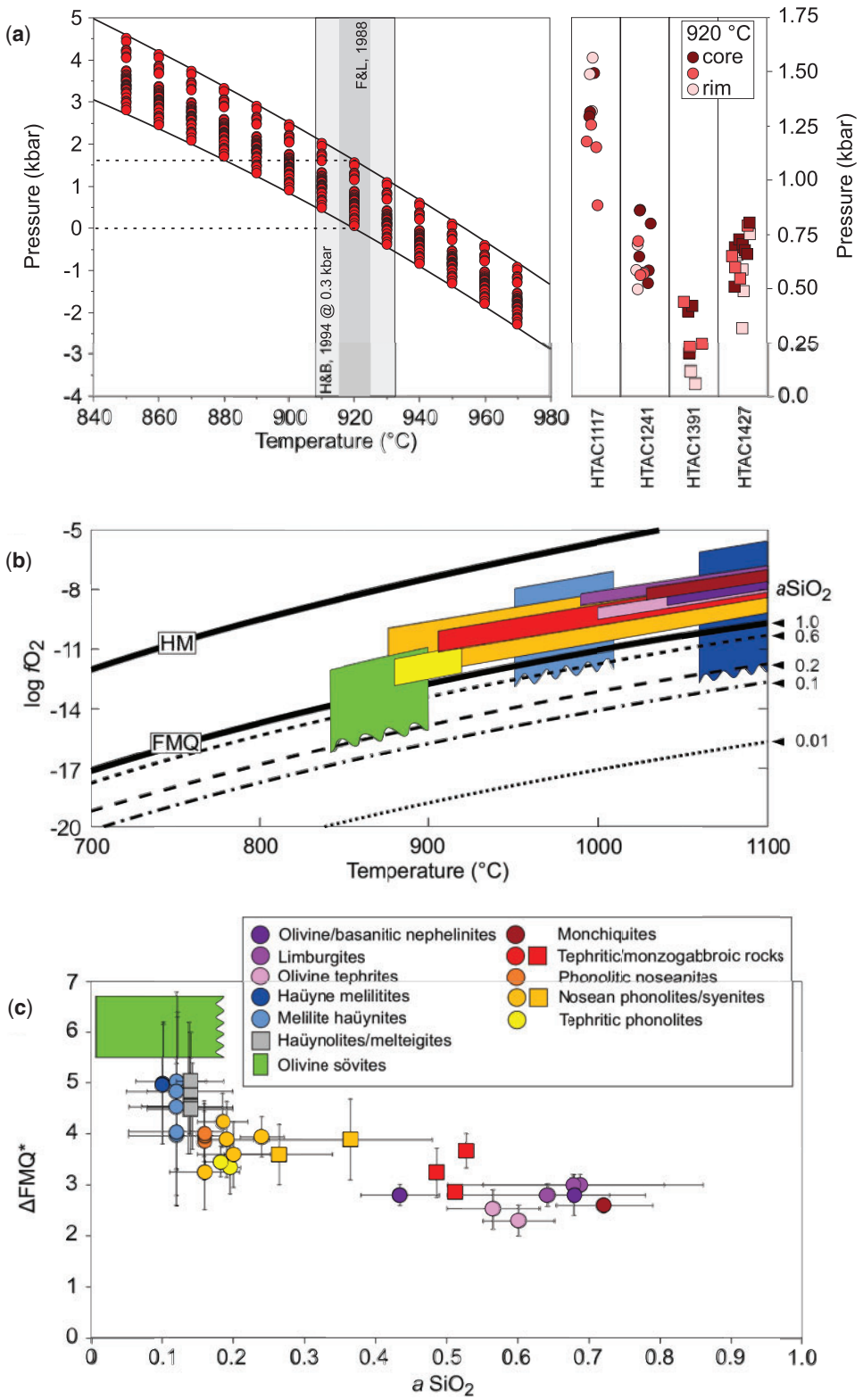


**Fig. 18.** Estimated crystallization conditions for the KVC rocks. (a) Pressure-temperature dependence (left side) of the Al-in hornblende barometer of Anderson & Smith (1995). Dark grey area represents the temperature interval calculated using the feldspar liquidus thermometer of Fuhrman & Lindsley (1988), bright grey area shows the temperature range obtained using the amphibole-plagioclase thermometer of Holland & Blundy (1994) at 0·3 kbar. On the right side, pressure estimates at 920°C are shown. Plutonic rocks are shown as rectangles whereas volcanic rocks are displayed as circles. (b) Temperature vs log $fO_2$ diagram with the FMQ and HM buffers curves shown as thick lines, whereas dashed lines illustrate the FMQ buffer curve at variable silica activities. (c) Estimated silica activity ($aSiO_2$) vs oxygen fugacity (expressed as ΔFMQ*) for the KVC. Symbols illustrate mean values whereas the error bars indicate the total possible range.

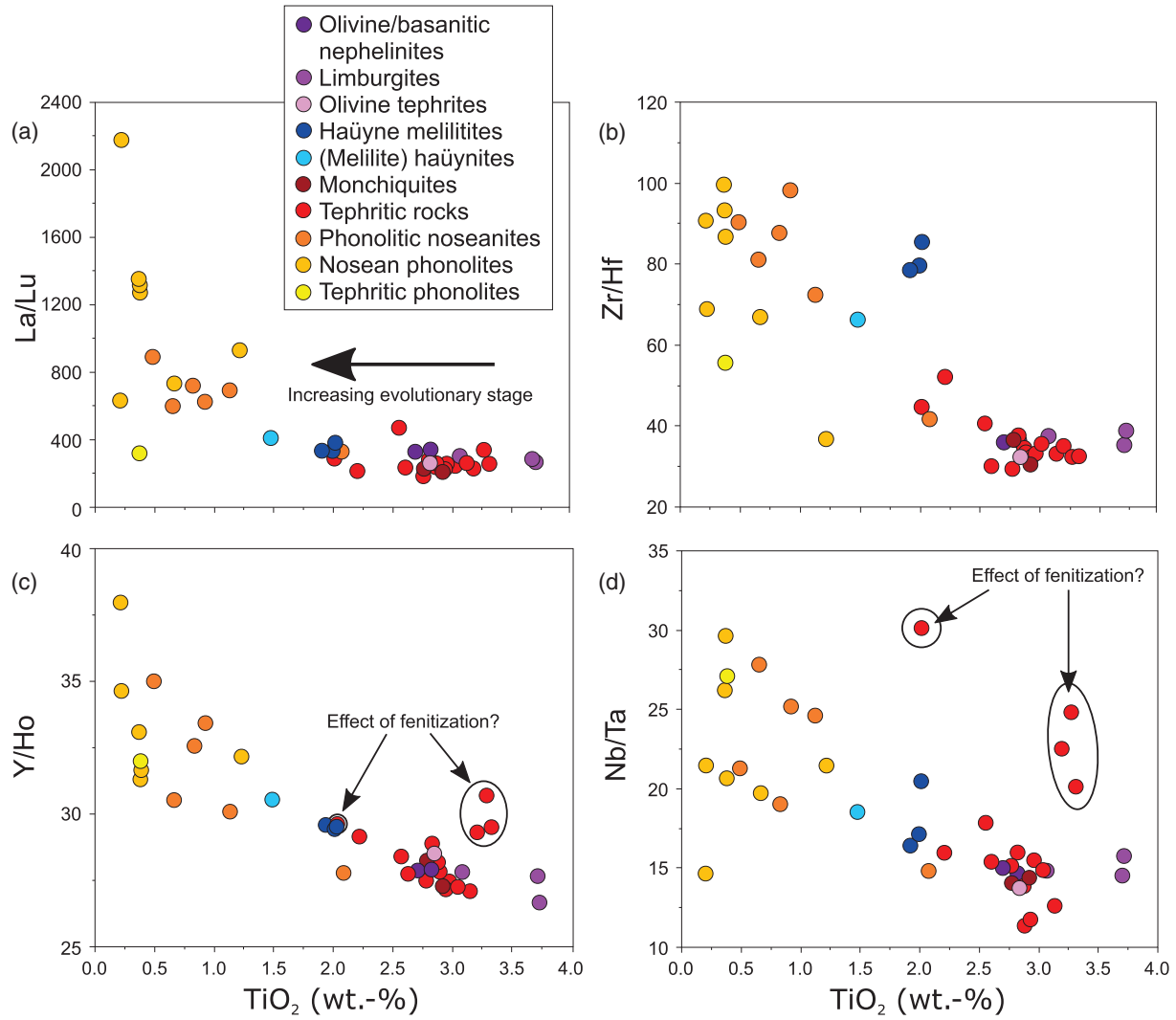


**Fig. 19.** Whole-rock La/Lu (a), Zr/Hf (b), Y/Ho (c) and Nb/Ta (d) vs $TiO_2$ illustrating the effects of titanite, perovskite and garnet fractionation (see text for details).

were collected in the immediate vicinity of the large sövite bodies and show subtle petrographic evidence for fenitization). Crystallization of titanite/perovskite and garnet are known to cause such fractionation effects (e.g. Chakhmouradian, 2006; Marks *et al.*, 2008*b*; Olin & Wolff, 2012; Chakhmouradian *et al.*, 2013).

Phonolitic rocks of the KVC with $Na_2O+K_2O$ concentrations $>$ 12 wt % cannot be explained by fractionation of the observed mineral phases and their chemical composition (Supplementary Data Fig. S2). We suggest that these rocks accumulated significant nosean and alkali feldspar (Supplementary Data Table S15). For some of these rocks, Sutherland (1967) proposed the importance of a metasomatic overprint and, in fact, some of them show abundant hydrothermally-formed zeolites (e.g. Weisenberger *et al.*, 2014), which could be responsible for their high and variable $Na_2O+K_2O$ contents. The potential importance of contamination with 'crustal material' for some of these rocks has been stressed previously (Schleicher *et al.*, 1990) and mixing of variably evolved magmas and uptake of already crystallized material during the genesis of this rock series seems likely, as suggested, e.g. by 'green-core' pyroxenes and rounded olivine (xeno)crysts in some of the rocks (see above; Ulianov *et al.*, 2007). All these factors add geochemical complexity and need to be invoked to fully explain the compositional scatter in the whole-rock data.

*A model for the evolution of nephelinitic to limburgitic and melilitic to haüynitic rocks.* Olivine/basanitic nephelinites are the most MgO- Ni- and Cr-rich rocks of the KVC (Figs 8 and 9) and olivine melilitites (grey field in Figs 8 and 9) occurring in close proximity to the KVC (e.g. Mahlberg, Urach and Hegau) are interpreted to be their parental magmas (Wilson *et al.*, 1995; Dunworth & Wilson, 1998; Ulianov *et al.*, 2007). Olivine/basanitic nephelinites can be modelled assuming fractionation of olivine, melilite and minor amounts of spinel,

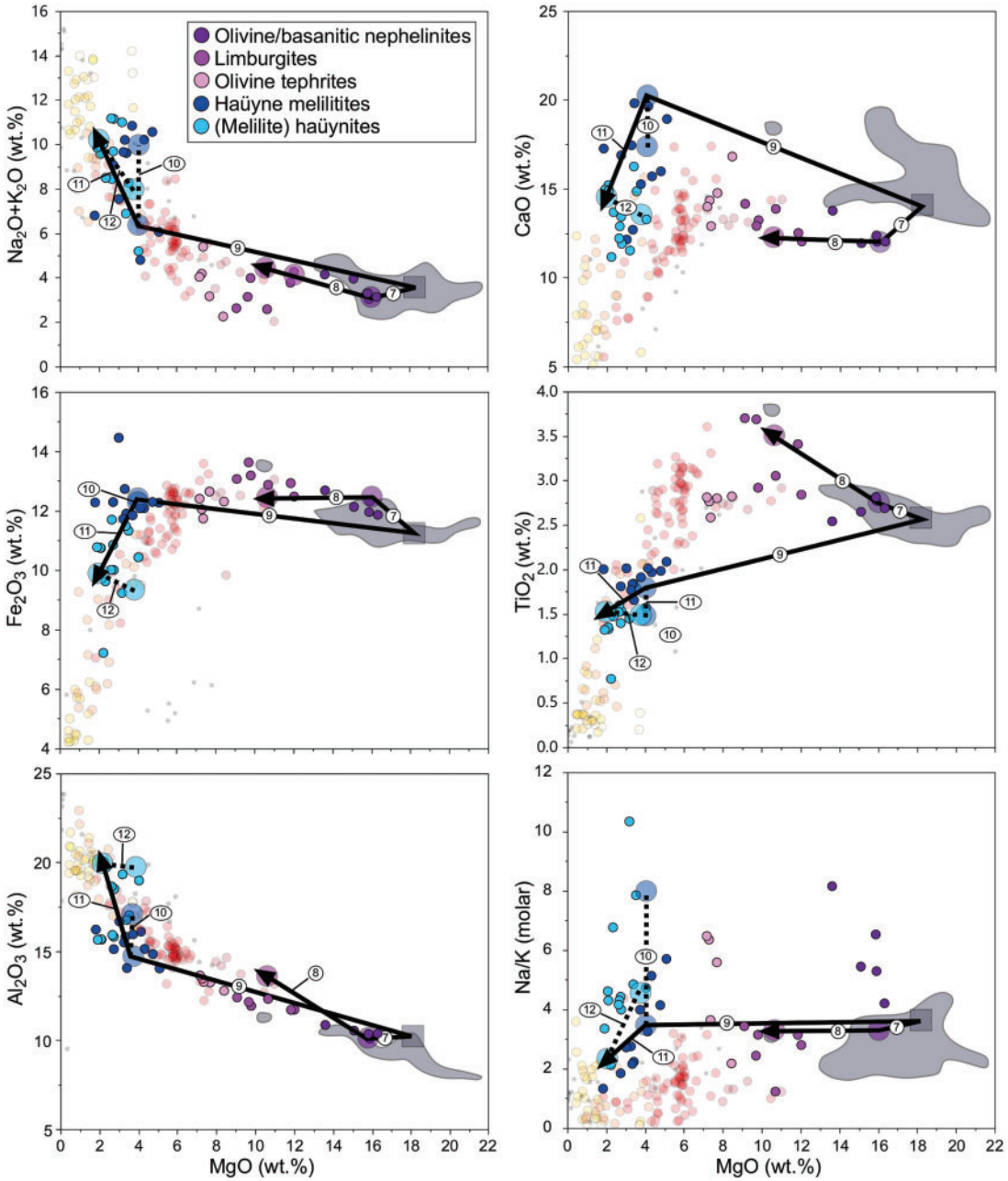


**Fig. 20.** Fractionation path for the nephelinitic to limburgitic and melilititic to haüynitic rock series. Numbers refer to Supplementary Data Table S15. Grey area illustrates the compositional range of olivine melilitites in SW Germany (Keller *et al.*, 1990; Wilson *et al.*, 1995).

perovskite and nepheline, using the Mahlberg olivine melilitite (Fig. 1b) as a starting composition; limburgites can be explained by further fractionation mainly of olivine and clinopyroxene (Fig. 20 and Supplementary Data Table S15). However, their highly variable Na/K ratios (Fig. 8) cannot be easily reproduced by such fractionation models (Fig. 20), which we suggest is due to variable alteration and weathering of nepheline and glass, and accompanying redistribution of Na and K (e.g. Nesbitt *et al.*, 1980; Quantin & Lorenzoni, 1992; Giampaolo *et al.*, 1997; Weisenberger *et al.*, 2014).

It has been suggested that, based on their (slightly) different Pb and Nd isotope compositions (Schleicher *et al.*, 1990, 1991), the olivine melilitites, olivine/basanitic nephelinites and limburgites were derived from a different mantle source compared with haüyne melilitites and (melilite) haüynites. However, (i) Pb concentrations in these rocks are very low (<35 ppm) and could be easily altered during the ascent of such melts, as proposed by Ray (2009) who assumed assimilation with lower crustal granulites for the KVC rocks; (ii) considering a typical uncertainty of about 0·5 $\varepsilon_{Nd}$ units (e.g.

Marks *et al.*, 2003, 2009), the Nd isotope compositions of these two groups largely overlap with each other; (iii) the $^{87}Sr/^{86}Sr$ values for both rock groups are very similar (Schleicher *et al.*, 1990). Furthermore, an isotopically heterogeneous mantle could also be responsible for the isotope variations (e.g. Bell, 1998). We suggest that nephelinitic to limburgitic and melilititic to haüynitic rocks may be derived from a common source. In fact, haüyne melilitites could have originated from olivine melilitites by fractionation of greater quantities of olivine and lesser quantities of melilite (Fig. 20 and Supplementary Data Table S15) and further fractionation of mainly melilite from the haüyne melilitites could generate melt compositions similar to (melilite) haüynites. The large scatter in Na/K ratios, $Na_2O+K_2O$ and CaO contents in the haüyne melilitites and (melilite) haüynites (Figs 8 and 20) can be explained by the accumulation of variable amounts of haüyne, clinopyroxene and melilite, combined with the compositional variation and variably intense alteration of abundant feldspathoid minerals, similar to what we propose for the phonolitic rocks (see above).

High $CO_2$ concentrations in a silica-undersaturated magma lead to a polymerization of the silicate melt (Mysen *et al.*, 1976) and hence, more polymerized minerals like melilite compared to olivine should crystallize. Since the solubility of $CO_2$ depends on pressure, olivine/basanitic nephelinitic or haüyne melilititic melts may reflect polybaric melting of a common mantle source (Mysen *et al.*, 1976; Yagi & Onuma, 1978). However, in addition to pressure, the solubility of $CO_2$ in a melt may also be influenced by the oxidation state (e.g. Pan *et al.*, 1991; Thibault & Holloway, 1994). Highly oxidized conditions may cause the release of $CO_2$ and a subsequent termination of melilite precipitation (Mysen *et al.*, 1976). For example, Dunworth & Wilson (1998) suggested variable redox conditions to be responsible for the highly variable melilite-olivine ratio in olivine melilitites in southwestern Germany. Since haüyne melilitites crystallized under more oxidized conditions than olivine/basanitic nephelinites (Fig. 18c), it seems likely that haüyne melilitites originated from a more oxidized part of the mantle. However, during fractionation from olivine melilitite to haüyne melilitite, the $CO_2$ concentration must increase, as melilite and magmatic carbonate are present in the haüyne melilitites.

## The genetic relation between silicate rocks and carbonatites

The similarity of carbon and oxygen isotope compositions of calcite crystals in sövites and haüyne melilitites imply a common origin (Hubberten *et al.*, 1988). Apatite textures and compositions in haüyne melilitites suggest that these may have nucleated in a silicate melt and continued to crystallize from a melt with carbonatitic affinity (Wang *et al.*, 2014). Further, similar $^{87}Sr/^{86}Sr$ isotope values of carbonatites and haüyne melilitites (Schleicher *et al.*, 1990) strengthen this hypothesis. As both the carbonatites and the haüyne melilitites formed at high redox conditions (Fig. 18), their close genetic affinity is further supported, although the actual process of carbonatite formation is still uncertain: are they direct mantle carbonate melts or are they products of fractionation/liquid immiscibility of mantle-derived silicate melts?

A primary melt directly derived by (carbonated) mantle melting seems unlikely, as most of the KVC carbonatites are calcitic (Keller, 1978, 1981; Lehnert, 1989), whereas primary carbonatitc magmas should be Mg-rich (e.g. Wallace & Green, 1988; Dalton & Wood, 1993; Dalton & Presnall, 1998; Wyllie & Lee, 1998; Litasov & Ohtani, 2009). However, during ascent, any primary carbonatitic magma should evolve towards more calcitic compositions by interaction with mantle peridotite and accompanying wehrlitization (e.g. Dalton & Wood, 1993; Lee & Wyllie, 2000). In contrast, the observed Ca/(Ca+Mg) ratios of the KVC carbonatites are $>0{\cdot}97$ and, therefore, much higher than would be expected based on experimental studies ($<0{\cdot}88$; Dalton & Wood, 1993; Lee & Wyllie, 2000).

The second possibility, fractional crystallization of a carbonate-bearing silicate liquid, resulting in the formation of (exsolved or residual) carbonatitic magmas (Gittins, 1989; Kjarsgaard & Peterson, 1991; Gittins & Jago, 1998; Halama *et al.*, 2005; Brooker & Kjarsgaard, 2011) appears, however, more likely in the case of the KVC. Based on the presence of primary magmatic carbonate in haüyne melilitites, it was concluded that these may represent the 'missing link' between the silicate melts and carbonatites (Keller, 1984*a*; Hubberten *et al.*, 1988). Liquid immiscibility with evolved haüyne melilitites representing the conjugate silicate melt can be excluded, because a hypothetical unexsolved precursor melt composition (carbonatite+haüyne melilitite) cannot be generated by simple fractionation of the parental olivine melilitite (Supplementary Data Fig. S3). However, since the $CO_2$ solubility in silicate liquids is highly pressure-dependent (e.g. Yoder, 1975; Mysen *et al.*, 1976), a hypothetical parental melt could have been decarbonated during ascent and hence, the melilititic rocks might not be appropriate for modelling derivation of the carbonatites by differentiation and accompanying $CO_2$ enrichment. Therefore, we assume that the direct precursor to the carbonatites might be present at lower crustal levels where pressure is high enough to prevent decarbonation reactions. However, whether the carbonatites formed by liquid immiscibility or by extreme magmatic differentiation of a carbonate-rich mafic/ultramafic silicate melt (possibly of olivine melilititic composition) remains speculative.

## Mantle source(s) of the KVC rocks

The olivine melilitites of SW Germany formed by partial melting at the base of the lithospheric mantle which previously had been enriched by K-depleted carbonated melts from the dolomite–garnet–peridotite stability field in the asthenosphere (e.g. Dunworth & Wilson, 1998). Ulianov *et al.* (2007) proposed a similar process for the

formation of the olivine/basanitic nephelinites at the KVC and suggested that the more calcic olivine melilitites formed from more strongly metasomatized (carbonated) mantle regions or from smaller degrees of partial melting. However, the lower concentrations of MgO and compatible elements such as Ni and Cr in olivine/basanitic nephelinites compared to olivine melilitites favour their formation by fractional crystallization rather than by the processes mentioned above. The osmium isotope systematics of Blusztajn & Hegner (2002) confirm the lithospheric mantle as the source region, but cannot exclude an asthenospheric contribution.

Monchiquites probably represent somewhat evolved magmas, as indicated by their low MgO, Ni and Cr contents (Figs 8 and 9). Their potassic character cannot be explained by fractionation from olivine melilitites and requires another source. For these rocks, an enriched lithospheric mantle, presumably a phlogopite- and amphibole-bearing spinel lherzolite, was assumed (Wilson & Downes, 1992). Indeed, phonolitic tephrite HTAC1117 contains MgO-rich mica (xeno)crysts which resemble those found in lithospheric mantle xenoliths in the Massif Central and the Rhenish Massif (Wilson & Downes, 1991). Whole-rock isotope data from Schleicher *et al.* (1990) strengthen the assumption of two magma sources, as the olivine/basanitic nephelinites exhibit lower $^{87}Sr/^{86}Sr$ isotope ratios ($^{87}Sr/^{86}Sr$ =0·7032–0·7040) than the monchiquites ($^{87}Sr/^{86}Sr$ =0·7039–0·7051).

In summary, at least, two types of parental magmas are necessary to explain the lithological variability of the silicate rocks of the KVC. We envisage that these magmas were produced from a mineralogically and isotopically heterogeneous mantle source, similar to what was proposed for comparable silicate rock-carbonatite complexes at Mt. Vulture (Melluso *et al.*, 1996) or Tamazeght (Marks *et al.*, 2008*a*).

### Redox conditions in carbonatite-producing mantle domains

The few carbonatites for which redox estimates are available (Oka, Chernigovskiy, Jacupiranga, Palabora; see above) contain baddeleyite, perovskite, monticellite or melilite, which suggests $aSiO_2$ values well below 0·2. Hence, silica-corrected redox conditions are actually several log units above the FMQ-buffer, very similar to our results for the KVC carbonatites (see above; Fig. 18c), and imply highly oxidized parental source regions for carbonatites.

One of the most oxidized mantle regions known are rift-related environments that can reach oxygen fugacities of up to $\Delta FMQ = +3{\cdot}5$ (Foley, 2011 and references therein) even without considering the silica-corrected FMQ-buffer (see above). Indeed, many carbonatite complexes, including the KVC, formed in rift settings, with the highest mantle redox estimates being determined for the Olmani peridotites derived from the lithospheric mantle below the East African Rift. Here, rising carbonate-bearing melts from the asthenosphere caused intense metasomatism (Rudnick *et al.*, 1993, 1994) that probably increased the oxidation state of the lithospheric mantle. Similar processes at the base of the mantle lithosphere are assumed for the source region of the olivine melilitites associated with the KVC (e.g. Dunworth & Wilson, 1998; see above). However, their apparently variable redox conditions (Dunworth & Wilson, 1998) may be caused by contrasting redox states at the boundary between lithospheric and asthenospheric mantle (e.g. Ballhaus, 1993; Ballhaus & Frost, 1994). These differences may have determined the major fractionating phases (olivine versus melilite) during further evolution of the olivine melilititic melts, leading to either nephelinitic–limburgitic or to melilititic–haüynitic rock series (see above). Since the parental liquids to carbonatites are generally assumed to originate from the sub-lithospheric mantle, the source region for those rocks must be heavily influenced by asthenospheric fluids or melts (Bell & Simonetti, 2010). Therefore, the high redox conditions for the rocks of the KVC reflect the interaction between the mantle lithosphere and carbonate-bearing melts or metasomatic fluids emanating from the asthenosphere. The presence of $CO_2$ during peridotite melting produces silica-undersaturated melts of carbonatitic and melilititic to nephelinitic composition (e.g. Wallace & Green, 1988; Dasgupta *et al.*, 2007). Such associations are found at many carbonatite complexes worldwide (e.g. Kaiserstuhl, Mt. Vulture, Magnet Cove, Tamazeght, Oldoinyo Lengai, Kerimasi) and the silicate rocks often contain mineral assemblages that indicate oxidized crystallization conditions (e.g. perovskite-magnetite-clinopyroxene or garnet-magnetite-wollastonite-clinopyroxene), even where carbonatites are lacking (e.g. Sadiman; Zaitsev *et al.*, 2012).

The oxidation of carbon stored as diamonds at the base of the lithosphere has been proposed as a process to generate carbonate-bearing magmas (carbonate redox melting; Foley *et al.*, 2009; Foley, 2011). As the oxygen fugacity of the mantle increases with decreasing pressure (Ballhaus & Frost, 1994; Woodland & Koch, 2003; Frost & McCammon, 2008), carbonatitic melts may be produced by lithospheric thinning, and hence are often associated with continental rifting. However, present and past subduction zones may equally be responsible for the formation of heterogeneously oxidized mantle domains that may be reactivated much later in an entirely different tectonic setting (e.g. Parkinson & Arculus, 1999; Frost & McCammon, 2008; Martin *et al.*, 2017), as suggested by subduction-like isotope signatures in some carbonatites (e.g. van Achterbergh *et al.*, 2002; Walter *et al.*, 2008; Hulett *et al.*, 2016).

## SUMMARY AND CONCLUSIONS

Based on the estimated crystallization parameters ($T$, $fO_2$ and $aSiO_2$) and fractional crystallization models, we propose that two different magma series are responsible for

the various rock types exposed at the KVC. The generally low Na/K ratio of the tephritic to phonolitic rock series implies a K-basanitic parental magma, as previously suggested by Keller (1984*a*, 1984*b*) and Kim (1985). The geochemistry and high formation temperatures of the monchiquites (above 1100°C) exclude a genetic link to the more primitive olivine/basanitic nephelinites and limburgites. The evolution of the tephritic–phonolitic rock series via fractional crystallization is characterized by decreasing silica activity and increasing oxygen fugacity, accompanied by mineralogical changes from olivine–clinopyroxene–spinel assemblages in the more primitive rocks via clinopyroxene-magnetite assemblages in the intermediate members to clinopyroxene–garnet-titanite assemblages in the most evolved lithologies. The parental magma of the nephelinitic, melilitic and haüynitic rocks, however, may be similar in composition to olivine melilitites from SW Germany. Variations in the redox state during differentiation may cause variable degrees of melilite versus olivine fractionation and could result in the formation of either olivine/basanitic nephelinites ($\Delta$FMQ* of around $+3$) or haüyne melilitites ($\Delta$FMQ* $=$ $+4$–6). Based on various geochemical arguments and their similarly high redox conditions ($\Delta$FMQ* $=$ $+6$–7), the carbonatites probably have a genetic relation to the haüyne melilitites.

The highly oxidized conditions of these melts seem to be typical of such complexes as the association of carbonatites with oxidized alkaline silicate rocks is a common feature worldwide. Therefore, we conclude that oxidizing and carbonated fluids/melts interacting with the mantle lithosphere is a major prerequisite for the subsequent genesis of mixed alkaline silicate rock-carbonatite complexes.

## ACKNOWLEDGMENTS

We would like to thank Simone Schafflick for sample preparation in Tübingen and are grateful to Wolfhard Wimmenauer (University of Freiburg), Anatoly Zaitsev (University of St. Petersburg), James Connolly (ETH Zürich), Filippo Ridolfi (University of Hannover) who helped with many hints and discussions. Special thanks to Philipp Seeger. The help of terratec Geophysical Services (Heitersheim, Germany) by sharing unpublished results of their ongoing geophysical investigations in the Kaiserstuhl area is highly acknowledged. The Landesamt für Rohstoff, Geologie and Bergbau (Geological Survey for Baden-Württemberg) is thanked for providing numerous samples. Constructive comments by Anton Chakhmouradian, Antonio Simonetti, an anonymous reviewer and editor Gerhard Wörner on an earlier version of this contribution are gratefully acknowledged.

## FUNDING

This work was supported by the Deutsche Forschungsgemeinschaft [grant number MA2563/12–1] and the European Union's Horizon 2020 research and innovation programme [grant number 689909].

## SUPPLEMENTARY DATA

Supplementary data are available at *Journal of Petrology* online.

## REFERENCES

Andersen, D. J., Lindsley, D. H. & Davidson, P. M. (1993). QUILF: a pascal program to assess equilibria among Fe-Mg-Mn-Ti oxides, pyroxenes, olivine, and quartz. *Computers & Geosciences* **19**, 1333–1350.

Anderson, J. L. & Smith, D. R. (1995). The effects of temperature and $fO_2$ on the Al-in-hornblende barometer. *American Mineralogist* **80**, 549–559.

Arató, R. & Audétat, A. (2017). Experimental calibration of a new oxybarometer for silicic magmas based on vanadium partitioning between magnetite and silicate melt. *Geochimica et Cosmochimica Acta* **209**, 284–295.

Armstrong, J. T. (1991). Quantitative elemental analysis of individual microparticles with electron beam Instruments. In: Heinrich, K. F. J. & Newbury, D. E. (eds) *Electron Probe Quantitation*. Springer, New York: Plenum, pp. 261–315.

Bakhashwin, M. (1975). Petrographische und geochemische Untersuchung der silikatischen Gesteine aus der Forschungsbohrung Kaiserstuhl 1970. PhD thesis, Universität Freiburg, 99 pp.

Ballhaus, C. (1993). Redox states of lithospheric and asthenospheric upper mantle. *Contributions to Mineralogy and Petrology* **114**, 331–348.

Ballhaus, C. & Frost, B. R. (1994). The generation of oxidized CO2-bearing basaltic melts from reduced CH4-bearing upper mantle sources. *Geochimica et Cosmochimica Acta* **58**, 4931–4940.

Beccaluva, L., Coltorti, M., Di Girolamo, P., Melluso, L., Milani, L., Morra, V. & Siena, F. (2002). Petrogenesis and evolution of Mt. Vulture alkaline volcanism (Southern Italy). *Mineralogy and Petrology* **74**, 277–297.

Bell, K. (1998). Radiogenic isotope constraints on relationships between carbonatites and associated silicate rocks—a brief review. *Journal of Petrology* **39**, 1987–1996.

Bell, K. & Simonetti, A. (2010). Source of parental melts to carbonatites–critical isotopic constraints. *Mineralogy and Petrology* **98**, 77–89.

Blust, G. (1993). Petrographie und Geochemie der silikatischen Ganggesteine der Bohrung KB3 Steinreise. Diplomathesis, Universität Freiburg, 83 pp.

Blusztajn, J. & Hegner, E. (2002). Osmium isotopic systematics of melilitites from the Tertiary Central European Volcanic Province in SW Germany. *Chemical Geology* **189**, 91–103.

Bouiflane, M. (2008). Cartographies aéromagnétique et magnétique multi-échelles: étude structurale d'une région du Fossé rhénan. PhD thesis, Université Louis Pasteur Strasbourg, 206 pp.

Brooker, R. & Kjarsgaard, B. (2011). Silicate–carbonate liquid immiscibility and phase relations in the system SiO2–Na2O–Al2O3–CaO–CO2 at 0· 1–2· 5 GPa with applications to carbonatite genesis. *Journal of Petrology* **52**, 1281–1305.

Bussweiler, Y., Foley, S. F., Prelević, D. & Jacob, D. E. (2015). The olivine macrocryst problem: new insights from minor and trace element compositions of olivine from Lac de Gras kimberlites, Canada. *Lithos* **220-223**, 238–252.

Carswell, D., Wilson, R. & Zhai, M. (1996). Ultra-high pressure aluminous titanites in carbonate-bearing eclogites at

Shuanghe in Dabieshan, central China. *Mineralogical Magazine* **60**, 461–471.
Chakhmouradian, A. R. (2006). High-field-strength elements in carbonatitic rocks: geochemistry, crystal chemistry and significance for constraining the sources of carbonatites. *Chemical Geology* **235**, 138–160.
Chakhmouradian, A. R., Reguir, E. P., Kamenetsky, V. S., Sharygin, V. V. & Golovin, A. V. (2013). Trace-element partitioning in perovskite: implications for the geochemistry of kimberlites and other mantle-derived undersaturated rocks. *Chemical Geology* **353**, 112–131.
Connolly, J. (1990). Multivariable phase diagrams: an algorithm based on generalized thermodynamics. *American Journal of Science* **290**, 666–718.
Cosca, M., Moecher, D. & Essene, E. (1986). Activity-composition relations for the join grossular-andradite and application to calc-silicate assemblages. *Geological Society of America, Abstracts with Programs* **18**, 572.
Czygan, W. (1977). Petrographie und Geochemie der Foidsyenit-Einschlüsse im Phonolith von Niederrotweil im Kaiserstuhl. *Berichte der Naturforschenden Gesellschaft Freiburg im Breisgau* **67**, 41–52.
Dalton, J. A. & Presnall, D. C. (1998). Carbonatitic melts along the solidus of model lherzolite in the system CaO-MgO-Al 2 O 3-SiO 2-CO 2 from 3 to 7 GPa. *Contributions to Mineralogy and Petrology* **131**, 123–135.
Dalton, J. A. & Wood, B. J. (1993). The compositions of primary carbonate melts and their evolution through wallrock reaction in the mantle. *Earth and Planetary Science Letters* **119**, 511–525.
Dasgupta, R., Hirschmann, M. M. & Smith, N. D. (2007). Water follows carbon: CO2 incites deep silicate melting and dehydration beneath mid-ocean ridges. *Geology* **35**, 135–138.
De Fino, M., La Volpe, L. & Piccarreta, G. (1982). Magma evolution at mount vulture (Southern Italy). *Bulletin Volcanologique* **45**, 115–126.
Dunworth, E. A. & Wilson, M. (1998). Olivine melilitites of the SW German Tertiary Volcanic Province: mineralogy and petrogenesis. *Journal of Petrology* **39**, 1805–1836.
Edel, J., Fuchs, K., Gelbke, C. & Prodehl, C. (1975). Deep structure of southern Rhinegraben area from seismic refraction investigations. *Journal of Geophysics-Zeitschrift für Geophysik* **41**, 333–356.
Farmer, G. L. & Boettcher, A. (1981). Petrologic and crystal-chemical significance of some deep-seated phlogopites. *American Mineralogist* **66**, 1154–1163.
Flohr, M. J. & Ross, M. (1990). Alkaline igneous rocks of Magnet Cove, Arkansas: mineralogy and geochemistry of syenites. *Lithos* **26**, 67–98.
Foley, S. F. (2011). A reappraisal of redox melting in the Earth's mantle as a function of tectonic setting and time. *Journal of Petrology* **52**, 1363–1391.
Foley, S. F., Prelevic, D., Rehfeldt, T. & Jacob, D. E. (2013). Minor and trace elements in olivines as probes into early igneous and mantle melting processes. *Earth and Planetary Science Letters* **363**, 181–191.
Foley, S. F., Yaxley, G., Rosenthal, A., Buhre, S., Kiseeva, E., Rapp, R. & Jacob, D. (2009). The composition of near-solidus melts of peridotite in the presence of CO2 and H2O between 40 and 60 kbar. *Lithos* **112**, 274–283.
Friel, J. & Ulmer, G. (1974). Oxygen fugacity geothermometry of the Oka carbonatite. *American Mineralogist* **59**, 314–318.
Frost, B. R. (1991). Introduction to oxygen fugacity and its petrologic importance. *Reviews in Mineralogy and Geochemistry* **25**, 1–9.
Frost, D. J. & McCammon, C. A. (2008). The redox state of Earth's mantle. *Annual Review of Earth and Planetary Sciences* **36**, 389–420.
Fuhrman, M. & Lindsley, D. H. (1988). Ternary-feldspar modeling and thermometry. *American Mineralalogist* **73**, 201–215.
Gaspar, J. C. & Wyllie, P. J. (1983). Magnetite in the carbonatites from the Jacupiranga Complex, Brazil. *American Mineralogist* **68**, 195–213.
Giampaolo, C., Godano, R. F., Di Sabatino, B. & Barrese, E. (1997). The alteration of leucite-bearing rocks: a possible mechanism. *European Journal of Mineralogy* **9**, 1277–1292.
Giehl, C., Marks, M. & Nowak, M. (2013). Phase relations and liquid lines of descent of an iron-rich peralkaline phonolitic melt: an experimental study. *Contributions to Mineralogy and Petrology* **165**, 283–304.
Gittins, J. (1989). The origin and evolution of carbonatite Magmas. In: Bell, K. (ed.). *Carbonatites: Genesis and Evolution.* London: Unwin Hyman, pp. 580–600.
Gittins, J. & Jago, B. (1998). Differentiation of natrocarbonatite magma at Oldoinyo Lengai volcano, Tanzania. *Mineralogical Magazine* **62**, 759–768.
Govindaraju, K. (1989). Compilation of working values and sample description for 272 geostandards. *Geostandards and Geoanalytical Research* **13**, 1–113.
Govindaraju, K. (1994). Compilation of working values and sample description for 383 geostandards. *Geostandards and Geoanalytical Research* **18**, 1–158.
Grapes, R. & Keller, J R. (2010). Fe2+-dominant rhonite in undersaturated alkaline basaltic rocks, Kaiserstuhl volcanic complex, Upper Rhine Graben, SW Germany. *European Journal of Mineralogy* **22**, 285–292.
Groschopf, R., Kessler, G., Leiber, J., Maus, H., Ohmert, W., Schreiner, A. & Wimmenauer, W. (1996). *Geologische Karte von Baden-Württemberg 1: 50000 Erläuterungen zum Blatt Freiburg i. Br. und Umgebung*. Freiburg i. Br.: Geologisches Landesamt Baden-Württemberg, 364 pp.
Grutzeck, M., Kridelbaugh, S. & Weill, D. (1974). The distribution of Sr and REE between diopside and silicate liquid. *Geophysical Research Letters* **1**, 273–275.
Guzmics, T., Mitchell, R. H., Szabó, C., Berkesi, M., Milke, R. & Ratter, K. (2012). Liquid immiscibility between silicate, carbonate and sulfide melts in melt inclusions hosted in co-precipitated minerals from Kerimasi volcano (Tanzania): evolution of carbonated nephelinitic magma. *Contributions to Mineralogy and Petrology* **164**, 101–122.
Halama, R., Vennemann, T., Siebel, W. & Markl, G. (2005). The Grønnedal-Ika carbonatite–syenite complex, South Greenland: carbonatite formation by liquid immiscibility. *Journal of Petrology* **46**, 191–217.
Hanson, G. N. (1980). Rare earth elements in petrogenetic studies of igneous systems. *Annual Review of Earth and Planetary Sciences* **8**, 371–406.
Harmer, R., Lee, C. & Eglington, B. (1998). A deep mantle source for carbonatite magmatism: evidence from the nephelinites and carbonatites of the Buhera district, SE Zimbabwe. *Earth and Planetary Science Letters* **158**, 131–142.
Holland, T. J. (1990). Activities of components in omphacitic solid solutions. *Contributions to Mineralogy and Petrology* **105**, 446–453.
Holland, T. & Blundy, J. (1994). Non-ideal interactions in calcic amphiboles and their bearing on amphibole-plagioclase thermometry. *Contributions to Mineralogy and Petrology* **116**, 433–447.
Holland, T. & Powell, R. (1998). An internally consistent thermodynamic data set for phases of petrological interest. *Journal of Metamorphic Geology* **16**, 309–343.
Holland, T. & Powell, R. (2003). Activity–composition relations for phases in petrological calculations: an asymmetric multicomponent formulation. *Contributions to Mineralogy and Petrology* **145**, 492–501.

Hubberten, H.-W., Katz-Lehnert, K. & Keller, J. (1988). Carbon and oxygen isotope investigations in carbonatites and related rocks from the Kaiserstuhl, Germany. *Chemical Geology* **70**, 257–274.

Hulett, S. R., Simonetti, A., Rasbury, E. T. & Hemming, N. G. (2016). Recycling of subducted crustal components into carbonatite melts revealed by boron isotopes. *Nature Geoscience* **9**, 904.

Keller, J. (1978). Primary olivine nephelinitic magmas in the Rhinegraben riftvalley volcanism (Central Europe). Abstract presented at the International Geodynamics Conference on 'Magma Genesis', pp. 270–271.

Keller, J. (1981). Carbonatitic volcanism in the Kaiserstuhl alkaline complex: evidence for highly fluid carbonatitic melts at the Earth's surface. *Journal of Volcanology and Geothermal Research* **9**, 423–431.

Keller, J. (1984a). Der jungtertiäre Vulkanismus Südwestdeutschlands: Exkursionen im Kaiserstuhl und Hegau. *Fortschritte der Mineralogie* **62**, 2–35.

Keller, J. (1984b). Geochemie und Magmenentwicklung im Kaiserstuhl. *Fortschritte der Mineralogie* **62**, 116–118.

Keller, J., Brey, G., Lorenz, V. & Sachs, P. (1990). IAVCEI 1990: Preconference Excursion 2A: Volcanism and Petrology of the Upper Rhine Graben (Urach-Hegau-Kaiserstuhl), IAVCEI, International Volcanological Congress, Mainz, 60 pp.

Kim, J. (1985). Petrologie und Geochemie der tephritischen Gesteine im Kaiserstuhl. PhD thesis, Unviersität Freiburg, 184 pp.

Kjarsgaard, B. & Peterson, T. (1991). Nephelinite-carbonatite liquid immiscibility at Shombole volcano, East Africa: Petrographic and experimental evidence. *Mineralogy and Petrology* **43**, 293–314.

Koberski, U. (1992). Anwendungen der Kathodolumineszenz auf Fragestellungen in der Petrologie. PhD thesis, Unviersität Freiburg, 213 pp.

Kraml, M., Pik, R., Rahn, M., Selbekk, R., Carignan, J. & Keller, J. (2006). A new multi-mineral age reference material for 40Ar/39Ar,(U-Th)/He and fission track dating methods: the Limberg t3 tuff. *Geostandards and Geoanalytical Research* **30**, 73–86.

Le Maitre, R., Streckeisen, A., Zanettin, B., Le Bas, M., Bonin, B., Bateman, P., Bellieni, G., Dudek, A., Efremova, A. & Keller, J. (2002). *Igneous Rocks. A Classification and Glossary of Terms. Recommendations of the IUGS Subcomission on the Systematics of Igneous Rocks*. Cambridge University Press, Cambridge, 236pp.

Leake, B. E., Woolley, A. R., Arps, C. E. S., Birch, W. D., Gilbert, M. C., Grice, J. D., Hawthorne, E., Kato, A., Kisch, H. J., Krivovichev, V. G., Linthout, K., Laird, J., Mandarino, J., Maresch, W. V., Nickel, E. H., Rock, N. M. S., Schumacher, J. C., Smith, D. C., Stephenson, N. C. N., Ungaretti, L., Whittaker, E. J. W. & Youzhi, G. (1997). Report. Nomenclature of amphiboles: report of the subcommittee on amphiboles of the international mineralogical association commission on new minerals and mineral names. *European Journal of Mineralogy* **9**, 623–321.

Leake, B. E., Woolley, A. R., Birch, W. D., Burke, E. A. J., Ferraris, G., Grice, J. D., Hawthorne, F. C., Kisch, H. J., Krivovichev, V. G., Schumacher, J. C., Stephenson, N. C. N. & Whittaker, E. J. W. (2004). Nomenclature of amphiboles: additions and revisions to the International Mineralogical Association's amphibole nomenclature. *Mineralogical Magazine* **68**, 209–215.

Lee, W.-J. & Wyllie, P. (2000). The system CaO-MgO-SiO 2-CO 2 at 1 GPa, metasomatic wehrlites, and primary carbonatite magmas. *Contributions to Mineralogy and Petrology* **138**, 214–228.

Léger, A., Rebbert, C. & Webster, J. (1996). Cl-rich biotite and amphibole from Black Rock forest, Cornwall, New York. *American Mineralogist* **81**, 495–504.

Lehnert, K. (1989). Petrologie der Gangkarbonatite im Kaiserstuhl. PhD thesis, Universität Freiburg, 290 pp.

Litasov, K. D. & Ohtani, E. (2009). Solidus and phase relations of carbonated peridotite in the system CaO–Al 2 O 3–MgO–SiO 2–Na 2 O–CO 2 to the lower mantle depths. *Physics of the Earth and Planetary Interiors* **177**, 46–58.

Locock, A. J. (2008). An Excel spreadsheet to recast analyses of garnet into end-member components, and a synopsis of the crystal chemistry of natural silicate garnets. *Computers & Geosciences* **34**, 1769–1780.

Markl, G. & Piazolo, S. (1999). Stability of high-Al titanite from low-pressure calcsilicates in light of fluid and host-rock composition. *American Mineralogist* **84**, 37–47.

Marks, M. A. & Markl, G. (2017). A global review on agpaitic rocks. *Earth-Science Reviews* **173**, 229–258.

Marks, M. A., Coulson, I. M., Schilling, J., Jacob, D. E., Schmitt, A. K. & Markl, G. (2008b). The effect of titanite and other HFSE-rich mineral (Ti-bearing andradite, zircon, eudialyte) fractionation on the geochemical evolution of silicate melts. *Chemical Geology* **257**, 153–172.

Marks, M. A., Neukirchen, F., Vennemann, T. & Markl, G. (2009). Textural, chemical, and isotopic effects of late-magmatic carbonatitic fluids in the carbonatite–syenite Tamazeght complex, High Atlas Mountains, Morocco. *Mineralogy and Petrology* **97**, 23.

Marks, M. A., Schilling, J., Coulson, I. M., Wenzel, T. & Markl, G. (2008a). The alkaline–peralkaline Tamazeght complex, High Atlas Mountains, Morocco: mineral chemistry and petrological constraints for derivation from a compositionally heterogeneous mantle source. *Journal of Petrology* **49**, 1097–1131.

Marks, M., Vennemann, T., Siebel, W. & Markl, G. (2003). Quantification of magmatic and hydrothermal processes in a peralkaline syenite–alkali granite complex based on textures, phase equilibria, and stable and radiogenic isotopes. *Journal of Petrology* **44**, 1247–1280.

Martin, A. M., Médard, E., Righter, K. & Lanzirotti, A. (2017). Intraplate mantle oxidation by volatile-rich silicic magmas. *Lithos* **292-293**, 320–333.

Melluso, L., Cucciniello, C., Le Roex, A. & Morra, V. (2016). The geochemistry of primitive volcanic rocks of the Ankaratra volcanic complex, and source enrichment processes in the genesis of the Cenozoic magmatism in Madagascar. *Geochimica et Cosmochimica Acta* **185**, 435–452.

Melluso, L., Morra, V. & Di Girolamo, P. (1996). The Mt. Vulture volcanic complex (Italy): evidence for distinct parental magmas and for residual melts with melilite. *Mineralogy and Petrology* **56**, 225–250.

Milani, L., Bolhar, R., Cawthorn, R. G. & Frei, D. (2016). In situ LA–ICP-MS and EPMA trace element characterization of Fe–Ti oxides from the phoscorite–carbonatite association at Phalaborwa, South Africa. *Mineralium Deposita* **52**, 747–768.

Munoz, J. (1984). F-OH and Cl-OH exchange in micas with applications to hydrothermal ore deposits. *Reviews in Mineralogy and Geochemistry* **13**, 469–493.

Mysen, B. O., Eggler, D. H., Seitz, M. & Holloway, J. R. (1976). Carbon dioxide in silicate melts and crystals; Part I, Solubility measurements. *American Journal of Science* **276**, 455–479.

Nesbitt, H. W., Markovics, G. & Price, R. C. (1980). Chemical processes affecting alkalis and alkaline earths during continental weathering. *Geochimica et Cosmochimica Acta* **44**, 1659–1666.

Nicholls, I. & Harris, K. (1980). Experimental rare earth element partition coefficients for garnet, clinopyroxene and amphibole coexisting with andesitic and basaltic liquids. *Geochimica et Cosmochimica Acta* **44**, 287–308.

Olin, P. H. & Wolff, J. A. (2012). Partitioning of rare earth and high field strength elements between titanite and phonolitic liquid. *Lithos* **128-131**, 46–54.

Palme, H. & O'Neill, H. S. C. (2003). Cosmochemical estimates of mantle composition. *Treatise on Geochemistry* **2**, pp 568.

Pan, V., Holloway, J. R. & Hervig, R. L. (1991). The pressure and temperature dependence of carbon dioxide solubility in tholeiitic basalt melts. *Geochimica et Cosmochimica Acta* **55**, 1587–1595.

Panina, L. & Stoppa, F. (2009). Silicate-carbonate-salt liquid immiscibility and origin of the sodalite-haüyne rocks: study of melt inclusions in olivine foidite from Vulture volcano, S. Italy. *Open Geosciences* **1**, 377–392.

Panina, L., Sharygin, V. & Keller, J. (2000). Evidence from melt inclusions in pyroxene. *Geochemistry International* **38**, 343–352.

Parkinson, I. J. & Arculus, R. J. (1999). The redox state of subduction zones: insights from arc-peridotites. *Chemical Geology* **160**, 409–423.

Prowatke, S. & Klemme, S. (2005). Effect of melt composition on the partitioning of trace elements between titanite and silicate melt. *Geochimica et Cosmochimica Acta* **69**, 695–709.

Pucher, R. (1991). Der Kaiserstuhl-Vulkan aus magnetischer Sicht. *Geologisches Jahrbuch* **E48**, 107–137.

Putirka, K., Johnson, M., Kinzler, R., Longhi, J. & Walker, D. (1996). Thermobarometry of mafic igneous rocks based on clinopyroxene-liquid equilibria, 0–30 kbar. *Contributions to Mineralogy and Petrology* **123**, 92–108.

Quantin, P. & Lorenzoni, P. (1992). Weathering of leucite to clay minerals in tephrites of the Vico volcano. *Mineralogica et Petrografica Acta* **35**, 289–296.

Ray, J. S. (2009). Radiogenic isotopic ratio variations in carbonatites and associated alkaline silicate rocks: role of crustal assimilation. *Journal of Petrology* **50**, 1955–1971.

Ridolfi, R. F., Zanetti, A., Renzulli, A., Perugini, D., Holtz, F. & Oberti, R. (2018). AMFORM, a new mass-based model for the calculation of the unit formula of amphiboles from electron microprobe analyses. *American Mineralogist: Journal of Earth and Planetary Materials* **103**, 1112–1125.

Robie, R. A. & Hemingway, B. S. (1995). Thermodynamic properties of minerals and related substances at 298.15 K and 1 bar ($10^5$ Pascals) pressure and at higher temperatures. *US Geological Survey Bulletin* **2131**, 461–461.

Rosatelli, G., Stoppa, F. & Jones, A. (2000). Intrusive calcite-carbonatite occurrence from Mt. Vulture volcano, southern Italy. *Mineralogical Magazine* **64**, 615–624.

Rosatelli, G., Wall, F. & Stoppa, F. (2007). Calcio-carbonatite melts and metasomatism in the mantle beneath Mt. Vulture (Southern Italy). *Lithos* **99**, 229–248.

Rudnick, R. L., McDonough, W. F. & Chappell, B. W. (1993). Carbonatite metasomatism in the northern Tanzanian mantle: petrographic and geochemical characteristics. *Earth and Planetary Science Letters* **114**, 463–475.

Rudnick, R. F. W., McDonough, W., & Orpin, A. (1994). Northern Tanzanian peridotite xenolith: a comparison with Kaapvaal peridotites and evidence for carbonatite interaction with ultra-refractory residues. In: Meyer, H. O. A. & Leonardos, O. (eds). *Proceedings of the 5th Int'l Kimberlite Conference: CPRM*, Brasilia. pp. 336–353.

Ryabchikov, I. D. & Kogarko, L. (2006). Magnetite compositions and oxygen fugacities of the Khibina magmatic system. *Lithos* **91**, 35–45.

Ryabchikov, I. D., Kogarko, L., Krivdik, S. & Ntaflos, T. (2008). Constraints of the formation of carbonatites in the Chernigovka Massif, Azov Region, Ukraine. *Geology of Ore Deposits* **50**, 423–432.

Schleicher, H., Baumann, A. & Keller, J. (1991). Pb isotopic systematics of alkaline volcanic rocks and carbonatites from the Kaiserstuhl, upper Rhine rift valley, FRG. *Chemical Geology* **93**, 231–243.

Schleicher, H., Keller, J. & Kramm, U. (1990). Isotope studies on alkaline volcanics and carbonatites from the Kaiserstuhl, Federal Republic of Germany. *Lithos* **26**, 21–35.

Schnetzler, C. & Philpotts, J. A. (1970). Partition coefficients of rare-earth elements between igneous matrix material and rock-forming mineral phenocrysts—II. *Geochimica et Cosmochimica Acta* **34**, 331–340.

Seeger, P. (2015). Fremdgesteinseinschlüsse im Ganggestein des Horberigs im Kaiserstuhl. BSc thesis, Universität Tübingen, 119 pp.

Shimizu, N. & Kushiro, I. (1975). The partitioning of rare earth elements between garnet and liquid at high pressures: preliminary experiments. *Geophysical Research Letters* **2**, 413–416.

Sigmund, J. (1996). Diatrembreccien, Mantelxenolithe und Karbonatite in der Kernbohrung KB2 im Kaiserstuhl. PhD thesis, Universität Freiburg, 154 pp.

Simmons, E. C. & Hedge, C. E. (1978). Minor-element and Sr-isotope geochemistry of Tertiary stocks, Colorado mineral belt. *Contributions to Mineralogy and Petrology* **67**, 379–396.

Speer, J. A. (1984). Micas in igneous rocks. *Reviews in Mineralogy and Geochemistry* **13**, 299–356.

Stoppa, F., Sharygin, V. V. & Jones, A. P. (2008). Mantle metasomatism and alkali carbonatite silicate phase reaction as inferred by Nyerereite inclusions in Vulture volcano carbonatite rocks. In: *Proceedings of the 9th International Kimberlite Conference*.

Sutherland, D. (1967). A note on the occurrence of potassium-rich trachytes in the Kaiserstuhl carbonatite complex, West Germany. *Mineralogical Magazine and Journal of the Mineralogical Society* **36**, 334–341.

Taylor, W. & Green, D. (1987). The petrogenetic role of methane: effect on liquidus phase relations and the solubility mechanism of reduced C–H Volatiles. In: Mysen, B. O. (ed.). *Magmatic Processes: Physicochemical Principles*. University Park, PA: Geochemical Society, pp. 121–138.

Thibault, Y. & Holloway, J. R. (1994). Solubility of CO 2 in a Ca-rich leucitite: effects of pressure, temperature, and oxygen fugacity. *Contributions to Mineralogy and Petrology* **116**, 216–224.

Treiman, A. H. & Essene, E. J. (1984). A periclase-dolomite-calcite carbonatite from the Oka complex, Quebec, and its calculated volatile composition. *Contributions to Mineralogy and Petrology* **85**, 149–157.

Tropper, P. & Manning, C. E. (2008). The current status of titanite–rutile thermobarometry in ultrahigh-pressure metamorphic rocks: the influence of titanite activity models on phase equilibrium calculations. *Chemical Geology* **254**, 123–132.

Ulianov, A., Müntener, O., Ulmer, P. & Pettke, T. (2007). Entrained macrocryst minerals as a key to the source region of olivine nephelinites: Humberg, Kaiserstuhl, Germany. *Journal of Petrology* **48**, 1079–1118.

van Achterbergh, E., Griffin, W. L., Ryan, C. G., O'Reilly, S. Y., Pearson, N. J., Kivi, K. & Doyle, B. J. (2002). Subduction

signature for quenched carbonatites from the deep lithosphere. *Geology* **30**, 743–746.

Wallace, M. E. & Green, D. H. (1988). An experimental determination of primary carbonatite magma composition. *Nature* **335**, 343–346.

Walter, M. J., Bulanova, G. P., Armstrong, L. S., Keshav, S., Blundy, J. D., Gudfinnsson, G., Lord, O. T., Lennie, A. R., Clark, S. M., Smith, C. B. & Gobbo, L. (2008). Primary carbonatite melt from deeply subducted oceanic crust. *Nature* **454**, 622.

Wang, L.-X., Marks, M. A., Wenzel, T., Von Der Handt, A., Keller, J., Teiber, H. & Markl, G. (2014). Apatites from the Kaiserstuhl Volcanic Complex, Germany: new constraints on the relationship between carbonatite and associated silicate rocks. *European Journal of Mineralogy* **26**, 397–414.

Weisenberger, T. B., Spürgin, S. & Lahaye, Y. (2014). Hydrothermal alteration and zeolitization of the Fohberg phonolite, Kaiserstuhl Volcanic Complex, Germany. *International Journal of Earth Sciences* **103**, 2273–2300.

Wilson, M. & Downes, H. (1991). Tertiary—Quaternary extension-related alkaline magmatism in western and central Europe. *Journal of Petrology* **32**, 811–849.

Wilson, M. & Downes, H. (1992). Mafic alkaline magmatism associated with the European Cenozoic rift system. *Tectonophysics* **208**, 173–182.

Wilson, M., Rosenbaum, J. M. & Dunworth, E. A. (1995). Melilitites: partial melts of the thermal boundary layer? *Contributions to Mineralogy and Petrology* **119**, 181–196.

Wimmenauer, W. (1952). Petrographische Untersuchungen an einigen basischen Eruptivgesteinen des Oberrheingebietes. *Neues Jahrbuch für Mineralogie - Abhandlungen* **83**, 375–432.

Wimmenauer, W. (1962). Beiträge zur Petrographie des Kaiserstuhls. Teil IV: Die Gesteine der phonolithischen Familie. Teil V: Die subvulkanischen Breccien. *Neues Jahrbuch für Mineralogie - Abhandlungen* **98**, 367–415.

Wimmenauer, W. (2003). *Geologische Karte von Baden-Württemberg 1: 25.000 Erläuterungen zum Blatt Kaiserstuhl*. Freiburg i. Br.: Geologisches Landesamt Baden-Württemberg, 280 pp.

Wood, B. (1979). Activity-composition relationships in Ca(Mg, Fe)$Si_2O_6$-$CaAl_2SiO_6$ clinopyroxene solid solutions. *American Journal of Science* **279**, 854–875.

Woodland, A. & Koch, M. (2003). Variation in oxygen fugacity with depth in the upper mantle beneath the Kaapvaal craton, Southern Africa. *Earth and Planetary Science Letters* **214**, 295–310.

Woolley, A. R. (2001). *The Alkaline Rocks and Carbonatites of the World. Part 3: Africa*. London: The Geological Society of London, 372 pp.

Woolley, A. R. & Kjarsgaard, B. A. (2008). Paragenetic types of carbonatite as indicated by the diversity and relative abundances of associated silicate rocks: evidence from a global database. *The Canadian Mineralogist* **46**, 741–752.

Wyllie, P. J. & Lee, W.-J. (1998). Model system controls on conditions for formation of magnesiocarbonatite and calciocarbonatite magmas from the mantle. *Journal of Petrology* **39**, 1885–1893.

Yagi, K. & Onuma, K. (1978). Genesis and differentiation of nephelinitic magma. *Bulletin Volcanologique* **41**, 466–472.

Ying, J., Zhou, X. & Zhang, H. (2004). Geochemical and isotopic investigation of the Laiwu–Zibo carbonatites from western Shandong Province, China, and implications for their petrogenesis and enriched mantle source. *Lithos* **75**, 413–426.

Yoder, H. (1975). Relationship of melilite-bearing rocks to kimberlite: a preliminary report on the system akermanite-CO2. *Physics and Chemistry of the Earth* **9**, 883–894.

Zaitsev, A., Marks, M., Wenzel, T., Spratt, J., Sharygin, V., Strekopytov, S. & Markl, G. (2012). Mineralogy, geochemistry and petrology of the phonolitic to nephelinitic Sadiman volcano, Crater Highlands, Tanzania. *Lithos* **152**, 66–83.

Ziegler, P. (1982). *Geological Atlas of Central and Western Europe*. Amsterdam: Shell International Petroleum, Maatschappij BV, 130 pp.

# Appendix IV

Accepted publication

*Study 4*

Walter, B.F., Parsapoor, A., Braunger, S., Marks, M.A.W., Wenzel, T., Martin, M., Markl, G., 2018. Pyrochlore as a monitor for magmatic and hydrothermal processes in carbonatites from the Kaiserstuhl volcanic complex (SW Germany). Chemical Geology 498, 1-16. http://dx.doi.org/10.1016/j.chemgeo.2018.08.008.

Chemical Geology 498 (2018) 1–16

Contents lists available at ScienceDirect

Chemical Geology

journal homepage: www.elsevier.com/locate/chemgeo

# Pyrochlore as a monitor for magmatic and hydrothermal processes in carbonatites from the Kaiserstuhl volcanic complex (SW Germany)

B.F. Walter[a,*], A. Parsapoor[a], S. Braunger[a], M.A.W. Marks[a], T. Wenzel[a], M. Martin[b], G. Markl[a]

[a] Eberhard Karls Universität Tübingen, Wilhelmstr. 56, D-72074 Tübingen, Germany
[b] Landesamt für Geologie, Rohstoffe und Bergbau, Baden-Württemberg, Albertstraße 5, D-79104 Freiburg i. Br., Germany

ARTICLE INFO

Editor: D.B. Dingwell

*Keywords:*
Carbonatites
HFSE
Mineralization
Ore deposit
Kaiserstuhl
Magmatic
Hydrothermal
Pyrochlore
REE
Exploration
Textures

ABSTRACT

Pyrochlore from the Kaiserstuhl volcanic complex (SW Germany) shows textural and compositional differences between various coarse-grained calcite-carbonatite bodies (Badberg, Degenmatt, Haselschacher Buck, Orberg) and extrusive carbonatites (Henkenberg, Kirchberg).

Oscillatory-zoned F-rich pyrochlore with up to 69 wt% $Nb_2O_5$ is common in all coarse-grained calcite-carbonatite bodies and probably formed during magmatic conditions. However, only in some of the samples from the Badberg, partly resorbed U- and Ta-enriched pyrochlore cores with up to 22 wt% $UO_2$ and 9 wt% $Ta_2O_5$ have been identified, which are interpreted as being inherited from underlying nosean syenites. Pyrochlore data from a drill core penetrating the Badberg indicate increasing contents of REE, U, and Ta with depth, while Nb, F and Na contents decrease. This may reflect the combined effects of fractional crystallization and assimilation (AFC) or indicates a multi-stage emplacement of the carbonatitic magma. Patchy-zoned ceriopyrochlore and REE- and Th-enriched pyrochlore with up to 19 wt% total $REE_2O_3$ and 6.5 wt% $ThO_2$ is largely restricted to samples from the Orberg and probably formed during hydrothermal conditions. This can be related to the relatively evolved character of the Orberg carbonatites, based on their relatively high whole-rock Nb/Ta and Zr/Hf mass ratios. This study demonstrates that the textural and compositional variation of pyrochlore in carbonatites is a powerful tool to distinguish magmatic, hydrothermal and weathering processes in carbonatitic systems.

## 1. Introduction

The so-called High Field Strength Elements (HFSE) include the rare earth elements (REE), yttrium (Y), zirconium (Zr), hafnium (Hf), niobium (Nb), and tantalum (Ta) that are essential for many high-tech applications, such as semiconductors, displays, batteries and high performance magnets (e.g., Humphries, 2010 and references therein). The industrial demand for this element suite largely increased during the last decades and recently, the European Commission recognized a significant risk of supply for some of the HFSE and defined them as critical metals (e.g., Du and Graedel, 2011; Hatch, 2012; Massari and Ruberti, 2013; EC, 2014).

Deposits for HFSE are mostly found in alkaline rocks and carbonatites, the latter being recently defined as rocks with ≥30 vol% primary igneous carbonate minerals (Mitchell, 2005). Most carbonatites are associated with various types of alkaline silicate rocks, ranging from ultramafic (e.g., olivinites and pyroxenites in Kovdor; Krasnova et al., 2004a) to felsic (e.g., nepheline syenites at Grønnedal-Ika, Greenland; Halama et al., 2005). Among the > 500 known occurrences, only 49 contain extrusive carbonatites (Woolley and Church, 2005; Woolley and Kjarsgaard, 2008).

The most common HFSE-carriers in carbonatites are pyrochlore-group minerals, perovskite and titanite-group minerals, baddeleyite ($ZrO_2$), zirconolite ($CaZrTi_2O_7$), calzirite ($Ca(Zr,Ca)_2Zr_4(Ti,Fe)_2O_{16}$), zircon and apatite (e.g., Chakhmouradian, 2006). Pyrochlore-group minerals are especially abundant in carbonatites and are a major Nb source to date (Mitchell, 2015). Three mines are in operation today: Araxá and Cataláo-II (Brasil) and St. Honoré (Canada). Numerous occurrences are under evaluation (e.g., Aley, Upper Fir in Canada, Tomtor in Russia, Lueshe in Dem. Rep. Congo) or re-evaluation (e.g., Panda Hill in Tanzania, Oka in Canada and Fen in Norway; Gendron et al., 1981; Issa Filho et al., 1984; Mariano, 1989, Lapin and Tolstov, 1995; Nasraoui and Bilal, 2000; Mitchell, 2015 and references therein). Some carbonatites are mined for REEs (e.g., Mount Weld in Australia; Humphries, 2010, Mountain Pass in USA; Castor, 2008; and Bayan Obo in Mongolia; Yang et al., 2011) and one occurrence (Kovdor in Russia; Ivanyuk et al., 2002; Krasnova et al., 2004b) is mined for Zr with baddeleyite being an ore mineral.

* Corresponding author.
*E-mail address:* benjamin.walter@uni-tuebingen.de (B.F. Walter).

https://doi.org/10.1016/j.chemgeo.2018.08.008
Received 9 January 2018; Received in revised form 16 July 2018; Accepted 9 August 2018
Available online 07 September 2018

The Kaiserstuhl volcanic complex (SW Germany) consists of a variety of alkaline silicate rocks associated with intrusive and extrusive carbonatites (e.g., Wimmenauer, 2003, Braunger et al., in press). This eroded volcanic complex (even though it is a subeconomic occurrence) was chosen by the HiTech AlkCarb project as a natural laboratory for studying the textural, mineralogical and geochemical relationships between intrusive and extrusive carbonatites and to investigate depth-dependent systematics, which could help to improve existing geomodels (e.g., Le Bas, 1987) and exploration methods for carbonatites. We focus here on pyrochlore-group minerals because this mineral group shows significant compositional variations in various magmatic, hydrothermal and weathering stages (e.g., Wall et al., 1996; Chakhmouradian, 2006; Lumpkin and Ewing, 1995; Williams et al., 1997; Zaitsev et al., 2012). Hence, the textural and compositional variability of pyrochlore-group minerals provides the opportunity to study the geochemical evolution of a carbonatite system in detail.

Previous studies indicate mineralogical and textural variations within and between the different carbonatite bodies of the complex (Blust, 1993; Katz and Keller, 1981; Keller, 1964, 1965, 1981, 1984a, 1984b, 1989; Keller et al., 1990; Sigmund, 1996). This present study is guided by the following questions that have both economic and fundamental significance:

(1) Are there systematic textural and compositional variations of the pyrochlore-group minerals between the different carbonatite types of the complex?
(2) Are there depth-depending textural and compositional variations of pyrochlore-group minerals in coarse-grained calcite-carbonatites?
(3) Is it possible to use these variations and differences for improving exploration methods for carbonatite-related HFSE mineralizations?

## 2. The Kaiserstuhl volcanic complex

The Kaiserstuhl volcanic complex (SW-Germany) is situated in the Upper Rhinegraben rift and is part of the Central European Magmatic Province (e.g., Wilson and Downes, 2006; Lustrino and Wilson, 2007; Fig. 1A). The complex is situated at the junction of four tectonic blocks and is affected by Neogene strike slip and horst-graben tectonics in the Rhinegraben (Fig. 1B & C; Beccaletto et al., 2010). The rocks of this partly eroded stratovolcano are of Miocene age (18–15 Ma) and are dominated by mostly tephritic lavas, ash beds, sills, and dykes that are interbedded with rare nephelinitic lavas and extrusive carbonatites (Fig. 1D). This sequence was intruded by several phonolite bodies and larger masses of sodalite monzogabbros. The latter are essentially confined to the central part of the complex (Fig. 1D; e.g., Wimmenauer, 2003 and references therein). Subsequently, polygenic diatreme breccias formed (e.g., Baranyi, 1971; Sigmund, 1996) and established pathways for several larger carbonatite bodies (Fig. 2A). These are in turn intruded by phonolites that are very rarely associated with medium- to coarse-grained nosean syenite (only in the Badberg area; see Braunger et al., in press; Giebel et al., submitted). The latter rocks are known to occur at depth, based on a scientific (unfortunately lost today) drilling at the Badberg (Forschungsbohrung Kaiserstuhl FB, Kirchheimer, 1973) and their presence as cm- to dm-sized xenoliths in various lithologies across the Kaiserstuhl (Wimmenauer, 2003; Seeger, 2015). Hence, nosean syenites underly at least parts of the complex, as has been postulated by Goodenough et al. (2016). Today, most of the Kaiserstuhl rocks show variable degrees of surficial weathering and are partly covered by several tens of meters of Quaternary fluviatile and aeolian sediments (loess).

The magmatic rocks of the Kaiserstuhl have been interpreted to represent two magma series: Sodic rocks (olivine nephelinites, haüyne melilitites and (melilite) haüynites) derived from a primitive magma and a more differentiated magma type that formed sodic-potassic rocks (tephrites, phonolites, e.g., Schleicher et al., 1990, Wimmenauer, 2003). Based on isotopic studies, Schleicher et al. (1990) found evidence for a genetic link between the carbonatites and the Na-series magmas of the Kaiserstuhl. The detailed processes that generated the carbonatites, however, are still under debate (e.g., Wimmenauer, 2003; Wang et al., 2014; Braunger et al., in press).

### 2.1. Investigated sample material

More than 200 samples from drill cores, surface outcrops and sample collections at the Universität Tübingen and the LGRB (Geological Survey of Baden-Württemberg) were investigated for this study. The complete sample list (including GPS positions) and details on the scientific drillings are given in Electronic supplements ES1 and ES2, respectively. Two of the four drill cores from the Kaiserstuhl (KB2 1991 and KB3 1991) are still available (see Fig. 2A for their locations). The 195 m deep KB2 drill core from Orberg quarry II (Electronic supplement ES3) consists of coarse-grained carbonatite underlain by polygenic diatreme breccias crosscut by sodalite monzogabbro and carbonatitic veins (Sigmund, 1996). The 400 m deep KB3 drill hole at the Steinreise location (on a small hill called Horberig immediately west of the Badberg) penetrated sodalite monzogabbros and alkaline dyke rocks and underlying coarse-grained carbonatite with nosean syenite (Fig. 2A, Electronic supplement ES4). The whole profile is crosscut by various carbonatitic and silicate dyke rocks (Blust, 1993). Not preserved are the cores of the 100 m deep KB1 (1991) in the Eichstetter Tal and the 500 m deep the Badloch drill cores (1970, Electronic supplement ES5). The KB1 drilling (100 m of coarse-grained calcite-carbonatite) failed and the cores of the Badloch drilling were destroyed in a fire. Based on petrographic descriptions from the 1970s (Kirchheimer, 1973), the Badloch drilling (FB) cored coarse-grained calcite-carbonatite underlain by nosean syenite (Fig. 2A & B), interrupted by phonolitic rocks. Again, the profile was crosscut by numerous carbonatitic and silicate dyke rocks. All surficial samples (with the exception of those taken from quarry faces) show variable degrees of surficial weathering (e.g., increased porosity, alteration of mica and magnetite to secondary FeOOH-phases).

### 2.2. Geology of the carbonatites

#### 2.2.1. Coarse-grained calcite-carbonatites

Coarse-grained calcite-carbonatites (sövites) are restricted to the central part of the Kaiserstuhl, where they occur as four larger bodies (Badberg, Haselschacher Buck, Degenmatt, Orberg) and two small satellite pipes (Katharinenberg and Kirchberg, Figs. 1 & 2). The largest of these bodies (Badberg) exhibits layering structures parallel to its contact towards the country rocks and contains elongated xenoliths of fenitized nosean syenites that are similarly aligned. The abundance of these xenoliths decreases from the upper to the lower parts of the body (Fig. 2B). A tabular geometry of the Badberg body is suggested, with a NW-dipping of about 60° and an inclination-corrected thickness of < 300 m (Wimmenauer, 1963; Fig. 2). The hanging wall consists of sodalite monzogabbros, the foot wall is represented by phonolites and nosean syenites and numerous dyke rocks crosscut the Badberg carbonatite (Kirchheimer, 1973; Fig. 2B). The Degenmatt and Haselschacher Buck occurrences resemble similar structures as the Badberg but their unsatisfactory outcrop situation does not allow for a detailed structural analysis. At the Orberg, coarse-grained calcite-carbonatite was mined in five quarries. Quarries I-III expose an up to 10 m thick NNE-SSW striking dyke-like body. The variable dip of this body (about 70° in quarry III but only about 25° in quarry II; Wimmenauer, 1963) and the variably oriented layering structures in quarries IV and V (Hubaux, 1964; Fig. 2) indicate a cauliflower-like structure consisting of several dyke/sill-like apophyses surrounded by polygenic diatreme breccias (Fig. 2).

The Kaiserstuhl is situated on the junction between four tectonic blocks (Fig. 2B) and is intersected by the regional Tuniberg fault (Figs. 1 & 2) with a down-throw towards the graben center and a vertical

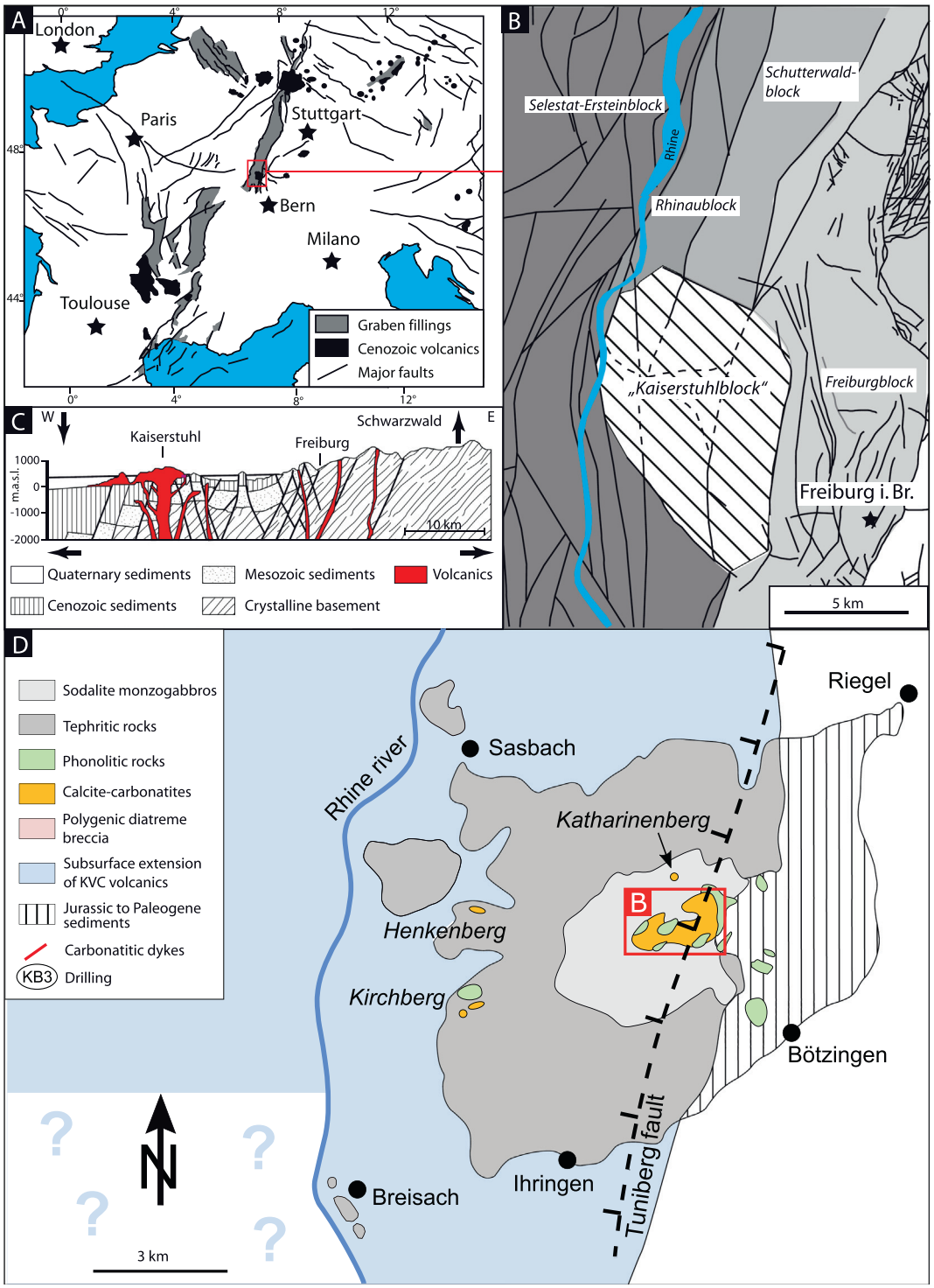


**Fig. 1.** (A) Overview map of the Central European Magmatic Province including Palaeogene rifts (grey) and volcanic products (black). (B) Subsurface tectonic map of the Kaiserstuhl area after the database of Beccaletto et al. (2010). The Kaiserstuhl is situated on four different tectonic blocks. (C) Cross section of the eastern Upper Rhine graben. Note that the extrusive rocks cover the Micocene surface, which is today mostly covered by Quaternary gravels. (D) Simplified geological map of the Kaiserstuhl volcanic complex (modified after Keller et al., 1990).

displacement of 1000–3000 m (Beccaletto et al., 2010). Therefore, we speculate that the Badberg, Degenmatt and Haselschacher Buck occurrences once belonged to a common sub-vertical pipe-like structure that was subsequently tilted and disrupted by Neogene strike-slip and horst-graben tectonics within the Upper Rhinegraben (Beccaletto et al., 2010). The Orberg occurrences may represent a larger apophysis of this hypothetical structure (e.g., Hubaux, 1964), whereas the small (< 10 m in diameter) and isolated occurrences at Kirchberg and Katharinenberg are interpreted as two minor pipe-like structures with unknown relationships to the main structure (Fig. 2).

### 2.2.2. *Medium- to fine-grained carbonatites*

Medium- to fine-grained calcite-carbonatites (alvikites) occur as (sub)vertical dykes with variable thickness (cm to m). Most of them are

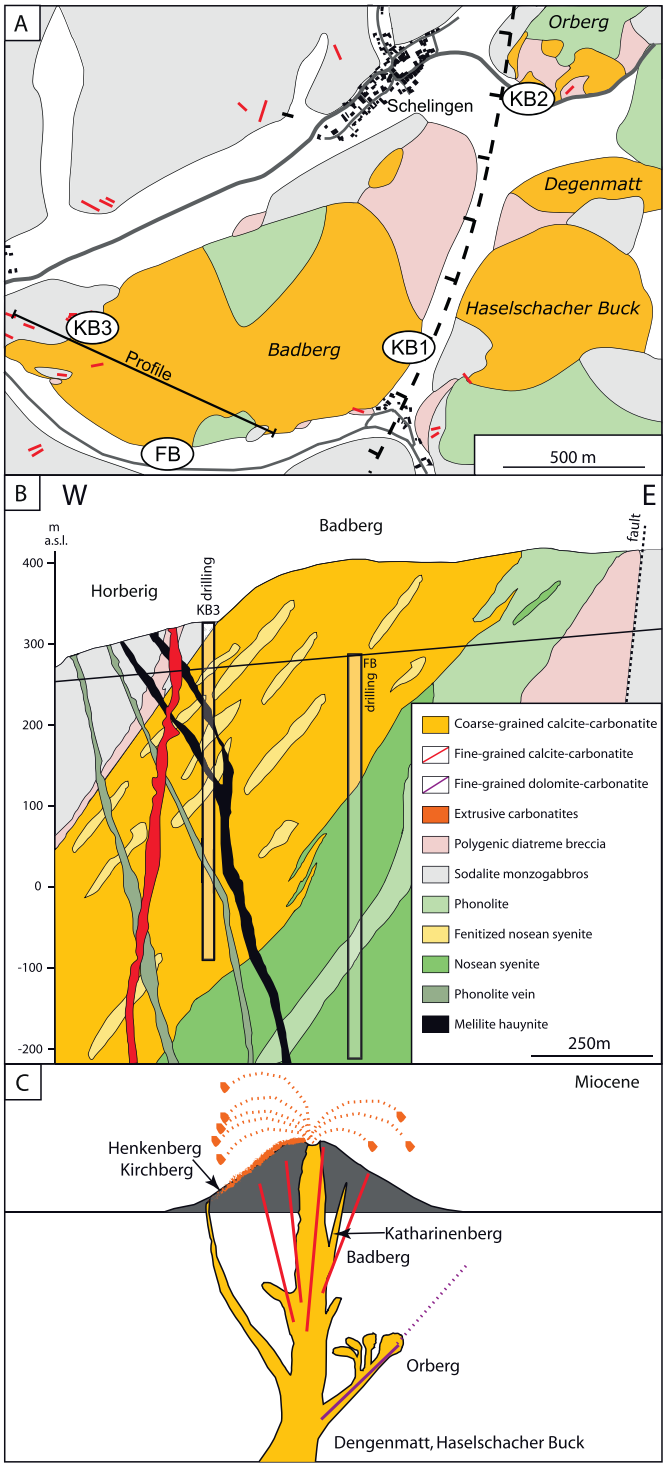


**Fig. 2.** Geology of the Karbonatites in the Kaiserstuhl. (A) Simplified map of the central part of the Kaiserstuhl (modified from Wimmenauer, 2003) with locations of the four scientific drillings. (B) Schematic W-E profile through the Horberig and western Badberg area. The profile is based on field observations and drill cores and logs. The black subhorizontal line indicates the valley S of the Badberg (see Fig. 2A). (C) Schematic illustration (not to scale) of the hypothetical, initially (sub)vertical, pipe-like structure showing the different carbonatite occurrences at the Kaiserstuhl.

disclosed in the central part of the complex, but few occur in the outer extrusive tephrites. They crosscut all other rock types (Fig. 2) and represent the youngest volcanic rocks of the complex (Katz and Keller, 1981). Most of them are assumed to belong to a radial dyke (cone sheet) system with its center below the Badberg (Lehnert, 1989).

Medium- to fine-grained dolomite-carbonatites (beforsites) rarely occur as cm- to m-sized dykes, apophyses, and irregularly formed bodies within coarse-grained calcite-carbonatites, close to the contact with the (Mg- and Fe-rich) host rocks. They occur in Orberg quarries II, III and V and in a previously not described occurrence at Degenmatt.

#### 2.2.3. Extrusive carbonatites

At the western flank of the complex, up to three layers (each 1–1.5 m thick) of extrusive carbonatites occur at Henkenberg and Kirchberg (Fig. 1D). They represent alternating sequences of carbonatitic crystal tuffs, lapillistones and lavas interbedded with tephritic and basanitic ashes and lavas (Keller, 1981, 1989; Woolley and Kjarsgaard, 2008). The distance between these two localities is about 1.5 km but because of intense anthropogenic land transformations in the 1970s only isolated outcrops are preserved and their original extent is unknown.

## 3. Petrography

### 3.1. Coarse-grained calcite-carbonatites

Detailed petrographic descriptions of these rocks are already available (e.g., Wimmenauer, 1963, 2003; Wimmenauer et al., 1977; Lehnert, 1989; Keller et al., 1990). These are briefly summarized here and we provide details on the observed textures for pyrochlore-group minerals, as these are the focus of the present study. Coarse-grained calcite-carbonatites are dominated by calcite and contain variable amounts of apatite, magnetite, phlogopite, pyrochlore-group minerals and rarely forsteritic olivine, monticellite and melilite. Common accessories include sulfides (pyrite, pyrrhotite, galena, sphalerite, chalcopyrite), barite and rare Nb-perovskite (only in some Badberg samples). The modal amount of non-carbonate minerals varies largely on the dm- to m-scale and in some areas mineral banding occurs, represented by alternating coarse-grained and finer-grained layers with very different modal amounts of apatite, magnetite and pyrochlore-group minerals.

Pyrochlore-group minerals occur in all investigated samples. They form up to 2 mm large anhedral to euhedral grains, in cases intergrown with apatite and sulfides. In samples from Badberg, Haselschacher Buck and Degenmatt, pyrochlore-group minerals typically show oscillatory zoning patterns (Fig. 3A–F). In Badberg samples taken in the vicinity of fenitized nosean syenites and from deeper levels of the KB3 drill core (see above), however, some pyrochlores contain BSE-bright cores that are partly resorbed and surrounded by the before-mentioned oscillatory-zoned mostly BSE-darker areas (Fig. 3D). Such cores were also recognized at Degenmatt and Haselschacher Buck (Fig. 3E & F). However, the bad outcrop situation at these locations does not allow to judge if these are related to fenitized nosean syenite xenoliths. At Orberg and Katharinenberg however, such bright cores (and xenoliths of fenitized nosean syenite) are typically missing (Fig. 4A–H) and pyrochlore group minerals are mostly oscillatory zoned (Fig. 4A–H) and contain late-stage BSE-bright rims (Fig. 4B) or show patchy zonation (with BSE-brighter alteration patches) textures that overprint the primary oscillatory zoning (Fig. 4F). Typically, the patchy overprinting starts at the grain boundary whereby an alteration front moves towards the core area of the pyrochlore (Fig. 4F). Furthermore, the common association with rosettes of apatite needles indicates that at least the pyrochlore group minerals in the banded carbonatites of the complex crystalized in-situ (Fig. 4C & D).

#### 3.1.1. Fenitized nosean syenites

At the Badberg, fenitized nosean syenites occur as up to several meters large xenoliths in the coarse-grained calcite-carbonatite (see above; Fig. 2B). These rocks show a primary mineralogy of haüyne ± alkali feldspar ± clinopyroxene ± garnet ± apatite ± magnetite ± titanite ± pyrochlore-group minerals that is variably metasomatized.

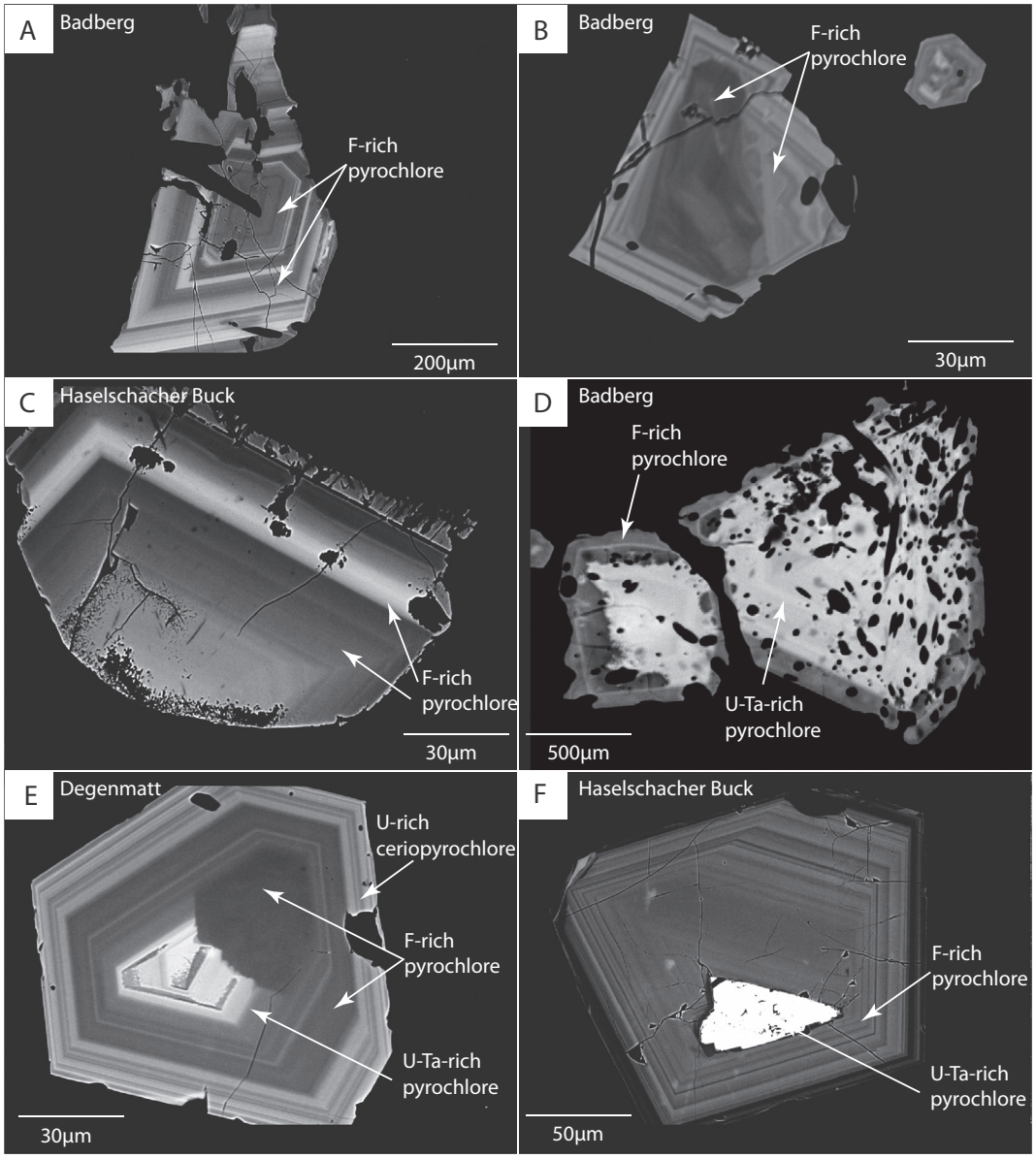


**Fig. 3.** Pyrochlore textures from coarse-grained calcite-carbonatites of the Kaiserstuhl (Badberg, Haselschacher Buck, Degenmatt). (A) & (B) Oscillatory zoned. F-rich pyrochlore from Badberg. (C) Oscillatory zoned F-rich pyrochlore from Haselschacher Buck. (D) Pyrochlore from Badberg with typical U-Ta-enriched cores overgrown by oscillatory zoned F-rich pyrochlore. (E) Oscillatory zoned pyrochlore with a BSE-bright core from Degenmatt. (F) Oscillatory zoned F-rich with BSE-bright U-Ta-enriched core from Haaelschacher Buck.

The samples contain variable amounts of coarse-grained interstitial calcite and former nosean or haüyne and alkali feldspar are largely now decomposed to various zeolite minerals and calcite. Clinopyroxene occurs mostly as pale green, sometimes patchy-colored subhedral and interstitial grains and if present, a dark brown garnet I is overgrown by a reddish-brownish garnet II that occasionally forms poikilitic aggregates that enclose former foid minerals (for details see Giebel et al., submitted). Pyrochlore-group minerals typically consist of BSE-bright cores that are partly resorbed and overgrown by oscillatory-zoned areas.

### 3.2. Medium- to fine-grained carbonatitic dykes

These rocks include banded, comb-layered, porphyritic and streaky varieties of medium-to fine-grained calcite-carbonatites described in detail in Katz and Keller (1981), Hubberten et al. (1988) and Lehnert (1989). Briefly, they consist of a groundmass of calcite with bands or striations of magnetite, apatite, pyrochlore (mostly unzoned) and Nb-perovskite. In some cases, calcite ocelli, phlogopite, rare alabandine and primary barite were recognized. Porphyritic varieties further contain rounded and deformed clasts of coarse-grained calcite and accessory garnet, pyrochlore, magnetite, amphibole, forsteritic olivine, zirconolite, calzirite and baddeleyite. Rare medium-to fine-grained dolomite-carbonatites consist of a fine-grained groundmass of dolomite-ankerite and contain the same non-carbonate minerals as medium-to fine-grained calcite-carbonatites, with additional bastnaesite and monazite (Wimmenauer, 2003).

### 3.3. Extrusive carbonatites

The petrography of the extrusive carbonatites from the complex has been described in detail before (e.g., Keller, 1981, 1989; Hubberten et al., 1988). Briefly, carbonatitic crystal tuffs from Henkenberg are mainly composed of sparry calcite with clasts of fenitized nosean syenites, coarse-grained calcite, magnetite, garnet and augitic pyroxene,

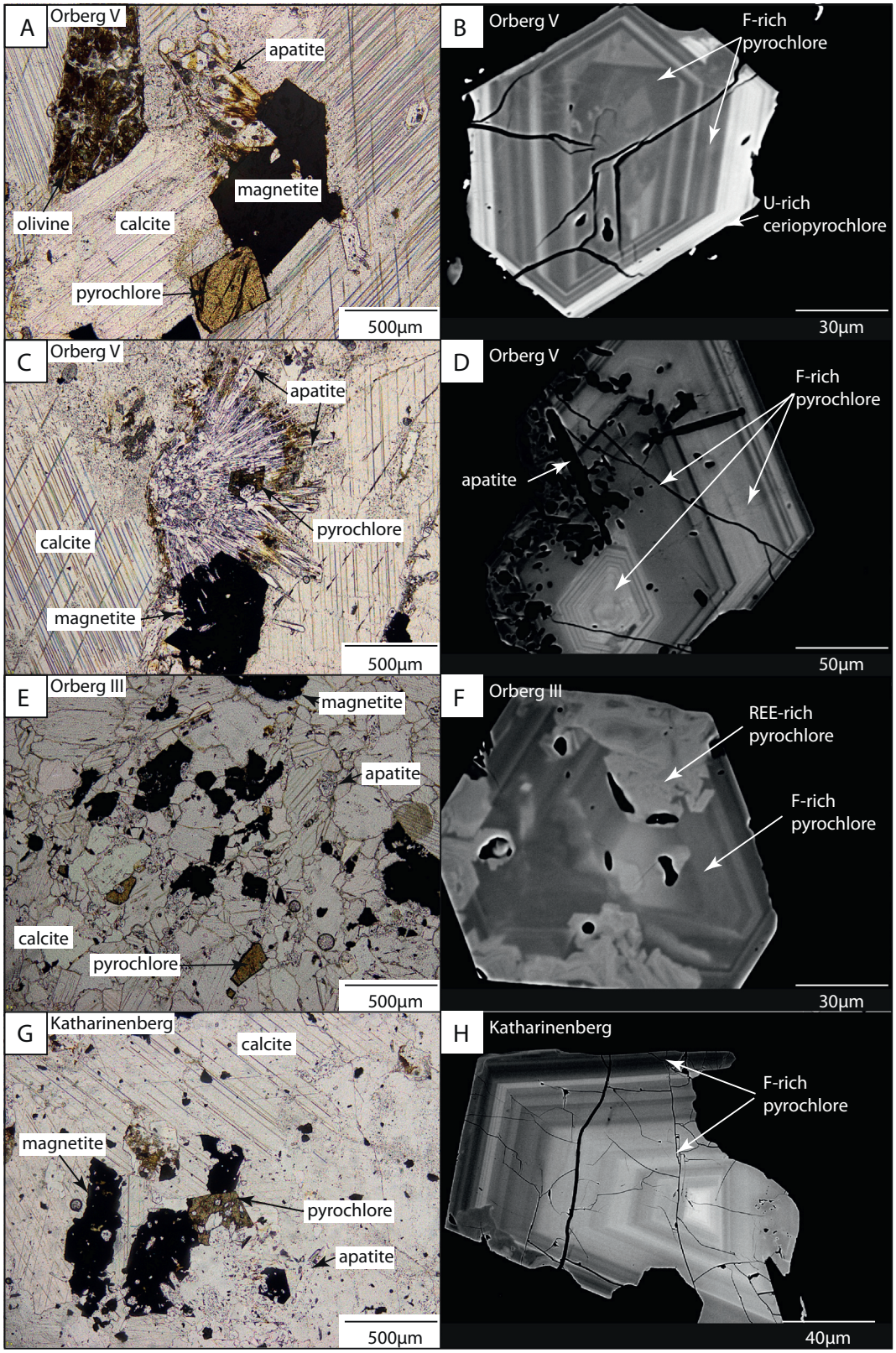


**Fig. 4.** Pyrochlore textures from coarse-grained calcite-carbonatites of the Kaiserstuhl (Orberg, Katharinenberg). (A) Euhedral pyrochlore associated with magnetite and apatite from Orberg quarry V. (B) Typically, at Orberg the U-Ta-enriched pyrochlore cores are missing. Often the oscillatory zoned Orberg pyrochlores contain U-rich ceriopyrochlore or U-REE-Th enriched pyrochlores rims. (C & D) At Orberg quarry V and elsewhere, rosettes of apatite needles are over- and intergrown with pyrochlore. (E & F) In the finer-grained calcite-carbonatite of Orberg quarry III pyrochlores often occur as euhedral grains with a patchy zonation that overprints the primary oscillatory zoning. (G & H). Pyrochlore from Katharinenberg is typically oscillatory zoned and lacks U-Ta-enriched BSE-bright cores.

and rare apatite and pyrochlore-group minerals. Carbonatitic lapilli tuffs consist of closely-packed lapilli of 0.5 to 10 mm diameter, cemented by secondary calcite. The lapilli have a porphyritic and trachytoid texture with phenocrysts of platy calcite, minor magnetite and accessory clinopyroxene, garnet, apatite, Nb-perovskite, and pyrochlore-group minerals. A carbonatite lava from Kirchberg consists of a fine-grained and altered carbonate-rich matrix with platy calcite phenocrysts accompanied by minor euhedral to subhedral magnetite, garnet, nepheline, and alkali feldspar.

## 4. Analytical methods

### 4.1. Whole-rock analyses

Prior to analysis, all samples (generally ≥1 kg) were liberated from weathering crusts and crushed. About 50 g representative sample aliquotes were then ground with an agate mill for 10 min. Loss on ignition was determined from 1 g sample material at 1000 °C.

Major elements were analysed by means of wavelength dispersive XRF at Universität Tübingen (Germany). For the fused beads 1.5000 g of dried sample powder (at 105 °C) was mixed with 7.5000 g MERCK spectromelt A12 (mixture of 66% Li-tetraborate and 34% Li-metaborate) and melted at 1200 °C beads using an Oxiflux system from CBR analytical service. Measurements were done using a Bruker AXS S4 Pioneer system (Rh-tube at 4 kW) with 32 standardised samples (Govindaraju, 1989). Analytical uncertainties are usually in the range of 0.1% (relative), and detection limits are in the range of 1–10 µg/g.

Trace element contents were determined with ICP-MS (X-series 2, Thermo Fisher Scientific) at the Karlsruhe Institute of Technology (Germany) using acid digestion of 100 mg of representative sample powder. To assure complete silicate decomposition, 40% HF (suprapur), 65% $HClO_4$ (normatom) and the pre-oxidized (65% $HNO_3$, subboiled) sample were heated in a closed Teflon vessel for 16 h at 120 °C. After evaporating the acids to incipient dryness, the residue was re-dissolved in 65% $HNO_3$ (subboiled) and evaporated again (three times) for purification purposes. The final residue was dissolved in 50 ml of ultrapure water. The quality assurance of the trace element ICP-MS measurements was done by including the certified reference material CRM-TMDW-A (High-Purity standards, Inc.) into the protocol (accuracy: ± 10% for most elements). Mathematical corrections of Eu, Gd, Tb and Er were necessary due to high concentrations of Ba and light REE. $^{151/153}$Eu was corrected for BaO interferences, $^{157}$Gd for PrO and $^{158}$Gd for CeO interferences, $^{159}$Tb and $^{167}$Er for NdO interferences. The mean value of both isotopes is given for Eu and Gd. To assure the quality of the whole procedure, six blanks and two certified reference materials (SY-2, SY-3; Govindaraju, 1994) were included into the digestions process (accuracy: mainly ± 10%). The reproducibility ( ± 5% for most elements) was checked by digesting a phonolitic sample in triplicate.

### 4.2. Electron microprobe analyses

For analyses of pyrochlore-group minerals a JEOL 8900 electron microprobe at the University of Tübingen was used with a beam current of 10 nA and an acceleration voltage of 20 kV in connection with a focused beam. For calibration, diopside was used for Ca and Si, albite for Na, hematite for Fe, bustamite for Mn, $ThO_2$ for Th, $SrTiO_3$ for Sr and Ti, $Li_2Ta_2O_6$ for Ta, $Al_2O_3$ for Al, $LiNb_2O_6$ for Nb, $ZrO_2$ for Zr, YAG-glass for Y, $UO_2$ for U, La-glass (REE16G) for La, Ce-glass (REE16G) for Ce, Pr-glass for Pr (REE16G), Sm-glass for Sm (REE16G), and $CaF_2$ was used for F. Counting times on the peak were 16 s for Ca, 30 s for Na, Si, Sr, Nb, Ta, Al, Y, Fe, Mn, La, Ce, Sm, Pr, Nd, Ti, Zr, U, Th and Sr and 60 s for F. Background counting times (upper and lower) where half the peak times. Data reduction was performed using the internal ZAF matrix correction software of JEOL (Bence and Albee, 1968; Armstrong, 1988, 1991). Details on the WDS configuration used and typical detection limits for the individual elements are given in the Electronic supplement ES6. High-precision quantitative analyses of F are difficult, as for light elements, significant peak shifts may occur that result in unreliable net peak intensities (e.g., Bastin et al., 1986; Wenzel et al., 2003). Therefore, the area intensity measurement mode was applied for determining F contents. Hereby, the WDX signal was step-wise integrated from the lower to the upper background along the F peak position on a F-rich pyrochlore of sample HTAC_1200.

## 5. Results

### 5.1. Whole rock data

All investigated samples (N = 43) are classified as calcio-carbonatites (Woolley and Kempe, 1989), as they are low in $Na_2O$ (< 1.4 wt%), $Fe_2O_3$ (< 8.4 wt%), and MgO (< 3.7 wt%), with no clear differences between intrusive and extrusive samples or localities (Electronic supplement ES7). As being typical for carbonatites, primitive-mantle normalized trace element patterns (Fig. 5A) show variable enrichment of LILE (e.g., Ba, Sr) and P, with some HFSE being strongly enriched (Nb, Ta, REE) and others showing variable depletion (Zr, Hf, U, Th, Ti). Compared to global carbonatite data (Chakhmouradian, 2006), the contents of Nb (up to 2700 µg/g) are relatively high, whereas Zr contents (< 300 µg/g) are rather low (Fig. 5B & C). All investigated samples have typical LREE-enriched patterns and the absolute REE contents (up to about 2700 µg/g) roughly correlate with $P_2O_5$ (Fig. 5D).

### 5.2. Compositional variation of pyrochlore-group minerals

The general formula of this mineral group is $A_{2-m}B_2X_{6-w}Y_{1-n}{\cdot}pH_2O$ (Lumpkin and Ewing, 1995; Atencio et al., 2010). At the A site, As, Ba, Bi, Ca, Cs, K, Mg, Mn, Na, Pb, REE, Sb, Sr, Th, U and Y are incorporated, the B site is normally occupied by Nb, Ta, Ti, Zr, $Fe^{3+}$, Al and Si, and the Y and X positions are filled with O, OH and F (Zurevinski and Mitchell, 2004). Vacancies are very common in the A and Y sites and increase with low-temperature weathering (Lumpkin and Ewing, 1995; Wall et al., 1996). In all, > 1200 EPMA analyses of pyrochlore-group minerals were carried out (Electronic supplement ES8), representative analyses are given in Table 1. The formulae have been calculated on the basis of 2 B-site cations and all analyses fall into the pyrochlore-subgroup (Fig. 6) following the classification of Hogarth (1977). The different pyrochlore types (resorbed cores, oscillatory zoned and patchy zoned; see above) show clear compositional differences (Fig. 7 and Electronic supplements ES9–ES11):

(i) The BSE-bright cores restricted to pyrochlores from Badberg, Degenmatt and Haselschacher Buck (Fig. 4D–F) are low in $Na_2O$ (≤4.1 wt%). They are enriched in $UO_2$ (up to 22.2 wt%) and $Ta_2O_5$ (up to 9.3 wt%), but have low $ZrO_2$ (≤0.1 wt%), $ThO_2$ (b.d.l.) and F (≤0.5 wt%), and moderate REE oxide (up to 7.1 wt%) contents.
(ii) Oscillatory-zoned pyrochlore occurs in all investigated samples (Fig. 3A–F; 5A-H) and is rich in CaO (up 23.2 wt%) and $Na_2O$ (up to 11.3 wt%). Compared to the above-mentioned BSE-bright cores, they are much lower in $UO_2$ (≤4.3 wt%), and $Ta_2O_5$ (≤1.9 wt%), but have similar REE oxide (up to 12.0 wt%) contents and reach higher contents of $ZrO_2$ (up to 5.8 wt%), $ThO_2$ (up to 1.4 wt%) and F (up to 3.4 wt%).
(iii) Patchy-zoned pyrochlore (Fig. 4F) from Orberg is relatively low in CaO (≤16.3 wt%) and $Na_2O$ (≤5.9 wt%), while $UO_2$ (up to 8.2 wt%), $Ta_2O_5$ (up to 4.8 wt%), $ThO_2$ (up to 6.5 wt%), $ZrO_2$ (up to 13.7 wt%) and the REE oxides total (up to 18.4 wt%) reach higher contents than in oscillatory-zoned pyrochlore. Some analyses indicate TREEs > 0.4 apfu and fulfill the criteria for the terminus ceriopyrochlore (Hogarth, 1977).

Pyrochlore from medium- to fine-grained calcite-carbonatites is generally unzoned but the compositional variations among grains of the

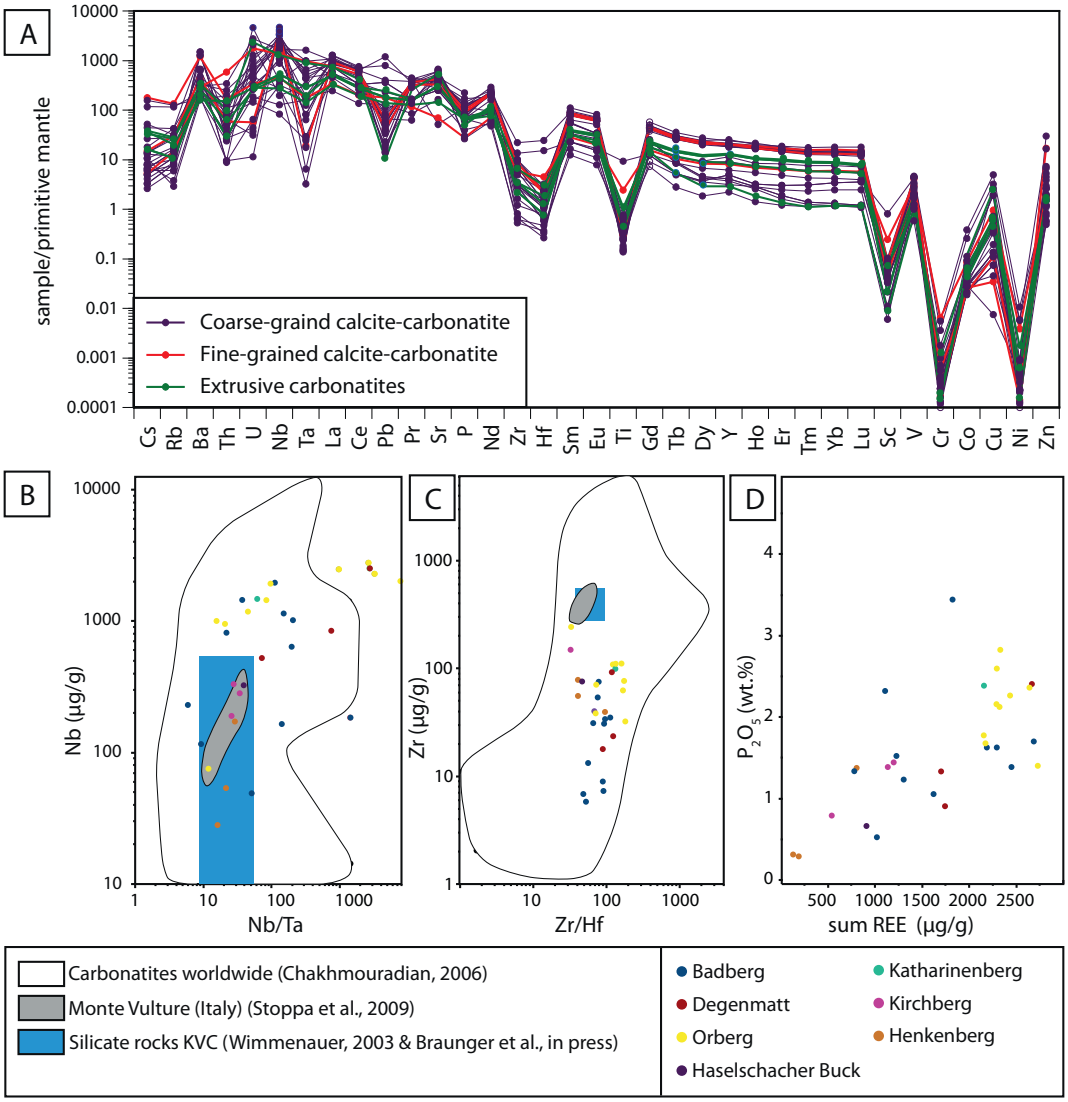


**Fig. 5.** Whole-rock data for Kaiserstuhl carbonatites. (A) Primitive mantle-normalized trace element patterns. (B) & (C) Plots of Nb and Zr concentration versus Nb/Ta and Zr/Hf ratios of the Kaiserstuhl carbonatites compared to global carbonatite data (Chakhmouradian, 2006); data for carbonatites from Mt. Vulture (Rosatelli et al., 2007) and data for Kaiserstuhl silicate rocks (Braunger et al., in press). (D) Correlation between whole-rock $P_2O_5$ (wt%) and sum of REEs (µg/g) for Kaiserstuhl carbonatites.

same sample are substantial. Compared to pyrochlore from coarse-grained calcite-carbonatites they contain moderate to high contents of CaO (8.9–17.0 wt%), $Na_2O$ (8.9–10.1 wt%), $Ta_2O_5$ (up to 2.5 wt%), $ZrO_2$ (up to 6.5 wt%), and $ThO_2$ (up to 2.0 wt%), variable amounts of REE oxides (2.1–18.9 wt%) and are low in $UO_2$ (b.d.l. – 1.6 wt%). Pyrochlore from medium- to fine-grained dolomite-carbonatites is relatively rich in CaO (11.5–18.7 wt%), but low in $Na_2O$ (3.3–8.7 wt%) with similar contents of $UO_2$, $ZrO_2$, $Ta_2O_5$, $ThO_2$ and REE oxides as in medium- to fine-grained calcite-carbonatites.

Unzoned pyrochlores from the lapilli tuff (Henkenberg) show high values of CaO (15.9–20.0 wt%) and $Na_2O$ (4.1–7.3 wt%). The contents of REE oxides (up to 5.2 wt%), $ThO_2$ (up to 0.8 wt%), $UO_2$ (up to 1.9 wt %), $ZrO_2$ (up to 2.7 wt%) and $Ta_2O_5$ (up to 0.9 wt%) are low.

The observed compositional variation in this large data set can be explained by the following set of substitution mechanisms that are of variable importance for the different textural types of pyrochlore (e.g., Kapustin, 1980; Hogarth, 1977; Hogarth et al., 2000; Electronic supplement ES11):

$Ta^{5+} \leftrightarrow Nb^{5+}$ (only B site involved) (1)

$Ca^{2+} + Ti^{4+} \leftrightarrow Na^{+} + Nb^{5+}$ (A and B site involved) (2)

$Ca^{2+} + Ti^{4+} \leftrightarrow Na^{+} + Ta^{5+}$ (A and B site involved) (3)

$Na^{+} + 3Nb^{5+} \leftrightarrow U^{4+} + 3Ti^{4+}$ (A and B site involved) (4)

$Ca^{2+} + 2Nb^{5+} \leftrightarrow U^{4+} + 2Ti^{4+}$ (A and B site involved) (5)

$Na^{+} + REE^{3+} \leftrightarrow 2Ca^{2+}$ (only A site involved) (6)

$REE^{3+} + 2Ti^{4+} \leftrightarrow Na^{+} + 2Nb^{5+}$ (A and B site involved) (7)

### 5.2.1. Depth-depending variations in the KB3 drill hole

The samples from surface outcrops combined with those from the KB3 drill cores allow for studying compositional variations in pyrochlore over a vertical depth of about 400 m within the Badberg body (Fig. 8). Whereas in the upper part of the sample profile, most element concentrations are roughly constant, compositional changes can be recognized below about 100 m above sea level (drill core meter 220–400). Below this depth, Na, Nb and F contents are relatively low, whereas U, REE, Ta, Fe, and Al conents are relatively high. Among the latter group, U contents gradually decrease in the lower part of the

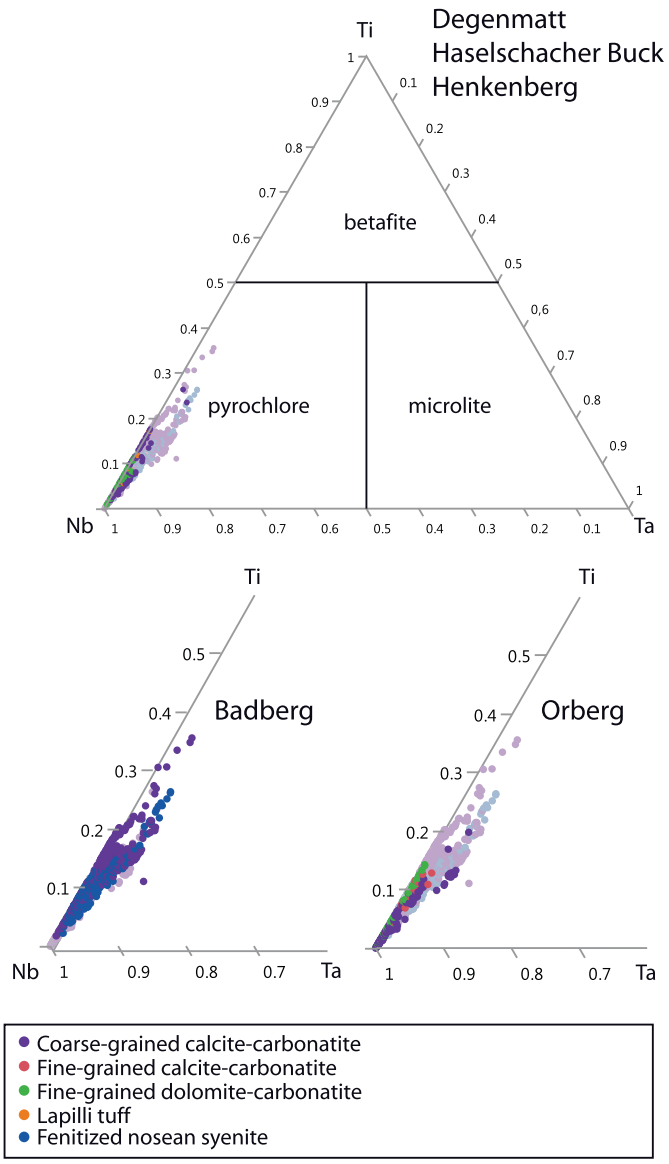


**Fig. 6.** Classification diagram for pyrochlore-group minerals with data from the various sample localities (after Hogarth, 1977). All compositions represent pyrochlore senso stricto.

profile, while REE contents increase further with depth. Other element contents either stay roughly constant throughout the profile (Ca, Sr, Mn, Y) or show rather unsystematic scatter (Zr, Ti, Th).

## 6. Discussion

### 6.1. Pyrochlore as a monitor for magmatic, hydrothermal and weathering processes

The textural and compositional variability in the Kaiserstuhl pyrochlores reveals important details on the magmatic and hydrothermal evolution of the various carbonatites of the complex. Similar textural complexity has been observed in several other occurrences of pyrochlore, as detailed below.

(i) An early population of U-Ta-enriched pyrochlore, which is commonly resorbed and surrounded by oscillatory-zoned F-enriched pyrochlore has been interpreted to reflect a multi-stage magmatic evolution in several carbonatites worldwide (e.g., Chakhmouradian and Zaitsev, 1999; Chakhmouradian and Mitchell, 2002; Zurevinski and Mitchell, 2004; Mitchell, 2005; Hogarth, 1977; Hogarth et al., 2000; Lee et al., 2006, Chakhmouradian, 2006). At the Kaiserstuhl, these U- and Ta-enriched pyrochlore cores are restricted to pyrochlores from some Badberg samples that occur in close proximity to fenitized nosean syenites. Therefore, we interpret the resorbed U- and Ta-rich cores as originally crystallized from a silicate magma and subsequently entrained in the carbonatite magma during emplacement. This is further supported by high Gamma Ray signatures related to U- and Ta-rich pyrochlore from the nosean syenites below the Badberg (Kirchheimer, 1973).

(ii) Oscillatory-zoned F-enriched pyrochlores from all localities probably crystallized directly from the carbonatite magma. Oscillatory zoning in pyrochlore is seen as a typical magmatic feature, originating from higher crystal growth rates than diffusion rates for the respective elements in the melt (e.g., Hogarth et al., 2000).

(iii) Pyrochlores from Orberg samples show intense patchy zonation and localized late-stage rims that crosscut earlier textures (Fig. 4F). These are exceptionally rich in Zr (up to 13.7 wt% $ZrO_2$), REE (up to 18.4 wt% REE oxides), Th (up to 6.5 wt% $ThO_2$), U (up to 8.2 wt % $UO_2$) and resemble pyrochlore and ceriopyrochlore compositions (Figs. 6 & 7; Hogarth, 1977). These textures are interpreted to reflect hydrothermal alteration. Such textures are much rarer in samples from the other localities, which may indicate a more evolved character of the Orberg rocks (see also below). Alternatively, this may be related to the much smaller size of the Orberg carbonatite bodies as it is presumably easier (in contrast to the much more competent sodalite monzogabbros in the vicinity of the Badberg) for Zr-REE-U-Th-rich fluids to ascent and percolate through the high-porosity polygenic diatreme breccias and into the carbonatite dykes and apophyses. Pyrochlores from the Kola peninsula evolve from initially Ca–Na-Th-rich towards Ba–Sr-(REE)-rich compositions by meteoric (metasomatic) fluids (Chakhmouradian and Williams, 2004) and a similar Ba-enrichment during hydrothermal stages has been described from the Sokli carbonatite in Finland (Lee et al., 2006). Late-stage REE-enriched pyrochlores and ceriopyrochlores from Kaiserstuhl are Ba-poor (always below detection limit). However, strong Ba-enrichment occurs in phlogopite from the Kaiserstuhl carbonatites (up to about 4.5 wt% BaO; Keller et al., 1990), while mica from the Sokli rocks (see above) is invariably Ba-poor ($\leq$1.4 wt% BaO).

(iv) Cracked and partly resolved pyrochlores typical of low-temperature (sub)surface weathering or late-stage hydrothermal alteration are characterized by A-site vacancies in the pyrochlore formula (e.g., Lumpkin and Ewing, 1995; Wall et al., 1996). At the Kaiserstuhl, pyrochlore data with significant A-site vacancies are depleted in Na-Ca-F. However, an increase in REE, Ti, Zr or Ba is not recognized, although this would be common for pyrochlores with high A-site vacancies related to a hydrothermal overprint (Lumpkin and Ewing, 1995). Hence, surficial weathering is seen as the dominant process that generates the A-site vacancies.

### 6.2. Fractionation of geochemical twins (Nb/Ta and Zr/Hf) during carbonatite evolution

Pyrochlores are likely to be the main carrier of Nb/Ta as supported by the rough correlation between the Nb/Ta ratios in pyrochlore and the respective whole-rock data (Fig. 9), especially considering the large variability of Nb/Ta ratios in the various textural types of pyrochlore (see above). Similarly, we assume that the major Zr and Hf hosts are pyrochlores as well, given the absence of notable Zr phases (such as baddeleyite or zircon) in the investigated samples. However, a direct comparison between whole-rock Zr/Hf ratios and pyrochlore data is not possible, as most EPMA analyses indicate Hf to be below the detection limit (~300 µg/g). Although some overlap exists, Orberg samples reach higher Nb/Ta and Zr/Hf ratios than samples from the Badberg and Nb

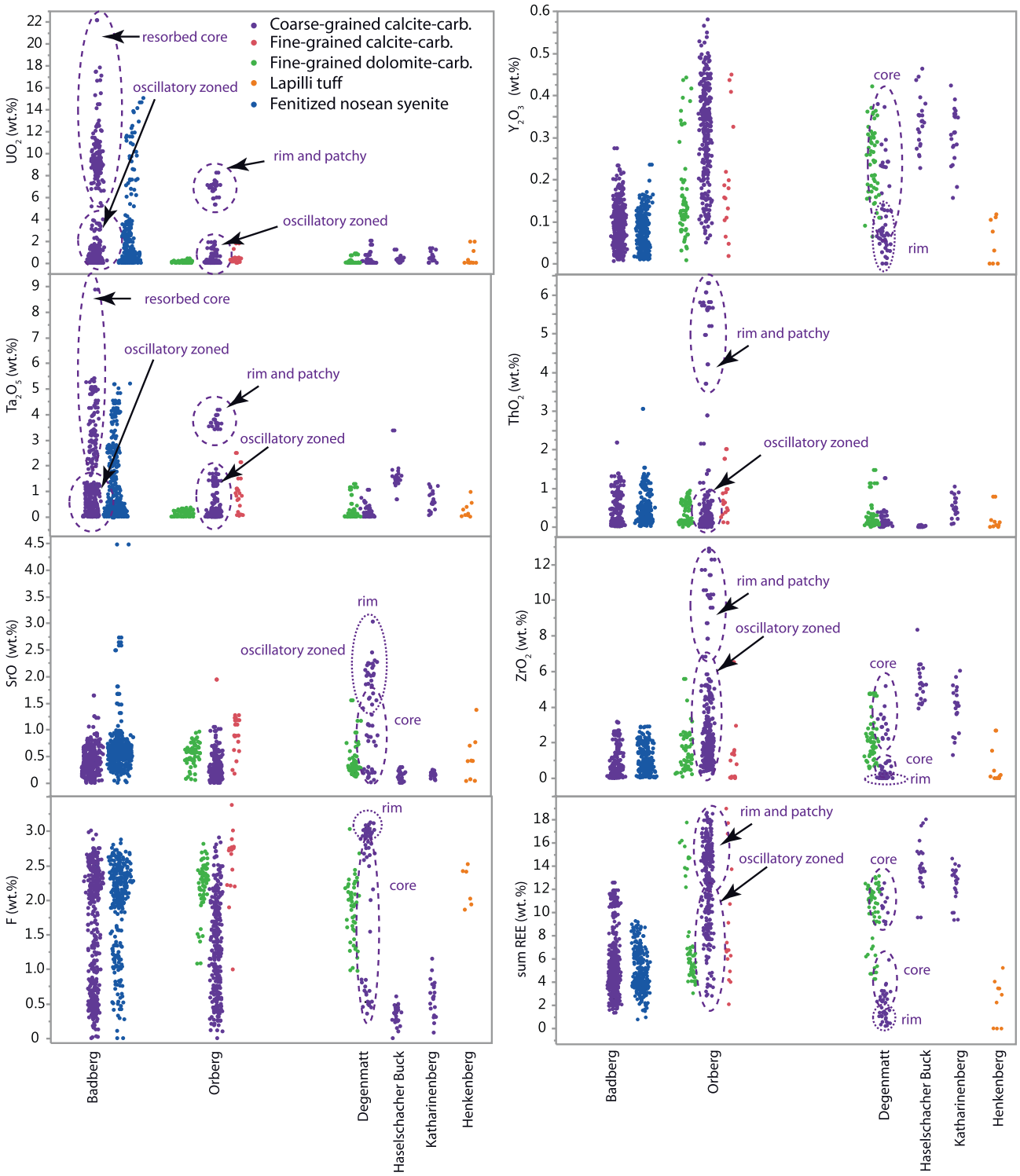


**Fig. 7.** Compositional variation of pyrochlore in the various Kaiserstuhl carbonatites and fenitized nosean syenites.

and Zr contents in Orberg samples are relatively high (Figs. 7 & 9), which is partly influenced by U- and Ta-enriched (and low Nb/Ta) resorbed pyrochlore cores in some Badberg samples and relatively high Zr contents in patchy-zoned REE-enriched pyrochlores and ceriopyrochlore from Orberg samples (Figs. 7 & 9). The significance of highly variable Nb/Ta and Zr/Hf ratios found in carbonatites (Fig. 5B & C) was discussed by Chakhmouradian (2006) and can be explained in the case of the Kaiserstuhl volcanic complex by fractional crystallization of pyrochlore. Starting with low Nb/Ta and Zr/Hf ratios and evolving towards high ratios during differentiation would imply that the Orberg carbonatites represent more evolved rocks than those from Badberg if a common origin of these two bodies is assumed (Lehnert, 1989). Compared to silicate rocks, carbonatites of the Kaiserstuhl are enriched in Nb and Ta but depleted in Zr, and show a much larger spread, reaching very high Nb/Ta and Zr/Hf ratios (Fig. 5B & C). However, due to a lack of Nb/Ta and Zr/Hf ratios from the presumably carbonatite-related haüynites and haüynite melilitites (Schleicher et al., 1990), it is not possible to shed more light on the processes that generated carbonatites

**Table 1**
Representative pyrochlore analyses from the Kaiserstuhl.

| Sample | HTAC_1232 | HTAC_1253 | HTAC_1353 | HTAC_284 | HTAC_1369 | HTAC_1366 | HTAC_1362 |
|---|---|---|---|---|---|---|---|
| Texture | Oscillatory | Oscillatory | Oscillatory | Patchy | Unzoned | Patchy | Resorbed core |
| Location | Badberg | Orberg | Orberg | Has. Buck | Henkenberg | Degenmatt | Badberg |
| $Na_2O$ | 3.59 | 4.19 | 7.40 | 2.03 | 4.11 | 4.23 | 2.59 |
| CaO | 17.79 | 16.20 | 15.45 | 18.55 | 22.02 | 15.48 | 17.21 |
| SrO | 0.30 | 0.09 | 0.43 | 0.24 | 0.70 | 0.16 | 0.02 |
| $La_2O_3$ | 0.66 | 1.30 | 1.05 | 1.48 | 0.07 | 1.30 | 0.06 |
| $Ce_2O_3$ | 5.90 | 9.40 | 5.99 | 9.98 | 2.03 | 8.05 | 2.92 |
| $Pr_2O_3$ | 0.26 | 0.68 | 0.44 | 0.62 | 0.09 | 0.70 | 0.21 |
| $Nd_2O_3$ | 0.42 | 1.75 | 1.10 | 1.25 | 0.05 | 1.70 | 0.39 |
| $Sm_2O_3$ | 0.07 | 0.26 | 0.14 | 0.20 | b.d.l. | 0.29 | 0.09 |
| $Y_2O_3$ | 0.09 | 0.25 | 0.16 | 0.35 | 0.08 | 0.36 | 0.00 |
| $ThO_2$ | b.d.l. | 0.66 | 0.49 | 0.03 | 0.78 | 1.47 | 0.35 |
| FeO | 3.41 | 2.39 | 0.98 | 2.69 | 0.68 | 2.11 | 3.28 |
| $SiO_2$ | b.d.l. | b.d.l. | 0.00 | b.d.l. | 0.26 | b.d.l. | 0.02 |
| MnO | 0.16 | 0.39 | 0.14 | 0.33 | 0.07 | 0.63 | 0.02 |
| $ZrO_2$ | 0.08 | 4.60 | 2.62 | 3.91 | 0.42 | 4.77 | 0.29 |
| $TiO_2$ | 5.35 | 3.24 | 4.26 | 1.97 | 7.13 | 2.81 | 9.30 |
| $Nb_2O_5$ | 51.24 | 51.24 | 57.07 | 52.19 | 57.38 | 52.25 | 34.56 |
| $Ta_2O_5$ | 1.01 | 1.20 | 1.48 | 1.39 | 0.06 | 1.28 | 7.65 |
| $Al_2O_3$ | 0.16 | 0.13 | 0.03 | 0.20 | b.d.l. | 0.14 | 0.29 |
| F | 1.25 | 2.24 | 4.78 | 0.97 | 4.43 | 3.14 | 0.00 |
| $UO_2$ | 8.22 | 0.63 | 1.26 | 0.21 | 0.27 | 0.85 | 19.12 |
| $H_2O$ | 1.80 | 1.22 | 0.22 | 1.73 | 0.48 | 0.76 | 2.29 |
| F (corr.) | 0.53 | 0.94 | 2.01 | 0.41 | 1.86 | 1.32 | 0.00 |
| Total | 99.95 | 100.85 | 7.40 | 98.58 | 100.63 | 101.72 | 98.37 |
| Formulae on the basis of 2 B-site cations | | | | | | | |
| Na | 0.45 | 0.53 | 0.91 | 0.26 | 0.50 | 0.53 | 0.36 |
| Ca | 1.24 | 1.13 | 1.05 | 1.32 | 1.47 | 1.07 | 1.32 |
| Sr | 0.01 | 0.00 | 0.02 | 0.01 | 0.03 | 0.01 | 0.00 |
| La | 0.02 | 0.03 | 0.02 | 0.04 | 0.00 | 0.03 | 0.00 |
| Ce | 0.14 | 0.22 | 0.14 | 0.24 | 0.05 | 0.19 | 0.08 |
| Pr | 0.01 | 0.02 | 0.01 | 0.02 | 0.00 | 0.02 | 0.01 |
| Nd | 0.01 | 0.04 | 0.02 | 0.03 | 0.00 | 0.04 | 0.01 |
| Sm | 0.00 | 0.01 | 0.00 | 0.00 | 0.00 | 0.01 | 0.00 |
| Y | 0.00 | 0.01 | 0.01 | 0.01 | 0.00 | 0.01 | 0.00 |
| Th | 0.00 | 0.01 | 0.01 | 0.00 | 0.01 | 0.02 | 0.01 |
| Fe | 0.19 | 0.13 | 0.05 | 0.15 | 0.04 | 0.11 | 0.20 |
| Si | 0.00 | 0.00 | 0.00 | 0.00 | 0.02 | 0.00 | 0.00 |
| Mn | 0.01 | 0.02 | 0.01 | 0.02 | 0.00 | 0.03 | 0.00 |
| Zr | 0.00 | 0.15 | 0.08 | 0.13 | 0.01 | 0.15 | 0.01 |
| Ti | 0.26 | 0.16 | 0.20 | 0.10 | 0.33 | 0.14 | 0.50 |
| Nb | 1.51 | 1.51 | 1.63 | 1.57 | 1.61 | 1.53 | 1.12 |
| Ta | 0.02 | 0.02 | 0.03 | 0.03 | 0.00 | 0.02 | 0.15 |
| Al | 0.01 | 0.01 | 0.00 | 0.02 | 0.00 | 0.01 | 0.02 |
| F | 0.26 | 0.46 | 0.95 | 0.20 | 0.87 | 0.64 | 0.00 |
| U | 0.11 | 0.01 | 0.02 | 0.00 | 0.00 | 0.01 | 0.27 |
| REE | 0.17 | 0.32 | 0.19 | 0.33 | 0.50 | 0.29 | 0.09 |
| A-site | 1.99 | 2.01 | 2.10 | 1.93 | 2.07 | 1.94 | 2.05 |
| B-site | 2.00 | 2.00 | 2.00 | 2.00 | 2.00 | 2.00 | 2.0 |
| F (corr.) total | 101.12 | 101.13 | 103.47 | 99.92 | 99.12 | 101.18 | 100.47 |

at the Kaiserstuhl volcanic complex (liquid immiscibility versus fractionation) in the context of partitioning of Nb, Ta, Zr and Hf between silicate and carbonatite melt (Veksler et al., 1998).

### 6.3. Pyrochlore compositions as an exploration indicator

#### 6.3.1. Depth-depending variations of pyrochlore composition

The depth-depending compositional variations in pyrochlore (see above) correlate well with geophysical data from the KB3 drilling that indicate increasing radioactivity at depth (Terra Tec, personal communication). The drill core meters below 100 m above sea level (drill core meter 220–400) reflects the central parts of a former vertical pipe structure (see above). In numerous elements (especially, Na, Nb, F, U, TREEs, Ta, Fe, Al) a significant and sharp compositional change in pyrochlore can be recognized. This may indicate a multi-stage emplacement of the carbonatitic magma or may reflect the combined effects of fractional crystallization and assimilation (AFC) as suggested by Giebel et al. (submitted). These results indicate that down-hole changes in pyrochlore compositions may have potential application as an exploration indicator.

#### 6.3.2. Relation between intrusive and extrusive carbonatites

Extrusive carbonatites of the Kaiserstuhl contain fragments of fenitized nosean syenites and rare Nb-perovskite (see above). These mineralogical features only occur in some Badberg samples. We therefore suggest that the extrusive carbonatites at the western flank of the

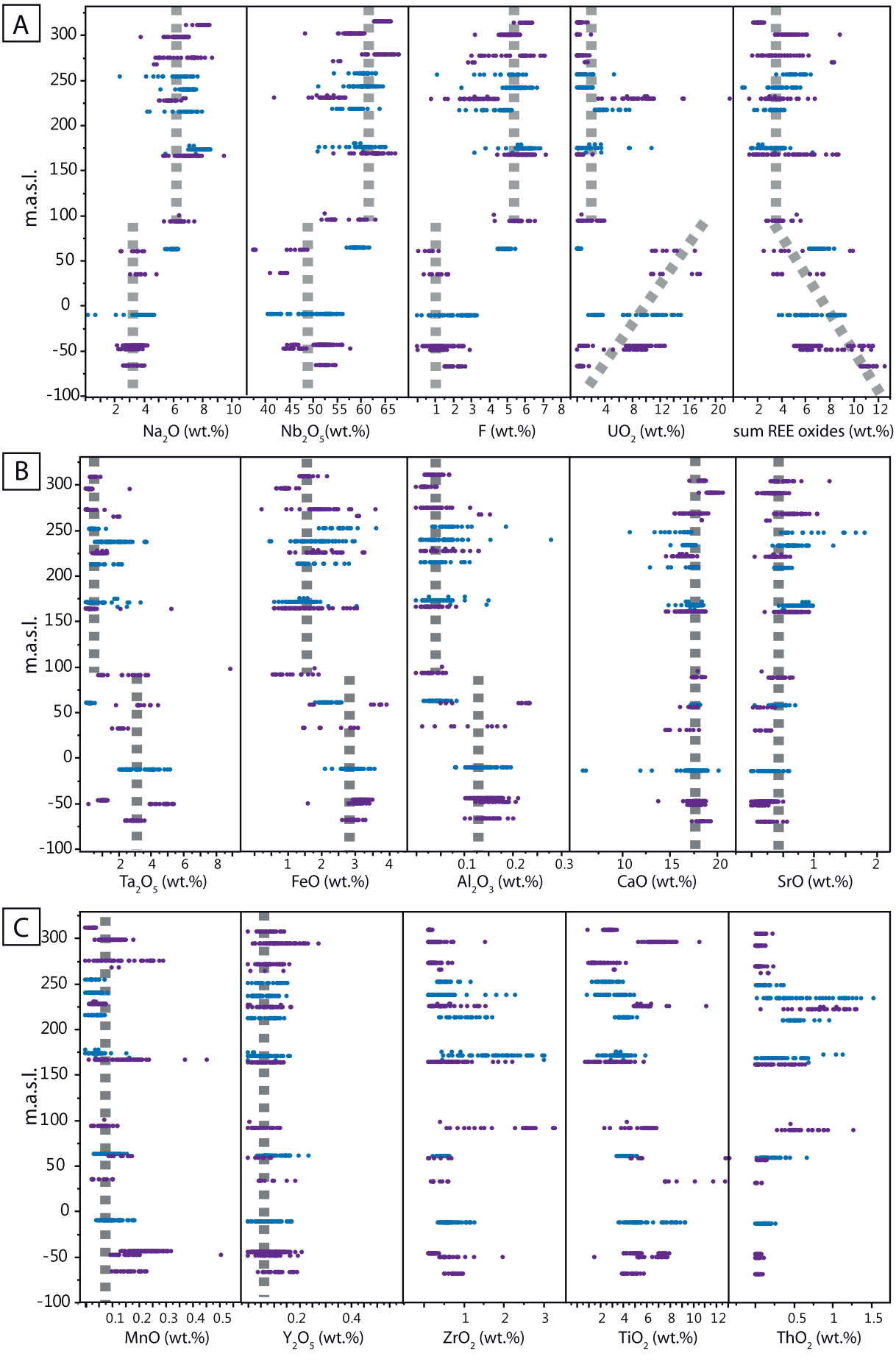


(caption on next page)

**Fig. 8.** Compositional variation of pyrochlore down-hole the KB3 drilling. Note the variable behavior of the various elements below a depth of about 100 m above sea level.

complex may represent erupted equivalents of the hypothetical Badberg-Degenmat-Haselschacher pipe (Fig. 2B; see above) body. Therefore, extrusive carbonatites may offer the principal opportunity to predict HFSE mineralization expected in genetically related intrusive equivalents at depth. Hence, the pyrochlores from extrusive carbonatites of the complex indicate a minimum content of > 6 wt% total REE oxides (< 19 wt% in intrusive carbonatites) in pyrochlore in the ore body at depth, > 1 wt% $ThO_2$ (< 6.5 wt%), > 3 wt% $ZrO_2$ (< 14 wt %), > 1 wt% $Ta_2O_5$ (< 9 wt%), > 11 wt% $TiO_2$ (< 13.5 wt%), > 2 wt % $UO_2$ (< 22 wt%) and > 68 wt% $Nb_2O_5$ (< 69 wt%). However, the modal amounts of pyrochlores in the extrusive carbonatites are much lower than in the intrusive rocks. Other physical-chemical effects, such as hydrothermal alteration (which is markedly different in the Badberg and Orberg bodies, see above), differentiation stage of the carbonatitic magma during eruption/intrusion, will certainly affect such an estimation, especially if the geometry of the body at depth is insufficiently constrained. Nevertheless, this approach may be applied during first stages of exploration.

*6.3.3. Element correlations of pyrochlore and whole-rock and their relation to geophysical exploration tools*

In this section, the mineral chemical controls of geophysical exploration parameters will be discussed (Fig. 10). At Orberg, high REE (up to 2500 µg/g) and variable Th contents (up to 60 µg/g) in whole-rocks and in pyrochlores (up to 18.6 wt% and up to 6.3 wt%, respectively) do not strictly correlate (Fig. 10A). This is because apatite is an important REE carrier in the Kaiserstuhl carbonatites as well (Fig. 5D), with up to 7 wt% REE (Wang et al., 2014; Giebel et al., submitted), but typically low Th contents < 10 µg/g (Wang et al., 2014). Therefore, high Th contents may or may not indicate REE-enrichment in carbonatites and the common approach “if you look for REE, go for the Th” may not always be applicable. This result is problematic with respect to geophysical exploration as apatite is not sensitive to U-, Th-, K-mapping, magnetic susceptibility and geo-electrics and hence, apatite-hosted REE enrichment cannot be detected easily. However, a positive correlation between Th and Zr in whole-rocks (Fig. 10B) enables to detect enrichment of Zr by airborne Th-mapping, but may not help to detect Nb and Ta enrichment, due to their lack of correlation with Th (Fig. 10C & D).

In contrast to pyrochlore compositions (Fig. 7), no significant differences between U and Ta contents in whole rock samples from the Badberg (< 90 µg/g and < 40 µg/g) and Orberg (< 70 µg/g and < 60 µg/g) exist (Fig. 10E & F). This is presumably related to a much higher modal amount of pyrochlore at Orberg (with relatively low U and Ta contents) whereas at Badberg pyrochlore occurs in lower abundances, but with higher U and Ta contents (Fig. 7). However, the positive correlation between U and Ta in whole-rock and pyrochlore (Fig. 10E) indicates that Ta-rich samples could be mapped by e.g., airborne U-mapping. Hence, further studies have to be carried out to shed light on the mineralogical and mineral chemical factors which control geophysical signatures with a focus not only on Th (e.g., U mapping and U-Ta correlation in pyrochlore or apatite detection by geophysical parameters).

## 7. Summary and conclusion

The textural and compositional differences in pyrochlore-group minerals between intrusive and extrusive carbonatites and between different intrusive bodies allow for deciphering details of the magmatic, hydrothermal and meteoric evolution of the carbonatitic system of the Kaiserstuhl volcanic complex. In a more general sense, several results of this study can potentially be used as exploration indicators for carbonatite-related HFSE mineralization at depth:

(i) The mineralogical composition of extrusive carbonatites of the Kaiserstuhl volcanic complex is similar to that of the coarse-grained calcite-carbonatites from Badberg, Degenmatt and Haselschacher Buck. Therefore, if extrusive carbonatites contain pyrochlore, a conservative estimate of HFSE content of pyrochlore in their intrusive equivalents appears possible.

(ii) Pyrochlore from Badberg samples frequently contain U- and Ta-rich cores that probably represent xenocrystic material derived from underlying nosean syenites. Their subsequent crystallization history within the carbonatite magma itself is recorded by oscillatory-zoned F-rich pyrochlore that overgrew and partly resorbed these cores. Pyrochlore from Orberg samples, however, lacks such resorbed cores, suggesting the absence of such rocks below the Orberg area.

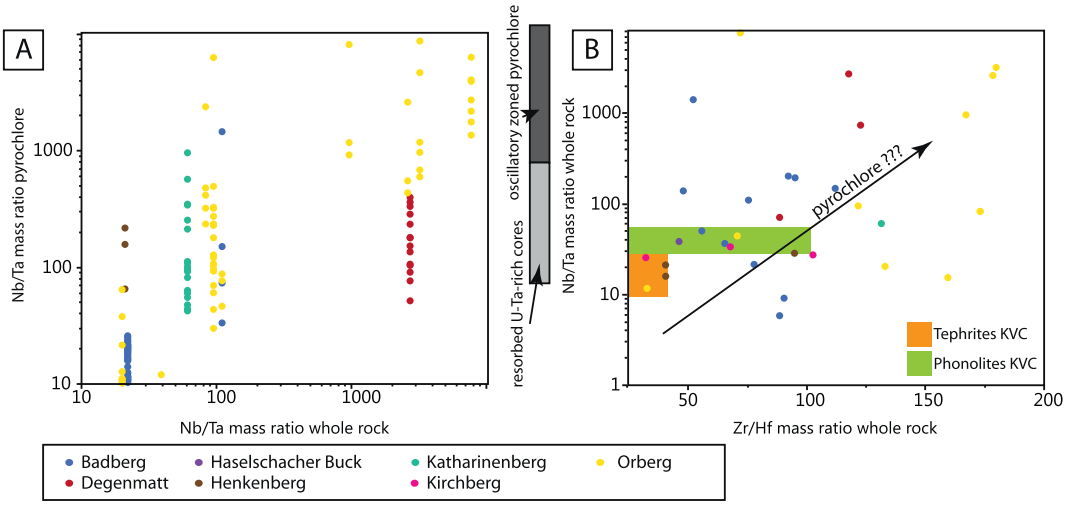


**Fig. 9.** Comparison of (A) Nb/Ta and (B) Zr/Hf ratios between pyrochlore and whole-rock data of Kaiserstuhl carbonatites.

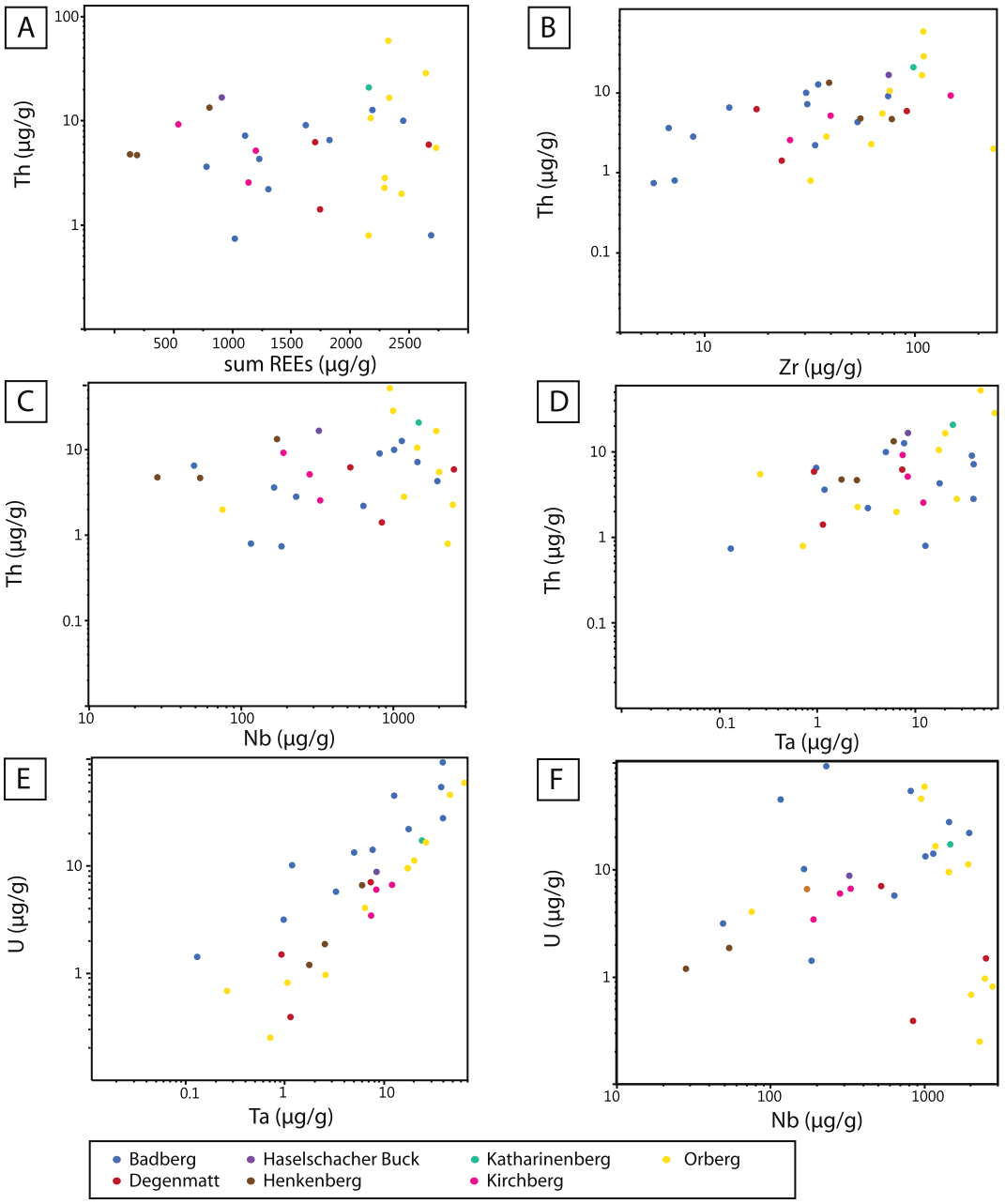


**Fig. 10.** (A–F) Correlations between the exploration parameters U and Th to Nb, Ta, Zr and REE. Note: In (B) and (E) Th is positively correlated to Zr and U to Ta.

(iii) The abundance of patchy zoned and Zr-REE-Th-U-enriched pyrochlore and ceriopyrochlore at the Orberg indicates a strong hydrothermal overprint of these rocks. They represent the highest values in all investigated samples, except for U, which is still higher in resorbed BSE-bright pyrochlore cores restricted to some of the Badberg samples.

Supplementary data to this article can be found online at https://doi.org/10.1016/j.chemgeo.2018.08.008.

## Acknowledgments

We would like to thank to Simone Schafflick for sample preparation in Tübingen. Furthermore, we would like to thank the Landesamt für Geologie, Rohstoffe und Bergbau (Geological Survey of Baden-Württemberg) for providing numerous samples. We are grateful to Wolfhard Wimmenauer (University of Freiburg), Pete Siegfried (GeoAfrica Prospecting Services), Klaus Brauch, Michael Tauchnitz, Claudia Pohl and Dietmar Kopp (Terratec Geophysical Services), Samuel Weatherley (Teck minerals), Graham Banks (Geological Survey of Denmark and Greenland), Kathryn Goodenough (British Geological Survey), Frances Wall (University of Exeter), Anatoly Zaitsev (University of St. Petersburg), Anton Chakhmouradian (University of Manitoba) and Udo Neumann (University of Tübingen) who helped with many hints and discussions. We thank Anatoly Zaitsev and an anonymous reviewer for their critical reviews that improve the manuscript significantly. Donald Dingwell is thanked for his editorial guidance. This study was supported by the European Union's Horizon 2020 research and innovation programme (grant agreement No 689909).

## References


Armstrong, J.T., 1988. Quantitative analysis of silicate and oxide minerals: comparison of Monte Carlo, ZAF and phi-rho-z procedures. Microbeam Anal. 23, 239–246.

Armstrong, J.T., 1991. Quantitative elemental analysis of individual microparticles with electron beam instruments. In: Electron Probe Quantitation. Springer, US, pp. 261–315.

Atencio, D., Andrade, M.B., Christy, A.G., Gieré, R., Kartashov, P.M., 2010. The pyrochlore supergroup of minerals: nomenclature. Can. Mineral. 48, 673–698.

Baranyi, I., 1971. Petrographie und Geochemie der subvulkanischen Breccien des Kaiserstuhls und seiner Umgebung (unpublished dissertation, 156 pp.). University of Freiburg.

Bastin, G.F., Heijligers, H.J.M., Van Loo, F.J.J., 1986. A further improvement in the Gaussian ϕ (ϱ) approach for matrix correction in quantitative electron probe microanalysis. Scanning 8, 45–67.

Beccaletto, L., Capar, L., Cruz-Mermy, D., Rupf, I., Nitsch, E., Oliviero, G., Elsass, P., Perrin, A., Stephane, M., 2010. The GeORG Project – Geological Potential of the Upper Rhine Graben - Situation, Goals and First Scientific Results. (Abstr., 23ème Réunion des Sciences de la Terre (RST2010), Bordeaux, BRGM, HAL Id: hal-00642768).

Bence, A.E., Albee, A.L., 1968. Empirical correction factors for the electron microanalysis of silicates and oxides. J. Geol. 76, 382–403.

Blust, G., 1993. Petrographie und Geochemie der silikatischen Ganggesteine der Bohrung KB3 Steinreise (unpublished diploma thesis, 83 pp.). Albert-Ludwigs-University Freiburg.

Castor, S.B., 2008. The Mountain Pass rare-earth carbonatite and associated ultrapotassic rocks, California. Can. Mineral. 46, 779–806.

Chakhmouradian, A.R., 2006. High-field-strength elements in carbonatitic rocks: geochemistry, crystal chemistry and significance for constraining the sources of carbonatites. Chem. Geol. 235, 138–160.

Chakhmouradian, A.R., Mitchell, R.H., 2002. The mineralogy of Ba-and Zr-rich alkaline pegmatites from Gordon Butte, Crazy Mountains (Montana, USA): comparisons between potassic and sodic agpaitic pegmatites. Contrib. Mineral. Petrol. 143, 93–114.

Chakhmouradian, A.R., Williams, C.T., 2004. Mineralogy of high-field-strength elements (Ti, Nb, Zr, Ta, Hf) in phoscoritic and carbonatitic rocks of the Kola Peninsula, Russia. In: Phoscorites and Carbonatites From Mantle to Mine: The Key Example of the Kola Alkaline Province. 10. pp. 293–340.

Chakhmouradian, A.R., Zaitsev, A.N., 1999. Calcite-amphibole-clinopyroxene rock from the Afrikanda Complex, Kola Peninsula, Russia; mineralogy and a possible link to carbonatites; I, oxide minerals. Can. Mineral. 37, 177–198.

Du, X., Graedel, T.E., 2011. Global rare earth in-use stocks in NdFeB permanent magnets. J. Ind. Ecol. 15, 836–843.

EC, 2014. EC Report on Critical Raw Materials for the EU. 2014.

Gendron, L., Biss, R., Rodrigue, M., 1981. Underground mining and pyrochlore ore processing at Niobec mine, Quebec, Canada. In: Niobium, pp. 79–96.

Goodenough, K.M., Schilling, J., Jonsson, E., Kalvig, P., Charles, N., Tuduri, J., Deady, E.A., Sadeghi, M., Schiellerup, H., Müller, A., Bertrand, G., Arvanitidisc, N., Eliopoulos, D.G., Shaw, R.A., Thranee, K., Keulene, N., 2016. Europe's rare earth element resource potential: an overview of REE metallogenetic provinces and their geodynamic setting. Ore Geol. Rev. 72, 838–856.

Govindaraju, K., 1989. Compilation of Working Values and Sample Description for 272 Geostandards (Special Issue of Geostandards Newsletter). vol. XIII.

Govindaraju, K., 1994. Compilation of working values and sample description for 383 geostandards. Geostand. Newslett. 18, 1–158.

Halama, R., Vennemann, T., Siebel, W., Markl, G., 2005. The Grønnedal-Ika carbonatite–syenite complex, South Greenland: carbonatite formation by liquid immiscibility. J. Pet. 46, 191–217.

Hatch, G.P., 2012. Dynamics in the global market for rare earths. Elements 8 (5), 341–346.

Hogarth, D.D., 1977. Classification and nomenclature of the pyrochlore group. Am. Mineral. 62, 403–410.

Hogarth, D.D., Williams, C.T., Jones, P., 2000. Primary Zoning in Pyrochlore Group Minerals From Carbonatites. pp. 683–697.

Hubaux, A., 1964. In: Van Wambeke, L. (Ed.), Structure des carbonatites de Schelingen, pp. 31–36 (1964, Bruxelles).

Hubberten, H.W., Katz-Lehnert, K., Keller, J., 1988. Carbon and oxygen isotope investigations in carbonatites and related rocks from the Kaiserstuhl, Germany. Chem. Geol. 70, 257–274.

Humphries, M., 2010. Rare Earth Elements: The Global Supply Chain. DIANE Publishing.

Issa Filho, A., Lima, P.R.A., Souza, O., 1984. Aspects of the geology of the Barreiro carbonatitic complex, Araxá, MG, Brazil. In: Carbonatitic Complexes of Brazil: Geology, pp. 19–44.

Ivanyuk, G.Y., Yakovenchuk, V.N., Pakhomovsky, Y.A., 2002. Kovdor. Laplandia Minerals. (Apatity: 326 pp.).

Kapustin, Y.L., 1980. Mineralogy of Carbonatites. Amerind Publishing, New Delhi, India (259 pp.).

Katz, K., Keller, J., 1981. Comb-layering in carbonatite dykes. Nature 294, 350–352.

Keller, J., 1964. Zur Vulkanologie des Burkheim-Sponeck-Gebietes im westlichen Kaiserstuhl. Ber. Naturforsch. Ges. Freibg. 54. pp. 107–130.

Keller, J., 1965. Eine Tuffbreccie vom Henkenberg bei Niederrotweil und ihre Bedeutung für die Magmatologie des Kaiserstuhls. Ber. Naturforsch. Ges. Freiburg im Breisgau. 55. pp. 349–364.

Keller, J., 1981. Carbonatitic volcanism in the Kaiserstuhl alkaline complex: evidence for highly fluid carbonatitic melts at the Earth's surface. J. Volcanol. Geotherm. Res. 9, 423–431.

Keller, J., 1984a. Der jungtertiäre Vulkanismus Südwestdeutschlands: Exkursionen im Kaiserstuhl und Hegau. Fortschr. Mineral. 62, 2–35.

Keller, J., 1984b. Geochemie und Magmenentwicklung im Kaiserstuhl. Fortschr. Mineral. 62, 116–118.

Keller, J., 1989. Extrusive carbonatites and their significance. In: Bell, K. (Ed.), Carbonatites: Genesis and Evolution. Unwin Hyman, London, pp. 70–88.

Keller, J., Brey, G., Lorenz, V., Sachs, P., Schleicher, H., 1990. IAVCEI 1990: Pre-conference Excursion 2A: Volcanism and Petrology of the Upper Rhinegraben (Urach-Hegau-Kaiserstuhl). (Unpublished field guide).

Kirchheimer, F., 1973. Weitere Mitteilungen über das Vorkommen radioaktiver Substanzen in Süddeutschland. Jh. geol. 15. Landesamt Baden-Württ, pp. 33–125.

Krasnova, N.I., Petrov, T.G., Balaganskaya, E.G., Garcia, D., Moutte, J., Zaitsev, A.N., Wall, F., 2004a. Introduction to phoscorites: occurrence, composition, nomenclature and petrogenesis. In: Wall, F., Zaitev, A.N. (Eds.), Phoscorites and Carbonatites From Mantle to Mine: The Key Example of the Kola Alkaline Province. The Mineralogical Society of Great Britain and Ireland, London, pp. 45–74.

Krasnova, N.I., Balaganskaya, E.G., Garcia, D., 2004b. Kovdor – classic phoasorites and carbonatites. In: Wall, F., Zaitev, A.N. (Eds.), Phoscorites and Carbonatites From Mantle to Mine: The Key Example of the Kola Alkaline Province. The Mineralogical Society of Great Britain and Ireland, London, pp. 99–132.

Lapin, A.V., Tolstov, A.V., 1995. Mineral Deposits in the Weathering Crust of Carbonatites. Nauka, Moscow (208 pp.).

Le Bas, M.J., 1987. Nephelinites and carbonatites. Geol. Soc. Lond., Spec. Publ. 30 (1), 53–83.

Lee, M.J., Lee, J.I., Garcia, D., Moutte, J., Williams, C.T., Wall, F., Kim, Y., 2006. Pyrochlore chemistry from the Sokli phoscorite-carbonatite complex, Finland: implications for the genesis of phoscorite and carbonatite association. Geochem. J. 40, 1–13.

Lehnert, K., 1989. Petrologie der Gangkarbonatite im Kaiserstuhl (unpublished dissertation, 210 pp.). Albert-Ludwigs-Universtity Freiburg.

Lumpkin, G.R., Ewing, R.C., 1995. Geochemical alteration of pyrochlore group minerals: pyrochlore subgroup. Am. Mineral. 80, 732–743.

Lustrino, M., Wilson, M., 2007. The circum-Mediterranean anorogenic Cenozoic igneous province. Earth Sci. Rev. 81, 1–65.

Mariano, A.N., 1989. Economic geology of rare earth elements. Rev. Mineral. Geochem. 21, 309–337.

Massari, S., Ruberti, M., 2013. Rare earth elements as critical raw materials: focus on international markets and future strategies. Res. Policy 38, 36–43.

Mitchell, R.H., 2005. Carbonatites and carbonatites and carbonatites. Can. Mineral. 43, 2049–2068.

Mitchell, R.H., 2015. Primary and secondary niobium mineral deposits associated with carbonatites. Ore Geol. Rev. 64, 626–641.

Nasraoui, M., Bilal, E., 2000. Pyrochlores from the Lueshe carbonatite complex (Democratic Republic of Congo): a geochemical record of different alteration stages. J. Asian Earth Sci. 18, 237–251.

Rosatelli, G., Wall, F., Stoppa, F., 2007. Calcio-carbonatite melts and metasomatism in the mantle beneath Mt. Vulture (Southern Italy). Lithos 99, 229–248.

Schleicher, H., Keller, J., Kramm, U., 1990. Isotope studies on alkaline volcanics and carbonatites from the Kaiserstuhl, Federal Republic of Germany. Lithos 26, 21–35.

Seeger, P., 2015. Fremdgesteinseinschlüsse im Ganggestein des Horberigs im Kaiserstuhl (BSC thesis, 132 pp.). University of Tübingen.

Sigmund, J., 1996. Diatrembreccien, Mantelxenolithe und Karbonatite in der Kernbohrung KB 2 im Kaiserstuhl (unpublished dissertation, 154 pp.). Albert-Ludwigs-Universtity Freiburg.

Veksler, I.V., Petibon, C., Jenner, G.A., Dorfman, A.M., Dingwell, D.B., 1998. Trace element partitioning in immiscible silicate–carbonate liquid systems: an initial experimental study using a centrifuge autoclave. J. Pet. 39, 2095–2104.

Wall, F., Williams, C.T., Woolley, A.R., Nasraoui, M., 1996. Pyrochlore from weathered carbonatite at Lueshe, Zaire. Mineral. Mag. 60, 731–750.

Wang, L.X., Marks, M.A., Wenzel, T., Von Der Handt, A., Keller, J., Teiber, H., Markl, G., 2014. Apatites from the Kaiserstuhl Volcanic Complex, Germany: new constraints on the relationship between carbonatite and associated silicate rocks. Eur. J. Mineral. 26, 397–414.

Wenzel, T., Nickel, K.G., Glaser, J., Meyer, H.J., Eyidi, D., Eibl, O., 2003. Electron probe microanalysis of Mg–B compounds: stoichiometry and heterogeneity of superconductors. Phys. Status Solidi 198, 374–386.

Williams, C.T., Wall, F., Woolley, A.R., Phillipo, S., 1997. Compositional variation in pyrochlore from the Bingo carbonatite, Zaire. J. Afr. Earth Sci. 25, 137–145.

Wilson, M., Downes, H., 2006. Tertiary-Quaternary intra-plate magmatism in Europe and its relationship to mantle dynamics. Geol. Soc. Lond. Mem. 32, 147–166.

Wimmenauer, W., 1963. Beiträge zur Petrographie des Kaiserstuhls, Teile VI und VII. Neues Jb. Mineral. Abh. 99, 213–276.

Wimmenauer, W., 2003. Geologische Karte von Baden-Württemberg Blatt Kaiserstuhl, mit Erläuterungen. Landesamt für Geologie, Rohstoffe und Bergbau Baden-Württemberg, Freiburg i. Br (280 pp.).

Wimmenauer, W., Bakhashwin, M., Baranyi, I., Hsiao, C., 1977. Neuere Befunde ilber den Untergrund des Kaiserstuhls. Ber. Naturforsch. 67. Ges. Freiburg im Breisgau, pp. 405–424.

Woolley, A.R., Church, A.A., 2005. Extrusive carbonatites: a brief review. Lithos 85, 1), 1–14.
Woolley, A.R., Kempe, D.R.C., 1989. Carbonatites: nomenclature, average chemical compositions and element distribution. In: Bell, K. (Ed.), Carbonatites: Genesis and Evolution. Unwin Hyman, London, pp. 1–14.
Woolley, A.R., Kjarsgaard, B.A., 2008. Carbonatite Occurrences of the World: Map and Database. Geological Survey of Canada.
Yang, K.F., Fan, H.R., Santosh, M., Hu, F.F., Wang, K.Y., 2011. Mesoproterozoic carbonatitic magmatism in the Bayan Obo deposit, Inner Mongolia, North China: constraints for the mechanism of super accumulation of rare earth elements. Ore Geol. Rev. 40 (1), 122–131.
Zaitsev, A.N., Williams, C.T., Wall, F., Zolotarev, A.A., 2012. Evolution of chemical composition of pyrochlore group minerals from phoscorites and carbonatites of the Khibina alkaline massif. Geol. Ore Deposits 54, 503–515.
Zurevinski, S.E., Mitchell, R.H., 2004. Extreme compositional variation of pyrochlore-group minerals at the Oka carbonatite complex, Quebec: evidence of magma mixing? Can. Mineral. 42, 1159–1168.

# Appendix V

Accepted publication

*Study 5*

Giebel, R.J., Parsapoor, A., Walter, B.F., Braunger, S., Marks, M.A.W., Wenzel, T., Markl, G., 2019. Evidence for Magma–Wall Rock Interaction in Carbonatites from the Kaiserstuhl Volcanic Complex (Southwest Germany). Journal of Petrology 60, 1163-1194. http://dx.doi.org/10.1093/petrology/egz028.

JOURNAL OF PETROLOGY

*Journal of Petrology*, 2019, Vol. 60, No. 6, 1163–1194
doi: 10.1093/petrology/egz028
Advance Access Publication Date: 14 May 2019
Original Article

OXFORD

# Evidence for Magma–Wall Rock Interaction in Carbonatites from the Kaiserstuhl Volcanic Complex (Southwest Germany)

**R. J. Giebel [1,2,*], A. Parsapoor[1,†], B. F. Walter[1,3], S. Braunger[1], M. A. W. Marks[1], T. Wenzel[1] and G. Markl[1]**

[1]Department of Geosciences, Eberhard Karls Universität Tübingen, Wilhelmstr. 56, 72074 Tübingen, Germany; [2]Department of Geology, University of the Free State, 250 Nelson-Mandela-Drive, Bloemfontein 9300, South Africa; [3]Institute for Applied Geosciences, Karlsruhe Institute of Technology, Adenauerring 20b, Karlsruhe 76131, Germany

*Corresponding author. Department of Geosciences, Eberhard Karls Universität Tübingen, Wilhelmstr. 56, 72074 Tübingen, Germany. Telephone: +49-(0)7071-29-73155. Fax: +49-(0)7071-29-3060. E-mail: r.j.giebel@gmx.de
[†]Joint first authorship.

Received June 6, 2018; and in revised form April 27, 2019; Accepted May 3, 2019

## ABSTRACT

The mineralogy and mineral chemistry of the four major sövite bodies (Badberg, Degenmatt, Haselschacher Buck and Orberg), calcite foidolite/nosean syenite xenoliths (enclosed in the Badberg sövite only) and rare extrusive carbonatites of the Kaiserstuhl Volcanic Complex in Southern Germany provide evidence for contamination processes in the carbonatitic magma system of the Kaiserstuhl. Based on textures and composition, garnet and clinopyroxene in extrusive carbonatites represent xenocrysts entrained from the associated silicate rocks. In contrast, forsterite, monticellite and mica in sövites from Degenmatt, Haselschacher Buck and Orberg probably crystallized from the carbonatitic magma. Clinopyroxene and abundant mica crystallization in the Badberg sövite, however, was induced by the interaction between calcite foidolite xenoliths and the carbonatite melt. Apatite and micas in the various sövite bodies reveal clear compositional differences: apatite from Badberg is higher in REE, Si and Sr than apatite from the other sövite bodies. Mica from Badberg is biotite- and comparatively $Fe^{2+}$-rich (Mg# = 72–88). Mica from the other sövites, however, is phlogopite (Mg# up to 97), as is typical of carbonatites in general. The typical enrichment of Ba due to the kinoshitalite substitution is observed in all sövites, although it is subordinate in the Badberg samples. Instead, Badberg biotites are strongly enriched in $^{IV}Al$ (eastonite substitution) which is less important in the other sövites. The compositional variations of apatite and mica within and between the different sövite bodies reflect the combined effects of fractional crystallization and carbonatite-wall rock interaction during emplacement. The latter process is especially important for the Badberg sövites, where metasomatic interaction released significant amounts of K, Fe, Ti, Al and Si from earlier crystallized nosean syenites. This resulted in a number of mineral reactions that transformed these rocks into calcite foidolites. Moreover, this triggered the crystallization of compositionally distinct mica and clinopyroxene crystals around the xenoliths and within the Badberg sövite itself. Thus, the presence and composition of clinopyroxene and mica in carbonatites may be useful indicators for contamination processes during their emplacement. Moreover, the local increase of silica activity during contamination enabled strong REE enrichment in apatite via a coupled substitution involving Si, which demonstrates the influence of contamination on REE mineralization in carbonatites.

**Key words:** contamination; carbonatite; Kaiserstuhl; mineral chemistry; calcite foidolite; REE mineralization; silicates in carbonatites

## INTRODUCTION

Carbonatites are mantle-derived magmatic rocks with more than 30% primary igneous carbonate minerals (Mitchell, 2005; Woolley & Kjarsgaard, 2008). In most of the ~ 550 known occurrences they form intrusive bodies (e.g. plugs, pipes, dykes, sills), whereas extrusive equivalents, such as lavas and tuffs are notably scarce, with only about 50 known occurrences (Woolley & Church, 2005). Depending on their predominant carbonate mineral, carbonatites are subdivided into calcite- (sövites and alvikites), dolomite- (beforsites), ferro- and natro-carbonatites (Le Maitre *et al.*, 2002). Calcite is the most common magmatic carbonate (sometimes with exsolution of dolomite), magmatic dolomite and ankerite are less common and other carbonates (e.g. strontianite, barytocalcite) and REE-carbonates (e.g. burbankite, bastnäsite) are generally minor constituents (e.g. Zaitsev *et al.*, 1998; Moore *et al.*, 2015; Giebel *et al.*, 2017).

In addition to carbonate minerals, most carbonatites contain variable amounts of apatite, magnetite (spinel group minerals) and phlogopite and a number of additional silicate minerals (e.g. forsterite, monticellite, melilite, clinopyroxene, amphibole, garnet, feldspathoids, alkali feldspar) have been reported, although it may be difficult to distinguish primary carbonatitic crystals from xenocrysts (e.g. Andersen, 1988; Hogarth, 1989; Barker, 2001; Brod *et al.*, 2001; Chakrabarty *et al.*, 2009; Reguir *et al.*, 2012; Chakhmouradian *et al.*, 2017). In addition, various sulfides (pyrrhotite, pyrite, chalcopyrite, galena, sphalerite) and HFSE- and REE-rich minerals (e.g. baddeleyite/zircon, perovskite/titanite, pyrochlore, zirconolite, calzirtite) are typically present (e.g. Chakhmouradian, 2006; Farrell *et al.*, 2010; Gomide *et al.*, 2013; Bell *et al.*, 2015). Due to the high abundance of apatite and some of the above-mentioned REE- and HFSE-rich minerals, carbonatites are of general economic interest and several occurrences are currently mined (e.g. Araxa, Bayan Obo, Catalao, Kovdor, Mount Weld, Niobec; Gendron *et al.*, 1984; de Oliveira & Imbernon, 1998; Ivanyuk et al., 2002; Krasnova *et al.*, 2004; Kanazawa & Kamitani, 2006; Yang *et al.*, 2011; Neumann & Medeiros, 2015).

Contamination by crustal or cogenetic intrusive rocks is generally not considered to play an important role during carbonatite magmatism, because carbonatitic melts have low densities and extremely low viscosities, enabling them to ascend rapidly (Treiman & Schedl, 1983; Jones *et al.*, 2013 and references therein). High-silica carbonatitic rocks in alkaline silicate–carbonatite complexes, which probably preserve the evidence of contamination of the parental magma, have often been ignored in previous studies, although there is evidence for the interaction between carbonatites and silicate rocks (Andrade *et al.*, 1999). However, potential contamination by silicate rocks in carbonatites cannot easily be detected by means of radiogenic isotope data (such as Sr, Nd and Pb isotope data) as carbonatites often have high concentrations of these elements and their isotope systems are thereby 'buffered' against contamination with silicate rocks, which normally have much lower concentrations of these elements (e.g. Bell & Tilton, 2002 and references therein). The composition of silicate minerals in carbonatites and their comparison with country rocks, mantle rocks and associated ultramafic cumulates and alkaline rocks, however, may allow for their identification as true primary carbonatitic crystals or xenocrysts, but such studies are very rare (e.g. Vuorinen & Skelton, 2004).

Carbonatites from the Kaiserstuhl Volcanic Complex (South Germany) have been investigated previously (e.g. Keller, 1981; Hay & O'Neil, 1983, Hubberten *et al.*, 1988; Wimmenauer, 2003; Wang *et al.*, 2014; Teiber *et al.*, 2015; Braunger *et al.*, 2018; Walter *et al.*, 2018) but no systematic study of their mineralogy and mineral chemistry is available to date. We provide a comprehensive data set for the mineralogical inventory and the compositional variations of the major minerals in sövites and extrusive carbonatites, namely calcite, apatite, spinel group minerals (magnetite-magnesioferrite) and silicate minerals (mica, forsterite, monticellite, clinopyroxene, garnet). Based on the compositional variation of these phases, we tested the suitability of apatite and mica to assess the extent of carbonatite–wall rock interaction (contamination) in one of the sövite bodies of the Kaiserstuhl Volcanic Complex.

## GEOLOCICAL SETTING AND OCCURENCE OF CARBONATITES IN THE KAISERSTUHL

The Kaiserstuhl Volcanic Complex (KVC) is situated in the Upper Rhine Graben (Fig. 1a), which is part of a larger extensional zone throughout central Europe that was established in a stress regime caused by Alpine orogenic processes in Tertiary times (e.g., Ziegler, 1982; Wilson & Downes, 1991). The emplacement of the KVC rocks along deep-reaching zones of weakness was enabled by lithospheric thinning (Hüttner, 1996; Edel *et al.*, 2006; Bourgeois *et al.*, 2007). The Upper Rhine Graben is characterized by numerous listric and mostly steep fault sets that are partly subparallel to the graben geometry. These faults and associated structures cause a horst and graben structure and a complex system of variably sized tectonic blocks (e.g. Beccaletto *et al.*, 2010).

The rocks of the KVC are of Miocene age (18–15 Ma; e.g. Kraml *et al.*, 2006 and references therein) and mainly consist of a tephritic to phonolitic rock series, accompanied by minor nephelinitic to limburgitic, and melilititic to haüynitic lithologies and carbonatites (e.g. Baranyi *et al.*, 1976; Keller *et al.*, 1990; Wimmenauer, 2003; Braunger *et al.*, 2018). The KVC rocks probably derive from several magma sources, with carbonatites being genetically related to the melilititic to haüynitic rocks (e.g. Schleicher *et al.*, 1990; Wang *et al.*, 2014).

The four major sövite bodies (Badberg, Degenmatt, Haselschacher Buck, Orberg) are spatially associated

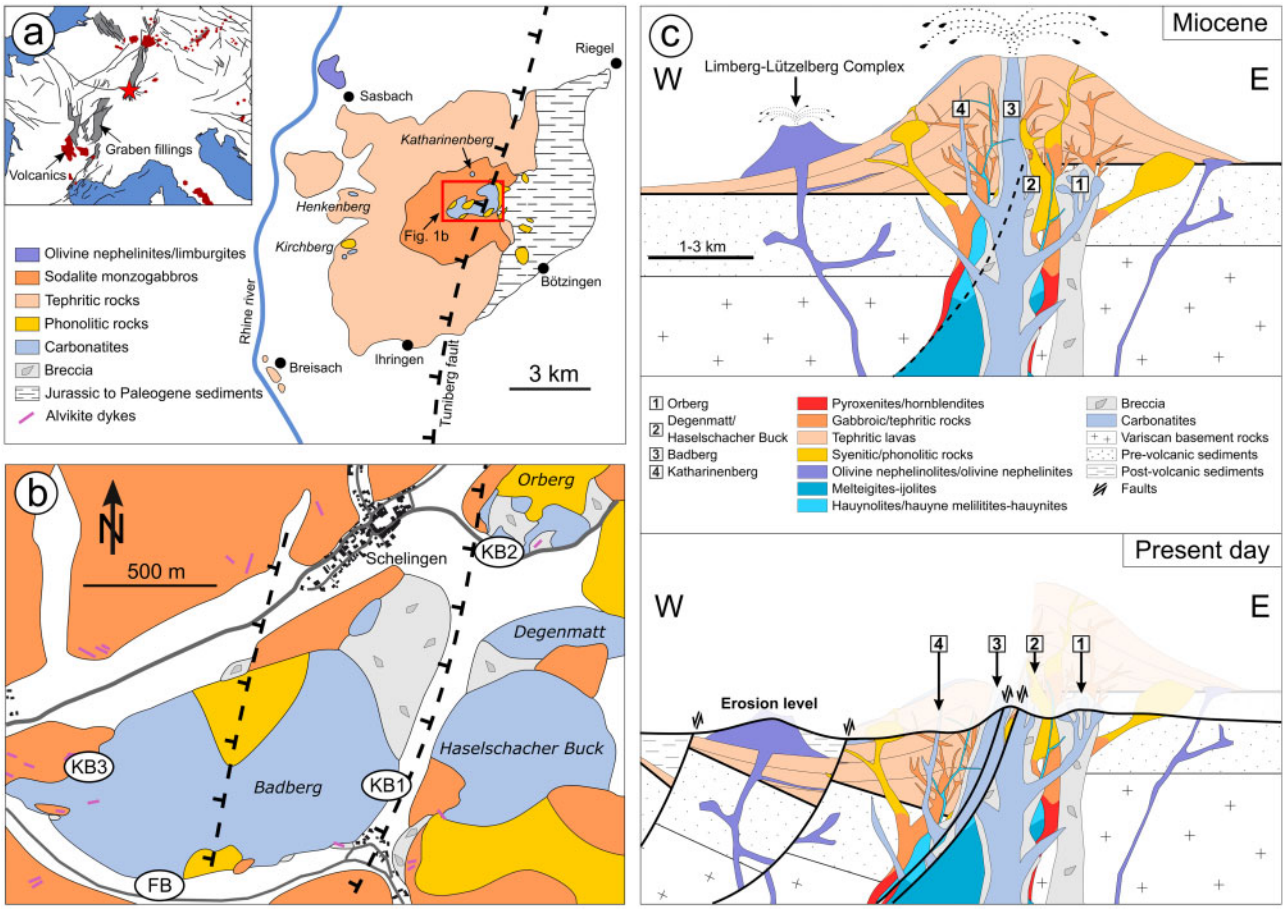


**Fig. 1.** Geology of the Kaiserstuhl Volcanic Complex (KVC). (a) Simplified geological map of the KVC (modified after Keller *et al.*, 1990) including an overview map of the European Cenozoic Volcanic Province (modified after Dèzes *et al.*, 2004), where the position of the KVC is indicated by a red star. (b) Detailed geological map of the central part of the KVC, which depicts several sövite bodies and the location of the four historic drill holes KB1, KB2, KB3 and FB. The schematic fault system is represented by a duplication of the Tuniberg normal fault. (c) Schematic cross section of the structural development of the carbonatites at the KVC.

with polygenetic breccias in the central area of the KVC and two small sövite occurrences (<10 m in diameter) are exposed at Katharinenberg and Kirchberg (Fig. 1a). The KVC is intersected by the regional Tuniberg Fault (Fig. 1), which causes a vertical displacement of ~1000 m north and ~3000 m south of the KVC, with a westwards down-throw towards the Rhine graben centre (Groschopf *et al.*, 1996; Beccaletto *et al.*, 2010). Geophysical evidence (seismic surveys; e.g. Brauch *et al.*, 2018 and references therein) suggests at least one sub-parallel structure further W that intersects the Badberg sövite body (Fig. 1b), but the vertical displacement of this structure is unknown.

The about 400 m thick, pipe-like Badberg body is banded and inclined at about 60° towards the northwest. It intrudes sodalite monzogabbros and phonolites and is partly underlain by foid syenites and phonolites as indicated by the scientific KB3 and FB drillings (Kirchheimer, 1973; Blust, 1993). Mineral banding in the sövite is subparallel to its contacts towards the country rocks and numerous cm- to m-sized rafts of calcite foidolites occur aligned parallel to the banding. The relative abundance of these xenoliths decreases from the top of the tilted Badberg body towards its deeper parts. The sövite bodies at Degenmatt and Haselschacher Buck probably reflect similar pipe-like geometries but are not exposed well enough to constrain this. However, geophysical data (gravimetric and magnetic) indicate a continuous pipe-like body below the Degenmatt/Haselschacher Buck bodies, whereas there is no evidence that the Badberg body continues to greater depth (Brauch *et al.*, 2018).

Sövites at Orberg are exposed in five quarries (designated as I–V) and display variable geometries. Sövite sills dipping by 25° towards the northeast are exposed in quarries I and II, quarry III exposes a 10 m thick sheet-like body with a dip of 70° towards the northwest , and quarries IV and V show irregular geometries implying a cauliflower-like structure. The emplacement of the Orberg sövites was probably promoted by distinct zones of weakness, reflected by pre-existing polygenic breccias (proved by KB2 scientific drilling in 1991 in quarry II; Hubaux, 1964).

Dolomite-bearing alvikites (still calcite-dominated, though) occur as fine- to medium-grained subvertical dykes, crosscutting all rock types and rare dolomite-

dominated varieties (beforsites) are known (e.g. Van Wambeke, 1964; Sigmund, 1996). Alvikites show variable thicknesses (cm- to m scale) and textures. They have been described in great detail previously (e.g. Katz & Keller, 1981; Sommerauer & Katz-Lehnert, 1985; Katz-Lehnert, 1989) and are not subject to the present study.

At Henkenberg and Kirchberg (Fig. 1a), three layers (each 1 to 1·5 m thick) of extrusive carbonatite, represented as alternating sequences of carbonatitic crystal tuff, lapillistones and lavas and interbedded with tephritic and basanitic pyroclastics, are preserved (Keller, 1978; Keller, 1981, Keller, 1989; Woolley & Kjarsgaard, 2008). The distance between these two localities is about 1·5 km, but the original extent of these deposits is unknown, due to intense anthropogenic land transformations in the 1970s.

## SAMPLE MATERIAL AND ANALYTICAL METHODS

The material investigated for this study is part of the sample set (N ≈ 400) of Walter *et al.* (2018) and includes 46 carefully selected samples from surface outcrops and from the scientific KB2 and KB3 drillings, covering the major sövite bodies and the two known occurrences of extrusive carbonatites in the KVC. A complete sample list is given in Table 1, along with locations, GPS coordinates and petrographic details.

Mineral compositions were acquired using a JEOL 8900 electron microprobe at the Institute of Geosciences, Universität Tübingen, Germany. Acceleration voltage was 15 kV (for apatite, phlogopite, clinopyroxene and carbonate) and 20 kV (for garnet and spinel group minerals) using a beam current of 10 nA (for apatite) and 20 nA (for other minerals). Depending on the mineral, the beam diameters varied from a focused beam (for olivine, spinel group minerals, pyroxene and zirconolite), 2 μm (mica), 5 μm (carbonates and garnet) to 10 μm (apatite). Natural and synthetic standards were used for calibration (see ES1, Supplementary Data; supplementary data are available for downloading at http://www.petrology.oxfordjournals.org). Data reduction was performed using the internal ZAF and φρz matrix correction software of JEOL (Armstrong, 1991). Details on the WDS configuration used and typical detection limits for the individual elements of various minerals are given in the Supplementary Data; supplementary data are available for downloading at http://www.petrology.oxfordjournals.org (ES1).

## PETROGRAPHY

### Sövites

Besides calcite, the most abundant minerals in the different sövites are apatite, mica, spinel group minerals and pyrochlore, with highly variable modal amounts (Table 1; Fig. 2) on a dm- to m-scale. Occasionally, mineral banding represented by alternating coarse-grained and finer grained layers of non-carbonate minerals occurs in some areas. Rarely, thin olivine-rich layers (Orberg) and in one case, a perovskite-rich layer (Badberg, see below) have been exposed. However, the major mineralogical differences between the sövite bodies are reflected by the presence/absence of clinopyroxene, olivine and monticellite.

Olivine is present in two samples from Haselschacher Buck and Katharinenberg and occurs as up to 500 μm large euhedral to subhedral grains, which are often serpentinized along cracks and grain boundaries and are occasionally replaced by calcite (Fig. 3a). Subhedral to anhedral monticellite occurs in one sample from Orberg V (Fig. 3b).

Apatite is the most abundant non-carbonate mineral and occurs in all investigated sövites. Textures range from large radial crystal aggregates (Fig. 3c), medium-sized prismatic grains to anhedral patches mostly enclosed by calcite and less commonly by phlogopite and spinel group minerals. Most apatites show variable zoning patterns, ranging from oscillatory zonation (Fig. 3d; with occasional resorbed cores) to patchy zonation.

Clinopyroxene was only observed in some of the Badberg samples, where it is mostly euhedral but typically cracked and altered along cleavages. In some cases it shows rounded grain boundaries towards calcite (Fig. 3e).

The abundance and general appearance of mica (Figs 3e and 4) differs between samples from Badberg (commonly very mica-rich) and the other localities (generally mica-poor). With the exception of the Badberg samples, mica occurs as <2 mm large euhedral to subhedral laths to stubby grains, mostly enclosed by calcite (Fig. 4a). It is almost colourless under plane-polarized light and is occasionally altered to chlorite. Mica from Orberg III and Katharinenberg is typically oscillatory zoned (Fig. 4b), while mica from the Degenmatt samples is less so, and mica from other localities lacks any visible zonation. Mica from the Badberg samples is much larger (up to 2 cm), exhibiting an olive-green to khaki appearance under plane-polarized light. Two different modes of occurrence in the Badberg samples are distinguished: (1) blocky crystals accumulated at the contact towards the calcite foidolites (Fig. 4c; see below) are classified as 'black-wall mica', whereas (2) bundles of large mica laths occur dispersed in the Badberg samples and are seemingly independent of the presence of calcite foidolite relicts (Fig. 4d).

Spinel group minerals are very common and generally occur as several mm-sized disseminated subhedral to euhedral grains (occasionally very porous; Fig. 3f). They are mostly enclosed by calcite and occasionally contain inclusions of apatite. In very few samples, however, they are overgrown by apatite. Abundant pyrochlore (see details in Walter *et al.*, 2018) and rare zirconolite (Van Wambeke, 1964; Sinclair & Eggleton, 1982; Keller, 1984) crystallized more or less simultaneously with spinel group minerals. Zirconolite was only found in a sample from Haselschacher Buck, where it

**Table 1:** List of samples investigated in this study along with their major mineralogy

| Locality | Rock type | Sample # | Depth | UTM coordinates | Ap | Phl | Mgt | Pcl | Cpx | Grt | Ol/ Mtc | Cal | Dol |
|---|---|---|---|---|---|---|---|---|---|---|---|---|---|
| Badberg | Calcite foidolite | HTAC 260 | Surface | 32 U 401310 5327748 | x | x | – | (tr) | X* | X | – | x | – |
| Badberg | Sövite | HTAC 1136 | KB3 (267 m) | 32 U 400940 5327843 | X | X | X* | – | X* | – | – | X | – |
| Badberg | Calcite foidolite | HTAC 1139 | KB3 (254 m) | 32 U 400940 5327843 | x* | x | – | – | X | X* | – | x | – |
| Badberg | Calcite foidolite | HTAC 1147 | KB3 (241 m) | 33 U 400940 5327844 | x* | x | – | – | X | X* | – | x | – |
| Badberg | Calcite foidolite | HTAC 1148 | KB3 (240 m) | 32 U 400940 5327843 | x | x* | – | (tr) | X | X | – | x | – |
| Badberg | Sövite | HTAC 1151 | KB3 (227m) | 32 U 400940 5327843 | X | X | x | x | x* | – | – | X* | – |
| Badberg | Sövite | HTAC 1156 | KB3 (215 m) | 32 U 400940 5327843 | X | X* | x | x | – | – | – | X | – |
| Badberg | Calcite foidolite | HTAC 1158 | KB3 (204 m) | 32 U 400940 5327843 | x | X | – | (tr) | X | X* | – | X | – |
| Badberg | Calcite foidolite | HTAC 1168 | KB3 (177 m) | 32 U 400940 5327843 | x | x | – | (tr) | X | X* | – | x | – |
| Badberg | Calcite foidolite | HTAC 1173 | KB3 (165 m) | 32 U 400940 5327843 | x | X | x | – | X | X* | – | x | – |
| Badberg | Calcite foidolite | HTAC 1178 | KB3 (150 m) | 32 U 400940 5327843 | x* | – | – | (tr) | X* | X | – | X | – |
| Badberg | Calcite foidolite | HTAC 1197 | KB3 (100 m) | 32 U 400940 5327843 | x | x | – | (tr) | X* | X | – | x | – |
| Badberg | Sövite | HTAC 1200 | KB3 (93m) | 32 U 400940 5327843 | X | X* | x | (tr) | – | – | – | X | – |
| Badberg | Calcite foidolite | HTAC 1200 | KB3 (93 m) | 32 U 400940 5327843 | x | X* | x | – | X | X* | – | x | – |
| Badberg | Sövite | HTAC 1215 | KB3 (35 m) | 32 U 400940 5327843 | X | x | X | x | x* | – | – | X | – |
| Badberg | Sövite | HTAC 1229 | KB3 (-10 m) | 32 U 400940 5327843 | X* | X | X | x | X* | – | – | X* | – |
| Badberg | Sövite | HTAC 1237 | KB3 (-48 m) | 32 U 400940 5327843 | X | X* | X | (tr) | x* | – | – | X* | – |
| Badberg | Sövite | HTAC 1245 | KB3 (-66 m) | 32 U 400940 5327843 | x | X* | X | (tr) | x | – | – | X | – |
| Badberg | Sövite | HTAC 1362 | Surface | 32 U 400763 5327907 | X | x | X | (tr) | x | – | – | X* | – |
| Orberg II | Sövite | HTAC 1253 | KB2 (4 m) | 32 U 402477 5328680 | x* | x | X | x | – | – | – | X* | x |
| Orberg II | Sövite | HTAC 1267 | KB2 (271 m) | 32 U 402477 5328680 | x | x | x | – | – | – | – | X* | x |
| Orberg II | Sövite | HTAC 1318 | KB2 (191.7 m) | 32 U 402477 5328680 | x | x* | x | – | – | – | – | X | x |
| Orberg II | Sövite | HTAC 1282 | KB2 (242 m) | 32 U 402477 5328680 | x | x | x | – | – | – | – | X* | x |
| Orberg II | Sövite | HTAC 1294 | KB2 (323 m) | 32 U 402477 5328680 | x | x | X | x | – | – | – | X* | – |
| Orberg III | Sövite | HTAC 1410 | Surface | 32 U 402555 5328668 | x* | x* | x* | x | – | – | – | X* | – |
| Orberg III | Sövite | HTAC 1413 | Surface | 32 U 402555 5328668 | x* | x* | x* | x | – | – | – | X | – |
| Orberg IV | Sövite | HTAC 0237 | Surface | 32 U 402691 5328724 | X* | x* | X* | x | – | – | – | X* | – |
| Orberg IV | Sövite | HTAC 0239 | Surface | 32 U 402691 5328724 | X* | – | x | x | – | – | – | X* | – |
| Orberg IV | Sövite | HTAC-1353 | Surface | 33 U 402691 5328724 | x* | x | x* | x | – | – | – | X | – |
| Orberg V | Sövite | HTAC 0222 | Surface | 32 U 402640 5328781 | x* | x* | – | x | – | – | – | X | X |
| Orberg V | Sövite | HTAC 0224 | Surface | 32 U 402640 5328781 | X | – | X* | X | – | – | – | X | – |
| Orberg V | Sövite | HTAC 0225 | Surface | 32 U 402640 5328781 | x* | x* | x* | X | – | – | – | X* | – |
| Orberg V | Sövite | HTAC 1356 | Surface | 32 U 402640 5328781 | x* | – | x | – | – | – | –/ X* | X* | – |
| Orberg V | Sövite | HTAC 1366 | Surface | 32 U 402620 5328185 | x* | x* | – | x | – | – | – | X* | – |
| Degenmatt | Sövite | HTAC 1399 | Surface | 32 U 403779 5326957 | X* | x* | – | x | – | – | – | X* | – |
| Haselschacher Buck | Sövite | HTAC 0284 | Surface | 32 U 402668 5327797 | X* | x* | x* | x | – | – | – | X* | – |
| Haselschacher Buck | Sövite | HTAC 1354 | Surface | 32 U 402668 5327797 | x* | x* | x* | – | – | – | x*/- | X* | – |
| Katharinenberg | Sövite | HTAC 1415b | Surface | 32 U 402288 5329644 | X | x* | X* | x | – | – | – | X* | – |
| Katharinenberg | Sövite | HTAC 1415c | Surface | 32 U 402288 5329644 | X* | x* | x* | x | – | – | X*/- | X* | – |
| Henkenberg | Crystal tuff | GM1 | Surface | 32 U 396571 5327645 | x | – | – | – | x* | x* | – | X* | – |
| Henkenberg | Crystal tuff | GM2 | Surface | 32 U 396571 5327645 | x | – | x* | (tr) | X* | x* | – | X* | – |
| Henkenberg | Crystal tuff | GM3 | Surface | 32 U 396570 5327645 | x* | x | x* | – | X | x* | – | X | – |
| Henkenberg | Crystal tuff | HTAC 1369 | Surface | 32 U 396571 5327640 | x | – | x | – | – | x* | – | X | – |
| Henkenberg | Crystal tuff | HTAC 1371 | Surface | 32 U 396571 5327640 | x | – | x* | – | – | x | – | X | – |
| Henkenberg | Lapilli stone | GM4 | Surface | 32 U 396570 5327647 | x | – | x* | – | x* | x* | – | X* | – |
| Kirchberg | Lava | HTAC 1337 | Surface | 32 U 396571 5327640 | – | – | x* | – | – | x* | – | X* | – |

X, major component; x, minor component; (tr), trace component.
*, EPMA data available.

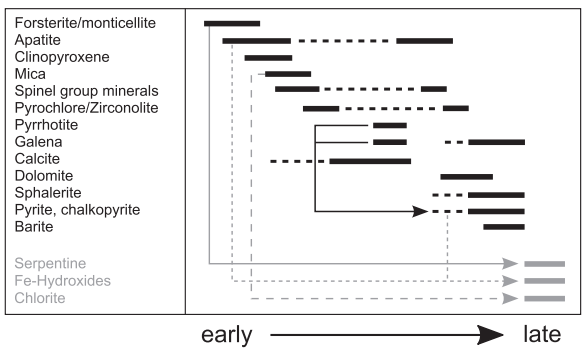


**Fig. 2.** Paragenetic scheme for sövites of the KVC including major alteration phases (in grey).

occurs as up to 30 μm large and occasionally zoned crystals (Fig. 4g). Perovskite (in the old literature called 'dysanalyte') was reported from a thin horizon at the Badloch quarry (southern Badberg; Wimmenauer, 1963; Hornig-Kjarsgaard, 1998). This outcrop is, however, lost and none of the investigated samples contains perovskite.

The main phase of calcite formation occurred relatively late, only rarely calcite occurs as small inclusions in apatite. Calcite exhibits equigranular and subhedral textures, with grain sizes varying from 100 μm up to several cm. Late-stage dolomitization of calcite is occasionally observed (Fig. 4h).

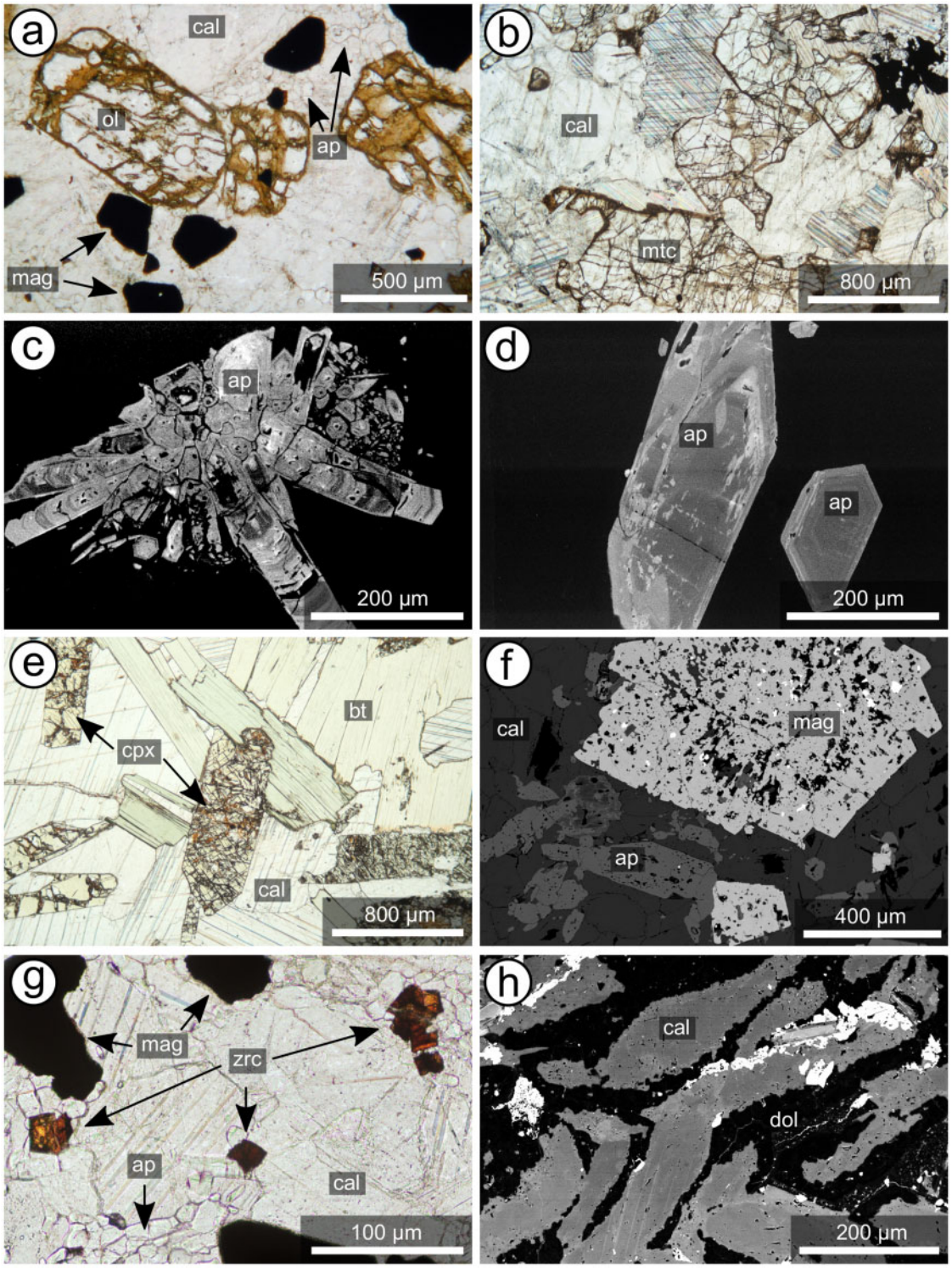


**Fig 3.** Photomicrographs (plane polarized light) and backscattered electron (BSE) images of the mineral assemblage of sövites from the KVC. (a) Coarse-grained olivine altered to serpentine (Haselschacher Buck). (b) Subhedral to anhedral monticellite (Orberg V). (c) Stellar aggregates of apatite (Orberg V). (d) REE- and Si-rich rims with REE- and Si-poor cores in apatite (Badberg). (e). Partly resorbed and altered clinopyroxene associated with biotite (Badberg). (f) Porous spinel group mineral (magnetite-magnesioferrite) associated with apatite and calcite (Orberg III). (g) Zirconolite (zrc) in olivine-bearing sövite (Haselschacher Buck). (h) Subhedral calcite surrounded and partly replaced by late-stage dolomite (Orberg II).

Abbreviations: ap, apatite; bt, biotite; cal, calcite; cpx, clinopyroxene; dol, dolomite; mag, spinel group mineral (magnetite–magnesioferrite); mtc, monticellite; ol, olivine; zrc, zircon.

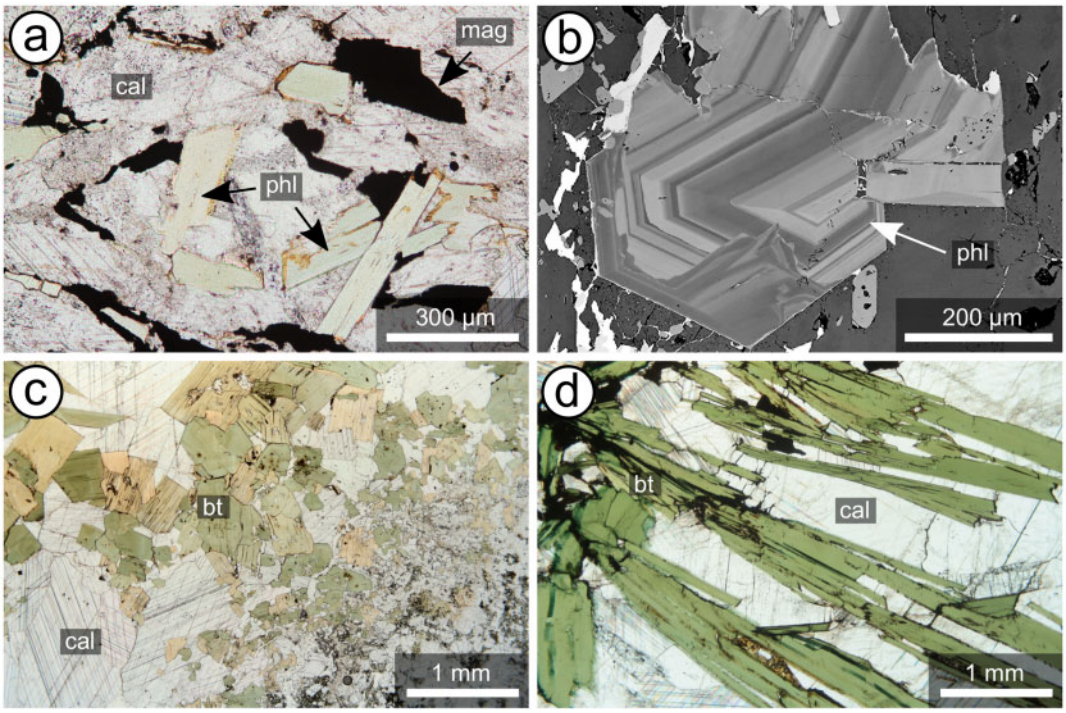


**Fig. 4.** Photomicrographs (plane polarized light) and backscattered electron (BSE) images of the different appearances of mica in sövites from the KVC. (a) Euhedral to subhedral laths of phlogopite enclosed by calcite and spinel group minerals (magnetite-magnesioferrite; Orberg V). (b) Oscillatory zoned Ba-rich phlogopite (Orberg III). (c) Coarse-grained 'black-wall' biotite (Badberg). (d) Coarse-grained bundles of biotite laths independent of the presence of calcite foidolite (Badberg). Abbreviations (see Fig. 3): bt, biotite; phl, phlogopite.

Rare pyrrhotite crystallized before calcite, but other sulphides (mainly pyrite, with minor galena and sphalerite) are of late-stage/hydrothermal origin and are often associated with fine-grained and interstitial barite.

## Extrusive carbonatites

Carbonatite lavas have only been observed at the Kirchberg (Fig. 1). They consist of up to 0·6 mm large oscillatory zoned calcite laths and up to 150 μm large euhedral spinel group mineral grains, set in a fine-grained groundmass of calcite, apatite and spinel group minerals (Fig. 5a). In some cases, the spinel group minerals show thin rims, which are BSE-dark (Fig. 5b). Occasional xenocrysts of nepheline (300 μm; Fig. 5a) and garnet (200 μm) have been observed.

Carbonatite lapillistones and crystal tuffs from the Henkenberg were described in detail by Keller (1981, 1989). Lapillistones consist of calcite laths and subrounded lapilli cemented by fine-grained secondary calcite. The 0·5 to 10 mm large lapilli contain, in addition to calcite, larger amounts of spinel group minerals and prismatic apatite, and rare grains of clinopyroxene and garnet (Fig. 5c). Crystal tuffs are mainly composed of fragments of calcite (showing mosaic textures), spinel group minerals, garnet and pyroxene, with rare apatite and pyrochlore, set in a groundmass of calcite (Fig. 5d). Occasionally intercalated clasts of calcite foidolite and sövite can be recognized.

## Calcite foidolites

Xenoliths of calcite foidolite (cm- to m-sized) occur only in the Badberg sövite (and rarely in carbonatitic tuff layers of the Henkenberg). Their abundance decreases towards the centre of the Badberg body, where they are strongly disaggregated compared to those in marginal zones. Sövite that contains strongly disaggregated xenoliths is exceptionally mica-rich (Fig. 6). Based on drill core loggings (Blust, 1993), the average carbonatite/xenolith ratio is about 5:1, but varies strongly from about 2:1 (marginal areas) to about 50:1 (central areas) over a range of tens of metres.

The contact between calcite foidolites and the surrounding sövite is characterized by coarse-grained seams of olive-green to khaki mica (see above) and an occasional transition zone consisting of strongly altered garnet and clinopyroxene, frequently intruded by carbonatitic veins (Fig. 7a). The central parts of these xenoliths consist of variable amounts of altered foid minerals (see below) and relict feldspar, with variable amounts of clinopyroxene, garnet and interstitial calcite (Fig. 7b–d).

Former nosean or haüyne (now decomposed to various zeolite minerals and calcite) is the most common phase. It mostly forms rounded grains of variable sizes and only rarely, euhedral grains containing small Fe-sulfide/oxide micro-inclusions are present (Fig. 7c). Rare relics of alkali feldspar are variably replaced by zeolites, calcite, mica and other minerals (Fig. 7d).

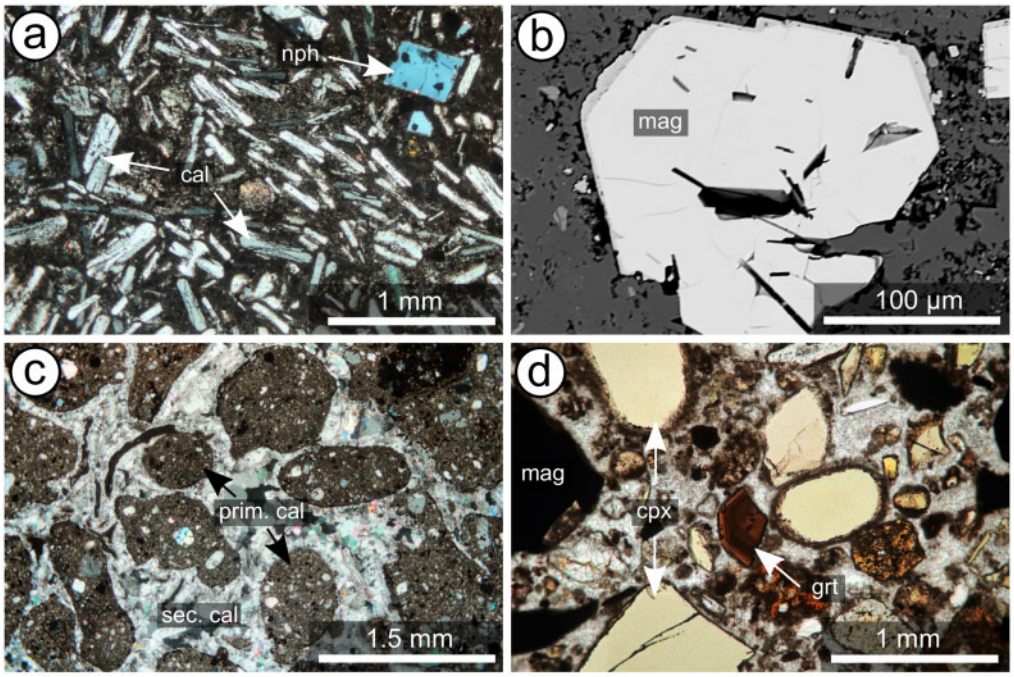


**Fig. 5.** Photomicrographs (plane and crossed polarized light) and backscattered electron (BSE) images of textural features of extrusive carbonatites from the KVC. (a) Carbonatite lava with calcite laths in a matrix of fine-grained calcite, apatite and spinel group minerals (magnetite–magnesioferrite). (b) Euhedral spinel group minerals with darker rims (enriched in Al) in carbonatite lava. (c) Lapillistone porphyritic lapilli in a fine-grained groundmass of calcite, spinel group minerals and apatite, cemented by secondary calcite. (d) Crystal tuff with fragments of clinopyroxene, garnet (grt) and spinel group minerals in groundmass of calcite.

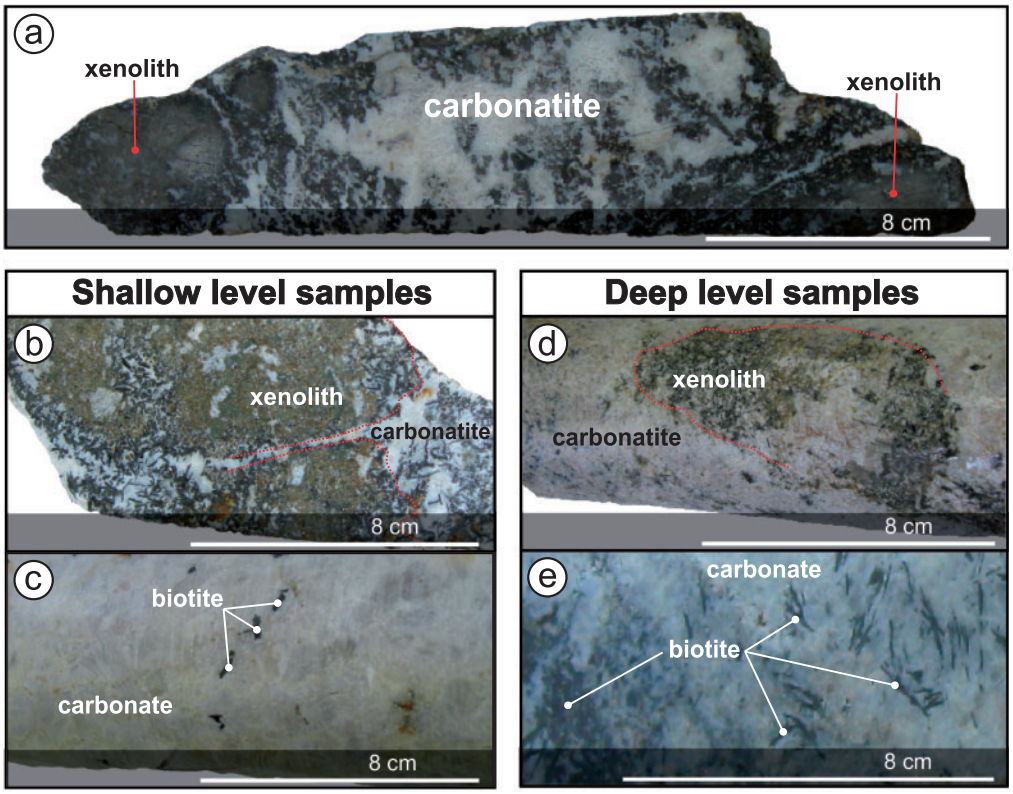


**Fig. 6.** Xenoliths in the Badberg carbonatites. (a) Carbonatite with a high xenolith proportion and strong proximal (to the xenolith) mica formation. (b) Xenolith from a 'shallow' drill core level (reflecting the marginal zone of the carbonatite pipe) showing significant mica formation around (black-wall mica) and in direct vicinity of the xenoliths. (c) Sections distal to a xenolith within a 'shallow' drill core level showing low mica formation. (d) Xenolith from a 'deep' drill core level (reflecting the central zone of the carbonatite pipe) showing strong disaggregation. The xenolith is nearly almost replaced by calcite. (e) Sections distal to xenolith within a 'deep' drill core level showing significant mica formation. The correlation between stronger disaggregated/resorbed xenoliths and the increased formation of mica shows a clear dependency.

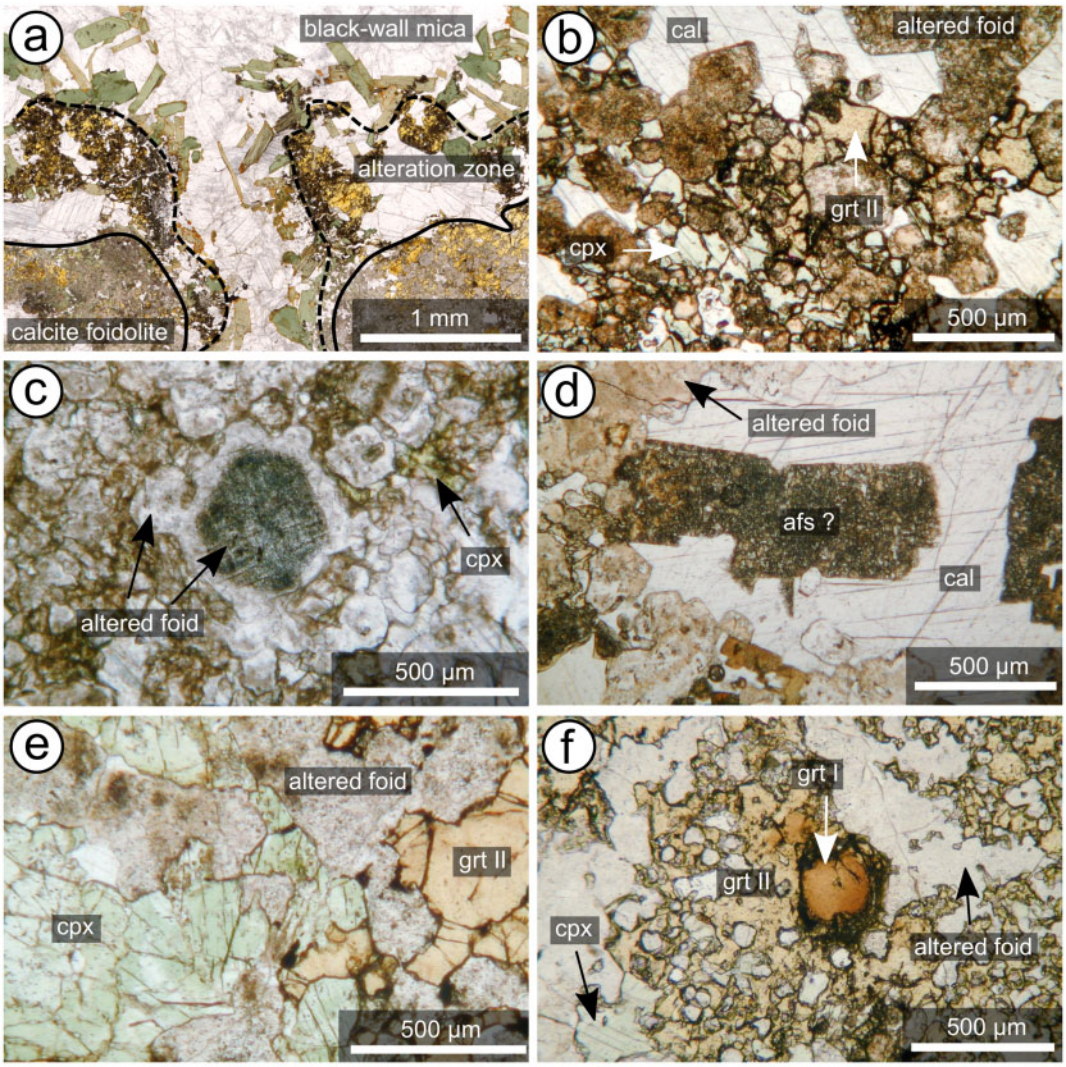


**Fig. 7.** Photomicrographs (plane polarized light) of the mineral assemblage and textural appearance of calcite foidolites from the KVC. (a) Coarse-grained biotite-rich 'black-wall' at the contact between carbonatite and calcite foidolite. (b) Recrystallized garnet (II) associated with recrystallized clinopyroxene (II), calcite and foid minerals (mostly altered to zeolites). (c) Euhedral nosean (or haüyne) decomposed to zeolite and calcite. (d) Alkali feldspar (afs) replaced by a mixture of zeolite, calcite, biotite, minor clinopyroxene (II) and garnet (II). (e) Clinopyroxene (II), garnet (II) and interstitial calcite in a calcite foidolite. (f) Dark brown and rounded (relict) garnet (I) overgrown by anhedral garnet (II).

Clinopyroxene occurs mostly as pale green, sometimes patchy-coloured subhedral and interstitial grains (Fig. 7e). If present, dark brown garnet I (relict cores) is overgrown by a reddish-brownish garnet II (recrystallized anhedral grains or masses; Fig. 7f). Garnet II is commonly zoned and occasionally forms poikilitic aggregates that enclose former foid minerals (Fig. 7f). Ubiquitous accessory minerals are apatite and titanite, only one sample contains primary spinel group minerals.

## MINERAL COMPOSITIONS

### Carbonates

Representative analyses are given in Table 2; formula calculations are based on one cation with $CO_2$ being calculated. Calcite in sövites contains variable, but generally minor amounts of Sr (<2 wt % SrO), Fe (<0·4 wt % FeO), Mg (<1·5 wt % MgO) and Mn (<1·5 wt %). Mean REE contents are generally <0·2 wt % $Ce_2O_3$ (similar to earlier data; Hornig-Kjarsgaard, 1998), but may occasionally reach higher values; however, the presence of REE-rich micro inclusions cannot be excluded. Calcite from Badberg samples is relatively Sr-rich but Mg-poor compared to calcite from other sövites (Fig. 8). Calcite in extrusive carbonatites is highly variable in composition. In the crystal tuff and lapillistone samples from Henkenberg, primary calcite is Sr-rich but Mg-poor compared to secondary calcite cement (Fig. 8).

### Apatite

Representative analyses are given in Table 3 and formula calculations were done using the method of Ketcham (2015). As typical of carbonatites

**Table 2:** Representative EPMA analyses of carbonates from the Kaiserstuhl Volcanic Complex

| Sample # | 1229 | 1237 | 1362 | 1267 | 1294 | 1267 | 1318 | 1316b | 1410 | 237 | 239 | 225 | 1356 | 1366 |
|---|---|---|---|---|---|---|---|---|---|---|---|---|---|---|
| Locality | Badberg | | | Orberg II | | | | | Orberg III | Orberg IV | | Orberg V | | |
| Mineral | Calcite | | | | | Dolomite | | Ankerite | Calcite | | | | | |
| Rock type | Sövite | | | | | | | | | | | | | |
| wt.% | | | | | | | | | | | | | | |
| CaO | 55·18 | 55·45 | 55·09 | 55·79 | 54·74 | 30·96 | 28·89 | 28·88 | 53·15 | 54·88 | 54·67 | 54·39 | 56·22 | 55·63 |
| MgO | 0·08 | 0·04 | 0·03 | 0·40 | 0·12 | 15·51 | 18·57 | 8·88 | 1·26 | 0·50 | 0·58 | 0·55 | 0·05 | 0·36 |
| FeO | bdl | 0·04 | bdl | 0·04 | 0·16 | 3·37 | 0·53 | 15·15 | bdl | 0·11 | bdl | 0·22 | 0·14 | 0·26 |
| MnO | 0·10 | 0·24 | 0·03 | bdl | 0·38 | 2·91 | 2·38 | 3·21 | 0·50 | 0·04 | 0·19 | bdl | bdl | bdl |
| SrO | 1·62 | 1·55 | 1·36 | 1·18 | 1·40 | 0·61 | 1·37 | 0·27 | 1·46 | 1·16 | 1·07 | 1·18 | 0·84 | 0·00 |
| $Ce_2O_3$ | 0·07 | 0·89 | 0·07 | 0·21 | 0·11 | 0·03 | 0·04 | bdl | bdl | 0·64 | 0·06 | bdl | 0·06 | bdl |
| $CO_2$ (calc.) | 44·17 | 44·75 | 43·89 | 44·83 | 44·07 | 45·38 | 45·35 | 43·75 | 44·01 | 44·46 | 44·13 | 43·92 | 44·64 | 44·21 |
| Total | 101·22 | 102·95 | 100·46 | 102·44 | 100·98 | 98·77 | 97·13 | 100·14 | 100·38 | 101·78 | 100·70 | 100·25 | 101·95 | 100·46 |
| Formula based on 1 cation | | | | | | | | | | | | | | |
| Ca | 0·98 | 0·97 | 0·99 | 0·98 | 0·97 | 0·54 | 0·50 | 0·52 | 0·95 | 0·97 | 0·97 | 0·97 | 0·99 | 0·99 |
| Mg | 0·002 | 0·001 | 0·001 | 0·01 | 0·003 | 0·37 | 0·45 | 0·22 | 0·03 | 0·01 | 0·01 | 0·01 | 0·001 | 0·01 |
| Fe | bdl | 0·00 | bdl | 0·00 | 0·002 | 0·05 | 0·01 | 0·21 | bdl | 0·002 | bdl | 0·003 | 0·002 | 0·004 |
| Mn | 0·001 | 0·003 | 0·00 | bdl | 0·01 | 0·04 | 0·03 | 0·05 | 0·01 | 0·001 | 0·003 | bdl | bdl | bdl |
| Sr | 0·02 | 0·01 | 0·01 | 0·01 | 0·01 | 0·01 | 0·01 | 0·00 | 0·01 | 0·01 | 0·01 | 0·01 | 0·01 | 0·00 |
| Ce | 0·001 | 0·008 | 0·001 | 0·002 | 0·001 | 0·0003 | 0·0003 | bdl | bdl | 0·01 | 0·001 | bdl | 0·001 | bdl |
| Total cations | 1·00 | 1·00 | 1·00 | 1·00 | 1·00 | 1·00 | 1·00 | 1·00 | 1·00 | 1·00 | 1·00 | 1·00 | 1·00 | 1·00 |

| Sample # | 284 | 1354 | 1399 | 1415b | 1415c | GM1 | GM2 | GM4 | GM4 | 1337 | 1337 |
|---|---|---|---|---|---|---|---|---|---|---|---|
| Locality | Haselschacher Buck | | Degenmatt | Katharinenberg | | Henkenberg | | | | Kirchberg | |
| Mineral | Calcite | | | | | | | | Sec. Calcite | Calcite | |
| Rock type | Sövite | | | | | Crystal tuff | | Lapilli stone | | Lava | |
| Wt % | | | | | | | | | | | |
| CaO | 54·86 | 54·93 | 51·87 | 55·31 | 53·13 | 56·44 | 55·03 | 56·35 | 56·14 | 54·82 | 55·65 |
| MgO | 0·31 | 0·18 | 0·48 | 0·53 | 1·19 | 0·43 | 0·05 | 0·08 | 0·82 | 0·03 | 0·04 |
| FeO | 0·29 | bdl | 0·13 | 0·09 | 0·07 | bdl | bdl | 0·06 | bdl | 0·40 | bdl |
| MnO | bdl | 0·13 | 1·17 | 0·14 | 0·46 | bdl | 0·15 | 0·02 | bdl | bdl | bdl |
| SrO | 0·87 | 0·72 | 0·26 | 0·38 | 1·12 | 0·00 | 1·48 | 1·00 | bdl | 1·36 | 1·15 |
| Ce2O3 | bdl | bdl | 0·06 | 0·17 | 0·09 | bdl | 0·09 | 0·08 | 0·05 | bdl | bdl |
| CO2 (calc.) | 43·94 | 43·69 | 42·18 | 44·36 | 43·83 | 44·76 | 44·00 | 44·82 | 44·97 | 43·88 | 44·21 |
| Total | 100·28 | 99·65 | 96·14 | 100·99 | 99·87 | 101·63 | 100·80 | 102·41 | 101·98 | 100·49 | 101·04 |
| Formula based on 1 cation | | | | | | | | | | | |
| Ca | 0·98 | 0·99 | 0·97 | 0·98 | 0·95 | 0·99 | 0·98 | 0·99 | 0·98 | 0·98 | 0·99 |
| Mg | 0·01 | 0·004 | 0·01 | 0·01 | 0·03 | 0·01 | 0·001 | 0·002 | 0·02 | 0·001 | 0·001 |
| Fe | 0·004 | bdl | 0·002 | 0·001 | 0·001 | bdl | bdl | 0·001 | bdl | 0·01 | bdl |
| Mn | bdl | 0·002 | 0·02 | 0·002 | 0·01 | bdl | 0·002 | 0·00 | bdl | bdl | bdl |
| Sr | 0·01 | 0·01 | 0·00 | 0·00 | 0·01 | 0·00 | 0·01 | 0·01 | bdl | 0·01 | 0·01 |
| Ce | bdl | bdl | 0·001 | 0·002 | 0·001 | bdl | 0·001 | 0·001 | 0·000 | bdl | bdl |
| Total cations | 1·00 | 1·00 | 1·00 | 1·00 | 1·00 | 1·00 | 1·00 | 1·00 | 1·00 | 1·00 | 1·00 |

bdl, below detection limit.

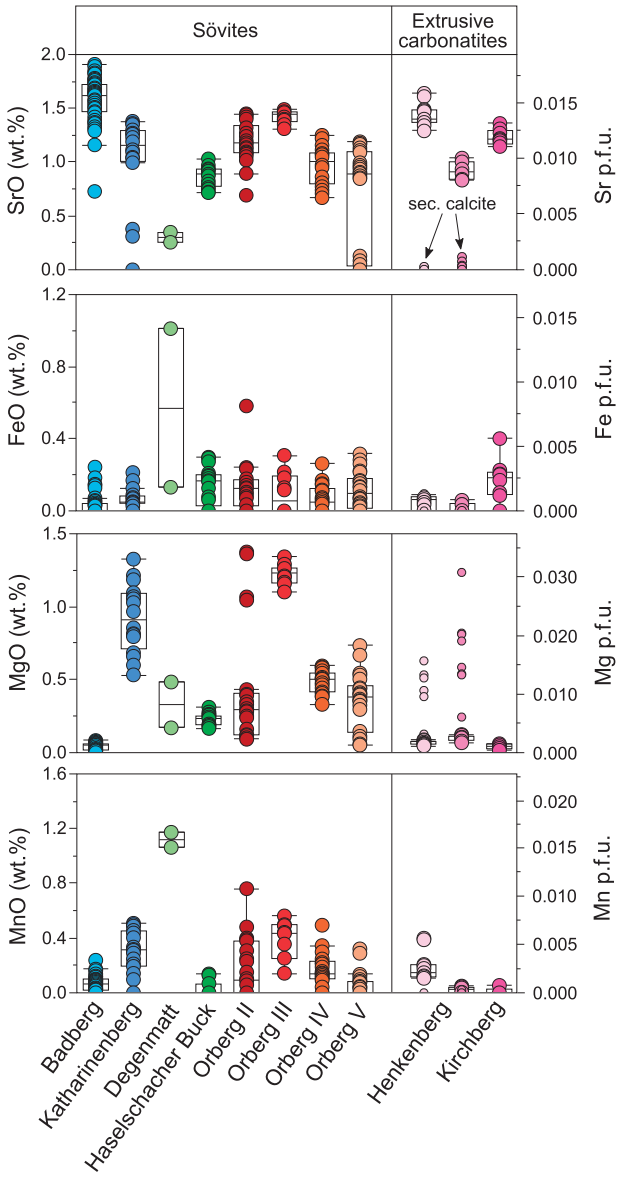


**Fig. 8.** Composition of calcite in sövites and extrusive carbonatites from the KVC shown as box plot diagrams.

(Chakhmouradian *et al.*, 2017), apatite from the KVC is fluorapatite to hydroxyapatite with variable F (1–2·8 wt %) and very low Cl contents (below 0·02 wt %; Table 4). Most data closely follow a substitution mechanism according to the apatite-britholite series ($Ca^{2+} + P^{5+} \leftrightarrow REE^{3+} + Si^{4+}$; Fig. 9a). Apatites from the Badberg sövites and calcite foidolites reach the highest levels of $REE_2O_3$ (up to 6·5 wt %), SrO (up to 4 wt %) and $SiO_2$ (up to 3·6 wt %), but are relatively low in $Na_2O$ (below 0·5 wt %) compared to other locations (Fig. 9). In contrast, apatites from Orberg are low in $REE_2O_3$ (<3 wt %), $SiO_2$ (<1·8 wt %) and SrO (<1·5 wt %), but in some cases show elevated $Na_2O$ (up to 1·2 wt %), following the coupled substitution mechanism $2Ca^{2+} + (3Ca^{2+}) \leftrightarrow REE^{3+} + Na^{+} + (3Sr^{2+})$ (apatite-belovite series). Most apatites are compositionally zoned with variable enrichments of REE and Si towards the rim of the crystals. In particular, apatites from the Badberg sövite show a distinct and sharp enrichment of a britholite component (Figs 3d and 9a) and commonly a slight decrease of Sr in their rims (Fig. 9c). Apatite data from samples of the KB3 drill hole (Badberg) show greater scatter in the upper parts of the drill hole than in the lower parts, with higher REE and Si but lower F and slightly lower Sr in the deeper parts of the drill hole (Fig. 10).

## Mica

Representative analyses are given in Table 4; formula calculations are based on an ideal trioctahedral mica formula ($XY_3[Z_4O_{10}][OH, F, Cl]_2$) and the data were normalized to 7 (tetrahedral [Z] plus octahedral [Y]) cations. Micas from the KVC are Mg-rich and show variable enrichment of Ba (Fig. 11a), with those from Badberg having lower Ba (<0·07 apfu) and Mg# (72–88) compared to micas from the other localities (up to 0·5 Ba pfu and Mg# 91–97), while tetrahedral $Fe^{3+}$ is similarly low at all localities (<0·05 and <0·07 $Fe^{3+}$ pfu, respectively). Accordingly, mica from Badberg is classified as biotite (after Foster, 1960), whereas mica from all other localities is phlogopite. A continuous 1:1 increase of Al with Ba is caused by the phlogopite-kinoshitalite substitution ($K^{+} + Si^{4+} \leftrightarrow Ba^{2+} + {}^{IV}Al^{3+}$). Deviations from the 1:1 slope towards higher Al indicate an additional effect of the phlogopite–eastonite substitution ($Mg^{2+} + Si^{4+} \leftrightarrow {}^{IV}Al^{3+} + {}^{VI}Al^{3+}$; Fig. 11b) with a shift from the ideal 1:1 line reflecting constant eastonite substitution with increasing kinoshitalite substitution. The distinct oscillatory zonation in phlogopites from Orberg III and Katharinenberg (Fig. 4b) exclusively reflects a variable kinoshitalite substitution. Based on specific chemical characteristics, three mica groups are distinguished:

1. Phlogopites from Degenmatt, Katharinenberg and Orberg III and V are characterized by a large spread in Ba and Al contents (Fig. 11b). Orberg III micas follow a nearly ideal kinoshitalite substitution, whereas for micas from Degenmatt, Katharinenberg and Orberg V the additional importance of the eastonite substitution is obvious (Fig. 11a). Phlogopites of this group are further characterized by intermediate Na and F (Na up to 0·09 apfu, F up to 0·4 apfu; Fig. 11c and d) and the lowest Ti and Mn contents (<0·02 and <0·03 apfu, respectively; Fig. 11e and f).
2. Phlogopites from Orberg II and IV and from Haselschacher Buck show a constant eastonite substitution with increasing kinoshitalite substitution (Ba <0·3 apfu; Fig. 11b) and are further characterized by the highest Na (up to 0·11 apfu), intermediate Ti, (up to 0·03 apfu) and low Mn (<0·03 apfu) and F (<0·15 apfu; Fig. 11c–f) contents.
3. Biotite from the Badberg shows the lowest Mg# (72–88) and although their Ba content is low (<0·07 apfu), they show strong Al enrichment during evolution suggesting the importance of the eastonite substitution (Fig. 11a and b). They are further characterized by the highest Mn (up to 0·1 apfu), low

**Table 3:** Representative EPMA analyses of apatite from the Kaiserstuhl Volcanic Complex

| Sample # | 1229 | 1139 | 1147 | 1178 | 1253 | 1413 | 1410 | 1353 | 239 | 237 | 222 | 222 | 225 | 1356 | 1399 | 284 | 1354 | 1415c | GM3 |
|---|---|---|---|---|---|---|---|---|---|---|---|---|---|---|---|---|---|---|---|
| Locality | Badberg | | | | Orberg II | Orberg III | | Orberg IV | | | Orberg V | | | | Degen-matt | Haselschacher Buck | | Katha-rinenberg | Henken-berg |
| Rock type | Calcite Foidolite | | Sövite | | | | | | | | | | | | | | | | Crystal tuff |
| wt % | | | | | | | | | | | | | | | | | | | |
| $Na_2O$ | 0·08 | 0·10 | 0·06 | 0·09 | 0·22 | 0·25 | 0·25 | 0·21 | 0·31 | 0·17 | 1·06 | 0·69 | 0·29 | 0·04 | 0·51 | 0·13 | 0·12 | 0·18 | 0·14 |
| CaO | 52·25 | 52·04 | 51·00 | 51·98 | 54·13 | 54·31 | 54·39 | 54·10 | 54·00 | 53·46 | 52·47 | 52·38 | 53·55 | 52·72 | 51·31 | 53·88 | 53·06 | 54·82 | 52·79 |
| SrO | 0·90 | 1·48 | 1·94 | 1·25 | 0·62 | 0·85 | 0·81 | 0·76 | 0·61 | 0·67 | 1·41 | 1·40 | 0·68 | 0·53 | 1·47 | 0·49 | 0·46 | 0·56 | 0·51 |
| $La_2O_3$ | 1·31 | 0·60 | 1·41 | 0·92 | 0·57 | 0·24 | 0·28 | 0·25 | 0·41 | 0·25 | 0·40 | 0·42 | 0·31 | 0·79 | 0·37 | 0·64 | 0·66 | 0·21 | 0·16 |
| $Ce_2O_3$ | 2·07 | 1·18 | 1·98 | 1·49 | 1·13 | 0·30 | 0·43 | 0·47 | 0·65 | 0·50 | 0·67 | 0·71 | 0·57 | 1·37 | 0·60 | 1·10 | 1·14 | 0·51 | 0·37 |
| $Pr_2O_3$ | 0·27 | 0·19 | 0·25 | 0·16 | 0·12 | bdl | 0·07 | 0·07 | 0·13 | bdl | 0·06 | 0·16 | 0·04 | 0·27 | 0·03 | 0·15 | 0·16 | bdl | bdl |
| $Nd_2O_3$ | 0·46 | 0·24 | 0·39 | 0·30 | 0·47 | 0·09 | 0·15 | bdl | 0·28 | 0·12 | 0·24 | 0·26 | 0·18 | 0·42 | 0·25 | 0·38 | 0·39 | 0·17 | 0·12 |
| FeO | bdl | 0·03 | 0·04 | 0·03 | bdl | 1·07 | 0·02 | bdl | bdl | bdl | 0·02 | 0·07 | bdl | bdl | 0·04 | bdl | 0·15 | bdl | 0·23 |
| $P_2O_5$ | 36·62 | 39·83 | 36·73 | 38·86 | 40·20 | 39·22 | 40·72 | 40·30 | 40·01 | 41·19 | 39·64 | 39·78 | 40·26 | 39·27 | 40·86 | 38·48 | 38·85 | 40·38 | 38·77 |
| $SiO_2$ | 2·55 | 0·87 | 2·50 | 1·29 | 0·84 | 0·21 | 0·33 | 0·48 | 0·52 | 0·35 | 0·02 | 0·17 | 0·72 | 1·50 | 0·04 | 1·62 | 1·92 | 0·53 | 0·98 |
| $SO_3$ | 0·38 | 0·08 | 0·34 | 0·12 | 0·14 | 0·17 | 0·24 | 0·27 | 0·22 | 0·14 | 0·32 | 0·24 | 0·32 | 0·20 | 0·12 | 0·44 | 0·24 | 0·23 | 0·97 |
| $As_2O_5$ | bdl | bdl | bdl | bdl | bdl | bdl | bdl | bdl | 0·03 | bdl | 0·03 | bdl | bdl | bdl | bdl | 0·04 | bdl | bdl | bdl |
| MnO | bdl | 0·04 | bdl | bdl | 0·02 | 0·08 | 0·05 | 0·02 | bdl | 0·02 | 0·12 | 0·08 | 0·04 | bdl | 0·07 | bdl | bdl | 0·04 | 0·03 |
| Cl | 0·05 | 0·05 | 0·02 | 0·01 | 0·03 | 0·03 | 0·03 | 0·02 | 0·05 | 0·03 | 0·02 | 0·04 | 0·05 | 0·01 | 0·01 | 0·07 | 0·03 | 0·04 | 0·62 |
| F | 1·41 | 2·51 | 1·09 | 2·08 | 1·62 | 1·70 | 1·66 | 1·44 | 1·42 | 1·71 | 1·93 | 2·08 | 1·33 | 1·11 | 2·73 | 0·99 | 1·14 | 1·45 | 2·30 |
| −O(F) | 0·60 | 1·06 | 0·46 | 0·88 | 0·68 | 0·72 | 0·70 | 0·61 | 0·60 | 0·72 | 0·81 | 0·87 | 0·56 | 0·47 | 1·15 | 0·42 | 0·48 | 0·61 | 0·97 |
| −O(Cl) | 0·01 | 0·01 | 0·00 | 0·00 | 0·01 | 0·01 | 0·01 | 0·00 | 0·01 | 0·01 | 0·00 | 0·01 | 0·01 | 0·00 | 0·00 | 0·02 | 0·01 | 0·01 | 0·14 |
| Corrected Total: | 97·76 | 98·17 | 97·28 | 97·70 | 99·42 | 97·78 | 98·72 | 97·79 | 98·02 | 97·87 | 97·56 | 97·58 | 97·76 | 97·75 | 97·26 | 97·94 | 97·81 | 98·49 | 96·90 |
| *OH wt.% | 1·93 | 0·99 | 2·23 | 1·38 | 1·83 | 1·72 | 1·80 | 1·99 | 1·99 | 1·77 | 1·52 | 1·37 | 2·08 | 2·27 | 0·82 | 2·35 | 2·24 | 1·98 | 0·91 |
| Net Cor. Total: | 99·68 | 99·16 | 99·51 | 99·08 | 101·25 | 99·50 | 100·52 | 99·78 | 100·01 | 99·64 | 99·08 | 98·95 | 99·84 | 100·02 | 98·08 | 100·29 | 100·05 | 100·47 | 97·81 |
| Formula calculation based on the method of Ketcham (2015) | | | | | | | | | | | | | | | | | | | |
| Na | 0·01 | 0·02 | 0·01 | 0·01 | 0·04 | 0·04 | 0·04 | 0·04 | 0·05 | 0·03 | 0·18 | 0·12 | 0·05 | 0·01 | 0·09 | 0·02 | 0·02 | 0·03 | 0·02 |
| Ca | 4·92 | 4·83 | 4·82 | 4·86 | 4·94 | 5·05 | 4·96 | 4·97 | 4·97 | 4·89 | 4·89 | 4·88 | 4·91 | 4·87 | 4·77 | 4·97 | 4·89 | 5·00 | 4·92 |
| Sr | 0·05 | 0·07 | 0·10 | 0·06 | 0·03 | 0·04 | 0·04 | 0·04 | 0·03 | 0·03 | 0·07 | 0·07 | 0·03 | 0·03 | 0·07 | 0·02 | 0·02 | 0·03 | 0·03 |
| La | 0·04 | 0·02 | 0·05 | 0·03 | 0·02 | 0·01 | 0·01 | 0·01 | 0·01 | 0·01 | 0·01 | 0·01 | 0·01 | 0·02 | 0·01 | 0·02 | 0·02 | 0·01 | 0·01 |
| Ce | 0·07 | 0·04 | 0·06 | 0·05 | 0·04 | 0·01 | 0·01 | 0·01 | 0·02 | 0·02 | 0·02 | 0·02 | 0·02 | 0·04 | 0·02 | 0·03 | 0·04 | 0·02 | 0·01 |
| Pr | 0·01 | 0·01 | 0·01 | 0·01 | 0·00 | bdl | 0·00 | 0·00 | 0·00 | bdl | 0·00 | 0·01 | 0·00 | 0·01 | 0·00 | 0·00 | 0·00 | bdl | bdl |
| Nd | 0·01 | 0·01 | 0·01 | 0·01 | 0·01 | 0·00 | 0·00 | bdl | 0·01 | 0·00 | 0·01 | 0·01 | 0·01 | 0·01 | 0·01 | 0·01 | 0·01 | 0·01 | 0·00 |
| Fe | bdl | 0·00 | 0·00 | 0·00 | bdl | 0·08 | 0·00 | bdl | bdl | bdl | 0·00 | 0·00 | bdl | bdl | 0·00 | bdl | 0·01 | bdl | 0·02 |
| P | 2·72 | 2·92 | 2·75 | 2·87 | 2·90 | 2·88 | 2·93 | 2·92 | 2·91 | 2·98 | 2·92 | 2·93 | 2·92 | 2·87 | 3·00 | 2·81 | 2·83 | 2·91 | 2·85 |
| Si | 0·22 | 0·08 | 0·22 | 0·11 | 0·07 | 0·02 | 0·03 | 0·04 | 0·04 | 0·03 | 0·00 | 0·01 | 0·06 | 0·13 | 0·00 | 0·14 | 0·16 | 0·05 | 0·09 |
| S | 0·03 | 0·00 | 0·02 | 0·01 | 0·01 | 0·01 | 0·02 | 0·02 | 0·01 | 0·01 | 0·02 | 0·02 | 0·02 | 0·01 | 0·01 | 0·03 | 0·02 | 0·01 | 0·06 |
| As | bdl | bdl | bdl | bdl | bdl | bdl | bdl | bdl | 0·00 | bdl | 0·00 | bdl | bdl | bdl | bdl | 0·00 | bdl | bdl | bdl |
| Mn | bdl | 0·00 | bdl | bdl | 0·00 | 0·01 | 0·00 | 0·00 | bdl | 0·00 | 0·01 | 0·01 | 0·00 | bdl | 0·01 | bdl | bdl | 0·00 | 0·00 |
| Cl | 0·01 | 0·01 | 0·00 | 0·00 | 0·00 | 0·00 | 0·00 | 0·00 | 0·01 | 0·00 | 0·00 | 0·01 | 0·01 | 0·00 | 0·00 | 0·01 | 0·00 | 0·01 | 0·09 |
| F | 0·39 | 0·69 | 0·30 | 0·57 | 0·44 | 0·47 | 0·45 | 0·39 | 0·39 | 0·46 | 0·53 | 0·57 | 0·36 | 0·30 | 0·75 | 0·27 | 0·31 | 0·39 | 0·63 |
| $OH^{(est.)}$ | 0·60 | 0·30 | 0·69 | 0·42 | 0·56 | 0·53 | 0·55 | 0·61 | 0·61 | 0·53 | 0·47 | 0·42 | 0·63 | 0·69 | 0·25 | 0·72 | 0·69 | 0·60 | 0·28 |
| Total cations | 8·08 | 8·00 | 8·06 | 8·03 | 8·05 | 8·15 | 8·05 | 8·05 | 8·07 | 7·99 | 8·14 | 8·09 | 8·03 | 8·00 | 8·00 | 8·07 | 8·03 | 8·06 | 8·01 |

*OH wt %, calculated from $OH^{(est.)}$. $OH^{(est.)}$, estimated after calculations of Ketcham (2015).
bdl, below detection limit. Noticeable variation of representative analyses in a single sample has been indicated by the addition of further analyses, reflecting the variation.

**Table 4:** Representative EPMA analyses of micas from the Kaiserstuhl Volcanic Complex

| Sample # | 1200 | 1200 | 1156 | 1148 | 1245 | 1237 | 1318 | 1318 | 1413 | 1413 | 1413 | 1410 | 237 | 222 | 225 | 1366 | 1354 | 284 | 1415b | 1415c |
|---|---|---|---|---|---|---|---|---|---|---|---|---|---|---|---|---|---|---|---|---|
| Locality | Badberg | | | | | | Orberg II | | Orberg III | | | | Orberg IV | Orberg V | | | Haselschacher Buck | | Katharinenberg | |
| Rock type | Sövite (Black Wall) | | | | Sövite | | | | | | | | | | | | | | | |
| wt % | | | | | | | | | | | | | | | | | | | | |
| $Na_2O$ | 0·23 | 0·23 | 0·22 | 0·29 | 0·36 | 0·41 | 0·17 | 0·13 | 0·40 | 0·50 | 0·58 | 0·52 | 0·64 | 0·29 | 0·51 | 0·42 | 0·66 | 0·66 | 0·38 | 0·48 |
| $K_2O$ | 9·69 | 10·16 | 9·89 | 9·26 | 9·39 | 9·33 | 9·81 | 10·63 | 4·62 | 5·25 | 6·77 | 7·16 | 7·33 | 7·93 | 6·58 | 8·90 | 8·23 | 6·66 | 6·33 | 7·46 |
| CaO | 0·02 | bdl | 0·06 | 0·03 | 0·05 | 0·04 | 0·18 | 0·26 | 0·19 | 0·01 | 0·12 | 0·07 | 0·05 | 0·04 | 0·02 | 0·04 | 0·07 | 0·23 | 0·04 | 0·05 |
| BaO | 1·74 | 0·24 | 0·82 | 2·42 | 2·09 | 2·29 | 2·56 | 0·44 | 14·76 | 12·57 | 8·12 | 8·11 | 6·81 | 7·44 | 10·15 | 3·21 | 4·21 | 8·66 | 10·83 | 7·20 |
| MgO | 24·02 | 21·79 | 20·33 | 21·40 | 21·03 | 22·67 | 25·62 | 27·43 | 23·97 | 24·42 | 24·85 | 24·97 | 24·06 | 26·21 | 25·23 | 27·02 | 24·67 | 24·41 | 24·82 | 25·62 |
| MnO | 1·03 | 1·36 | 1·17 | 1·08 | 0·75 | 0·69 | 0·36 | 0·40 | 0·13 | 0·17 | 0·21 | 0·23 | 0·35 | 0·20 | 0·14 | 0·26 | 0·29 | 0·30 | 0·11 | 0·24 |
| $FeO^S$ | 5·20 | 9·25 | 10·46 | 7·40 | 8·82 | 7·71 | 2·24 | 1·89 | 0·73 | 1·78 | 1·86 | 2·22 | 4·21 | 1·60 | 1·30 | 1·36 | 3·72 | 2·72 | 1·60 | 2·26 |
| $Fe_2O_3^S$ | 0·69 | 0·01 | 0·25 | 0·96 | 0·18 | 0·13 | 0·00 | 0·00 | 1·15 | 0·00 | 0·40 | 0·11 | 0·04 | 0·05 | 0·32 | 1·11 | 0·00 | 0·20 | 0·08 | 0·16 |
| $Al_2O_3$ | 13·74 | 11·87 | 13·16 | 15·39 | 15·08 | 14·99 | 15·06 | 12·25 | 20·11 | 19·29 | 18·02 | 18·12 | 17·07 | 15·77 | 18·30 | 13·87 | 17·81 | 18·65 | 18·87 | 16·57 |
| $TiO_2$ | 0·17 | 0·76 | 0·37 | 0·22 | 0·55 | 0·57 | 1·00 | 0·18 | 0·15 | 0·17 | 0·29 | 0·13 | 0·31 | 0·22 | 0·15 | 0·22 | 0·39 | 0·23 | 0·13 | 0·11 |
| $Cr_2O_3$ | bdl | 0·05 | 0·02 | bdl | bdl | 0·01 | 0·01 | bdl | bdl | 0·03 | 0·05 | 0·03 | 0·02 | 0·01 | bdl | bdl | 0·01 | bdl | bdl | 0·03 |
| $SiO_2$ | 39·51 | 40·27 | 39·10 | 37·38 | 37·90 | 38·85 | 38·70 | 42·68 | 29·77 | 31·95 | 34·40 | 35·33 | 36·01 | 37·17 | 34·34 | 39·20 | 37·13 | 34·63 | 33·40 | 36·49 |
| Cl | bdl | 0·01 | 0·02 | 0·01 | bdl | 0·01 | bdl | bdl | 0·01 | 0·02 | 0·02 | bdl | 0·02 | 0·02 | 0·01 | bdl | bdl | bdl | bdl | bdl |
| F | 2·09 | 1·26 | 1·32 | 1·27 | 0·08 | 0·19 | 1·58 | 3·10 | 1·14 | 0·80 | 0·85 | 0·93 | 0·69 | 1·55 | 0·88 | 1·41 | 0·17 | 0·15 | 0·79 | 0·92 |
| $-O=(F, Cl)_2$ | 0·88 | 0·53 | 0·56 | 0·54 | 0·04 | 0·08 | 0·67 | 1·31 | 0·48 | 0·34 | 0·36 | 0·39 | 0·30 | 0·66 | 0·37 | 0·59 | 0·07 | 0·06 | 0·33 | 0·39 |
| Total | 98·13 | 97·26 | 97·19 | 97·10 | 96·28 | 97·90 | 97·29 | 99·39 | 97·13 | 96·94 | 96·54 | 97·93 | 97·61 | 98·50 | 97·92 | 97·02 | 97·36 | 97·50 | 97·38 | 97·57 |
| $H_2O^*$ | 3·17 | 3·51 | 3·44 | 3·47 | 4·05 | 4·09 | 3·43 | 2·82 | 3·34 | 3·57 | 3·64 | 3·67 | 3·77 | 3·39 | 3·65 | 3·52 | 4·12 | 4·02 | 3·65 | 3·68 |
| Formula based on 7 (tetrahedral [Z] plus octahedral [Y]) cations | | | | | | | | | | | | | | | | | | | | |
| Na | 0·03 | 0·03 | 0·03 | 0·04 | 0·05 | 0·06 | 0·02 | 0·02 | 0·06 | 0·07 | 0·08 | 0·07 | 0·09 | 0·04 | 0·07 | 0·06 | 0·09 | 0·09 | 0·05 | 0·07 |
| K | 0·89 | 0·94 | 0·93 | 0·87 | 0·88 | 0·85 | 0·90 | 0·95 | 0·46 | 0·51 | 0·64 | 0·67 | 0·68 | 0·73 | 0·62 | 0·81 | 0·75 | 0·62 | 0·60 | 0·69 |
| Ca | 0·001 | bdl | 0·005 | 0·002 | 0·004 | 0·003 | 0·01 | 0·02 | 0·02 | 0·001 | 0·01 | 0·01 | 0·004 | 0·003 | 0·001 | 0·003 | 0·01 | 0·02 | 0·003 | 0·004 |
| Ba | 0·05 | 0·01 | 0·02 | 0·07 | 0·06 | 0·06 | 0·07 | 0·01 | 0·45 | 0·37 | 0·24 | 0·23 | 0·20 | 0·21 | 0·29 | 0·09 | 0·12 | 0·25 | 0·32 | 0·21 |
| Mg | 2·57 | 2·36 | 2·23 | 2·34 | 2·30 | 2·42 | 2·74 | 2·86 | 2·75 | 2·74 | 2·73 | 2·71 | 2·61 | 2·83 | 2·77 | 2·87 | 2·61 | 2·66 | 2·75 | 2·77 |
| Mn | 0·06 | 0·08 | 0·07 | 0·07 | 0·05 | 0·04 | 0·02 | 0·02 | 0·01 | 0·01 | 0·01 | 0·01 | 0·02 | 0·01 | 0·01 | 0·02 | 0·02 | 0·02 | 0·01 | 0·01 |
| $Fe^{2+}$ | 0·31 | 0·56 | 0·64 | 0·45 | 0·54 | 0·46 | 0·13 | 0·11 | 0·05 | 0·11 | 0·11 | 0·14 | 0·26 | 0·10 | 0·08 | 0·08 | 0·22 | 0·17 | 0·10 | 0·14 |
| $Fe^{3+}$ | 0·04 | 0·00 | 0·01 | 0·05 | 0·01 | 0·01 | 0·00 | 0·00 | 0·07 | 0·00 | 0·02 | 0·01 | 0·00 | 0·00 | 0·02 | 0·06 | 0·00 | 0·01 | 0·00 | 0·01 |
| Al | 1·16 | 1·02 | 1·14 | 1·33 | 1·30 | 1·26 | 1·27 | 1·01 | 1·83 | 1·71 | 1·57 | 1·55 | 1·47 | 1·35 | 1·59 | 1·17 | 1·49 | 1·61 | 1·65 | 1·42 |
| Ti | 0·01 | 0·04 | 0·02 | 0·01 | 0·03 | 0·03 | 0·05 | 0·01 | 0·01 | 0·01 | 0·02 | 0·01 | 0·02 | 0·01 | 0·01 | 0·01 | 0·02 | 0·01 | 0·01 | 0·01 |
| Cr | bdl | 0·003 | 0·001 | bdl | bdl | 0·001 | 0·001 | bdl | bdl | 0·001 | 0·003 | 0·002 | 0·001 | 0·001 | bdl | bdl | 0·001 | bdl | bdl | 0·001 |
| Si | 2·84 | 2·93 | 2·88 | 2·74 | 2·78 | 2·78 | 2·78 | 2·99 | 2·29 | 2·41 | 2·54 | 2·57 | 2·62 | 2·69 | 2·53 | 2·79 | 2·64 | 2·53 | 2·48 | 2·65 |
| Cl | bdl | 0·001 | 0·002 | 0·002 | 0·000 | 0·001 | bdl | bdl | 0·001 | 0·002 | 0·003 | bdl | 0·002 | 0·002 | 0·001 | bdl | bdl | bdl | bdl | bdl |
| F | 0·48 | 0·29 | 0·31 | 0·30 | 0·02 | 0·04 | 0·36 | 0·68 | 0·28 | 0·19 | 0·20 | 0·21 | 0·16 | 0·36 | 0·21 | 0·32 | 0·04 | 0·04 | 0·19 | 0·21 |
| Total cations | 7·97 | 7·98 | 7·99 | 7·98 | 7·99 | 7·98 | 8·01 | 8·00 | 7·98 | 7·96 | 7·97 | 7·98 | 7·97 | 7·99 | 7·99 | 7·96 | 7·96 | 7·98 | 7·98 | 7·97 |

$H_2O^*$, calculated from OH (F+Cl+OH = 2). S, $Fe^{2+}/Fe^{3+}$ ratios calculated from stoichiometry.
bdl, below detection limit. Noticeable variation of representative analyses in a single sample has been indicated by the addition of further analyses, reflecting the variation.

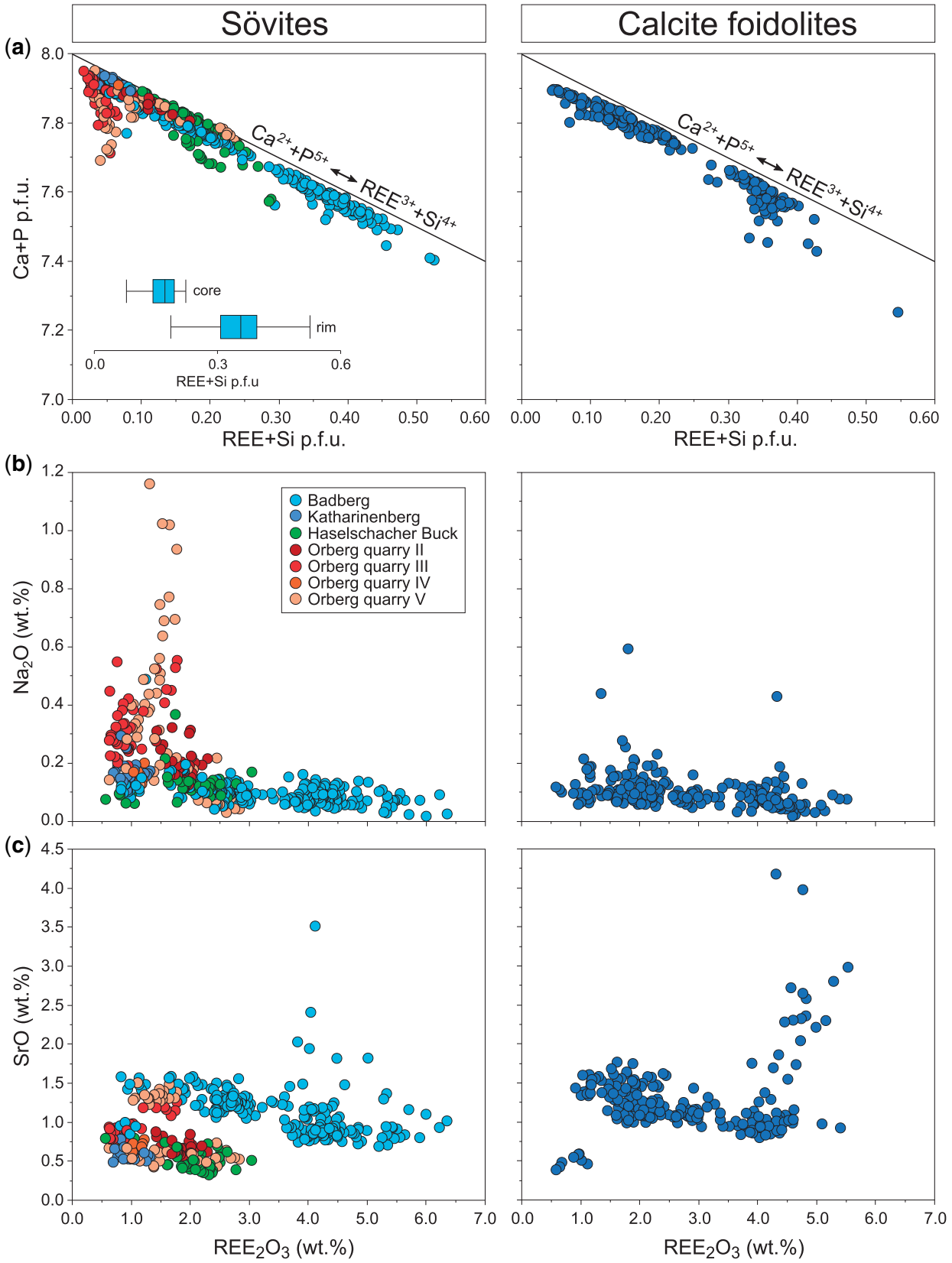


**Fig. 9.** Chemical variations of apatite in sövites and calcite foidolites from the KVC. (a) Ca+P vs REE+Si representing the apatite-britholite substitution mechanism ($Ca^{2+} + P^{5+} \leftrightarrow REE^{3+} + Si^{4+}$). (b) and (c) Variations of $Na_2O$ and SrO vs $REE_2O_3$.

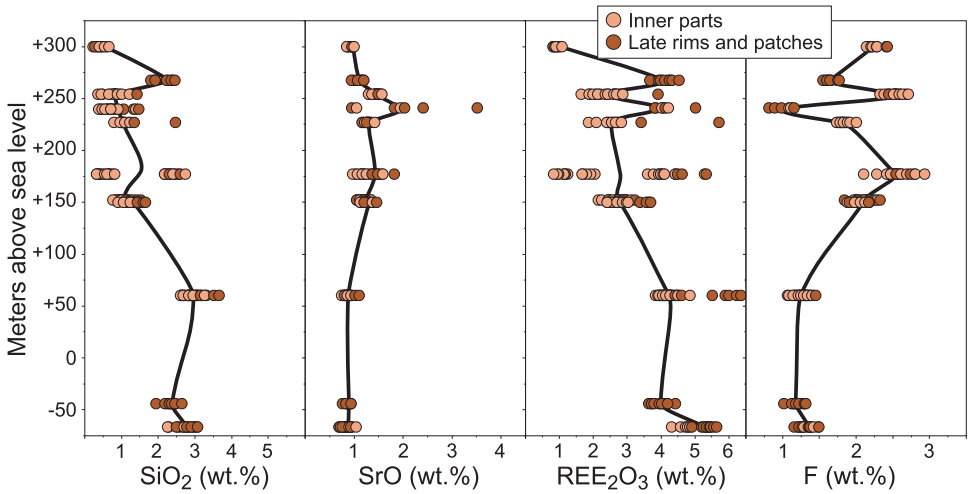


**Fig. 10.** Compositional variations of apatite with depth (given as m above sea level) in the KB3 drill hole (Badberg). Note: According to the tilting of the Badberg sövite (Fig. 1c), this variation depicts only a restricted depth variation within the sövite pipe, but reflects an additional centre-margin effect.

to intermediate Na (<0·07 apfu) and F (<0·5 apfu) and intermediate to high Ti (<0·06 apfu; Fig. 11c–f). Amongst the Badberg micas, those from black-walls around calcite foidolites (Fig. 7a) show lower Ti and Na, but higher F and Mn contents (Fig. 11c–f), but are otherwise compositionally similar to those formed far away from xenoliths.

## Olivine and monticellite

Representative analyses are given in Table 5; formula calculations are based on four oxygens. Olivine in two of the sövites is Mg-rich ($Fo_{96–90}$) but shows a large range in the larnite component, varying from 0·1 to 1·5 mol % (0·06–1·17 wt % CaO; Fig. 12a). The negative correlation between forsterite and larnite components (Fig. 12a) implies a preferred incorporation of Ca with decreasing Mg (Jurewicz & Watson, 1988; Libourel, 1999). The Mn contents (up to 3·0 wt % MnO) are much higher than in the associated silicate rocks of the KVC (grey fields in Fig. 12b), while Ni contents rarely exceed the detection limit (NiO <0·03 wt %). Monticellite (about 75 mol %) is present in one sample (Orberg V) and contains about 20 mol % kirschsteinite ($CaFeSiO_4$) and 5 mol % glaucochroite ($CaMnSiO_4$).

## Clinopyroxene

Formula calculations are based on four cations and six oxygens; representative analyses are listed in Table 6. Clinopyroxene in the investigated samples is invariably diopside-rich (Fig. 12c and d). However, clinopyroxene in sövites and calcite foidolites is higher in MnO (up to 1·4 wt %) but lower in $TiO_2$ (<0·9 wt %) compared to clinopyroxene in extrusive carbonatites (MnO <0·3 wt % and up to 4·1 wt % $TiO_2$; Fig. 12c and d). The concentration of $Cr_2O_3$ (up to 0·27 wt %) is only elevated in some extrusive carbonatites (Table 6).

## Spinel group minerals

Representative analyses are given in Table 7 and formula calculations are based on three cations and four oxygens. Spinel group minerals in the investigated samples are classified as magnetite–magnesioferrite. In sövites they are poor in Ti (<0·13 apfu) and Al (<0·32 apfu), but relatively rich in Mn (up to 0·22 apfu), compared to those from extrusive carbonatites (Fig. 12e). In extrusive carbonatites, their Mg contents are relatively constant (0·26 to 0·36 apfu) compared to the large range observed in the sövite samples (0·08–0·65 apfu). Amongst the sövites, samples from Orberg reach the highest Mg content, implying a relatively large magnesioferrite component (up to 63 mol %), when considering endmembers magnetite ($Fe^{2+}Fe^{3+}_2O_4$), magnesioferrite ($MgFe^{3+}_2O_4$) and jacobsite ($MnFe^{3+}_2O_4$). Spinel group mineral rims in a carbonatitic lava sample (Fig. 5b) that appear distinctly darker in BSE have high Mg (0·63–0·69 apfu) and Al (0·42–0·56 apfu) concentrations, i.e. are spinel-rich.

## Garnet

Representative analyses are listed in Table 8; formula calculations are based on eight cations and twelve oxygens, using the calculation scheme of Locock (2008). Most analyses show a very good 1:1 correlation between Ti + $Fe^{3+}$ and Si + Al (Fig. 13a), indicating solid solution between grossular (0–26%) andradite (47–84%), schorlomite (0–18%) and morimotoite (0–29%) endmembers (Fig. 13b). These garnets are best described as Ti-bearing andradites. They are commonly called 'melanite', but this name is not accepted by the IMA. The contents of Nb, Zr and REE are generally low (<0·02, <0·02 and <0·01 apfu, respectively) but garnet II from the calcite foidolites may reach much higher Nb (up to 0·2 apfu) and Zr (up to 0·2 apfu), whilst REE contents are similarly low (Fig. 13c–e). Such Nb- and Zr-rich

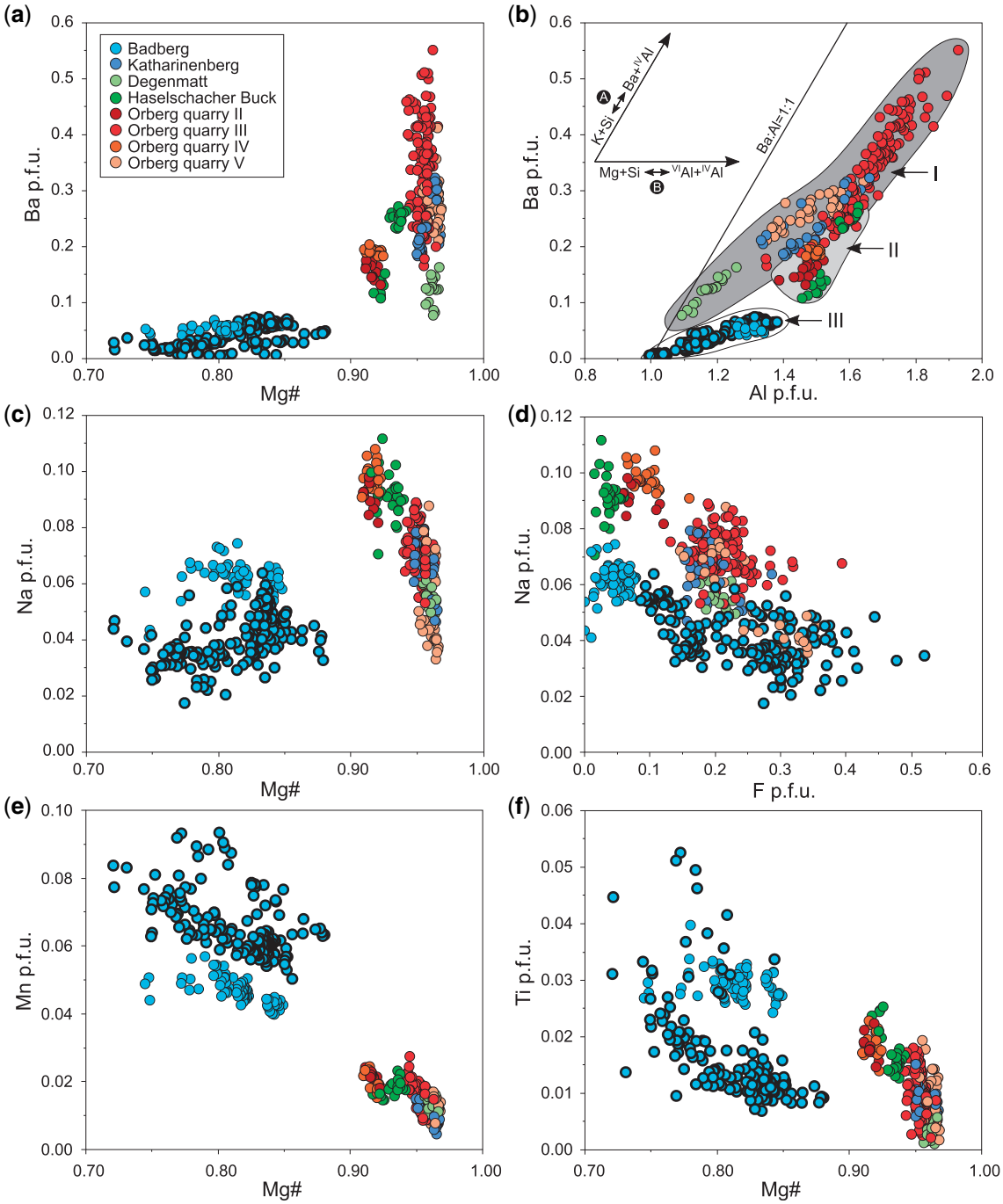


**Fig. 11.** Compositional variation of mica in sövites from the KVC. (a) Binary diagram of Ba vs Mg#. (b) Binary diagram of Ba versus Al. Inset depicts substitution tendencies: (A) Kinoshitalite substitution, (B) eastonite substitution (for details see text). (c) and (d) Na vs Mg# and F, respectively. (e) and (f) Mn and Ti vs Mg# respectively. Note the separation of biotite from Badberg compared to phlogopite from the other localities, as well as a separation between 'black-wall' mica (marked by heavier outline) and mica which is seemingly 'independent' of the presence of calcite foidolite in the Badberg samples.

analyses show clear deviations from the ideal Ti + $Fe^{3+}$ - Si + Al 1:1 correlation (Fig. 13a). Based on their Mg–Ti characteristics, garnet I and II from the calcite foidolites can be clearly distinguished from each other, with garnet from the extrusive carbonatites plotting in between these two groups (Fig. 13f).

## Zirconolite

Representative analyses are given in Table 9; formula calculations are based on four cations. We analysed zirconolite in a sövite from Haselschacher Buck, where it is rich in Nb (up to 21·5 wt % $Nb_2O_5$) and Ta (up to 4·4 wt % $Ta_2O_5$) with relatively low amounts of REE+Y (up to

**Table 5:** Representative EPMA analyses of olivine and monticellite from the Kaiserstuhl Volcanic Complex

| Sample # | 1415 | 1415 | 1354 | 1354 | 1356 |
|---|---|---|---|---|---|
| Locality | Katharinenberg | | Haselschacher Buck | | Orberg V |
| Mineral | Forsterite | | | | Monticellite |
| wt.% | | | | | |
| $SiO_2$ | 43·01 | 42·54 | 41·64 | 42·27 | 38·06 |
| FeO | 1·78 | 4·13 | 6·29 | 5·52 | 8·45 |
| MnO | 1·88 | 2·82 | 2·97 | 2·67 | 2·41 |
| MgO | 54·28 | 50·98 | 48·77 | 50·05 | 18·98 |
| NiO | bdl | bdl | bdl | bdl | bdl |
| CaO | 0·06 | 0·52 | 0·86 | 0·41 | 32·82 |
| Total | 101·03 | 100·99 | 100·53 | 100·92 | 100·74 |
| Formula based on 4 oxygens | | | | | |
| Si | 1·01 | 1·02 | 1·01 | 1·02 | 1·02 |
| Fe | 0·04 | 0·08 | 0·13 | 0·11 | 0·19 |
| Mn | 0·04 | 0·06 | 0·06 | 0·05 | 0·05 |
| Mg | 1·90 | 1·82 | 1·77 | 1·79 | 0·76 |
| Ni | bdl | bdl | bdl | bdl | bdl |
| Ca | 0·00 | 0·01 | 0·02 | 0·01 | 0·95 |
| Total cations | 2·99 | 2·98 | 2·99 | 2·98 | 2·98 |

bdl, below detection limit.

4·5 wt % $REE_2O_3 + Y_2O_3$), U (up to 1·2 wt % $UO_2$) and Th (up to 1·7 wt % $ThO_2$), plotting in the Nb+Ta-rich corner of the known compositional range (Fig. 14).

## DISCUSSION

### Origin of silicate minerals in the Kaiserstuhl carbonatites

Many carbonatites contain minor amounts of silicate minerals (in particular ferromagnesian silicates) with mica being the most common one (Reguir *et al.*, 2012). Their stability largely depends on silica activity, which is generally very low in carbonatites, in addition to temperature and other chemical potentials (Barker, 2001; Massuyeau *et al.*, 2015). Therefore, it is important to distinguish different genetic types of silicate minerals in carbonatites (e.g. Barker, 2001), including:

1. Silicates that crystallized from the carbonatitic magma, either due to a pristine sufficiently high silica activity ('true' primary magmatic silicates; type Ia) or because of a (local) change in silica activity (and the activity of other chemical components), for example by the interaction with wall rocks or xenoliths (type Ib).
2. Entrained crystals from the source rock or from wall rocks encountered during ascent and emplacement of the carbonatitic magma, including crystals from genetically related magmatic silicate rocks (xenocrysts; type II).
3. Subsolidus phases that formed during final cooling due to the interaction with hydrothermal or meteoric fluids (type III).

While a subsolidus origin (type III) can be easily recognized based on characteristic textures (e.g. exsolutions, pseudomorphs, veinlets), it is not easy to distinguish primary (carbonatitic) crystals (type I) from xenocrysts (type II) because there is a broad range of compositional variations of these phases in carbonatites (Chakhmouradian & Zaitsev, 2002; Reguir *et al.*, 2009; Reguir *et al.*, 2012). Also, depending on their composition and reaction kinetics, entrained xenocrysts may or may not be partly resorbed and/or chemically modified by diffusion-controlled reactions with the carbonatite magma. Therefore, only careful textural analyses combined with a detailed comparison between the composition of the mineral in question in the carbonatite with that of mantle rocks (e.g. olivine) and surrounding silicate rocks may provide the opportunity to determine the origin of such silicate minerals. In the following, we discuss the potential origin of the various silicate phases present in the Kaiserstuhl carbonatites.

Mica is the major K-bearing phase in most carbonatites and is typically $Fe^{2+}$-poor and variably enriched in Ba and Al (Giebel *et al.*, 2019 and references therein). At the KVC, mica in all sövites, except for the Badberg samples, shares these characteristics (Figs 11 and 15) and occurs as a minor phase more or less evenly dispersed in the rocks (Fig. 4a). We suggest that mica in these samples crystallized from the carbonatitic magma itself as a 'true' primary magmatic silicate at sufficiently high silica activities (type Ia). Mica in the Badberg samples, however, is compositionally distinct (Figs 11 and 15), much more abundant compared to the other sövites and partly occurs as seams around xenoliths (Figs 4 and 6). We assume that mica in the Badberg samples formed due to the interaction between entrained xenoliths and the carbonatitic magma (discussed in more detail below) and represents a type Ib phase.

Monticellite is stable at very low silica activities only (Barker, 2001) and is, therefore, commonly found in carbonatites (e.g. Nesbitt & Kelly, 1977; Stoppa & Lupini, 1993; Guzmics *et al.*, 2011), but is exceedingly rare in silicate rocks. None of the silicate lithologies at the KVC contains this phase. Olivine, in contrast, is a typical phase in mantle rocks and in many silicate rocks, including some of the KVC silicate lithologies. However, the high forsterite content, combined with high Mn (Fig. 12b) and very low Ni contents (Braunger *et al.*, 2018) is atypical of xenocrystic or mantle-derived olivine, but is typically observed in carbonatites (e.g. Lee *et al.*, 2004). At the KVC, olivine and monticellite (both Mn-enriched) are fairly rare and only occur in relatively mica-poor samples. Due to their cracked appearance, occasional rounded edges, serpentinization/iddingitization and partial resorption, a xenocrystic origin cannot be excluded. However, the absence of even small-scale compositional modifications (for example compositional zoning as would be expected by diffusional processes) renders this unlikely. Hence, we suggest that monticellite and olivine may represent silicate minerals of type I, probably representing 'true' primary magmatic silicates (type Ia), although it cannot be completely

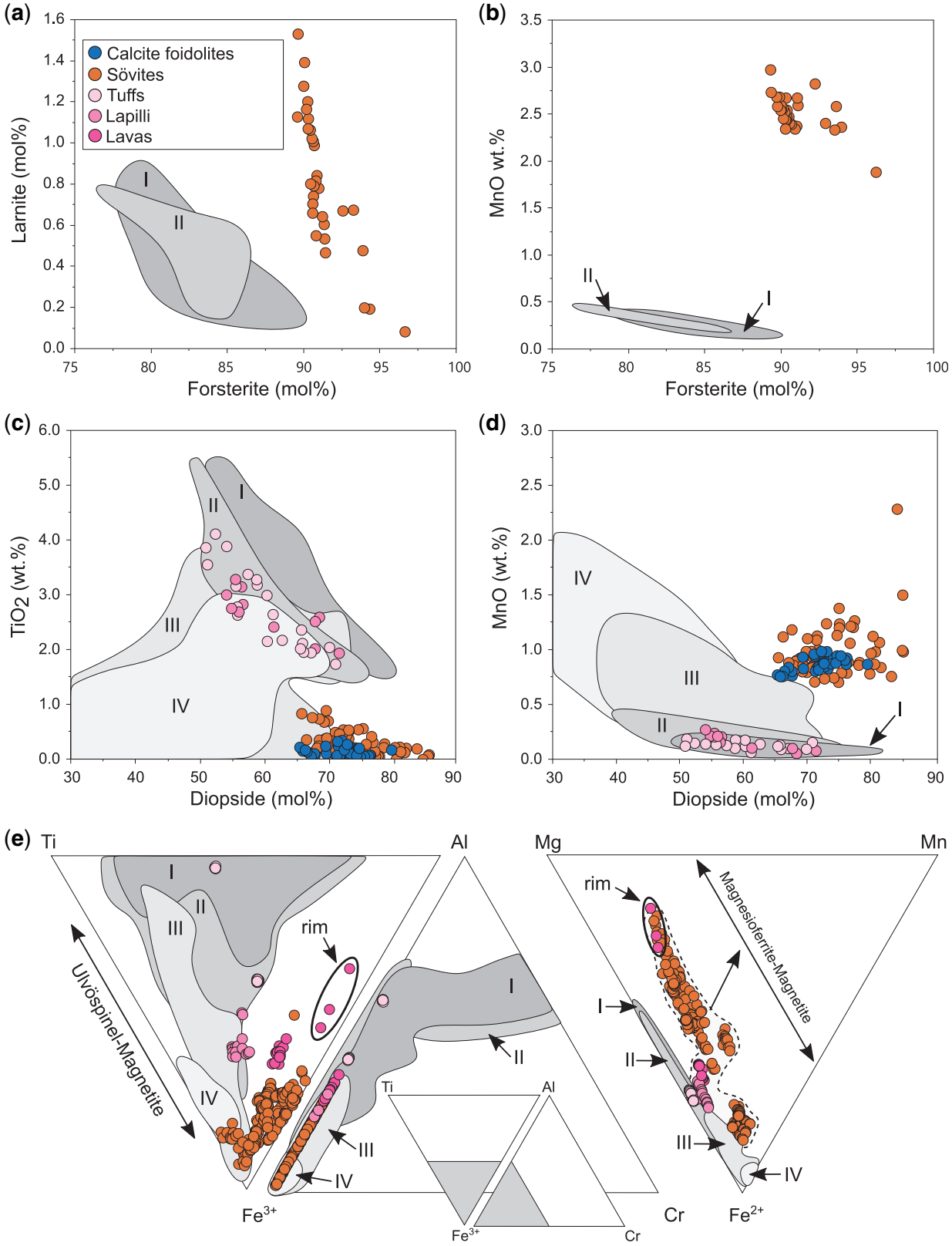


**Fig. 12.** Composition of olivine, clinopyroxene and spinel group minerals (magnetite-magnesioferrite) from carbonatites and calcite foidolites of the KVC. (a) Larnite vs forsterite components. (b) MnO (wt %) vs forsterite component in olivine. (c) and (d) Concentrations of $TiO_2$ (wt %) and MnO (wt %) vs diopside component in clinopyroxene. (e) Spinel group mineral compositions from carbonatites of the KVC. Grey fields represent data (olivine, clinopyroxene and spinel group minerals, respectively) for the KVC silicate rocks (Braunger *et al.*, 2018): (I) Olivine nephelinites and limburgites, (II) tephritic rocks, (III) melilititic and haüynitic/haüynolitic rocks, (IV) phonolitic/syenitic rocks, (V) haüynilites and melteigites.

**Table 6:** Representative EPMA analyses of pyroxene from the Kaiserstuhl Volcanic Complex

| Sample # | 260 | 1197 | 1151 | 1229 | 1215 | 1178 | 1237 | GM1 | GM2 | GM4 |
|---|---|---|---|---|---|---|---|---|---|---|
| Locality | Badberg | | | | | | | Henkenberg | | |
| Rock type | Calcite foidolite | | | | | | | Crystal tuff | | Lapili stone |
| wt % | | | | | | | | | | |
| $SiO_2$ | 53·44 | 49·16 | 49·40 | 49·20 | 49·74 | 51·84 | 50·74 | 44·37 | 45·04 | 44·89 |
| $TiO_2$ | 0·05 | 0·11 | 0·21 | 0·58 | 0·33 | 0·10 | 0·17 | 3·30 | 2·30 | 2·64 |
| $Al_2O_3$ | 1·60 | 3·60 | 3·61 | 3·58 | 3·30 | 1·08 | 2·81 | 9·37 | 8·52 | 8·38 |
| $Cr_2O_3$ | bdl | bdl | bdl | bdl | bdl | bdl | bdl | 0·04 | 0·04 | 0·03 |
| FeO | 6·15 | 8·81 | 8·61 | 7·97 | 7·25 | 5·96 | 6·58 | 7·53 | 7·35 | 7·75 |
| MnO | 0·94 | 0·81 | 0·83 | 0·95 | 0·89 | 1·14 | 0·99 | 0·13 | 0·15 | 0·15 |
| MgO | 13·93 | 12·52 | 12·67 | 12·71 | 13·22 | 14·26 | 13·65 | 11·53 | 11·83 | 11·51 |
| CaO | 24·70 | 23·90 | 24·35 | 23·96 | 24·23 | 23·90 | 24·35 | 22·77 | 23·65 | 23·64 |
| $Na_2O$ | 0·38 | 0·47 | 0·41 | 0·51 | 0·40 | 0·51 | 0·37 | 0·53 | 0·42 | 0·51 |
| Total | 101·19 | 99·38 | 100·11 | 99·47 | 99·37 | 98·81 | 99·67 | 99·65 | 99·32 | 99·56 |
| Formula based on 4 cations and 6 oxygens | | | | | | | | | | |
| Si | 1·96 | 1·84 | 1·84 | 1·84 | 1·86 | 1·94 | 1·88 | 1·66 | 1·68 | 1·68 |
| Ti | 0·00 | 0·003 | 0·01 | 0·02 | 0·01 | 0·003 | 0·005 | 0·09 | 0·06 | 0·07 |
| Al | 0·07 | 0·16 | 0·16 | 0·16 | 0·15 | 0·05 | 0·12 | 0·41 | 0·38 | 0·37 |
| Cr | bdl | bdl | bdl | bdl | bdl | bdl | bdl | 0·001 | 0·001 | 0·001 |
| $Fe^{3+}$ | 0·04 | 0·18 | 0·18 | 0·17 | 0·15 | 0·11 | 0·12 | 0·12 | 0·15 | 0·16 |
| $Fe^{2+}$ | 0·15 | 0·09 | 0·08 | 0·08 | 0·08 | 0·08 | 0·08 | 0·12 | 0·08 | 0·09 |
| Mg | 0·76 | 0·70 | 0·70 | 0·71 | 0·74 | 0·79 | 0·76 | 0·64 | 0·66 | 0·64 |
| Mn | 0·03 | 0·03 | 0·03 | 0·03 | 0·03 | 0·04 | 0·03 | 0·004 | 0·005 | 0·005 |
| Ca | 0·97 | 0·96 | 0·97 | 0·96 | 0·97 | 0·96 | 0·97 | 0·91 | 0·95 | 0·95 |
| Na | 0·03 | 0·03 | 0·03 | 0·04 | 0·03 | 0·04 | 0·03 | 0·04 | 0·03 | 0·04 |
| Total cations | 4·00 | 4·00 | 4·00 | 4·00 | 4·00 | 4·00 | 4·00 | 4·00 | 4·00 | 4·00 |
| Mg# | 0·84 | 0·88 | 0·89 | 0·89 | 0·91 | 0·91 | 0·90 | 0·85 | 0·90 | 0·88 |

bdl, below detection limit.

excluded that they are the product of small-scale contamination (type Ib).

Clinopyroxene (cpx) and garnet in extrusive carbonatites are broken and partly rounded (Fig. 5d). As they chemically resemble those of the silicate rocks (Figs 12 and 13), both phases are interpreted as being entrained from the KVC silicate rocks during eruption, representing type II silicates. In sövites, cpx only occurs in the Badberg samples, where it is mostly euhedral and compositionally distinct from those found in extrusive carbonatites and the known silicate rocks of the KVC, but very similar to the recrystallized cpx of calcite foidolites (Fig. 12c and d). Therefore, we suggest that cpx in the Badberg sövites formed similarly to mica (see above) by the interaction between xenoliths and carbonatite magma, representing a type Ib silicate. A possible entrainment of recrystallized cpx from calcite foidolites or an entrainment of original cpx (both representing a type II silicate) from the calcite foidolite precursor lithology (before alteration) is considered unlikely, as cpx in sövite is mostly euhedral (Fig. 3e), whereas it is interstitial and completely recrystallized in calcite foidolites (Fig. 7e). Also, a lack of small-scale compositional modifications (zoning) by xenocryst–carbonatite magma interactions render an entrainment of the original cpx improbable.

## Mineralogical and mineral chemical differences among the KVC carbonatites

Based on geophysical and structural data (Brauch *et al.*, 2018; see above) we assume that the various sövite bodies of the KVC once belonged to a common subvertical pipe structure that was intersected, displaced and tilted by subsequent tectonic activity within the Rhine Graben system (Fig. 1c). Consequently, sövites at the Badberg may represent a higher emplacement level (shallower level of the pipe) than the Haselschacher Buck and Degenmatt occurrences. Orberg sövites may represent a large apophysis of this structure (e.g. Hubaux, 1964; Katz-Lehnert, 1989) and based on pyrochlore textures and compositions, these rocks experienced an intense hydrothermal overprint (Walter *et al.*, 2018). Although it is assumed that all four carbonatite localities belong to one batch of melt, major mineralogical and mineral chemical differences between the Badberg sövites and the other carbonatite bodies are prominent:

1. only Badberg sövites contain variable amounts of calcite foidolites (Figs 6 and 7);
2. only Badberg sövites are comparatively rich in mica that is texturally and compositionally distinct from mica in the other sövite occurrences (Figs 4c, d and 6);
3. only some Badberg sövites contain clinopyroxene (Fig. 3e);
4. only apatite in Badberg sövites shows exceptionally Si- and REE-rich rims (Fig. 9a).

In the following we discuss the significance of the calcite foidolites and the possible reasons for the presence of compositional distinct mica and apatite in the Badberg sövites, including contamination, magmatic differentiation and hydrothermal overprint.

**Table 7:** Representative EPMA analyses of magnetite from the Kaiserstuhl Volcanic Complex

| Sample | 1237 | 1136 | 1215 | 1151 | 1362 | 1410 | 1413 | 1353 | 237 | 225 | 224 | 1354 | 284 | 1415b | 1415c | 1371 | GM2 | GM3 | GM4 | 1337 |
|---|---|---|---|---|---|---|---|---|---|---|---|---|---|---|---|---|---|---|---|---|
| Locality | Badberg | | | | | Orberg III | | Orberg IV | | Orberg V | | Haselschacher Buck | | Katharinenberg | | Henkenberg | | | | Kirchberg |
| Rock type | Sövite | | | | | | | | | | | | | | | Crystal tuff | | | Lapilli stone | Lava |
| wt % | | | | | | | | | | | | | | | | | | | | |
| $SiO_2$ | 0·02 | 0·09 | 0·12 | 0·04 | 0·10 | 0·04 | 0·04 | 0·04 | 0·02 | 0·02 | 0·02 | 0·03 | 0·03 | 0·12 | 0·05 | 0·31 | 0·05 | 0·15 | 0·10 | 0.04 |
| $TiO_2$ | 2·81 | 9·41 | 3·60 | 2·07 | 5·64 | 1·24 | 1·91 | 1·23 | 1·51 | 1·29 | 1·48 | 1·74 | 3·04 | 2·23 | 2·80 | 4·04 | 3·52 | 7·57 | 2·34 | 1.79 |
| $Fe_2O_3$ | 62·87 | 46·64 | 61·37 | 65·25 | 56·20 | 65·74 | 64·94 | 67·16 | 68·68 | 66·04 | 65·35 | 64·87 | 64·11 | 64·51 | 63·38 | 57·31 | 61·56 | 51·17 | 62·75 | 65.90 |
| FeO | 17·87 | 30·68 | 26·70 | 25·84 | 22·13 | 18·42 | 25·93 | 15·82 | 15·35 | 18·69 | 19·99 | 26·88 | 22·06 | 18·84 | 20·92 | 24·08 | 27·20 | 28·19 | 18·06 | 15.54 |
| MnO | 3·99 | 0·65 | 3·08 | 3·96 | 3·46 | 4·62 | 3·69 | 4·76 | 4·85 | 4·18 | 3·72 | 2·89 | 5·50 | 4·29 | 4·31 | 2·87 | 2·69 | 1·74 | 3·99 | 5.02 |
| MgO | 8·54 | 6·73 | 3·64 | 2·43 | 8·08 | 6·53 | 2·38 | 8·18 | 8·54 | 6·75 | 6·36 | 2·30 | 4·25 | 7·25 | 6·17 | 6·44 | 3·36 | 6·37 | 8·30 | 8.55 |
| $V_2O_3$ | 0·41 | 0·15 | 0·19 | 0·25 | 0·22 | 0·47 | 0·18 | 0·38 | 0·59 | 0·59 | 0·31 | 0·18 | 0·91 | 0·31 | 0·24 | 0·08 | 0·20 | 0·15 | 0·41 | 0.52 |
| $Al_2O_3$ | 5·51 | 7·39 | 2·85 | 1·57 | 6·36 | 4·20 | 1·79 | 4·07 | 2·73 | 4·21 | 4·45 | 2·33 | 1·18 | 4·15 | 4·01 | 6·77 | 2·59 | 6·22 | 6·16 | 4.35 |
| $Cr_2O_3$ | 0·03 | 0·04 | 0·01 | 0·01 | 0·03 | 0·03 | 0·01 | 0·02 | 0·04 | 0·04 | 0·02 | 0·01 | 0·05 | 0·02 | 0·01 | 0·01 | 0·01 | 0·01 | 0·03 | 0.03 |
| ZnO | 0·29 | 0·07 | 0·13 | 0·20 | 0·20 | 0·28 | 0·16 | 0·31 | 0·28 | 0·29 | 0·28 | 0·19 | 0·30 | 0·24 | 0·30 | 0·14 | 0·13 | 0·12 | 0·28 | 0.33 |
| Total | 102·34 | 101·85 | 101·67 | 101·62 | 102·43 | 101·58 | 101·04 | 101·97 | 102·59 | 102·08 | 102·00 | 101·43 | 101·45 | 101·95 | 102·20 | 102·04 | 101·31 | 101·67 | 102·42 | 102.09 |
| Formula based on 3 cations and 4 oxygens | | | | | | | | | | | | | | | | | | | | |
| Si | 0·001 | 0·003 | 0·004 | 0·002 | 0·003 | 0·001 | 0·001 | 0·001 | 0·000 | 0·001 | 0·001 | 0·001 | 0·001 | 0·004 | 0·002 | 0·011 | 0·002 | 0·005 | 0·004 | 0.001 |
| Ti | 0·07 | 0·24 | 0·10 | 0·06 | 0·14 | 0·03 | 0·05 | 0·03 | 0·04 | 0·03 | 0·04 | 0·05 | 0·08 | 0·06 | 0·07 | 0·11 | 0·09 | 0·20 | 0·06 | 0.05 |
| $Fe^{3+}$ | 1·62 | 1·21 | 1·68 | 1·81 | 1·45 | 1·75 | 1·81 | 1·76 | 1·80 | 1·75 | 1·73 | 1·80 | 1·76 | 1·70 | 1·68 | 1·49 | 1·69 | 1·34 | 1·62 | 1.72 |
| $Fe^{2+}$ | 0·52 | 0·88 | 0·81 | 0·80 | 0·63 | 0·56 | 0·80 | 0·47 | 0·45 | 0·55 | 0·60 | 0·83 | 0·68 | 0·56 | 0·62 | 0·70 | 0·83 | 0·83 | 0·52 | 0.45 |
| Mn | 0·12 | 0·02 | 0·10 | 0·12 | 0·10 | 0·14 | 0·12 | 0·14 | 0·14 | 0·12 | 0·11 | 0·09 | 0·17 | 0·13 | 0·13 | 0·08 | 0·08 | 0·05 | 0·12 | 0.15 |
| Mg | 0·43 | 0·34 | 0·19 | 0·13 | 0·41 | 0·34 | 0·13 | 0·42 | 0·44 | 0·35 | 0·32 | 0·13 | 0·23 | 0·37 | 0·32 | 0·33 | 0·18 | 0·32 | 0·42 | 0.44 |
| V | 0·01 | 0·002 | 0·003 | 0·004 | 0·003 | 0·01 | 0·003 | 0·01 | 0·01 | 0·01 | 0·004 | 0·003 | 0·01 | 0·004 | 0·003 | 0·001 | 0·003 | 0·002 | 0·01 | 0.01 |
| Al | 0·22 | 0·30 | 0·12 | 0·07 | 0·25 | 0·17 | 0·08 | 0·16 | 0·11 | 0·17 | 0·18 | 0·10 | 0·05 | 0·17 | 0·17 | 0·28 | 0·11 | 0·25 | 0·25 | 0.18 |
| Cr | 0·001 | 0·001 | 0·00 | 0·00 | 0·001 | 0·001 | 0·00 | 0·001 | 0·001 | 0·001 | 0·001 | 0·00 | 0·001 | 0·00 | 0·00 | 0·00 | 0·00 | 0·00 | 0·001 | 0.001 |
| Zn | 0·01 | 0·002 | 0·004 | 0·01 | 0·01 | 0·01 | 0·004 | 0·01 | 0·01 | 0·01 | 0·01 | 0·01 | 0·01 | 0·01 | 0·01 | 0·004 | 0·004 | 0·003 | 0·01 | 0.01 |
| Total cations | 3·00 | 3·00 | 3·00 | 3·00 | 3·00 | 3·00 | 3·00 | 3·00 | 3·00 | 3·00 | 3·00 | 3·00 | 3·00 | 3·00 | 3·00 | 3·00 | 3·00 | 3·00 | 3·00 | 3.00 |

**Table 8:** Representative EPMA analyses of garnet from the Kaiserstuhl Volcanic Complex

| Sample # | 1158 | 1158 | 1168 | 1168 | 1147 | 1147 | 1173 | 1173 | GM1 | GM2 | GM2 | GM3 | 1369 | 1369 | GM4 | 1337 | 1337 |
|---|---|---|---|---|---|---|---|---|---|---|---|---|---|---|---|---|---|
| Location | Badberg | | | | | | | | Henkenberg | | | | | | | Kirchberg | |
| Rock type | Calcite foidolite | | | | | | | | Crystal tuff | | | | | | Lapilli stone | Lava | |
| wt % | | | | | | | | | | | | | | | | | |
| $SiO_2$ | 36·36 | 33·52 | 36·67 | 34·21 | 35·34 | 27·57 | 32·00 | 34·72 | 32·88 | 33·62 | 30·35 | 33·55 | 28·38 | 31·12 | 32·29 | 32·83 | 34·95 |
| $TiO_2$ | 2·08 | 3·48 | 0·82 | 3·11 | 2·66 | 8·60 | 9·34 | 4·81 | 7·02 | 5·55 | 10·55 | 5·45 | 13·52 | 9·77 | 7·27 | 7·10 | 3·78 |
| $ZrO_2$ | 0·17 | 1·12 | 0·17 | 2·67 | 0·44 | 3·93 | 0·12 | 0·08 | 0·33 | 0·17 | 0·38 | bdl | 0·55 | bdl | 0·07 | 0·19 | 0·32 |
| $Y_2O_3$ | bdl | bdl | 0·07 | bdl | bdl | bdl | bdl | bdl | bdl | 0·15 | 0·10 | bdl | 0·14 | bdl | 0·17 | bdl | bdl |
| $Al_2O_3$ | 5·55 | 3·91 | 4·62 | 2·63 | 3·03 | 1·93 | 1·41 | 1·17 | 2·24 | 2·66 | 3·34 | 2·63 | 4·20 | 2·22 | 3·24 | 1·66 | 2·77 |
| $Fe_2O_3$ | 22·16 | 22·82 | 23·98 | 23·99 | 24·87 | 20·56 | 25·07 | 26·84 | 24·40 | 25·12 | 22·24 | 24·76 | 20·04 | 22·13 | 22·81 | 25·78 | 25·84 |
| MnO | 0·56 | 0·55 | 0·58 | 0·79 | 0·62 | 0·73 | 0·49 | 0·50 | 0·78 | 0·63 | 0·52 | 0·76 | 0·49 | 0·62 | 0·62 | 0·58 | 0·94 |
| MgO | 0·69 | 0·89 | 0·55 | 0·89 | 0·69 | 1·25 | 0·46 | 0·27 | 0·62 | 0·49 | 0·95 | 0·46 | 0·95 | 0·90 | 0·88 | 0·45 | 0·22 |
| CaO | 32·37 | 33·16 | 33·11 | 32·47 | 31·87 | 31·59 | 32·27 | 32·73 | 32·50 | 33·05 | 32·63 | 32·19 | 31·67 | 31·93 | 32·82 | 32·29 | 32·57 |
| $Na_2O$ | 0·01 | 0·02 | 0·03 | 0·07 | 0·04 | 0·17 | 0·26 | 0·21 | 0·12 | 0·06 | 0·08 | 0·12 | 0·11 | 0·09 | 0·07 | 0·14 | 0·08 |
| $ThO_2$ | bdl | bdl | 0·04 | bdl | bdl | bdl | bdl | bdl | bdl | bdl | 0·04 | 0·04 | bdl | 0·06 | bdl | bdl | bdl |
| $UO_2$ | bdl | bdl | bdl | bdl | bdl | bdl | bdl | bdl | bdl | bdl | bdl | bdl | bdl | bdl | bdl | bdl | bdl |
| $Ta_2O_5$ | bdl | 0·17 | bdl | bdl | bdl | 0·13 | bdl | bdl | bdl | 0·07 | bdl | 0·12 | 0·03 | 0·06 | bdl | bdl | bdl |
| $Nb_2O_5$ | 0·16 | 1·57 | 0·49 | 1·19 | 0·45 | 5·19 | bdl | 0·11 | 0·13 | bdl | 0·14 | bdl | bdl | 0·22 | 0·27 | bdl | 0·09 |
| SrO | bdl | bdl | bdl | bdl | bdl | bdl | bdl | bdl | bdl | bdl | bdl | bdl | bdl | bdl | bdl | bdl | bdl |
| $La_2O_3$ | bdl | bdl | bdl | bdl | bdl | bdl | bdl | bdl | bdl | bdl | bdl | bdl | bdl | bdl | bdl | bdl | bdl |
| $Ce_2O_3$ | bdl | bdl | 0·10 | 0·12 | bdl | 0·10 | bdl | bdl | bdl | bdl | bdl | bdl | bdl | 0·08 | bdl | 0·07 | 0·07 |
| $Nd_2O_3$ | bdl | bdl | bdl | 0·09 | bdl | bdl | bdl | bdl | bdl | bdl | bdl | bdl | bdl | bdl | bdl | 0·05 | 0·07 |
| $Pr_2O_3$ | bdl | 0·06 | 0·05 | bdl | bdl | bdl | bdl | bdl | bdl | 0·04 | bdl | bdl | 0·06 | bdl | 0·07 | bdl | 0·07 |
| $Sm_2O_3$ | bdl | bdl | bdl | bdl | bdl | bdl | bdl | bdl | bdl | bdl | bdl | bdl | bdl | 0·05 | 0·04 | bdl | 0·03 |
| F | bdl | bdl | bdl | bdl | bdl | bdl | bdl | bdl | bdl | bdl | bdl | bdl | bdl | bdl | bdl | bdl | bdl |
| Total | 100·11 | 101·27 | 101·27 | 102·23 | 100·01 | 101·75 | 101·43 | 101·45 | 101·01 | 101·62 | 101·30 | 100·08 | 100·13 | 99·25 | 100·61 | 101·13 | 101·79 |
| Formula based on 8 cations and 12 oxygens | | | | | | | | | | | | | | | | | |
| Si | 2·98 | 2·78 | 2·99 | 2·84 | 2·95 | 2·38 | 2·67 | 2·88 | 2·74 | 2·78 | 2·52 | 2·81 | 2·39 | 2·64 | 2·69 | 2·74 | 2·88 |
| Ti | 0·13 | 0·22 | 0·05 | 0·19 | 0·17 | 0·56 | 0·59 | 0·30 | 0·44 | 0·34 | 0·66 | 0·34 | 0·86 | 0·62 | 0·45 | 0·45 | 0·23 |
| Zr | 0·01 | 0·05 | 0·01 | 0·11 | 0·02 | 0·17 | 0·01 | 0·00 | 0·01 | 0·01 | 0·02 | bdl | 0·02 | bdl | 0·00 | 0·01 | 0·01 |
| Y | bdl | bdl | 0·003 | bdl | bdl | bdl | bdl | bdl | bdl | 0·01 | 0·004 | bdl | 0·01 | bdl | 0·01 | bdl | bdl |
| Al | 0·54 | 0·38 | 0·44 | 0·26 | 0·30 | 0·20 | 0·14 | 0·11 | 0·22 | 0·26 | 0·33 | 0·26 | 0·42 | 0·22 | 0·32 | 0·16 | 0·27 |
| $Fe^{2+}$ | 0·16 | 0·06 | 0·08 | 0·16 | 0·18 | 0·32 | 0·20 | 0·15 | 0·13 | 0·08 | 0·12 | 0·12 | 0·23 | 0·20 | 0·06 | 0·17 | 0·14 |
| $Fe^{3+}$ | 1·21 | 1·36 | 1·40 | 1·34 | 1·39 | 1·01 | 1·38 | 1·53 | 1·40 | 1·48 | 1·27 | 1·44 | 1·05 | 1·22 | 1·36 | 1·45 | 1·46 |
| Mn | 0·04 | 0·04 | 0·04 | 0·06 | 0·04 | 0·05 | 0·03 | 0·04 | 0·05 | 0·04 | 0·04 | 0·05 | 0·04 | 0·04 | 0·04 | 0·04 | 0·07 |
| Mg | 0·08 | 0·11 | 0·07 | 0·11 | 0·09 | 0·16 | 0·06 | 0·03 | 0·08 | 0·06 | 0·12 | 0·06 | 0·12 | 0·11 | 0·11 | 0·06 | 0·03 |
| Ca | 2·85 | 2·94 | 2·90 | 2·88 | 2·85 | 2·92 | 2·89 | 2·91 | 2·90 | 2·93 | 2·91 | 2·89 | 2·86 | 2·91 | 2·93 | 2·89 | 2·88 |
| Na | 0·002 | 0·00 | 0·00 | 0·01 | 0·01 | 0·03 | 0·04 | 0·03 | 0·02 | 0·01 | 0·01 | 0·02 | 0·02 | 0·01 | 0·01 | 0·02 | 0·01 |
| Th | bdl | bdl | 0·00 | bdl | bdl | bdl | bdl | bdl | bdl | bdl | 0·00 | 0·00 | bdl | 0·00 | bdl | bdl | bdl |
| U | bdl | bdl | bdl | bdl | bdl | bdl | bdl | bdl | bdl | bdl | bdl | bdl | bdl | bdl | bdl | bdl | bdl |
| Ta | bdl | 0·004 | bdl | bdl | bdl | 0·003 | bdl | bdl | bdl | 0·001 | bdl | 0·003 | 0·001 | 0·001 | bdl | bdl | bdl |
| Nb | 0·01 | 0·06 | 0·02 | 0·04 | 0·02 | 0·20 | bdl | 0·004 | 0·01 | bdl | 0·01 | bdl | bdl | 0·01 | 0·01 | bdl | 0·003 |
| Sr | bdl | bdl | bdl | bdl | bdl | bdl | bdl | bdl | bdl | bdl | bdl | bdl | bdl | bdl | bdl | bdl | bdl |
| REE total | bdl | bdl | 0·004 | 0·006 | bdl | 0·003 | bdl | bdl | bdl | bdl | bdl | bdl | 0·002 | 0·005 | 0·003 | 0·004 | 0·007 |
| F | bdl | bdl | bdl | bdl | bdl | bdl | bdl | bdl | bdl | bdl | bdl | bdl | bdl | bdl | bdl | bdl | bdl |
| Total cations | 8·00 | 8·00 | 8·00 | 8·00 | 8·00 | 8·00 | 8·00 | 8·00 | 8·00 | 8·00 | 8·00 | 8·00 | 8·00 | 8·00 | 8·00 | 8·00 | 8·00 |

bdl, below detection limit. Noticeable variation of representative analyses in a single sample has been indicated by the addition of further analyses, reflecting the variation.

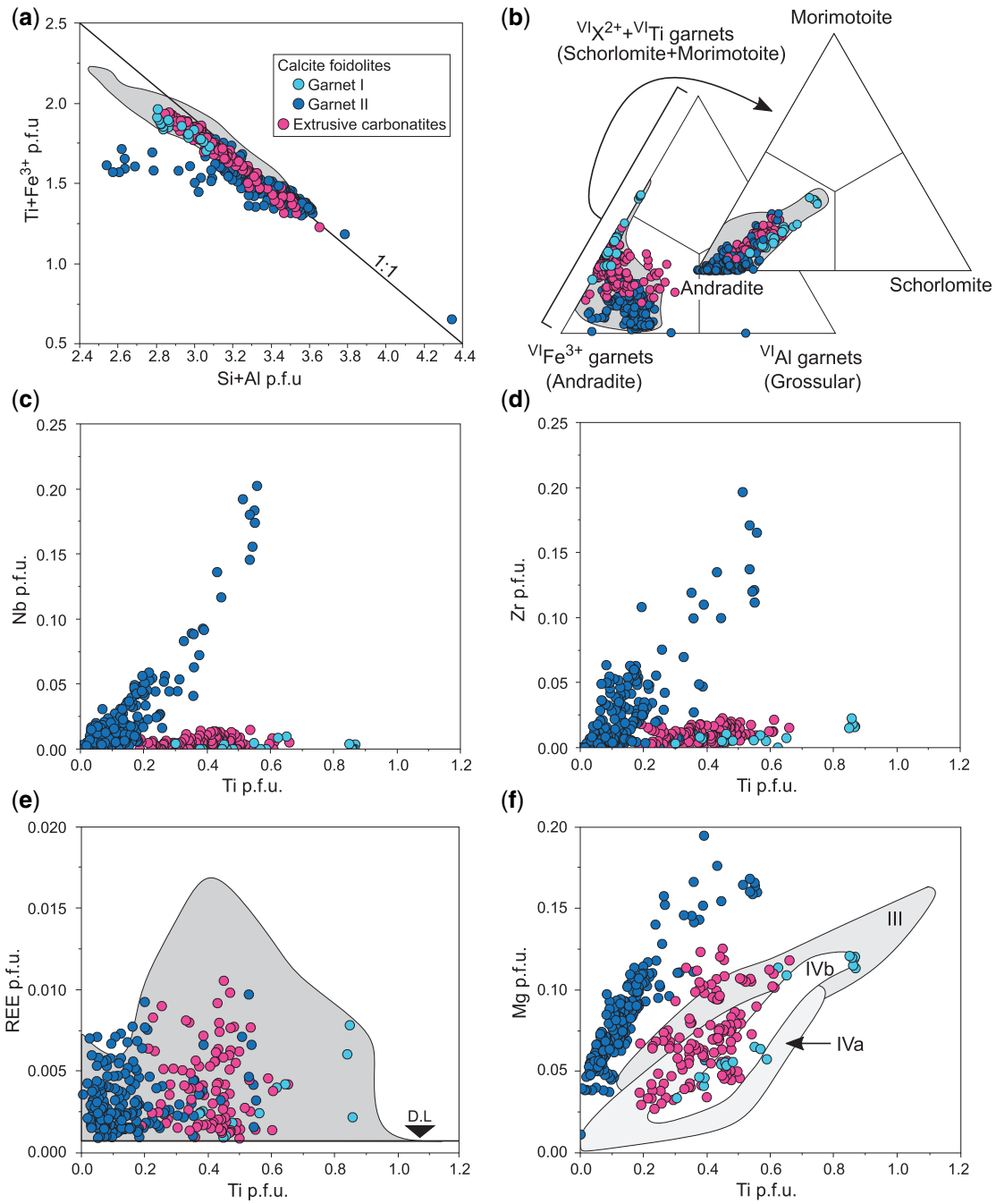


**Fig. 13.** Compositional variation of garnet from carbonatites and calcite foidolites of the KVC. (a) Ti+$Fe^{3+}$ vs Si+Al. The solid line illustrates the ideal 1:1 substitution. (b) Garnet composition based on the octahedral-site occupations $Fe^{3+}$, $X^{2+}$+Ti (X= Mg, $Fe^{2+}$) and Al and based on the endmembers andradite, morimotoite and schorlomite. (c)–(f) Concentrations of Nb, Zr, REE and Mg vs Ti, with data from the KVC silicate rocks shown as grey fields for comparison (Braunger *et al.*, 2018): (III) melilititic and haüynitic/haüynolitic rocks, melteigites, IVa) nosean syenites (former 'ledmorites'), (IVb) phonolites and nosean syenite inclusions therein.

## Significance of calcite foidolites (carbonatite magma–xenolith interaction)

Calcite foidolites in the Badberg sövites (Figs 6 and 7) probably do not represent cumulates of the carbonatite magma itself, since their mineralogy is very different from the sövites and large differences in the modal abundances would be expected. Also, feldspar, which is found as relicts in the calcite foidolites, is generally unstable at the low silica activities expected for carbonatite magmas (Barker, 2001; Massuyeau *et al.*, 2015). Therefore, we assume that these rocks represent equivalents of previously emplaced silicate rocks entrained in and subsequently resorbed and metasomatized by the intruding carbonatitic magma.

Despite their textural resemblance to haüynolites that occur as xenoliths in some phonolitic rocks (Czygan, 1977), the chemical composition of relict garnet (garnet type I) in calcite foidolites suggests that the

**Table 9:** Representative EPMA analyses of zirconolite from the Kaiserstuhl Volcanic Complex

| Sample # | 1354 | 1354 | C 71 | C 72 |
|---|---|---|---|---|
| Locality | Haselschacher Buck | | Kaiserstuhl | |
| Rock type | Sövite | | | |
| wt % | | | | |
| CaO | 12·56 | 12·52 | 11·38 | 12·20 |
| $Na_2O$ | bdl | bdl | n.a. | n.a. |
| SrO | 0·29 | bdl | n.a. | n.a. |
| $La_2O_3$ | 0·16 | 0·30 | n.a. | n.a. |
| $Ce_2O_3$ | 1·71 | 2·02 | 0·77 | 0·90 |
| $Pr_2O_3$ | 0·37 | 0·34 | n.a. | n.a. |
| $Nd_2O_3$ | 1·03 | 1·13 | 1·10 | n.a. |
| $Sm_2O_3$ | 0·27 | 0·19 | 0·27 | n.a. |
| $Y_2O_3$ | 0·48 | 0·49 | n.a. | n.a. |
| $ZrO_2$ | 33·75 | 32·68 | 30·51 | 34·80 |
| $UO_2$ | 1·04 | 1·23 | 1·22 | 1·40 |
| $ThO_2$ | 1·18 | 1·65 | 5·13 | 4·10 |
| $TiO_2$ | 10·81 | 10·66 | 13·56 | 22·70 |
| $Nb_2O_5$ | 21·20 | 21·53 | 22·07 | 15·70 |
| $Ta_2O_5$ | 4·10 | 4·45 | 3·08 | n.a. |
| MgO | n.a. | n.a. | 0·85 | n.a. |
| $Al_2O_3$ | 0·91 | 0·82 | n.a. | n.a. |
| FeO | 8·00 | 7·77 | 7·41 | 7·60 |
| MnO | 0·98 | 1·03 | 0·94 | 0·20 |
| $SiO_2$ | bdl | bdl | n.a. | n.a. |
| F | bdl | bdl | n.a. | n.a. |
| Total | 98·83 | 98·80 | 98·29 | 99·60 |
| Formula based on 4 cations | | | | |
| Ca | 0·90 | 0·91 | 0·84 | 0·87 |
| Na | bdl | bdl | n.a. | n.a. |
| Sr | 0·01 | bdl | n.a. | n.a. |
| REE+Y | 0·10 | 0·12 | 0·05 | 0·02 |
| Zr | 1·11 | 1·07 | 1·02 | 1·08 |
| U | 0·01 | 0·02 | 0·02 | 0·02 |
| Th | 0·02 | 0·03 | 0·08 | 0·06 |
| Ti | 0·55 | 0·54 | 0·70 | 1·10 |
| Nb | 0·64 | 0·66 | 0·67 | 0·46 |
| Ta | 0·07 | 0·08 | 0·06 | n.a. |
| Mg | n.a. | n.a. | 0·09 | n.a. |
| Al | 0·07 | 0·07 | n.a. | n.a. |
| Fe | 0·45 | 0·44 | 0·42 | 0·38 |
| Mn | 0·06 | 0·06 | 0·05 | 0·01 |
| Si | bdl | bdl | n.a. | n.a. |
| F | bdl | bdl | n.a. | n.a. |
| Total cations | 4·00 | 4·00 | 4·00 | 4·00 |

bdl, below detection limit. n.a., not analysed.
C71: Data from Keller (1984). C72: Data from Sinclair & Eggleton (1982).

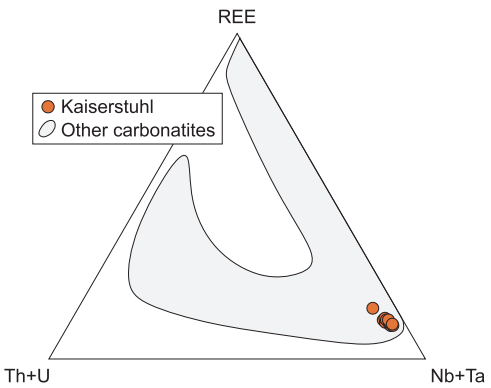


**Fig. 14.** Compositional variation of zirconolite from the KVC in comparison with other carbonatites (data from Williams & Gieré, 1996; Hurai *et al.*, 2018).

nosean syenites that underlie the Badberg body (as evidenced by the FB drill core; see Walter *et al.*, 2018), are the most likely protolith (Fig. 13). However, in contrast to nosean syenites, calcite foidolites have a higher proportion of sodalite-group minerals, alkali feldspar is almost absent and clinopyroxene and garnet are subhedral to anhedral. We attribute these mineralogical and textural differences to the interaction with the carbonatite magma (Fig. 16).

Carbonatites reach liquidus temperatures above 1000 °C (e.g. Kharlomov, 1981; Panina, 2005; Guzmics *et al.*, 2011) and contain large amounts of volatile phases (e.g. F and $H_2O$; Treiman & Essene, 1984; Jago & Gittins, 1991). Therefore, they can cause intense metasomatism (Elliot *et al.*, 2018) and may be capable of partly assimilating silicate rocks. Textural evidence for the interaction between the entrained xenoliths and the carbonatite magma includes: (i) the almost complete replacement of precursor alkali feldspar by foids; (ii) the compositional change of nosean to haüyne; (iii) blackwall-like mica seams around the xenoliths; (iv) the occurrence of recrystallized garnet (garnet type II) with relics of original garnet cores (garnet type I); and (v) crosscutting carbonatitic veins (Figs 6 and 7). The modifications in nosean syenites can be expressed by the schematic mineral reactions (1) – (3):

alkali feldspar + nosean (nosean syenite) → haüyne (calcite foidolite)

$$2\ KAlSi_3O_8 + Na_8Al_6Si_6O_{24}SO_4 + CaSO_4(melt) + CaO\ (melt) = Ca_2Na_6Al_6Si_6O_{24}(SO_4)_2 + Al_2O_3 + 6\ SiO_2 + K_2O + Na_2O$$

(reaction 1)

original cpx (nosean syenite) → recrystallized cpx (calcite foidolite)

$$10\ Ca_{0.8}Na_{0.2}Mg_{0.4}Fe^{2+}{}_{0.3}Fe^{3+}{}_{0.3}Al_{0.1}Si_{1.9}O_6 + 2\ CaO\ (melt) + 3\ MgO\ (melt) + 0.5\ Al_2O_3(\text{reaction 1}) = 10\ CaMg_{0.7}Fe^{2+}{}_{0.1}Fe^{3+}{}_{0.2}Al_{0.2}Si_{1.8}O_6 + 3\ FeO + Na_2O + SiO_2 + 0.25\ O_2$$

(reaction 2)

original garnet I (nosean syenite) → recrystallized garnet II (calcite foidolite)

$$10\ (Ca_{2.9}Mg_{0.1})(Fe^{2+}{}_{0.3}Fe^{3+}{}_{1.2}Ti_{0.5})(Al_{0.2}Si_{2.8})O_{12} + 0.5\ ZrO_2(melt) + 0,25\ Nb_2O_5(melt) + 0.5\ Al_2O_3(\text{reaction 1}) + 0.125\ O_2(melt) = 10\ (Ca_{2.9}Mg_{0.1})(Fe^{2+}{}_{0.2}Fe^{3+}{}_{1.3}Ti_{0.3}[Zr,\ Nb]_{0.1}Al_{0.1})(Al_{0.2}Si_{2.8})O_{12} + 2\ TiO_2$$

(reaction 3)

Garnet II has relatively high Nb and Zr contents (Fig. 13), reflecting the importance of the carbonatitic magma during metasomatism, as carbonatites are typically enriched in these elements (usually stored in pyrochlore, perovskite, baddeleyite and zirconolite). Similar modifications of silicate rocks by carbonatitic melts have been described as 'antiskarn'

metasomatism (Anenburg & Mavrogenes, 2018) and reflect the mutual interaction during contamination.

Importantly, xenoliths in the lower sections of the KB3 drill hole, which represents the central part of the tilted Badberg body, are much more strongly disaggregated, which may indicate higher degrees of resorption compared to the marginal parts of the body. This may be attributed to a longer lasting heat flow that predominantly occurred in the central area of the carbonatite pipe, while marginal zones experienced an earlier and more rapid cooling. Consequently, this central zone contains more silica that may have induced the observed exceptional mica enrichment in those parts (Fig. 6). In these samples (down-hole below +100 metres above sea level), pyrochlore is enriched in $Fe^{2+}$, Al and Ti (Walter *et al.*, 2018), which was probably released by the resorption of xenoliths. Note that such enrichment of $Fe^{2+}$ and Al in pyrochlore is confined to the Badberg locality and does not exist at the other carbonatite localities of the KVC.

## The significance of mica composition

The enhanced formation of mica (and the formation of diopside instead of monticellite/olivine) in the Badberg samples cannot be ascribed to magmatic differentiation, since silicates in carbonatites crystallize early, which would decrease the $SiO_2$ concentration and silica activity in the carbonatite magma with fractionation (e.g. Krasnova *et al.*, 2004; Lee *et al.*, 2004). However, strong textural evidence and mineral compositions (see above) suggest a connection between the formation of mica (and cpx) and the entrainment of xenoliths in the sövites from Badberg.

In contrast to mica from the other sövite bodies of the KVC (which are dominated by the kinoshitalite substitution), mica at Badberg is dominated by the eastonite substitution (see above). This indicates that the availability of Al exceeds the availability of Ba, most likely due to the provision of Al by the resorption of feldspar (reaction 1). Furthermore, Badberg mica shows an unusual enrichment in octahedral $Fe^{2+}$. This is atypical for the other sövites of the KVC and carbonatites in general (e.g. Kovdor, Palabora, Sokli and Jacupiranga; Fig. 15), where the formation of tetraferriphlogopite (incorporation of $Fe^{3+}$) or Fe-poor phlogopite is preferred over the formation of $Fe^{2+}$-rich mica (biotite; e.g. Lee *et al.*, 2003; Krasnova *et al.*, 2004; Giebel *et al.*, 2019). While all other localities of the KVC show 'typical carbonatite micas' with respect to their Mg, Al and Fe concentrations, Badberg micas are more similar to micas from silicate rocks (Fig. 15), which we ascribe to the metasomatic interaction with the calcite foidolite clasts and rafts (see above). Alteration reactions (1) – (3) above demonstrate the release of K, Al, Si and $Fe^{2+}$, which are consumed to form $Fe^{2+}$-bearing mica (Figs 4c and 7a) according to the schematic reaction:

$$K_2O\ (\text{see reaction 1}) + Al_2O_3(\text{see reaction 1}) + 6\ SiO_2(\text{see reactions 1 and 2}) + FeO\ (\text{see reaction 2}) + 5\ MgO\ (\text{melt}) + 2\ H_2O\ (\text{melt}) = 2\ KMg_{2.5}Fe_{0.5}AlSi_3O_{10}(OH)_2 \quad \text{(reaction 4)}$$

Besides the $Fe^{2+}$-enrichment, the micas of the Badberg contain elevated amounts of Ti and Mn. While Mn and also F are preferably incorporated into the mica precipitating directly on the resorbed clasts (black-wall

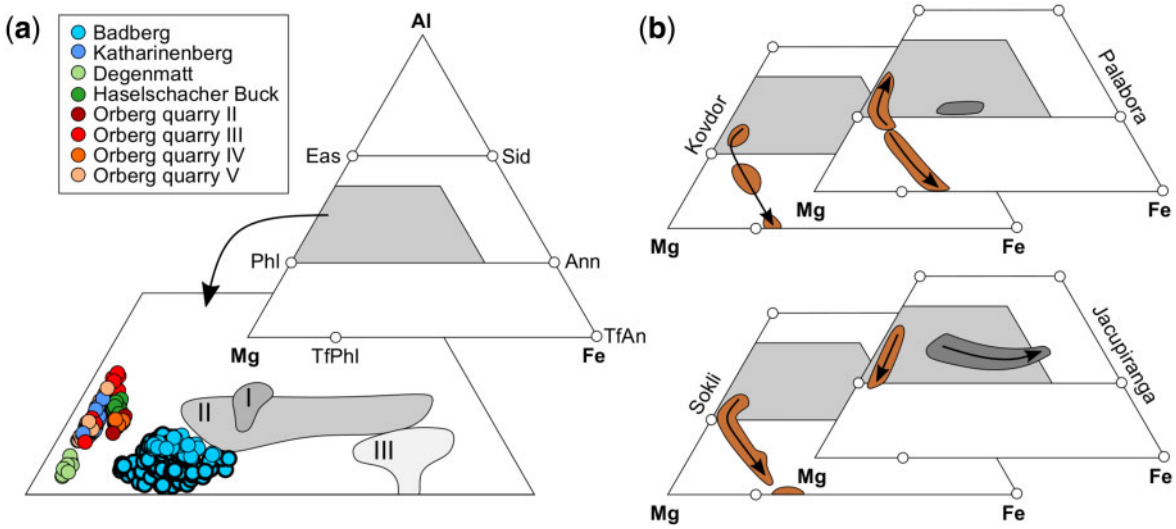


**Fig. 15.** (a) Ternary diagrams of $Mg–Al_{total}–Fe_{total}$ reflecting the compositional characteristics of mica from the sövites of the KVC, with numbered grey areas representing mica compositions from the silicate rocks of the KVC (Braunger *et al.*, 2018): (I) olivine nephelinites; (II) tephritic rocks; (III) haüyne melilitites. (b) Mica compositions from other carbonatites with brown fields indicating mica compositions in carbonatites and dark grey field mica compositions from associated silicate rocks (Palabora, Kovdor, Sokli and Jacupiranga; Brod *et al.*, 2001; Lee *et al.*, 2003; Krasnova *et al.*, 2004; Giebel *et al.*, 2019). Ann, annite; Eas, eastonite; Sid, siderophyllite; Phl, phlogopite; TfPhl, tetraferriphlogopite; TfAn, tetraferriannite.

mica), Ti, Na and Ba behave mostly conversely and appear to have been enriched in the carbonate melt, further distant from the resorbed clasts (Fig. 11). The enhanced crystallization of mica at Badberg and the related consumption of Mg from the carbonatite melt may also be the reason for the relative depletion of Mg in subsequently crystallized calcite (Fig. 8), due to the generally very rapid diffusion in carbonatite melts and their resulting very fast equilibration (e.g. Anenburg *et al.*, 2018 and references therein). Besides Mg, Ba was also derived from the carbonatite melt itself, while the enrichment of Ti (reaction 3) and additional Mn is probably related to the resorption and recrystallization of clinopyroxene and garnet I. The absence of $Fe^{2+}$-poor mica cores suggests that the entire mica crystallization in the Badberg sövites took place during nosean syenite–carbonatite magma interaction. Hence, mica composition cannot be easily used to track magmatic differentiation at Badberg, but may still be applicable at the other localities.

Enrichment of Ba in carbonatites is generally ascribed to differentiation because of its incompatible character (e.g. Kogarko *et al.*, 2012; McCormick & Heathcote, 1987; McCormick & Le Bas, 1996). Moreover, Ba is efficiently mobilized in carbonatites, is strongly concentrated in residual liquids and dissolves favourably in aqueous fluids (Anenburg & Mavrogenes, 2018). Thus, the strong enrichment of Ba in the mica from the Orberg sövites (Fig. 11) confirms the assumption of Walter *et al.* (2018) that the Orberg sövites are evolved and hydrothermally overprinted. The high Mg# of Orberg mica is attributed to the relative enrichment of Mg over Fe during differentiation (fractional crystallization) due to the contemporaneous formation of Fe-rich spinel group minerals. This is the reverse of what is typically expected during silicate-magma differentiation (dependent on the redox state of the magma; e.g. Heathcote & McCormick, 1989; Giebel *et al.*, 2019). A comparison between the enrichment of Ba and the increase of the Mg# in these micas suggests a much stronger sensitivity of the former in terms of mica evolution. In conclusion, mica does not only record differentiation, but also contamination processes in carbonatites exceptionally well.

## The significance of apatite composition

The local increase in silica activity in the carbonatite melt (reactions 1 & 2) enhanced the incorporation of Si in apatite (Figs 9 and 10) and favoured simultaneous REE incorporation due to the britholite substitution (e.g. Hammouda *et al.*, 2010). In contrast to cores of Badberg apatites, which generally reveal a lower britholite substitution, rims are significantly more strongly affected (Fig. 9a). The sharp contact between the cores and rims suggests an abrupt and strong compositional change of the carbonatite magma during apatite formation, which excludes continuous magma differentiation, although the generally high Sr contents in Badberg apatites (Fig. 9c) indicate a relatively evolved character for the Badberg sövites.

In contrast to a few apatites from the Orberg that occur in strongly hydrothermally altered samples and experienced a belovite substitution (see above; Fig. 9), which is typical for hydrothermal apatite evolution in many carbonatites (e.g. de Toledo *et al.*, 2004; Doroshkevich *et al.*, 2009), a hydrothermal origin of the Badberg apatites in respect of the increased britholite substitution (0·3–0·5 REE+Si pfu) in its rims is also unlikely. This phenomenon is restricted to magmatic temperatures (>600 °C), while hydrothermal conditions (including sufficient $SiO_2$) promote the formation of REE-poorer apatite and REE-rich silicate minerals (e.g. cerite; Anenburg & Mavrogenes, 2018; Anenburg *et al.*, 2018). In addition, typical hydrothermal interaction textures (reprecipitation/replacement reactions; e.g. Giebel *et al.*, 2017) are typically absent in Badberg sövites.

We assume that the enhanced britholite substitution in apatites is related to the interaction between the carbonatite magma and silicate xenoliths. The core–rim variation records the time-dependent effect of contamination. This is additionally reflected by the increasing Si and REE content in apatite in the deeper sections of drill core KB3 (Fig. 10; central zones of the pipe), where a stronger disaggregation of xenoliths caused an increased release of silica (see above). Experimental data (Klemme & Dalpé, 2003) confirm enhanced partitioning of REE into apatite with increasing $SiO_2$ content in the melt. This emphasizes the potential importance of contamination of carbonatitic magmas for REE mineralization; the local enrichment of Si favours an early (magmatic) incorporation of REE into apatite, which inhibits the subsequent enrichment of REE in residual liquids/fluids. These late-stage fluids, however, are the most common source for the deposit-quality enrichment of REE-minerals and/or REE-rich minerals in carbonatites (Wall & Mariano, 1996). This connection is convincingly indicated by a comparison of the REE concentrations in apatite and pyrochlore between the Badberg and other carbonatite bodies (Fig. 17). While Badberg apatites are REE-rich (due to contamination; Fig. 9a), the incorporation of REE in Badberg (late-stage) pyrochlore seems to be largely unaffected. In contrast, apatites at other localities are relatively REE-poor, while hydrothermally overprinted pyrochlore at these localities is strongly REE-enriched (see details in Walter *et al.*, 2018). This potentially has economic implications, although it should be noted that calcite (due to its high modal content) further contributes to the REE budget of the rocks.

## Mica in carbonatites – a potential clue to wall rock interaction processes?

Many carbonatites contain appreciable amounts of mica (e.g. Brod *et al.*, 2001; Lee *et al.*, 2003; Reguir *et al.*,

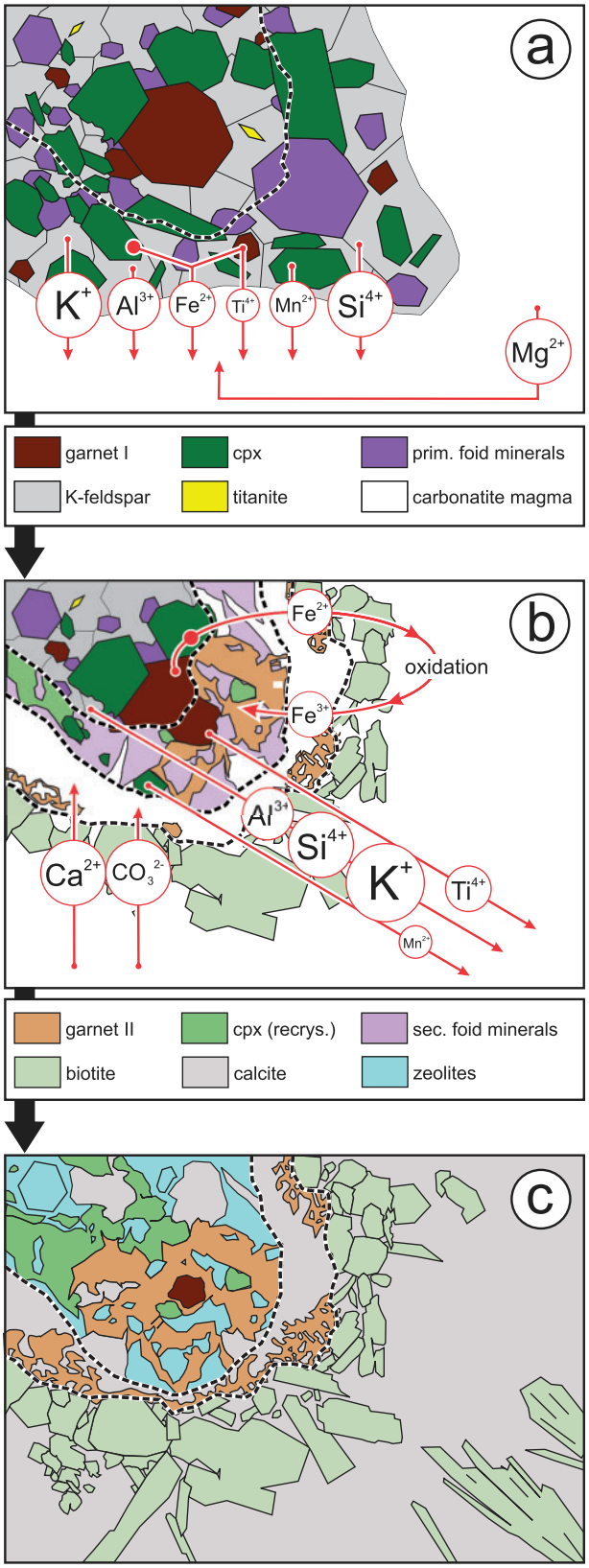


**Fig. 16.** Schematic diagram illustrating processes during contamination of carbonatitic melt by wall rock. (a) Interaction of carbonatitic melt with xenoliths of nosean syenite leads to resorption of primary minerals in marginal zones and associated release of some elements into the melt. (b) The released elements cause the formation of mica in black-walls, with Mg mostly provided by the carbonatitic melt. Contemporaneously $Fe^{3+}$, Ca and $CO_3^{2-}$ are incorporated in recrystallized garnet II, diopsidic clinopyroxene II and calcite. (c) Completely resorbed/recrystallized xenolith (now represented as calcite foidolite) with relictic garnet I; primary nosean is completely replaced by zeolite.

2009; Giebel *et al.*, 2019). In many carbonatites mica is more or less equally distributed in the rock, but some carbonatites contain cm- to m-sized mica-rich areas as schlieren and lenses and even mica-dominated rocks (glimmerites) occur in some cases at the contact between carbonatites and the host rocks (glimmeritization; e.g. Gittins *et al.*, 1975; Hoatson *et al.*, 2011).

Our study shows that interaction of carbonatite magma with silicate rocks may induce mica crystallization in carbonatites due to the mobilization and redistribution of K, Si, Al, Mg, Fe and $H_2O$ (reaction 4). Similarly, Vuorinen & Skelton (2004) and Chakhmouradian *et al.* (2008) showed that mica with an unusual $Fe^{2+}$-rich composition in the Alnö and Eden Lake sövites most probably is the product of the reaction between the carbonatite melt and the silicate host rocks. Thereby, the general question arises whether 'pure' carbonatites are capable of crystallizing mica in larger quantities at all, or whether an additional enrichment of K, Al, Si and Fe by contamination and interaction with silicate wall rocks is critically important. Sufficient Mg occurs in the carbonatite magma itself and experimental studies have shown that carbonate melts are capable of containing relatively high concentrations of $H_2O$ (e.g. 10 wt % at 1 kbar; Keppler, 2003). However, the available experimental data indicate that carbonatites can dissolve only minor amounts of Al (usually $<$1 wt % $Al_2O_3$; Brooker & Kjarsgaard, 2011) and Si ($<$2·9 wt % $SiO_2$) at conditions pertinent to the KVC (750–1200 °C, subvolcanic pressures; Weidendorfer *et al.*, 2017).

We performed mass balance calculations based on these experimental constraints, typical Al and Si concentrations in mica from the Badberg (and various other carbonatites) and carbonatite melt densities (2·2–2·6 g/cm$^3$) estimated for middle to shallow crustal levels at 800–1200 °C (e.g. Wolff, 1994; Genge *et al.*, 1995; Dobson *et al.*, 1996; Kono *et al.*, 2014). These calculations indicate that only minor modal amounts of mica ($<$7%) can form from a carbonatitic melt – assuming that sufficient K, Mg and $H_2O$ are available and no other silicate minerals are present (ES1, Supplementary Data; supplementary data are available for downloading at http://www.petrology.oxfordjournals.org). Consequently, larger amounts of mica in carbonatites would require an additional external introduction of Si and Al. In fact, the enrichment of Al in some carbonatites has been ascribed to the resorption of feldspar from fenitized wall rocks (McCormick & Le Bas, 1996), which obviously also releases alkalis and Si. Further, because of the relatively early fractionation of mica in

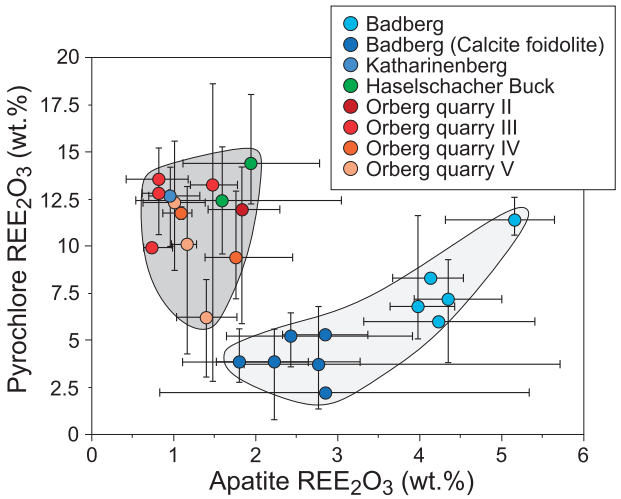


**Fig. 17.** Comparison of REE concentrations in pyrochlore and apatite in sövites from different localities in the KVC. The error bars represent the maximum or the minimum values, respectively, for pyrochlore/apatite within a sample.

carbonatites, rather mica-poor carbonatites are generally expected at shallow crustal levels. This further excludes the possibility that a compositionally distinct carbonatite magma is responsible for the unusual enrichment of mica in the Badberg sövites. Hence, contamination may play a key-role for enhanced mica formation in evolved carbonatitic systems, such as the KVC. This notion is most likely also applicable for the formation of other silicate minerals (e.g. Anenburg & Mavrogenes, 2018). Here, though, different processes have to be distinguished, including: (1) assimilation of wall rocks/crystals (occurrence of xenoliths/xenocrysts); (2) interaction with wall rocks via diffusion along compositional gradients (wall rock modifications); and (3) introduction of alkali-rich fluids (not easily detectable).

## CONCLUSIONS AND IMPLICATIONS

It is generally supposed that crustal contamination plays a negligible role during carbonatite intrusion due to the high rate of magma ascent, extremely low viscosity and occasionally extraordinary low temperatures of carbonatitic magmas (Treiman & Schedl, 1983; Jones *et al.*, 2013 and references therein). At the same time, carbonatitic magmas are known to be extremely reactive because of their massive compositional contrast to almost all crustal rock types and cogenetic silicate rocks (the strong geochemical gradients result in intense diffusional processes) and because of their high amounts of fluxing agents such as P, F and other volatiles, causing various types of metasomatic reactions in deep-seated mantle regions as well as at shallow crustal levels.

Especially shallow-level carbonatites in active rift zones, of which the Kaiserstuhl Volcanic Complex (Southwest Germany) is a good example, may be associated with brittle deformation during and after magma emplacement, which may support disaggregation and entrainment of fragments and rafts of country rocks and/or cogenetic intrusive rocks. Sub-surface levels may even promote the fragmentation of wall rocks by explosive eruptions, where fragments of wall rock may be partly resorbed by carbonatite melt prior to consolidation.

Our study presents textural and geochemical evidence that intense interaction between carbonatite magma and fragments of earlier, cogenetic, intrusive silicate rocks at a shallow emplacement level can indeed influence the mineralogy and mineral chemistry of sövites. This contamination process causes a mineralogical and geochemical modification of both carbonatite and silicate rocks.

Mica that crystallized from such locally contaminated carbonatites may incorporate relatively high amounts of octahedral $Fe^{2+}$, which is atypical of carbonatites in general. Such contamination processes may even influence the timing, type and intensity of REE mineralization and hence may be able to cause a relocation of economic levels in a carbonatitic system. In the Badberg case, wall rock interaction causes preferred incorporation of REE in apatite during the magmatic stage. This resulted in relative REE depletion during the late-magmatic/hydrothermal stages. At Orberg, however, contamination processes probably did not play an important role and indeed, REE enrichment in pyrochlore in these samples is much more intense during the hydrothermal stage. However, the otherwise commonly observed formation of late magmatic and hydrothermal REE-F-carbonate minerals (e.g. bastnäsite, synchysite, parisite) in carbonatites is largely lacking at the KVC.

## ACKNOWLEDGEMENTS

We thank Wolfhard Wimmenauer (University of Freiburg) and Manfred Martin (LRGB Freiburg) for providing sample material. Wolfhard Wimmenauer was of invaluable help during field work and we are very grateful that he took the time to show one of us (B.W.) outcrops forgotten for decades. We especially thank Klaus Brauch, Michael Tauchnitz, Claudia Pohl, Dietmar Kopp, Gregory Symons (terratec Geophysical Services), Samuel Weatherley, Graham Banks and Björn Heincke (Geological Survey of Denmark and Greenland), Pete Siegfried (Geo-Africa Prospecting Services cc) and Kathryn Goodenough (British Geological Survey), for insightful discussions on the structural framework of the KVC. Anatoly Zaitsev (University of St. Petersburg), Anton Chakhmouradian (University of Manitoba) and Udo Neumann (University of Tübingen) are gratefully acknowledged for constructive discussions on various topics related to this study. We further thank Rainer Babiel and Stefan Kreissl for their continuous support during analytical sessions and Simone Schafflick for thin section preparation. Finally, we thank Michael Anenburg, Ingrid Hornig-Kjarsgaard, Alasdair Skelton

and an anonymous reviewer, as well as Editor Gerhard Wörner, for their attentive reviews that allowed us to improve this manuscript significantly.

## FUNDING

This work was supported by the Alexander von Humboldt Foundation [sponsorship of A. Parsapoor–Georg Forster Research Fellowship] and has further received funding from the European Union's Horizon 2020 research and innovation programme [grant agreement No 689909]. R.J. Giebel and S. Braunger are supported by the Deutsche Forschungsgemeinschaft [grants MA 2563/10 and MA2563/12, respectively].

## SUPPLEMENTARY DATA

Supplementary data are available at *Journal of Petrology* online.

## REFERENCES

Andersen, T. (1988). Evolution of peralkaline calcite carbonatite magma in the Fen complex, southeast Norway. *Lithos* **22**, 99–112.

Anenburg, M., Burnham, A. D. & Mavrogenes, J. A. (2018). Ree redistribution textures in altered fluorapatite: symplectites, veins, and phosphate-silicate-carbonate assemblages from the Nolans Bore P-REE-Th deposit, Northern Territory, Australia. *The Canadian Mineralogist* **56**, 331–354.

Anenburg, M. & Mavrogenes, J. A. (2018). Carbonatitic versus hydrothermal origin for fluorapatite REE-Th deposits: Experimental study of REE transport and crustal "antiskarn" metasomatism. *American Journal of Science* **318**, 335–366.

Andrade, F., Möller, P., Lüders, V., Dulski, P. & Gilg, H. (1999). Hydrothermal rare earth elements mineralization in the Barra do Itapirapuã carbonatite, southern Brazil: behaviour of selected trace elements and stable isotopes (C, O). *Chemical Geology* **155**, 91–113.

Armstrong, J. T. (1991). Quantitative elemental analysis of individual microparticles with electron beam instruments. In: Heinrich, K. F. J. and Newbury, D. E. (eds) *Electron Probe Quantitation*. New York: Plenum Press, pp. 261–315.

Baranyi, I., Lippolt, H. J. & Todt, W. (1976). K-Ar Altersbestimmungen an tertiaren Vulkaniten des Oberrheingraben-Gebietes: II Die Alterstraverse vom Hegau nach Lothringen. *Oberrheinische Geologische Abhandlungen* **25**, 41–62.

Barker, D. S. (2001). Calculated silica activities in carbonatite liquids. *Contributions to Mineralogy and Petrology* **141**, 704–709.

Beccaletto, L., Capar, L., Cruz-Mermy, D., Rupf, I., Nitsch, E., Oliviero, G., Elsass, P., Perrin, A. & Marc, S. (2010). The GeORG Project - Geological Potential of the Upper Rhine Graben - Situation, goals and first scientific results, 23ème Réunion des Sciences de la Terre (RST2010). BRGM, Bordeaux, France, HAL ID: hal-00642768.

Bell, K. & Tilton, G. R. (2002). Probing the mantle: the story from carbonatites. *Eos, Transactions American Geophysical Union* **83**, 273–277.

Bell, K., Zaitsev, A., Spratt, J., Fröjdö, S. & Rukhlov, A. (2015). Elemental, lead and sulfur isotopic compositions of galena from Kola carbonatites, Russia–implications for melt and mantle evolution. *Mineralogical Magazine* **79**, 219–241.

Blust, G. (1993). Petrographie und Geochemie der silikatischen Ganggesteine der Bohrung KB3 Steinreise. PhD thesis, Albert-Ludwigs University Freiburg, p. 83.

Bourgeois, O., Ford, M., Diraison, M., De Veslud, C. L. C., Gerbault, M., Pik, R., Ruby, N. & Bonnet, S. (2007). Separation of rifting and lithospheric folding signatures in the NW-Alpine foreland. *International Journal of Earth Sciences* **96**, 1003–1031.

Brauch, K. W., Pohl, C. M., Symons, G. & Tauchnitz, M. (2018). *Paper on Instrument Test and Best Practice for Carbonatites and Alkaline Rocks. Horizon2020 Internal Report, HiTechAlkCarb Project No.689909*. Terratec Geoservices. D4.2. p. 78.

Braunger, S., Marks, M., Walter, B. F., Neubauer, R., Reich, R., Wenzel, T., Parsapoor, A. & Markl, G. (2018). The petrology of the Kaiserstuhl Volcanic Complex, SW Germany: the importance of oxidized lithosphere for carbonatite generation. *Journal of Petrology* **59**, 1731–1762.

Brod, J., Gaspar, J., De Araújo, D., Gibson, S., Thompson, R. & Junqueira-Brod, T. (2001). Phlogopite and tetra-ferriphlogopite from Brazilian carbonatite complexes: petrogenetic constraints and implications for mineral-chemistry systematics. *Journal of Asian Earth Sciences* **19**, 265–296.

Brooker, R. & Kjarsgaard, B. (2011). Silicate-carbonate liquid immiscibility and phase relations in the system $SiO_2$–$Na_2O$–$Al_2O_3$–CaO–$CO_2$ at 0.1-2.5 GPa with applications to carbonatite genesis. *Journal of Petrology* **52**, 1281–1305.

Chakhmouradian, A., Mumin, A., Demény, A. & Elliott, B. (2008). Postorogenic carbonatites at Eden Lake, Trans-Hudson Orogen (northern Manitoba, Canada): geological setting, mineralogy and geochemistry. *Lithos* **103**, 503–526.

Chakhmouradian, A. R. (2006). High-field-strength elements in carbonatitic rocks: geochemistry, crystal chemistry and significance for constraining the sources of carbonatites. *Chemical Geology* **235**, 138–160.

Chakhmouradian, A. R., Reguir, E. P., Zaitsev, A. N., Couëslan, C., Xu, C., Kynický, J., Mumin, A. H. & Yang, P. (2017). Apatite in carbonatitic rocks: compositional variation, zoning, element partitioning and petrogenetic significance. *Lithos* **274**, 188–213.

Chakhmouradian, A. R. & Zaitsev, A. N. (2002). Calcite–amphibole–clinopyroxene rock from the Afrikanda complex, Kola Peninsula, Russia: mineralogy and a possible link to carbonatites. III. Silicate minerals. *The Canadian Mineralogist* **40**, 1347–1374.

Chakrabarty, A., Sen, A. K. & Ghosh, T. K. (2009). Amphibole—a key indicator mineral for petrogenesis of the Purulia carbonatite, West Bengal, India. *Mineralogy and Petrology* **95**, 105–112.

Czygan, W. (1977). Petrographie und Geochemie der Foidsyenit-Einschlusse im Phonolith von Niederrotweil im Kaiserstuhl. *Berichte der Naturforschenden Gesellschaft Freiburg im Breisgau* **67**, 41–52.

de Oliveira, S. M. B. & Imbernon, R. A. L. (1998). Weathering alteration and related REE concentration in the Catalão I carbonatite complex, central Brazil. *Journal of South American Earth Sciences* **11**, 379–388.

de Toledo, M. C. M., Lenharo, S. L., Ferrari, V. C., Fontan, F., de Parseval, P. & Leroy, G. (2004). The compositional evolution of apatite in the weathering profile of the Catalão I alkaline-carbonatitic complex, Goiás, Brazil. *The Canadian Mineralogist* **42**, 1139–1158.

Dèzes, P., Schmid, S. & Ziegler, P. (2004). Evolution of the European Cenozoic Rift System: interaction of the Alpine

and Pyrenean orogens with their foreland lithosphere. *Tectonophysics* **389**, 1–33.

Dobson, D. P., Jones, A. P., Rabe, R., Sekine, T., Kurita, K., Taniguchi, T., Kondo, T., Kato, T., Shimomura, O. & Urakawa, S. (1996). In-situ measurement of viscosity and density of carbonate melts at high pressure. *Earth and Planetary Science Letters* **143**, 207–215.

Doroshkevich, A. G., Viladkar, S. G., Ripp, G. S. & Burtseva, M. V. (2009). Hydrothermal REE mineralization in the Amba Dongar carbonatite complex, Gujarat, India. *The Canadian Mineralogist* **47**, 1105–1116.

Edel, J.-B., Whitechurch, H. & Diraison, M. (2006). Seismicity wedge beneath the Upper Rhine Graben due to backwards Alpine push? *Tectonophysics* **428**, 49–64.

Elliott, H., Wall, F., Chakhmouradian, A., Siegfried, P., Dahlgren, S., Weatherley, S., Finch, A., Marks, M., Dowman, E. & Deady, E. (2018). Fenites associated with carbonatite complexes: a review. *Ore Geology Reviews* **93**, 38–59.

Farrell, S., Bell, K. & Clark, I. (2010). Sulphur isotopes in carbonatites and associated silicate rocks from the Superior Province, Canada. *Mineralogy and Petrology* **98**, 209–226.

Foster, M. D. (1960). Interpretation of the composition of trioctahedral micas. *U.S. Geological Survey Professional Paper*, 49.

Gendron, L., Bis, R. & Rodrigue, M. (1984). Underground mining and pyrochlore ore processing at Niobec Mine, Quebec, Canada. In: Stuart, H. (ed.) *Niobium, Proceedings of the International Symposium of the Metallurgical Society of AIME (American Institute of Mining, Metallurgical and Petroleum Engineers)*. Warrendale, Pennsylvania, pp. 79–96.

Genge, M. J., Price, G. D. & Jones, A. P. (1995). Molecular dynamics simulations of CaCO3 melts to mantle pressures and temperatures: implications for carbonatite magmas. *Earth and Planetary Science Letters* **131**, 225–238.

Giebel, R. J., Gauert, C. D. K., Marks, M. A. W., Costin, G. & Markl, G. (2017). Multi-Stage formation of REE minerals in the Palabora Carbonatite Complex, South Africa. *American Mineralogist* **102**, 1218–1233.

Giebel, R. J., Marks, M. A. W., Gauert, C. D. K. & Markl, G. (2019). A model for the formation of carbonatite-phoscorite assemblages based on the compositional variation of mica and apatite from the Palabora Carbonatite Complex, South Africa. *Lithos* **324–325**, 89–104.

Gittins, J., Allen, C. & Cooper, A. (1975). Phlogopitization of pyroxenite; its bearing on the composition of carbonatite magmas. *Geological Magazine* **112**, 503–507.

Gomide, C. S., Brod, J. A., Junqueira-Brod, T. C., Buhn, B. M., Santos, R. V., Barbosa, E. S. R., Cordeiro, P. F. O., Palmieri, M., Grasso, C. B. & Torres, M. G. (2013). Sulfur isotopes from Brazilian alkaline carbonatite complexes. *Chemical Geology* **341**, 38–49.

Groschopf, R., Kessler, G., Leiber, J., Maus, H., Ohmert, W., Schreiner, A. & Wimmenauer, W. (1996). *Erläuterungen zur Geologischen Karte Von Baden-Württemberg Freiburg i. Br. und Umgebung*. Freiburg: Geologische Landesamt Baden-Würrtemberg.

Guzmics, T., Mitchell, R. H., Szabó, C., Berkesi, M., Milke, R. & Abart, R. (2011). Carbonatite melt inclusions in coexisting magnetite, apatite and monticellite in Kerimasi calciocarbonatite, Tanzania: melt evolution and petrogenesis. *Contributions to Mineralogy and Petrology* **161**, 177–196.

Hammouda, T., Chantel, J. & Devidal, J.-L. (2010). Apatite solubility in carbonatitic liquids and trace element partitioning between apatite and carbonatite at high pressure. *Geochimica et Cosmochimica Acta* **74**, 7220–7235.

Hay, R. & O'Neil, J. (1983). Carbonatite tuffs in the Laetolil Beds of Tanzania and the Kaiserstuhl in Germany. *Contributions to Mineralogy and Petrology* **82**, 403–406.

Heathcote, R. C. & McCormick, G. R. (1989). Major-cation substitution in phlogopite and evolution of carbonatite in the Potash Sulphur Springs complex, Garland County, Arkansas. *American Mineralogist* **74**, 132–140.

Hoatson, D. M., Jaireth, S. & Miezitis, Y. (2011). The major rare-earth-element deposits of Australia: geological setting, exploration and resources. Canberra: Geoscience Australia.

Hogarth, D. (1989). Pyrocholre, apatite and amphibole: distinctive minerals in carbonatite. In: Bell, K. (ed.) *Carbonatites: Genesis and Evolution*. London: Unwin Hyman, pp. 105–148.

Hornig-Kjarsgaard, I. (1998). Rare earth elements in sövitic carbonatites and their mineral phases. *Journal of Petrology* **39**, 2105–2121.

Hubaux, A. (1964). Sructure des carbonatites de Schelingen. In: Van Wambeke, L. (ed.) *Les Roches Alcalines et Les Carbonatites du Kaiserstuhl*. Brussels: European Atomic Energy Community (EURATOM). Mineralogy Geochemistry Section, pp. 31–46.

Hubberten, H.-W., Katz-Lehnert, K. & Keller, J. (1988). Carbon and oxygen isotope investigations in carbonatites and related rocks from the Kaiserstuhl, Germany. *Chemical Geology* **70**, 257–274.

Hurai, V., Huraiová, M., Gajdošová, M., Konečný, P., Slobodník, M. & Siegfried, P. R. (2018). Compositional variations of zirconolite from the Evate apatite deposit (Mozambique) as an indicator of magmatic-hydrothermal conditions during post-orogenic collapse of Gondwana. *Mineralogy and Petrology* **112**, 279–296.

Hüttner, R. (1996). Tektonik im Grundgebirge. In: Groschopf, R., Kessler, G., Leiber, J., Maus, H., Ohmert, A., Schreiner, A. & Wimmenauer, A. (eds) *Geologische Karte Von Baden-Württemberg 1: 50000, Freiburg i.Br. und Umgebung*. Freiburg im Breisgau, Germany: Landesamt für Geologie, Rohstoffe und Bergbau Baden-Württemberg, pp. 119–228.

Ivanyuk, G. Y., Yakovenchuk, V. & Pakhomovsky, Y. A. (2002). *Kovdor*. Apatity, Russia: Laplandia Minerals, p. 326.

Jago, B. C. & Gittins, J. (1991). The role of fluorine in carbonatite magma evolution. *Nature* **349**, 56.

Jones, A. P., Genge, M. & Carmody, L. (2013). Carbonate melts and carbonatites. *Reviews in Mineralogy and Geochemistry* **75**, 289–322.

Jurewicz, A. J. & Watson, E. B. (1988). Cations in olivine, Part 2: diffusion in olivine xenocrysts, with applications to petrology and mineral physics. *Contributions to Mineralogy and Petrology* **99**, 186–201.

Kanazawa, Y. & Kamitani, M. (2006). Rare earth minerals and resources in the world. *Journal of Alloys and Compounds* **408**, 1339–1343.

Katz, K. & Keller, J. (1981). Comb-layering in carbonatite dykes. *Nature* **294**, 350–352.

Katz-Lehnert, K. (1989). Petrologie der Gangkarbonatite im Kaiserstuhl. PhD thesis, Albert-Ludwigs University Freiburg, p. 290.

Keller, J. (1978). Karbonatitische Schmelzen im Oberflächenvulkanismus des Kaiserstuhls. *Fortschritte der Mineralogie* **56**, 1–58.

Keller, J. (1981). Carbonatitic volcanism in the Kaiserstuhl alkaline complex: evidence for highly fluid carbonatitic melts at the earth's surface. *Journal of Volcanology and Geothermal Research* **9**, 423–431.

Keller, J. (1984). Der jungtertiäre Vulkanismus Südwestdeutschlands: Exkursionen im Kaiserstuhl und Hegau. *Fortschritte der Mineralogie* **62**, 2–35.

Keller, J. (1989). Extrusive carbonatites and their significance. In: Bell, K. (ed.) *Carbonatites: genesis and Evolution*. London: Unwin Hyman, pp. 70–88.

Keller, J., Brey, G., Lorenz, V., Sachs, P. & Schleicher, H. (1990). Pre-conference excursion 2A: volcanism and petrology of the Upper Rhinegraben (Urach-Hegau-Kaiserstuhl). *IAVCEI International Volcanic Congress Mainz*, p. 60.

Keppler, H. (2003). Water solubility in carbonatite melts. *American Mineralogist* **88**, 1822–1824.

Ketcham, R. A. (2015). Calculation of stoichiometry from EMP data for apatite and other phases with mixing on monovalent anion sites. *American Mineralogist* **100**, 1620–1623.

Kharlomov, Y. S. (1981). Origin of carbonatites of the Kovdor deposit. *International Geology Review* **23**, 865–880.

Kirchheimer, F. (1973). Weitere Mitteilungen über das Vorkommen radioaktiver Substanzen in Süddeutschland. *Jahresheft des Geologischen Landesamtes Baden-Württemberg* **15**, 33–125.

Klemme, S. & Dalpé, C. (2003). Trace-element partitioning between apatite and carbonatite melt. *American Mineralogist* **88**, 639–646.

Kogarko, L. N., Ryabchikov, I. D. & Kuzmin, D. V. (2012). High-Ba mica in olivinites of the Guli massif (Maimecha–Kotui province, Siberia). *Russian Geology and Geophysics* **53**, 1209–1215.

Kono, Y., Kenney-Benson, C., Hummer, D., Ohfuji, H., Park, C., Shen, G., Wang, Y., Kavner, A. & Manning, C. E. (2014). Ultralow viscosity of carbonate melts at high pressures. *Nature Communications* **5**, 5091.

Kraml, M., Pik, R., Rahn, M., Selbekk, R., Carignan, J. & Keller, J. (2006). A new multi-mineral age reference material for 40Ar/39Ar,(U-Th)/He and fission track dating methods: The Limberg t3 Tuff. *Geostandards and Geoanalytical Research* **30**, 73–86.

Krasnova, N., Balaganskaya, E. & Garcia, D. (2004). Kovdor - classic phoscorites and carbonatites. In: Wall, F. & Zaitev, A. N. (eds) *Phoscorites and Carbonatites from Mantle to Mine: The Key Example of the Kola Alkaline Province.* London, GB: Mineralogical Society of Great Britain and Ireland, pp. 99–132.

Le Maitre, R., Streckeisen, A., Zanettin, B., Le Bas, M., Bonin, B., Bateman, P., Bellieni, G., Dudek, A., Efremova, A. & Keller, J. (2002). Igneous rocks. A classification and glossary of terms. *Recommendations of the IUGS Subcomission on the Systematics of Igneous Rocks.* Cambridge: Cambridge University Press, p. 236.

Lee, M., Garcia, D., Moutte, J., Williams, C. & Wall, F. (2004). Carbonatites and phoscorites from the Sokli Complex, Finland. In: Wall, F. & Zaitev, A. N. (eds) *Phoscorites and Carbonatites from Mantle to Mine: The Key Example of the Kola Alkaline Province.* London, UK: Mineralogical Society, pp. 133–162.

Lee, M. J., Garcia, D., Moutte, J. & Lee, J. I. (2003). Phlogopite and tetraferriphlogopite from phoscorite and carbonatite associations in the Sokli massif, Northern Finland. *Geosciences Journal* **7**, 9–20.

Libourel, G. (1999). Systematics of calcium partitioning between olivine and silicate melt: implications for melt structure and calcium content of magmatic olivines. *Contributions to Mineralogy and Petrology* **136**, 63–80.

Locock, A. J. (2008). An Excel spreadsheet to recast analyses of garnet into end-member components and a synopsis of the crystal chemistry of natural silicate garnets. *Computers & Geosciences* **34**, 1769–1780.

Massuyeau, M., Gardès, E., Morizet, Y. & Gaillard, F. (2015). A model for the activity of silica along the carbonatite–kimberlite–mellilitite–basanite melt compositional joint. *Chemical Geology* **418**, 206–216.

McCormick, G. R. & Heathcote, R. C. (1987). Mineral chemistry and petrogenesis of carbonatite intrusions, Perry and Conway Counties, Arkansas. *American Mineralogist* **72**, 59–66.

McCormick, G. R. & Le Bas, M. J. (1996). Phlogopite crystallization in carbonatitic magmas from Uganda. *The Canadian Mineralogist* **34**, 469–478.

Mitchell, R. H. (2005). Carbonatites and carbonatites and carbonatites. *The Canadian Mineralogist* **43**, 2049–2068.

Moore, M., Chakhmouradian, A. R., Mariano, A. N. & Sidhu, R. (2015). Evolution of rare-earth mineralization in the Bear Lodge carbonatite, Wyoming: Mineralogical and isotopic evidence. *Ore Geology Reviews* **64**, 499–521.

Nesbitt, B. E. & Kelly, W. C. (1977). Magmatic and hydrothermal inclusions in carbonatite of the Magnet Cove Complex, Arkansas. *Contributions to Mineralogy and Petrology* **63**, 271–294.

Neumann, R. & Medeiros, E. B. (2015). Comprehensive mineralogical and technological characterisation of the Araxá (SE Brazil) complex REE (Nb-P) ore and the fate of its processing. *International Journal of Mineral Processing* **144**, 1–10.

Panina, L. I. (2005). Multiphase carbonate-salt immiscibility in carbonatite melts: data on melt inclusions from the Krestovskiy massif minerals (Polar Siberia). *Contributions to Mineralogy and Petrology* **150**, 19–36.

Reguir, E., Chakhmouradian, A., Halden, N., Malkovets, V. & Yang, P. (2009). Major-and trace-element compositional variation of phlogopite from kimberlites and carbonatites as a petrogenetic indicator. *Lithos* **112**, 372–384.

Reguir, E. P., Chakhmouradian, A. R., Pisiak, L., Halden, N. M., Yang, P., Xu, C., Kynický, J. & Couëslan, C. G. (2012). Trace-element composition and zoning in clinopyroxene-and amphibole-group minerals: implications for element partitioning and evolution of carbonatites. *Lithos* **128**, 27–45.

Schleicher, H., Keller, J. & Kramm, U. (1990). Isotope studies on alkaline volcanics and carbonatites from the Kaiserstuhl, Federal Republic of Germany. *Lithos* **26**, 21–35.

Sigmund, J. (1996). Diatrembreccien, Mantelxenolithe und Karbonatite in der Kernbohrung KB 2 im Kaiserstuhl. PhD thesis, Albert-Ludwigs University, Freiburg, p. 154.

Sinclair, W. & Eggleton, R. (1982). Structure refinement of zirkelite from Kaiserstuhl, West Germany. *American Mineralogist* **67**, 615–620.

Sommerauer, J. & Katz-Lehnert, K. (1985). A new partial substitution mechanism of $CO_3^{2-}/CO_3OH^{3-}$ and $SiO_4^{4-}$ for the $PO_4^{3-}$ group in hydroxyapatite from the Kaiserstuhl alkaline complex (SW-Germany). *Contributions to Mineralogy and Petrology* **91**, 360–368.

Stoppa, F. & Lupini, L. (1993). Mineralogy and petrology of the Polino monticellite calciocarbonatite (Central Italy). *Mineralogy and Petrology* **49**, 213–231.

Teiber, H., Marks, M. A., Arzamastsev, A. A., Wenzel, T. & Markl, G. (2015). Compositional variation in apatite from various host rocks: clues with regards to source composition and crystallization conditions. *Neues Jahrbuch für Mineralogie - Abhandlungen* **192**, 151–167.

Treiman, A. H. & Essene, E. J. (1984). A periclase-dolomite-calcite carbonatite from the Oka complex, Quebec and its calculated volatile composition. *Contributions to Mineralogy and Petrology* **85**, 149–157.

Treiman, A. H. & Schedl, A. (1983). Properties of carbonatite magma and processes in carbonatite magma chambers. *The Journal of Geology* **91**, 437–447.

Van Wambeke, L. (1964). Geochemie minerale des carbonatites du Kaiserstuhl. In: Van Wambeke, L. (ed.) *Les Roches Alcalines et Les Carbonatites du Kaiserstuhl*. Brussels: European Atomic Energy Community (EURATOM). Mineralogy Geochemistry Section, pp. 65–92.

Vuorinen, J. H. & Skelton, A. D. (2004). Origin of silicate minerals in carbonatites from Alnö Island, Sweden: magmatic crystallization or wall rock assimilation? *Terra Nova* **16**, 210–215.

Wall, F. & Mariano, A. N. (1996). Rare earth minerals in carbonatites: a discussion centred on the Kangankunde Carbonatite, Malawi. In: Jones, A. P., Wall, F. & Williams, C. T. (eds) *Rare Earth Minerals: Chemestry, Origin and Ore Deposits. Mineralogical Society Series*. London: Chapman and Hall, pp. 193–226.

Walter, B. F., Parsapoor, A., Braunger, S., Marks, M. A. W., Wenzel, T., Martin, M. & Markl, G. (2018). Pyrochlore as a monitor for magmatic and hydrothermal processes in carbonatites from the Kaiserstuhl volcanic complex, SW Germany *Chemical Geology* **498**, 1–16.

Wang, L.-X., Marks, M. A., Wenzel, T., Von Der Handt, A., Keller, J., Teiber, H. & Markl, G. (2014). Apatites from the Kaiserstuhl Volcanic Complex, Germany: new constraints on the relationship between carbonatite and associated silicate rocks. *European Journal of Mineralogy* **26**, 397–414.

Weidendorfer, D., Schmidt, M. W. & Mattsson, H. B. (2017). A common origin of carbonatite magmas. *Geology* **45**, 507–510.

Williams, C. & Gieré, R. (1996). Zirconolite: a review of localities worldwide and a compilation of its chemical compositions. *Bulletin of the Natural History Museum London* **52**, 1.

Wilson, M. & Downes, H. (1991). Tertiary-Quaternary extension-related alkaline magmatism in western and central Europe. *Journal of Petrology* **32**, 811–849.

Wimmenauer, W. (1963). Beiträge zur Petrographie des Kaiserstuhls. *Teil VI: Die Karbonatite; Teil VII: Zur Petrogenese des Kaiserstuhls. Neues Jahrbuch der Mineralogie, Abhandlungen* **99**, 231–276.

Wimmenauer, W. (2003). Kaiserstuhl. In: *Geologische Karte Von Baden-Württemberg 1: 25.000 Mit Erläuterungen*. Freiburg: Landesamt für Geologie, Rohstoffe und Bergbau Baden-Württemberg.

Wolff, J. (1994). Physical properties of carbonatite magmas inferred from molten salt data and application to extraction patterns from carbonatite–silicate magma chambers. *Geological Magazine* **131**, 145–153.

Woolley, A. & Church, A. (2005). Extrusive carbonatites: a brief review. *Lithos* **85**, 1–14.

Woolley, A. R. & Kjarsgaard, B. A. (2008). *Carbonatite Occurrences of the World: Map and Database*. Geological Survey of Canada. Open File 5796.

Yang, K.-F., Fan, H.-R., Santosh, M., Hu, F.-F. & Wang, K.-Y. (2011). Mesoproterozoic carbonatitic magmatism in the Bayan Obo deposit, Inner Mongolia, North China: constraints for the mechanism of super accumulation of rare earth elements. *Ore Geology Reviews* **40**, 122–131.

Zaitsev, A. N., Wall, F. & Le Bas, M. J. (1998). REE-Sr-Ba minerals from the Khibina carbonatites, Kola Peninsula, Russia: their mineralogy, paragenesis and evolution. *Mineralogical Magazine* **62**, 225–250.

Ziegler, P. (1982). Triassic rifts and facies patterns in Western and Central Europe. *Geologische Rundschau* **71**, 747–772.

# Appendix VI

Submitted manuscript

*Study 6*

Braunger, S., Scharrer, M., Marks, M. A. W., Wenzel, T., Markl, G., submitted. Hydrothermal halite precipitation in mafic volcanic rocks: the case of the Buggingen salt deposit, SW Germany. Canadian Mineralogist.

# HYDROTHERMAL HALITE PRECIPITATION IN MAFIC VOLCANIC ROCKS: THE CASE OF THE BUGGINGEN SALT DEPOSIT, SW GERMANY

**SIMON BRAUNGER[§], MANUEL SCHARRER, MICHAEL A.W. MARKS, THOMAS WENZEL, AND GREGOR MARKL**

*Department of Geosciences, Eberhard-Karls-Universität Tübingen, Wilhelmstrasse 56, 72074 Tübingen, Germany*

[§] *Corresponding author e-mail address: simonbraunger@hotmail.com*

ABSTRACT

Dykes of primitive olivine melilitites and monchiquites intruded into a Rupelian (Palaeogene) potash salt deposit near Buggingen (SW Germany). Ocelli and amygdules reveal distinct mineral assemblages, depending on whether the dyke rocks are in direct contact to the potash layer or to bituminous shales (*Fish Shale*). Samples in contact with the potash salt layer show roundish textures that contain smectite±talc±chlorite, calcite, and in cases anhydrite and halite, while those close to the bituminous shale mainly comprise smectite, calcite, zeolites and analcime.

No textural or mineralogical evidence for high-temperature (magmatic) interaction between the dyke rocks and the evaporites was observed. This is presumably related to (i) a very low orthomagmatic water activity in the magma, which prevented exsolution of aqueous fluids and appreciable dissolution of the salt, and (ii) fast cooling of the magmas, inhibiting melting of the

salt deposits and potential liquid mingling and/or assimilation processes. Halite formation in the dyke rocks is rather related to a later, post-magmatic hydrothermal fluid that previously interacted with the salt-rich host rocks. Alteration of the initially glassy groundmass to smectites and zeolites caused an enrichment of Na in the residual fluid, but halite saturation was not reached, as recorded by the absence of groundmass halite. Only fluid rock interaction in mm-sized vugs caused halite-precipitation via desiccation by swelling of previously formed clay minerals. Locally, datolite formed in pseudomorphs after olivine. Its precipitation was controlled by Si and B supply provided by the breakdown of serpentine and smectite.

*Keywords: potash salt deposit, clay minerals, hydration, olivine melilitite, monchiquite*

## INTRODUCTION

Little is known about the interaction between silicate magmas and salt rocks, where the large chemical contrast provides potential for intense magmatic and hydothermal processes. Studies on basaltic rocks that intruded into the Zechstein evaporates (Upper Permian) of the Werra-Fulda region (Central Germany) report peperite textures and glassy halite inclusions that were interpreted to indicate carnallite-magma mingling (Schofield *et al.*, 2014) and partial melting of salts (Koch & Vogel, 1980). Hydrothermal redistribution of the salt is demonstrated by halite-bearing amygdules and altered ocelli (e.g. Koch, 1978, Knipping, 1989). Besides the Werra-Fulda region, primitive dyke rocks that contain halite-bearing amgydules/ocelli were also reported from the potash salt deposit at Buggingen in southwest Germany (e.g. Wimmenauer, 1951, Braitsch *et al.*, 1964, Hurrle, 1973, Esslinger, 1976, Hurrle, 1976). Despite a detailed petrographic investigation of the dyke rocks by Hurrle (1973), the precipitation mechanism for such salt textures was not investigated so far. Especially intriguing and not

understood is the fact that salt crystals do not occur in the groundmass but are restricted to amygdules/ocelli. We shed light on this peculiarity based on a detailed textural, mineralogical and mineral chemical characterization of the monchiquitic and olivine melilititic dyke rocks at the Buggingen salt deposit.

## GEOLOGY

The 4.5 m thick potash salt deposit near Buggingen is situated in the Upper Rhine Graben, about 25 km southwest of Freiburg (Fig. 1a), and was mined from 1928 to 1973 at a depth level of 800 to 1000 m (Esslinger, 1976). The deposit is of Rupelian age (34 to 28 Ma; Braitsch *et al.*, 1964, Sissingh, 1998), and is part of the Upper Saliferous Zone that consists of sylvite, halite, anhydrite and marl. It is underlain by brackish-marine calcite- and dolomite-bearing marls of the Middle Saliferous Zone (Zone fossilière). The hanging wall comprises evaporate-rich marls bearing anhydrite, gypsum and halite (Fig. 1b). A progression of the Paratethys and a subsequent regression is indicated by the uppermost layers which consist of bituminous marine shales (Fish Shale), marine-brackish (Meletta Beds) and limnic marls (Cyrena Marls). Unconformable Quaternary sediments (sands and gravel) cover the sequence. Magmatism of the Upper Rhine Graben and outside to the east at Urach and Hegau is part of the European Cenozoic Volcanic Province (Fig. 1a; Wilson & Downes, 1991). The famous Kaiserstuhl volcano (e.g. Braunger *et al.*, 2018, Walter *et al.*, 2018, Giebel *et al.*, 2019) is only 20 km away. The first dyke rocks at Buggingen were discovered during mining in 1936 and intruded along two fault zones: The dyke system consists of several olivine melilitites, with additional monchiquites in its western part. A rough estimate of the dyke rock age is given by the nearby, mineralogically similar olivine nephelinites at Eichstetten, Lehen and Mahlberg, which indicate an age of ~13-19 Ma (based on whole rock K-Ar, and U-Pb in perovskite; Baranyi *et al.*, 1976; Binder, personal communication).

## SAMPLE LOCALITIES

The investigated samples were provided by the Regierungspräsidium Freiburg, Landesamt für Geologie, Rohstoffe und Bergbau (Geological Survey of Baden-Württemberg) and were collected in the 1950´s and 1960´s. Samples from the western dyke zone were taken from the 793 m working horizon within the potash salt deposit and comprise olivine melilitites and monchiquites. At the eastern dyke zone, olivine melilitites in contact to the Fish Shale Zone were sampled in the shaft Heitersheim at a depth of 185-190 meters (Fig. 1b).

## METHODS

The investigated thin sections were prepared and polished completely dry (water-free) in order to prevent dissolution and redistribution of halite and sylvite. Mineral compositions were analyzed using a JEOL JXA8900 electron microprobe in wave-length dispersive mode at the Department of Geosciences, University of Tübingen (Germany) with an acceleration voltage of 20 kV and a beam current of 20 nA. Peak counting times for major elements were 16 s and between 30 and 60 s for minor elements while the background counting times were half as long. Natural and synthetic standards were used for calibration. Peak overlap corrections involving Ba-Ti, Ti-Ba, V-Ti, V-Cr, Al-Ba, F-Fe, Sm-Ce and Pr-La were implemented and the internal ZAF (for spinel group minerals, garnet, perovskite and titanite) or φ□z correction was applied for the raw data (Armstrong, 1991). Measurements were done with a focused beam except for amphibole and biotite which were measured with a 2 µm spot.

## MINERALOGY AND PETROGRAPHY

According to the guidelines of the International Union of Geological Sciences, Subcommission on the Systematics of Igneous Rocks (Le Maitre *et al.*, 2002), the two types of

dyke rocks at Buggingen are monchiquites and olivine melilitites (formerly also described as ankaratrites, a biotite-bearing variety of olivine nephelinites). In the following, the general mineral assemblages of the two dyke rock types as well as the mineralogical differences between dyke rocks associated with the Fish Shale and the potash salt layer are described in more detail. Paragenetic schemes summarize the crystallization sequence for the olivine melilitites and the monchiquites (Fig. 2) and representative mineral compositions for olivine, clinopyroxene, spinel group minerals, amphibole, biotite, garnet, titanite and perovskite are given (Tables 1-4).

*General mineral assemblages*

*Olivine melilitite* Precursor olivine macrocrysts of up to 1 mm in size are completely altered (Fig. 3a) and replaced by serpentine minerals and smectites (nontronite-saponite; note that the identification of smectites in this study is based on X-ray diffraction analyses of Hurrle, 1973). Diopsidic clinopyroxene (50-80 mol %) typically forms small needles and is only rarely present as phenocrysts (Fig. 3b). Chromian spinel (up to 1.1 wt.% $Cr_2O_3$) occurs as inclusions in olivine pseudomorphs (Fig. 3c) and in the groundmass, where it commonly shows a sieve-like texture (Fig. 3d) frequently overgrown by magnetite (<0.5 apfu Ti; Fig. 3c). In sample M110 and M156, some magnetites show an atoll-shaped texture with a core of garnet (schorlomite-morimotoite-grossular solid solutions) or titanite (Fig. 3e). Groundmass melilite is completely altered to chlorite (Fig. 3f). In some samples, purple pseudomorphs after haüyne were found which consist of a very fine-grained mixture of unidentified secondary minerals (Fig. 3g). Further groundmass constituents are apatite needles and interstitial biotite (Fig. 3h). The latter can be distinguished into a Mg-rich ($X_{Mg}$=0.7-0.8) and a Fe-rich ($X_{Mg}$=0.0-0.6) variety (Table 3). Much of the formerly glassy groundmass consists of very fine-grained secondary minerals including smectites, zeolites, calcite and chlorite.

Based on whole-rock analyses, Wimmenauer (1951) suggested that the fine-grained groundmass originally consisted of melilite, leucite and nepheline.

*Monchiquite* Monchiquites contain up to 3 mm large, sub- to anhedral and partly rounded olivine macrocrysts (Fig. 4a) that are heavily altered and commonly replaced by serpentine minerals and smectites (nontronite; Hurrle, 1973). The olivine relicts tend to higher forsterite components ($Fo_{92}$ to $Fo_{83}$), higher Ni (0.28-0.37 wt.% NiO) and lower Ca (0.02-0.12 wt.% CaO) concentrations compared to olivine microphenocrysts of the groundmass ($Fo_{87}$ to $Fo_{84}$; 0.17-0.32 wt.% NiO; 0.1-0.3 wt.% CaO; Fig.4b). Diopsidic clinopyroxene (50-80 mol %) forms several mm large, euhedral to subhedral macrocrysts, which typically consist of a bright sieved core, a plain transitional zone and a brown rim (Fig. 4c). Occasionally, there is an irregularly shaped bright clinopyroxene generation within the sieved core (Fig. 4d) which reveals the highest enstatite component (7-20 mol %) and the highest Cr concentrations (up to 1.65 wt.% $Cr_2O_3$). Green core clinopyroxenes are rare (Fig. 4e). The groundmass is dominated by brown elongated clinopyroxene grains. Chromian spinel (up to 1.1 wt.% $Cr_2O_3$) occurs as inclusions in olivine, the bright sieved clinopyroxene and within the groundmass where it sometimes reveals a sieve texture. Titanomagnetite (up to 0.6 apfu Ti) only is present in the groundmass. The groundmass additionally comprises partly altered glass (fine-grained zeolites, calcite, chlorite, talc), apatite, small tabular kaersutite and biotite ($X_{Mg}$=0.4-0.6; Fig. 4b; Table 3). Notable are roundish areas consisting of chlorite, talc and calcite which are surrounded by a zone of amphiboles and biotite grains (Fig. 4f).

*Textural and mineralogical differences of the dyke rocks depending on the host rock (bituminous shales versus potash salt layers)*

Both olivine melilitites and monchiquites contain roundish textures (Fig. 5). In olivine melilitites, the spheroidal to sometimes lobate textures contain diopside and perovskite at the

146 marginal zones and Hurrle (1973) described additional melilite and nepheline. Hence, these
147 spheroids are interpreted as ocelli that represent immiscible droplets of a "carbonatitic" magma.
148 However, some roundish textures in these rocks do not show any indication for primary
149 magmatic mineral phases and presumably represent refilled amygdules. The spheroids in
150 monchiquites show a concentric texture and lack evidence for magmatic mineral phases.
151 Consequently, they are interpreted as amygdules (c.f. Hurrle, 1973, Hurrle, 1976). Other
152 roundish areas that are surrounded by seams of biotite and amphibole resemble vitreous melt
153 residues that have subsequently been altered.

154

155 *Mineralization associated with the Fish Shale* At the contact to the Fish Shale, the
156 ocelli of the olivine melilitite comprise variable amounts of irregularly distributed aggregates
157 of smectite, natrolite and small amounts of calcite (Fig. 6a&b). Biotite may additionally occur
158 at the ocelli rim. The amygdules typically consist of a marginal zone of smectite and a centre
159 with variable amounts of tabular or needle-shaped natrolite (Fig. 6b&c), euhedral analcime and
160 late-stage calcite (Fig. 6d). In some amygdules, marginal smectite is missing (Fig. 6f). Pyrite
161 may occur at the rim of the ocelli (Fig. 6e), but also replaces parts of the groundmass (Fig. 6f).

162

163 *Mineralization associated with the potash salt layer* Ocelli of the olivine
164 melilitite associated with the potash salt deposit consist of marginal smectite and sometimes
165 biotite, while the central parts of the ocelli are dominated by halite (Fig. 7a). Hematite was
166 rarely found but then typically grew on top of the smectite seam (Fig. 7b). Tabular anhydrite
167 grains and barite are particularly common in sample M67 and M156 with the latter sample
168 additionally comprising small amounts of celestite (Fig. 7b). Notably, the ocelli margins of
169 sample M156 also contain isometric garnet with inclusions of small needle-shaped
170 clinopyroxene (Fig. 7c) and dark green aegirine needles replacing diopside (Fig. 7a).

171 Furthermore, sample M156 is characterized by halite pseudomorphs after olivine (Fig. 7d).
172 Datolite grains occur in altered olivine, either associated with halite (Fig. 7d) or serpentine and
173 smectite (Fig. 7e). Amygdules generally consist of a small rim of smectite minerals, marginal
174 calcite, sometimes anhydrite, and a core of halite (Fig. 7f).

175 The amygdules of the monchiquites have a concentric succession from rim to core consisting
176 of chlorite, smectite, talc, calcite and halite. A thin seam of pyrite sometimes occurs between
177 talc and halite (Fig. 7g). In some amygdules, halite is missing (Fig. 7h), which, however, may
178 be a 3-D-effect.

179

180 ## DISCUSSION

181 *Crystallization conditions*

182 The anhedral olivine macrocrysts of the monchiquits (forsterite content up to 92 %)
183 show high Ni (≥0.3 wt % NiO) and low Ca (≤0.1 wt. % CaO) concentrations which are typical
184 of mantle xenocrysts (Foley *et al.*, 2013, Bussweiler *et al.*, 2015). Moreover, depth estimates
185 were obtained by the clinopyroxene barometer of Nimis & Ulmer (1998) which was applied to
186 the various clinopyroxene types of the monchiquites (Fig. 8). White core clinopyroxenes
187 demonstrate high crystallization depths roughly between 40 and 20 km (depth estimates below
188 10 km are based on altered clinopyroxenes) and may represent mantle xenocrysts or early
189 orthomagmatic crystals. Green core clinopyroxenes presumably demonstrate the involvement
190 of percolative melts at lower crustal conditions (Pilet *et al.*, 2002). The sieve-like textured
191 clinopyroxenes (Fig. 4c) and spinels indicate a partial resorption of the macrocrysts during
192 magma ascent (e.g. Qi *et al.*, 1995, Shaw *et al.*, 2006). Groundmass clinopyroxenes
193 (transitional/brown clinopyroxenes) typically show values below those expected by an
194 overburden of ~1000 m (approximately 0.3 kbar) which may be related to the high uncertainty

of the calculated values (σ=1.75 kbar) and the fact that the barometer was initially calibrated for anhydrous systems. However, groundmass amphibole and mica in the monchiquites provide prove of a considerable water concentration of the melt at late stage conditions. Pressure estimates therefore are underestimated by ~1 kbar per wt.% $H_2O$ in the melt (Nimis & Ulmer, 1998). Based on coexisting olivine microphenocrysts and brown clinopyroxene, the groundmass temperature could be determined to approximately 950 °C (Andersen *et al.*, 1993).

*Reason for the absence of salt rock-magma interactions*

The large chemical contrast between the mafic dykes and the potash salts provide potential for intense assimilation and metasomatic processes. However, no textural or chemical differences in the magmatic mineral phases could be observed between the olivine melilitites in contact to the Fish Shale and those surrounded by the potash salt layer. Note, that slightly elevated Cl concentrations in biotite associated with the salt deposit (Table 3) may be caused by Cl diffusion into magmatically formed biotite (high $X_{Mg}$) during interaction with the NaCl-rich fluid, or may hint to a hydrothermal formation of biotite (low $X_{Mg}$). Sodium- and chlorine-rich mineral phases such as sodalite, which could be expected to form during magmatic interaction between a silica- undersaturated magma and salt rocks, are absent. Since spheroidal textures occur in all investigated dyke rocks, independent of the surrounding host rock, we exclude the possibility that the halite textures in these spheroidal structures demonstrate a salt-magma mingling, or even a salt-liquid immiscibility due to intense magmatic assimilation of the halite-bearing host rock. We suggest that the absence of salt rock-melt interactions is mainly related to two facts:

i) monchiquites and olivine melilitites are characterized by the absence of OH-bearing phenocryst minerals. Thus, the melts presumably had a rather low water activity during the orthomagmatic stage which prevented the exsolution of large amounts of fluids and a

220 subsequent dissolution of the salt rock. Moreover, carnallite, a hydrous salt mineral that already
221 decomposes at low temperatures <170 °C (Braitsch, 1971) is relatively rare in the salt deposit
222 of Buggingen, and hence could not provide significant amounts of water (Braitsch & Herrmann,
223 1964). However, the amount of primary brines in the host rock is uncertain.

224 ii) the dyke magma cooled rapidly. Knipping (1989) calculated the temperature for salt rocks
225 that were intruded by basaltic magmas in the Werra Fulda region. He assumed a dyke
226 thicknesses of 0.3, 1.0 and 1.8 m, a magma temperature of 1150 °C, and a wall rock temperature
227 of 50 °C. These parameters can also be applied to our study, where the dike widths vary between
228 a few cm to a maximum of 4 m (Esslinger, 1976), the magma temperature is estimated to be
229 above 950 °C, and the reported air temperature of the mine at 1000 m depth was about 50 °C
230 (Markl, 2017; we assume little erosion of the overburden since the intrusion of the dyke rocks).
231 Based on these input parameters, the calculated wall-rock temperature at the contact to the dyke
232 always remained below 790 °C, which prevented melting of halite and even sylvite (melting
233 point of ~800 and ~790 °C respectively). This coincides with the straight contact between the
234 salt rock and the dyke at Buggingen which does not indicate partial melting of the wall-rock.
235 However, at branching dykes, between (almost) contemporaneously emplaced intrusions, or if
236 salt fragments got entrapped into the magma, heat could act from more than one side and the
237 salt may locally have reached the melting temperature, as suggested by Koch & Vogel (1980)
238 in the Werra-Fulda region in Central Germany. From the same region, Schofield *et al.* (2014)
239 described some peperite structures at the contact between salt and dyke rocks which also
240 indicate a magmatic interaction. However, this process was caused by heating and dehydration
241 of carnallite, which is relatively rare at Buggingen (Braitsch & Herrmann, 1964).

242

*Fluid conditions*

The minimum temperature of the fluid responsible for the precipitation of halite in amygdules and ocelli was estimated to ~50 °C based on the current temperature of the mine at ~1000 m depth. Evidence for a somewhat higher minimum temperature of a hydrothermal event is shown by sample M156, where the presence of garnet and aegirine-rich clinopyroxene in the ocelli illustrates temperatures of at least 200 °C (Easton *et al.*, 1977, Decarreau *et al.*, 2004). Moreover, the core of atoll-shaped magnetite in sample M110 and M156 consists of garnet or titanite, and may demonstrate a replacement of Ti-rich magnetite by relatively hot fluids that penetrated the grain along cracks. However, a direct link between these relatively hot fluids and the halite-bearing spheroids is uncertain. While textural observations of Wimmenauer (1951) suggest that the salt layer in contact to the dyke rock is almost completely impoverished in KCl, Braitsch *et al.* (1964) demonstrated by chemical analyses that the contact zones still contain high KCl concentrations of up to 40 wt.%. We therefore suggest that the hydrothermal fluid contained a mixture of dissolved KCl and NaCl. Due to the high variations of the KCl concentration in the salt layers (between 3 and 40 wt.% KCl; Braitsch *et al.*, 1964), and the high temperature dependence of the KCl solubility (Braitsch, 1971), we omit a quantitative calculation for the salt content of the fluid.

The hydrothermal fluid that interacted with the olivine melilitites associated with the Fish Shale most likely equilibrated in this bituminous, pyrite-bearing marl (Böcker & Littke, 2014, Eichentopf *et al.*, 2017). This is consistent with the high amounts of zeolite, analcime and calcite in the ocelli and amygdule fillings, as well as with the presence of pyrite in the groundmass.

*The crystallization process for halite-bearing amygdules and ocelli*

Evaporation can be excluded as the precipitation mechanism for the hydrothermal formation of halite because the mafic dyke rocks were sampled at depth. In the following, we discuss a possible crystallization process for the halite-bearing spheroids (Fig. 9a). Due to the complex cation incorporation and adsorption capacity of smectites (e.g. Kloprogge *et al.*, 1999), the importance of kinetics (Gysi & Stefánsson, 2011) as well as the large number of uncertain parameters (e.g. fluid composition; fluid/dyke rock temperature; groundmass mineralogy of pristine dyke rocks), we chose not to construct a thermodynamic model of the fluid evolution. We present a geologically sound, but qualitative approach instead (Fig. 9b).

Assuming that the fine-grained groundmass of the monchiquites and the olivine melilitites mainly consisted of nepheline (as being typical of most silica-undersaturated primitive rocks), the hydrothermal alteration to clay minerals ± zeolites (Fig. 9a-1) should result in an increase of the sodium concentration of the fluid. Indeed, whole-rock analyses (after subtracting halite and anhydrite) of the heavily altered dyke rocks at Buggingen have lower Na concentrations than relatively fresh rock samples (Hurrle, 1973). In contrast, the K concentration of hydrothermally strongly overprinted rock samples is higher compared to the rather fresh dyke rocks. This also conforms with chemical analyses of the clay minerals, which typically consist of K-bearing smectites (Hurrle, 1973). Such a groundmass alteration process typically releases more Na than it consumes K (reaction 1),

$$2.33\ NaAlSiO_4\ (Nepheline) + 0.33\ K^+ + 1.34\ Si^{4+} + 2.66\ H_2O =$$

$$K_{0.33}Al_2Si_{3.67}Al_{0.33}O_{10}(OH)_2\ (K\text{-}smectite) + 2.33\ Na^+ + 3.34\ H^+ \quad \text{(reaction 1)}$$

The uptake of sodium into a salt-saturated fluid should immediately lead to the precipitation of halite. However, as no halite was observed in the groundmass (note that the thin sections were prepared completely dry, hence excluding a preparation-based salt dissolution), we suggest that

290 the initial fluid was not saturated with halite before penetrating the dyke rock, possibly due to
291 mixing and diluting with meteoric water. During interaction with the groundmass, the Na
292 concentration of the fluid steadily increased (while the K concentration decreased) but
293 obviously did not yet reach NaCl saturation. As soon as the fluid hit an amygdule, smectites
294 formed at the rim and the fluid became trapped (Fig. 9a-2). The Na concentration of the fluid
295 further increased during interaction with the marginal zone while the salt-rich fluids finally
296 desiccated in the vugs due to swelling of smectites (e.g. Usuki *et al.*, 1993). Consequently, NaCl
297 saturation was reached and halite precipitated in the vugs (Fig. 9a-3). In the amygdules, the
298 crystallization of talc additionally removed $H_2O$ from the fluid and drove it towards NaCl
299 saturation. A similar halite precipitation process can be assumed for the ocelli. In two olivine
300 melilitites, Hurrle (1973) found ocelli with only partly altered nepheline and a core of calcite,
301 which possibly demonstrates the primary magmatic ocelli filling. We assume that calcite
302 dissolved during interaction with the fluid, while smectites formed at the ocelli rim by alteration
303 of the marginal mineral assemblage of the ocelli (Fig. 10). Subsequent desiccation of the
304 trapped fluids by clay mineral swelling led to the crystallization of halite.

305 Smectite and zeolite formation in the groundmass presumably cemented possible fluid paths
306 (Fig. 9a-3), which would indicate that the salt-rich spheroids formed by a single hydrothermal
307 event. In amygdules, halite comprises up to ~12-20 vol.%, which is in the same order of
308 magnitude as the 16.5 vol.% halite that can precipitate from an NaCl-saturated (~30 wt.% NaCl)
309 fluid at ~50 °C, assuming equimolar $Na^+$ and $Cl^-$ (Driesner & Heinrich, 2007). As a
310 consequence, we suggest that the fluid was near NaCl saturation when it got trapped in the vugs
311 and finally desiccated by clay mineral swelling. Due to the uncertainty about the dissolved
312 amount of former mineral phases in the ocelli, we omit similar calculations for this spheroid
313 type.

The effect of clay mineral swelling is also illustrated by the mineral proportions in the ocelli/amygdules. Based on the simplified assumption, that the OH-bearing mineral phases of the ocelli/amygdules have an average volume of 140 $cm^3$/mol (halite 30 $cm^3$/mol; Blanc *et al.*, 2012 and references therein), and only contain 1 OH-group per formula unit (no interlayer water), the observed amount of smectite in the amygdules/ocelli (~85 vol.%) that formed due to the interaction between the spheroid rim and the NaCl-saturated fluid, is approximately 9 times too low. The absence of a prominent clay rim in some amygdules (Fig. 7f) implies that nearby clay minerals of the groundmass additionally bound $H_2O$ in their interlayers. Indeed, the lack of OH-bearing minerals at the amygdule rims is restricted to the olivine melilitites, which in contrast to the monchiquites, contain much more smectite minerals in the groundmass.

*Crystallization of datolite*

Datolite [$CaB(SiO_4)(OH)$] only occurs in one olivine melilitite sample (M156) as pseudomorphs after olivine, either associated with serpentine and smectite (Fig. 7e) or halite (Fig. 7d), but it is never present within ocelli. The required boron presumably derived from ocean-related sedimentary rocks (e.g. Leeman & Sisson, 1996, Garrett, 1998). The salt rocks at Buggingen are unlikely to represent the source of the boron since the concentrations are very low (< 10 ppm; Braitsch *et al.*, 1964), but the clay-rich layers of the salt horizon contain up to 600 ppm boron. Braitsch *et al.* (1964) did not believe in this boron source in the country rocks and suggested a magmatic origin since they could not detect significant variations in the boron content between the clay-rich layers in contact to the dyke rocks and those further away. However, we suggest that boron-leaching of the wall rock would have too little effect to be detectable, since boron is adsorbed by clays and should have been balanced again by circulating fluids over the course of the years. The high Ca concentration of the fluid required for the

crystallization of datolite most likely derived from the anhydrite-rich parts of the host rock, which is consistent with high amounts of anhydrite in ocelli of sample M156 (Fig. 7b).

The formation of datolite presumably was caused by a two-step process. This is in accordance with the restriction of datolite to only one rock sample of the present study (it has been found more often in other sample suites, though; Braitsch *et al.*, 1964, Markl, 2017), since clay mineral and zeolite precipitation generally cement the fluid paths. However, in case of sample M156, new cracks possibly formed due to tectonic stress (Wimmenauer, 1951). The first fluid batch equilibrated with the dyke rock by the alteration of olivine to serpentine and Mg-rich smectites (e.g. saponite; Hurrle, 1973). Boron thereby was incorporated into serpentine (e.g. Pabst *et al.*, 2011) and was adsorptively bound in the clay minerals (e.g. Gu & Lowe, 1990, Goldberg *et al.*, 1993, Karahan *et al.*, 2006). A second fluid batch which then was in disequilibrium with the olivine alteration phases dissolved serpentine and Mg-rich smectite. The high amounts of released boron and silica finally led to the crystallization of datolite grains. In contrast to the ocelli and amygdules, anhydrite is absent as presumably all available Ca was incorporated in datolite.

## SUMMARY AND CONCLUSION

No evidence for a magmatic interaction between the primitive dyke magma and the salt layers at Buggingen in SW Germany was observed. This is presumably related to (i) relatively dry orthomagmatic melt conditions and to (ii) a too fast cooling of the dyke. Instead, halite-bearing spheroids in the olivine melilitites and the monchiquites represent amygdules, respectively hydrothermally altered ocelli. Low temperature NaCl-bearing fluids from the surrounding salt layers reacted with the dyke rock groundmass, thereby forming smectites and zeolites. During alteration of the groundmass, the NaCl concentration of the fluid steadily increased but remained below NaCl saturation. As soon as the fluid hit a vug, smectites formed

at the margin and the fluid got trapped. Clay mineral swelling gradually consumed water from the fluid and finally led to the precipitation of halite. The presence of datolite is restricted to pseudomorphs after olivine. Serpentine/smectite breakdown provided the required Si and boron for its formation.

## ACKNOWLEDGMENTS

We would like to thank the Landesamt für Geologie, Rohstoffe und Bergbau (Geological Survey for Baden-Württemberg) in Freiburg for providing the rock samples studied here. This work was supported by the Deutsche Forschungsgemeinschaft (grant number MA2563/12–1).

## REFERENCES

ANDERSEN, D. J., LINDSLEY, D. H. & DAVIDSON, P. M. (1993). Quilf - a Pascal Program to Assess Equilibria among Fe-Mg-Mn-Ti Oxides, Pyroxenes, Olivine, and Quartz. *Computers & Geosciences* **19**, 1333-1350.

ARMSTRONG, J. T. (1991). Quantitative elemental analysis of individual microparticles with electron beam instruments. *Electron probe quantitation*: Springer, 261-315.

BARANYI, I., LIPPOLT, H. & TODT, W. (1976). Kalium-Argon-Altersbestimmungen an tertiären Vulkaniten des Oberrheingraben-Gebietes: II Die Alterstraverse vom Hegau nach Lothringen. *Oberrhein. Geol. Abh* **25**, 41-62.

BLANC, P., LASSIN, A., PIANTONE, P., AZAROUAL, M., JACQUEMET, N., FABBRI, A. & GAUCHER, E. C. (2012). Thermoddem: A geochemical database focused on low temperature water/rock interactions and waste materials. *Applied Geochemistry* **27**, 2107-2116.

BÖCKER, J. & LITTKE, R. (2014). Source rock characterisation and thermal maturity of the Rupelian Fish Shale (Bodenheim Fm./Hochberg Subfm.) in the central Upper Rhine Graben. *Zeitschrift der Deutschen Gesellschaft für Geowissenschaften* **165**, 247-273.

390 BRAITSCH, O. (1971). *Salt deposits their origin and composition*. Berlin-Heidelberg-New York:
391 Springer Verlag.
392 BRAITSCH, O., GUNZERT, G., WIMMENAUER, W. & THIEL, R. (1964). Über ein
393 Datolithvorkommen am Basaltkontakt im Kaliwerk Buggingen (Südbaden). *Beiträge*
394 *zur Mineralogie und Petrographie* **10**, 111-124.
395 BRAITSCH, O. & HERRMANN, A. G. (1964). Zur Geochemie des Broms in salinaren Sedimenten
396 Teil II: Die Bildungstemperaturen primärer Sylvin- und Carnallit-Gesteine. *Geochimica*
397 *et Cosmochimica Acta* **28**, 1081-1109.
398 BRAUNGER, S., MARKS, M. A. W., WALTER, B. F., NEUBAUER, R., REICH, R., WENZEL, T.,
399 PARSAPOOR, A. & MARKL, G. (2018). The Petrology of the Kaiserstuhl Volcanic
400 Complex, SW Germany: The Importance of Metasomatized and Oxidized Lithospheric
401 Mantle for Carbonatite Generation. *Journal of Petrology* **59**, 1731-1762.
402 BUSSWEILER, Y., FOLEY, S. F., PRELEVIC, D. & JACOB, D. E. (2015). The olivine macrocryst
403 problem: New insights from minor and trace element compositions of olivine from Lac
404 de Gras kimberlites, Canada. *Lithos* **220**, 238-252.
405 DECARREAU, A., PETIT, S., VIEILLARD, P. & DABERT, N. (2004). Hydrothermal synthesis of
406 aegirine at 200°C. *European Journal of Mineralogy* **16**, 85-90.
407 DÈZES, P., SCHMID, S. M. & ZIEGLER, P. A. (2004). Evolution of the European Cenozoic Rift
408 System: interaction of the Alpine and Pyrenean orogens with their foreland lithosphere.
409 *Tectonophysics* **389**, 1-33.
410 DRIESNER, T. & HEINRICH, C. A. (2007). The system H2O–NaCl. Part I: Correlation formulae
411 for phase relations in temperature–pressure–composition space from 0 to 1000°C, 0 to
412 5000bar, and 0 to 1 XNaCl. *Geochimica et Cosmochimica Acta* **71**, 4880-4901.
413 EASTON, A. J., HAMILTON, D., KEMPE, D. R. C., SHEPPARD, S. M. F. & AGRELL, S. O. (1977).
414 Low-Temperature Metasomatic Garnets in Marine Sediments [and Discussion].
415 *Philosophical Transactions of the Royal Society of London. Series A, Mathematical and*
416 *Physical Sciences* **286**, 253-271.
417 EICHENTOPF, H., BÖCKER, J. & LITTKE, R. (2017). Source rock characterisation of the Rupelian
418 Fish Shale (Bodenheim Fm./Hochberg Sbfm.)–An organic geochemical profile from the
419 clay pit. *Zeitschrift der Deutschen Gesellschaft für Geowissenschaften* **168**, 217-232.
420 ESSLINGER, G. (1976). Vorkommen und Tektonik der Basalte im Kalisalzlager Buggingen
421 (Südbaden). *Jahresheft des Geologischen Landesamtes in Baden-Württemberg* **18**, 7-
422 18.

FOLEY, S. F., PRELEVIC, D., REHFELDT, T. & JACOB, D. E. (2013). Minor and trace elements in olivines as probes into early igneous and mantle melting processes. *Earth and Planetary Science Letters* **363**, 181-191.

GARRETT, D. E. (1998). *Borates: Handbook of deposits, processing, properties, and use*: Elsevier.

GIEBEL, R. J., PARSAPOOR, A., WALTER, B. F., BRAUNGER, S., MARKS, M. A. W., WENZEL, T. & MARKL. (2019). Evidence for magma – wall rock interaction in carbonatites from the Kaiserstuhl Volcanic Complex (Southwest Germany). *Journal of Petrology*.

GOLDBERG, S., FORSTER, H. S. & HEICK, E. L. (1993). Boron Adsorption Mechanisms on Oxides, Clay Minerals, and Soils Inferred from Ionic Strength Effects. *Soil Science Society of America Journal* **57**, 704-708.

GU, B. & LOWE, L. E. (1990). STUDIES ON THE ADSORPTION OF BORON ON HUMIC ACIDS. *Canadian Journal of Soil Science* **70**, 305-311.

GYSI, A. P. & STEFÁNSSON, A. (2011). CO2–water–basalt interaction. Numerical simulation of low temperature CO2 sequestration into basalts. *Geochimica et Cosmochimica Acta* **75**, 4728-4751.

HURRLE, H. (1973). Ocelli-und Mandelbildung der Melilithankaratrite im Kalisalzlager Buggingen und im Kristallin des Schwarzwaldes. Verlag nicht ermittelbar.

HURRLE, H. (1976). Ocelli-und Mandelbildung der ultrabasischen Basalte im Kalisalzlager Buggingen und im Kristallin des Schwarzwaldes. *Jh. geol. Landesamt Baden-Württemberg* **18**, 19-37.

KARAHAN, S., YURDAKOÇ, M., SEKI, Y. & YURDAKOÇ, K. (2006). Removal of boron from aqueous solution by clays and modified clays. *Journal of Colloid and Interface Science* **293**, 36-42.

KLOPROGGE, J. T., KOMARNENI, S. & AMONETTE, J. E. (1999). Synthesis of Smectite Clay Minerals: A Critical Review. *Clays and Clay Minerals* **47**, 529-554.

KNIPPING, B. J. (1989). Basalt Intrusions in Evaporites. *Lecture Notes in Earth Sciences, Berlin Springer Verlag* **24**.

KOCH, K. (1978). Zur Entstehung von Tonmineralen im Kontaktbereich Basalt-Salinar. *Z. geol. Wiss* **6**, 733-747.

KOCH, K. & VOGEL, J. (1980). Zu den Beziehungen von Tektonik, Silvinitbildung und Basaltintrusion im Werra-Kaligebiet (DDR): mit 2 Tabellen. Dt. Verlag für Grundstofindustrie.

456 LE MAITRE, R., STRECKEISEN, A., ZANETTIN, B., LE BAS, M., BONIN, B., BATEMAN, P.,
457 BELLIENI, G., DUDEK, A., EFREMOVA, A. & KELLER, J. (2002). Igneous rocks. A
458 classification and glossary of terms. Recommendations of the IUGS Subcomission on
459 the Systematics of Igneous Rocks. Cambridge University Press, Cambridge.
460 LEEMAN, W. & SISSON, V. (1996). Geochemistry of boron and its implications for crustal and
461 mantle processes. Boron: mineralogy, petrology and geochemistry. *Rev. Mineral.* **33**,
462 645-708.
463 MARKL, G. (2017). *Schwarzwald-Lagerstätten und Mineralien aus vier Jahrhunderten-Band 4-*
464 *Südlicher Schwarzwald*. Salzhemmendorf-Lauenstein, Germany: Bodeverlag.
465 NIMIS, P. & ULMER, P. (1998). Clinopyroxene geobarometry of magmatic rocks Part 1: An
466 expanded structural geobarometer for anhydrous and hydrous, basic and ultrabasic
467 systems. *Contributions to Mineralogy and Petrology* **133**, 122-135.
468 PABST, S., ZACK, T., SAVOV, I. P., LUDWIG, T., ROST, D. & VICENZI, E. P. (2011). Evidence for
469 boron incorporation into the serpentine crystal structure. *American Mineralogist* **96**,
470 1112-1119.
471 PILET, S., HERNANDEZ, J. & VILLEMANT, B. (2002). Evidence for high silicic melt circulation
472 and metasomatic events in the mantle beneath alkaline provinces: the Na–Fe-augitic
473 green-core pyroxenes in the Tertiary alkali basalts of the Cantal massif (French Massif
474 Central). *Mineralogy and Petrology* **76**, 39-62.
475 QI, Q. U., TAYLOR, L. A. & ZHOU, X. (1995). Petrology and Geochemistry of Mantle Peridotite
476 Xenoliths from SE China. *Journal of Petrology* **36**, 55-79.
477 SCHOFIELD, N., ALSOP, I., WARREN, J., UNDERHILL, J. R., LEHNÉ, R., BEER, W. & LUKAS, V.
478 (2014). Mobilizing salt: Magma-salt interactions. *Geology* **42**, 599-602.
479 SHAW, C. S. J., HEIDELBACH, F. & DINGWELL, D. B. (2006). The origin of reaction textures in
480 mantle peridotite xenoliths from Sal Island, Cape Verde: the case for "metasomatism"
481 by the host lava. *Contributions to Mineralogy and Petrology* **151**, 681.
482 SISSINGH, W. (1998). Comparative Tertiary stratigraphy of the Rhine Graben, Bresse Graben
483 and Molasse Basin: correlation of Alpine foreland events. *Tectonophysics* **300**, 249-284.
484 USUKI, A., KAWASUMI, M., KOJIMA, Y., OKADA, A., KURAUCHI, T. & KAMIGAITO, O. (1993).
485 Swelling behavior of montmorillonite cation exchanged for ω-amino acids by ∈-
486 caprolactam. *Journal of Materials Research* **8**, 1174-1178.
487 WALTER, B. F., PARSAPOOR, A., BRAUNGER, S., MARKS, M. A. W., WENZEL, T., MARTIN, M. &
488 MARKL, G. (2018). Pyrochlore as a monitor for magmatic and hydrothermal processes

in carbonatites from the Kaiserstuhl volcanic complex (SW Germany). *Chemical geology* **498**, 1-16.

WILSON, M. & DOWNES, H. (1991). Tertiary—Quaternary extension-related alkaline magmatism in western and central Europe. *Journal of Petrology* **32**, 811-849.

WIMMENAUER, W. (1951). Petrographische Untersuchungen über das Ankaratrit-Vorkommen, im Kalisalzlager von Buggingen in Baden. Mitt. *Bl. bad. geol. Landesamt*, 117-128.

TABLE 1. REPRESENTATIVE EPMA ANALYSES OF OLIVINE AND CLINOPYROXENE

| Rock type | Monchiquite | | | | | | | | | Olivine melilitite | | | |
|---|---|---|---|---|---|---|---|---|---|---|---|---|---|
| Sample # | M164 | M63 | M13 | 8111 | 8111 | M164 | M13 | M63 | M13 | M34 | M156 | M109 | M110 |
| Association | Potash salt | | | | | | | | | Potash salt | | Fish Shale | |
| Mineral | Olivine | | | | Clinopyroxene | | | | | Clinopyroxene | | | |
| Mineral type | Large-anhedral | | Small-euhedral | | White core | Sieved | Transitional | Brown | Green core | | | | |
| Location | core | rim | core | rim | | | | | | Groundmass | Ocellus | Groundmass | Ocellus |
| wt.% | | | | | | | | | | | | | |
| $SiO_2$ | 41.74 | 41.16 | 40.87 | 40.83 | 52.76 | 49.94 | 42.33 | 47.39 | 50.21 | 46.45 | 46.72 | 47.62 | 47.71 |
| $TiO_2$ | na | na | na | na | 0.61 | 1.42 | 4.69 | 3.03 | 0.91 | 2.87 | 3.46 | 2.45 | 3.36 |
| $ZrO_2$ | na | na | na | na | bdl | bdl | 0.04 | 0.03 | 0.07 | 0.06 | 0.06 | bdl | 0.14 |
| $Al_2O_3$ | bdl | 0.03 | 0.07 | 0.05 | 3.88 | 4.70 | 9.67 | 6.05 | 5.32 | 5.94 | 5.02 | 5.10 | 4.71 |
| $Cr_2O_3$ | na | na | na | na | 0.80 | 1.12 | 0.23 | bdl | bdl | bdl | bdl | 0.10 | bdl |
| $Fe_2O_3$* | | | | | 1.23 | 2.43 | 5.67 | 2.51 | 4.08 | 4.83 | 4.28 | 4.88 | 3.52 |
| FeO* | 7.50 | 10.74 | 11.83 | 11.67 | 2.93 | 2.33 | 2.41 | 4.71 | 6.83 | 2.54 | 3.45 | 1.63 | 2.57 |
| MnO | 0.14 | 0.18 | 0.16 | 0.16 | 0.14 | 0.06 | 0.06 | 0.11 | 0.25 | 0.09 | 0.15 | 0.12 | 0.16 |
| MgO | 50.52 | 47.67 | 47.25 | 46.65 | 17.26 | 14.88 | 11.50 | 13.02 | 10.21 | 13.20 | 12.90 | 13.83 | 13.86 |
| NiO | 0.34 | 0.31 | 0.20 | 0.27 | na | na | na | na | na | na | na | na | na |
| CaO | 0.02 | 0.12 | 0.18 | 0.19 | 20.11 | 23.04 | 23.10 | 22.62 | 20.59 | 23.69 | 23.41 | 24.32 | 23.78 |
| $Na_2O$ | na | na | na | na | 0.87 | 0.55 | 0.49 | 0.52 | 1.99 | 0.36 | 0.51 | 0.34 | 0.48 |
| $K_2O$ | na | na | na | na | bdl | bdl | bdl | bdl | bdl | bdl | 0.02 | bdl | bdl |
| Total | 100.27 | 100.20 | 100.55 | 99.82 | 100.59 | 100.48 | 100.19 | 99.99 | 100.45 | 100.03 | 99.98 | 100.40 | 100.30 |
| *Formula based on 4 oxygens (olivine), respectively 4 cations and 6 oxygens (clinopyroxene)* | | | | | | | | | | | | | |
| Si | 1.01 | 1.01 | 1.00 | 1.01 | 1.90 | 1.83 | 1.59 | 1.77 | 1.87 | 1.73 | 1.75 | 1.76 | 1.77 |
| Ti | na | na | na | na | 0.02 | 0.04 | 0.13 | 0.08 | 0.03 | 0.08 | 0.10 | 0.07 | 0.09 |
| Zr | na | na | na | na | bdl | bdl | 0.00 | 0.00 | 0.00 | 0.00 | 0.00 | bdl | 0.00 |
| Al | 0.00 | 0.00 | 0.00 | 0.00 | 0.16 | 0.20 | 0.43 | 0.27 | 0.23 | 0.26 | 0.22 | 0.22 | 0.21 |
| Cr | na | na | na | na | 0.02 | 0.03 | 0.01 | bdl | bdl | bdl | bdl | 0.00 | bdl |
| $Fe^{3+}$ | | | | | 0.03 | 0.07 | 0.16 | 0.07 | 0.11 | 0.14 | 0.12 | 0.14 | 0.10 |
| $Fe^{2+}$ | 0.15 | 0.22 | 0.24 | 0.24 | 0.09 | 0.07 | 0.08 | 0.15 | 0.21 | 0.08 | 0.11 | 0.05 | 0.08 |
| Mn | 0.00 | 0.00 | 0.00 | 0.00 | 0.00 | 0.00 | 0.00 | 0.00 | 0.01 | 0.00 | 0.00 | 0.00 | 0.01 |
| Mg | 1.82 | 1.74 | 1.73 | 1.72 | 0.93 | 0.81 | 0.64 | 0.72 | 0.57 | 0.73 | 0.72 | 0.76 | 0.77 |
| Ni | 0.01 | 0.01 | 0.00 | 0.01 | na | na | na | na | na | na | na | na | na |
| Ca | 0.00 | 0.00 | 0.00 | 0.00 | 0.78 | 0.90 | 0.93 | 0.90 | 0.82 | 0.95 | 0.94 | 0.96 | 0.94 |
| Na | na | na | na | na | 0.06 | 0.04 | 0.04 | 0.04 | 0.14 | 0.03 | 0.04 | 0.02 | 0.03 |
| K | na | na | na | na | bdl | bdl | bdl | bdl | bdl | bdl | 0.00 | bdl | bdl |
| Total cations | 2.00 | 2.00 | 2.00 | 2.00 | 4.00 | 4.00 | 4.00 | 4.00 | 4.00 | 4.00 | 4.00 | 4.00 | 4.00 |

na: not analyzed; bdl: below detection limit; *Fe2O3-FeO ratio for clinopyroxene was calculated.

TABLE 2. REPRESENTATIVE EPMA ANALYSES OF SPINEL GROUP MINERALS

| Rock type | Monchiquite | | | Olivine melilitite | | | | | | |
|---|---|---|---|---|---|---|---|---|---|---|
| Sample # | M164 | M13 | M13 | M34 | M156 | M34 | M67 | M89 | M110 | M110 |
| Association | Potash salt | | | Potash salt | | | | Fish Shale | | |
| Mineral | Chromite | Spinel | Magnetite | Chromite | Spinel | Magnetite | Magnetite (altered) | Spinel | Magnetite | Magnetite (altered) |
| wt.% | | | | | | | | | | |
| $SiO_2$ | 0.10 | 0.11 | 0.13 | 0.08 | 0.11 | 0.13 | 0.09 | 0.11 | 0.19 | 0.15 |
| $TiO_2$ | 4.05 | 1.70 | 17.86 | 1.69 | 4.75 | 12.10 | 8.53 | 4.67 | 7.28 | 12.10 |
| $Al_2O_3$ | 9.52 | 26.13 | 6.27 | 11.76 | 16.42 | 6.68 | 0.34 | 18.03 | 9.58 | 0.64 |
| $V_2O_3$ | 0.19 | 0.15 | 0.38 | 0.08 | 0.12 | 0.12 | 0.30 | 0.11 | 0.19 | 0.25 |
| $Cr_2O_3$ | 40.25 | 33.04 | 0.00 | 43.92 | 19.37 | 0.07 | bdl | 20.51 | 16.58 | bdl |
| $Fe_2O_3$* | 15.13 | 27.34 | 29.20 | 13.86 | 26.74 | 41.88 | 51.39 | 24.95 | 30.46 | 43.61 |
| FeO* | 20.95 | 24.61 | 40.53 | 16.97 | 20.83 | 29.50 | 38.14 | 19.88 | 27.92 | 38.90 |
| MnO | 0.17 | 0.10 | 0.65 | 0.13 | 0.28 | 0.52 | 0.59 | 0.24 | 0.88 | 2.73 |
| MgO | 10.46 | 13.99 | 4.93 | 11.93 | 11.40 | 8.72 | 0.11 | 12.36 | 7.27 | 0.09 |
| NiO | 0.28 | 0.22 | 0.03 | 0.10 | 0.10 | 0.07 | 0.02 | 0.11 | 0.03 | 0.02 |
| ZnO | 0.09 | 0.11 | 0.08 | 0.09 | 0.07 | 0.06 | 0.05 | 0.07 | 0.12 | 0.46 |
| Total | 101.18 | 101.09 | 100.05 | 100.59 | 100.20 | 99.85 | 99.56 | 101.03 | 100.48 | 98.94 |
| *Formula based on 3 cations and 4 oxygens* | | | | | | | | | | |
| Si | 0.00 | 0.00 | 0.00 | 0.00 | 0.00 | 0.00 | 0.00 | 0.00 | 0.01 | 0.01 |
| Ti | 0.10 | 0.04 | 0.47 | 0.04 | 0.11 | 0.31 | 0.25 | 0.11 | 0.19 | 0.35 |
| Al | 0.37 | 0.92 | 0.26 | 0.45 | 0.62 | 0.27 | 0.02 | 0.67 | 0.38 | 0.03 |
| V | 0.00 | 0.00 | 0.01 | 0.00 | 0.00 | 0.00 | 0.00 | 0.00 | 0.00 | 0.00 |
| Cr | 1.05 | 0.78 | 0.00 | 1.12 | 0.49 | 0.00 | bdl | 0.51 | 0.45 | bdl |
| $Fe^{3+}$ | 0.37 | 0.21 | 0.78 | 0.34 | 0.65 | 1.09 | 1.48 | 0.59 | 0.78 | 1.26 |
| $Fe^{2+}$ | 0.58 | 0.41 | 1.20 | 0.46 | 0.56 | 0.85 | 1.22 | 0.52 | 0.80 | 1.25 |
| Mn | 0.00 | 0.00 | 0.02 | 0.00 | 0.01 | 0.02 | 0.02 | 0.01 | 0.03 | 0.09 |
| Mg | 0.51 | 0.62 | 0.26 | 0.58 | 0.55 | 0.45 | 0.01 | 0.58 | 0.37 | 0.01 |
| Ni | 0.01 | 0.01 | 0.00 | 0.00 | 0.00 | 0.00 | 0.00 | 0.00 | 0.00 | 0.00 |
| Zn | 0.00 | 0.00 | 0.00 | 0.00 | 0.00 | 0.00 | 0.00 | 0.00 | 0.00 | 0.01 |
| Total cations | 3.00 | 3.00 | 3.00 | 3.00 | 3.00 | 3.00 | 3.00 | 3.00 | 3.00 | 3.00 |

bdl: below detection limit; *Fe2O3-FeO ratio was calculated.

TABLE 3. REPRESENTATIVE EPMA ANALYSES OF AMPHIBOLE AND MICA

| Rock type | Monchiquite | | | | | Olivine melilitite | | | | | |
|---|---|---|---|---|---|---|---|---|---|---|---|
| Sample # | M63 | M63 | 8111 | M13 | M63 | M34 | M156 | M156 | M89 | M110 | M89 |
| Association | Potash salt | | | | | Potash salt | | | Fish Shale | | |
| Mineral | Amphibole | | | Mica | | Mica | | | | | |
| Location | Groundmass | | | | | Groundmass | Ocellus | | Groundmass | Ocellus | Groundmass |
| wt.% | | | | | | | | | | | |
| $SiO_2$ | 36.53 | 36.07 | 36.20 | 33.28 | 33.50 | 35.59 | 35.77 | 36.77 | 33.36 | 36.43 | 37.99 |
| $TiO_2$ | 6.85 | 7.41 | 7.87 | 8.35 | 6.82 | 5.50 | 5.54 | 2.97 | 7.19 | 5.84 | 6.60 |
| $ZrO_2$ | 0.05 | 0.04 | 0.04 | bdl | 0.02 | 0.02 | 0.02 | 0.02 | bdl | bdl | bdl |
| $Al_2O_3$ | 13.75 | 15.00 | 14.02 | 16.23 | 15.58 | 14.11 | 15.05 | 6.97 | 14.70 | 14.26 | 7.44 |
| $Cr_2O_3$ | bdl | 0.03 | bdl | bdl | bdl | bdl | bdl | bdl | bdl | bdl | bdl |
| $Fe_2O_3$* | 7.12 | 8.99 | 7.96 | | | | | | | | |
| FeO* | 9.74 | 4.16 | 5.94 | 13.87 | 19.16 | 12.15 | 10.55 | 31.05 | 12.26 | 9.29 | 23.41 |
| MnO | 0.30 | 0.16 | 0.26 | 0.14 | 0.19 | 0.25 | 0.18 | 0.63 | 0.25 | 0.14 | 0.65 |
| MgO | 8.56 | 10.92 | 10.38 | 12.66 | 9.79 | 16.75 | 17.48 | 8.39 | 15.07 | 18.92 | 9.24 |
| CaO | 11.38 | 11.45 | 11.44 | 0.11 | 0.09 | 0.04 | 0.07 | 0.22 | 0.24 | 0.04 | 0.10 |
| BaO | 0.33 | 0.45 | 0.51 | 3.67 | 3.21 | 2.27 | 3.26 | 1.00 | 4.81 | 3.32 | 0.59 |
| $Na_2O$ | 2.54 | 2.42 | 2.21 | 0.94 | 0.80 | 0.48 | 0.48 | 0.15 | 0.43 | 0.55 | 0.33 |
| $K_2O$ | 1.61 | 1.73 | 1.87 | 7.24 | 7.66 | 8.68 | 8.39 | 8.87 | 7.87 | 8.41 | 9.09 |
| F | 0.17 | 0.22 | 0.13 | 0.35 | 0.34 | 0.45 | 0.64 | 0.29 | 0.72 | 0.98 | 0.64 |
| Cl | 0.10 | 0.09 | 0.08 | 0.04 | 0.11 | 0.04 | 0.06 | 0.04 | bdl | 0.02 | bdl |
| $H_2O$** | 0.73 | 0.52 | 0.53 | 3.65 | 3.58 | 3.70 | 3.65 | 3.54 | 3.49 | 3.54 | 3.39 |
| -O≡F,Cl | 0,09 | 0.11 | 0.07 | 0.15 | 0.17 | 0.20 | 0.28 | 3.84 | 0.30 | 0.41 | 0.27 |
| Total | 99.66 | 99.54 | 99.36 | 100.38 | 100.67 | 99.84 | 100.86 | 100.79 | 100.09 | 101.32 | 99.18 |
| *Formula based on 16 cations and 23 oxygens (Amphibole), respectively 22 oxygens (Mica)* | | | | | | | | | | | |
| Si | 5.64 | 5.49 | 5.56 | 5.03 | 5.17 | 5.34 | 5.29 | 5.96 | 5.10 | 5.33 | 6.00 |
| Ti | 0.80 | 0.85 | 0.91 | 0.95 | 0.79 | 0.62 | 0.62 | 0.36 | 0.83 | 0.64 | 0.78 |
| Zr | 0.00 | 0.00 | 0.00 | bdl | 0.00 | 0.00 | 0.00 | 0.00 | 0.00 | bdl | bdl |
| Al | 2.50 | 2.69 | 2.54 | 2.89 | 2.83 | 2.49 | 2.63 | 1.33 | 2.65 | 2.46 | 1.38 |
| Cr | bdl | 0.00 | bdl | bdl | bdl | bdl | bdl | bdl | bdl | bdl | bdl |
| $Fe^{3+}$ | 0.82 | 1.01 | 0.90 | 0.00 | | | | | | | |
| $Fe^{2+}$ | 1.24 | 0.52 | 0.75 | 1.75 | 2.47 | 1.52 | 1.31 | 4.21 | 1.57 | 1.14 | 3.09 |
| Mn | 0.04 | 0.02 | 0.03 | 0.02 | 0.02 | 0.03 | 0.02 | 0.09 | 0.03 | 0.02 | 0.09 |
| Mg | 1.97 | 2.48 | 2.38 | 2.85 | 2.25 | 3.74 | 3.86 | 2.03 | 3.43 | 4.13 | 2.17 |
| Ca | 1.88 | 1.87 | 1.88 | 0.02 | 0.02 | 0.01 | 0.01 | 0.04 | 0.04 | 0.00 | 0.02 |
| Ba | 0.02 | 0.03 | 0.03 | 0.22 | 0.19 | 0.13 | 0.19 | 0.06 | 0.29 | 0.19 | 0.04 |
| Na | 0.76 | 0.71 | 0.66 | 0.28 | 0.24 | 0.14 | 0.14 | 0.05 | 0.13 | 0.16 | 0.10 |
| K | 0.32 | 0.34 | 0.37 | 1.40 | 1.51 | 1.66 | 1.58 | 1.83 | 1.53 | 1.57 | 1.83 |
| Total cations | 16.00 | 16.00 | 16.00 | 15.41 | 15.50 | 15.69 | 15.64 | 15.95 | 15.59 | 15.65 | 15.50 |
| F | 0.08 | 0.11 | 0.06 | 0.16 | 0.16 | 0.21 | 0.30 | 0.15 | 0.35 | 0.46 | 0.32 |
| Cl | 0.03 | 0.02 | 0.02 | 0.01 | 0.03 | 0.01 | 0.01 | 0.01 | bdl | 0.00 | 0.00 |
| OH | 0.75 | 0.52 | 0.54 | 3.82 | 3.81 | 3.78 | 3.69 | 3.84 | 3.65 | 3.54 | 3.68 |
| O | 1.15 | 1.35 | 1.38 | | | | | | | | |
| Total anions | 2.00 | 2.00 | 2.00 | 4.00 | 4.00 | 4.00 | 4.00 | 4.00 | 4.00 | 4.00 | 4.00 |

bdl: below detection limit; *Fe2O3-FeO ratio was calculated; **H2O was calculated.

TABLE 4. REPRESENTATIVE EPMA ANALYSES OF GARNET, TITANITE AND PEROVSKITE

| Rock type | Olivine melilitite | | | | | | | | |
|---|---|---|---|---|---|---|---|---|---|
| Sample # | M156 | M156 | M110 | M67 | M110 | M110 | M156 | M156 | M110 |
| Association | Potash salt | | Fish Shale | Potash salt | Fish Shale | | Potash salt | | Fish Shale |
| Mineral | Garnet | | | Perovskite | | | Titanite | | |
| Location | Ocellus | | Groundmass | Ocellus | Groundmass | Ocellus | Groundmass | | |
| wt.% | | | | | | | | | |
| $SiO_2$ | 35.77 | 33.99 | 31.74 | bdl | 0.07 | bdl | 31.90 | 30.52 | 32.66 |
| $TiO_2$ | 3.37 | 5.89 | 10.81 | 54.31 | 55.53 | 54.31 | 30.71 | 34.10 | 28.61 |
| $ZrO_2$ | 0.17 | bdl | bdl | bdl | bdl | bdl | 0.24 | 0.23 | bdl |
| $Al_2O_3$ | 8.52 | 2.70 | 4.59 | bdl | 0.07 | 0.05 | 2.00 | 0.21 | 5.48 |
| $Fe_2O_3$* | 15.68 | 20.83 | 13.10 | 1.18 | 0.82 | 1.07 | 4.28 | 3.65 | 1.78 |
| FeO* | 0.35 | 1.65 | 4.34 | | | | | | |
| MnO | 0.17 | 0.19 | 0.06 | bdl | 0.04 | 0.03 | 0.05 | 0.03 | 0.02 |
| MgO | 0.90 | 0.78 | 0.25 | bdl | 0.07 | 0.04 | 0.36 | 0.05 | 0.28 |
| CaO | 34.28 | 33.03 | 32.79 | 36.82 | 38.81 | 36.81 | 26.53 | 26.82 | 27.55 |
| $Na_2O$ | 0.03 | 0.12 | 0.19 | 1.38 | 0.85 | 1.12 | 0.08 | 0.35 | 0.33 |
| $Nb_2O_5$ | 0.13 | 0.15 | bdl | 2.13 | 1.65 | 2.01 | bdl | 1.72 | bdl |
| $Ta_2O_5$ | bdl | bdl | bdl | 0.08 | bdl | 0.07 | bdl | 0.07 | bdl |
| SrO | bdl | bdl | bdl | 0.81 | 0.97 | 1.13 | bdl | 0.55 | bdl |
| $La_2O_3$ | bdl | bdl | bdl | bdl | bdl | bdl | bdl | bdl | bdl |
| $Ce_2O_3$ | bdl | 0.08 | bdl | 0.37 | bdl | 0.64 | bdl | bdl | bdl |
| $Pr_2O_3$ | bdl | bdl | bdl | 0.19 | 0.07 | 0.19 | bdl | bdl | bdl |
| $Nd_2O_3$ | bdl | bdl | bdl | 0.17 | 0.06 | 0.31 | bdl | bdl | bdl |
| $Sm_2O_3$ | bdl | bdl | bdl | 0.09 | bdl | 0.07 | 0.04 | bdl | bdl |
| $Y_2O_3$ | bdl | bdl | 0.09 | bdl | bdl | bdl | bdl | bdl | bdl |
| $ThO_2$ | bdl | bdl | bdl | 0.11 | 0.06 | 0.20 | bdl | bdl | bdl |
| F | 0.04 | bdl | bdl | 0.34 | 0.15 | 0.12 | bdl | bdl | 0.03 |
| Cl | bdl | bdl | 0.02 | bdl | bdl | bdl | 0.36 | bdl | 0.03 |
| $H_2O$** | | | | | | | 3.23 | 1.66 | 3.65 |
| -O≡F,Cl | 0,02 | bdl | 0.00 | 0.14 | 0.06 | 0.05 | 0.00 | 0.00 | 0.02 |
| Total | 99.39 | 99.39 | 97.97 | 97.82 | 99.15 | 98.11 | 99.78 | 99.94 | 100.41 |
| *Formula based on 8 cations and 12 oxygens (Garnet), 3 oxygens (Perovskite) or 1 Si cation (Titanite)* | | | | | | | | | |
| Si | 2.89 | 2.84 | 2.68 | bdl | 0.00 | bdl | 1.00 | 1.00 | 1.00 |
| Ti | 0.21 | 0.37 | 0.69 | 0.97 | 0.97 | 0.97 | 0.72 | 0.84 | 0.66 |
| Zr | 0.01 | bdl | bdl | bdl | bdl | bdl | 0.00 | 0.00 | bdl |
| Al | 0.81 | 0.27 | 0.46 | bdl | 0.00 | 0.00 | 0.07 | 0.01 | 0.20 |
| $Fe^{3+}$ | 0.95 | 1.31 | 0.83 | 0.01 | 0.01 | 0.01 | 0.10 | 0.09 | 0.04 |
| $Fe^{2+}$ | 0.02 | 0.12 | 0.31 | | | | | | |
| Mn | 0.01 | 0.01 | 0.00 | bdl | 0.00 | 0.00 | 0.00 | 0.00 | 0.00 |
| Mg | 0.11 | 0.10 | 0.03 | bdl | 0.00 | 0.00 | 0.02 | 0.00 | 0.01 |
| Ca | 2.97 | 2.96 | 2.97 | 0.93 | 0.96 | 0.93 | 0.89 | 0.94 | 0.90 |
| Na | 0.01 | 0.02 | 0.03 | 0.06 | 0.04 | 0.05 | 0.00 | 0.02 | 0.02 |
| Nb | 0.00 | 0.01 | bdl | 0.02 | 0.02 | 0.02 | 0.00 | 0.03 | bdl |
| Ta | bdl | bdl | bdl | 0.00 | bdl | 0.00 | 0.00 | 0.00 | bdl |
| Sr | bdl | bdl | bdl | 0.01 | 0.01 | 0.02 | 0.00 | 0.01 | bdl |
| La | bdl | bdl | bdl | bdl | bdl | bdl | bdl | bdl | bdl |
| Ce | bdl | 0.00 | bdl | 0.00 | bdl | 0.01 | bdl | bdl | bdl |
| Pr | bdl | bdl | bdl | 0.00 | 0.00 | 0.00 | bdl | bdl | bdl |
| Nd | bdl | bdl | bdl | 0.00 | 0.00 | 0.00 | bdl | bdl | bdl |
| Sm | bdl | bdl | bdl | 0.00 | bdl | 0.00 | 0.00 | bdl | bdl |
| Y | bdl | bdl | 0.00 | bdl | bdl | bdl | bdl | bdl | bdl |
| Th | bdl | bdl | bdl | 0.00 | 0.00 | 0.00 | bdl | bdl | bdl |
| Total cations | 8.00 | 8.00 | 8.00 | 2.02 | 2.01 | 2.01 | 2.82 | 2.95 | 2.83 |
| F | 0.01 | bdl | bdl | 0.01 | 0.01 | 0.00 | bdl | bdl | 0.00 |
| Cl | bdl | bdl | 0.00 | | | | 0.02 | bdl | 0.00 |
| OH | | | | | | | 0.72 | 0.37 | 0.79 |
| O | 11.99 | 12.00 | 12.00 | 2.99 | 2.99 | 3.00 | 4.26 | 4.63 | 4.21 |
| Total anions | 12.00 | 12.00 | 12.00 | 3.00 | 3.00 | 3.00 | 5.00 | 5.00 | 5.00 |

bdl: below detection limit; *$Fe_2O_3$-FeO ratio was calculated; **$H_2O$ was calculated.

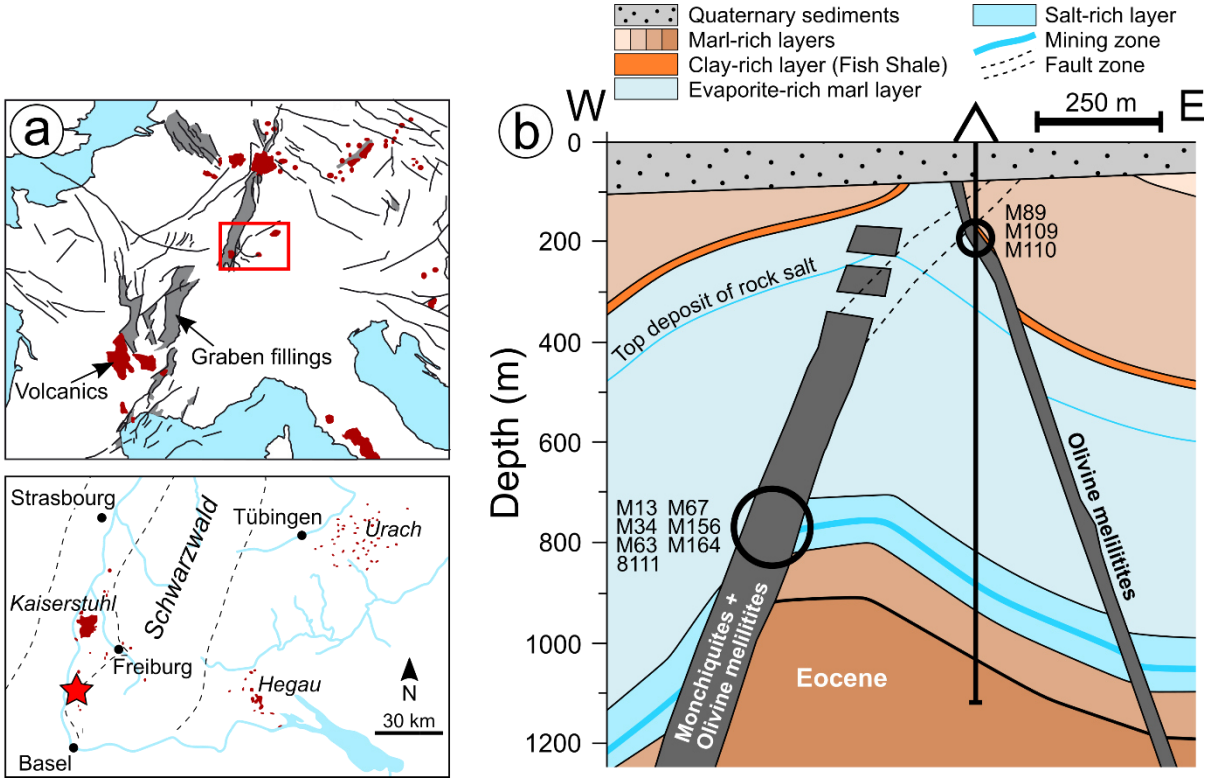


Fig. 1: Geology of Buggingen. A) Overview map of the European Cenozoic Volcanic Province and the Cenozoic magmatic occurrences in southwest Germany (modified after Dèzes *et al.*, 2004). Buggingen is located at the red star. B) Cross-section showing the geology of Buggingen and the sample sites (modified after Esslinger, 1976).

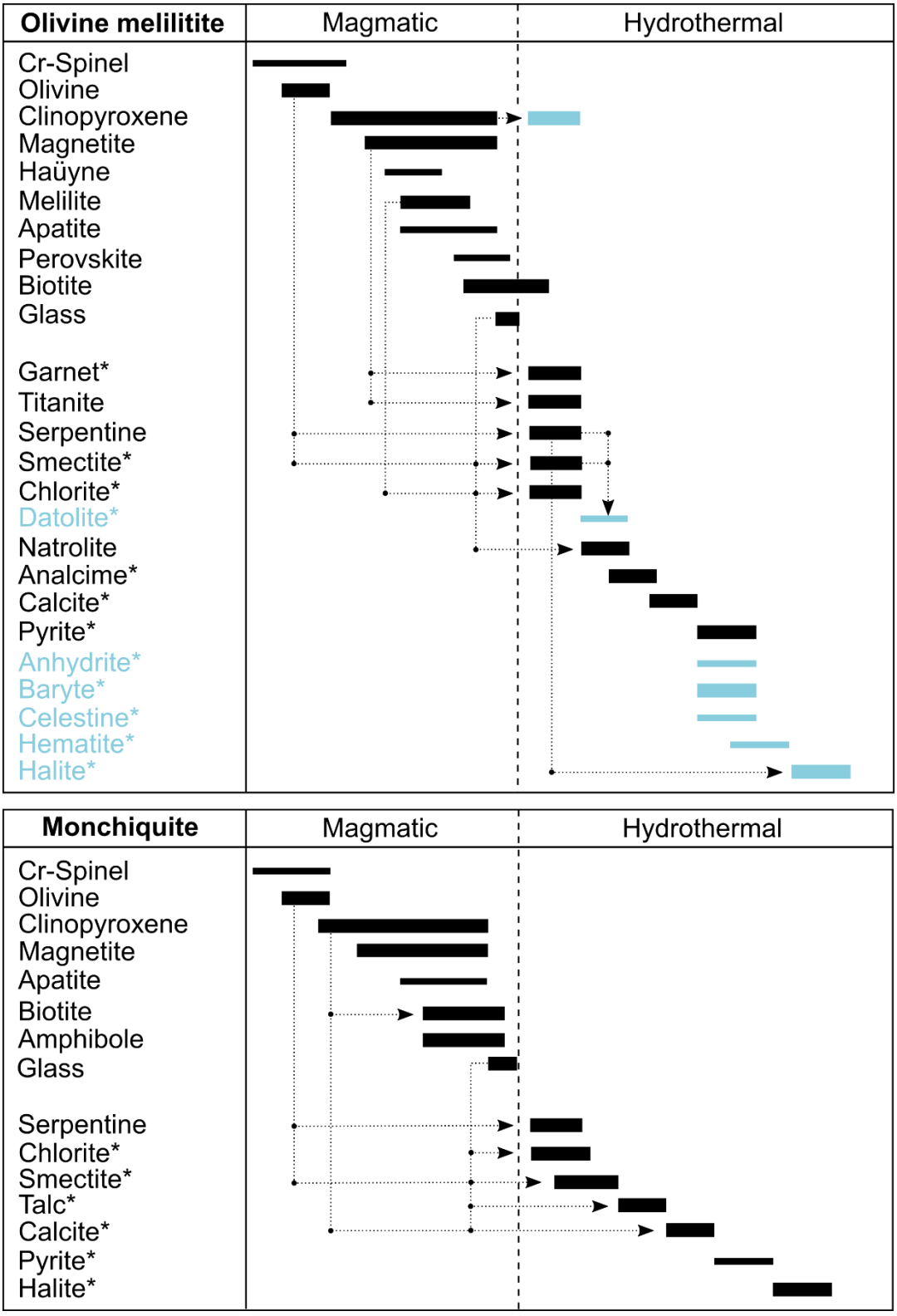


Fig. 2: Paragenetic scheme for the olivine melilitite and the monchiquites from Buggingen. Alteration processes are indicated by arrows. Mineral phases of the olivine melilitite that only occur in association with the salt layer are indicated in blue. Mineral phases highlighted by the star are present in ocelli/amygdules.

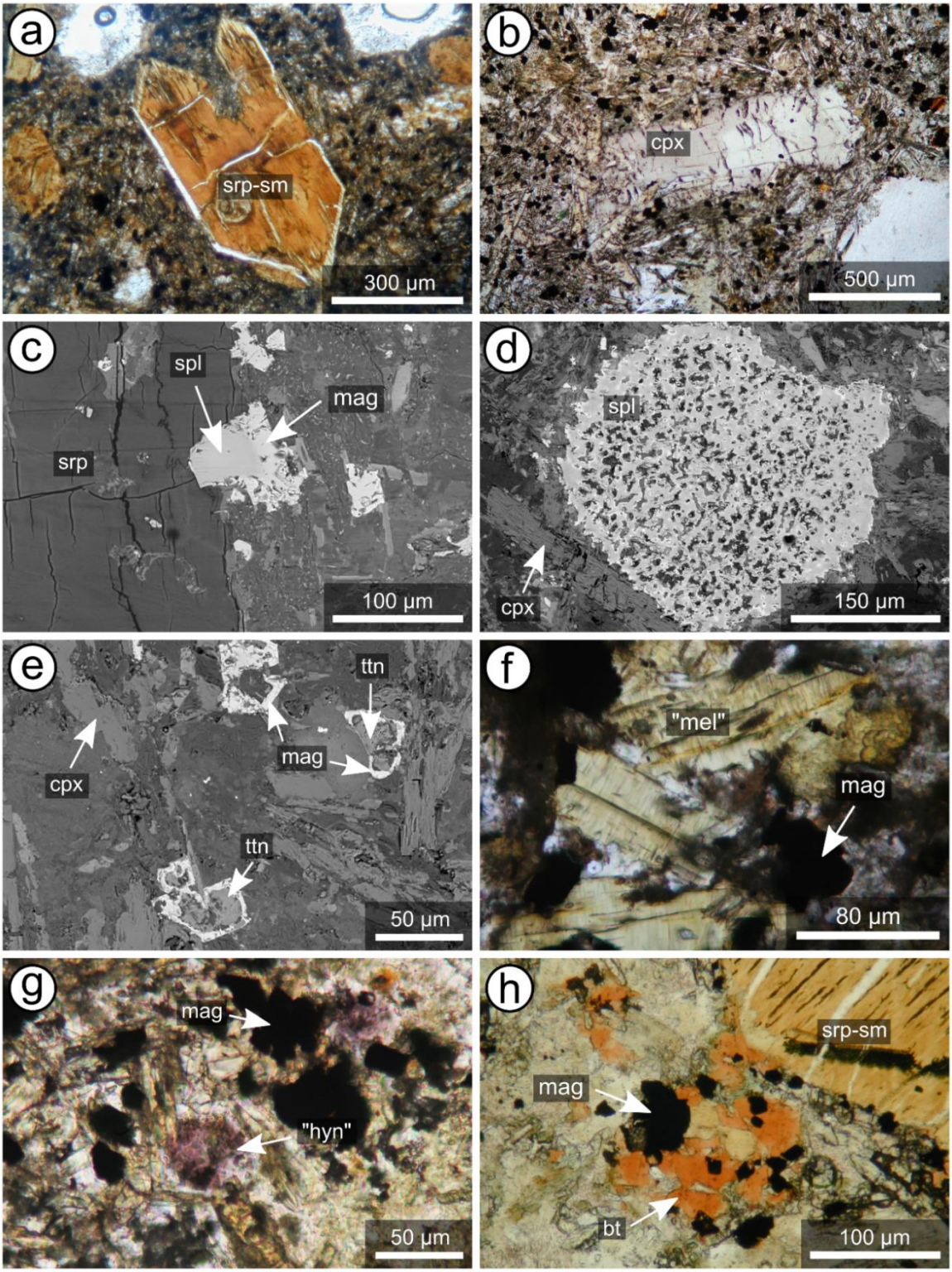


Fig. 3: Mineral textures in the olivine melilitites from Buggingen (transmitted light microscopy and BSE images [c,d,e]). a) Euhedral olivine macrocryst totally replaced by serpentine (srp) and smectite (sm) minerals. b) Clinopyroxene (cpx) macrocryst in a groundmass consisting of plenty clinopyroxene needles. c) Spinel (spl) at the rim of an serpentinized olivine. Those parts of the spinel that are not enclosed by former olivine are surrounded by magnetite (mag). d) Spinel showing a sieve texture. e) Atoll-shaped magnetite with a core of titanite (ttn). f) Melilite (mel) being totally altered to chlorite. g) Purple pseudomorphs after haüyne (hyn) consisting of a mixture of fine-grained secondary minerals. e) Interstitial biotite (bt).

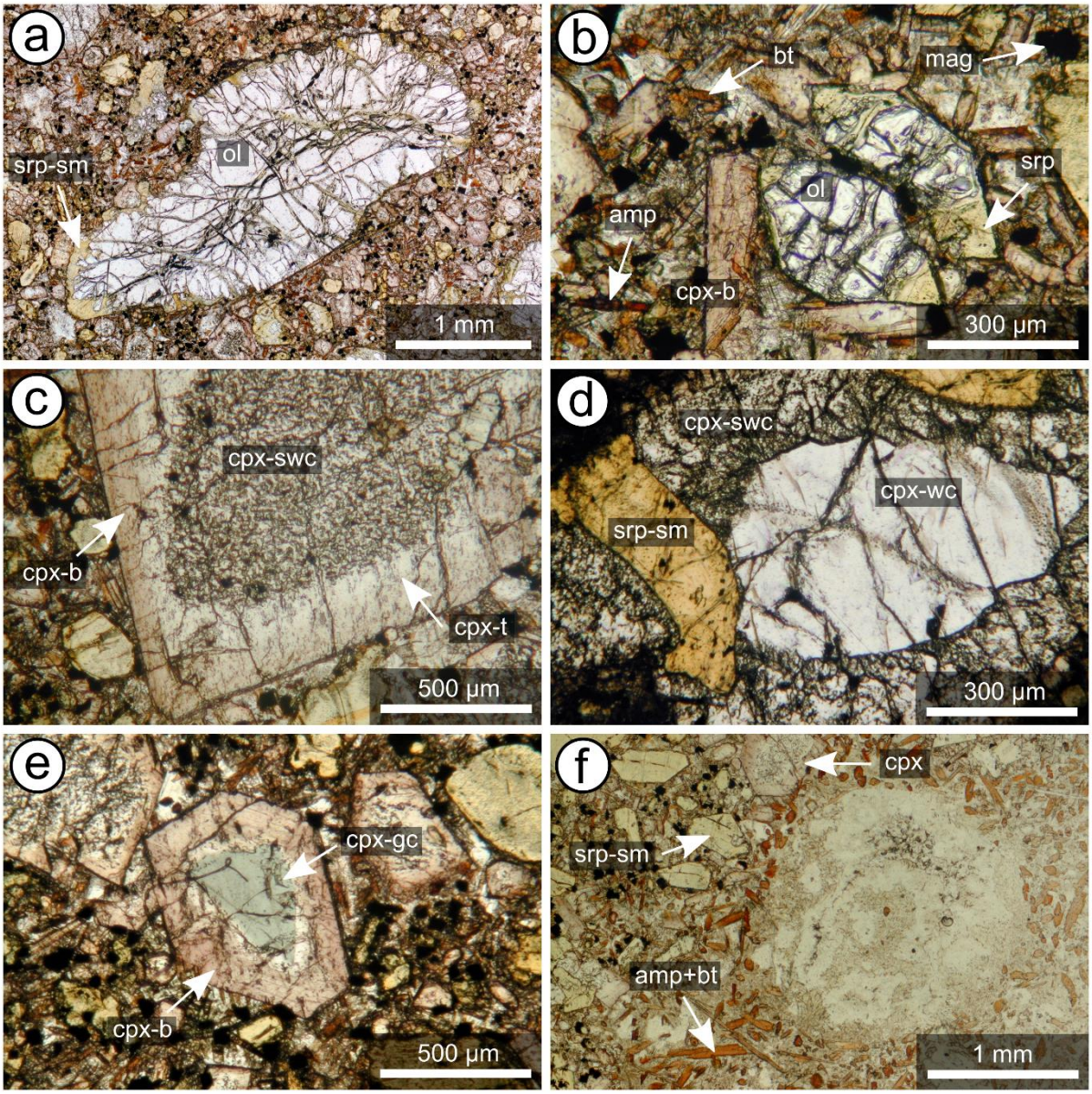


Fig. 4: Mineral textures in the monchiquites from Buggingen (transmitted light microscopy images). a) Large, rounded olivine (ol) macrocryst partly replaced by serpentine and smectite minerals. b) Euhedral olivine, brown clinopyroxene needles and small tabular amphibole (amp) and biotite constitute the groundmass. c) Clinopyroxene consisting of a sieved white core (cpx-swc), a plain transitional zone (cpx-t) and a brown rim (cpx-b). d) Clinopyroxene with an irregularly shaped white core (cpx-wc), surrounded by sieved white clinopyroxene and olivine that is completely replaced by serpentine and smectite minerals. e) Green-core clinopyroxene (cpx-gc) rimmed by brown clinopyroxene. f) Roundish zone consisting of a fine-grained mixture of chlorite, talc and calcite, surrounded by amphiboles and biotite.

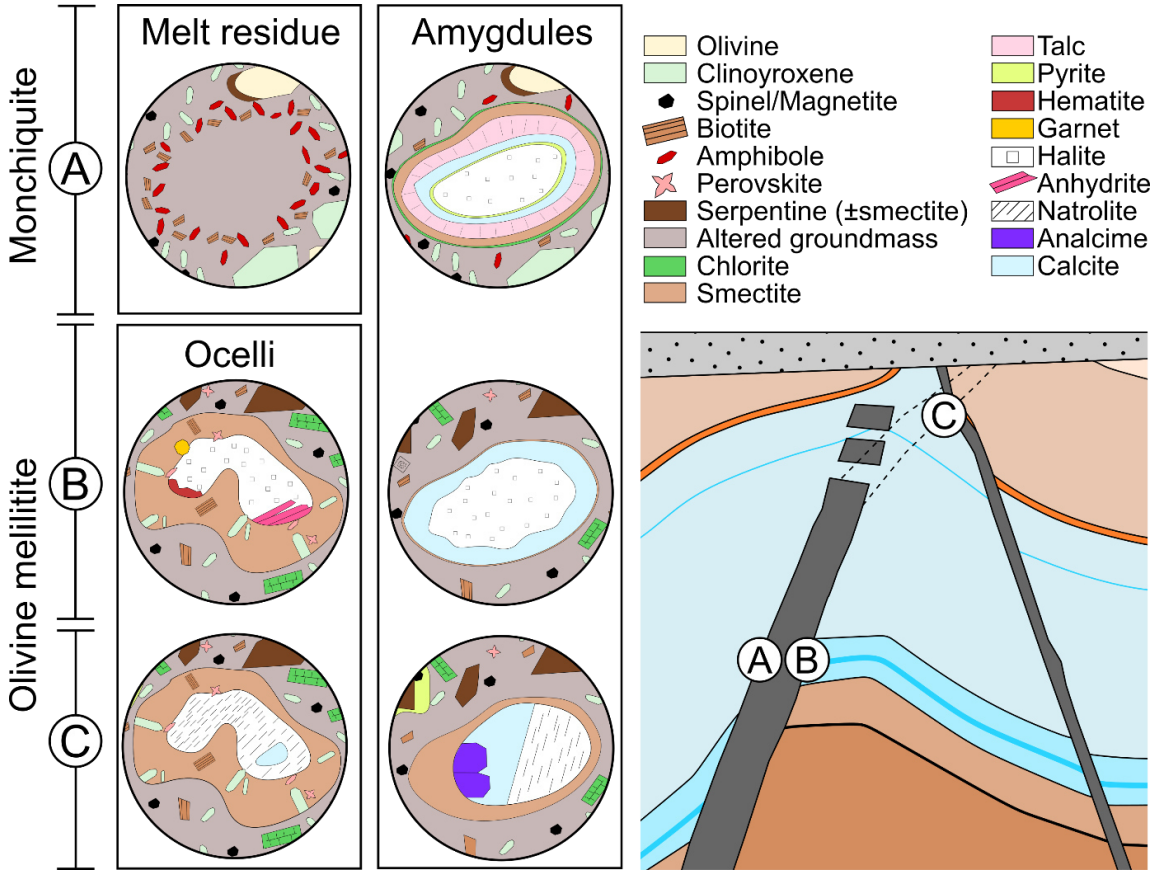


Fig. 5: Schematic overview of the spheroidal textures in the monchiquites and the olivine melilitites.

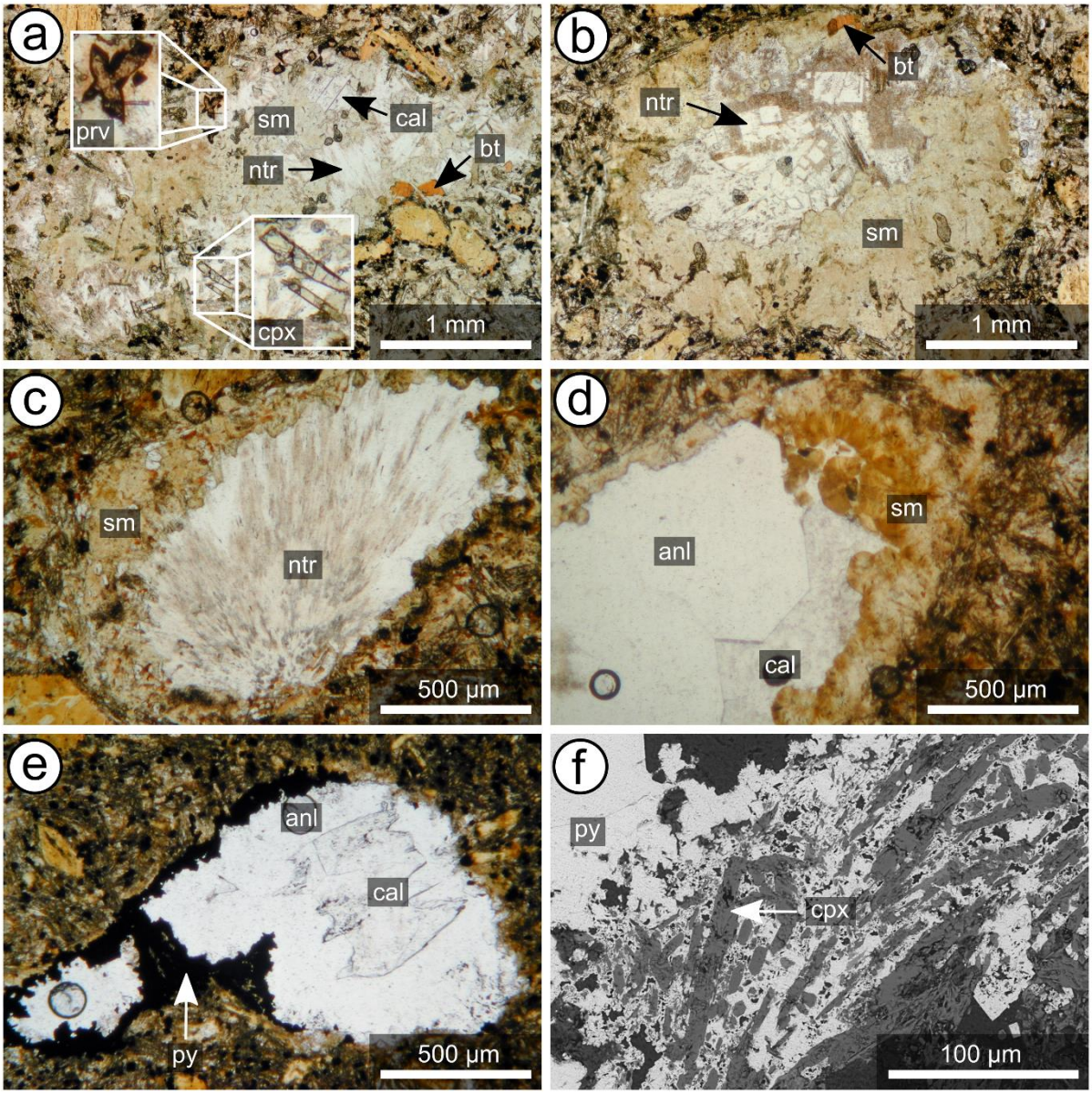


Fig. 6: Mineral textures of the ocelli in the olivine melilitites associated with the Fish Shale (transmitted light microscopy images. a) Biotite, clinopyroxene and perovskite (prv) sometimes occur at the rim of ocelli. Calcite (cal), smectite and natrolite are further common constituents. b) Ocellus with a rim mainly consisting of smectite and rare biotite, and a core of natrolite (ntr). c) Ocellus with marginal smectite minerals and a core of natrolite. d) Ocellus consisting of smectites, calcite and analcime (anl). e) Ocellus with marginal pyrite (py), analcime and calcite. f) Parts of the groundmass are replaced by pyrite.

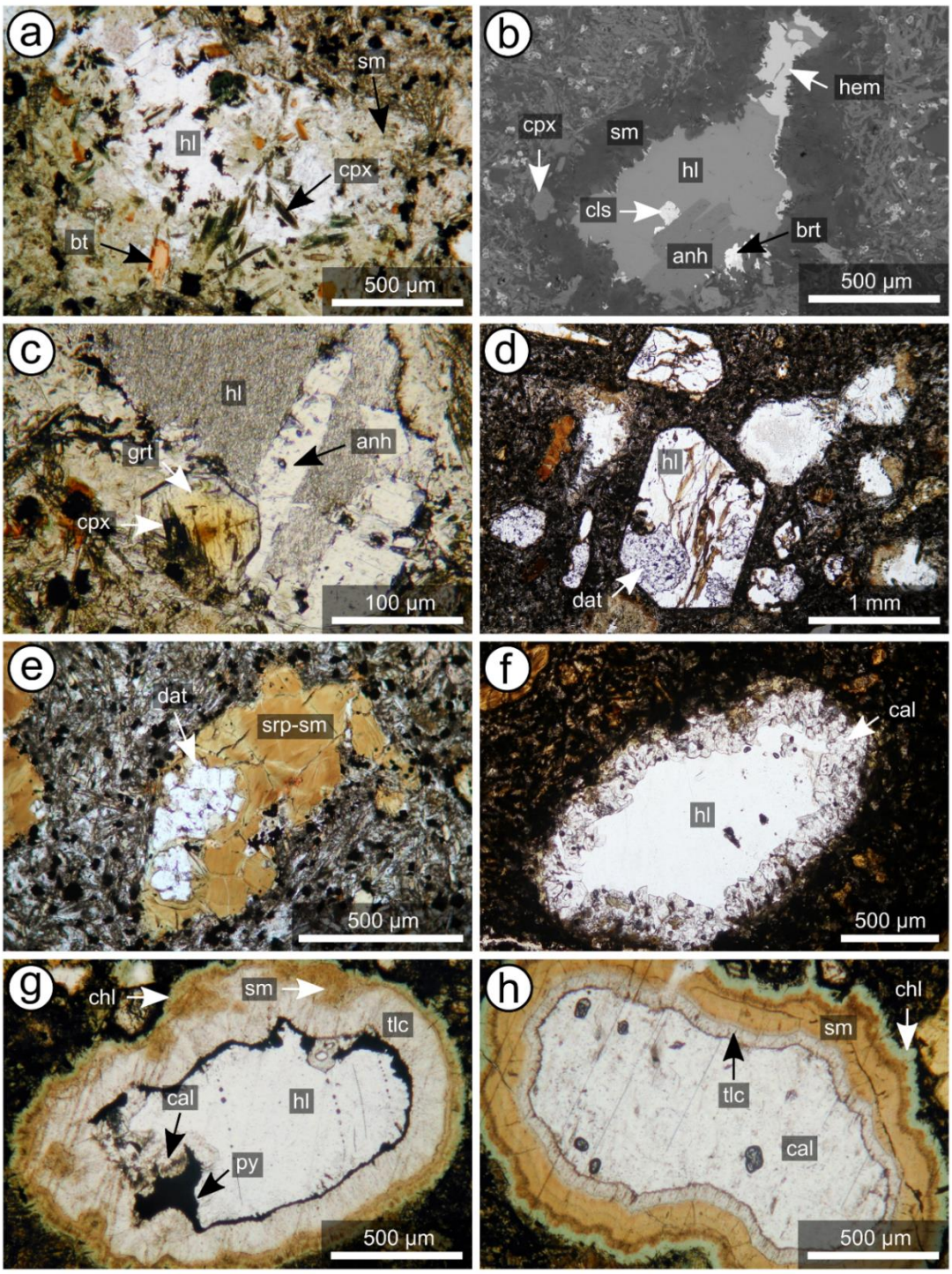


Fig. 7: Mineral textures of the ocelli and amygdules in the olivine melilitites and the monchiquites associated with the potash salt layer (transmitted light microscopy and BSE images [b]). a) Ocellus with a rim of biotite, aegirine and smectites, and a core of halite. b) Ocellus consisting of smectites, hematite (hem), barite (brt), anhydrite (anh), celestine (cls) and halite. c) In sample M156, euhedral garnet (grt) with inclusions of clinopyroxene sometimes occur at the rim of ocelli. d) Halite and datolite (dat) pseudomorph after olivine. e) Serpentine, smectite and datolite pseudomoprh after olivine. f) Amygdule consisting of marginal calcite and a core of halite. g) Amygdule with a concentric succession of chlorite (chl), smectite, talc (tlc), calcite, pyrite (py) and halite. h) Amygdule showing a concentric succession of chlorite, smectite, talc and calcite.

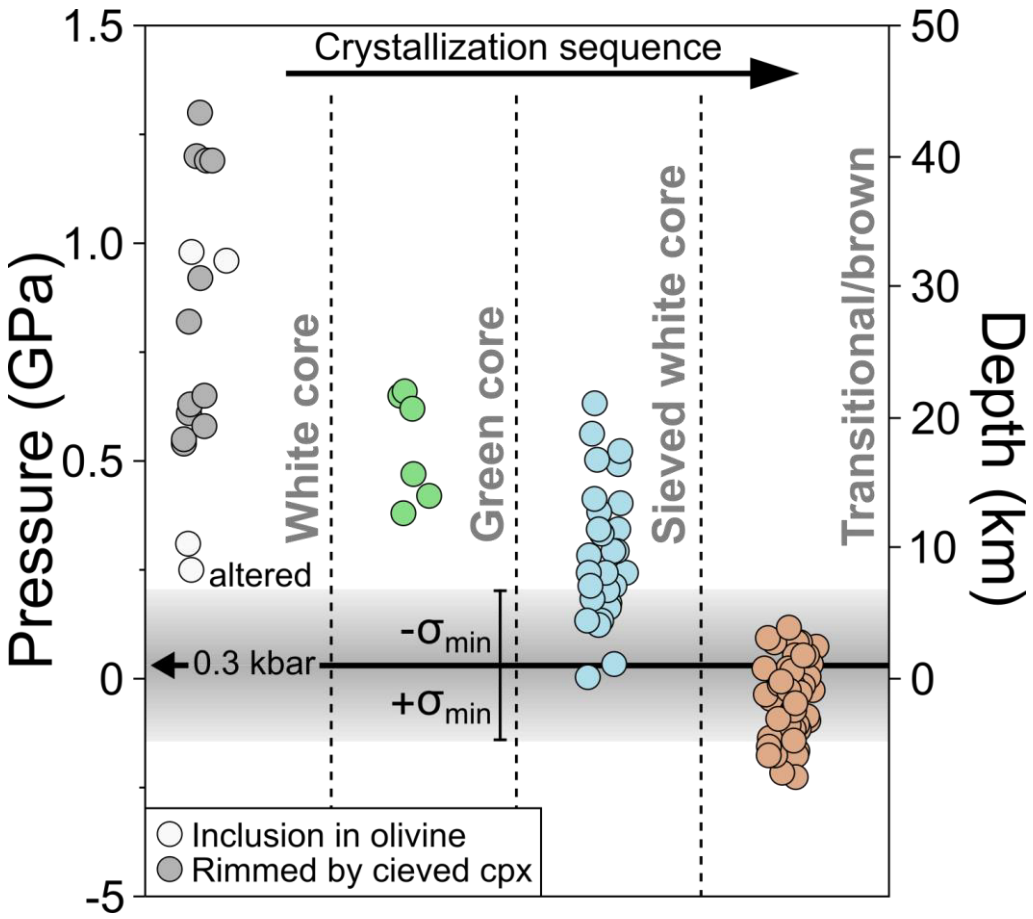


Fig.8: Crystallization depth for the various clinopyroxene types in the monchiquites from Buggingen. Pressure estimates are based on Nimis & Ulmer (1998) and indicate a minimum uncertainty of σ=1.75 kbar. The negative pressure estimates for many of the transitional/brown clinopyroxenes might additionally be caused by the fact that the barometer is calibrated for anhydrous systems (note that late-stage clinopyroxenes coexist with amphibole and mica). The line at 0.3 kbar demonstrates the expected minimum pressure during groundmass crystallization due to an overburden of ~1000 m.

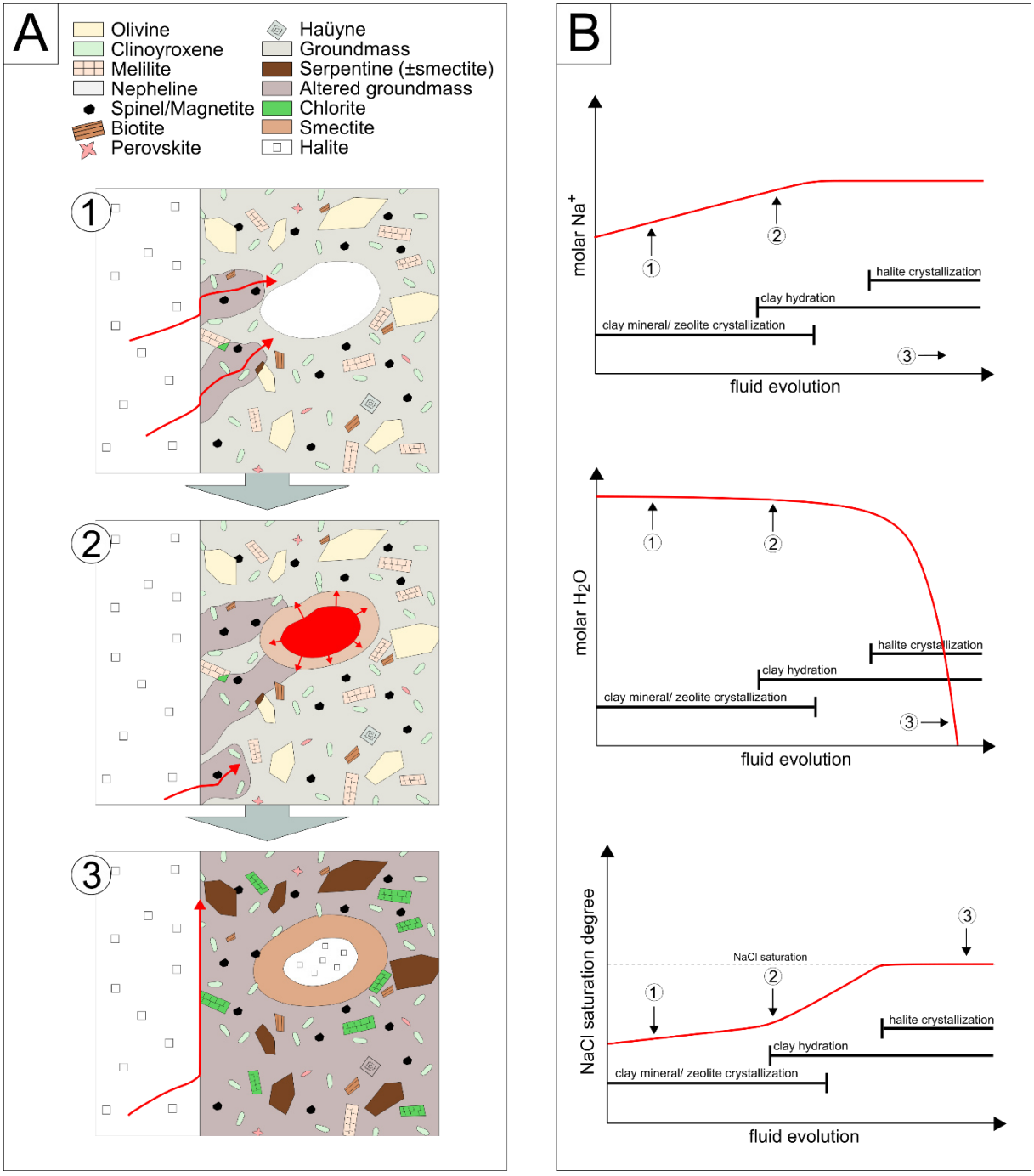


Fig. 9: Precipitation mechanism for the halite-bearing amygdules/ocelli. A) Schematic evolution of the dyke rock mineral assemblage. 1) NaCl-saturated fluid (red arrow) interacts with the groundmass, thereby producing Na- and OH-bearing alteration phases (smectites and zeolites). 2.) Fluid hits a vug, forms marginal smectite minerals and gets trapped. 3) Gradual removal of $H_2O$ from the fluid by clay mineral swelling results in NaCl precipitation. The formation of smectites and zeolites cements possible fluid paths and prevents further fluids from entering the dyke rock (blue arrow). B) Schematic evolution of the fluid composition. The upper two xy-diagram demonstrate the evolution of the molar $Na^+$, respectively $H_2O$ concentration of the fluid with respect to the initial fluid composition. The lower xy-diagram demonstrates the NaCl saturation degree during fluid evolution.

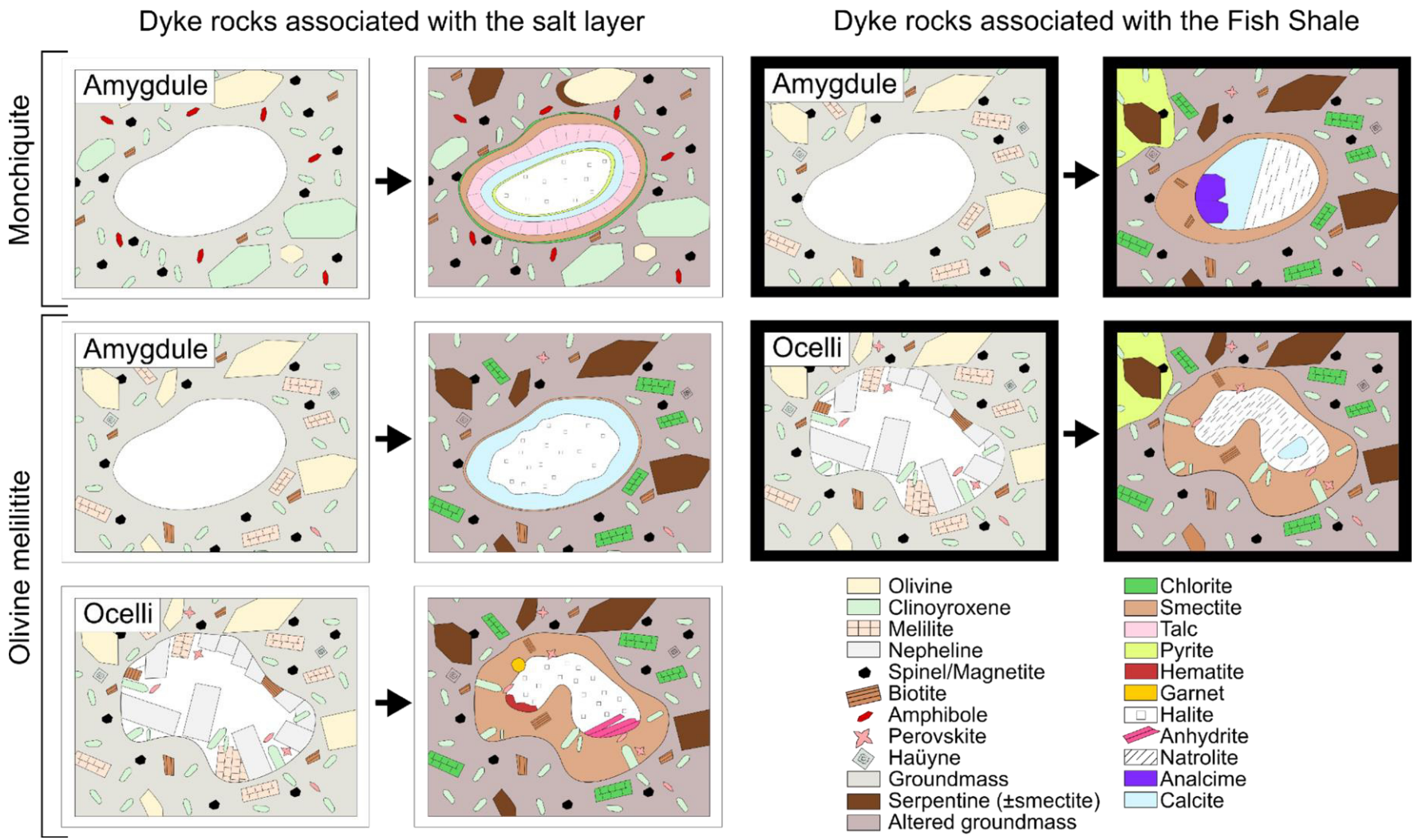


Fig. 10: Schematic diagram illustrating the mineral assemblage of amygdules and ocelli before and after the hydrothermal overprint.

# Appendix VII

Accepted publication

*Study 7*

Braunger, S., Marks, M.A.W., Wenzel, T., Chmyz, L., Guitarrari Azzone, R., Markl, G., 2020. Do carbonatites and alkaline rocks reflect variable redox conditions in their upper mantle source? Earth and Planetary Science Letters 533, 116041. http://dx.doi.org/10.1016/j.epsl.2019.116041.

Earth and Planetary Science Letters 533 (2020) 116041

Contents lists available at ScienceDirect

Earth and Planetary Science Letters

www.elsevier.com/locate/epsl

# Do carbonatites and alkaline rocks reflect variable redox conditions in their upper mantle source?

Simon Braunger [a,*], Michael A.W. Marks [a], Thomas Wenzel [a], Luanna Chmyz [b], Rogério Guitarrari Azzone [b], Gregor Markl [a]

[a] Department of Geosciences, Eberhard-Karls-Universität Tübingen, Wilhelmstrasse 56, 72074 Tübingen, Germany
[b] Institute of Geosciences, Universidade de São Paulo, Rua do Lago 562, 05508-080 São Paulo, Brazil

ARTICLE INFO

*Article history:*
Received 4 July 2019
Received in revised form 3 December 2019
Accepted 17 December 2019
Available online xxxx
Editor: R. Dasgupta

*Keywords:*
carbonatites
alkaline silicate rocks
redox conditions
oxygen fugacity
mantle

ABSTRACT

A detailed investigation on seven carbonatites and associated alkaline rock complexes (Kaiserstuhl, Sokli, Kovdor, Palabora, Oka, Magnet Cove, Jacupiranga), together with a world-wide comparison between carbonatites, alkaline silicate rocks and mantle xenoliths, implies peculiar redox conditions for carbonatite-bearing alkaline complexes: Carbonatites and associated alkaline rocks in continental settings crystallize from relatively oxidized magmas, on average 1.4 log units ($\sigma = 1.7$) and 1.3 log units ($\sigma = 1.1$) above the synthetic fayalite-magnetite-quartz (FMQ) buffer. In contrast, alkaline rocks in continental settings that lack associated carbonatites reveal rather reduced conditions (mean $\Delta$FMQ $= -1.1$; $\sigma = 1.4$). The calculated redox conditions for carbonatites and associated silicate rocks demonstrate that these crystallize from relatively oxidized mantle-derived melts compared to the general range found for alkaline rocks in continental settings.



## 1. Introduction

Carbonatites are carbonate-rich magmatic rocks that typically occur in continental intraplate settings, such as at the edge of cratons or within rifts (Woolley and Kjarsgaard, 2008). Carbonatitic magmas can evolve from strongly $SiO_2$-undersaturated and carbonate-bearing parental silicate melts by fractional crystallization and liquid immiscibility, with the latter being especially important in alkali-rich systems (e.g. Jones et al., 2013; Martin et al., 2013). They may also form directly by partial melting of carbonate-bearing peridotite (e.g. Beccaluva et al., 2017; Chmyz et al., 2019).

Carbonatites are typically not pure carbonate rocks but contain variable amounts of silicates (e.g. olivine, mica, garnet), oxides (e.g. magnetite, pyrochlore, perovskite), sulfides (e.g. pyrrhotite, galena, pyrite), and phosphates (particularly apatite). In a few cases, carbonatites are associated with apatite-magnetite-olivine±carbonate rocks (phoscorites) which are related to carbonatites by crystal fractionation or liquid immiscibility from a common parental magma (Krasnova et al., 2004b; Giebel et al., 2019a). However, most carbonatites are spatially and temporally associated with variable alkaline silicate rocks, which suggests a genetic link between both rock groups. The silicate rocks include ultramafic, mafic, intermediate and evolved lithologies. Depending on the erosion level of the magmatic complex, their textures range from coarse-grained cumulitic (e.g., Palabora, Kovdor) to fine-grained and porphyritic (sub)volcanic textures (e.g., in the East Africa Rift); mixed examples exist as well (e.g., Magnet Cove, Kaiserstuhl). Based on the associated silicate rocks, carbonatites are divided into several genetic types, with nephelinite- and melilitite-clan carbonatites representing the most abundant ones. Other genetic types include for example kimberlite- and ailikite-clan carbonatites (Mitchell, 2005).

The source region for most carbonatites and associated alkaline silicate rocks is the metasomatized lithospheric and/or sublithospheric (asthenospheric) mantle (e.g. Bell and Simonetti, 2010; Braunger et al., 2018). However, carbonatites and spatially associated alkaline silicate rocks do not necessarily derive from the same magma source, as demonstrated by various isotope studies (Bell, 1998). In cases, carbonatites are cogenetic with only some of the exposed silicate rocks (Kaiserstuhl; Braunger et al., 2018) or even none of them (Jacupiranga; Beccaluva et al., 2017; Chmyz et al., 2019). The variable genetic relationships between carbonatites and spatially associated alkaline rocks reflect the heterogeneity of the metasomatized lithospheric mantle. Depending on their scale, these heterogeneities cause the formation of compositionally diverse melt volumes that may evolve and differentiate indepen-

* Corresponding author.
*E-mail address:* simonbraunger@hotmail.com (S. Braunger).

https://doi.org/10.1016/j.epsl.2019.116041
0012-821X/

dently from each other or may mix with each other, eventually forming a carbonatite-alkaline silicate rock complex.

Depending on oxygen fugacity ($f_{O2}$), carbon in the mantle is present either as reduced species (graphite, diamond, carbides and $CH_4$) or in its oxidized form ($CO_2$ and carbonates; Frost and McCammon, 2008; Dasgupta and Hirschmann, 2010; Stagno, 2019). Redox conditions of the (sub)lithospheric mantle vary by more than 8 log units around the synthetic fayalite-magnetite-quartz (FMQ) buffer (e.g. Foley, 2011). This heterogeneity is related to different tectonic settings: thick cratonic lithosphere is variably reduced (mean of $\Delta$FMQ $= -2.8$, being more reduced at greater depth) due to the pressure-dependent stability of $Fe^{2+}$- and/or $Fe^{3+}$-bearing minerals (e.g. Ballhaus and Frost, 1994). In contrast, the mantle above subduction zones shows high redox conditions (mean of $\Delta$FMQ $= +0.5$) because of the interaction with oxidizing melts from the subducted slab (Parkinson and Arculus, 1999). Digestion of crustal rocks by the mantle leads to further heterogeneity with respect to redox conditions over time (e.g. Foley, 2011; Rohrbach and Schmidt, 2011). Although the oxidation state of the upper mantle has been assumed to be stable over the past 3800 Ma (e.g. Canil, 2002; Li and Lee, 2004), recent studies suggest an increase of the redox conditions since the Archean (e.g. Gaillard et al., 2015; Aulbach and Stagno, 2016). For the asthenosphere, estimates based on investigations of abyssal (oceanic) peridotites or Mid Ocean Ridge basalts reveal average redox conditions slightly more reduced than for the lithosphere, possibly due to the loss of oxidative fluids and melts that infiltrated the overlying mantle (Frost and McCammon, 2008; Foley, 2011). Alternatively, the convecting upper mantle (at least to 150 km depth) might not follow the $f_{O2}$-depth correlation mentioned above and, hence, is more oxidized than the continental lithosphere. This was recently suggested by Eguchi and Dasgupta (2018) for redox conditions of subducted lithologies, but it remains to be tested, if such assumptions can be extrapolated to asthenospheric peridotites.

Those alkaline silicate rocks that occur in similar settings as carbonatites (such as intraplate environments) show a similarly large spread in their redox conditions as the upper mantle, namely from $\Delta$FMQ $= -4$ to $+6$. This variability is qualitatively expressed by the mafic minerals in alkaline rocks: Clinopyroxene-garnet±titanite assemblages seem to be indicative for relatively oxidized crystallization conditions, whereas olivine-clinopyroxene-magnetite assemblages indicate variable, but mostly reduced conditions. In some extreme cases, rather unusual sodic clinopyroxene-amphibole-eudialyte±aenigmatite assemblages, so-called agpaitic rocks, crystallize from some of the most reduced magmas known on Earth (Marks and Markl, 2017). Subduction zone-related lamprophyric lavas belong to the most oxidized silicate rocks known (Carmichael, 1991), but these are not considered further here because of their different tectonic setting.

Very little is known about redox conditions for carbonatitic magmas and even less so about redox conditions for carbonatites and their spatially associated alkaline silicate rocks. Here, we present the results of thermodynamic calculations for seven igneous complexes (Kaiserstuhl, Sokli, Kovdor, Palabora, Magnet Cove, Oka, Jacupiranga) that constrain redox conditions for carbonatites and associated alkaline silicate rocks. Our results, augmented by literature data, provide insight into the variable redox conditions under which alkaline silicate rocks may form and indicate that carbonatites (and their associated alkaline silicate rocks) crystallize from remarkably oxidized mantle-derived magmas, compared to alkaline rocks in general.

## 2. Geology and petrography

We investigated carbonatites, phoscorites and associated alkaline silicate rocks (ultramafic, melilititic and nephelinitic rocks) that contain appropriate mineral assemblages for deducing their crystallization conditions (Table 1). We used well-known examples from Europe (Kaiserstuhl, Germany; Sokli, Finland; Kovdor, Russia), Africa (Palabora, South Africa), North America (Magnet Cove, USA; Oka, Canada) and South America (Jacupiranga, Brazil). These examples cover a range of ages (Proterozoic to Cenozoic) and emplacement depths (close to surface to >5 km) and are considered to represent typical carbonatite-alkaline silicate rock associations (Mitchell, 2005).

### 2.1. Kaiserstuhl (Germany)

The Kaiserstuhl volcanic complex (q.v. Braunger et al., 2018 and references therein) was active between 19 and 16 Ma and predominantly consists of porphyritic tephritic rocks, medium-grained sodalite monzogabbros (in the centre), and several phonolite domes that are all assumed to derive from a rather potassic basanitic parental magma. Minor melilititic, nephelinitic, and basanitic rocks represent a more sodic rock series, probably genetically related with the carbonatites of the Kaiserstuhl complex. The examined coarse-grained calcite carbonatites contain variable amounts of magnetite, euhedral but partly altered olivine or monticellite, apatite and small amounts of phlogopite and pyrochlore (Fig. 1a).

### 2.2. Sokli (Finland)

The Sokli alkaline complex (q.v. Lee et al., 2004 and references therein) is part of the Palaeozoic Kola Alkaline Province and intruded 370-360 Ma ago. It shows a concentric structure and is divided into an outer zone consisting of carbonate-rich metasomatic facies that replaced ultramafic rocks (mainly clinopyroxenites) and a magmatic core composed of three phoscorite-carbonatite stages and two subsequent dolomite carbonatite stages. The investigated phoscorites and carbonatites are characterized by variable amounts of olivine, magnetite, apatite, phlogopite, baddeleyite and carbonate. Phoscorite type 3 lacks olivine but contains individual ilmenite grains instead (Fig. 1b).

### 2.3. Kovdor (Russia)

The Devonian (~420-370 Ma) Kovdor massif (q.v. Krasnova et al., 2004a and references therein) also belongs the Palaeozoic Kola Alkaline Province and is a multiphase alkali-ultrabasic pluton with olivinites, clinopyroxenites, melilitolites and marginal ijolites to melteigites. The subsequently intruded phoscorite-carbonatite complex in the west of the massif includes five main phoscorite types (P1-P5) with the last three being associated with paired carbonatites (C1-C3). The phoscorites consist of variable amounts of olivine, magnetite and apatite while phlogopite, baddeleyite and carbonate represent minor mineral phases. Carbonatites have a similar mineral assemblage but are obviously carbonate-rich. Irregular ilmenite patches and variably shaped spinel grains (Fig. 1c) occur as exsolutions in magnetite while C2 carbonatites also contain ilmenite-magnetite assemblages of the composite type. The general grain size of the phoscorites and the magnetite content increases from P1 to P3 and from P4 to P5, while the olivine concentration decreases. Phoscorite P4 and its associated carbonatite contain tetraferriphlogopite instead of phlogopite and in C3 carbonatites, dolomite is the predominant carbonate phase.

### 2.4. Palabora (South Africa)

The 2060 Ma old Palabora carbonatite complex (q.v. Giebel et al., 2019a and references therein) is exposed as an elongated tripartite pipe-like body that predominantly consists of clinopyroxenites and small satellite bodies of syenites. The central Loolekop

**Table 1**
Mineral assemblages and intrinsic parameters for investigated rock types.

| Locality | | Rock type | Mineral assemblage | Temperature (°C) | ΔFMQ** |
|---|---|---|---|---|---|
| Kaiserstuhl | | Carbonatite | Cal+ap+**mag**±**ol**±**mtc**+**phl** | 840-900$^{OM}$ | +1.8 ± 0.8$^{OM}$ |
| | | Nephelinite-basanite | **Cpx**+nph+**ol**+**mag**+sp+**pl**±**afs** | 990-1050$^{B18}$ | +2.1 ± 0.9$^{B18}$ |
| | | Melilite-haüynite | Sgm+**cpx**+**grt**+**mll**+nph+**mag**+**prv**+ap | 950-1120$^{B18}$ | +1.9 ± 3.4$^{B18}$ |
| | | Melteigite | Nph+**cpx**+**grt**+**mag**+**pl**+**ttn**+**prv**±ap | ~1000$^{E}$ | +1.8 ± 0.7$^{B18}$ |
| | | Sodalite Monzogabbros-Tephrites | **Cpx**+**pl**+**mag**±**ol**+sgm+**afs**±**amp**±phl±**ttn**±ap | 880-1220$^{B18}$ | +1.7 ± 1.3$^{B18}$ |
| | | Phonolites | **Afs**+sgm+**grt**+**cpx**±nph±**wo**±**pl**±**ttn**±**mag**+ap | 880-1130$^{B18}$ | +1.2 ± 0.9$^{B18}$ |
| Sokli | | Phoscorite 1 | Cal+**mag**+**ol**+ap+**phl**+dol+bdy+ilm | 530-770$^{OM}$ | |
| | | Carbonatite 2 | Cal+**ol**+**mag**+**ilm**+ap+**phl**+dol+bdy | 590-700$^{OM}$ | |
| | | Phoscorite 3 | Dol+**mag**+**ilm**+cal+ap+phl+bdy | 510-670$^{IM}$ | 0 ± 0.9$^{IM}$ |
| Kovdor | | Phoscorite 1 | **Ol**+ap+**mag**+**phl**+cal±dol+bdy+**ilm** | 590-660$^{IM}$; 440-790$^{OM}$ | +2.3 ± 1.0$^{IM}$ |
| | | Phoscorite 2 | **Mag**+ap+**ol**+cal±dol+**phl**+bdy+**ilm** | 500-880$^{OM}$ | |
| | pair | Phoscorite 3 | **Mag**+ap+cal+**ol**±dol+**phl**+bdy+**ilm** | 590-840$^{OM}$ | |
| | pair | Carbonatite 1 | Cal+**mag**+**ol**+**phl**+ap±dol+bdy+**ilm** | 590-640$^{IM}$; 550-630$^{OM}$ | +1.9 ± 0.6$^{IM}$ |
| | pair | Phoscorite 4 | **Mag**+ap+**ol**+**tphl**+cal±dol+bdy+**ilm** | 550-590$^{IM}$; 580-750$^{OM}$ | |
| | | Carbonatite 2 | Cal+**mag**±**ol**+**tphl**+ap±dol+bdy+**ilm** | 560-620$^{IM}$; 470-570$^{OM}$ | +2.4 ± 0.4$^{IM}$ |
| | pair | Phoscorite 5 | **Mag**+**ol**+**phl**+dol+cal+ap+bdy+**ilm** | 400-850$^{OM}$ | |
| | | Carbonatite 3 | Dol+cal+**mag**+phl+ap+bdy+**ilm** | 520-540$^{IM}$ | |
| Palabora | pair | Phoscorite | **Mag**+**ol**+cal+dol+ap+**phl**+bdy+**ilm** | 610-650$^{IM}$; 510-860$^{OM}$ | +1.2 ± 0.8$^{IM}$ |
| | | Banded carbonatite | Cal+**Ol**+**mag**+dol+ap+**phl**+bdy+**ilm** | 530-580$^{IM}$; 450-600$^{OM}$ | |
| | | Transgressive carbonatite | Cal+**Ol**+**mag**+dol+ap+**phl**+bdy+**ilm** | 570-650$^{IM}$; 510-760$^{OM}$ | +0.9 ± 0.4$^{IM}$ |
| Magnet Cove | | Carbonatite | Cal+ap+**mtc**+**mag**+**prv**+**grt**+**sp**+**ilm** | >850$^{SM}$ | +0.1 ± 0.3$^{F}$ |
| | | Clinopyroxenite-ijolite | **Cpx**±nph±**grt**+**mag**±**ttn**+**prv**+ap | ~1000$^{E}$ | +1.8 ± 1.5$^{F}$ |
| | | Syenite | Afs+**cpx**+pl+**mag**+phl+**ttn**+ap | ~900$^{E}$ | +1.2 ± 0.7$^{F}$ |
| Oka | | Calcite-rich okaite | **Mll**+cal+**prv**+**mag**+**cpx**+**sp**+**ilm**+**phl**+ap | 620-680$^{IM}$; >800$^{SM}$ | +0.8 ± 0.9$^{IM}$; +1.6 ± 0.4$^{F}$ |
| Jacupiranga | | Carbonatite | Cal+ap+phl+**mag**+**ilm** | 580-660$^{IM}$ | +1.3 ± 0.7$^{IM}$ |
| | | Clinopyroxenite | **Cpx**+**mag**+**ilm**+**prv**+ap | ~1000$^{E}$ | +0.8 ± 2.3$^{F}$ |
| | | Monzonite-syenite | **Afs**±**pl**+**cpx**+**mag**+**ilm**+phl+**ttn**±**amp**+ap | >800$^{A}$ | +1.2 ± 0.9$^{F}$ |

*Note:* Mineral phases are listed in descending order of frequency with the bold phases being used to calculate the crystallization conditions.
**Only redox estimates at $T \geq 600$ °C are listed because of unpredictable redox changes during further cooling (compare Fig. 3).
Abbreviations: afs = alkali feldspar; amp = amphibole; ap = apatite; bdy = baddeleyite; cal = calcite; cpx = clinopyroxene; dol = dolomite; grt = garnet; ilm = ilmenite; mag = magnetite; mll = melilite; mtc = monticellite; nph = nepheline; ol = olivine; (t)phl = (tetraferri)phlogopite; pl = plagioclase; prv = perovskite; sgm = sodalite-group minerals; sp = spinel; ttn = titanite; wo = wollastonite.
*Crystallization conditions constrained using:* [A] Amphibole; [B18] Braunger et al., 2018; [E] Estimation; [IM] Ilmenite-magnetite; [OM] Olivine-magnetite. [F] Further mineral phase equilibria. See text for further information.

pipe additionally contains phoscorites and associated banded carbonatites that are partly penetrated by a transgressive carbonatite. The mineralogy of the different phoscorites and carbonatites is very similar but with variable amounts of olivine, magnetite (Fig. 1d), apatite, phlogopite, baddeleyite and carbonate. The core of magnetite commonly contains ilmenite and spinel exsolutions, while ilmenite-magnetite of the composite type is typical for the banded carbonatites.

### 2.5. Oka (Canada)

The 126-115 Ma old Oka carbonatite complex (q.v. Chen and Simonetti, 2013 and references therein) comprises two intrusive centres with an early formed ring of alternating carbonatites and silicate rocks and a later central carbonatite plug. The silicate rocks predominantly consist of ijolites and okaites with the latter only occurring in the northern ring and at least partly representing a transition to carbonatites. The calcite-rich okaite (up to 20% carbonate) consists of euhedral melilite, perovskite and clinopyroxene, euhedral to anhedral biotite and small amounts of apatite (Fig. 1e). Variably sized and shaped spinel exsolutions and rare ilmenite exsolutions are present within the subhedral magnetite grains.

### 2.6. Magnet Cove (USA)

The mid-Cretaceous (100±5 Ma) Magnet Cove alkaline complex (e.g. Eby, 1987) is an elliptically shaped ring-dyke consisting of marginal foid syenites, clinopyroxenites (north-western and northeaster edge of the complex), trachytes and phonolites that crop out as an intermediate ring, and central ijolites which were intruded by several carbonatite bodies. The studied carbonatites contain large columnar grains of apatite, subhedral monticellite, and magnetite whose core commonly consists of spinel and sometimes ilmenite exsolutions. Perovskite forms euhedral to subhedral crystals of various sizes and is occasionally associated with anhedral garnet. Large calcite crystals surround all previously mentioned mineral phases (Fig. 1f).

### 2.7. Jacupiranga (Brazil)

The early Cretaceous (135-131 Ma) Jacupiranga carbonatite complex (q.v. Chmyz et al., 2017 and references therein) can be divided into two silicate intrusions: 1) the norther part comprises peridotites (dunites and scarce wehrlites) that are surrounded by a heterogeneous zone of primitive to evolved rock types (e.g. lamprophyres, diorites, monzonites, syenites) while 2) a clinopyroxenite plug, with some occurrence of ijolites, melteigites and 5 pipe-like carbonatite bodies are present in the south. Besides calcite, the main mineral phases in the investigated carbonatites are apatite, phlogopite and magnetite. Ilmenite is present as individual grains but also surrounds magnetite and occurs as exsolutions in the latter (Fig. 1g).

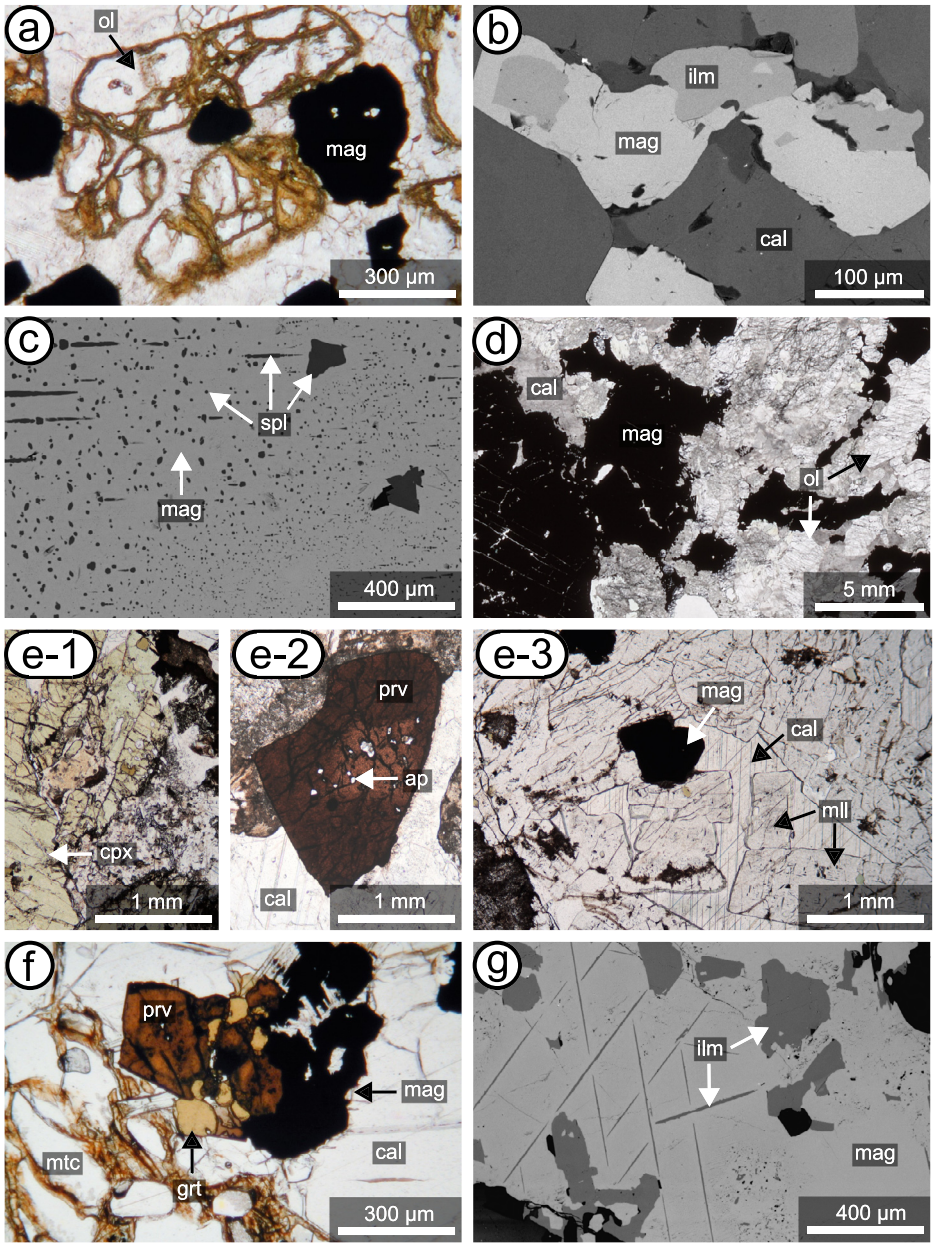


**Fig. 1.** Mineral textures in carbonatitic rocks (transmitted light microscopy [a, d, e, f] and BSE images). (a) Carbonatite from Kaiserstuhl consisting of partly altered olivine and magnetite. (b) Carbonatite from Sokli with an ilmenite-magnetite assemblage of composite type. (c) Phoscorite from Kovdor with elongated, rounded and irregularly shaped spinel exsolutions in magnetite. (d) Phoscorite from Palabora with large magnetite, olivine and calcite. (e) Okaite from Oka containing clinopyroxene (e-1), perovskite (e-2), melilite, magnetite and calcite (e-3). (f) Carbonatite from Magnet Cove consisting of perovskite (with apatite inclusions), garnet, magnetite and monticellite. (g) Carbonatite from Jacupiranga showing trellis-type and irregularly shaped ilmenite exsolutions in magnetite.

## 3. Methods

### 3.1. Analytical methods

Mineral compositions were analyzed using a JEOL JXA8900 electron microprobe in wave-length dispersive mode at the Department of Geosciences, University of Tübingen (Germany). An acceleration voltage of 20 kV and a beam current of 12 nA for garnet, perovskite and titanite, respectively 20 nA for all other mineral analyses was chosen. Peak counting times for major elements were 16 s and between 30 and 60 s for minor elements while the background counting times were half as long. Natural and synthetic standards were used for calibration. Peak overlaps between Ba-Ti, Ti-Ba, V-Ti, V-Cr, Al-Ba, F-Fe, Sm-Ce and Pr-La were corrected and an internal ZAF (spinel group minerals, ilmenite, garnet) or $\phi$rz correction was applied for the raw data (Armstrong, 1991). Measurements were executed with a focused beam for olivine group minerals, pyroxene, melilite, spinel group minerals and ilmenite, but was widened to 2 µm for amphibole. In order to avoid a destruction of the grains due to the long measurement time for garnet, perovskite and titanite, the beam spot was set to 5 µm for these minerals.

### 3.2. Quantification of intrinsic parameters

Temperature and oxygen fugacity ($f_{O2}$) during the crystallization of carbonatites and associated alkaline silicate rocks were calculated by applying several thermometers (magnetite-spinel exsolution, olivine-spinel, amphibole; Lehmann and Roux, 1986; Andersen et al., 1993; Ridolfi and Renzulli, 2012) and thermo-

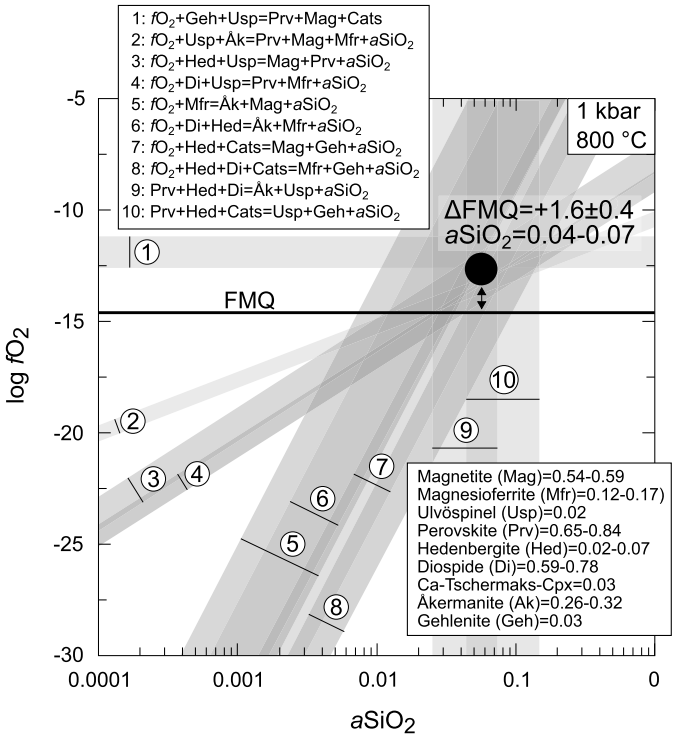


**Fig. 2.** Estimated oxygen fugacity and silica activity for the okaite from Oka, based on coexisting mineral assemblages. Reactions were performed with activity-corrected endmember compositions at a temperature of 800-900 °C and a pressure of 1 kbar. The black dot overlaps with all mineral equilibria and is the best fit for the redox conditions ($\Delta$FMQ = +1.1-2.5) and the silica activity ($a\mathrm{SiO_2}$ = 0.04-0.07).

oxybarometers (ilmenite-magnetite; Andersen and Lindsley, 1985), as well as the Perple_X software package (Connolly, 1990) for computing activity-corrected phase diagrams (cf. Braunger et al., 2018 for the applied mineral endmember solution models) using appropriate mineral assemblages and textures. The implemented thermodynamic database of Holland and Powell (1998) was extended by thermodynamic properties for perovskite (Robie and Hemingway, 1995) and was checked for internal consistency. Pressure estimates were taken from literature data, except for Jacupiranga where they are based on amphibole barometry (Ridolfi and Renzulli, 2012) in associated monzonites.

The calculated intrinsic parameters were then augmented by literature data on crystallization conditions of carbonatites and associated silicate rocks. In order to avoid over-representation by multiple redox determinations for the same or similar rock types within a complex, the different rock types were summarized into subgroups according to their state of evolution. A t-test was performed to check the statistical significance of the differences between carbonatites, respectively associated silicate rocks and alkaline silicate rocks without association to carbonatites with regard to redox conditions (see the electronic supplement for a complete compilation of the data and methods used in this study).

## 4. Results

High temperatures (typically above 750 °C) were obtained for phoscorites from Sokli, Kovdor and Palabora, and for carbonatites from the Kaiserstuhl using core analyses of olivine and magnetite. In cases where magnetite cores show exsolution textures, the primary chemical composition was reintegrated. Associated carbonatites at Sokli, Kovdor and Palabora indicate lower maximum temperatures (570-760 °C), while calculations using magnetite and olivine rim analyses generally yield >200 °C lower temperatures. The carbonatitic rocks from Magnet Cove and Oka also yield high temperatures (>800 °C) based on spinel exsolutions in magnetite. Temperatures for carbonatites from Jacupiranga were estimated to ≤660 °C (ilmenite-magnetite equilibria). For the other carbonatites and phoscorites, ilmenite-magnetite assemblages yield temperatures in the range of 530 to 680 °C. Silicate rocks reveal temperatures typically above 800 °C (e.g. amphibole thermometry for monzonites at Jacupiranga), although some temperatures are rough estimates only (e.g. clinopyroxenites at Magnet Cove and Jacupiranga; Table 1).

Redox conditions for the carbonatites from Kaiserstuhl ($\Delta$FMQ = +1.8 ± 0.8) were calculated using coexisting olivine-magnetite pairs assuming a silica activity slightly below the diopside stability (Fig. 6 in Braunger et al., 2018), since the latter is only present where the carbonatitic magma interacted with the silicate wall-rock, leading to a raised silica activity (see details in Giebel et al., 2019b). Redox conditions for carbonatites and phoscorites from Sokli ($\Delta$FMQ = 0 ± 0.9), Kovdor ($\Delta$FMQ= +2.2±1.0) and Palabora ($\Delta$FMQ = +1.2 ± 0.8), as well as for the okaite from Oka ($\Delta$FMQ = +0.8 ± 0.9) and the carbonatites from Jacupiranga ($\Delta$FMQ = +1.3 ± 0.7) were determined by ilmenite-magnetite assemblages. More complex mineral assemblages including minerals like clinopyroxene, melilite, magnetite, garnet and perovskite (Fig. 2) constrain the redox conditions for the carbonatites from Magnet Cove ($\Delta$FMQ = +0.1 ± 0.3), the okaite from Oka ($\Delta$FMQ = +1.6 ± 0.4), and for the alkaline silicate rocks at Kaiserstuhl ($\Delta$FMQ = +1.9 ± 3.4), Magnet Cove ($\Delta$FMQ = +1.8 ± 1.5) and Jacupiranga ($\Delta$FMQ = +0.8 ± 2.3).

## 5. Discussion

### 5.1. Crystallization interval of carbonatites

The temperature interval recorded in various carbonatites by variable techniques is very broad (Fig. 3a). The highest (probably near-liquidus) temperatures of up to about 1000 °C are indicated by homogenization temperatures for melt inclusions in various

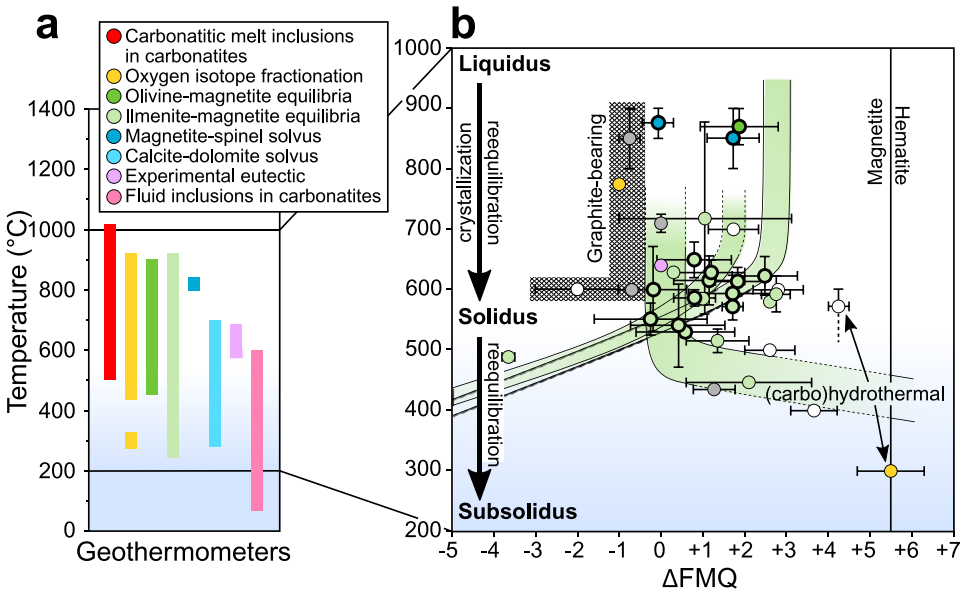


**Fig. 3.** Crystallization conditions for carbonatitic rocks. (a) Temperature interval constrained by several geothermometers. (b) Redox conditions in dependence of temperature. The color code of the dots refers to the applied geothermometers of Fig. 3a, grey dots represent further temperature determinations, white dots are rough estimates, bold-rimmed data points are new calculations of this study. Each data point refers to a specific redox calculation method applied to a particular carbonatitic rock type of a locality. Green paths indicate redox-temperature changes based on ilmenite-magnetite equilibria (extrapolated parts are highlighted by dashed lines) for carbonatites from Palabora, Kovdor (low redox conditions at low temperature) and Newania. Carbo-(hydrothermal) processes presumably result in an increase of the redox conditions, while dry thermal reequilibration lead to a decrease of ΔFMQ (see the electronic supplement for references of the literature data). (For interpretation of the colors in the figure(s), the reader is referred to the web version of this article.)

early magmatic minerals (such as olivine, monticellite, clinopyroxene and magnetite; (e.g. Guzmics et al., 2011). Oxygen isotope fractionation between apatite, magnetite, olivine and phlogopite (e.g. Doroshkevich et al., 2010) as well as magnetite-ilmenite equilibria preserve temperatures of up to around 900 °C (e.g. at Kaiserstuhl, Sokli, Kovdor, Palabora). The spread to much lower apparent temperatures (down to about 300 °C) is caused by variable reequilibration processes during cooling. For example, the apparently lower temperatures for carbonatites compared to their associated phoscorites (see above) are probably related to the smaller grain size of olivine and magnetite, which facilitates intense syn- to postmagmatic diffusion (e.g. Ozawa, 1984). Similar effects probably cause the overlapping temperature interval between ilmenite exsolutions in magnetite (synmagmatic or subsolidus?) and presumably magmatic composite ilmenite-magnetite assemblages (Fig. 3a). Near-solidus temperatures ($\leq$700 °C) are recorded by e.g. dolomite exsolutions in calcite (Zaitsev and Polezhaeva, 1994) and experimental data constrain the eutectic of simple carbonatitic compositions to ~650 °C (Lee et al., 2000). The transition from magmatic to (carbo)hydrothermal conditions is determined by fluid inclusion homogenization temperatures (up to 600 °C; Rankin, 1975) and even lower temperatures (down to 530 °C) are indicated by melt inclusions trapped in late-stage carbonate that roughly mark the carbonatite solidus (e.g. Sokolov, 2014). In summary, carbonatites record a liquidus-solidus interval from ~1000 °C to roughly 500 °C (depending on composition). In the following only redox estimates calculated at temperatures above 600 °C are taken into consideration in order to minimize potential fractional crystallization and thermal reequilibration issues (Fig. 3b).

### 5.2. Redox conditions during the crystallization of alkaline rocks and carbonatites

On average, alkaline silicate rocks that are not associated with carbonatites formed under statistically significant ($p < 0.001$) more reduced conditions (mean $\Delta FMQ = -1.1$, $\sigma = 1.4$; Fig. 4a) than alkaline silicate rocks associated with carbonatites (mean $\Delta FMQ = +1.4$, $\sigma = 1.7$; Fig. 4b) and carbonatites themselves (mean $\Delta FMQ = +1.3$, $\sigma = 1.1$; Fig. 4c). In our compilation, we only included alkaline silicate rocks from continental settings since carbonatites mainly occur in such geodynamic environments. Carbonatites at present subduction zones are so far only known from Mt. Vulture (Italy), but it is debated that carbonatite genesis at this locality is not related to the subduction process itself (cf. D'Orazio et al., 2007; Stoppa et al., 2008). We also excluded very rare carbonatites from ocean islands reported only from the Canary Islands, Cape Verdes and Kerguelen (Woolley and Kjarsgaard, 2008) and rare graphite- or diamond-bearing carbonatites (e.g. Chernigovsky, Chagatai, Yonghwa) as these constitute only <2% of all carbonatite complexes worldwide and would therefore be overrepresented in our compilation (they would constitute 30% of the carbonatite complexes for which redox conditions are available; Fig. 4c). Group I kimberlites are genetically closely related to carbonatites as they also occur in intraplate settings (mainly within cratons), require a carbonate-rich mantle source, are characterized by extreme levels of silica undersaturation and may contain significant amounts of carbonate (Mitchell, 1986). Kimberlites have been frequently studied but, mostly because of their hybrid nature (Russell et al., 2013) and $CO_2$ degassing processes (Dongre and Tappe, 2019), their redox conditions vary by more than 16 log units (see electronic supplement Fig. 1). We therefore chose not to integrate them into our compilation and will not further discuss the kimberlite group.

### 5.3. Redox conditions of the source region of alkaline rocks and carbonatites

It is widely assumed that primitive mantle-derived rocks inherit the oxidation state of their source region (e.g. Carmichael, 1991), although some variance in the redox estimates may result from fractional crystallization of Fe-bearing minerals and degassing processes (Gaillard et al., 2015). Although evolved rocks are generally more susceptible to such effects, a very similar range of redox conditions compared to the primitive rocks exists (Fig. 4a&b). The

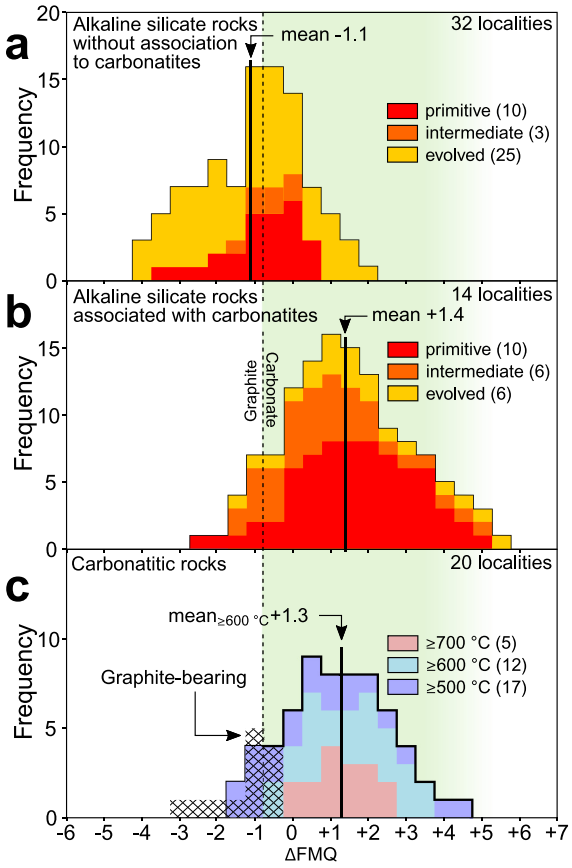


**Fig. 4.** Histograms compiling redox conditions for (a) alkaline silicate rocks without association to carbonatites, (b) those being related to carbonatites and (c) carbonatitic rocks. Alkaline silicate rocks are distinguished into primitive, intermediate and evolved types, carbonatites are sub-classified based on temperature. Numbers in brackets indicate the sample size for each group. The vertical dashed line in all three subfigures shows the stability field of graphite-, respectively carbonate-bearing peridotite.

good accordance between carbonatites and (primitive) associated silicate rocks indicates that the former may also reflect the redox state of their mantle source. However, during partial melting of a mantle rock, ferric iron preferably partitions into the melt while ferrous iron remains in its residue (e.g. Canil and O'Neill, 1996). Hence, the melt tends to record higher redox conditions than the source rock prior and after melt extraction. In contrast, the $f_{O2}$-P dependency of a basaltic melt in a closed system differs from that of solid mineral assemblages leading to a relatively more reduced oxidation state of the melt at crustal conditions compared to the oxidation state of the mantle source. Moreover, the $f_{O2}$-P path of synthetic buffers like FMQ deviates from those of basaltic melts and solid mineral assemblages which further complicates the comparison of ΔFMQ at mantle pressure with that at crustal levels (e.g. O'Neill et al., 2006). The interplay of all these factors has not yet been sufficiently investigated and further studies in this regard are warranted. We assume that the complications mentioned above should on average have similar affects for alkaline complexes with and without associated carbonatites. Therefore, we suggest that differences in the calculated oxygen fugacity of igneous rocks are an effect of variable redox conditions of the mantle.

Support for relatively oxidized conditions in the source region of carbonatites comes from redox estimates on mantle xenoliths that show trace element signatures characteristic for the interaction between mantle and carbonate-rich liquids. These mantle fragments are up to 4 log units more oxidized than typical lithospheric mantle (Fig. 5) and were found in various geodynamic environments, such as orogenic massifs (Pyrenees; Woodland et al., 1996), cratons (Slave, Kaapvaal; Creighton et al., 2010; Hanger et al., 2015) and other intraplate settings (Massif Central; e.g. Uenver-Thiele et al., 2017) including continental rift environments (East African rift; Rudnick et al., 1994). The Massif Central and particularly the East African Rift also comprise several carbonatite occurrences. We suggest that such xenoliths not only reflect interaction between lithospheric mantle and (asthenosphere-derived) carbonate-rich liquids, but that the xenoliths derive from a mantle that may reflect one possible source for carbonatite-bearing complexes.

Also thermodynamic calculations indicate that the redox conditions for carbonatites and associated alkaline rocks might reflect the oxidation state of their mantle source. The minimum redox conditions for the melting of carbonated peridotite are constrained by the enstatite-magnesite-olivine-diamond/graphite buffer reaction, which marks the stability limit for carbonates in peridotite (EMOD/G in Fig. 5) for pressures above 2 GPa. At lower pressures, $CO_2$ is stable instead of carbonate and the minimum redox conditions are limited by the graphite-$CO_2$ buffer (D/G$CO_2$ in Fig. 5). The most oxidized mantle rocks known (Foley, 2011) define an empirical upper $f_{O2}$ which strongly depends on pressure ($-0.7\Delta$FMQ/GPa; Fig. 5) due to the stability shift towards $Fe^{2+}$ instead of $Fe^{3+}$-bearing mineral phases with depth (e.g. Ballhaus and Frost, 1994). Note that the upper $f_{O2}$ limit for carbonated peridotite and the $f_{O2}$-depth correlation of the mantle is solely based on data from lithospheric xenoliths, but we suggest that the asthenospheric mantle should behave similarly because of its similar mineralogy.

Carbonatites often occur in intraplate-rift settings or at the thinned edge of cratons, consistent with the formation of nephelinitic to melilititic melts at mantle depths between 50-130 km (Hirose and Kushiro, 1993; Gudfinnsson and Presnall, 2005). Based

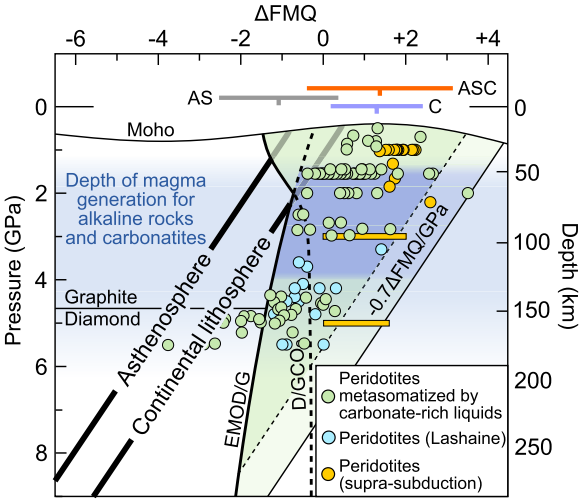


**Fig. 5.** Pressure and redox conditions for the solidus of carbonated peridotite limited by the enstatite-magnesite-olivine-graphite/diamond (EMOD/G) buffer, the diamond/graphite-$CO_2$ (D/G$CO_2$) equilibrium and an empirically constrained boundary (slope of $-0.7\Delta$FMQ/GPa; shift towards lower $\Delta$FMQ by excluding outliers; Ballhaus and Frost, 1994). At pressures <2 GPa, peridotite is in equilibrium with $CO_2$ instead of carbonate. Mean redox estimates (with standard deviation) of (AS) alkaline silicate rocks without association to carbonatites, (ASC) alkaline silicate rocks associated with carbonatites and (C) carbonatitic rocks are shown for comparison. Peridotite xenoliths that occur in carbonatitic tuffs from Lashaine (Tanzania) are presumably metasomatized by a silica-rich melt and are not directly related to carbonatite generation (Rudnick et al., 1994; Bell and Simonetti, 2010).

on experiments (e.g. Wyllie et al., 1990), the parental melts for carbonatites originate from depths >75 km (>2 GPa). The depth interval of 75-130 km constrains the redox conditions of the source region of most carbonatitic melts to $\Delta$FMQ $= -1$ to $+3$ (Fig. 5), which also agrees with the oxidation state of carbonatites and their associated alkaline silicate rocks (Fig. 4b&c). The lower $f_{O2}$ conditions determined for alkaline complexes that lack carbonatites imply an ordinary or even reduced mantle source (Fig. 5). However, most carbonatites derive from oxidized magmas at rather shallow depth, since the stability field of carbonate-bearing peridotite continuously diminishes with depth. Furthermore, the redox state of the mantle decreases with depth, which makes it more difficult to oxidize graphite/diamond to carbonate (Fig. 5). Indeed, carbonatites that are cogenetic with lamprophyres and kimberlites may originate from greater depths (>150 km; e.g. Tappe et al., 2017), but these account for only a minor fraction of the known carbonatite occurrences (Woolley and Kjarsgaard, 2008).

## 6. Implications and conclusions

Although carbonatites and spatially associated alkaline silicate rocks do not always derive from the same magma source, carbonatites and associated silicate rocks in the 7 investigated complexes all indicate oxidized conditions (Table 1), suggesting that mantle oxidation processes must have affected all tapped mantle domains. Similarly, our world-wide compilation demonstrates that carbonatites and alkaline silicate rocks associated with carbonatites formed under rather oxidized conditions compared to the general range found for alkaline rocks in intraplate settings.

Especially the average asthenosphere, except for the uppermost part, is presumably too reduced to stabilize $CO_2$ or carbonate (Fig. 5, Foley, 2011). However, since partial melting processes within the mantle strongly affect its oxygen fugacity (Canil and O'Neill, 1996), there still may be domains oxidized enough for the formation of carbonates, and hence for carbonate-rich melts. A relatively high oxidation state of the mantle can also be achieved by the digestion of subducted crustal material (e.g. Yaxley and Brey, 2004; Rohrbach and Schmidt, 2011), the influence of which has been revealed for many young (<300 Ma) carbonatites by boron isotopes (Hulett et al., 2016). Carbonate-bearing sediments and altered oceanic crust, which contains around 2.5 wt.% $CO_2$ in the top few hundred meters (Alt and Teagle, 1999; Yaxley et al., 2019), additionally raises the carbonate concentration of the mantle and further promotes the formation of carbonate-rich melts. (note that altered oceanic crust reveals carbon isotope systematics very similar to the average mantle and carbonatites; Deines, 2002; Shilobreeva et al., 2011). Such C-enriched and oxidized asthenospheric mantle domains may be the ultimate source for carbonatite complexes, or they function as an intermediate stage by providing carbonate-rich melts that infiltrate the base of the lithosphere, thereby finally preconditioning the source region for carbonatites and associated silicate rocks (Foley and Fischer, 2017).

An oxidized mantle with a sufficiently high carbonate content is not the only prerequisite for the formation of carbonatite complexes. The mantle beneath subduction zones is generally oxidized enough to stabilize carbonate (Foley, 2011) but carbonatites directly related to subduction processes seem to be lacking and Yaxley et al. (2019) argue that this is because of the reversed temperature gradient of the mantle wedge above the subducting plate. Potential carbonate-bearing melts would react with the overlying mantle, thereby being strongly modified and diluted. Ocean island volcanics and xenoliths from oceanic environments also indicate elevated oxygen fugacities (mean $\Delta$FMQ $\approx +0.6$; Ballhaus, 1993; Mallmann and O'Neill, 2007; Foley, 2011). Moreover, ocean island basalts reveal similar radiogenic isotope signatures as carbonatites and are suggested to form by the involvement of recycled oceanic crust (e.g. Hauri et al., 1993; Bell and Simonetti, 2010). The absence of carbonatites at most ocean islands is therefore not a result of too reduced conditions, but of a too thin oceanic lithosphere leading to primitive melt compositions that will not evolve into the carbonatite-silicate miscibility gap. Exceptions are the carbonatite occurrences at the Cape Verdes and Canary Islands, which are situated on a much thicker oceanic lithosphere and whose primitive silicate melts have an extraordinary low silica and high alkali content, allowing the formation of carbonatites during fractionation (e.g. Martins et al., 2010; Martinez-Arevalo et al., 2013; Weidendorfer et al., 2016; Schmidt and Weidendorfer, 2018).

Because of the known heterogeneity in the source region, the absence of carbonatites in some oxidized alkaline silicate complexes (e.g. Katzenbuckel, Ankaratra, Itatiaia; Mann et al., 2006; Cucciniello et al., 2017; Melluso et al., 2017) may therefore reflect a lack of carbon in the mantle source, crystallization of the

silicate melt before an exsolved/residual carbonatitic magma could form, decarbonation reactions in the melt which released $CO_2$-rich fluids, or simply lack of outcrop. Likewise, silicate rocks associated with carbonatites may form under reduced conditions as well, as suggested by existing examples of olivine-clinopyroxene-magnetite syenites associated with carbonatites. In the special case of Khibina (Russia), carbonatites are associated with peralkaline foid syenites that probably formed under very reduced conditions. There, the carbonatites are of carbothermal rather than magmatic origin and the reduced silicate rocks derive from a different mantle source (Kramm and Kogarko, 1994).

Despite all limitations and exceptions, the contrasting redox conditions between alkaline complexes that contain carbonatites and many alkaline complexes devoid of carbonatites is striking (Fig. 4) and is probably related to highly variable redox conditions in the mantle. Alkaline complexes that show reduced crystallization conditions are generally characterized by the absence of carbonatites, presumably because of the absence of oxidized and carbonate-involving metasomatism processes. Alkaline silicate rocks that are genetically associated with carbonatites, however, belong to the most oxidized alkaline rocks at continental settings, consistent with the prerequisite of an oxidized, carbonate-bearing mantle.

## Declaration of competing interest

The authors declare that they have no known competing financial interests or personal relationships that could have appeared to influence the work reported in this paper.

## Acknowledgements

We thank Simone Schafflick for sample preparation and are grateful to Johannes Giebel, Anatoly Zaitsev, Jacques Mouttes, Mi Jung Lee, Corbin Cannon and Antonio Simonetti for providing samples, thin sections and data. Special thanks to Benjamin Walter for his help with collection of fluid inclusions data, to Tatjana Epp for her help with statistical analyses, and to James Connolly for his help with thermodynamic calculations. We further appreciate insightful comments by Rajdeep Dasgupta, Sebastian Tappe and an anonymous reviewer, as well as constructive comments by Dennis Brown, Dante Canil and two anonymous reviewers on an earlier version of this manuscript. This work was funded by the Deutsche Forschungsgemeinschaft (grant MA2563/12-1).

## Appendix A. Supplementary material

Supplementary material related to this article can be found online at https://doi.org/10.1016/j.epsl.2019.116041.

## References

Alt, J.C., Teagle, D.A.H., 1999. The uptake of carbon during alteration of ocean crust. Geochim. Cosmochim. Acta 63, 1527–1535. https://doi.org/10.1016/S0016-7037(99)00123-4.

Andersen, D., Lindsley, D.H., 1985. New (and final!) models for the Ti-magnetite/ilmenite geothermometer and oxygen barometer. In: Abstracts of American Geophysical Union 1985 Spring Meeting. American Geophysical Union.

Andersen, D.J., Lindsley, D.H., Davidson, P.M., 1993. Quilf - a Pascal program to assess equilibria among Fe-Mg-Mn-Ti oxides, pyroxenes, olivine, and quartz. Comput. Geosci. 19, 1333–1350. https://doi.org/10.1016/0098-3004(93)90033-2.

Armstrong, J.T., 1991. Quantitative elemental analysis of individual microparticles with electron beam instruments. In: Electron Probe Quantitation. Springer, pp. 261–315.

Aulbach, S., Stagno, V., 2016. Evidence for a reducing Archean ambient mantle and its effects on the carbon cycle. Geology 44, 751–754. https://doi.org/10.1130/G38070.1.

Ballhaus, C., 1993. Redox states of lithospheric and asthenospheric upper-mantle. Contrib. Mineral. Petrol. 114, 331–348. https://doi.org/10.1007/Bf01046536.

Ballhaus, C., Frost, B.R., 1994. The generation of oxidized CO2-bearing basaltic melts from reduced CH4-bearing upper-mantle sources. Geochim. Cosmochim. Acta 58, 4931–4940. https://doi.org/10.1016/0016-7037(94)90222-4.

Beccaluva, L., Bianchini, G., Natali, C., Siena, F., 2017. The alkaline-carbonatite complex of Jacupiranga (Brazil): magma genesis and mode of emplacement. Gondwana Res. 44, 157–177. https://doi.org/10.1016/j.gr.2016.11.010.

Bell, K., 1998. Radiogenic isotope constraints on relationships between carbonatites and associated silicate rocks—a brief review. J. Petrol. 39, 1987–1996. https://doi.org/10.1093/petroj/39.11-12.1987.

Bell, K., Simonetti, A., 2010. Source of parental melts to carbonatites–critical isotopic constraints. Mineral. Petrol. 98, 77–89. https://doi.org/10.1007/s00710-009-0059-0.

Braunger, S., Marks, M.A.W., Walter, B.F., Neubauer, R., Reich, R., Wenzel, T., Parsapoor, A., Markl, G., 2018. The petrology of the Kaiserstuhl volcanic complex, SW Germany: the importance of metasomatized and oxidized lithospheric mantle for carbonatite generation. J. Petrol. 59, 1731–1762. https://doi.org/10.1093/petrology/egy078.

Canil, D., 2002. Vanadium in peridotites, mantle redox and tectonic environments: archean to present. Earth Planet. Sci. Lett. 195, 75–90. https://doi.org/10.1016/S0012-821X(01)00582-9.

Canil, D., Bellis, A.J., 2006. Ferric iron in $CaTiO_3$ perovskite as an oxygen barometer for kimberlite magmas II: applications. J. Petrol. 48, 231–252. https://doi.org/10.1093/petrology/egl067.

Canil, D., O'Neill, H.S.C., 1996. Distribution of ferric iron in some upper-mantle assemblages. J. Petrol. 37, 609–635. https://doi.org/10.1093/petrology/37.3.609.

Carmichael, I.S.E., 1991. The redox states of basic and silicic magmas: a reflection of their source regions? Contrib. Mineral. Petrol. 106, 129–141. https://doi.org/10.1007/BF00306429.

Chen, W., Simonetti, A., 2013. In-situ determination of major and trace elements in calcite and apatite, and U–Pb ages of apatite from the Oka carbonatite complex: insights into a complex crystallization history. Chem. Geol. 353, 151–172. https://doi.org/10.1016/j.chemgeo.2012.04.022.

Chmyz, L., Arnaud, N., Biondi, J.C., Azzone, R.G., Bosch, D., 2019. Hf-Pb isotope and trace element constraints on the origin of the Jacupiranga Complex (Brazil): insights into carbonatite genesis and multi-stage metasomatism of the lithospheric mantle. Gondwana Res. 71, 16–27. https://doi.org/10.1016/j.gr.2019.01.012.

Chmyz, L., Arnaud, N., Biondi, J.C., Azzone, R.G., Bosch, D., Ruberti, E., 2017. Ar-Ar ages, Sr-Nd isotope geochemistry, and implications for the origin of the silicate rocks of the Jacupiranga ultramafic-alkaline complex (Brazil). J. South Am. Earth Sci. 77, 286–309. https://doi.org/10.1016/j.jsames.2017.05.009.

Connolly, J.A.D., 1990. Multivariable phase-diagrams - an algorithm based on generalized thermodynamics. Am. J. Sci. 290, 666–718. https://doi.org/10.2475/ajs.290.6.666.

Creighton, S., Stachel, T., Eichenberg, D., Luth, R.W., 2010. Oxidation state of the lithospheric mantle beneath Diavik diamond mine, central Slave craton, NWT, Canada. Contrib. Mineral. Petrol. 159, 645–657. https://doi.org/10.1007/s00410-009-0446-x.

Cucciniello, C., Melluso, L., le Roex, A.P., Jourdan, F., Morra, V., de' Gennaro, R., Grifa, C., 2017. From olivine nephelinite, basanite and basalt to peralkaline trachyphonolite and comendite in the Ankaratra volcanic complex, Madagascar: 40Ar/39Ar ages, phase compositions and bulk-rock geochemical and isotopic evolution. Lithos 274–275, 363–382. https://doi.org/10.1016/j.lithos.2016.12.026.

Dasgupta, R., Hirschmann, M.M., 2010. The deep carbon cycle and melting in Earth's interior. Earth Planet. Sci. Lett. 298, 1–13. https://doi.org/10.1016/j.epsl.2010.06.039.

Deines, P., 2002. The carbon isotope geochemistry of mantle xenoliths. Earth-Sci. Rev. 58, 247–278. https://doi.org/10.1016/S0012-8252(02)00064-8.

Dongre, A., Tappe, S., 2019. Kimberlite and carbonatite dykes within the Premier diatreme root (Cullinan Diamond Mine, South Africa): new insights to mineralogical-genetic classifications and magma CO2 degassing. Lithos 338–339, 155–173. https://doi.org/10.1016/j.lithos.2019.04.020.

D'Orazio, M., Innocenti, F., Tonarini, S., Doglioni, C., 2007. Carbonatites in a subduction system: the Pleistocene alvikites from Mt. Vulture (Southern Italy). Lithos 98, 313–334. https://doi.org/10.1016/j.lithos.2007.05.004.

Doroshkevich, A.G., Ripp, G.S., Moore, K.R., 2010. Genesis of the Khaluta alkaline-basic Ba-Sr carbonatite complex (West Transbaikala, Russia). Mineral. Petrol. 98, 245–268. https://doi.org/10.1007/s00710-009-0063-4.

Eby, G.N., 1987. Fission-track geochronology of the Arkansas alkaline province. Citeseer.

Eguchi, J., Dasgupta, R., 2018. Redox state of the convective mantle from CO2-trace element systematics of oceanic basalts. Geochem. Perspect. Lett. 8, 17–21. https://doi.org/10.7185/geochemlet.1823.

Fedortchouk, Y., Canil, D., 2004. Intensive variables in kimberlite magmas, Lac de Gras, Canada and implications for diamond survival. J. Petrol. 45, 1725–1745. https://doi.org/10.1093/petrology/egh031.

Fedortchouk, Y., Canil, D., Carlson, J.A., 2005. Dissolution forms in Lac de Gras diamonds and their relationship to the temperature and redox state of kimberlite magma. Contrib. Mineral. Petrol. 150, 54–69. https://doi.org/10.1007/s00410-005-0003-1.

Foley, S.F., 2011. A reappraisal of redox melting in the Earth's mantle as a function of tectonic setting and time. J. Petrol. 52, 1363–1391. https://doi.org/10.1093/petrology/egq061.

Foley, S.F., Fischer, T.P., 2017. An essential role for continental rifts and lithosphere in the deep carbon cycle. Nat. Geosci. 10, 897–902. https://doi.org/10.1038/s41561-017-0002-7.

Frost, D.J., McCammon, C.A., 2008. The redox state of Earth's mantle. Annu. Rev. Earth Planet. Sci. 36, 389–420. https://doi.org/10.1146/annurev.earth.36.031207.124322.

Gaillard, F., Scaillet, B., Pichavant, M., Iacono-Marziano, G., 2015. The redox geodynamics linking basalts and their mantle sources through space and time. Chem. Geol. 418, 217–233. https://doi.org/10.1016/j.chemgeo.2015.07.030.

Giebel, R.J., Marks, M.A., Gauert, C.D., Markl, G., 2019a. A model for the formation of carbonatite-phoscorite assemblages based on the compositional variations of mica and apatite from the Palabora Carbonatite Complex, South Africa. Lithos 324, 89–104. https://doi.org/10.1016/j.lithos.2018.10.030.

Giebel, R.J., Parsapoor, A., Walter, B.F., Braunger, S., Marks, M.A.W., Wenzel, T., Markl, G., 2019b. Evidence for magma – wall rock interaction in carbonatites from the Kaiserstuhl Volcanic Complex (Southwest Germany). J. Petrol. 60 (6), 1163–1194. https://doi.org/10.1093/petrology/egz028.

Gudfinnsson, G.H., Presnall, D.C., 2005. Continuous gradations among primary carbonatitic, kimberlitic, melilititic, basaltic, picritic, and komatiitic melts in equilibrium with garnet lherzolite at 3–8 GPa. J. Petrol. 46, 1645–1659. https://doi.org/10.1093/petrology/egi029.

Guzmics, T., Mitchell, R.H., Szabó, C., Berkesi, M., Milke, R., Abart, R., 2011. Carbonatite melt inclusions in coexisting magnetite, apatite and monticellite in Kerimasi calciocarbonatite, Tanzania: melt evolution and petrogenesis. Contrib. Mineral. Petrol. 161, 177–196. https://doi.org/10.1007/s00410-010-0525-z.

Hanger, B.J., Yaxley, G.M., Berry, A.J., Kamenetsky, V.S., 2015. Relationships between oxygen fugacity and metasomatism in the Kaapvaal subcratonic mantle, represented by garnet peridotite xenoliths in the Wesselton kimberlite, South Africa. Lithos 212, 443–452. https://doi.org/10.1016/j.lithos.2014.09.030.

Hauri, E.H., Shimizu, N., Dieu, J.J., Hart, S.R., 1993. Evidence for hotspot-related carbonatite metasomatism in the oceanic upper mantle. Nature 365, 221–227. https://doi.org/10.1038/365221a0.

Hirose, K., Kushiro, I., 1993. Partial melting of dry peridotites at high pressures: determination of compositions of melts segregated from peridotite using aggregates of diamond. Earth Planet. Sci. Lett. 114, 477–489. https://doi.org/10.1016/0012-821x(93)90077-M.

Holland, T.J.B., Powell, R., 1998. An internally consistent thermodynamic data set for phases of petrological interest. J. Metamorph. Geol. 16, 309–343. https://doi.org/10.1111/j.1525-1314.1998.00140.x.

Hulett, S.R.W., Simonetti, A., Rasbury, E.T., Hemming, N.G., 2016. Recycling of subducted crustal components into carbonatite melts revealed by boron isotopes. Nat. Geosci. 9, 904. https://doi.org/10.1038/Ngeo2831.

Jones, A.P., Genge, M., Carmody, L., 2013. Carbonate melts and carbonatites. Carbon in Earth 75, 289–322. https://doi.org/10.2138/rmg.2013.75.10.

Kramm, U., Kogarko, L.N., 1994. Nd and Sr isotope signatures of the Khibina and Lovozero agpaitic centres, Kola Alkaline province, Russia. Lithos 32, 225–242. https://doi.org/10.1016/0024-4937(94)90041-8.

Krasnova, N., Balaganskaya, E., Garcia, D., 2004a. Kovdor—classic phoscorites and carbonatites. In: Phoscorites and Carbonatites from Mantle to Mine: the Key Example of the Kola Alkaline Province. Mineralogical Society, London, pp. 99–132.

Krasnova, N., Petrov, T., Balaganskaya, E., Garcia, D., Moutte, J., Zaitsev, A., Wall, F., 2004b. Introduction to phoscorites: occurrence, composition, nomenclature and petrogenesis. In: Wall, F., Zaitev, A.N. (Eds.), Phoscorites and Carbonatites from Mantle to Mine: the Key Example of the Kola Alkaline Province. The Mineralogical Society of Great Britain and Ireland, London, pp. 45–74.

Lee, M., Garcia, D., Moutte, J., Williams, C., Wall, F., 2004. Carbonatites and phoscorites from the Sokli Complex, Finland. In: Wall, F., Zaitev, A.N. (Eds.), Phoscorites and Carbonatites from Mantle to Mine: the Key Example of the Kola Alkaline Province. The Mineralogical Society of Great Britain and Ireland, London, pp. 133–162.

Lee, W.-J., Fanelli, M., Cava, N., Wyllie, P., 2000. Calciocarbonatite and magnesiocarbonatite rocks and magmas represented in the system CaO-MgO-CO2-H2O at 0.2 GPa. Mineral. Petrol. 68, 225–256. https://doi.org/10.1007/s007100050011.

Lehmann, J., Roux, J., 1986. Experimental and theoretical-study of (Fe2+, Mg)(Al, Fe3+)2O4 spinels - activity-composition relationships, miscibility gaps, vacancy contents. Geochim. Cosmochim. Acta 50, 1765–1783. https://doi.org/10.1016/0016-7037(86)90138-9.

Le Pioufle, A., Canil, D., 2012. Iron in monticellite as an oxygen barometer for kimberlite magmas. Contrib. Mineral. Petrol. 163, 1033–1046. https://doi.org/10.1007/s00410-011-0714-4.

Li, Z.-X.A., Lee, C.-T.A., 2004. The constancy of upper mantle fO2 through time inferred from V/Sc ratios in basalts. Earth Planet. Sci. Lett. 228, 483–493. https://doi.org/10.1016/j.epsl.2004.10.006.

Mallmann, G., O'Neill, H.S.C., 2007. The effect of oxygen fugacity on the partitioning of Re between crystals and silicate melt during mantle melting. Geochim. Cosmochim. Acta 71, 2837–2857. https://doi.org/10.1016/j.gca.2007.03.028.

Mann, U., Marks, M., Markl, G., 2006. Influence of oxygen fugacity on mineral compositions in peralkaline melts: the Katzenbuckel volcano, Southwest Germany. Lithos 91, 262–285. https://doi.org/10.1016/j.lithos.2005.09.004.

Marks, M.A.W., Markl, G., 2017. A global review on agpaitic rocks. Earth-Sci. Rev. 173, 229–258. https://doi.org/10.1016/j.earscirev.2017.06.002.

Martin, L.H.J., Schmidt, M.W., Mattsson, H.B., Guenther, D., 2013. Element partitioning between immiscible carbonatite and silicate melts for dry and H2O-bearing systems at 1–3 GPa. J. Petrol. 54, 2301–2338. https://doi.org/10.1093/petrology/egt048.

Martinez-Arevalo, C., Mancilla, F.d.L., Helffrich, G., Garcia, A., 2013. Seismic evidence of a regional sublithospheric low velocity layer beneath the Canary Islands. Tectonophysics 608, 586–599. https://doi.org/10.1016/j.tecto.2013.08.021.

Martins, S., Mata, J., Munhá, J., Mendes, M.H., Maerschalk, C., Caldeira, R., Mattielli, N., 2010. Chemical and mineralogical evidence of the occurrence of mantle metasomatism by carbonate-rich melts in an oceanic environment (Santiago Island, Cape Verde). Mineral. Petrol. 99, 43–65. https://doi.org/10.1007/s00710-009-0078-x.

Melluso, L., Gennaro, R.d., Guarino, V., Morra, V., Lustrino, M., 2017. The REE- and HFSE-bearing phases in the Itatiaia alkaline complex (Brazil) and geochemical evolution of feldspar-rich felsic melts. Mineral. Mag. 81, 217–250. https://doi.org/10.1180/minmag.2016.080.122.

Mitchell, R., 1973. Composition of olivine, silica activity and oxygen fugacity in kimberlite. Lithos 6, 65–81. https://doi.org/10.1016/0024-4937(73)90080-7.

Mitchell, R.H., 1986. Kimberlites: Mineralogy, Geochemistry, and Petrology. Springer, Boston, MA.

Mitchell, R.H., 2005. Carbonatites and carbonatites and carbonatites. Can. Mineral. 43, 2049–2068. https://doi.org/10.2113/gscanmin.43.6.2049.

O'Neill, H.S.C., Berry, A.J., McCammon, C.C., Jayasuriya, K.D., Campbell, S.J., Foran, G., 2006. An experimental determination of the effect of pressure on the Fe3+/∑Fe ratio of an anhydrous silicate melt to 3.0 GPa. Am. Mineral. 91, 404–412. https://doi.org/10.2138/am.2005.1929.

Ozawa, K., 1984. Olivine-spinel geospeedometry: analysis of diffusion-controlled Mg-Fe2+ exchange. Geochim. Cosmochim. Acta 48, 2597–2611. https://doi.org/10.1016/0016-7037(84)90308-9.

Parkinson, I.J., Arculus, R.J., 1999. The redox state of subduction zones: insights from arc-peridotites. Chem. Geol. 160, 409–423. https://doi.org/10.1016/S0009-2541(99)00110-2.

Rankin, A., 1975. Fluid inclusion studies in apatite from carbonatites of the Wasaki area of western Kenya. Lithos 8, 123–136. https://doi.org/10.1016/0024-4937(75)90020-1.

Ridolfi, F., Renzulli, A., 2012. Calcic amphiboles in calc-alkaline and alkaline magmas: thermobarometric and chemometric empirical equations valid up to 1,130 °C and 2.2 GPa. Contrib. Mineral. Petrol. 163, 877–895. https://doi.org/10.1007/s00410-011-0704-6.

Robie, R.A., Hemingway, B.S., 1995. Thermodynamic properties of minerals and related substances at 298.15 K and 1 bar (105 Pascals) pressure and at higher temperatures. US Government Printing Office, Washington.

Rohrbach, A., Schmidt, M.W., 2011. Redox freezing and melting in the Earth's deep mantle resulting from carbon–iron redox coupling. Nature 472, 209–212. https://doi.org/10.1038/nature09899.

Rudnick, R., McDonough, W.F., Orpin, A.R., 1994. Northern Tanzanian peridotite xenolith: a comparison with Kaapvaal peridotites and evidence for carbonatite interaction with ultra-refractory residues. In: Proc. 5th Int'l Kimberlite Conference. CPRM, pp. 336–353.

Russell, J.K., Porritt, L.A., Hilchie, L., 2013. Kimberlite: rapid ascent of lithospherically modified carbonatitic melts. In: Pearson, D.G., Grütter, H.S., Harris, J.W., Kjarsgaard, B.A., O'Brien, H., Rao, N.V.C., Sparks, S. (Eds.), Proceedings of 10th International Kimberlite Conference. Springer India, New Delhi, pp. 195–210.

Schmidt, M.W., Weidendorfer, D., 2018. Carbonatites in oceanic hotspots. Geology 46, 435–438. https://doi.org/10.1130/G39621.1.

Shilobreeva, S., Martinez, I., Busigny, V., Agrinier, P., Laverne, C., 2011. Insights into C and H storage in the altered oceanic crust: results from ODP/IODP Hole 1256D. Geochim. Cosmochim. Acta 75, 2237–2255. https://doi.org/10.1016/j.gca.2010.11.027.

Sokolov, S.V., 2014. The formation conditions of labuntsovite-group minerals in the Kovdor massif, Kola Peninsula. Geol. Ore Depos. 56, 671–674. https://doi.org/10.1134/S1075701514080108.

Stagno, V., 2019. Carbon, carbides, carbonates and carbonatitic melts in the Earth's interior. J. Geol. Soc. 176, 375–387. https://doi.org/10.1144/jgs2018-095.

Stoppa, F., Principe, C., Giannandrea, P., 2008. Comments on: Carbonatites in a subduction system: the Pleistocene alvikites from Mt. Vulture (southern Italy) by d'Orazio et al., (2007). Lithos 103, 550–556. https://doi.org/10.1016/j.lithos.2007.10.012.

Tappe, S., Romer, R.L., Stracke, A., Steenfelt, A., Smart, K.A., Muehlenbachs, K., Torsvik, T.H., 2017. Sources and mobility of carbonate melts beneath cratons, with implications for deep carbon cycling, metasomatism and rift initiation. Earth Planet. Sci. Lett. 466, 152–167. https://doi.org/10.1016/j.epsl.2017.03.011.

Uenver-Thiele, L., Woodland, A.B., Seitz, H.-M., Downes, H., Altherr, R., 2017. Metasomatic processes revealed by trace element and redox signatures of the lithospheric mantle beneath the Massif Central, France. J. Petrol. 58, 395–422. https://doi.org/10.1093/petrology/egx020.

Weidendorfer, D., Schmidt, M.W., Mattsson, H.B., 2016. Fractional crystallization of Si-undersaturated alkaline magmas leading to unmixing of carbonatites on Brava Island (Cape Verde) and a general model of carbonatite genesis in alkaline magma suites. Contrib. Mineral. Petrol. 171, 43. https://doi.org/10.1007/s00410-016-1249-5.

Woodland, A.B., Kornprobst, J., McPherson, E., Bodinier, J.L., Menzies, M.A., 1996. Metasomatic interactions in the lithospheric mantle: petrologic evidence from the Lherz massif, French Pyrenees. Chem. Geol. 134, 83–112. https://doi.org/10.1016/S0009-2541(96)00082-4.

Woolley, A.R., Kjarsgaard, B.A., 2008. Carbonatite occurrences of the world: map and database. Geol. Surv. Can., 28. https://doi.org/10.4095/225115.

Wyllie, P.J., Baker, M.B., White, B.S., 1990. Experimental boundaries for the origin and evolution of carbonatites. Lithos 26, 3–19. https://doi.org/10.1016/0024-4937(90)90037-2.

Yaxley, G.M., Brey, G.P., 2004. Phase relations of carbonate-bearing eclogite assemblages from 2.5 to 5.5 GPa: implications for petrogenesis of carbonatites. Contrib. Mineral. Petrol. 146, 606–619. https://doi.org/10.1007/s00410-003-0517-3.

Yaxley, G.M., Ghosh, S., Kiseeva, E.S., Mallik, A., Spandler, C., Thomson, A.R., Walter, M.J., 2019. CO2-rich melts in Earth. In: Deep Carbon: Past to Present. Cambridge University Press.

Zaitsev, A., Polezhaeva, L., 1994. Dolomite-calcite textures in early carbonatites of the Kovdor ore deposit, Kola-Peninsula, Russia - their genesis and application for calcite-dolomite geothermometry. Contrib. Mineral. Petrol. 115, 339–344. https://doi.org/10.1007/Bf00310772.